



The
University
Of
Sheffield.

**Techno-economic assessment and
optimization of wind and concentrating
solar power with thermal energy storage
under arid climatic conditions**

By:

Ali J. Sultan

A thesis submitted in partial fulfilment of the requirements for the
degree of Doctor of Philosophy (PhD)

The University of Sheffield
Faculty of Engineering
Department of Mechanical Engineering

May 2022

Declaration

The work presented in this thesis is that of the author and has not been previously submitted for a degree at this, or any other, university. The information about the published work from the thesis is provided in the “Scientific Journal Publications” Section, starting from page (iii), and within the thesis.

This copy has been supplied on the understanding that it is copyright material and that no quotation from the thesis may be published without proper acknowledgement.

The right of Ali J. Sultan to be identified as the author of this work has been asserted by him in accordance with the Copyright, Designs and Patents Act 1988.

© 2022 The University of Sheffield and Ali J. Sultan.

Scientific Journal Publications

(1) Peer-reviewed original research article (published):

Ali J. Sultan, Kevin J. Hughes, Derek B. Ingham, Lin Ma, Mohamed Pourkashanian. Techno-economic competitiveness of 50 MW concentrating solar power plants for electricity generation under Kuwait climatic conditions [1]. *Renewable and Sustainable Energy Reviews* 2020;134:110342. Available from: <https://doi.org/10.1016/j.rser.2020.110342>.

(2) Peer-reviewed original research article (published):

Ali J. Sultan, Derek B. Ingham, Kevin J. Hughes, Lin Ma, Mohamed Pourkashanian. Optimization and performance enhancement of concentrating solar power in a hot and arid desert environment [2]. *Renewable and Sustainable Energy Reviews* 2021;149:111411. Available from: <https://doi.org/10.1016/J.RSER.2021.111411>.

(3) Peer-reviewed original research article (under revising process):

Ali J. Sultan, Derek B. Ingham, Lin Ma, Kevin J. Hughes, Mohamed Pourkashanian. Comparative techno-economic assessment and minimization of the levelized cost of electricity for increasing capacity wind power plants by row and angle layout optimization.

(4) Peer-reviewed supplementary material (published):

Ali J. Sultan, Kevin J. Hughes, Derek B. Ingham, Lin Ma, Mohamed Pourkashanian. Supplementary material for research article 110342 “Techno-economic competitiveness of 50 MW concentrating solar power plants for electricity generation under Kuwait climatic conditions” [3]. *Renewable and Sustainable Energy Reviews* 2020;134:110342. Available from: <https://doi.org/10.1016/j.rser.2020.110342> (download from “Appendix A. Supplementary data” in DOI).

(5) Peer-reviewed supplementary material (published):

Ali J. Sultan, Derek B. Ingham, Kevin J. Hughes, Lin Ma, Mohamed Pourkashanian. Supplementary material for research article 111411 “Optimization and performance enhancement of concentrating solar power in a hot and arid desert environment” [4]. *Renewable and Sustainable Energy Reviews* 2021;149:111411. Available from: <https://doi.org/10.1016/j.rser.2021.111411> (download from “Appendix A. Supplementary data” in DOI).

(6) Peer-reviewed supplementary material (under revising process):

Ali J. Sultan, Derek B. Ingham, Lin Ma, Kevin J. Hughes, Mohamed Pourkashanian. Supplementary material for research article. Comparative techno-economic assessment and minimization of the levelized cost of electricity for increasing capacity wind power plants by row and angle layout optimization.

Acknowledgements

I want to express my deepest gratitude to several people and institutions for their support during my PhD journey. Firstly, I would like to thank my supervisors, Prof. Derek B. Ingham, Dr. Kevin J. Hughes, Prof. Lin Ma, and Prof. Mohamed Pourkashanian, for their continuous guidance. In addition, I would like to thank the Kuwait Institute for Scientific Research for the financial support to pursue my degree of Doctor of Philosophy in Mechanical Engineering and for supporting this study. Moreover, I would like to thank the Kuwait Ministry of Electricity and Water for making its fossil-based power plant data available, which was used in this study. Finally, I would like to thank all of my family and friends for their constant encouragement and understanding throughout the past years.

Abstract

This work presents multiple techno-economic assessment and optimization results for utilizing the Concentrating Solar Power - Parabolic Trough (CSP-PT) with Thermal Energy Storage (TES) and wind power technologies. The evaluation is performed for electricity generation under arid climatic conditions and limited water resources to promote the mega-scale implementation of renewable energy in the Middle East and North Africa (MENA), including the Gulf Cooperation Council (GCC) region. The coordination of these technologies is considered for the case of Kuwait, which is a MENA/GCC member. The scope is technically challenging since Kuwait has a strategic target for achieving a 15% penetration in electricity demand from renewable energy by the year 2030. The results obtained constitute an attempt to provide recommendations on the validation, optimal design configurations, and operating conditions for future possibilities of CSP-PT/TES and wind power plant installations.

The CSP-PT/TES technology performance is evaluated in a hot desert environment with a comparative viewpoint. The techno-economic assessment is performed on an existing power plant in Spain (i.e., the world's largest installed CSP shareholder), and the model is validated using published data. It is revealed that the Direct Normal Irradiance (DNI) of Spain exceeds that of Kuwait by a difference of 176.2 kWh/m² yr, but the overall performance of the Kuwait case exceeds that of Spain. With a wet-cooled condenser system, the Kuwait case performance exceeds that of Spain for the annual overall plant efficiency (η_{overall}) by 2.9%, and the annual efficiency of the Solar Field (SF) system by 4.1%. Additionally, the annual net electricity output of the Kuwait case exceeds that of Spain by 14,534 MWh_e. With a dry-cooled condenser system, the Kuwait case performance exceeds that of Spain for η_{overall} by 1.1%, and the annual efficiency of the SF system by 3.0%. However, the annual net electricity output of the Spain case exceeds that of Kuwait by only 749.8 MWh_e. The better performance of the Kuwait case is due to the DNI impact on the number of full load hours of steam turbine, ambient temperature, wind speed, and SF heat loss/dumped energy. The results are realistic because the findings of the number of full load hours of steam turbine are as follows: 3003 h (wet cooling, Spain), 2709 h (dry cooling, Spain), 3306 h (wet cooling, Kuwait), and 2792 h (dry cooling, Kuwait). Additionally,

the annual mean ambient temperature in Kuwait (25.8 °C) is higher than that of Spain (14.9 °C), and the annual mean wind speed in Kuwait (4 m/s) is lower than that of Spain (6.7 m/s). Furthermore, the percentage reduction in water consumption is 96.61% (Spain case) and 97.05% (Kuwait case) due to replacing a wet-cooled condenser with a dry-cooled one. Due to limited water resources in the chosen location within Kuwait, the techno-economic assessment also considered 589 design configurations using a dry-cooled condenser system. The Solar Multiple (SM) and the number of full load hours of storage (N_h^{TES}) are varied to identify optimal configurations. It is concluded that the optimal SM is at 3.3, corresponding to the lowest Levelized Cost of Electricity (LCOE) of 15.0663 ¢/kWh for 16 h of storage. The performance of the dry-cooled CSP-PT design configurations is further evaluated to identify 19 optimal configurations for the Kuwait case based on the LCOE-minimization criterion. Such configurations have optimal SM values based on the lowest LCOE. From the optimization results, it is concluded that the SM value for optimal CSP-PT/TES configurations increases with an increasing number of N_h^{TES} . Also, the N_h^{TES} value has significant effects on the annual energy generation, capacity factor, and LCOE. However, the impact of N_h^{TES} on $\eta_{overall}$ is insignificant. Further, the periods of 24 h continuous electricity generation from CSP-PT/TES without fossil backup have been identified.

In addition, an evaluation of mega-scale wind power plants is performed under the climatic conditions of Kuwait. The coinciding peaks in electrical load and solar/wind resources have been revealed, promoting cogeneration from CSP-PT/TES and wind power with significant benefits. Also, the wind speed is found to be at maximum levels at high altitudes in the early daytime and late nighttime. Whereas in the afternoon, it reaches maximum values at low altitudes. The calculated wind shear is between 0.14-0.18 and shows a cyclic behaviour, promoting mega-scale wind power generation. Moreover, techno-economic assessment and optimization are performed for multi-row design configurations of several wind power plants. The optimal selection comes after evaluating 2220 configurations from which 60 optimal configurations are determined for different values of the number of rows in the wind power plant (N_r) based on the LCOE-minimization criterion. The 60 optimal configurations have optimal values of wind power plant layout angle (θ_{plant}) based on the lowest LCOE. It is concluded that the N_r and θ_{plant} values impact the LCOE, wake losses, performance ratio, and capacity factor. Further, the wind power

density is calculated to be 289 W/m^2 and it is concluded that June and July have high levels of generation, wind speed, temperature, and humidity. Also, the locally estimated scatterplot smoothing regression analyses on the wind resource confirm prevailing wind with a consistent northwest component.

Table of contents

Declaration.....	ii
Scientific Journal Publications.....	iii
Acknowledgements.....	v
Abstract.....	vi
Table of contents	ix
List of Figures	xiv
List of Tables.....	xxvi
Nomenclature	xxix
1. Introduction.....	1
1.1. Chapter journal publications	1
1.2. Reference concentrating solar power plant	1
1.3. Justification for concentrating solar power assessment	4
1.4. Assessment approach for concentrating solar power	11
1.5. The 2030 vision and renewable energy.....	12
1.6. Coordination of wind and concentrating solar power with thermal energy storage	13
1.7. Reference wind power plant and technology selection.....	15
1.8. Justification for wind power assessment.....	17
1.9. Chapter conclusion.....	17

2. Literature Review	19
2.1. Chapter journal publications.....	19
2.2. Background	19
2.3 Experiences of the Middle East and North Africa, and the Gulf Cooperation Council.....	23
2.3.1 Distinguished Middle East and North Africa experience of Morocco.....	23
2.3.2 Distinguished Gulf Cooperation Council experience of United Arab Emirates.....	25
2.4 Kuwait experience.....	26
2.4.1 Total carbon dioxide emission	27
2.4.2 Nationally determined contributions.....	29
2.4.3 Greenhouse gas inventory.....	29
2.4.4 Development plan.....	31
2.4.5 Land assessment.....	31
2.4.6 Installed capacity and electricity generation	32
2.4.7 Electrical load.....	33
2.4.8 Fuel types and consumptions.....	40
2.4.9 Renewable energy projects	42
2.5 Survey on simulation software(s) and tools for performance modelling.....	43
2.6 Survey on specifications of concentrating solar power plants	43
2.7 Research and knowledge gaps.....	54
2.8. Chapter conclusion.....	56
3. Methodology.....	59
3.1. Chapter journal publications.....	59
3.2 Model description	59
3.2.1 System components and energy balance.....	59
3.2.2 Justification for simulation model selection	69
3.2.3 Computational algorithm and control	70

3.3 Techno-economic competitiveness of concentrating solar power plants with thermal energy storage	73
3.4. Optimization and performance enhancement of concentrating solar power plants	75
3.4.1 Parametric analyses	75
3.4.2. Modelling approach	78
3.5. Comparative techno-economic assessment and optimization of wind power plants	79
3.5.1 Parametric analyses	79
3.5.2 Modelling approach	82
3.6. Chapter conclusion.....	83
4. Natural Resources and Meteorological Characteristics.....	85
4.1. Chapter journal publications	85
4.2. Meteorological data.....	85
4.3. Methodology for reliable meteorological data.....	90
4.4. Resource and weather characteristics	91
4.5. Location characteristics.....	98
4.6. Meteorological characteristics.....	99
4.7. Prevailing conditions.....	99
4.8. Chapter conclusion.....	102
5. Techno-economic Competitiveness of Concentrating Solar Power Plants with Thermal Energy Storage	103
5.1. Chapter journal publications.....	103
5.2. Climatic conditions	103
5.3. Reference concentrating solar power plant.....	104

5.4. Cooling options for condenser system	108
5.5. Description of thermal energy storage system	116
5.6. Mathematical description.....	118
5.7. Results and discussions.....	125
5.7.1. Validation	125
5.7.2. Effects of temperature and solar irradiance.....	128
5.7.3. Evaluation of thermal energy storage	138
5.7.4. Parametric analysis.....	142
5.7.4.1. Electricity output	142
5.7.4.2. Dumped thermal energy	143
5.7.4.3. Techno-economic analysis	145
5.8. Chapter conclusion.....	149
5.8.1. Concluding remarks.....	149
5.8.2. Recommendations	150
6. Optimization and Performance Enhancement of Concentrating Solar Power Plants.....	152
6.1. Chapter journal publications	152
6.2. Design parameters.....	152
6.3. Dry-cooled condenser	152
6.4. Performance enhancement using thermal energy storage.....	153
6.5. Performance enhancement using wind power	154
6.6. Mathematical formulation.....	156
6.7. Results and discussions.....	156
6.7.1. Levelized cost of electricity	156
6.7.2. Capacity factor	158
6.7.3. Thermal power produced by the solar field.....	159
6.7.4. Annual energy generation.....	161
6.7.5. Annual overall plant efficiency	162

6.7.6. Cycle electrical power output	163
6.7.7. Performance enhancement strategies	167
6.7.7.1. Dispatch control of thermal energy storage.....	167
6.7.7.2. Integration of wind power	173
6.7.7.3. Cogeneration with temperature derating effect	175
6.7.7.4. Cogeneration with load consideration	178
6.8. Chapter conclusion.....	181
7. Comparative Techno-economic Assessment and Optimization of Wind Power Plants.....	182
7.1. Chapter journal publications.....	182
7.2. Technology description	182
7.3. Mathematical description.....	185
7.4. Results and discussions.....	186
7.4.1 Locally estimated scatterplot smoothing regression analyses	186
7.4.2 Optimization analyses	191
7.4.2.1. Impact on levelized cost of electricity.....	191
7.4.2.2. Impact on wake losses.....	191
7.4.2.3. Impact on performance ratio	192
7.4.2.4. Impact on capacity factor	192
7.4.2.5. Impact of wind resource	192
7.4.3. Monthly performance assessment	198
7.4.4. Hourly performance assessment	205
7.4.5. Full load generation at rated wind speed	206
7.4.6. Economic analysis.....	217
7.5. Chapter conclusion.....	224
8. Conclusion and Future Work	226
8.1. Chapter journal publications	226
8.2. Benefits and applications.....	226

8.3. Novelty	227
8.4. Challenges and solutions	228
8.5. Study justification	229
8.6. Selection criteria	230
8.7. Optimization and assessment approach.....	232
8.8. Natural resources and meteorological characteristics	233
8.9. Techno-economic competitiveness of concentrating solar power plants with thermal energy storage	233
8.10. Optimization and performance enhancement of concentrating solar power plants	234
8.11. Comparative techno-economic assessment and optimization of wind power plants	235
8.12. Future work and recommendations.....	237
References	238
Appendices.....	274
Appendix A. Thermophysical properties of the Heat Transfer Fluid (HTF).....	274
Appendix B. Thermophysical properties of the Thermal Energy Storage (TES) medium.....	277
Appendix C. Process flow diagrams for the reference 50 MW CSP-PT plant (wet/dry)	278
Appendix D. Input data to the model.....	282
D.1. Input data to the CSP-PT/TES model.....	282
D.2. Input data to the wind power model	295
Appendix E. Mathematical modelling	300
E.1. Wind power density.....	300

E.2. Betz's coefficient	301
E.3. Betz's limit.....	302
E.4. Condenser systems (wet and dry).....	303
Appendix F. Supplementary figures.....	305
Appendix G. Supplementary tables.....	325
Appendix H. Estimated costs	326

List of Figures

Figure 1. 1 Main system components inside a CSP-PT plant	2
Figure 1. 2 Illustration of the leading CSP technologies and their installed ratio worldwide [6].....	3
Figure 1. 3 Comparisons between different TES materials [10].....	4
Figure 1. 4 Maps of Kuwait: (A) Kuwait and the other GCC countries in dark-blue colour, and (B) Kuwait governorates named and coloured differently – (Kuwait capital is shown in red star) [11].....	5
Figure 1. 5 The reference 50 MW plant (Andasol-1) in the Granada Province in Spain with the PB system and TES system at the plant centre and surrounded by the SF system [12].	5
Figure 1. 6 Schematic illustrating the SF system layout of the Andasol-1 plant [13].....	6
Figure 1. 7 Schematic illustrating the TES system layout of the Andasol-1 plant [14].....	6
Figure 1. 8 Comparison based on electricity consumption and CO ₂ emissions (the size of bubbles shows the gross domestic product per capita in 2019) [27].	7
Figure 1. 9 Subsidised electricity prices in the GCC region and the USA as of 2011, with Kuwait having the lowest rate (y-axis unit: US-\$/kWh) [21,22].....	8
Figure 1. 10 Kuwait map showing the western region with minimal oil and gas field concentrations [32].	9
Figure 1. 11 Kuwait map showing the western region with minimal transmission networks [30].	9
Figure 1. 12 LCOE estimations of renewable power projects [38] (the horizontal black-coloured line is added to the figure to indicate the average actual cost of electricity from the fossil-based power plants in Kuwait).....	11
Figure 1. 13 Global installed CSP capacities by technology and magnitude of the PB system in which the CSP-PT technology and the 50 MW capacity rating dominate globally [5].....	12

Figure 2. 1 Global technology shares for electricity production [57].	19
Figure 2. 2 Global technology shares: capacity of CSP (2007-2017) with Spain (the location of the reference CSP-PT plant in this work) holding the maximum share [57].	19
Figure 2. 3 Annual variations for energy use per capita in the Middle East (i), and energy use in Middle Eastern countries showing Kuwait at the top rank (ii, iii, iv) [68,74].	21
Figure 2. 4 Electricity generation by source in the Middle East [75].	22
Figure 2. 5 Global estimates: (i) electricity generation between 1971-2016 by fuel (in TWh) [58], (ii) gross production by source for 2016 [76], and (iii) consumption by sector for 1974-2016 [76].	22
Figure 2. 6 Grid interconnection in the Middle East (solid line: “existing”; dashed line: “not operational/island operation”; dotted line: “under consideration,-study, - construction”) [88].	24
Figure 2. 7 CO2 emissions in Kuwait according to BP from 2007 to 2017.	27
Figure 2. 8 CO2 emissions in Kuwait according to IEA from 1971 to 2015 (the labels indicate maximum data points).	28
Figure 2. 9 CO2 emissions in Kuwait according to the World Bank from 1946 to 2014 (the labels indicate maximum points).	28
Figure 2. 10 Distribution of emissions by sector and GHG type in 1994 [50].	30
Figure 2. 11 Breakdown of GHG emissions associated with energy activities in 1994 [50].	30
Figure 2. 12 Minimum/peak load, installed capacity, and population from 1997 to 2016 in Kuwait.	33
Figure 2. 13 Monthly profile of the peak/minimum load and average peak/minimum load for 2016 in Kuwait.	34
Figure 2. 14 Hourly electrical load profiles for hours 00:00 to 05:00 from the fossil-based power plants during 2016 in Kuwait.	35

Figure 2. 15 Hourly electrical load profiles for hours 06:00 to 11:00 from the fossil-based power plants during 2016 in Kuwait.	36
Figure 2. 16 Hourly electrical load profiles for hours 12:00 to 17:00 from the fossil-based power plants during 2016 in Kuwait.	37
Figure 2. 17 Hourly electrical load profiles for hours 18:00 to 23:00 from the fossil-based power plants during 2016 in Kuwait.	38
Figure 2. 18 Annual profiles from 1997 to 2016 in Kuwait: peak load, capacity, peak load as a percentage of capacity, and reserve.....	39
Figure 2. 19 Electrical load profile of August 15 th (the day of maximum peak load in 2016) from all fossil-based power plants in Kuwait.....	39
Figure 2. 20 Annual profiles from 1997 to 2016 in Kuwait: minimum/peak load, installed capacity, and per capita peak load share.	39
Figure 2. 21 Consumption of fuels at the fossil-based power plants in Kuwait.	40
Figure 2. 22 Annual profiles for peak load, maximum relative humidity, and maximum temperature during 1997-2016 in Kuwait.	40
Figure 2. 23 Percentage of the electricity generation share of Kuwait relative to the Middle East and the world.	41
Figure 3. 1 Illustration of the transmission network for grid connection, the reference wind power-generating unit, and the design configuration of the reference CSP-PT/TES plant with energy balance parameters.....	60
Figure 3. 2 Process flow diagram for the reference 50 MW CSP-PT plant with the wet cooling option (see Appendix C for the dry cooling option).....	61
Figure 3. 3 Description of the HCE components – (drawing vs actual) [220].	62
Figure 3. 4 Description of the HCE internal housings [221].	62
Figure 3. 5 Energy balance for the HCE (receiver) – the control volume (box) encompasses the HTF [188].	62
Figure 3. 6 Schematic diagram of a single unit of SCA used in the SF system in which the HCE (receiver) is shown as a red line (left) [222,223].....	63

Figure 3. 7 The SF system (top) with other CSP-PT plant systems (bottom) [224].	63
Figure 3. 8 HTF temperature increase as it flows through one [219].	68
Figure 3. 9 Heat loss as a function of HTF temperature [219].	68
Figure 3. 10 Heat loss per unit length of HCE vs average HTF temperature for Schott PTR70 2008 used in this work within the SF system [190,219].	68
Figure 3. 11 Illustration of the modelling pyramid in SAM [228].	70
Figure 3. 12 System computational algorithm in SAM [229].	71
Figure 3. 13 Control flow diagram for the CSP-PT/TES model in SAM [188].	72
Figure 4. 1 Monthly profiles of the hourly DNI (mean) in Kuwait.	88
Figure 4. 2 Monthly profiles of the dry-bulb temperature in Kuwait and Spain.	89
Figure 4. 3 Monthly temperature and humidity profiles based on ground measurements at 10 m in Kuwait.	89
Figure 4. 4 Hourly and monthly DNI levels in Kuwait (W/m ²).	91
Figure 4. 5 Monthly profiles of the temperature and humidity based on different measurement heights: (i) maximum values at 98 m, (ii) mean values at 98 m, and (iii) mean values at a low height (< 10 m).	94
Figure 4. 6 Monthly profiles of the wind speed at 100 m with maximum values occurring during the early day and late night.	95
Figure 4. 7 Monthly statistics of the wind speed at different RLMs: (i) maximum, (ii) mean, and (iii) minimum – (based on a 10-minute analysis).	96
Figure 4. 8 Frequency of the wind direction and wind speed at different RLMs: (i) RLM = 1B (at 97.8 m), (ii) RLM = 2 (at 80 m), (iii) RLM = 3 (at 60 m), (iv) RLM = 4 (at 40 m), and (v) RLM < 10 m – (colours: wind speed ranges, a: hourly analysis, b: 10-minute analysis).	97
Figure 4. 9 A topographical map with elevation for Kuwait [45].	100
Figure 4. 10 Sandstorm seasons in Kuwait: (i) storm on 25 March 2011 [257], (ii) regional trajectories [258], and (iii) dust deposition rate [259,260].	101

Figure 5. 1 Description of critical CSP-PT plant components: (i) a PT collector with thermal gradient [265], (ii) a single unit of SCA [266], (iii) a schematic diagram of a typical evacuated receiver [267], and (iv) HCE manufacturing processes [266].	105
Figure 5. 2 Dispatch flexibility of the CSP and PV technologies under the same solar resource condition [51].....	106
Figure 5. 3 Total installed cost reduction by source for a 160 MW CSP-PT power plant in 2015 and 2025 [269].	106
Figure 5. 4 Total installed cost reduction by source for a 160 MW CSP-PT power plant in 2015 and 2025 [268].	107
Figure 5. 5 Schematics of a wet cooling system [284,285,290].....	110
Figure 5. 6 Schematics of a dry cooling system [284,285,290].	113
Figure 5. 7 Categorizations of the solar TES system [298,299].....	116
Figure 5. 8 Classifications of various materials, latent heat storage, and PCMs [299].	117
Figure 5. 9 Main TES system configurations for CSP technologies in which molten salt is used as a medium in direct and indirect design configurations.	117
Figure 5. 10 Schematic of the processing of solar heat between CSP-PT plant systems [51].	118
Figure 5. 11 Monthly profiles of the net electricity output using wet/dry cooling options, the DNI level (kWh/m ² /month), and the wet/dry bulb temperatures for the Spain and Kuwait cases.	128
Figure 5. 12 Monthly profiles of the overall plant efficiency using wet/dry cooling, the DNI level (kWh/m ² /month), and the wet/dry bulb temperatures for the Spain and Kuwait cases.	129
Figure 5. 13 Comparison of the number of hours for different ranges of DNI (W/m ²) during each month for the Spain and Kuwait cases.	130
Figure 5. 14 Frequency of DNI (W/m ²) during a typical year in Spain and Kuwait....	132

Figure 5. 15 Monthly profiles of the dumped energy with the wet/dry cooling options and the DNI level (kWh/m ² /month) for the Spain and Kuwait cases (y-axis $\leq 10,000$ MWht).	133
Figure 5. 16 Comparison of the monthly DNI level (kWh/m ² /month) and the wet/dry bulb temperatures in Spain and Kuwait.	134
Figure 5. 17 The effects of the wet/dry bulb temperatures and DNI levels on the PB cycle efficiency with the wet/dry cooling options for the Spain and Kuwait cases. .	135
Figure 5. 18 Cycle cooling water mass flow rate (makeup) with the wet/dry cooling options for the Spain and Kuwait cases.....	136
Figure 5. 19 Annual profiles (sum) of the DNI in Spain and Kuwait.	138
Figure 5. 20 Comparison between the charged and discharged TES energy levels for the Spain and Kuwait cases using both the wet/dry cooling options.	140
Figure 5. 21 Total charged and discharged TES energy using the wet cooling option for the Spain and Kuwait cases.	141
Figure 5. 22 Total charged and discharged TES energy using the dry cooling option for the Spain and Kuwait cases.	141
Figure 5. 23 The annual net electricity output and the number of full load hours when the PB system operates at the rated design condition using the wet/dry cooling options for the Spain and Kuwait cases.....	143
Figure 5. 24 The dumped energy and the number of hours when the DNI value is less than or equal to a particular IAD value using the wet cooling option for the Spain and Kuwait cases.	144
Figure 5. 25 The dumped energy and the number of hours when the DNI value is less than or equal to a particular IAD value using the dry cooling option for the Spain and Kuwait cases.	145
Figure 5. 26 The LCOE values of 589 different design configurations for 50 MW CSP-PT power plants.	147
Figure 6. 1 Profiles of LCOE using a dry-cooled condenser: (i) 3-D variation of LCOE, (ii) LCOE as a function of SM, and (iii) LCOE as a function of NhTES.....	158

Figure 6. 2 Profiles of capacity factor using a dry-cooled condenser: (i) 3-D variation of capacity factor, (ii) capacity factor for 589 design configurations, (iii) capacity factor as a function of SM, and (iv) capacity factor as a function of NhTES.	159
Figure 6. 3 Profiles of thermal power produced by the SF system using a dry-cooled condenser: (i) 3-D variation of power, (ii) power for 589 design configurations, (iii) power as a function of SM, and (iv) power as a function of NhTES.....	160
Figure 6. 4 Profiles of Eele, a using a dry-cooled condenser: (i) 3-D variation of Eele, a, (ii) Eele, a for 589 design configurations, (iii) Eele, a as a function of SM, and (iv) Eele, a as a function of NhTES.....	161
Figure 6. 5 Profiles of η_{overall} using dry-cooled condenser: (i) 3-D variation of η_{overall} , (ii) η_{overall} for 589 design configurations, (iii) η_{overall} as a function of SM, and (iv) η_{overall} as a function of NhTES.	163
Figure 6. 6 Cycle electrical power output of a sample winter month (January profile) showing the 19 optimal design configurations with optimal SM values based on the lowest LCOE for $0 \leq \text{NhTES} \leq 18$	164
Figure 6. 7 Cycle electrical power output of a sample winter month (February profile) showing the 19 optimal design configurations with optimal SM values based on the lowest LCOE for $0 \leq \text{NhTES} \leq 18$	165
Figure 6. 8 Cycle electrical power output of a sample summer month (July profile) showing the 19 optimal design configurations with optimal SM values based on the lowest LCOE for $0 \leq \text{NhTES} \leq 18$	166
Figure 6. 9 Cycle electrical power output of a sample summer month (August profile) showing the 19 optimal design configurations with optimal SM values based on the lowest LCOE for $0 \leq \text{NhTES} \leq 18$	167
Figure 6. 10 Role of TES dispatch control fractions in maximizing Eele, a in the reference 50 MW CSP-PT plant for $0 \leq \text{FWSTES} \leq 1$ with the following variations: (i) FWSTES= 0, (ii) FWSTES= 0.5, and (iii) FWSTES= 1.	169
Figure 6. 11 Simulation results for the reference 50 MW CSP-PT plant performance during a typical day in the chosen location in Kuwait.	170

Figure 6. 12 Cycle electrical power output and direct/beam normal irradiance (i.e., DNI) during a sample winter month with high cloud presence (January profile) with maximization of TES role by increasing the value of FWOSTES as follows: (i) 0 and (ii) 0.3 – (low values of FWOSTES).....	171
Figure 6. 13 Cycle electrical power output and direct/beam normal irradiance (i.e., DNI) during a sample winter month with high cloud presence (January profile) with maximization of TES role by increasing the value of FWOSTES as follows: (i) 0.6 and (ii) 0.9 – (high values of FWOSTES).....	172
Figure 6. 14 A map of Kuwait showing the locations of two meteorological masts (about 10 km apart) in the chosen location: MM-1 at 100 m and MM-2 at 10 m.....	173
Figure 6. 15 Monthly statistics for α based on 10-minute calculations at different RLCs: (i) maximum, (ii) mean, and (iii) minimum.	176
Figure 6. 16 Frequency of ambient temperature in °C unit and characteristics of the reference 2 MW wind turbine used in this work: (i) frequency of ambient temperature exceeding a specific value, (ii) wind turbine power curve, and (iii) temperature derating effect on turbine performance.	177
Figure 6. 17 Potential periods for TES charging (orange-shaded) and discharging (green-shaded) for the day of maximum peak load during 2016 (August 15 th) in Kuwait under the zero renewable penetration scenario – (i.e., combined load from all fossil-based power plants).....	178
Figure 6. 18 Coordination between the wind resource from the MM-1 mast at 100 m, solar resource, and electrical load in Kuwait.....	179
Figure 7. 1 A simplified illustration of a single row configuration with grid connection, substations, overhead lines, and residential units.	183
Figure 7. 2 Power curve for the reference 2 MW wind turbine used in this work.....	183
Figure 7. 3 Profiles for the wind speed and α at different height levels during one day.	186
Figure 7. 4 Results of the LOESS regression analyses (monthly) for the wind resource during hours 0 to 23 for a typical year in the chosen location in this work.	189

Figure 7. 5 Monthly profiles for the wind speed frequency (left) at the reference wind turbine's hub height with normal distributions (right).....	190
Figure 7. 6 Monthly profiles for the wind direction frequency (left) at the reference wind turbine's hub height with normal distributions (right).....	190
Figure 7. 7 Impact of varying N_r and θ_{plant} on the LCOE and annual gross energy: (a) for 2220 configurations, (b) for 2220 configurations, and (c) for 60 optimal configurations.	194
Figure 7. 8 Impact of varying N_r and θ_{plant} on the wake losses and annual gross energy: (a) for 2220 configurations, (b) for 2220 configurations, and (c) for 60 optimal configurations.....	195
Figure 7. 9 Impact of varying N_r and θ_{plant} on the performance ratio and annual gross energy: (a) for 2220 configurations, (b) for 2220 configurations, and (c) for 60 optimal configurations.....	196
Figure 7. 10 Impact of varying N_r and θ_{plant} on the capacity factor and annual gross energy: (a) for 2220 configurations, (b) for 2220 configurations, and (c) for 60 optimal configurations.....	197
Figure 7. 11 MFPs and AFPs with their intersection areas (January to March months) for assessment parameters 1 to 12, namely from left to right, wind speed, wind direction, ambient temperature, atmospheric pressure, and generation of the selected 8 of the 60 optimal configurations (the optimal 1, 2, 3, 4, 40, 46, 52, and 58-row configurations): (i) MFPs (white areas), (ii) AFPs (dark-blue areas), and (iii) intersection areas (light-blue areas).....	201
Figure 7. 12 MFPs and AFPs with their intersection areas (April to June months) for assessment parameters 1 to 12, namely from left to right, wind speed, wind direction, ambient temperature, atmospheric pressure, and generation of the selected 8 of the 60 optimal configurations (the optimal 1, 2, 3, 4, 40, 46, 52, and 58-row configurations): (i) MFPs (white areas), (ii) AFPs (dark-blue areas), and (iii) intersection areas (light-blue areas).....	202
Figure 7. 13 MFPs and AFPs with their intersection areas (July to September months) for assessment parameters 1 to 12, namely from left to right, wind speed, wind direction, ambient temperature, atmospheric pressure, and generation of the	

selected 8 of the 60 optimal configurations (the optimal 1, 2, 3, 4, 40, 46, 52, and 58-row configurations): (i) MFPs (white areas), (ii) AFPs (dark-blue areas), and (iii) intersection areas (light-blue areas)..... 203

Figure 7. 14 MFPs and AFPs with their intersection areas (October to December months) for assessment parameters 1 to 12, namely from left to right, wind speed, wind direction, ambient temperature, atmospheric pressure, and generation of the selected 8 of the 60 optimal configurations (the optimal 1, 2, 3, 4, 40, 46, 52, and 58-row configurations): (i) MFPs (white areas), (ii) AFPs (dark-blue areas), and (iii) intersection areas (light-blue areas)..... 204

Figure 7. 15 HFPs and AFPs with their intersection areas (00:00 to 02:00 hours) for assessment parameters 1 to 12, namely from left to right, wind speed, wind direction, ambient temperature, atmospheric pressure, and generation of the selected 8 of the 60 optimal configurations (the optimal 1, 2, 3, 4, 40, 46, 52, and 58-row configurations): (i) HFPs (white areas), (ii) AFPs (dark-red areas), and (iii) intersection areas (light-red areas). 207

Figure 7. 16 HFPs and AFPs with their intersection areas (03:00 to 05:00 hours) for assessment parameters 1 to 12, namely from left to right, wind speed, wind direction, ambient temperature, atmospheric pressure, and generation of the selected 8 of the 60 optimal configurations (the optimal 1, 2, 3, 4, 40, 46, 52, and 58-row configurations): (i) HFPs (white areas), (ii) AFPs (dark-red areas), and (iii) intersection areas (light-red areas). 208

Figure 7. 17 HFPs and AFPs with their intersection areas (06:00 to 08:00 hours) for assessment parameters 1 to 12, namely from left to right, wind speed, wind direction, ambient temperature, atmospheric pressure, and generation of the selected 8 of the 60 optimal configurations (the optimal 1, 2, 3, 4, 40, 46, 52, and 58-row configurations): (i) HFPs (white areas), (ii) AFPs (dark-red areas), and (iii) intersection areas (light-red areas). 209

Figure 7. 18 HFPs and AFPs with their intersection areas (09:00 to 11:00 hours) for assessment parameters 1 to 12, namely from left to right, wind speed, wind direction, ambient temperature, atmospheric pressure, and generation of the selected 8 of the 60 optimal configurations (the optimal 1, 2, 3, 4, 40, 46, 52, and 58-row configurations): (i) HFPs (white areas), (ii) AFPs (dark-red areas), and (iii) intersection areas (light-red areas). 210

Figure 7. 19 HFPs and AFPs with their intersection areas (12:00 to 14:00 hours) for assessment parameters 1 to 12, namely from left to right, wind speed, wind direction, ambient temperature, atmospheric pressure, and generation of the selected 8 of the 60 optimal configurations (the optimal 1, 2, 3, 4, 40, 46, 52, and 58-row configurations): (i) HFPs (white areas), (ii) AFPs (dark-red areas), and (iii) intersection areas (light-red areas). 211

Figure 7. 20 HFPs and AFPs with their intersection areas (15:00 to 17:00 hours) for assessment parameters 1 to 12, namely from left to right, wind speed, wind direction, ambient temperature, atmospheric pressure, and generation of the selected 8 of the 60 optimal configurations (the optimal 1, 2, 3, 4, 40, 46, 52, and 58-row configurations): (i) HFPs (white areas), (ii) AFPs (dark-red areas), and (iii) intersection areas (light-red areas). 212

Figure 7. 21 HFPs and AFPs with their intersection areas (18:00 to 20:00 hours) for assessment parameters 1 to 12, namely from left to right, wind speed, wind direction, ambient temperature, atmospheric pressure, and generation of the selected 8 of the 60 optimal configurations (the optimal 1, 2, 3, 4, 40, 46, 52, and 58-row configurations): (i) HFPs (white areas), (ii) AFPs (dark-red areas), and (iii) intersection areas (light-red areas). 213

Figure 7. 22 HFPs and AFPs with their intersection areas (21:00 to 23:00 hours) for assessment parameters 1 to 12, namely from left to right, wind speed, wind direction, ambient temperature, atmospheric pressure, and generation of the selected 8 of the 60 optimal configurations (the optimal 1, 2, 3, 4, 40, 46, 52, and 58-row configurations): (i) HFPs (white areas), (ii) AFPs (dark-red areas), and (iii) intersection areas (light-red areas). 214

Figure 7. 23 Full load generation at the rated wind speed for selected 4 of the 60 optimal configurations (the optimal 1, 2, 3, and 4-row configurations) – (optimal low row-count configurations)..... 215

Figure 7. 24 Full load generation at the rated wind speed for selected 4 of the 60 optimal configurations (the optimal 40, 46, 52, and 58-row configurations) – (optimal high row-count configurations)..... 216

Figure 7. 25 The installed cost per watt as a function of Nr for the 60 optimal configurations of wind power plants (the optimal 1-row to 60-row configurations from left to right).....	217
Figure 7. 26 Multiple profiles for the 60 optimal configurations (the optimal 1-row to 60-row configurations from left to right): (a) the present value of annual energy, (b) the net present value (annual costs), (c) the annual energy, and (d) the annual gross energy.	218
Figure 7. 27 Multiple profiles for the 60 optimal design configurations of (the optimal 1-row to 60-row configurations from left to right): (a) the internal rate of return at the end of the analysis period (i.e., 25 years), (b) the project return (i.e., after-tax project maximum internal rate of return), and (c) the required PPA price.	219
Figure 7. 28 Multiple profiles for the 60 optimal design configurations (the optimal 1-row to 60-row configurations from left to right): (a) the flip actual percentage, (b) the flip target percentage, and (c) the flip target year.....	220
Figure 7. 29 Illustration (3D) of the cash flow over the project lifetime (25 years) for the selected 8 of the 60 optimal configurations (the optimal 1, 2, 3, 4, 40, 46, 52, and 58-row configurations).	221
Figure 7. 30 Illustration (2-D) of the cash flow over the project lifetime (25 years) for selected 4 of the 60 optimal configurations (the optimal 1, 2, 3, and 4-row configurations) – (optimal low row-count configurations).....	222
Figure 7. 31 Illustration (2D) of the cash flow over the project lifetime (25 years) for selected 4 of the 60 optimal configurations (the optimal 40, 46, 52, and 58-row configurations) – (optimal high row-count configurations).	223

List of Tables

Table 1. 1 Thermophysical properties of the HTF used within the SF system in the reference CSP-PT plant	3
Table 1. 2 Thermophysical properties of the TES medium used in the reference CSP-PT plant.....	4
Table 1. 3 Summary of the subsidized electricity prices for different consumer categories in Kuwait.	10
Table 2. 1 Energy consumption in selected countries in the Middle East [68]......	20
Table 2. 2 Subsidised electricity prices as of 2014 in the GCC countries [20]......	26
Table 2. 3 Capacity of renewable energy technologies in the GCC countries (wind, PV, CSP, and biomass/waste) [20].	27
Table 2. 4 Total GHG emissions in Kuwait [50].	30
Table 2. 5 GHG emissions of energy activities in Kuwait [50]......	30
Table 2. 6 Total installed power capacity at each of the fossil-based power plants in Kuwait as of 2016.....	33
Table 2. 7 Conventional power technologies and installed capacities at the fossil-based power plants as of 2016 in Kuwait.....	41
Table 2. 8 Summary of software(s) and tools for performance modelling.....	44
Table 2. 9 List of selected operational CSP plants worldwide.....	49
Table 2. 10 List of selected operational CSP plants worldwide.....	50
Table 3. 1 Design parameters for the reference CSP-PT/TES plant (Andasol-1) used in this work.	76
Table 4. 1 Statistical results for the DNI and meteorological parameters during a typical year in Kuwait.	87

Table 4. 2 Statistical comparisons between the DNI and GHI during a typical year in Kuwait.	93
Table 5. 1 Design climatic conditions for CSP-PT plants in the chosen location in this work.....	104
Table 5. 2 Typical estimated costs for the 50 MW CSP-PT plant [282].	107
Table 5. 3 Main input data to the model for the wet and dry-cooled condensers in this work.	111
Table 5. 4 Simulation and comparison of Andasol plant for wet and dry cooling systems [285].....	114
Table 5. 5 Main characteristics of different cooling systems [285].....	115
Table 5. 6 Actual and simulated results for the performance of the reference 50 MW CSP-PT plant (Andasol-1) used in this work under the climatic conditions of Spain.	126
Table 5. 7 Percentage difference values with actual and simulated results for the performance of the reference 50 MW CSP-PT plant (Andasol-1) used in this work under the climatic conditions of Spain.....	127
Table 5. 8 Performance results for the reference 50 MW CSP-PT plant (Andasol-1) under the wet/dry cooling options for the Kuwait and Spain cases.	131
Table 5. 9 Cycle cooling water mass flow rate (makeup) for the reference 50 MW CSP-PT plant (Andasol-1) under the wet/dry cooling options for the Kuwait and Spain cases.....	136
Table 5. 10 Energy balance results of the reference 50 MW CSP-PT plant (Andasol-1) under the wet/dry cooling options for the Spain and Kuwait cases.	137
Table 5. 11 Comparison of the statistical results for the DNI levels during a typical year in Spain and Kuwait.....	139
Table 5. 12 Comparison between the optimal design configurations and their performance measures using the validated CSP-PT model for the reference plant (50 MW capacity) with optimal SM values based on the lowest LCOE.....	148

Table 6. 1 Established RLMs for some measured meteorological elements from the MM-1 mast at 100 m.	174
Table 6. 2 Statistics of calculated α values based on a 10-minute analysis during a typical year.	175
Table 7. 1 Design characteristics for the reference wind turbine used in this work.	184
Table 7. 2 Statistical results (annual) for primary meteorological data at the reference wind turbine's hub height during a typical year.	190

Nomenclature

Acronyms

AFPs	Annual Frequency Profile(s)
BP	British Petroleum
CSP-PT	Concentrating Solar Power - Parabolic Trough
GCC	Gulf Cooperation Council
GHG	Greenhouse Gas
DLR	German Aerospace Center
EPA	Environment Public Authority (Kuwait)
HCEs	Heat Collecting Element(s)
HFPs	Hourly Frequency Profile(s)
HTF	Heat Transfer Fluid
IEA	International Energy Agency
IEC	International Electrotechnical Commission
LOESS	Locally Estimated Scatterplot Smoothing (regression)
MENA	Middle East and North Africa
MEW	Ministry of Electricity and Water (Kuwait)
MFPs	Monthly Frequency Profile(s)
MM	Meteorological Mast
NDCs	Nationally Determined Contribution(s)
NREL	National Renewable Energy Laboratory
NDCs	Nationally Determined Contribution(s)
NG	Natural Gas
PB	Power Block
PCMs	Phase Change Material(s)
PPA	Power Purchase Agreement
PT	Parabolic Trough
PV	Photovoltaic
SAM	System Advisor Model
SCA	Solar Collector Assembly
SEGS	Solar Energy Generating Systems
SF	Solar Field

SRW	Meteorological file type (for wind power modelling)
TES	Thermal Energy Storage
TMY	Typical Meteorological Year (for CSP-PT modelling)
TRNSYS	Transient System Simulation
UNFCCC	United Nations Framework Convention on Climate Change
US/USA	United States of America
2-D	Two-dimensional
3-D	Three-dimensional

Units

a	annual
bb1	barrel of oil
boe	barrel of oil equivalent
BTU	British Thermal Unit
C	Celsius
d	day
E	exa (10^{18})
EJ	exajoule
Fils	Currency value (1 Kuwaiti Dinar = 1000 Fils)
G	giga (10^9)
GW	gigawatt
GWh	gigawatt hour
GWh _t	gigawatt hour thermal
h/hr	hour
k	kilo
M	mega (10^6)
m	meter
m ²	square meter
MW	megawatt
MWh	megawatt hour
MW _e	megawatt electric
MWh _e	megawatt hour electric
MWh _t	megawatt hour thermal
s	second

SCF	Standard Cubic Foot
t	ton
T	tera (10^{12})
TWh	terawatt hour
W	watt
yr	year
\$	US Dollar
¢	US cent (1 \$ = 100 ¢)
°	degree

Symbols

A_{ap}	total aperture area of the solar field (m^2)
A_b	wind turbine blade area/blade's swept area (m^2)
$A_{collector}$	collector area (m^2)
AEP	Annual Electricity Production (kWh)
C_p	wind turbine power coefficient (%)
CO_2	Carbon dioxide (–)
ConcRat	Concentration Ratio (–)
DNI	Direct Normal Irradiance (W/m^2)
$E(N_h^{cr})$	amount of electricity produced by a renewable power technology, e.g. CSP-PT and wind power (kWh_e)
$E_{aux,cond}$	condenser auxiliaries consumption (kWh_e)
E_{boiler}	resulting thermal input to the power block (kWh_t)
$E_{ele,a}$	annual energy generation/net electricity output (MWh_e)
$E_{ele,aux,SF}$	solar field auxiliaries consumption (kWh_e)
$E_{ele,net,PB}$	net power output from power block (MWh_e)
$E_{ele,pump}$	condensate and feedwater pump consumption (kWh_e)
$E_{ele,turb}$	steam turbine electric power output (MWh_e)
E_{HTF}	the net thermal power transferred to the heat transfer fluid flowing in the collectors (kWh)
$E_{loss,piping}$	piping thermal losses (kWh_t)
$E_{receiver}$	the theoretical power available on the absorber tube surface (kWh_t)

E_{sun}	radiative solar power incident on net aperture area (MWh)
$E_{\text{th,loss}}$	collector thermal energy loss (kWh _t)
E_y	electricity generation in the year y (–)
$F_{\text{fou,glass}}$	factor counting fouling of envelope glass (–)
$F_{\text{fou,mirror}}$	factor counting fouling of mirror (–)
F_R	collector heat removal factor (–)
$F_R U_L$	collector loss coefficient (W/m ² °C)
$F_R(\tau\alpha)_n$	the efficiency when the solar radiation is absorbed by the plate and removed by the fluid flowing through the collector (–)
F_{track}	factor embodying all remaining losses as tracking errors (–)
F_y	fuel expenditures in the year y
$F_{\text{gross}}^{\text{TES}}$	turbine-storage adjustment gross output factor (–)
$F_{\text{WS}}^{\text{TES}}$	storage dispatch fraction with solar (–)
$F_{\text{WOS}}^{\text{TES}}$	storage dispatch fraction without solar (–)
F_{η}^{TES}	turbine-storage adjustment efficiency factor (–)
FCR	Fixed Charge Rate (–)
FOC	Fixed Operating Cost, or operations and maintenance costs (\$)
F'	collector efficiency factor (–)
$F' U_L$	modified loss coefficient based on $F_R U_L$ (W/m ² °C)
GHI	Global Horizontal Irradiance (W/m ²)
I_{beam}	the amount of beam solar radiation incident on the collector surface (W/m ²)
I_t	the amount of solar radiation incident on the plane of the collector surface (W/m ²)
IAD	Irradiation At Design (W/m ²)
IAM	Incidence Angle Modifier (–)
ICC	Installed Capital Cost (\$)
k	lifetime of the plant
$K(\theta)$	penalty coefficient, dependent on θ (–)
L	collector length (m)
LCOE	Levelized Cost of Electricity (¢/kWh)

M	number of rows of collectors in series (–)
M_y	operation and maintenance expenditures in the year y
\dot{m}	mass flow rate of fluid (kg/h)
N	number of parallel lines (–)
N_h^{cr}	number of critical hours (–)
$N_{parallel}$	number of series collector strings in parallel (–)
N_r	number of rows in the wind power plant (–)
N_{SCA}	total number of collectors (–)
N_{series}	number of collectors in series (–)
N_h^{TES}	number of full load hours of storage (–)
P_w	the output of the wind power-generating unit (kW)
PLSC	Peak Load Shaving Capability (–)
Q_{dump}	dumped thermal energy from the solar field (MWh _t)
Q_u	thermal power output of collector/solar field (MWh _t)
$Q_m^{frm TES}$	maximum power from storage (kW)
$Q_{in,th}^{PB}$	the design turbine thermal input, which is the design-point thermal requirement (MWh _t)
Q_m^{TES}	maximum thermal storage capacity (MWh _t)
$Q_m^{to TES}$	maximum power to storage (kW)
r	discount rate
R_1	constant modifier (–)
R_2	constant modifier (–)
RLCs	Reference Level of Calculation(s) (–)
RLMs	Reference Level of Measurement(s) (–)
SM	Solar Multiple (–)
S_y	investment expenditures in the year y
T_{amb}	ambient temperature (°C)
T_d	dry-bulb temperature (°C)
T_{in}	the temperature of the fluid entering the collector array (°C)
T_{max}	the maximum temperature at which the fluid may exit the collector array (°C)
T_{out}	temperature of fluid exiting the collector array (°C)
u_h	wind speed at the wind turbine's hub height (m/s)
U_L	loss coefficient (W/m ² °C)

u_1	wind speed at a higher altitude (m/s)
u_2	wind speed at a lower altitude (m/s)
VOC	Variable Operating Cost, or operations and maintenance costs per unit of annual electricity production (\$/kWh)
W_{ap}	collector aperture width (m)
y	counting variable for the year (–)
z_1	higher altitude (m)
z_2	lower altitude (m)

Greek Symbols

α	wind shear/exponent (–)
α_r	receiver absorptivity (–)
γ	intercept factor (°)
$\eta_{aux,SF}$	efficiency of solar field auxiliary (%)
$\eta_{d,c}$	cycle efficiency of the power plant with the conventional dry cooling system (%)
$\eta_{d,i}$	cycle efficiency of the power plant with the ideal dry cooling system (%)
$\eta_{net,PB}$	net power block efficiency (%)
$\eta_{optical}$	optical efficiency (%)
$\eta_{overall}$	annual overall plant efficiency (%)
η_{piping}	piping efficiency (%)
η_{shadow}	efficiency considering mutual shading (%)
$\eta_{thermal}$	thermal efficiency (%)
θ	incidence angle (°)
θ_{plant}	wind power plant layout angle (°)
ρ	air density (kg/m ³)
ρ_{clean}	parabolic mirror reflectivity in clean conditions (–)
τ_{glass}	vacuum/glass transmissivity (–)

1. INTRODUCTION

1.1. Chapter journal publications

Some of the work that appears in this chapter is associated with peer-reviewed scientific journal publications. This chapter is associated with publications (1) to (6). The detailed information of these publications is listed in the “Scientific Journal Publications” Section, starting from page (iii) of this thesis.

1.2. Reference concentrating solar power plant

There are four main types of Concentrating Solar Power (CSP) technologies, namely CSP-Parabolic Trough (PT), CSP-Tower, CSP-Fresnel, and CSP-Dish (see Figure 1. 2). The CSP-PT technology is the most popular and represents 76.6-82% of the global installed CSP capacity share, of which 45.9% have 50 MW capacity ratings [5,6]. Built between 1984 and 1991, the largest operating group of solar power plants in the world, with a total capacity of 354 MW_e is the Solar Energy Generating Systems (SEGS) I-IX. The SEGS I-IX group is located within the Mohave desert in southern California in the United States of America (USA) and consists of nine systems [7]. In 2007, the first mega-scale CSP-PT plant without Thermal Energy Storage (TES) in the world (i.e., Nevada Solar One) started operation in the USA. The plant has a net electricity output of 64 MW_e with a solar-only Rankine cycle, and the plant generates 130 GWh of peak power annually with a capacity factor of 23%.

On the other hand, the first mega-scale CSP-PT plant in Europe with TES is the Andasol-1 plant, which has been operational since 2009 in Spain [8]. The Andasol-1 plant is a milestone for this particular technology because it is the first CSP-PT plant in the world with TES capability. Therefore, Andasol-1 is used as the reference plant in this work for assessment purposes, including optimization and performance enhancement. The Andasol-1 plant has a gross capacity of 50 MW and is equipped with a two-tank molten salt TES system. In addition, it has a thermal capacity of nearly 964 MWh along with an oversized Solar Field (SF) to enable TES charging in the daytime and discharging in the nighttime for up to 7.5 h. In summer, it can operate for 20 h at full load on solar energy without the need for a backup system.

Due to its integrated TES system, the reference 50 MW CSP-PT plant (Andasol-1) generates more than the previously-mentioned Nevada Solar One plant, which lacks a TES system and has a larger capacity (64 MW). Several plants worldwide use the design configuration of Andasol-1 since it represents the state-of-the-art configuration of combined CSP-PT with TES. Within the reference CSP-PT plant, the PT collectors are arranged north-south to track the sun movement during the cycle of each day. The consecutive collectors (four to six) are arranged in two rows and connected to a loop (see Figure 1. 1), and the loops are supplied with Heat Transfer Fluid (HTF) from the cold header pipes by a manifold. Then, the hot header pipes collect the heated HTF and direct it to the heat exchanger system.

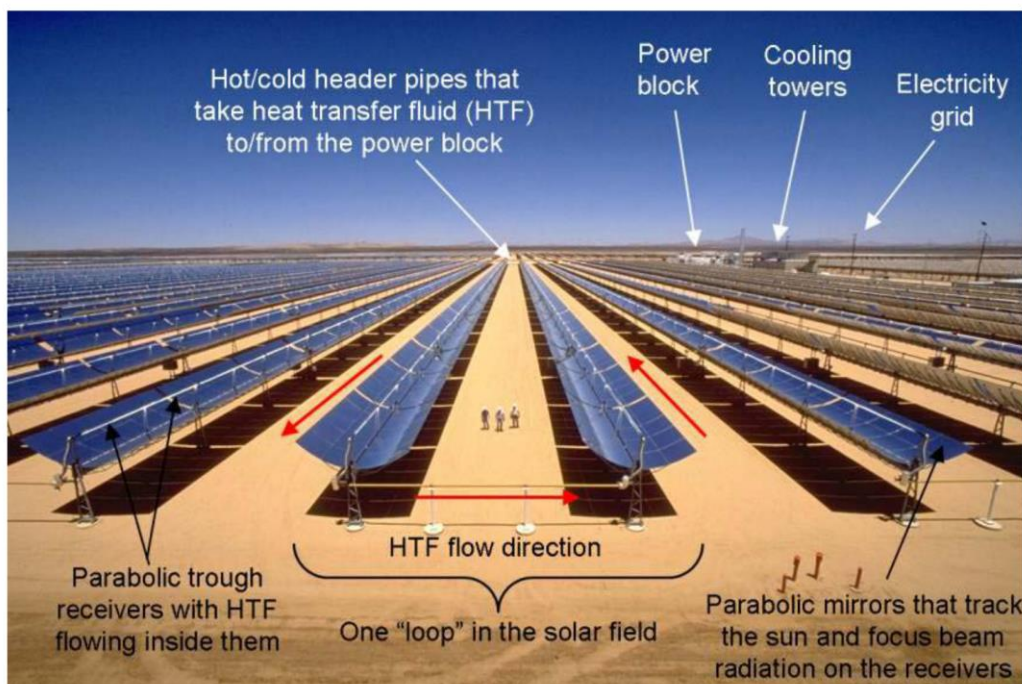


Figure 1. 1 Main system components inside a CSP-PT plant.

Additionally, in the reference CSP-PT plant, the PT collectors are aligned in a north-south direction in the SF system, consisting of 156 loops on an area of 510,120 m². The HTF (Dowtherm A, see Appendix A) flows with a temperature of 293 °C at the inlet and 393 °C at the outlet. Table 1. 1 shows the HTF thermophysical properties of the HTF used within the SF system in the reference CSP-PT plant. The SF system size is selected such that under normal conditions, the rated power is produced while the TES system is fully charged. The TES medium consists of 28,500 t of molten salt, a mixture of 60% sodium nitrate (NaNO₃) and 40% potassium nitrate (KNO₃), inside two tanks (hot and cold) with 14 m in height and 36 m in diameter.

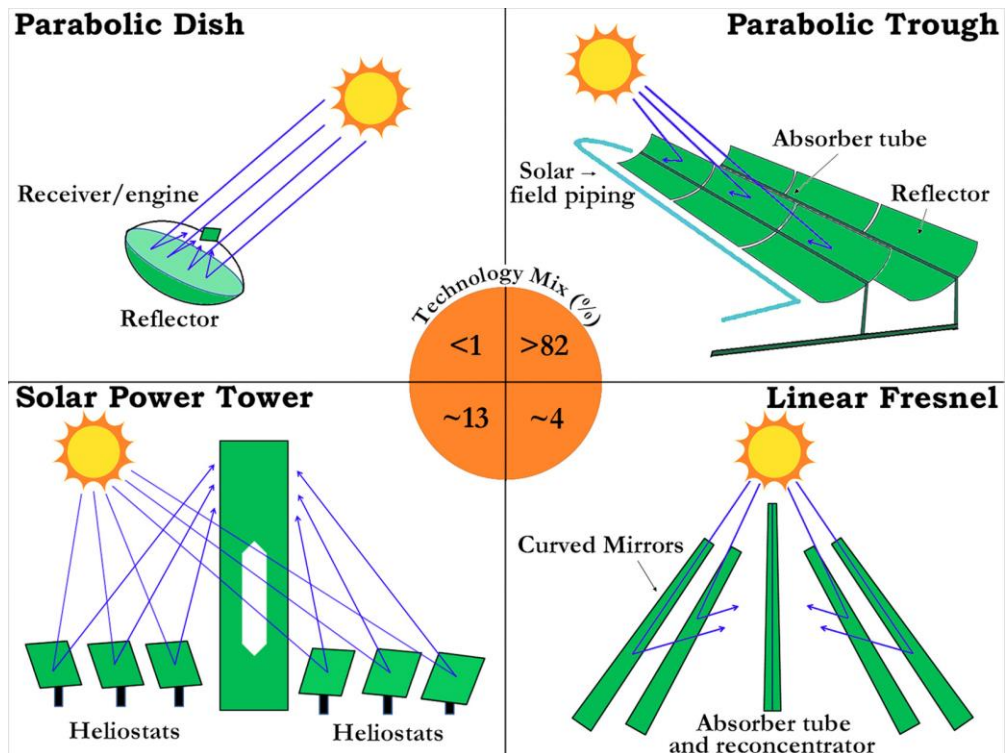


Figure 1. 2 Illustration of the leading CSP technologies and their installed ratio worldwide [6].

Table 1. 1 Thermophysical properties of the HTF used within the SF system in the reference CSP-PT plant

Temperature, °C	Specific Heat, KJ/kg-K	Density, kg/m ³	Viscosity, Pa-s	Kinematic viscosity, m ² -s	Conductivity, W/m-K	Enthalpy, J/kg
15	1.558	1063.5	0.005	4.70E-06	0.1395	23370
65	1.701	1023.7	0.00158	1.54E-06	0.1315	110565
105	1.814	990.7	0.00091	9.19E-07	0.1251	190470
155	1.954	947.8	0.00056	5.91E-07	0.1171	302870
205	2.093	902.5	0.00038	4.21E-07	0.1091	429065
255	2.231	854	0.00027	3.16E-07	0.1011	568905
305	2.373	801.3	0.0002	2.50E-07	0.0931	723765
355	2.527	742.3	0.00016	2.16E-07	0.0851	897085
405	2.725	672.5	0.00012	1.78E-07	0.0771	1.10E+06
600	2.725	672.5	0.00012	1.78E-07	0.0071	1.64E+06

The reference CSP-PT plan uses PT mirrors to heat the HTF to 393 °C. Then, some of the HTF is fed directly to the oil-to-steam heat exchanger to produce power, while the rest of the HTF is passed through an oil-to-salt heat exchanger to heat molten salt in the TES system in an insulated tank at 386 °C [9]. Then, power can be produced as needed when the molten salt heats the HTF, producing superheated steam to feed the PB system [9]. Figure 1. 3 shows a comparison between different

storage media in which it can be concluded that the TES medium (molten salt), which is used in this work, a mixture of 60% sodium nitrate (NaNO_3) and 40% potassium nitrate (KNO_3), has the advantage of a higher working temperature limit with a high melting point (see Table 1. 2 and Appendix B).

TES Material	Melting Point (°C)	Upper Temp limit (°C)	Density ($\text{kg}\cdot\text{m}^{-3}$)	Thermal Conductivity ($\text{W}\cdot\text{m}\cdot\text{K}^{-1}$)	Heat Capacity ($\text{kJ}\cdot\text{kg}\cdot\text{K}^{-1}$)
Mineral Oil	—	300	770	0.12	2.6
Synthetic Oil	—	400	900	0.11	2.3
Silicone Oil	—	400	900	0.10	2.1
Biphenyl/diphenyl oxide (Therminol VP1 oil)	13	400	815	0.21	2.3
Solar salts	220	600	1899	0.52	1.46
Hitec	142	535	1640	0.57	1.6
Hitec XL	120	500	1992	0.53	1.8

*Solar salt (40% KNO_3 +60% NaNO_3), Hitec(53% KNO_3 + 7% NaNO_3 +40% NaNO_2), Hitec XL (45% KNO_3 +48% $\text{Ca}(\text{NO}_3)_2$ +7% NaNO_3)

Figure 1. 3 Comparisons between different TES materials [10].

Table 1. 2 Thermophysical properties of the TES medium used in the reference CSP-PT plant.

Property (unit)	Value
Melting point (°C)	220
Boiling point (°C)	565
Thermal conductivity (W/m K)	0.53
Density (kg/m^3)	1804
Specific heat capacity (kJ/kg K)	1.52
Dynamic viscosity (Pa s)	0.00169
Prandtl number	4.85

1.3. Justification for concentrating solar power assessment

One of the main objectives of this work is to evaluate the techno-economic competitiveness of CSP-PT plants for electricity generation under arid climatic conditions and limited water resources. In addition, the aim is to support the future mega-scale implementation of the CSP-PT technology in the Middle East and North Africa (MENA), including the Gulf Cooperation Council (GCC) region. Such regions

have the advantage of high solar resources and limited water resources, which are needed for wet cooling processes at power plants. Figure 1. 4 shows the locations of some MENA/GCC countries and a detailed map of Kuwait. Figure 1. 5 shows a typical CSP-PT plant layout in Spain with the Power Block (PB) system at the centre and surrounded by the SF system consisting of PT collectors.

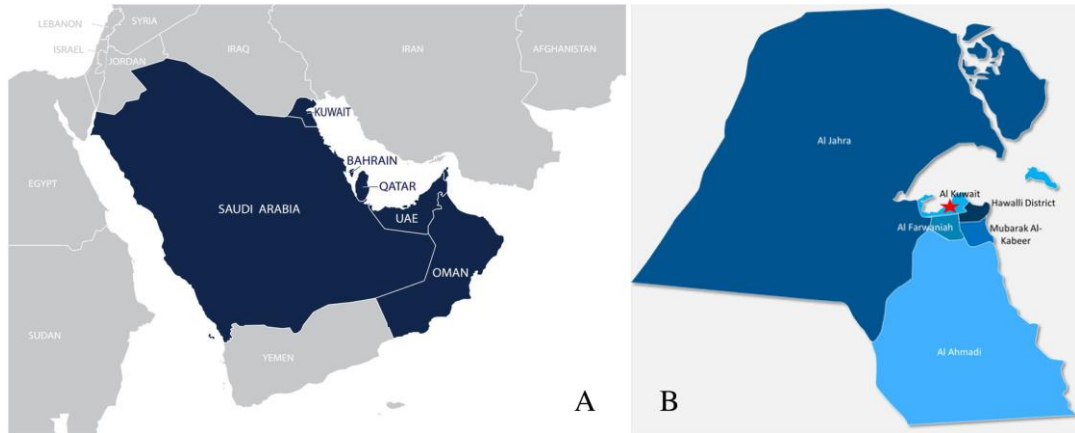


Figure 1. 4 Maps of Kuwait: (A) Kuwait and the other GCC countries in dark-blue colour, and (B) Kuwait governorates named and coloured differently – (Kuwait capital is shown in red star) [11].



Figure 1. 5 The reference 50 MW plant (Andasol-1) in the Granada Province in Spain with the PB system and TES system at the plant centre and surrounded by the SF system [12].

In this work, the performance assessment, enhancement, and optimization objectives are achieved using the reference Andasol-1 plant in Spain, the world's largest installed shareholder of CSP. It should be mentioned that the Andasol-1 plant is located 10 km east of Guadix in the municipal area of Aldeire and La Calahorra in the Marquesado del Zenete region, Granada Province, Spain [12]. Figure 1. 6 shows a schematic illustrating the SF system layout of the Andasol-1 plant. Figure 1. 7 shows a schematic illustrating the TES system layout of the Andasol-1 plant. Furthermore, techno-economic comparisons are drawn with the performance of the same reference plant under the arid climatic conditions of Kuwait.

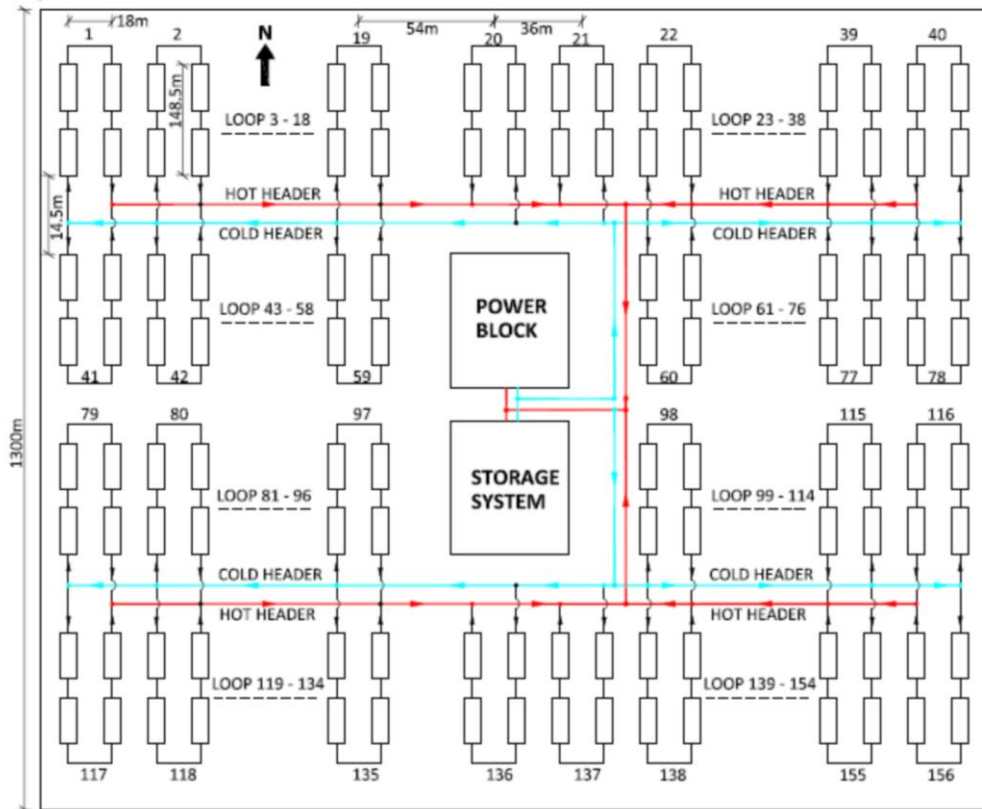


Figure 1. 6 Schematic illustrating the SF system layout of the Andasol-1 plant [13].

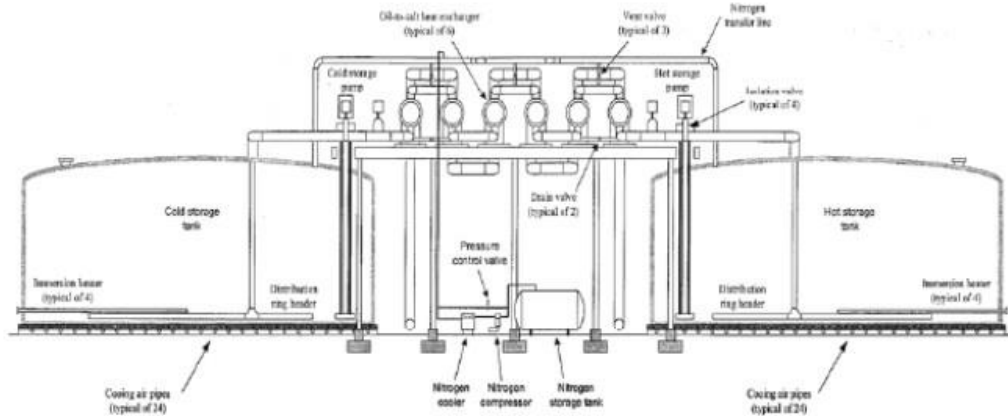


Figure 1. 7 Schematic illustrating the TES system layout of the Andasol-1 plant [14].

The following are the reasons for investigating the Kuwait case: (i) a detailed techno-economic assessment of the CSP-PT technology under the arid climatic conditions of Kuwait has not, as yet, been published prior to this work, (ii) Kuwait experiences extreme conditions; for example, the maximum temperature reached 54 °C during July 2016 in the shade, reported as the hottest reliably measured air temperature on Earth [15–19], (iii) Kuwait has one of the heavily subsidized prices of electricity worldwide with 0.66 US-¢/kWh from fossil-based plants [20–22]; therefore, the

Kuwait case represents a challenging one for evaluating the techno-economic competitiveness of renewable technologies, such as CSP-PT and wind power, (iv) Kuwait has a strategic target for achieving 15% of the electricity demand from renewables by the year 2030, and the technology mix shares have not, as yet, been finalized, (v) Kuwait is a MENA/GCC member [11], (vi) the CSP-PT technology has the advantage for retrofit applications within existing fossil-based power plants by employing only the SF system, leading to minimizing investment cost, (vii) the exclusive electricity provider in Kuwait is government-owned and reliant on fossil fuels; hence, assessing CSP-PT performance for electricity generation in a major oil-producing country, such as Kuwait, is highly encouraged for oil conservation, (viii) dispatchable renewable power, such as combined CSP-PT with TES, should be considered as an attractive solution for electricity generation because such configuration has the advantage of providing electricity on demand similar to conventional technologies, (ix) Kuwait had held the world's lowest comparative price of residential electricity in 2005 [23], and (x) Kuwait had held the world's largest comparative size of per capita residential electricity consumption in 2010 [23]. Moreover, Figure 1. 8 compares countries based on electricity consumption and carbon dioxide (CO₂) emissions, with Kuwait among the top [23–27].

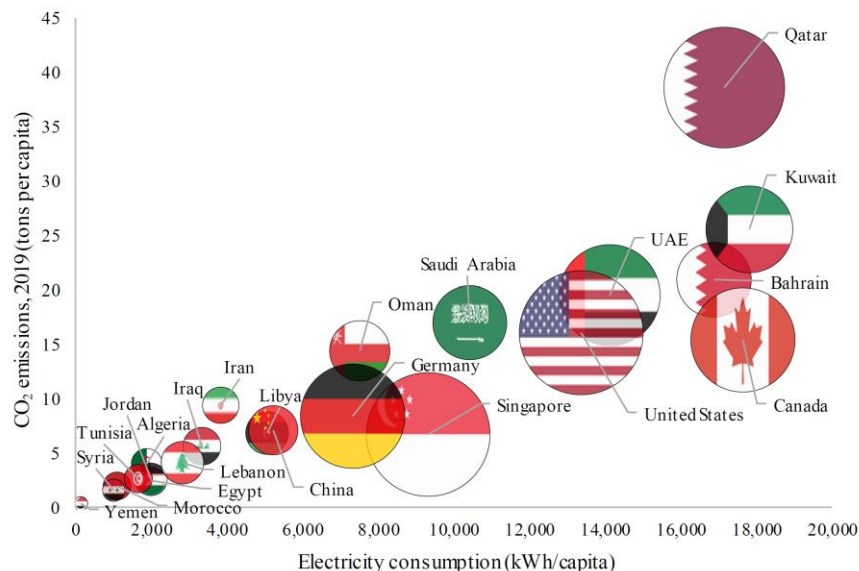


Figure 1. 8 Comparison based on electricity consumption and CO₂ emissions (the size of bubbles shows the gross domestic product per capita in 2019) [27].

Kuwait has one of the heavily subsidized electricity prices in the world, with 0.66 ¢/kWh from fossil-based power plants, as shown in Figure 1. 9 [20–22]. It should be noted that the Levelized Cost of Electricity (LCOE) from the CSP-PT technology is

currently approaching the global fossil-fuel cost range with promises of further LCOE reductions in the future.

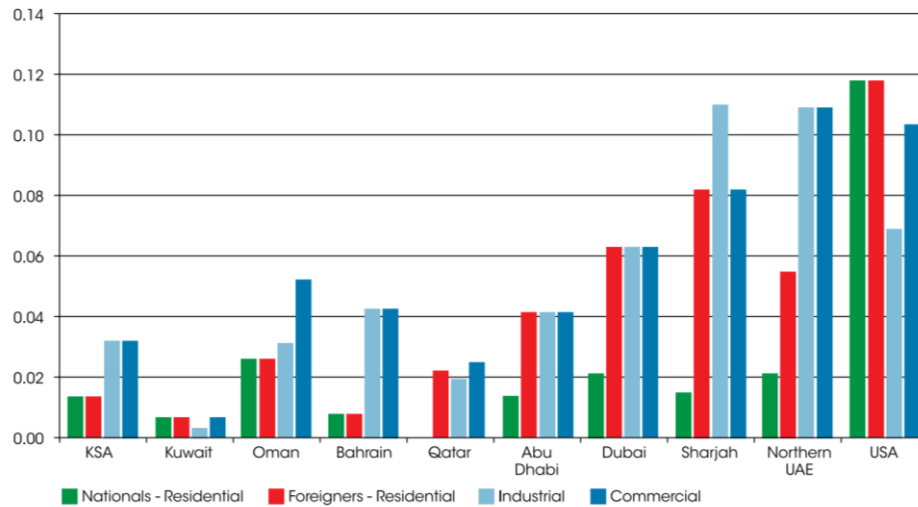


Figure 1. 9 Subsidised electricity prices in the GCC region and the USA as of 2011, with Kuwait having the lowest rate (y-axis unit: US-\$/kWh) [21,22].

The performance of the CSP-PT technology with a dry-cooled condenser system is assessed to evaluate several technical aspects, including the total water consumption savings. Such assessment is needed because one of the highest solar resources is located in Shagaya (i.e., the chosen location in this work), which has limited water resources within the western region of Kuwait [28]. Moreover, the chosen location has minimal oil/gas field concentrations and has one of the highest wind resources [28,29]. After considering the distribution of the transmission networks in Kuwait [30], it can be observed that the capacity factor of future networks in the chosen location can be maximized. This can be achieved if the coinciding peaks in the solar and wind resources are considered in determining future renewable power technology shares. Furthermore, such an approach can minimise the LCOE through renewable technology hybridization, especially since CSP-PT is dispatchable once combined with TES [31], but wind power is not. Alternatively, various grid services can be offered, such as spinning reserves with dispatchable power. Figure 1. 10 shows that the chosen location in the western region has minimal oil and gas field concentrations. Figure 1. 11 illustrates a map of Kuwait showing the western region with minimal transmission networks. From Figure 1. 11, it should be recognized that the capacity factor of future networks in the chosen location can be maximized due to the peak in the solar and wind resources. Hence, detailed assessment and optimization to minimize the LCOE from hybridizing

optimal design configurations of solar and wind power plants are highly encouraged, emphasizing the importance of this work.

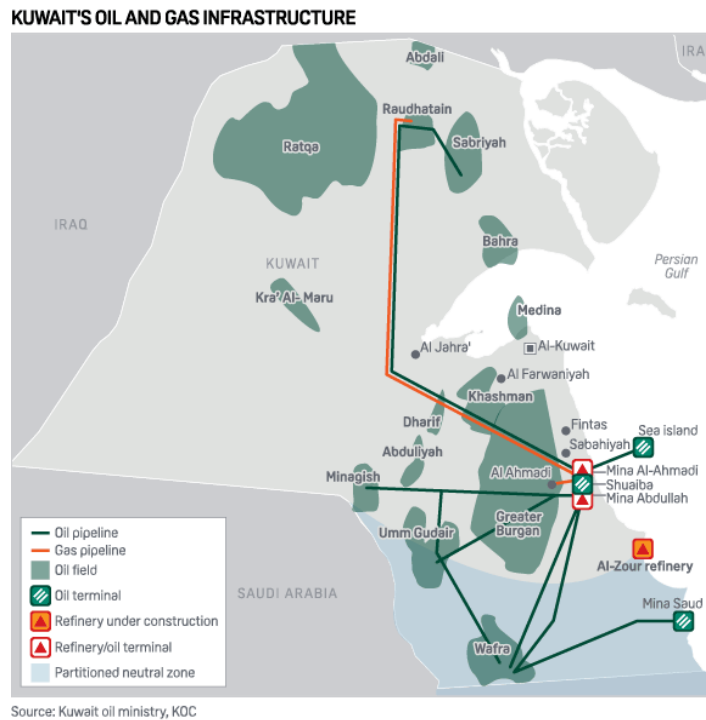


Figure 1. 10 Kuwait map showing the western region with minimal oil and gas field concentrations [32].

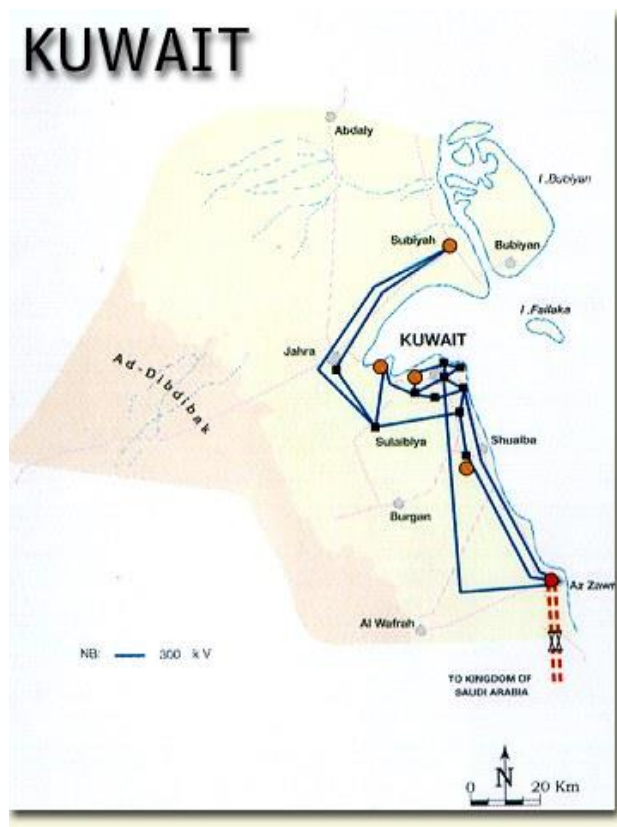


Figure 1. 11 Kuwait map showing the western region with minimal transmission networks [30].

As mentioned earlier, solar and wind resources are at peak levels in the chosen location, with minimal oil and gas field concentrations [28,29,32–34]. Therefore, utilizing the CSP-PT technology for electricity generation can provide economic benefits for Kuwait compared to the current business-as-usual scenario, which is the production of electricity from fossil-based power plants and then selling at heavily subsidized rates as low as 0.66 ¢/kWh (see Table 1. 3). Generally, most consumers in Kuwait are in the residential sector and pay about 6% (i.e., 0.66 ¢/kWh) of the average actual cost of electricity due to the massive subsidies. It should be noted that the average actual cost of electricity in the conventional plants of Kuwait is 14 ¢/kWh [35–37]. For CSP, the power capacity of a plant has a high impact with different ranges on the LCOE (economy of scale). Also, the LCOE estimations for CSP technologies are progressively approaching the fossil-fuel cost range [38]. Hence, CSP will play an essential role in the global energy mix in the future. Figure 1. 12 shows the LCOE comparisons between renewable power projects with the fossil-fuel cost range.

Table 1. 3 Summary of the subsidized electricity prices for different consumer categories in Kuwait.

Sector	Category	Prior to 2017		From 2017		Monthly electricity consumption range, kWh
		Fils/kWh	¢/kWh	Fils/kWh	¢/kWh	
Residential	Private houses	2	0.66	2	0.66	All ranges
	Apartments	2	0.66	5	1.65	≤ 1,000
		2	0.66	10	3.30	1,001 – 2,000
		2	0.66	15	4.95	> 2,000
Governmental		2	0.66	25	8.25	All ranges
Commercial		2	0.66	5	1.65	All ranges
Industrial	Productive	2	0.66	3	0.99	All ranges
	Non-Productive	2	0.66	5	1.65	All ranges
Agricultural	Productive	2	0.66	3	0.99	All ranges
	Non-Productive	2	0.66	5	1.65	All ranges
Others (e.g., chalets)		2	0.66	12	3.96	All ranges

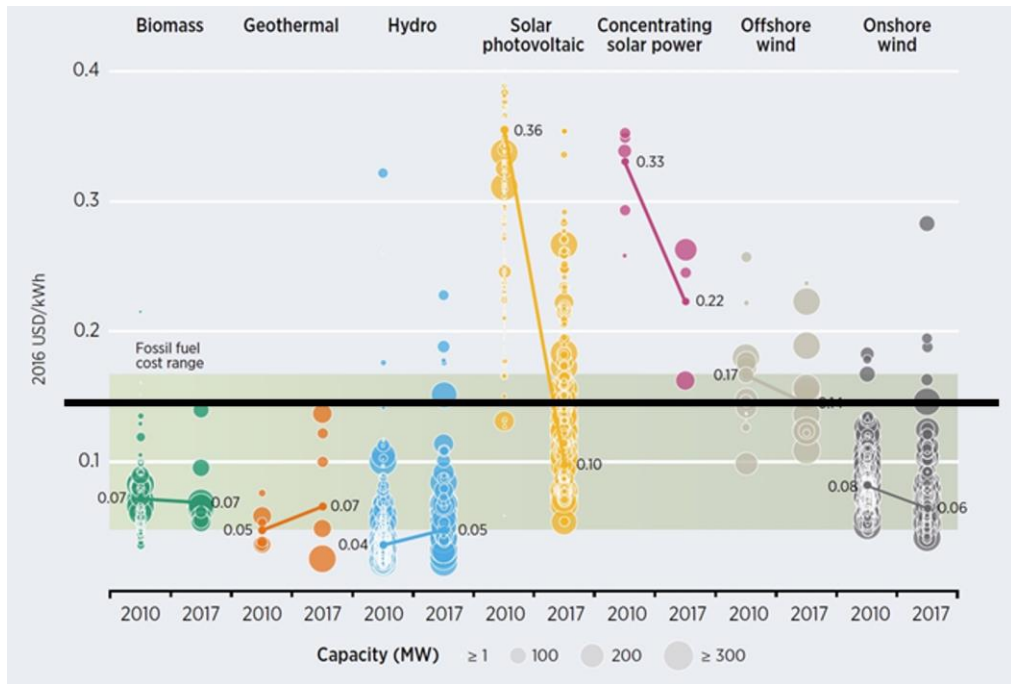


Figure 1. 12 LCOE estimations of renewable power projects [38] (the horizontal black-coloured line is added to the figure to indicate the average actual cost of electricity from the fossil-based power plants in Kuwait).

1.4. Assessment approach for concentrating solar power

The oil reserve of Kuwait is ranked in sixth place with 102 Gbbl (i.e., 6% of the global reserve). The oil sector accounts for 40% of the gross domestic product and 92% of the export revenues. However, the reliance on oil export is no longer viable, given the unpredictable global market shifts. In Kuwait, initial studies on natural resources and renewable energy technology assessments have encouraged the future establishment of mega-scale renewable energy projects [28,33,39–43]. The studies share at least one objective: to preserve the natural resources of Kuwait and protect its environment [44].

In this work, one of the goals is to assess the performance of CSP-PT design configurations. The assessment considers several CSP-PT design configurations, including 19 optimal configurations specific to the climatic conditions of the chosen location in Kuwait. The 19 optimal configurations have optimal Solar Multiple (SM) values based on the lowest LCOE. After evaluating 589 different design configurations through a detailed parametric analysis and validating a 50 MW CSP-PT model, the selection of the 19 optimal configurations is performed. It should

be recognized that the SM value is used to determine the SF system area as a multiple of the rated capacity of the PB system (i.e., the design turbine gross output). It should be mentioned that the chosen location has an annual Direct Normal Irradiance (DNI) of approximately 1857.1 kWh/m²yr.

As mentioned earlier, the CSP technologies consist of four technologies: CSP-PT, CSP-Tower, CSP-Fresnel, and CSP-Dish. The CSP-PT technology represents 76.6% of the global installed share, of which 45.9% are rated as 50 MW [5] (see Figure 1. 13). In general, an investment in a mega-scale renewable power plant, such as CSP-PT, begins with some critical stages. One of these stages is design optimization, which varies based on location and climatic conditions. Different locations should have different optimal configurations, depending on the plant’s operational philosophy and design criteria. In most scenarios, the design is approved once demonstrated through performance simulation to achieve the desired economic feasibility for the proposed project lifetime, highlighting the importance of this work.

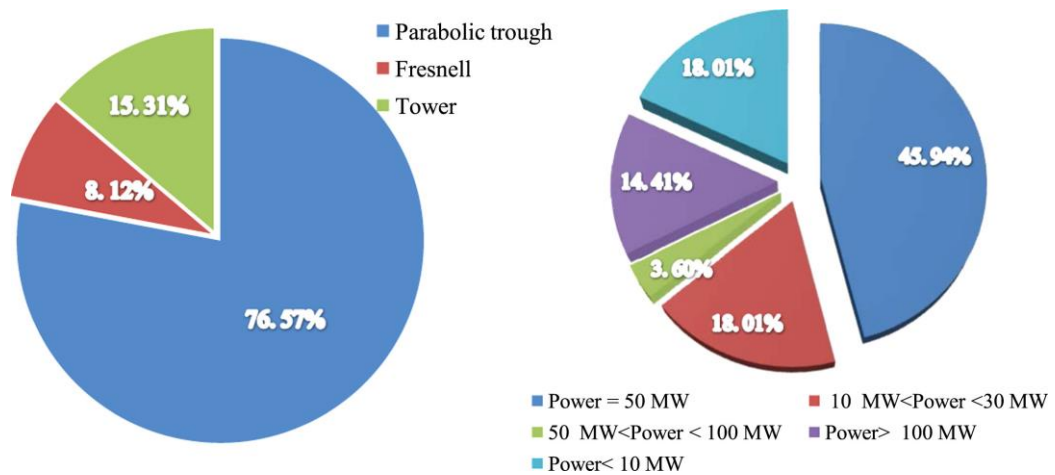


Figure 1. 13 Global installed CSP capacities by technology and magnitude of the PB system in which the CSP-PT technology and the 50 MW capacity rating dominate globally [5].

1.5. The 2030 vision and renewable energy

The techno-economic assessment and optimization of wet and dry-cooled CSP-PT plants for electricity generation are to be evaluated for the chosen location in Kuwait, with an average DNI of about 5.1 kWh/m²/d. By the year 2030, Kuwait should invest in approximately 4,500 MW of renewable power to reach a strategic target of achieving 15% of electricity demand from renewables. Kuwait has already ratified the framework convention on climate change in 1995 and the Kyoto protocol in 2005. Furthermore, Kuwait submitted the initial national communications in 2012 and the

Nationally Determined Contributions (NDCs) in 2015 as part of the Paris Agreement. The NDCs included proposed projects and steps demonstrating a sustainable development plan until 2035.

The government-owned power sector in Kuwait is reliant primarily on fossil fuel-based operations. Therefore, the current focus should be on achieving the 15% of electricity demand from renewables by utilizing wind and solar resources, which are abundant. Hence, the potential challenges facing CSP-PT and wind power should be evaluated due to the heavily subsidized electricity prices in a major oil-producing country like Kuwait. In this work, optimization, performance evaluation, and enhancement strategies are studied to assess the implementation of renewable power technologies, which are relatively new to Kuwait. Furthermore, the current focus for advancing the CSP-PT technology is to increase its feasibility under the arid climatic conditions of the MENA regions, including the GCC, since these regions have the advantage of both high solar and wind resources. Therefore, some of the technical and economic challenges for CSP-PT and wind power implementations to achieve the above target (15%) are to be evaluated since Kuwait experiences extreme arid climatic conditions and is both a MENA and GCC member [11].

1.6. Coordination of wind and concentrating solar power with thermal energy storage

Kuwait had held the world's lowest comparative price of residential electricity in 2005 and the largest comparative size of per capita residential electricity consumption in 2010 [23]. Besides, Kuwait has an arid desert environment, one of the harshest in the MENA/GCC regions. In 2016, the maximum temperature reached 54 °C in the shade, reported as the hottest reliably measured air temperature on Earth [15–19]. The total area of Kuwait is approximately 17,818 km² [45], primarily flat desert land. Although there is limited research on wind power and CSP-PT/TES coordination, none of the published studies provides a detailed performance assessment and optimization of these technologies under Kuwait's climatic conditions. It should be mentioned that the intermittency in the wind resource can be overcome by introducing an optimal TES system to the CSP-PT technology to offer beneficial dispatchability features [31]. This approach is helpful, especially since wind power is currently more economically competitive than CSP-PT.

One of the motivations of this work is that studies in line with the enerMENA project framework are highly encouraged. Such studies should prepare the ground for mega-scale CSP-PT implementation in the MENA/GCC regions and the proposed connection to the European grid network. Therefore, research and development are critical for reducing and improving renewable technologies in these regions, mainly developing countries [46].

This work aims to assess, optimize, and enhance the performance of CSP-PT/TES and wind power for electricity cogeneration under arid climatic conditions. The future implementations of CSP-PT and wind power technologies in the MENA/GCC regions have already been planned on a mega-scale level by introducing and announcing strategic national targets by many countries. However, the technical challenges in the implementation process are inevitable. Some of these challenges should be investigated because such regions have the advantage of high solar and wind resources but limited water resources for cooling processes needed in power plants, as in the case of Kuwait.

The detailed coordination of CSP-PT/TES and wind power has never been investigated for the Kuwait case prior to this work. Furthermore, the topic is challenging considering the various economic, environmental, and political constraints facing Kuwait, including the national target for achieving 15% penetration in electricity demand from renewable technologies by 2030. In Kuwait, the CO₂ emission rate has increased from 73.1 Mt in 2007 to 99.4 Mt in 2017 within only a decade [47–50]. It should be noted that renewable technology mix shares have not been finalized yet to achieve the 15% target for Kuwait. One of the essential objectives of this work is to utilize the dispatchability of CSP-PT/TES [51] to reduce the intermittency in the solar and wind resources, especially when accompanied by wind power.

In this work, the CSP-PT/TES performance using dry-cooled and wet-cooled condensers is assessed since the highest solar resource (i.e., DNI) is located in the chosen location, with limited water resources [28]. In addition, this location has high wind resources with minimal transmission networks to accommodate the 15% target mentioned above [28–30,32–34]. Furthermore, the location has minimal concentrations of oil and gas fields [29,52]. Therefore, the capacity factor of future networks at this location can be maximized if the coinciding peaks in the solar and wind resources are appropriately considered, as will be shown in Chapter 4.

This work supports implementing CSP-PT/TES and wind power for electricity cogeneration in an arid desert environment, which experiences high solar/wind resources, limited water resources, and minimal transmission networks. The dry-cooled CSP-PT performance is evaluated along with the wet-cooled one to overcome technical limitations. Furthermore, the coordinated scheme potential between CSP-PT/TES and wind power is also studied to maximize the capacity factor of future transmission networks in the chosen location by reporting optimal design configurations of various CSP-PT and wind power plant capacities. These optimal configurations are specific to the chosen location's climatic conditions. In addition, a detailed evaluation of the wind speed profiles in this location is performed since wind contributes to the initiation of sandstorms in desert regions and because sandstorms contribute to the degradation of CSP-PT performance. Especially since the sandstorm effect can be observed in the erosion of the reflectors and PT collectors in hot and arid environments similar to Kuwait.

1.7. Reference wind power plant and technology selection

In a typical wind power plant, the most effective method to increase the energy yield is to accurately predict wind availability, directly impacting electricity generation from wind turbines. Extending this understanding to the entire plant's lifetime emphasizes the importance of a reliable and detailed wind resource assessment before the design and optimization stages to maximize wind availability estimation for a specific location. In addition to reliable resource assessment at the wind turbine's hub height, understanding the turbine design characteristics, such as power curve, is critical for predicting energy generation accurately. Based on physical principles, the prevailing wind's kinetic energy is the primary determinant that allows wind energy extraction through the turbines' blades when sufficient wind speeds are encountered. Generally, wind density is influenced significantly by ambient temperature, atmospheric pressure, and relative humidity. Thus, wind density and wind speed define the kinetic energy in the blowing wind (see Appendix E). However, in a desert region like Kuwait, the ambient temperature is at extreme levels. Hence, the impact of harsh conditions should be investigated, along with the wind resource and wind turbine's design characteristics, significantly since the wind

resource can be affected by complex factors impacting the reliability and feasibility of generation.

Ideally, wind speed and direction measurements should be obtained, preferably at the reference wind turbine's hub height. Furthermore, it is critical to estimate the wind shear (α), which is the change in the wind speed with height above ground. In addition, ambient temperature, atmospheric pressure, and relative humidity are necessary for density calculation concerning any location under consideration as they directly affect the turbine's power output.

Indeed, many countries have focused on implementing renewable power technologies in the last few decades due to their electricity prices, which have shown competitiveness with fossil-based generation. Certainly, Kuwait is one of the countries that showed initial interest in the renewable energy arena as a MENA/GCC member [11]. Therefore, some studies [28,33,39–43] have promoted the initiation of wind and solar projects. Several advantages have been reported for establishing a renewable energy presence in an oil-rich country, such as Kuwait, including environmental benefits and enhancing the quality of life and health [44].

One of the main objectives of this work is to perform a techno-economic assessment and optimize wind power design configurations for electricity generation to suit Kuwait desert's wind resource and climatic conditions. It should be recalled that the chosen location is approximately 100 km from the capital city. Additionally, this location is at an elevation of roughly 240 m above sea level. Furthermore, the location is characterized by a plain topography and simple terrain without significant obstacles from the surroundings that would influence the wind and disturb its flow. Also, the location has no existing vegetation and obstructions that would promote shading effects or wind disturbances.

Another objective is to perform detailed parametric analyses and identify optimal design configurations for wind power plants with various capacity ratings. The chosen location in this work has an existing 10 MW wind power plant (5×2 MW), which is the first wind power plant in Kuwait and has a recent commission date. After one year of operation, it was revealed that the plant had produced energy production numbers that exceeded the industry average [53–56]. Hence, this work will perform a detailed techno-economic assessment and optimization for higher capacity wind power plants using a 2 MW rated wind turbine (i.e., the reference

wind turbine). This 2 MW turbine is used in the existing 10 MW wind power plant mentioned above.

1.8. Justification for wind power assessment

According to a study [53], the monthly calculated capacity factor was obtained during the first year of operation for the existing 10 MW plant mentioned above and found to be near-record numbers reported worldwide. Thus, it is essential to assess larger capacities of wind power plants for mega-scale commercial installations in the future to achieve Kuwait's 15% strategic target by 2030. Hence, a detailed techno-economic assessment and optimization of wind power plants for electricity generation under Kuwait's arid climate is performed in this work. One of the objectives is to provide necessary technical and economic data to aid in achieving this target to maximize renewable penetration. The chosen location has one of the highest wind and solar resources with minimal transmission networks [28–30,32–34]. Furthermore, this location has minimal concentrations of oil and gas fields [29,52]. Therefore, the capacity factor of future networks can be maximized if the wind resource peaks are identified for wind power dispatch scheduling. Also, using wind power for electricity generation will provide economic benefits for Kuwait compared to the current business-as-usual scenario. This work supports implementing wind power for electricity generation in a desert environment with high wind resource potential, limited water resources, and minimal transmission networks. A detailed evaluation of the wind resource is performed since wind initiates sandstorms, which contribute to the degradation of wind turbine performance. The effect of sandstorms can be seen in the erosion of the turbine blades in hot and arid environments.

1.9. Chapter conclusion

The main findings are summarized as follows:

- i. the CSP-PT technology is the most popular and represents 76.6-82% of the global installed CSP capacity share. Therefore, the CSP-PT technology is to be investigated in this work for performance assessment, optimization, and enhancement purposes,

- ii. the Andasol-1 power plant in Spain is a milestone for the CSP-PT technology because it is the first CSP-PT plant in the world with TES capability,
- iii. approximately 45.9% of the global CSP-PT installations have 50 MW capacity ratings [5,6]. Therefore, a CSP-PT plant with a 50 MW capacity (Andasol-1) is selected for performance assessment and optimization of the CSP-PT/TES technology,
- iv. Kuwait experiences extreme climatic conditions; for example, the maximum temperature reached 54 °C in July 2016 in the shade, reported as the hottest reliably measured air temperature on Earth [15–19],
- v. Kuwait has a strategic target for achieving 15% of the electricity demand from renewable technologies by 2030, and the technology mix shares have not, as yet, been finalized,
- vi. Kuwait is a MENA/GCC member [11] and has one of the heavily subsidized prices of electricity in the world, with 0.66 ¢/kWh from fossil-based power plants [20–22],
- vii. dispatchable renewable power, such as combined CSP-PT with TES, should be considered an attractive solution for electricity generation in Kuwait because such configurations offer the advantage of providing electricity on demand, similar to fossil-based power technologies (e.g., gas turbines),
- viii. dispatchable CSP-PT/TES accompanied with wind power can minimize the intermittences in the solar and wind resources,
- ix. the detailed coordination of CSP-PT/TES and wind power has never been investigated for the Kuwait case prior to this work, and
- x. the Kuwait case represents a challenging one for evaluating the techno-economic competitiveness of renewable technologies such as CSP-PT/TES and wind power due to various economic, environmental, and political constraints, including the national target for achieving a 15% penetration in electricity demand from solar and wind power technologies by the year 2030.

2. LITERATURE REVIEW

2.1. Chapter journal publications

Some of the work that appears in this chapter is associated with peer-reviewed scientific journal publications. This chapter is associated with publications (1) to (6). The detailed information of these publications is listed in the “Scientific Journal Publications” Section, starting from page (iii) of this thesis.

2.2. Background

By the end of 2017, renewable energy had a 26.5% electricity production share, and the global capacity of CSP reached 4.9 GW [57], as shown in Figure 2. 1. The USA and Spain are where most CSP plants are located, with Spain having the largest installed share of CSP in the world, as shown in Figure 2. 2. It should be noted that wind power has the maximum share (5.6%) of the total renewable energy electricity production (26.5%), leaving the non-renewable electricity share accounting for the remaining 73.5%.

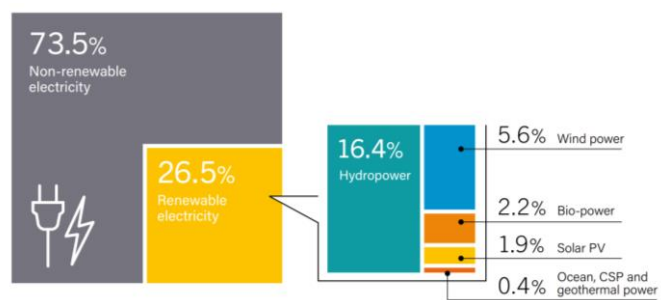


Figure 2. 1 Global technology shares for electricity production [57].

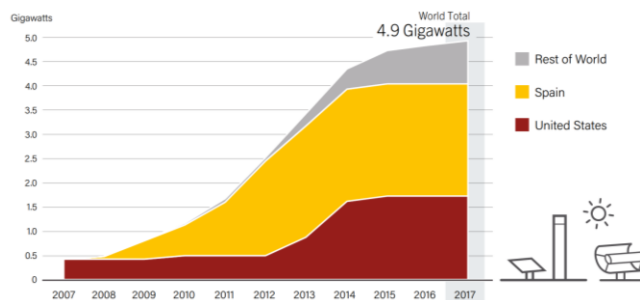


Figure 2. 2 Global technology shares: capacity of CSP (2007-2017) with Spain (the location of the reference CSP-PT plant in this work) holding the maximum share [57].

According to the International Energy Agency (IEA) [58], the country rankings in electricity generation and fuel sources are as follows: (i) China, USA, India, and Japan for using coal, (ii) Saudi Arabia, Japan, Iraq, and Kuwait for using oil, (iii) USA, Russia, Japan, and Iran for using Natural Gas (NG), and (iv) China, USA, Brazil, and Canada for using renewables. In the Middle East, energy consumption increases rapidly because most countries are developing (industrial growth effect). The rates of the increase in energy consumption for different countries are as follows: (i) Iran by 502% during 25 years (1980-2009) [59,60], (ii) Jordan by 27% during 13 years (1979-2010) [61], (iii) United Arab Emirates (UAE) by 152% during 14 years (1996-2010) [62,63], (iv) Bahrain by 234% during 15 years (1977-1992) [64], (v) Kuwait by 77% during 10 years (1995-2005) [65], (vi) Oman by 130% during 6 years (1990-1996) [66], and (vii) Syria by 50% during 7 years (2000-2007) [67] (see Table 2. 1).

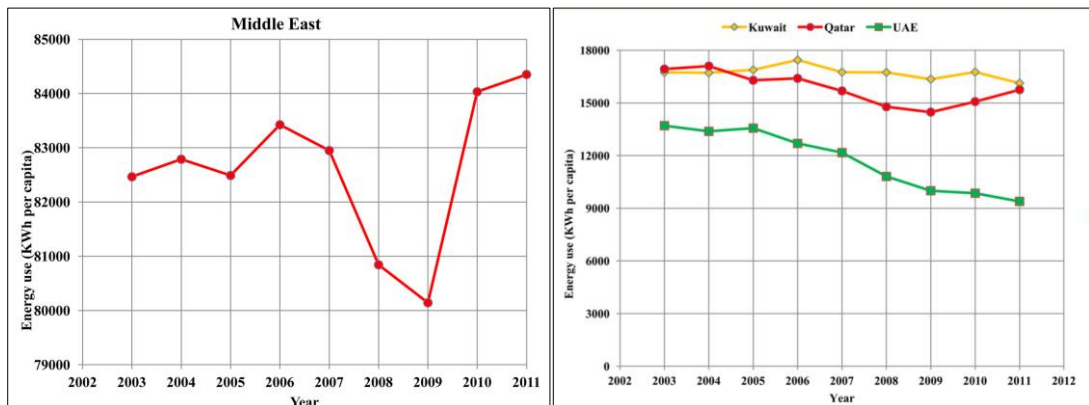
Table 2.1 Energy consumption in selected countries in the Middle East [68].

Country	Energy consumption	Unit	Year	Reference
Iran	193.20	Mbbl	1980	[59]
	650.70	Mbbl	2000	[59]
	1,164.00	Mbbl	2009	[60]
Jordan	10.28	Mbbl	1997	[61]
	12.76	Mbbl	2004	[61]
	13.07	Mbbl	2010	[61]
Saudi Arabia	1.11	Mbbl	1970	[69]
	271.74	Mbbl	1983	[70]
	1,020.00	Mbbl	2008	[69]
UAE	228.80	Mbbl	1996	[62]
	397.60	Mbbl	2005	[63]
	575.70	Mbbl	2010	[63]
Egypt	250.00	Mbbl	1994	[71]
	250.83	Mbbl	1996	[71]
	185.52	Mbbl	2008	[72]
Bahrain	refined gasoline: 638,000	US-bbl	1977	[64]
	refined gasoline: 2,131,000	US-bbl	1992	[64]
Kuwait	85.00	Mbbl	1995	[65]
	150.00	Mbbl	2005	[65]
Oman	18.02	Mbbl	1990	[66]
	41.37	Mbbl	1996	[66]
Syria	107.85	Mbbl	2000	[67]
	149.73	Mbbl	2005	[67]
	161.40	Mbbl	2007	[67]

For the per capita electricity consumption, Kuwait is at the top rank [73,74] in the range of 16,000-17,000 kWh per capita from 2003 to 2011 [68] (see Figure 2. 3). It is worth mentioning that NG development in the Middle East is due mainly to the power generation and petrochemical sectors. Furthermore, the share of oil in electricity production decreased (54% in 1971 and 28% in 2016) [75], as shown in

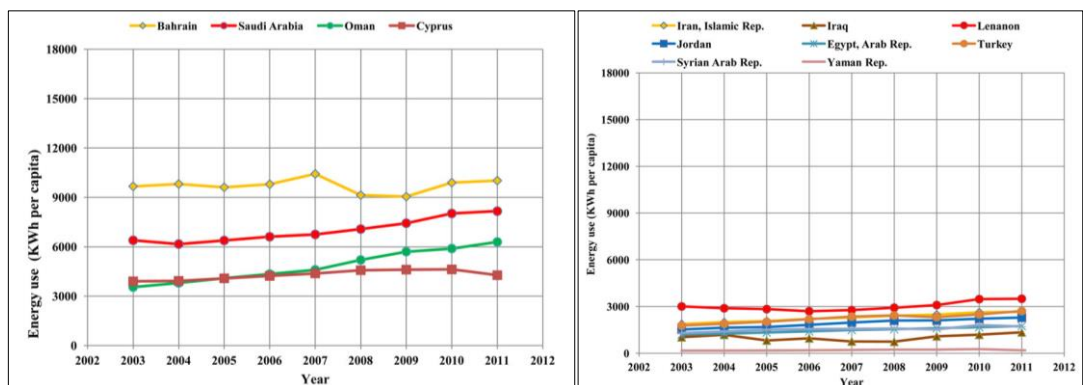
Figure 2. 4. On the whole, the breakdown of the world gross electricity production is as follows [76]: (i) 65.1% from fossil fuels (coal, oil, NG), (ii) 2.3% from biofuels, waste, (iii) 16.6% from hydroelectric plants including pumped storage, (iv) 10.4% from nuclear plants, (v) 5.6% from geothermal, solar, wind, tidal, other sources, and (vi) 2.3% from biofuels and waste.

According to IEA [76], the following shares are allocated: (i) the combined share for the total consumption of the residential sector along with the commercial and public service sector has increased from 48.4% in 1974 to 62.9% in 2016, (ii) the amount of electricity consumption in the industry sector has increased from 1874 TWh (1974) to 3031 TWh (2016) [76], and (iii) the industry share of total electricity consumption has decreased from 48.7% (1974) to 31.9% (2016). As of 2016 [58], the global electricity generation is 24,973 TWh with the following share distributions: (i) 38.4% coal, (ii) 3.7% oil, (iii) 23.2% NG, (iv) 10.4% nuclear, (v) 16.3% hydro, and (vi) 8% non-hydro renewables/waste (see Figure 2. 5).



(i)

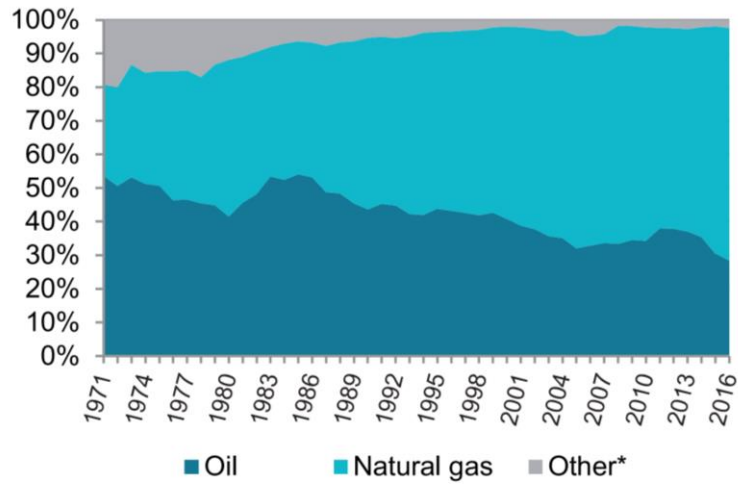
(ii)



(iii)

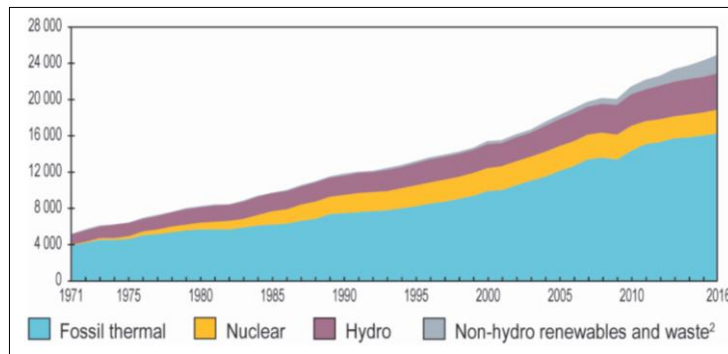
(iv)

Figure 2. 3 Annual variations for energy use per capita in the Middle East (i), and energy use in Middle Eastern countries showing Kuwait at the top rank (ii, iii, iv) [68,74].

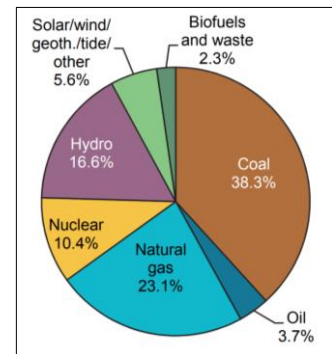


* Includes coal, nuclear, hydro, other renewables, biofuels and waste.

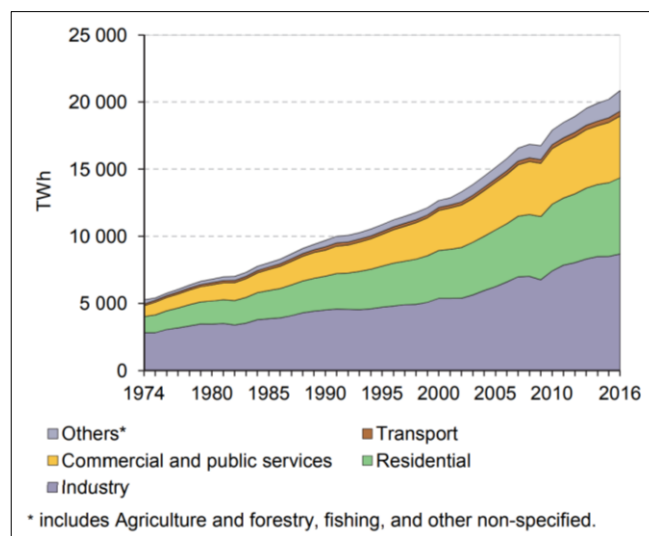
Figure 2. 4 Electricity generation by source in the Middle East [75].



(i)



(ii)



(iii)

Figure 2. 5 Global estimates: (i) electricity generation between 1971-2016 by fuel (in TWh) [58], (ii) gross production by source for 2016 [76], and (iii) consumption by sector for 1974-2016 [76].

2.3 Experiences of the Middle East and North Africa, and the Gulf Cooperation Council

2.3.1 Distinguished Middle East and North Africa experience of Morocco

In Morocco, the Greenhouse Gas (GHG) emissions from fuel combustion are estimated at 42.1 Mt of CO₂ for 2008, with an expected rise to double that amount by 2020-2025 due to the growth in the residential and energy sectors. It should be mentioned that Morocco signed the United Nations Framework Convention on Climate Change (UNFCCC) in the year 1992 and ratified it in the year 1995. The country formed a national committee on climate change in 1996 and a national scientific and technical committee in 2000. In 2001, Morocco submitted the first national communication on climate change and ratified the Kyoto Protocol in 2002 [77,78]. Morocco's energy consumption distribution is as follows: 61.9% petroleum, 22.5% coal, 6.9% electricity trade, 1% wind, 3% hydropower, and 4.6% NG. The electricity production profiles are as follows: 53.4% coal, 15.8% import, 0.8% wind, 6.1% hydropower, 12.1% gas, and 11.8% oil. The installed capacity targets in 2020 are categorized as follows: 14% solar power, 27% coal, 10% fuel, 21% gas, 14% hydropower, and 14% wind power [79]. In 2008, the government set renewable energy implementation targets. The renewable energy share in 2020 is expected to be 42% of the installed capacity, which is 2 GW of solar power, 2 GW of wind power, and 2 GW of hydropower. The electricity demand increased by an annual average of 6.8% between 2000 and 2011. As a result, consumption per capita increased by 5.2% per year on average. Some estimates reveal that the consumption could double by 2020 and quadruple by 2030 [80]. Moreover, Morocco was dependent on energy imports within the last decade since only 1% of the consumed fossil fuels have been produced locally [46,81].

According to a study [82], the most advanced technology for solar thermal power is CSP. The MENA desert has the advantage of high solar resources, which contributes to the popularity of CSP [83,84]. The initiative to utilize MENA desert lands to construct future CSP plants and electricity export to Europe is the most encouraging near-term prospect for CSP [85,86]. The German Aerospace Center

(DLR) has promoted renewable energy in the MENA region. There exists a network of meteorological stations under cooperation between DLR, international research institutes, and industry partners [87]. The aim is to provide reliable meteorological data of the MENA region, critical for CSP performance predictions. This network was established as part of the enerMENA initiative to shut down nuclear plants in Germany by 2022. The existing and planned grid interconnection (see Figure 2. 6) between countries in GCC, MENA, and Europe has encouraged Germany to support this initiative, which motivated the creation of the Europe-MENA partnerships with Morocco [88].

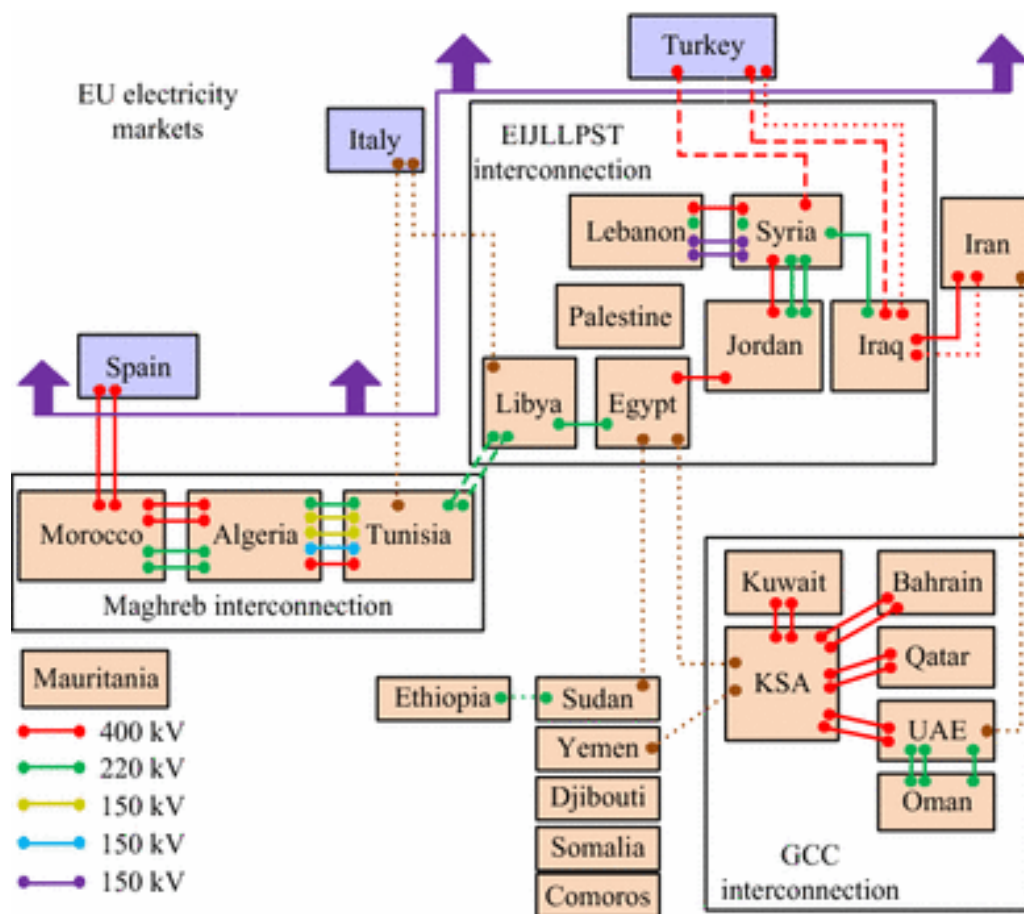


Figure 2. 6 Grid interconnection in the Middle East (solid line: "existing"; dashed line: "not operational/island operation"; dotted line: "under consideration, -study, -construction") [88].

The announced proposal was to use areas in Morocco to export electricity to Europe from future CSP projects. According to a DLR study [89], it was assumed that by 2025 most renewable power technologies will be cheaper than conventional ones, and renewable energy will dominate the Mediterranean region. Although the study promoted a broad mix of renewable technologies, it concluded that solar thermal technologies would play the leading role. Furthermore, the total CSP capacity in the

Mediterranean region will be more than the total combined capacity of wind, Photovoltaic (PV), biomass, and geothermal since CSP can produce up to double the energy production once combined with a TES system, underlining the importance of this work. It should be noted that CSP is a strong candidate for maximizing solar energy benefits. Once an optimal TES system is combined with CSP, the dispatch flexibility and capacity factor are maximized [90,91]. Moreover, the advantage of CSP is that it is capable, through TES, to overcome the intermittency in the solar resource due to diurnal variation and cloud cover effects [92].

2.3.2 Distinguished Gulf Cooperation Council experience of United Arab Emirates

The UAE has a 5.8% share of the global proven oil reserve, estimated at 97.8 Gbbl [49,93]. The crude oil production is approximately 2.97 Mbbbl/d, putting the country in eighth place among the largest oil-producing countries and the world's third-largest oil exporter with a 2.4 Mbbbl/d production rate. The proven NG reserve is estimated as 6,091 Bm³ with a marketed production of 54,085.7 Mm³. The NG exports amount to 12,109 Mm³ [94]. According to IEA [95,96], the breakdown of the total final energy consumption in the UAE is as follows: (i) industry with the largest share of 63% (1.2 EJ), (ii) transportation sector with 22% (0.4 EJ), and (iii) residential/commercial sector with 15% (0.3 EJ). In the UAE, electricity is generated mainly from NG, accounting for 15% of the total energy consumption. For the power generation fuel share, NG accounts for 99% [97]. According to the UAE government [98], most electricity generation, which is 110,000 GWh, used NG as input fuel in power plants in 2013. The UAE plan is to integrate NG distribution networks in all its emirates, which will alleviate peak demand shortfalls. In 2012, the total installed capacity was 27,200 MW. The UAE is considering a balanced energy mix to sustain the rising demand. The UAE is the first GCC country to start a new energy strategy involving nuclear power and solar/NG power. It should be recognized that the UAE is aiming to raise its power generation target concerning clean energy to 30% in 2030 by achieving 25-30% of electricity from nuclear and solar energy. The UAE has already committed to producing at least 7% of total power generation from renewable resources by 2020.

One of the applications of PV is to lower peak demand during the daytime [99]. CSP can perform the same application and address nighttime peak demand once

integrated with TES. According to a study [20], the following technologies were considered for electricity generation in the UAE: PV, wind, CSP, cogeneration, waste to energy, and nuclear power. The nighttime generation was promoted as a characteristic of CSP once combined with TES, allowing flexibility and coverage of nighttime peaks. In another study [100], the following sustainable energy transition visions were examined: (i) behaviour of supply options under high/low DNI for the “lead” 2030 vision, and (ii) electricity and desalination capacity deployment. In addition, the impacts and dynamics of an integrated sustainable energy transition plan for the UAE were studied. The sustainable energy transition plan provides benefits, such as minimizing installed conventional power capacity, driven by the reduction in overall demand due to demand-side-management measures. In addition, the compatibility and dependability drive other benefits from PV and CSP with TES. This means that PV covers afternoon peak demand, and CSP/TES covers nighttime peak in the UAE plan. The outcome of the plan is the reduction in conventional electricity supply capacity by more than 40%, from 38.9 GW in 2030 (“current” case) to 21.3 GW (“lead” case).

2.4 Kuwait experience

Kuwait has one of the heavily subsidized prices of electricity worldwide, with 0.66 ¢/kWh (see Table 2. 2) [20–22]. As of 2014, the GCC's total installed renewable capacities were: 0.6 MW for Bahrain, 0.2 MW for Kuwait, 0.7 MW for Oman, 28.2 MW for Qatar, 25 MW for Saudi Arabia, and 134.9 MW for UAE [20], as shown in Table 2. 3 [20]. Furthermore, it should be mentioned that the GCC renewable energy sectors are still at an early stage, and deployment projects have slowed down except for the UAE. Nevertheless, the GCC countries have set strategic targets for renewable energy implementation. Still, they are to be executed into mega-scale projects with ambitious plans in the short and medium terms.

Table 2. 2 Subsidised electricity prices as of 2014 in the GCC countries [20].

(US cents/kWh)							
	Bahrain	Kuwait	Oman	Qatar	Saudi Arabia	Abu Dhabi	Dubai
Residential Tariffs	0.8	0.7	2.6	2.2 - 6.0	1.3	5.6 - 8.7	7.8 - 12.1
Commercial Tariffs	0.8	0.7	5.2	2.5 - 4.9	3.2	4.2	7.8 - 12.1
Industrial Tariffs	3.8	0.4	4.2	2.2	4.1	4.2 - 8.0	7.8 - 12.1

Note: The tariff changes effective from January 2016 in Saudi Arabia and Abu Dhabi are included.
Sources: (RSB, 2015), (DEWA, 2015), (RCREEE, 2015a)

Table 2. 3 Capacity of renewable energy technologies in the GCC countries (wind, PV, CSP, and biomass/waste) [20].

Countries/ Capacity (MW)	2011	2012	2013	2014				
	Total RE*	Total RE*	Total RE*	Total RE*	Wind	PV	CSP	Biomass and Waste
 Bahrain	0.6	0.6	0.6	0.6	0.5	0.1	0	0
 Kuwait	0.1	0.1	0.2	0.2	0	1	0	0
 Oman**	0	0	0	0.7	0	0.7	0	0
 Qatar	25	28.2	28.2	28.2	0	3.2	0	25
 Saudi Arabia	0	19	25	25	0	25	0	0
 UAE, Abu Dhabi	19.5	20	134.9	134.9	0.9	33	100	1
Total	45.2	67.9	188.9	190.4	1.4	63	100	26

*RE = renewable energy

**Oman's 7 MW_{th} enhanced oil recovery plant is not included because this table addresses only electricity.

Source: IRENA Renewable Energy Statistics; (REN21, MOFA and IRENA, 2013); (RCREEE, 2015b)

2.4.1 Total carbon dioxide emission

British Petroleum (BP) company has estimated the CO₂ emissions globally [49]. According to BP, the rate of CO₂ emissions have increased from 73.1 Mt (2007) to 99.4 Mt (2017) in Kuwait (see Figure 2. 7).

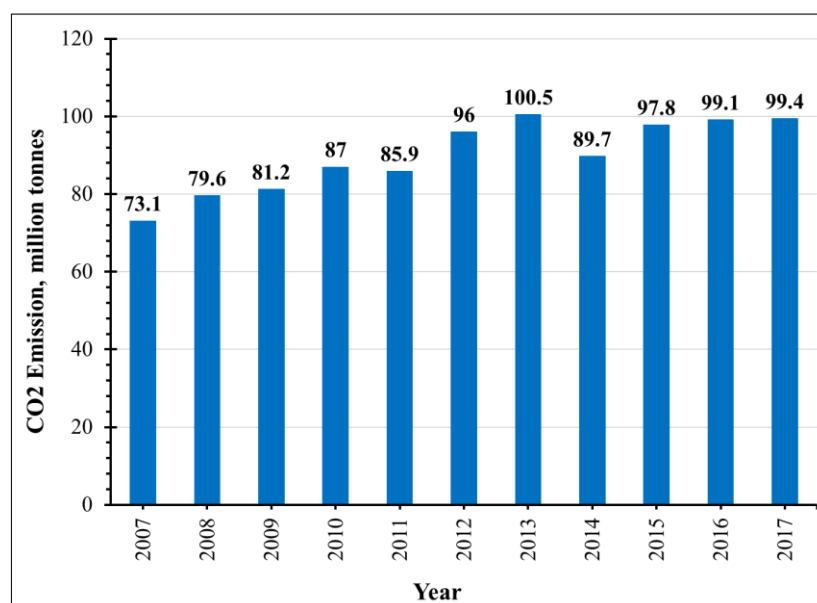


Figure 2. 7 CO₂ emissions in Kuwait according to BP from 2007 to 2017.

Additionally, the IEA has estimated the CO₂ emissions for various countries [47]. Figure 2. 8 shows the CO₂ emissions for Kuwait. Moreover, the World Bank has estimated the CO₂ emissions in Kuwait [48], as shown in Figure 2. 9. Currently, there is no active strategy for a carbon mitigation plan in Kuwait with advertised targets for each of the major contributors of CO₂ emissions at the national level. Instead, the

Environment Public Authority (EPA) of Kuwait continues to implement the rules, regulations, and guidelines set in 2001 for major criteria air pollutants. Moreover, the EPA of Kuwait has funded major projects to assess air quality within the country [44].

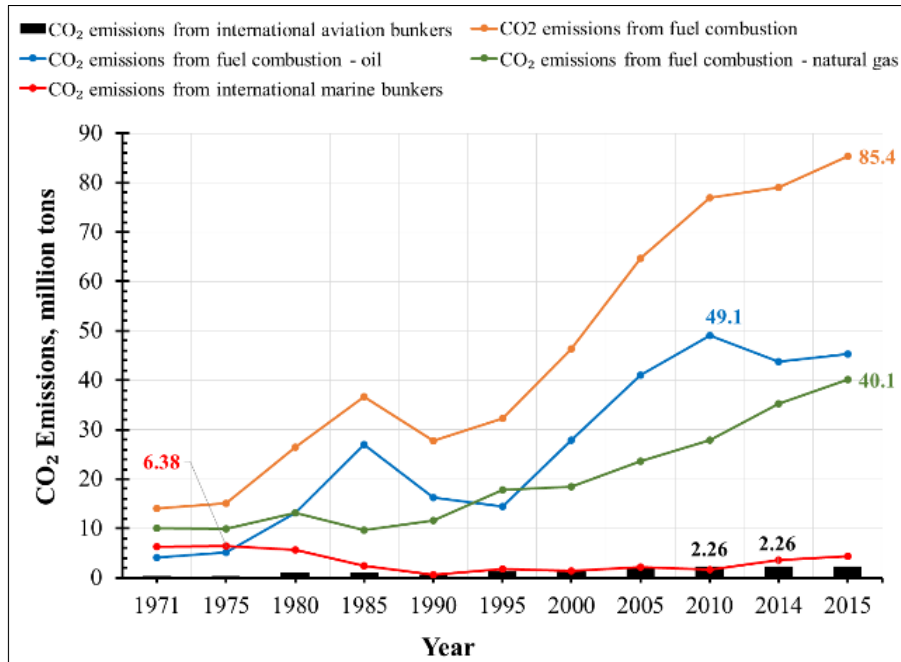


Figure 2. 8 CO₂ emissions in Kuwait according to IEA from 1971 to 2015 (the labels indicate maximum data points).

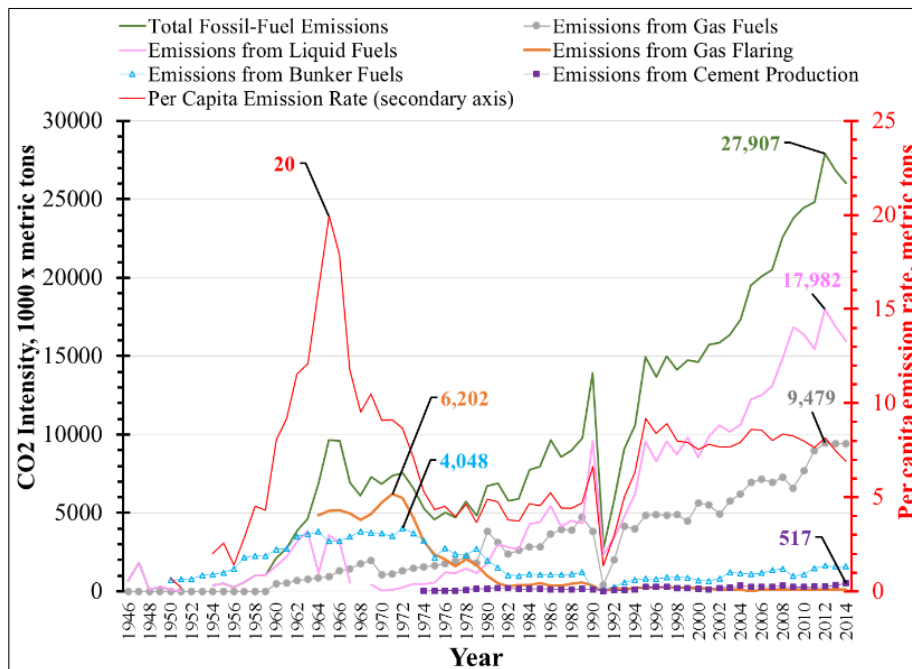


Figure 2. 9 CO₂ emissions in Kuwait according to the World Bank from 1946 to 2014 (the labels indicate maximum points).

2.4.2 Nationally determined contributions

Kuwait ratified the UNFCCC in 1995 and the Kyoto Protocol in 2005. For the Paris Agreement, Kuwait submitted the initial national communications in 2012 and the NDCs of Kuwait in 2015. The NDCs consisted of a proposal demonstrating the country's sustainable development plan until 2035. However, the proposal did not set a CO₂ reduction target percentage. According to the NDCs of Kuwait, the goals are summarized as follows: (i) diversifying energy sources, which contribute towards avoiding an increase of CO₂ and GHG emissions by the year 2035, and (ii) imposing sustainable development standards.

It should be noted that the contributions are based on planned projects which are still under development for the most part. Some of the projects that Kuwait intend to implement are as follows: (i) improving petroleum products by producing clean fuels according to environmental specifications to supply conventional plants by 2020, in addition to constructing a new refinery (Alzour) to replace the country's oldest oil refinery (Shuaiba), (ii) proposed projects focusing on energy production from municipal solid waste, (iii) energy production from renewable sources, (iv) mass transit project (metro system), and (v) making use of district cooling systems in new residential areas.

2.4.3 Greenhouse gas inventory

For the submission of the NDCs of Kuwait to UNFCCC in 2015, a GHG inventory was developed. The outcomes were that the energy-related activities accounted for the dominant portion of the GHG emissions. The distribution of GHG emissions was as follows [50] (also see Figure 2. 10, Figure 2. 11, Table 2. 4, and Table 2. 5):

- i. 95.3% of the GHG emissions were associated with the combustion of fossil fuels and the release of fugitive emissions from oil/gas operations,
- ii. waste management accounted for 2.4% of the GHG emissions,
- iii. industrial process emissions accounted for 2.1%,
- iv. agriculture emissions accounted for 0.2%, and
- v. managed tree plantations throughout the country sequestered less than 0.1% of the GHG emissions.

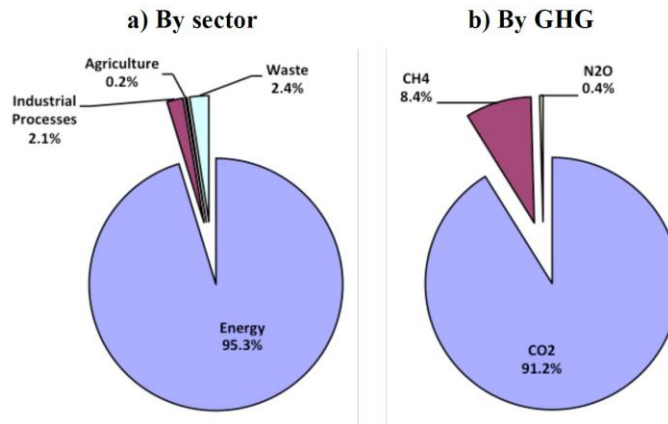


Figure 2.10 Distribution of emissions by sector and GHG type in 1994 [50].

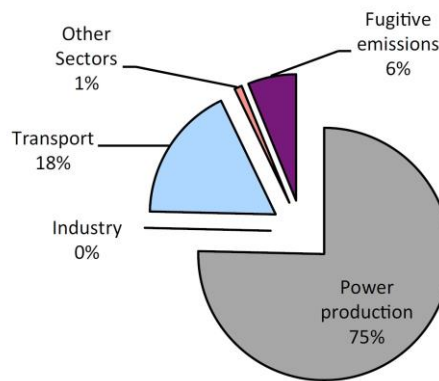


Figure 2.11 Breakdown of GHG emissions associated with energy activities in 1994 [50].

Table 2.4 Total GHG emissions in Kuwait [50].

GHG Sources & Sinks	CO ₂ e	CO ₂	CH ₄	N ₂ O	NO _x	CO	NM VOC	SO ₂
1 Energy	30,855	28,856	92.69	0.17	113	544	522	320
2 Industrial Processes	668	668	0.00	0.00	0	0	0	0
3 Solvent & Other Product Use	0	0	0.00	0.00	0	0	0	0
4 Agriculture	66	0	2.70	0.03	0	0	0	0
5 Land-Use Change & Forestry	-22	-22	0.00	0.00	0	0	0	0
6 Waste	784	0	33.80	0.24	0	0	0	0
Total National Emissions	32,373	29,524	129.19	0.44	113	544	522	320
Net National Emissions	32,351	29,502	129.19	0.44	113	544	522	320

Table 2.5 GHG emissions of energy activities in Kuwait [50].

GHG Source Categories	CO ₂ e	CO ₂	CH ₄	N ₂ O	NO _x	CO	NM VOC	SO ₂
All energy emissions	30,855	28,856	92.69	0.17	113	544	522	320
A Fuel Combustion Activities	28,944	28,856	1.69	0.17	113	502	95	204
1 Energy Industries	23,255	23,210	0.36	0.12	63	7	2	204
2 Manufacture/construction	0	0	0.00	0.00	0	0	0	0
3 Transport	5,393	5,351	1.28	0.05	50	495	93	0
4 Other Sectors	296	295	0.05	0.00	0	0	0	0
B Fugitive Emissions from Fuels	1,911	0	91.00	0.0	0	42	427	115
1 Solid Fuels	0	0	0.00	0.0	0	0	0	0
2 Oil and Natural Gas	1,911	0	91.00	0.0	0	42	427	115
Memo Items	3,474	3,474	0.00	0.0	0	0	0	0
International Bunkers	3,474	3,474	0.00	0.0	0	0	0	0
CO ₂ Emissions from Biomass	0	0	0.00	0.0	0	0	0	0

2.4.4 Development plan

It should be mentioned that the promises to achieve the NDCs of Kuwait could be fulfilled by engaging the private sector in the electricity/water sector and the oil/gas sector. Article 4.7 of UNFCCC states that the extent to which developing parties, including Kuwait, fulfil their obligations under UNFCCC depends on the developed party's support to the developing parties with finance and technology transfer to ensure adequate global cooperation.

Kuwait's second development plan (2015-2020) vision is to transform the country into a financial and commercial centre by the year 2035. This vision has addressed various sectors, including the energy sector, by presenting targets for the oil and electricity sectors focusing on capacity and performance. During the launch of the "New Kuwait" project, the Kuwait oil minister mentioned that a 50% stake in a power and water company could be sold to the private sector in the future [101]. This approach is expected to lead to the creation of three new power companies emphasizing renewable energy.

2.4.5 Land assessment

Kuwait has a total area of 17,818 km², consisting primarily of flat desert lands [45]. There exist nine islands in which Boubyan Island, the largest island with an area of 863 km², is located in the northeast part of the Gulf water. This island is linked to the mainland by a metal bridge. Most of the islands are in the planning stage for future development projects with no existing transmission networks connecting them. In this work, the chosen location in the western region has no future development plans, which makes it ideal for development projects toward the 15% target to fulfil local electricity demand from renewable energy. Besides, this location has minimal oil and gas field concentrations [52]. Furthermore, the location experiences peaks in solar and wind resources. Kuwait has practical plans for development in which it will require the use of most of its land. Currently, mega-scale projects are scheduled for growth in the northern sub-regional area [102]. The national physical plan strategy for 2005-2030 has determined the exact boundaries for development projects and size estimations of new population settlements [103]. It should be noted that the national development plan for 2035 has a living environment pillar [104], which is achieving a 15% renewable energy penetration.

2.4.6 Installed capacity and electricity generation

The oil reserve of Kuwait is ranked globally in sixth place with 102 Gbbl, 6% of the global reserve as of 2012 [105]. Furthermore, Kuwait has sufficient solar resources that could improve the economic feasibility of electricity generation from renewable technologies. However, the arid climatic conditions impose technical challenges.

In Kuwait, the oil and gas sector accounts for about 40% of the gross domestic product and about 92% of the export revenues [106]. As of 2018, the oil production reached 2.7 Mbbbl/d, and the marketed production of NG reached 17.1 Bm³ [106]. It can be estimated that approximately 342,842 bbl were used for electricity generation in 2016 [107], the exclusive electricity and water provider. This estimation corresponds to 12.7% of domestic oil production. It should be mentioned that the locally consumed fossil fuels are as follows: gas oil, crude oil, heavy oil, and NG [108]. In addition, the domestic oil consumption for electricity generation is estimated to reach 1 Mbbbl/d by 2030 [109,110]. This consumption equals approximately 37% of the 2017 oil production, leaving Kuwait with 63% for oil exports in case the 2030 oil production remains as that of 2017.

In particular, the Kuwait Ministry of Electricity and Water (MEW), the exclusive electricity and water provider, has estimated that the peak load could reach 33,000 MW in 2030, rising from 13,390 MW in 2016 [107]. Currently, MEW operates eight fossil-based power plants listed in Table 2. 6 with their capacities. Furthermore, MEW is exclusively responsible for generating, transmitting, and distributing electricity in Kuwait. The total installed power assets are about 18,850.4 MW [107] (i.e., 47.6% steam turbines, 12.2% combined cycle gas turbines, and 40.2% open cycle gas turbines). Most of these assets are categorized under thermal generation units with high potential for retrofit applications with CSP-PT to provide feed-in steam to existing steam turbines.

Moreover, Figure 2. 12 shows the minimum/peak load, installed capacity at the fossil-based power plants, and population in Kuwait from 1997 to 2016. Also, Figure F. 1 illustrates that the summertime represented by the third quarter (Q3) is when peak generation occurs due to the excess air conditioning load (comfort cooling in buildings).

Table 2. 6 Total installed power capacity at each of the fossil-based power plants in Kuwait as of 2016.

Plant Name	Total installed power capacity, MW
Shuwaikh	252
Shuaiba North	875.5
Shuaiba South	720
Doha East	1,158
Doha West	2,541
Alzour North	1,631.4
Alzour South	5,805.8
Sabiya	5,866.7
Total	18,850.4

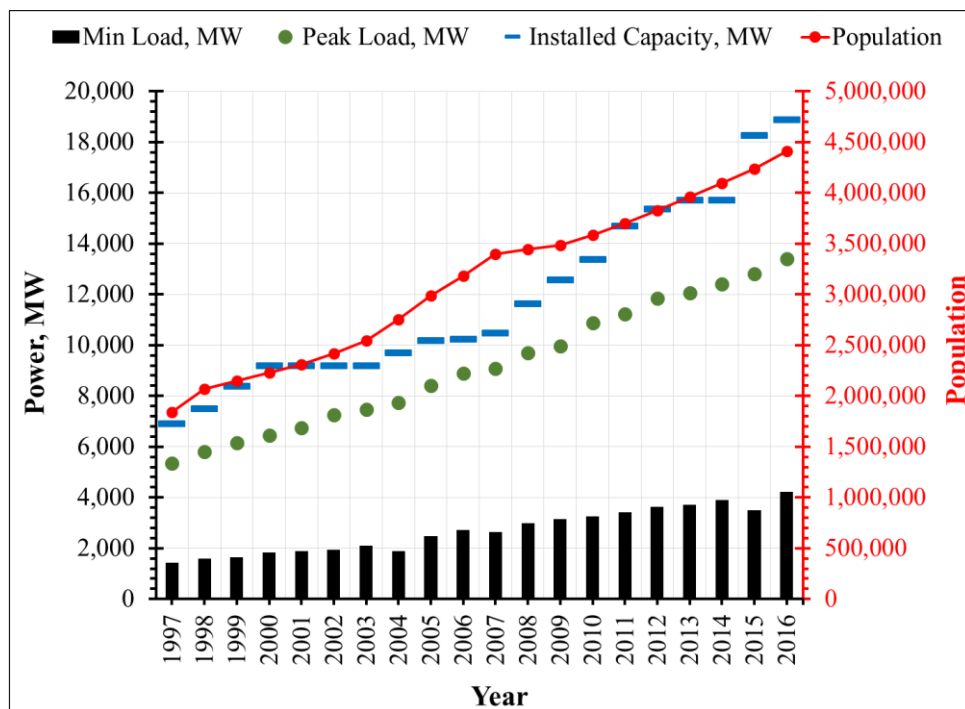


Figure 2. 12 Minimum/peak load, installed capacity, and population from 1997 to 2016 in Kuwait.

2.4.7 Electrical load

Figure 2. 13 illustrates the monthly peak/minimum load and average peak/minimum load at MEW plants for 2016, confirming that the peak load is in the summer. Also, it should be recognized that the previous years followed a similar trend (see Figure F. 2 to Figure F. 6). Figure F. 3 and Figure F. 4 show that maximal load values occur between hours 13:00 to 16:00 (afternoon) during the summer months (April to October). Additionally, it is observed that minimal load values occur between hours

03:00 to 05:00 (early morning) during the winter months. Furthermore, it should be noted from Figure F. 3 and Figure F. 4 that during the winter months, maximal load values occur during the nighttime between hours 17:00 to 19:00 due to the minimal effect of air conditioning load (comfort cooling in buildings). Figure F. 5 and Figure F. 6 show that maximal load values occur at exactly 15:00 during the summer months (April to October). Also, it is observed that minimal load values occur at exactly 04:00 during the winter months. In addition, it should be noted from Figure F. 5 and Figure F. 6 that during the winter months, maximal load values occur during the nighttime at exactly 18:00 due to the minimal effect of air conditioning load (comfort cooling in buildings).

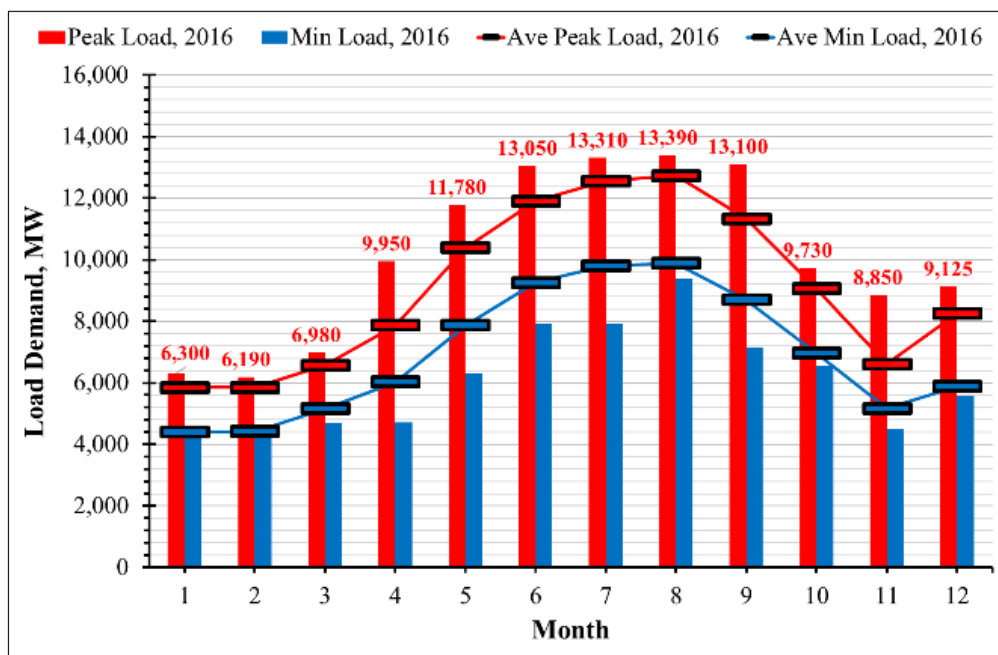


Figure 2.13 Monthly profile of the peak/minimum load and average peak/minimum load for 2016 in Kuwait.

Figure 2.14 to Figure 2.17 show the hourly electrical load profiles for hours 00:00 to 23:00 during 2016 in Kuwait. It is observed that there exists a summer consistent peak trend (i.e., red-coloured areas), which is apparent in the hourly electrical load profiles throughout the year.

Moreover, Figure 2.14 to Figure 2.17 reveal a remarkable resemblance between the electrical load profiles and the solar resource. The similarity highlights the need for further evaluation of the solar resource later in Chapter 4, especially since the solar resource frequently peaks during summer in Kuwait.

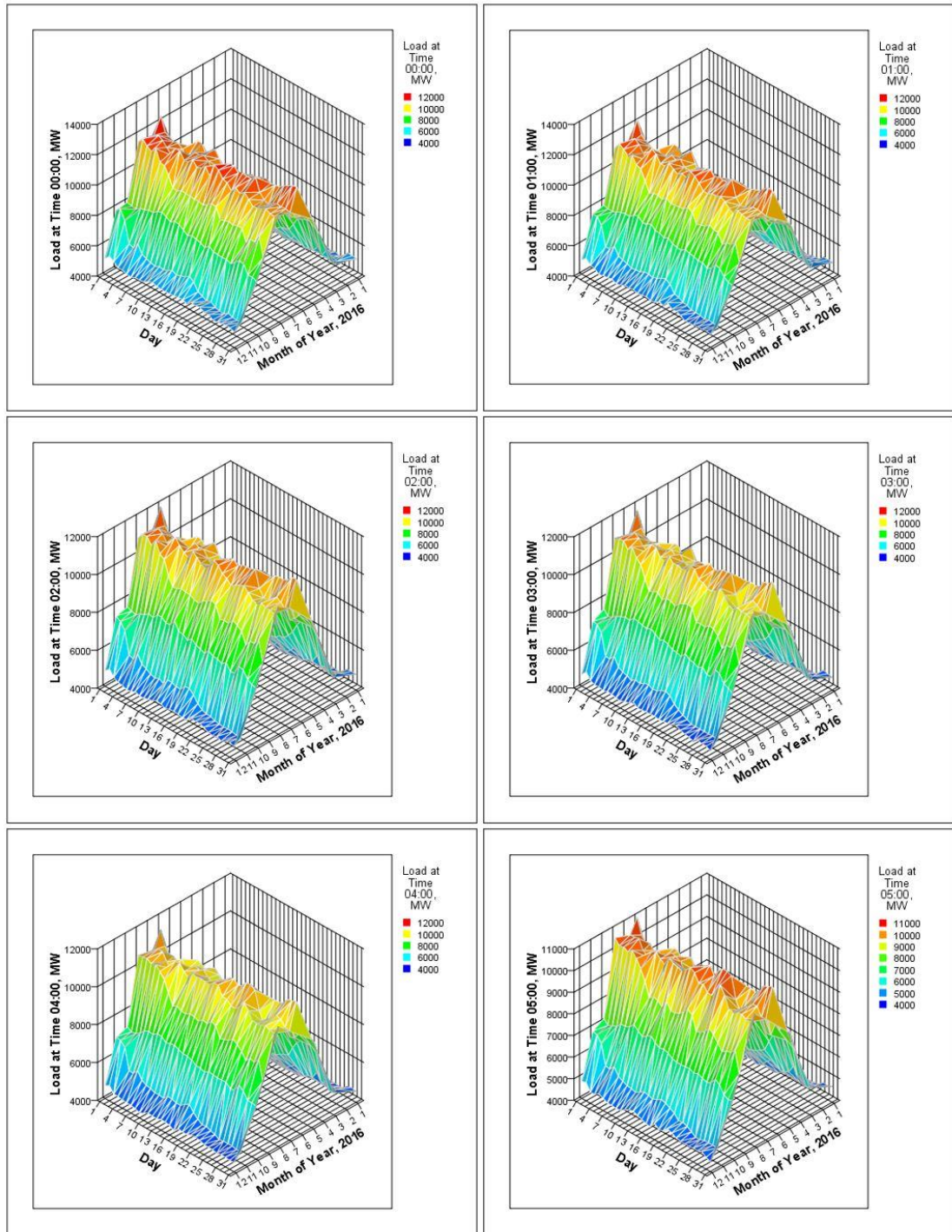


Figure 2. 14 Hourly electrical load profiles for hours 00:00 to 05:00 from the fossil-based power plants during 2016 in Kuwait.

During 2006-2007, a scheduled power shutdown routine was implemented in Kuwait to prevent failure in meeting demand when the peak load as a percentage of installed capacity was 87% (i.e., 13% reserve), as shown in Figure 2. 18. Furthermore, Figure 2. 19 shows the load profile of August 15th (the day of maximum peak load in 2016) from MEW plants in Kuwait.

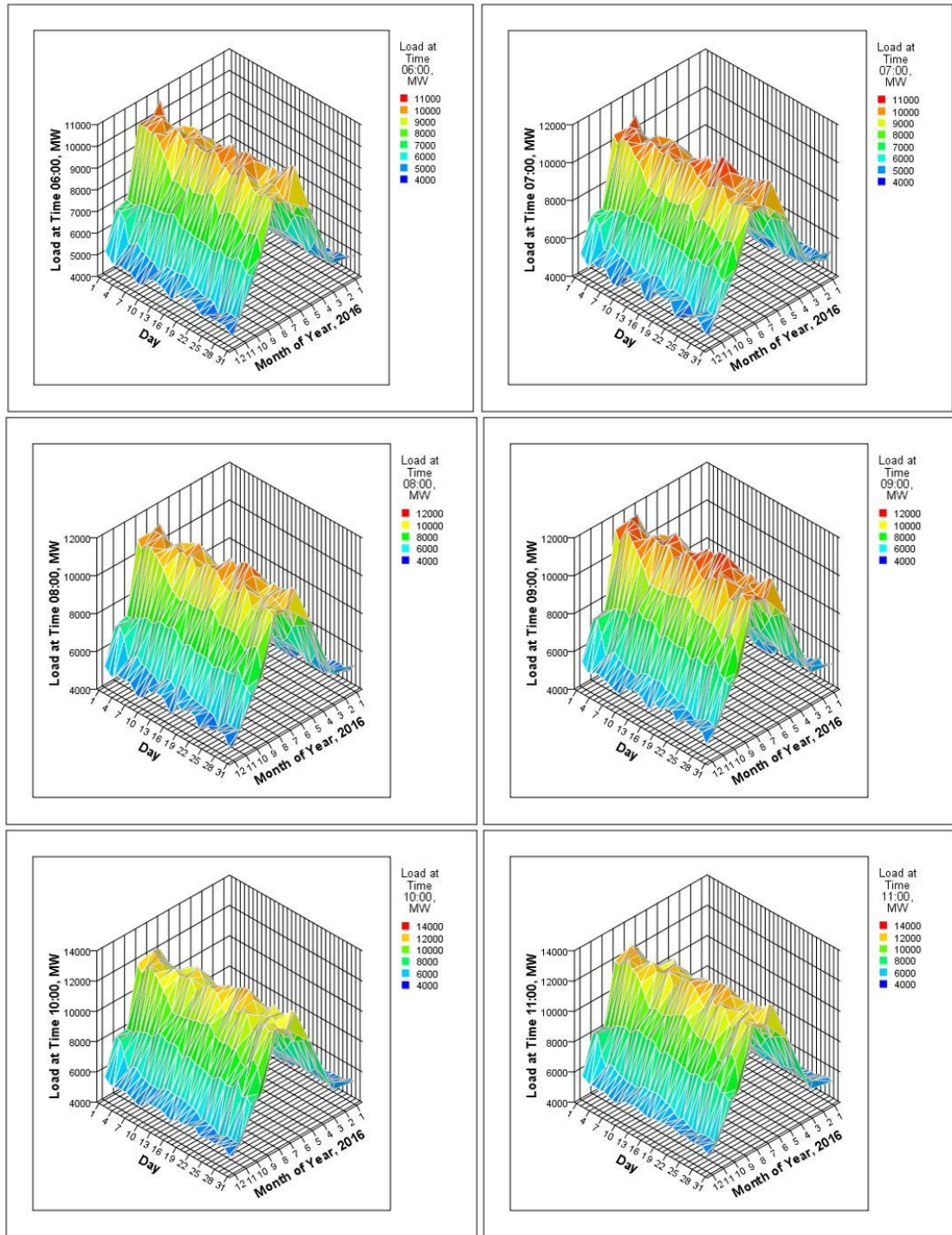


Figure 2. 15 Hourly electrical load profiles for hours 06:00 to 11:00 from the fossil-based power plants during 2016 in Kuwait.

Figure 2. 20 shows the annual profiles from 1997 to 2016 for the minimum/peak load, installed capacity, and per capita peak load share. According to MEW [107], the projections of total installed capacity are as follows 18447, 18947, 20327, 20627, 20627, and 20627 MW for the years 2017-2022, respectively.

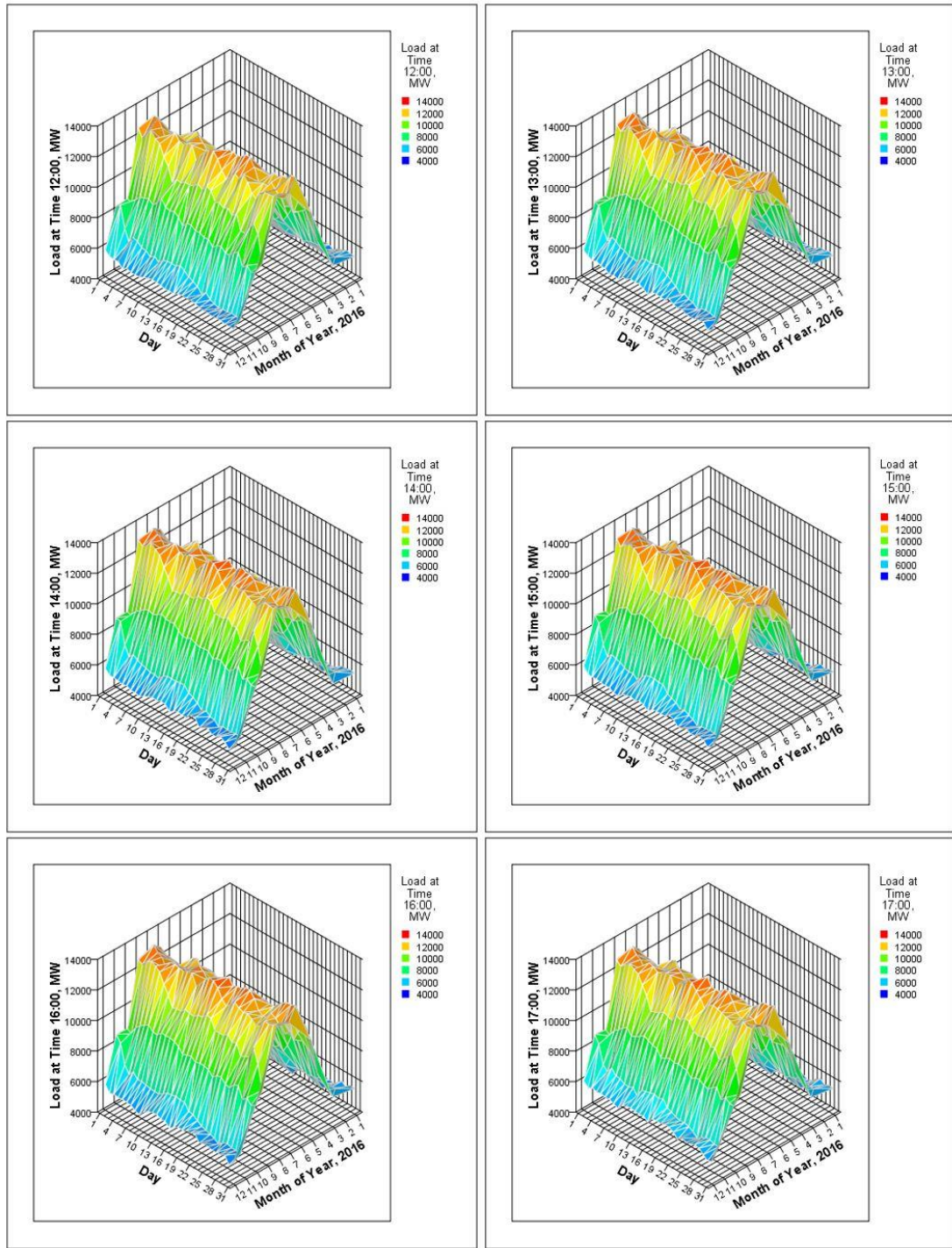


Figure 2. 16 Hourly electrical load profiles for hours 12:00 to 17:00 from the fossil-based power plants during 2016 in Kuwait.

It should be recognized that these projections represent the additions of future steam and gas turbines. The conventional power plants are currently in eastern coastal areas to ease access to the Gulf water used in evaporative cooling.

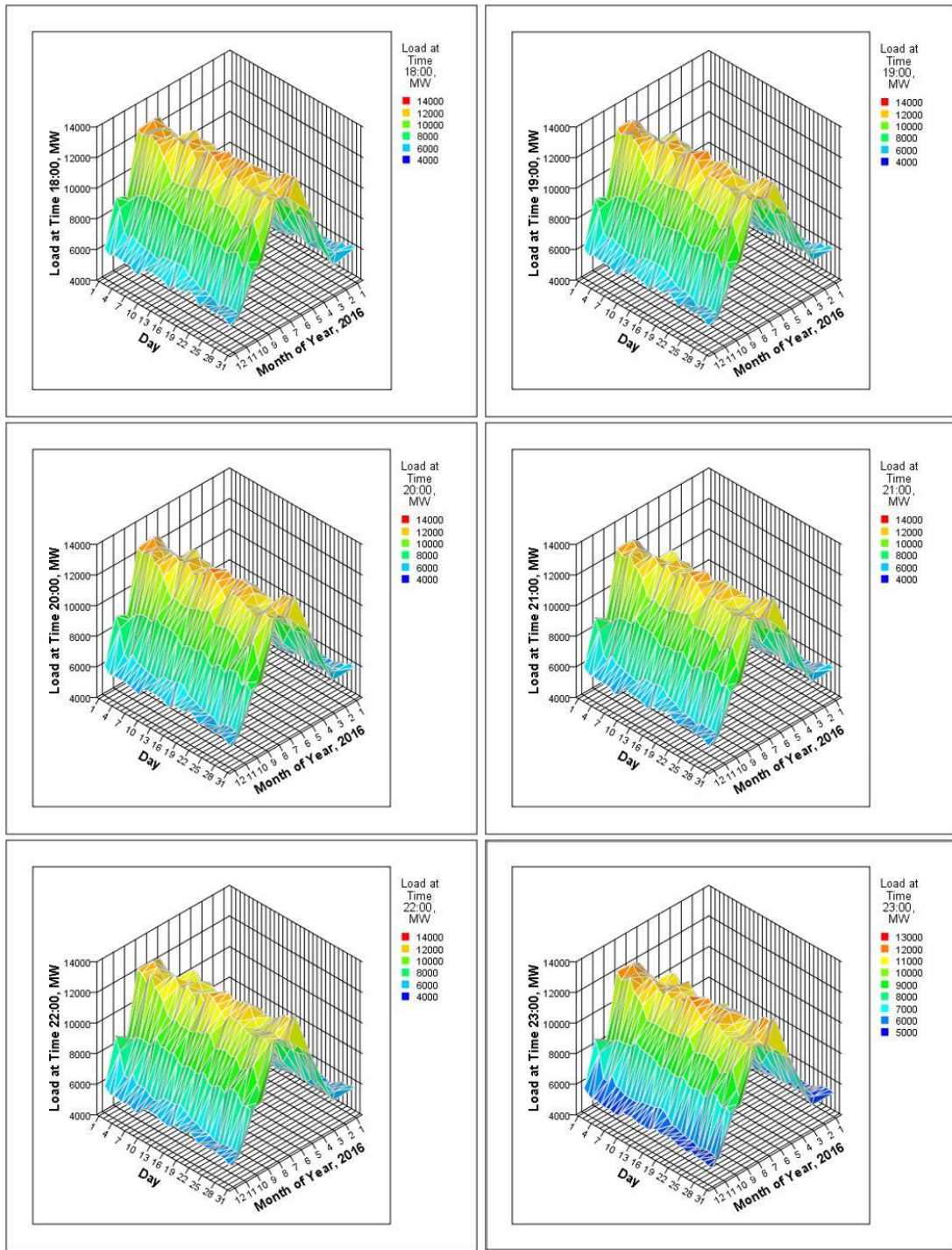


Figure 2. 17 Hourly electrical load profiles for hours 18:00 to 23:00 from the fossil-based power plants during 2016 in Kuwait.

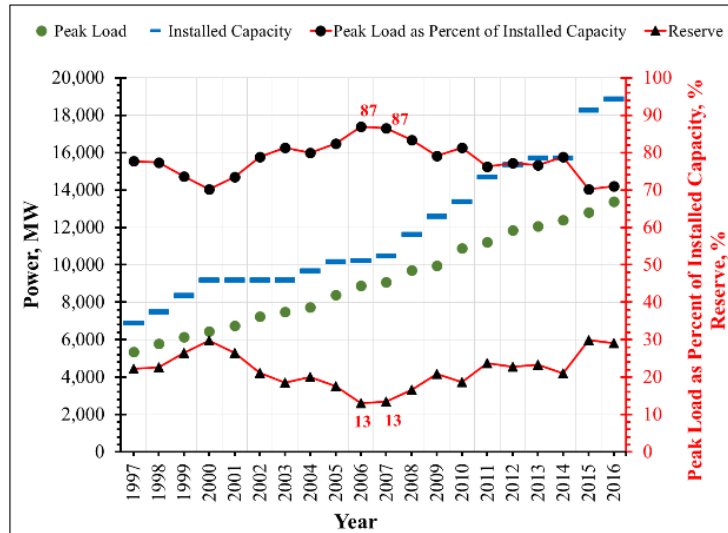


Figure 2. 18 Annual profiles from 1997 to 2016 in Kuwait: peak load, capacity, peak load as a percentage of capacity, and reserve.

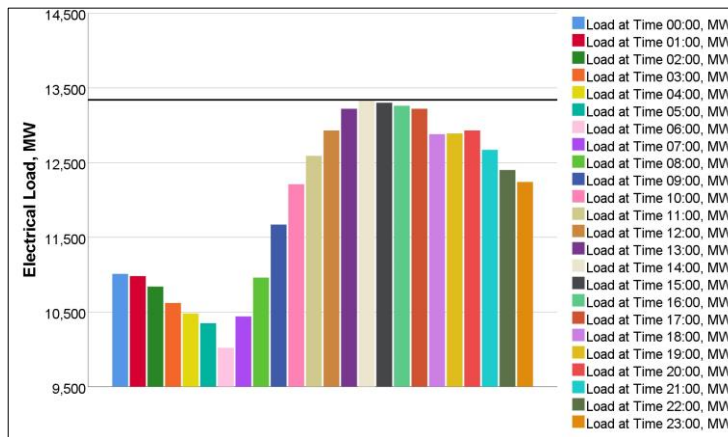


Figure 2. 19 Electrical load profile of August 15th (the day of maximum peak load in 2016) from all fossil-based power plants in Kuwait.

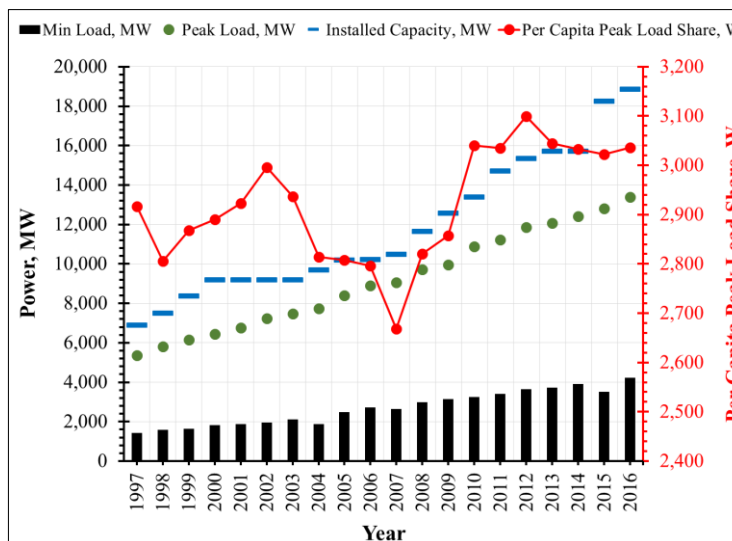


Figure 2. 20 Annual profiles from 1997 to 2016 in Kuwait: minimum/peak load, installed capacity, and per capita peak load share.

2.4.8 Fuel types and consumptions

Figure 2. 21 shows the consumption of fuels at MEW plants from 2005 to 2016 in Kuwait, in which the fuel consumption for electricity and water production accounted for 55%. Most consumers are in the residential sector, the largest consuming sector. It should be mentioned that under the electricity consumption category, the residential sector's fuel consumption share equals 34% [108]. Figure 2. 22 shows the profiles of peak load, maximum relative humidity at peak load, and maximum temperature at peak load at the fossil-based power plants. It can be concluded that the peak load during 1997-2016 occurred at maximum temperatures up to 50 °C. According to a study and official announcements, the cost of electricity production from these plants is averaged at approximately 14 ¢/kWh [35–37].

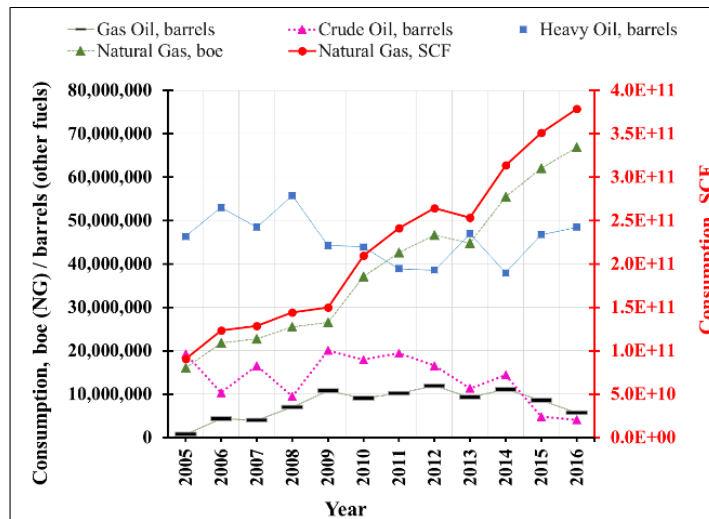


Figure 2. 21 Consumption of fuels at the fossil-based power plants in Kuwait.

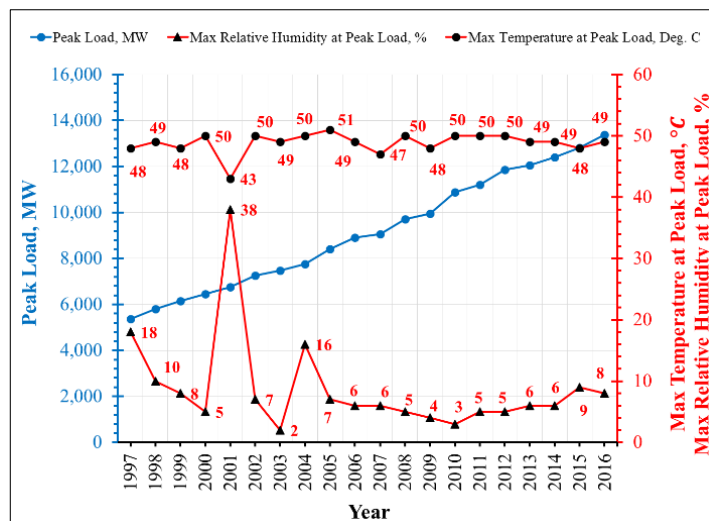


Figure 2. 22 Annual profiles for peak load, maximum relative humidity, and maximum temperature during 1997-2016 in Kuwait.

However, most residential consumers pay as low as 6% of this average actual cost, as shown in Table 1. 3. Furthermore, Figure 2. 23 shows the percentage of the electricity generation share of Kuwait relative to the Middle East and the world. Also, Table 2. 7 shows the conventional power technologies and installed capacities at the fossil-based power plants as of 2016 in Kuwait. Additionally, Figure F. 7 shows the annual profiles of electricity generation and the number of consumers in Kuwait from 1997 to 2016.

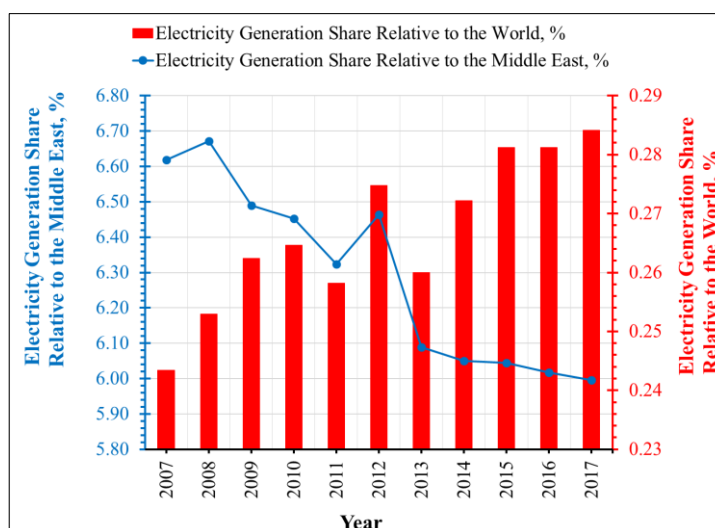


Figure 2. 23 Percentage of the electricity generation share of Kuwait relative to the Middle East and the world.

Table 2. 7 Conventional power technologies and installed capacities at the fossil-based power plants as of 2016 in Kuwait.

Power technology	Installed capacity, MW	Percentage share, %
Steam turbines	8,970	47.53
Combined cycle gas turbines	2,294.4	12.16
Open cycle gas turbines	7,586	40.20
Total	18,850.4	100

Figure F. 8 shows the type of electricity consumers for 2014-2016 in Kuwait. Figure F. 9 shows the NG consumption in SCF/boe units and the thermal energy in SCF/BTU units. Figure F. 10 shows the primary energy consumption for 2007-2017 and fuel type for 2016-2017 in boe/toe units. Figure F. 11 shows the calculated thermal energy consumption and electricity generation at MEW plants for 2015 and 2016. Figure F. 12 shows the calculated thermal energy consumption and related fossil fuel costs at these plants for 2015 and 2016. Figure F. 11 reveals the relationship between electricity generation and calculated thermal energy consumption at the fossil-based power plants in Kuwait for 2015 and 2016. This analysis approach provides an overview of the thermal efficiency of these plants. It should be noted that MEW

employs steam turbines, which make up 47.53% of its installed capacity. The gas turbines represent 40.2%, used during emergencies and peak load periods. The remaining 12.16% consists of combined cycle gas turbines. The thermal efficiency indicator for electricity generation from fossil fuels is illustrated in Figure F. 11. Figure F. 12 shows the calculated thermal energy consumption and the corresponding cost of fossil fuels in which the average actual cost of electricity generation is 14 ¢/kWh. It should be noted that this economic indicator reflects the cost of fuels only, which means that the following costs are excluded from the analysis: capital, operations, and maintenance costs.

2.4.9 Renewable energy projects

One of the early studies [39] in which a wind farm (6×5 kW) was installed in Kuwait for powering wireless service stations was completed by the Kuwait Institute for Scientific Research (KISR) in 2009 in Shagaya. The main objective of this study was to provide electricity to remote desert locations and therefore reduce the operating costs, such as diesel fuel and transportation costs. Furthermore, several studies on wind/solar resources and renewable technology assessments [28,33,39–43] have encouraged mega-scale renewable energy projects, such as the Shagaya Renewable Energy Park (SREP), managed by KISR. Also, it should be mentioned that KISR has launched its renewable energy program as a core part of its seventh strategic plan. As an initial step, the program includes the implementation of SREP (Phase I), consisting of 70 MW of commercially proven renewable technologies. One of the primary purposes of SREP establishment is to evaluate various renewable technologies to select the optimal shares to achieve 15% of local electricity demand from renewables by 2030. As a result, KISR has installed different meteorological stations across Kuwait for reliable data collection and forecasting purposes.

It should be noted that MEW has estimated the future peak load in 2030 to reach 33 GW, which is 41% more than the recorded 2016 peak load (13.4 GW) and 57% more than the 2016 installed conventional power capacity (18.9 GW). Furthermore, the following is a statement from MEW [107]: “There is a moral obligation from Kuwait to produce 15% from total power production by sustainable energy (renewable energy) in 2030, which is expected to be 4,500 MW”. In addition, the MEW deputy minister confirmed that the objective is to fulfil 15% of the peak load demand in 2030 from renewable energy [111]. Also, one of the seven pillars of the

Kuwait national development plan towards 2035 is to promote 15% renewable penetration [104].

Renewable technologies, such as CSP-PT and wind power, can provide sustainable and economic opportunities for Kuwait with benefits, such as reducing local consumption of fossil fuels and ensuring new sources for generating additional revenues. The most critical requirement in selecting a location for a CSP-PT plant is the availability of suitable DNI. Shagaya has one of Kuwait's highest solar and wind resource levels. Additionally, it is situated in a suitable terrain in a flat desert, mainly classified as undeveloped land. Besides, it does not feature any considerable change in topography with no significant obstacles for construction or for becoming potential causes of shading [45]. Thus, the chosen location in this work is selected to be Shagaya after thorough consideration.

2.5 Survey on simulation software(s) and tools for performance modelling

Table 2. 8 provides a detailed review in the form of a survey on the following various software(s) and tools to aid in performing modelling objectives: SolarTherm, AEETES, SGHAT, ASAP, TIM, CAVITY, SIMPLY, CIRCE, ThermoSysPro, DELSOL, CPLEX, Dish Field System Model, CSDS, DRAC/TOPAZ, Prosim, CosmosWorks/ANSYS/Visual HFLCAL, RESYSpro, FLUENT, SolarPILOT, GATECYCLE, INSEL, HELIOS, MESSAGE, MIRVAL, REMix-CEM, RADSOLVER, REMix-OptiMo, SAM, REMix-EnDAT, SOLERGY, Dymola/Modelica, SOLTRACE, RETScreen, STEAMPRO, PolySun, T-BRD, Simulink-MATLAB, TROUGH HELIOS, PLEXOS, TRNSYS, and IPSEpro.

2.6 Survey on specifications of concentrating solar power plants

Table 2. 9 provides a survey result, which includes a detailed review focusing on the specifications of selected CSP plants worldwide [112,113,122–131,114,132–137,115–121]. As part of the provided survey results, the following are included for each selected CSP plant: (i) plant name and location, (ii) CSP technology, (iii) TES medium, (iv) nominal temperature, (v) TES option, (vi) plant capacity, and (vii) TES capacity.

Table 2. 8 Summary of software(s) and tools for performance modelling.

Software/Tool	Description	Comments
SolarTherm	For analyzing the viability and overall impact of CSP components and system designs. It is an open-source simulation tool that includes a simulation framework and a library of flexible CSP components and control strategies.	Its library of flexible CSP components and control strategies can be adapted or replaced with new designs to meet the particular needs of end-users [138].
AEETES	For modelling the dish-cavity receiver, specifically for geometries with asymmetric incident fluxes [139–142].	It predicts the thermal performance of pool-boiler and heat-pipe reflux receivers.
SGHAT	For evaluating the effect of glint and glare from CSP technologies.	Sandia imposed restrictions. The tool was developed initially for internal Sandia uses only. The glare code and algorithm are available for licensing from Sandia [143].
ASAP	For modelling of optics for CSP technologies [144], optical design and performance, Gaussian-beam decomposition, polarization ray tracing, and other wave-optics phenomena [145,146].	Compatible with SolidWorks/CosmosWorks for modelling gravity and wind effects, for example, on heliostats.
TIM	For modelling CSP-Tower by analyzing the heliostat field and reflected glare with a 3-D interface. The approaches are annulus, point-per-group, up-aiming, and single-point-focus [143].	Tower Illuminance Model (TIM) evaluates the solar irradiance and feather temperature of birds flying through the receiver [147].
CAVITY	For modelling of energy transfer in CSP-Tower receivers. Generally, it assesses receiver performance [144] and determines tube/fluid temperature distributions. Also, it calculates thermal losses and efficiencies.	No maintenance or updated versions are currently delivered. Instead, FLUENT [148,149] can be used to model the receiver performance of the CSP-Tower.
SIMPLY	A compiler based on a declarative language for CSP modelling (standard SMT-LIB format). It uses SMT solvers.	More development is needed to make it competitive with advanced software tools for CSP modelling [150].
CIRCE	For modelling the optical performance of dish systems and linear concentrating systems [151,152], and analyses on the solar collector component, such as an analysis of a point-focus concentrator with a flat target.	It provides users with a design tool that is easy to implement without a longer processing time to obtain results.

Table 2. 8 Cont. Summary of software(s) and tools for performance modelling.

Software/Tool	Description	Comments
ThermoSysPro	The tool uses component models from the ThermoSysPro (Modelica-based) library. It provides a generic library for simulating plant performance, including CSP.	Its library has been validated against several test cases belonging to plant performance modelling (nuclear, thermal, biomass, and solar domains) [153].
DELSOL	For modelling of CSP-Tower, and optical design and performance of heliostat [154–157].	It is used for implementing an analytical approach to designing and evaluating performance. It can be combined with SOLERGY for more capability.
CPLEX	CPLEX solver based on the YALMIP/MATLAB used in CSP modelling. Thermal/electrical demands and operating objectives are used as inputs to minimize operating costs.	The optimization model is solved as a Mixed Integer Linear Programming (MILP) problem [158].
Dish Field System Model	For evaluation of the impact on the shaded performance of staggering the field layout for maintenance reasons [159]	For optimizing the layout of dishes and cost/benefit ratios.
CSDS	Concentrating Solar Deployment System Model (CSDS) is a multi-regional/time-period, GIS, and linear programming model. The tool is used in capacity expansion for electricity sectors.	It focuses on the principal market and policy issues related to the penetration of CSP technologies for electricity generation [160].
DRAC/TOPAZ	The tool analyzes the fluid flow and piping heat transfer of CSP-Tower [161,162]. For assessing receiver performance [157,161,163].	No maintenance or updated versions are currently delivered.
Prosim	The tool contains an extensive component library for conventional and nonconventional plants.	It has the disadvantage of a long calculation time for mega-scale applications [164].
CosmosWorks/ ANSYS/Visual HFLCAL	For finite element analyses to examine thermal performance [165–168].	It is used with ASAP/CIRCE to evaluate the impact on optical performance and determine the stress on receiver tubes.

Table 2. 8 Cont. Summary of software(s) and tools for performance modelling.

Software/Tool	Description	Comments
RESYSpro	It is used in evaluating the performance of water and power systems, including wind, PV, and conventional technologies.	It is capable of performing technical, economic, and ecological performance [169]
FLUENT	It is used in solar receiver performance [170]. Also, it is used for heat transfer and hydraulic analyses to perform computational fluid dynamics analyses [171].	It is used in heat transfer analysis for TES components, piping layout, and receivers.
SolarPILOT	Solar Power Tower Integrated Layout and Optimization Tool (SolarPILOT) is used in the performance assessment of the CSP-Tower.	It is used in calculating annualized thermal efficiency with minimum optimization performed on design [172]
GATECYCLE	It is used in the modelling of PB systems [173,174]. In addition, it is a commercially available heat and mass balance program for the analysis of a variety of types of plants.	Its library does not include a solar collector. Instead, the software predicts solar power generation [175].
INSEL	INSEL (INtegrated Simulation Environment Language) was used for calculating hourly generation from thermal power generating units, such as CSP.	It is used for calculating hourly electricity generation from PV plants [176].
HELIOS	It is used in modelling the optical behaviour of reflecting solar concentrators (e.g., solar flux density from heliostat fields using cone optics) [177,178].	No maintenance or updated versions are currently delivered
MESSAGE	It is used as an optimization tool to minimize the total cost associated with expanding energy systems.	It provides the user with the least-cost energy estimation and predicts electricity supply mix scenarios [179].
MIRVAL	It models solar flux density from a heliostat field using ray tracing [154,157,180,181]. Also, it is used in analyzing the optical design and performance of heliostats.	No maintenance or updated versions are currently delivered.

Table 2. 8 Cont. Summary of software(s) and tools for performance modelling.

Software/Tool	Description	Comments
REMix-CEM	It contains several modules for power generation technologies, including CSP.	The CSP module allows the modelling of dry and wet-cooled CSP-PT plants [182].
RADSOLVER	For modelling of energy transfer of CSP-Tower receiver [183], and for analyzing receiver performance [157].	No maintenance or updated versions are currently delivered.
REMix-OptiMo	It uses meteorological data to calculate time-series power outputs of main renewable technologies, including CSP.	It makes decisions on the operation protocols for renewable systems by considering cost figures in the calculations [184].
System Advisor Model (SAM)	For performance analysis of CSP-PT and other technologies with TES capability (PV, high concentrating PV, wind, biomass, and geothermal power) [185]. Also, it models HTF transport, exchange, storage, and PB [186–191].	Detailed processes (e.g., optics) are modelled in SAM, which combines annual time-series power production models with financial models to estimate the LCOE [192–194] and other financial metrics for renewable energy technologies.
REMix-EnDAT	It evaluates the least cost and operation of power systems.	It minimizes costs from expenditures arising from the installation of new assets [195].
SOLERGY	It models CSP-Tower [157,196] and evaluates the effect of plant dispatch strategies on net electricity output. It models CSP in which the energy collection and production subsystems are connected through TES.	It uses FORTRAN, and it is considered as a quasi-steady-state plant model with a constant time step.
Dymola/Modelica	It is used to develop validated control algorithms for CSP collector fields [197,198].	It is based on the open Modelica language.
SOLTRACE	A ray-tracing code for complex solar optical systems [199,200]. For optical design and performance of heliostat.	No maintenance or updated versions are delivered.

Table 2. 8 Cont. Summary of software(s) and tools for performance modelling.

Software/Tool	Description	Comments
RETScreen	It is based on Microsoft Excel and is freely available. Also, it evaluates energy production, savings, and costs for leading renewable technologies [201].	Its analysis steps are as follows: energy model, cost analysis, GHG analysis, financial summary, and sensitivity and risk analysis
STEAMPRO	It is used for modelling steam power cycles [202,203].	It shares many features with GATECYCLE.
PolySun	It is a commercial product that simulates solar thermal, PV, and geothermal systems.	It conducts financial analyses, such as payback period, annual savings/costs, and net present value [201].
T-BRD	It is used to model the Solar Two (CSP-Tower) receiver system dynamics and test initial design concepts. Also, it is used in the dynamic simulation of tubular receivers [204].	No maintenance or updated versions are currently delivered.
Simulink-MATLAB	The model of CSP-Tower plants can be built using Simulink-MATLAB [205].	No built-in economic features of CSP performance.
TROUGH HELIOS	It models the optics of CSP-PT and predicts the incident flux [206,207].	No maintenance or updated versions are currently delivered.
PLEXOS	The tool is used in cost minimization routines. Also, it optimizes various power systems by minimizing costs from fuel/emission, operations/maintenance, start-ups, etc.	The cost minimization routine in PLEXOS does not optimize the CSP operation from the plant owner's perspective [208].
TRNSYS	Modular software for modelling different power systems, including solar power systems and components [209,210].	TRNSYS is used within the performance modelling engine of the SAM software.
IPSEpro	It performs PB cycle modelling [211,212].	It is used in calculating heat balance and assessing process simulation [213].

Table 2. 9 List of selected operational CSP plants worldwide.

Plant name and location	CSP technology	TES medium	Nominal temperature, °C		TES option	Plant capacity	TES capacity	Reference
			Cold	Hot				
IEA-SSPS, Almeria - Spain	PT	Santotherm 55	225	295	One tank thermocline	1.2 MW _t	5 MWh _t	[112–114]
Irrigation pump, Coolidge AZ - USA	Tower	Oil	200	228	One tank thermocline	NA	3 MWh _t	[115,116]
Nevada Solar One, Nevada - USA	PT	Dowtherm A	318	393	Oversized field piping	64 MW _e	0.5 h	[117,118]
Aalborg CSP, Brønderslev - Denmark	PT	NA	252	312	Without TES	16.6 MW	NA	[119]
Holaniku Keahole Point Hawaii - USA	PT	Water	NA	200	Indirect	2 MW _t , 500 kW _e	2 h	[120,121]
Arcosol 50, Cádiz - Spain	PT	Molten salt 28,500 t 60% sodium nitrate, 40% potassium nitrate	293	393	Indirect two-tank	49.9 MW	7.5 h	[122]

Table 2. 10 List of selected operational CSP plants worldwide.

Plant name and location	CSP technology	TES medium	Nominal temperature, °C		TES option	Plant capacity	TES capacity	Reference
			Cold	Hot				
Planta Solar-10, Sevilla - Spain	Tower	Pressurized water	240	260	Steam accumulator	11 MW _e	50 min/20 MWh _t	[117,123,124]
ASE Demo, Massa Martana - Italy	PT	Molten salt 50 t 60% NaNO ₃ and 40% KNO ₃	290	550	Direct two-tank	0.35 MW	4.27 MWh _t	[125]
Casablanca - Morocco	PT	Molten salt 60% NaNO ₃ and 40% KNO ₃	293	393	Indirect two-tank	50 MW	7.5 h	[214]
Planta Solar-20, Sevilla - Spain	Tower	Pressurized water	NA	250-300	Steam accumulator	20 MW _e	50 min	[112,117]
La Florida, Badajoz - Spain	PT	Molten salt 29,000 t 60% NaNO ₃ and 40% KNO ₃	292	386	Indirect two-tank	50 MW _e	7.5 h	[117,127]
Gujarat Solar One, Kutch - India	PT	Molten salt 60% NaNO ₃ and 40% KNO ₃	293	393	Indirect two-tank	28 MW	9 h	[128]
Andasol-1, Granada - Spain	PT	Molten salt 28,500 t 60% NaNO ₃ and 40% KNO ₃	292	386	Indirect two-tank	50 MW _e	7.5 h/964 MWh _t	[117,127,129]

Table 2. 9 Cont. List of selected operational CSP plants worldwide.

Plant name and location	CSP technology	TES medium	Nominal temperature, °C		TES option	Plant capacity	TES capacity	Reference
			Cold	Hot				
Gulang, Wuwei – China	PT	Molten salt 60% NaNO ₃ and 40% KNO ₃	293	393	Indirect two-tank	50 MW	9 h	[215,216]
Andasol-2, Granada - Spain	PT	Molten salt 60% NaNO ₃ and 40% KNO ₃ 28,500 t	292	386	Indirect two-tank	50 MW _e	7.5 h/1010 MWh _t	[117,127,129]
Ilanga I, Upington - South Africa	PT	Molten salt mixed nitrates	293	393	Indirect two-tank	100 MW	5 h	[131]
Extresol-1, Badajoz - Spain	PT	Molten salt 60% NaNO ₃ and 40% KNO ₃	292	386	Indirect two-tank	50 MW _e	7.5 h/1010 MWh _t	[117,127,132]

Table 2. 9 Cont. List of selected operational CSP plants worldwide.

Plant name and location	CSP technology	TES medium	Nominal temperature, °C		TES option	Plant capacity	TES capacity	Reference
			Cold	Hot				
Kathu Solar Park, Kathu - South Africa	PT	Molten salt mixed nitrates 45,000 t	293	393	Indirect two-tank	100 MW	4.5 h	[133]
Manchasol-1, Ciudad Real - Spain	PT	Molten salt 60% NaNO ₃ and 40% KNO ₃ 28,500 t	292	386	Indirect two-tank	50 MW _e	7.5 h/375 MWh _t	[112,117,127]
KaXu Solar One, Poffader - South Africa	PT	Molten salt mixed nitrates	NA	NA	Indirect two-tank	100 MW	2.5 h	[134]
Manchasol-2, Ciudad Real - Spain	PT	Molten salt 60% NaNO ₃ and 40% KNO ₃ 28,500 t	292	386	Indirect two-tank	50 MW _e	7.5 h	[117,127]
KVK Energy Solar, Askandra – India	PT	Molten salt mixed nitrates	NA	NA	Indirect two-tank	100 MW	4 h/1010 MWh _t	[135]
La Dehesa, Badajoz - Spain	PT	Molten salt 60% NaNO ₃ and 40% KNO ₃ 29,000 t	292	386	Indirect two-tank	50 MW _e	7.5 h	[112,117,127]

Table 2. 9 Cont. List of selected operational CSP plants worldwide.

Plant name and location	CSP technology	TES medium	Nominal temperature, °C		TES option	Plant capacity	TES capacity	Reference
			Cold	Hot				
Puerto Errado 1, Murcia - Spain	Fresnel	Saturated steam	NA	270	Steam accumulator	1.4 MW _e	NA	[112,117]
Archimede, Sicily - Italy	PT	Molten salt 60% NaNO ₃ and 40% KNO ₃ 50 t	290	550	Direct two-tank	5 MW _e	8 h/100 MWh _t	[112,117]
Torresol Gemasolar, Seville - Spain	Tower	Molten salt 60% NaNO ₃ and 40% KNO ₃	290	565	Direct two-tank	17 MW _e	15 h	[112,127]
Dahan, Beijing – China	Tower	Saturated steam/oil	220	350	Steam accumulator/ concrete	1 MW _e	1 MWh _t	[112,136,137]

2.7 Research and knowledge gaps

This work aims to offer optimal design configurations to expand the implementation of renewable technologies, specifically in the CSP-PT and wind power arenas. One objective is to suggest potential mega-scale applications of these technologies in the MENA/GCC region. Another objective is to assess the feasibility of electricity generation by investigating the technical and economic performance in a hot desert environment. It should be noted that the outcomes to be obtained will include a detailed techno-economic assessment for the establishment of stand-alone power plants and an investigation of the economics of scale for larger power capacities and future expansion. In addition, this work will offer new knowledge about the optimal performance of CSP-PT and wind power plants under the harsh climate of Kuwait for mega-scale deployment, which has never been investigated before. Additionally, both the power and industrial sectors will benefit from offering new power supply solutions, among other possibilities, such as heat augmentation or industrial process heat applications using the CSP-PT/TES technology. The long-term benefits also extend to reducing CO₂ emissions and saving strategic commodities, such as oil and NG, from excessive consumption for steam production at conventional power plants in Kuwait. Especially since the Kyoto protocol mandates GHG emission reduction in which CO₂ is the primary gas. Hence, the recommendations to be provided could enable Kuwait to exchange its CO₂ quota in the future.

One focus area of this work is the CSP-PT technology with considerations of DNI, ambient conditions, operating conditions, HTF flow characteristics (Dowtherm A, see Appendix A), and heat losses. In general, the PT collector thermal efficiency should be maximized throughout the plant's lifetime by continuously maintaining the optimal design conditions. After that, the overall energy and economic yields can improve and become competitive. Furthermore, the DNI, which is naturally transient, is the heat source in a CSP-PT plant. Hence, it is necessary to provide recommendations on the validation, optimal design configurations, and operating conditions for future possibilities of CSP-PT/TES plant installations in Kuwait. Only then one can analyze the thermal efficiency to locate and quantify heat losses and performance degradation accurately.

Furthermore, the heat collection in the PT collectors is performed by the Heat Collecting Element (HCE). Therefore, performance evaluation and investigation of

the thermal efficiency are critical because the HCE is the component that delivers solar heat to the medium (HTF), which absorbs the heat inside the HCE. Furthermore, the analytical approach in this work is critical because maximum thermal energy extraction from the DNI is a continuous challenge for the solar energy industry, not only the CSP-PT technology.

Consequently, the HCE and HTF operating temperatures should be maintained close to specific ranges based on engineering design. If the temperatures increase or decrease beyond those ranges, HTF decomposition and accompanying hydrogen permeation into the vacuum annulus of the HCE will occur eventually. As a result, the hydrogen in the annulus space will increase heat losses and decrease thermal efficiency. Therefore, a CSP-PT model to evaluate the thermal efficiency is needed to be investigated, specifically for a location with an arid desert environment like Kuwait, since the operational problems are more frequent in such a region. Furthermore, recommendations are to be provided for validation and operating conditions of future CSP-PT plant installations. This is achieved by utilizing an existing CSP-PT plant (Andasol-1) for performance evaluation, enhancement, and optimization. Then, optimal CSP-PT plant design configurations specific to the climatic conditions of Kuwait are determined to maximize the overall plant efficiency.

It should be noted that global financial lenders (e.g., World Bank) consider the ratio of thermal efficiency of the power plant versus the average thermal efficiency of the existing fleet of plants in the base year as a key performance indicator to approve loans for plant development [217]. Hence, this indicator supports the analysis approach in this work since thermal efficiency is a rational indicator for assigning CSP-PT plant monetary values ($\$/\text{kWh}$ or LCOE). Also, such an approach is imperative because one of the main objectives of this work is to provide data on the economic and technical limitations of the CSP-PT technology in the arid climate of Kuwait (dust storms, high humidity, extreme temperatures). Besides, periodic evaluation of the thermal performance is critically needed because it improves the plant's economic feasibility by increasing the annual energy production, reducing the operational challenges, and decreasing the LCOE.

Moreover, this work aims to assess and optimize future wind power plant installations to achieve Kuwait's strategic target by modelling various mega-scale wind power plant capacities. The performance assessment and optimization are

performed by integrating specific design parameters, operating conditions, ambient conditions, and onsite measured meteorological data (wind speed, wind direction, etc.). This objective is imperative to provide recommendations for optimal design configurations, performance degradation evaluation, and overall wind power plant performance throughout the plant's lifetime. Additionally, the economic feasibility of different optimal wind power design configurations is determined.

2.8. Chapter conclusion

The main findings are summarized as follows:

- i. renewable energy had a 26.5% electricity production share, and the global capacity of CSP reached 4.9 GW [57], with Spain having the largest installed share of CSP in the world,
- ii. it should be noted that wind power has the maximum share (5.6%) of the total renewable energy electricity production share (26.5%), and the non-renewable electricity share accounts for 73.5%,
- iii. an existing CSP-PT plant in Spain is selected as the reference plant in this work for performance assessment and optimization of the CSP-PT technology,
- iv. concerning per capita electricity consumption, Kuwait is at the top rank [73,74] within the range of 16,000-17,000 kWh per capita during 2003-2011 [68],
- v. according to a study [82], the most advanced technology for solar thermal power is CSP. The MENA desert has the advantage of high solar resources, which contributes to the popularity of CSP [83,84]. Therefore, the initiative to utilize MENA desert lands to construct future CSP plants and electricity export to Europe is the most encouraging near-term prospect for CSP [85,86],
- vi. the DLR has promoted renewable energy in the MENA region. There exists a network of meteorological stations under the cooperation between DLR, international research institutes, and industry partners [87]. The aim is to provide reliable meteorological data, which is critical for CSP performance predictions,

- vii. this network of meteorological stations was established as part of the enerMENA initiative to shut down nuclear plants in Germany by 2022. The existing and planned grid interconnection between countries in the GCC, MENA, and Europe has encouraged Germany to support this initiative, which motivated the creation of the Europe-MENA partnerships with Morocco [88],
- viii. Kuwait is part of the grid interconnection in the Middle East [88]; therefore, the Kuwait case is investigated in this work to assess and optimize CSP-PT/TES performance under arid climatic conditions,
- ix. Kuwait has one of the heavily subsidized prices of electricity worldwide, with 0.66 ¢/kWh . As of 2014, Kuwait's total installed renewable energy capacity was 0.2 MW [20],
- x. the chosen location (Shagaya) in Kuwait has no future development plans, making it ideal for future development projects toward the 15% target to fulfil local electricity demand from renewable energy by 2030. The location in the western region has limited water resources, and the majority of the population resides within/or close to the eastern coastal areas. Besides, the location has minimal oil and gas field concentrations [52]. Furthermore, the location experiences peaks in solar and wind resources. Hence, investigating the different optimal design configurations of dispatchable CSP-PT with TES accompanied with wind power should minimize the intermittences in the solar and wind resources (i.e., an advantage),
- xi. Kuwait's oil/gas sector accounts for about 40% of the gross domestic product and about 92% of the export revenues [106]. As of 2018, Kuwait's oil production reached 2.7 Mbbbl/d, and the marketed production of NG reached 17.1 Bm³ [106]. It can be estimated that approximately 342,842 bbl were used for electricity generation in 2016 [107]. This estimation corresponds to 12.7% of domestic oil production,
- xii. Kuwait's domestically consumed fossil fuels are gas oil, crude oil, heavy oil, and NG [108]. Such domestic oil consumption in electricity generation is estimated to reach 1 Mbbbl/d by 2030 [109,110]. This consumption equals approximately 37% of the 2017 oil production, leaving Kuwait with 63% for oil exports in case the 2030 oil production remains as that of 2017,

- xiii. MEW has estimated that the peak load would reach 33,000 MW in 2030, rising from 13,390 MW in 2016 [107],
- xiv. Kuwait's total installed power assets are about 18,850.4 MW [107] (i.e., 47.6% steam turbines, 12.2% combined cycle gas turbines, and 40.2% open cycle gas turbines). Most of these assets are categorized under thermal generation units with high potential for retrofit applications with CSP-PT,
- xv. the third quarter (Q3, summer) is when peak generation occurs due to the excess air conditioning load (comfort cooling in buildings) in Kuwait, and the peak load occurs during the summer.
- xvi. The fuel consumption for electricity and water production accounted for 55% in Kuwait,
- xvii. according to a study and official announcements, the cost of electricity production from fossil-based power plants is averaged at approximately 14 ¢/kWh in Kuwait [35–37]. However, most residential consumers pay as low as 6% of this average actual cost,
- xviii. detailed review material on various software(s) and tools for performance modelling are provided. Therefore, SAM has been selected for performance assessment and optimization of wind power and CSP-PT, along with other time-series analysis software(s), and
- xix. the result of a detailed review on the specifications of selected CSP plants worldwide is provided [112,113,122–131,114,132–137,115–121]. The Andasol-1 plant in Spain, with TES capability and 50 MW capacity rating [5,6], is selected in this work as a reference plant for performance assessment, enhancement, and optimization of the CSP-PT technology.

3. METHODOLOGY

3.1. Chapter journal publications

Some of the work that appears in this chapter is associated with peer-reviewed scientific journal publications. This chapter is associated with publications (1) to (6). The detailed information of these publications is listed in the “Scientific Journal Publications” Section, starting from page (iii) of this thesis.

3.2 Model description

3.2.1 System components and energy balance

In this work, the main model components consist of the following: (i) a transmission network for grid connection, (ii) wind power-generating units using a reference 2 MW wind turbine, and (iii) a reference 50 MW CSP-PT plant (i.e., Andasol-1 in Spain). It should be noted that the CSP-PT plant's components were determined after assessment of the used model in Ref. [218]. Figure 3. 1 provides an illustration of the main model components with energy balance parameters. The CSP-PT plant consists mainly of the SF, TES, and PB systems. Figure 3. 2 shows the process flow diagram for the reference CSP-PT plant. The process flow diagrams for the reference plant with the wet and dry cooling options are provided in Appendix C. A detailed breakdown of the estimated costs for the reference 50 MW CSP-PT plant, including the condenser system, is provided in Appendix H. In this work, the energy balance equations are expressed in a comprehensive approach for the complete thermal analysis of a CSP-PT plant. It should be recognized that Figure 3. 3, Figure 3. 4, and Figure 3. 5 (HCE energy balance) illustrate the main components of the HCE where the initial heat gain process takes place inside the PT collector within the SF system in a CSP-PT plant.

Figure 3. 3 and Figure 3. 4 illustrate the HCE design and how it allows the HTF to absorb the heat from the sun. It should be noted that the annulus between the absorber tube and the glass envelope is evacuated [219]. This setup prevents heat

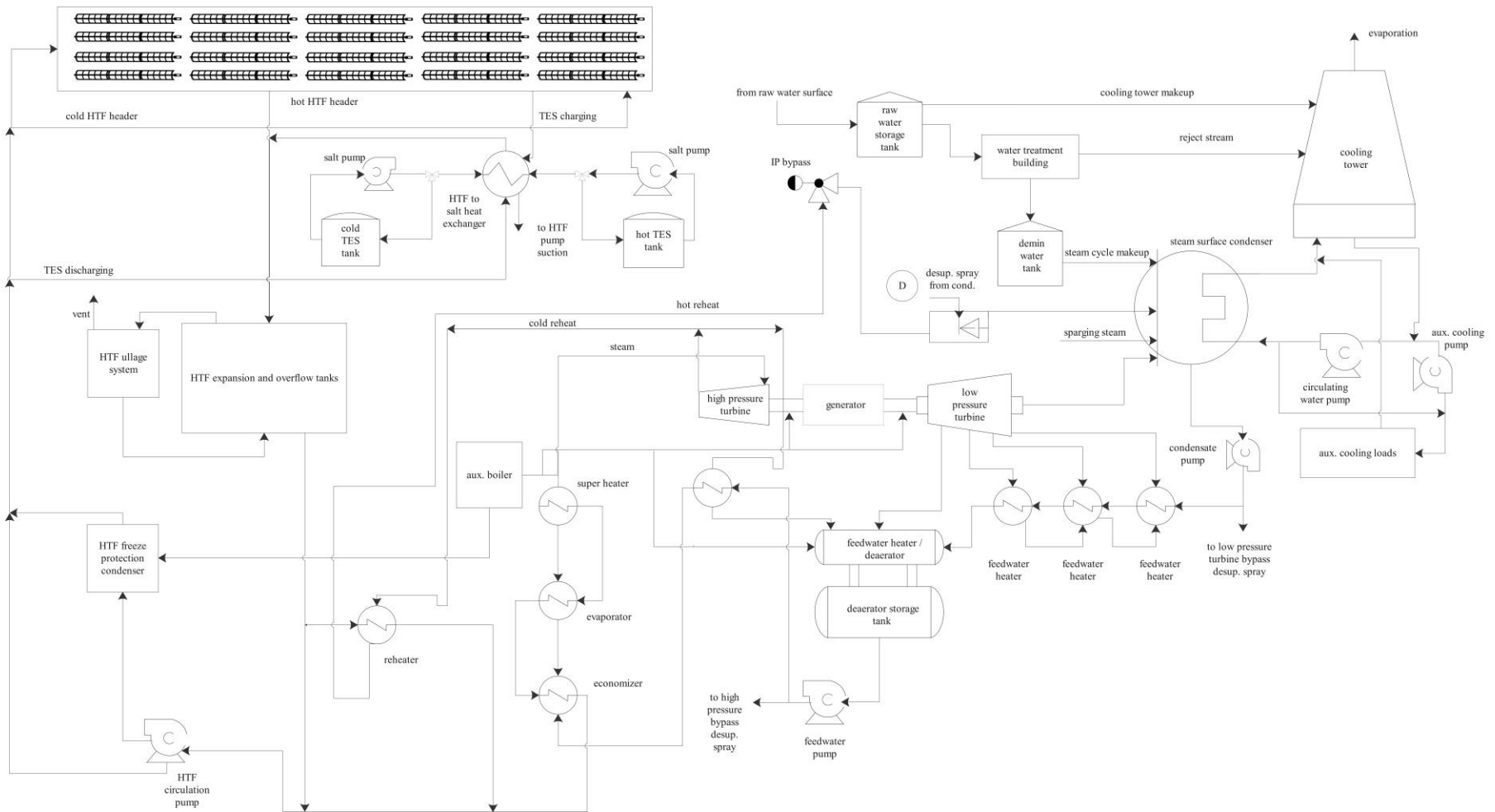


Figure 3. 2 Process flow diagram for the reference 50 MW CSP-PT plant with the wet cooling option (see Appendix C for the dry cooling option).

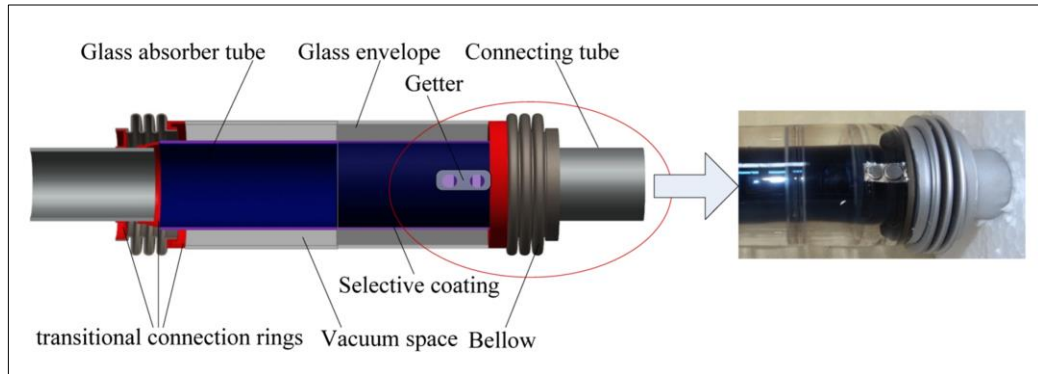


Figure 3.3 Description of the HCE components – (drawing vs actual) [220].

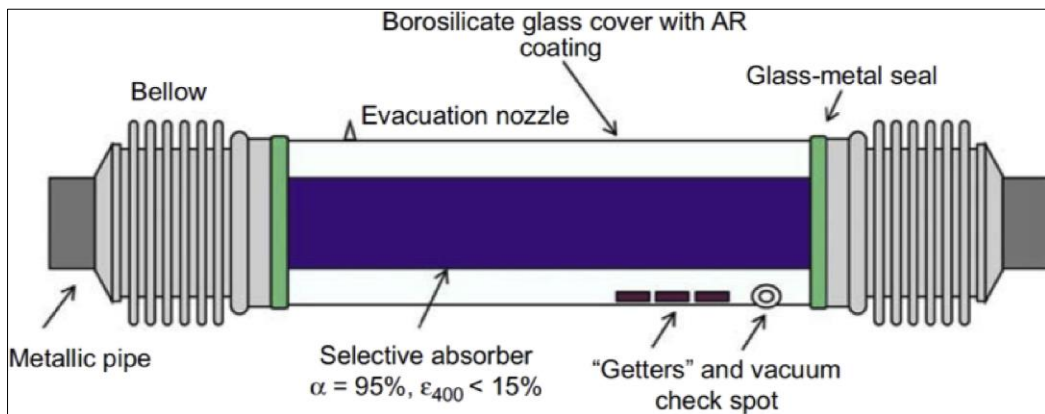


Figure 3.4 Description of the HCE internal housings [221].

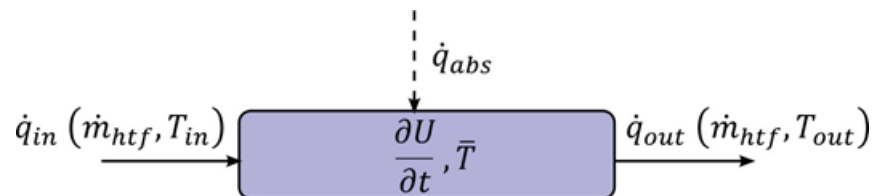


Figure 3.5 Energy balance for the HCE (receiver) – the control volume (box) encompasses the HTF [188].

It should be noted that the mass flow rate and temperature of the HTF (Dowtherm A, see Appendix A) travelling inside the HCE affect the plant's thermal efficiency. This means that higher mass flow rates and/or higher temperatures of the HTF lead to higher thermal efficiency. Therefore, the operating conditions of the PT collector and HTF characteristics should be considered in a detailed analysis using a validated model, which calculates the efficiency profiles for the reference 50 MW CSP-PT plant. It should be recognized that Dowtherm A (see Appendix A) is a synthetic organic HTF and an eutectic mixture of two very stable compounds, biphenyl ($C_{12}H_{10}$) and ($C_{12}H_{10}O$).

The collectors are fueled by a transient source (i.e., DNI), which continually changes magnitude; therefore, the model should incorporate the characteristics, operating conditions, and ambient conditions of the chosen location in Kuwait. Furthermore, the HCE, which collects the solar heat in the collector, is housed inside the Solar Collector Assembly (SCA) with support structures (see Figure 3. 6) within the SF system (see Figure 3. 7). The SF system consists of numerous SCA units and HCEs through which the HTF flows and absorbs heat from incident solar radiation from sunrise (east) to sunset (west).

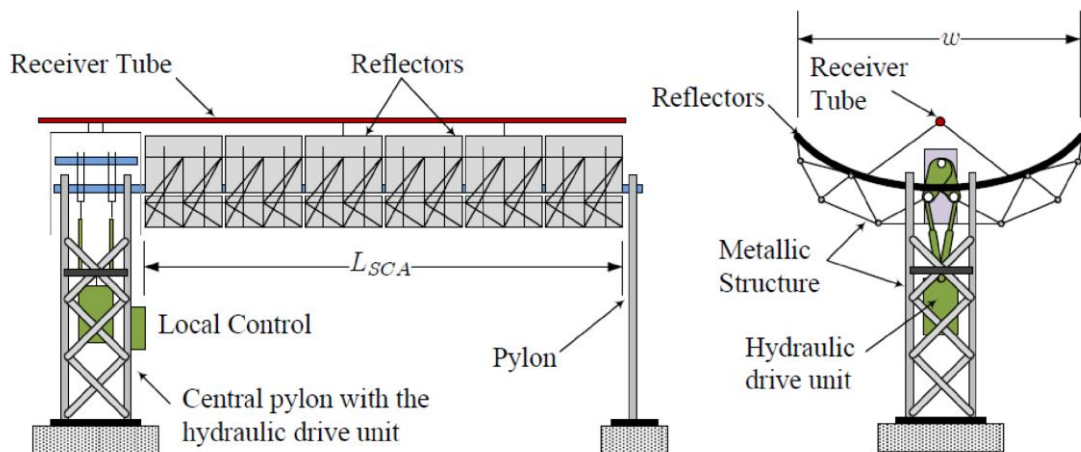


Figure 3. 6 Schematic diagram of a single unit of SCA used in the SF system in which the HCE (receiver) is shown as a red line (left) [222,223].

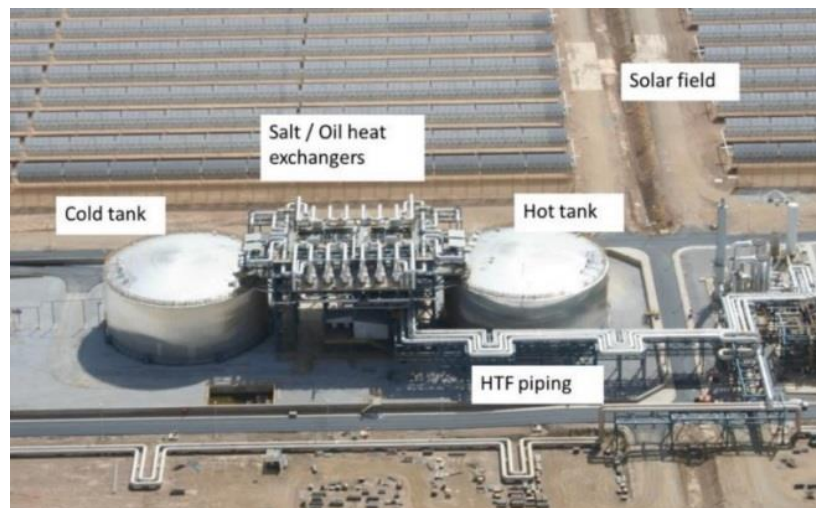


Figure 3. 7 The SF system (top) with other CSP-PT plant systems (bottom) [224].

Whenever the heat losses in the HCEs are at minimal levels, the HTF temperature can be estimated proportional to the receiving heat flux from solar radiation. Therefore, an assessment of the heat losses considering the solar radiation rate of change should be coupled with a thermal efficiency analysis to comprehensively

understand the heat collection process within the CSP-PT plant. Similarly, the process in which solar radiation (heat gain) affects the HTF temperature should be understood as it impacts thermal efficiency calculations. Contrary to conventional generation processes, the heat absorbed in the PT collectors comes from solar radiation, which changes with considerable daily and hourly fluctuations. It should be recognized that analyzing such behaviour requires a model to investigate the thermal efficiency profiles based on variable ambient conditions (throughout the year) and several design parameter inputs (see Appendix D). Especially since the heat absorbed by the collectors should be monitored during the plant's lifetime even after passing the following tests, which CSP-PT plants initially undergo: (i) performance testing, (ii) provisional acceptance testing, and (iii) reliability test run at the stage of plant handover.

It is critical to understand the thermal response in PT collectors because they contain different heat transfer processes for collecting and transferring heat. Generally, the HCE in the collectors heats the HTF, a medium that processes heat and dissipates it at different rates depending on the operating and ambient conditions. Therefore, the vital role of the collectors highlights the need for detailed thermal analysis from the viewpoint of efficient input fuel (i.e., solar heat gain) and HTF flow rate. Furthermore, the collector is driven by solar heat from the HCE; therefore, the ambient conditions (e.g., temperature, solar radiation) will significantly affect thermal efficiency calculations. Hence, sufficient measures need to be checked through modelling due to the existence of hundreds of collectors in a CSP-PT plant.

The previous tests may be performed under steady-state conditions in some instances in CSP-PT plants. However, the trend of solar radiation is naturally transient. This makes the solar radiation's effective vector component (used in the thermal efficiency calculation) follows a similar trend. Thus, there is a need to set assumptions regarding each of the following: (i) the Irradiation At Design (IAD), (ii) the heat losses due to thermal inertia effects, (iii) the HTF incompressibility, and (iv) the mass flow control effectiveness. Therefore, some assumptions are required so that the HTF outlet temperature satisfies steady-state conditions for efficiency calculation purposes. Furthermore, it is critical to investigate the steady-state conditions under the assumption that the change in HTF flow rate follows the variation in solar radiation (heat input). Thus, the HTF flow rate is adjusted by control functionality during plant testing to ensure close to constant HTF outlet

temperature. It should be noted that later in Chapter 5, the IAD effects are investigated. It should be recognized that a control strategy is utilized within the SF system in the reference CSP-PT plant. The HTF mass flow rate is monitored so that the loop outlet temperature (see Figure 1. 1) performs as per the design point. The HTF temperature is calculated iteratively because the receiver heat loss and surface temperature are functions of HTF temperature, which is a function of HTF mass flow rate. This is achieved through an initial estimate for the field mass flow rate and temperature values, and then the mass flow rate is recalculated and adjusted until the outlet temperature converges to the design value.

One of the essential needs to utilize a validated model in this work is to calculate thermal efficiency profiles considering solar radiation changes and perform the tests mentioned above, including the reliability test run. Here, reliability is the overall consistency of thermal performance under the same operating conditions. It should be recognized that a CSP-PT plant would be considered highly reliable if it has consistent thermal efficiency under the same testing conditions.

According to a study [188], a header pipe supplies each loop with an equal HTF flow rate in the SF system, and another header returns the hot HTF to the PB system or the TES system. Each loop contains multiple SCAs and HCEs. This looping incrementally heats the HTF to the design outlet temperature for the CSP-PT plant. In this work, it should be recognized that the SCA is treated as the lowest discretisation level in modelling, and each SCA is considered an independent node within the loop inside the SF system. The steady-state HCE model determines the temperature rise across the node, HTF mass flow rate through the HCE, and HTF specific heat. The energy balance for node i is represented as follows:

$$\Delta T_i = T_{out,i} - T_{in,i} = \frac{\dot{q}_{abs}}{\dot{m}_{HTF} C_{HTF}}$$

3.1

In the SF system, attention should be given to the transient effect produced by the HTF thermal mass in the headers/receiver piping and the HTF change in energy, internal energy ($\frac{\partial U}{\partial t}$), which is a function of time (t). Figure 3. 5 shows the energy balance for a single SCA node in which it can be observed that the heat flows are dependent on \dot{m}_{HTF} , $T_{out,i}$, and $T_{in,i}$. Further, it should be noted that $\frac{\partial U}{\partial t}$ is defined as the change in energy of the node, which is dependent on t and calculated as follows:

$$\frac{\partial U}{\partial t} = (m c_{HTF} + (m c)_{b,SCA} L) \frac{\partial T}{\partial t}$$

3. 2

Here, m is the HTF mass in the node, L is the SCA length, and c_{HTF} is the HTF specific heat, the term $(m c)_{b,SCA} L$ is to account for the thermal mass of piping, joints, insulation, and other SCA components that thermally cycle with the HTF. It should be recognized that the term $(m c)_{b,SCA} L$ is dimensionally equivalent to the HTF capacitance term $m c_{HTF}$ and is represented by a single value. Also, it should be noted that this term is dimensionally defined to describe the thermal energy (per collector length) required to raise the temperature of the node one degree K. The temperature of node i from the previous time step is stored, and the inlet temperature is adjusted equivalent to the outlet temperature of the previous node. In order to analyze the change in HTF temperature, there is a need to perform an energy balance in the control volume as follows:

$$\dot{q}_{in} + \dot{q}_{abs} = \frac{\partial U}{\partial t} + \dot{q}_{out}$$

3. 3

One of the essential parameters to examine is the inlet and outlet heat flows, which can be calculated as follows:

$$\dot{q}_{in} - \dot{q}_{out} = \dot{m}_{HTF} c_{HTF} (T_{in} - T_{out}) = 2 \dot{m}_{HTF} c_{HTF} (T_{in} - \bar{T})$$

3. 4

where \bar{T} is the average temperature. After considering the above relation along with the definition for the internal energy and solving for the first differential, the following is obtained:

$$\frac{d\bar{T}}{dt} = \frac{2 \dot{m}_{HTF} c_{HTF} (T_{in} - \bar{T}) + \dot{q}_{abs}}{m c_{HTF} + (m c)_{b,SCA}}$$

3. 5

The general solution to the above relation is as follows:

$$\bar{T} = \frac{\dot{q}_{abs}}{2 \dot{m}_{HTF} c_{HTF} (T_{in} - \bar{T})} + C_1 e \left[-\frac{2 \dot{m}_{HTF} c_{HTF} (T_{in} - \bar{T})}{m c_{HTF} + (m c)_{b,SCA}} \Delta t \right] + T_{in}$$

3. 6

where C_1 is solved after enforcing boundary conditions as follows (when $t=0$):

$$\bar{T}_0 = \frac{\dot{q}_{abs}}{2 \dot{m}_{HTF} c_{HTF}} + C_1 \exp^0 + T_{in}$$

$$C_1 = \bar{T}_0 - \frac{\dot{q}_{abs}}{2 \dot{m}_{HTF} c_{HTF}} - T_{in}$$

3.7

Substituting C_1 into the above general solution, the outlet temperature from each SCA ($\bar{T}_{0,i}$) can be calculated as follows:

For $i = 1$ to N_{SCA} :

$$\bar{T}_{0,i} = 2 \bar{T}_i - T_{in,i} = \frac{\dot{q}_{abs,i}}{\dot{m}_{HTF} c_{HTF,i}} + T_{in,i} + 2 \left[\bar{T}_{0,i} - \frac{\dot{q}_{abs,i}}{2 \dot{m}_{HTF} c_{HTF,i}} - T_{in,i} \right] \exp \left[\frac{-2 \dot{m}_{HTF} c_{HTF,i} \Delta t}{m_i c_{HTF,i} + m_{c_{i,b,SCA}} L_i} \right]$$

3.8

The above relation is concerned with each node i in the loop within the SF system in the CSP-PT plant, where $T_{in,i}$ is equivalent to the outlet temperature from the previous node in the loop, $T_{in,i-1}$. It should be understood that the calculated temperature for each node depends on the inlet temperature from the previous node and the node temperature from the previous time step; therefore, such values should be considered as boundary conditions within the system. In the modelling algorithm, the temperature of the node at the previous time step is stored in between time steps. Additionally, the inlet temperature is set equal to the outlet temperature of the previous node. Additionally, the HTF mass of each node is calculated as a function of the receiver piping volume ($L_i A_{SCA,i}$) and the local HTF density (ρ_{HTF}) as follows:

For $i = 1$ to N_{SCA} :

$$m_i = \rho_{HTF} L_i A_{SCA,i}$$

3.9

According to a study [219], the HTF temperature increase as it flows through one loop was analyzed. In the study, the heat loss testing of the Schott PTR70 2008 receiver, which is used in this work, has been performed. Figure 3.8 shows the HTF temperature rise, which looks linear with a slight down curve. It was concluded that the temperature rise (per meter) decreased from 0.18 °C (at $T_{HTF} = 293$ °C) to 0.16 °C (at $T_{HTF} = 391$ °C). In addition, the net energy gain decreases as the fluid

passes through the loop since the heat loss increases as the HTF temperature increases, as a result.

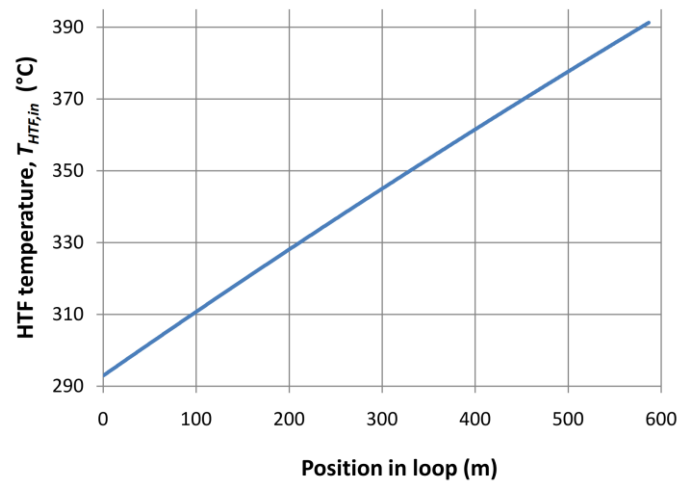


Figure 3. 8 HTF temperature increase as it flows through one [219].

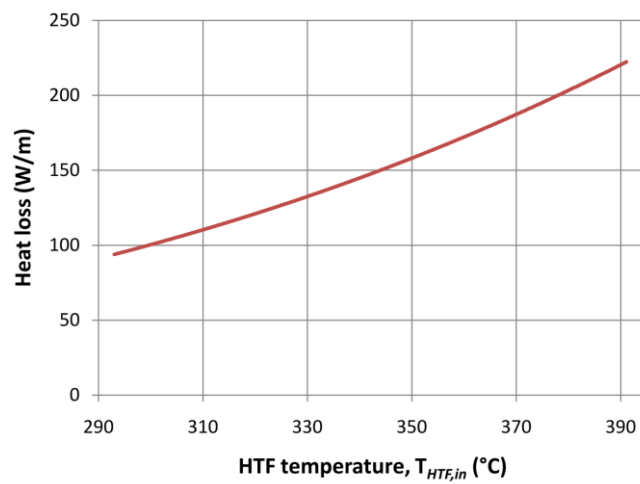


Figure 3. 9 Heat loss as a function of HTF temperature [219].

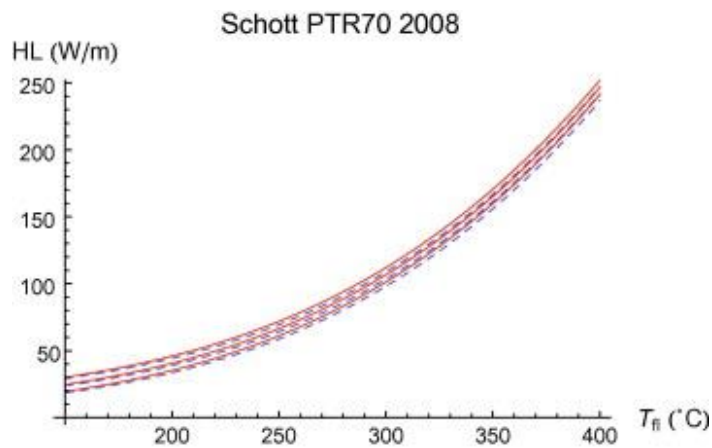


Figure 3. 10 Heat loss per unit length of HCE vs average HTF temperature for Schott PTR70 2008 used in this work within the SF system [190,219].

Figure 3. 10 shows that the solid red curves use an average HTF temperature, assuming a temperature jump of 100 °C between input and output HTF temperatures. Also, the dashed blue curves assume a constant HTF temperature throughout the receiver. Additionally, the lower curves correspond to an ambient temperature of 40 °C, middle curves to 20 °C and upper curves to 0 °C [190].

3.2.2 Justification for simulation model selection

In this work, the following reasons contributed to the selection of the SAM software, based on the Transient System Simulation (TRNSYS), for CSP-PT/TES and wind power performance modelling: (i) detailed performance analysis from the viewpoint of total system-level simulation, (ii) availability of input datasets for design parameters of plant components (see Appendix D), and (iii) ability to run a large number of simulations by employing the writing of scripts and codes using several programming languages to perform parametric analyses. It should be recognized that a detailed review has been conducted to demonstrate various software(s) and tools available for CSP-PT and wind power modelling [138,139,148–157,140,158–167,141,168–174,176–178,142,179–187,189,143,190–199,144,200–209,145,210–213,146,147]. These software(s) and tools are listed in Table 2. 8, as previously mentioned.

According to SAM developers [188], the software is based on hourly simulations interacting with performance and financial models to calculate energy outcomes and costs/cash flows. SAM allows for exchanging data with external software for further detailed analysis, such as using advanced statistical tools, as in this work's case. Most inputs can be used as parametric variables (see Appendix D) to investigate the impacts of variations in technical performance and economic indicators, such as LCOE. SAM system uses a performance engine (TRNSYS software), which includes customized components, developed at the University of Wisconsin. It should be recognized that TRNSYS is a time-series simulation program that can simulate system component performance, and it is integrated into SAM for faster simulation run time. The default source code folder `\SAM\<version number>\exelib\trnsys\source` contains the FORTRAN code for each TRNSYS module as follows:

- i. `sam_mw_trough_Type250.f90` (the SF system),
- ii. `sam_mw_trough_Type251.f90` (the TES system and dispatch),

- iii. sam_mw_pt_Type224.f90 (the PB system), and
- iv. the shared HTF property subroutines sam_mw_pt_Type229.f90 and sam_mw_pt_propmod.

It should be noted that the aim of the PB system model is to characterize off-design performance and provide flexibility in dealing with the steam Rankine cycle. Instead of directly incorporating a detailed model into TRNSYS, process-simulation software is used to construct a representative cycle. Then, the output is converted into an off-design performance. It should be noted that SAM uses the design of experiments statistical approach [225] to characterize variable dependencies and generate response surfaces [226,227].

3.2.3 Computational algorithm and control

The SAM software is demonstrated as software that handles the comprehensive performance of CSP/TES and wind power technologies. In general, total system analysis software(s), such as SAM, evaluate the overall performance metrics (e.g., LCOE) and energy outputs depending on detailed processes with information concerning the performance of subcomponents [228] (see Figure 3. 11 and Figure 3. 12).

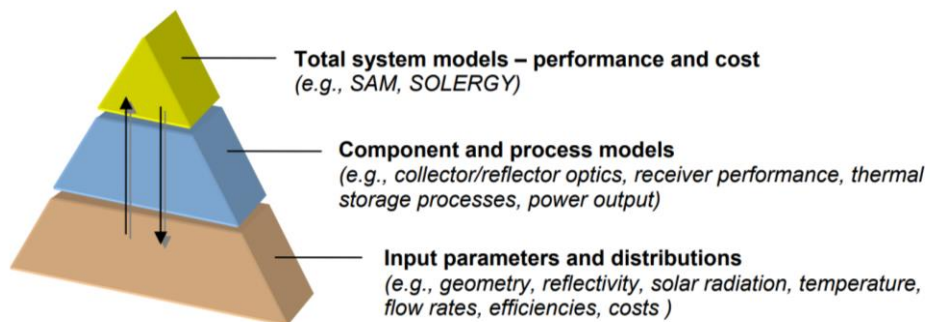


Figure 3. 11 Illustration of the modelling pyramid in SAM [228].

The complex process models in SAM require input parameters (see Appendix D) and distributions for uncertainty and sensitivity analyses obtained from surveys of power plants, operational tests, detailed reviews, and expert judgments. The framework for modelling complex systems relies on passing information from various process models to prioritize modelling and characterization for the objectives that impact the financial and performance metrics. In one study [229], the algorithms in SAM for analyzing the components, parameters, and time-dependent inputs are explained.

The control flow diagram for the physical CSP-PT model is provided by the National Renewable Energy Laboratory (NREL) [188] (see Figure 3. 13). SAM is usually used for total system-level simulation by estimating the technical performance and economics through the integration of elements from DELSOL and TRNSYS, which is used within the performance modelling engine of SAM. Additionally, SAM uses embedded models for both piping (a source of heat loss) and TES systems, which are treated as lumped systems. The performance and economic models are taken from the Excel-based model EXCELERGY (i.e., developed by NREL), which provides a framework for analyzing system costs and performance.

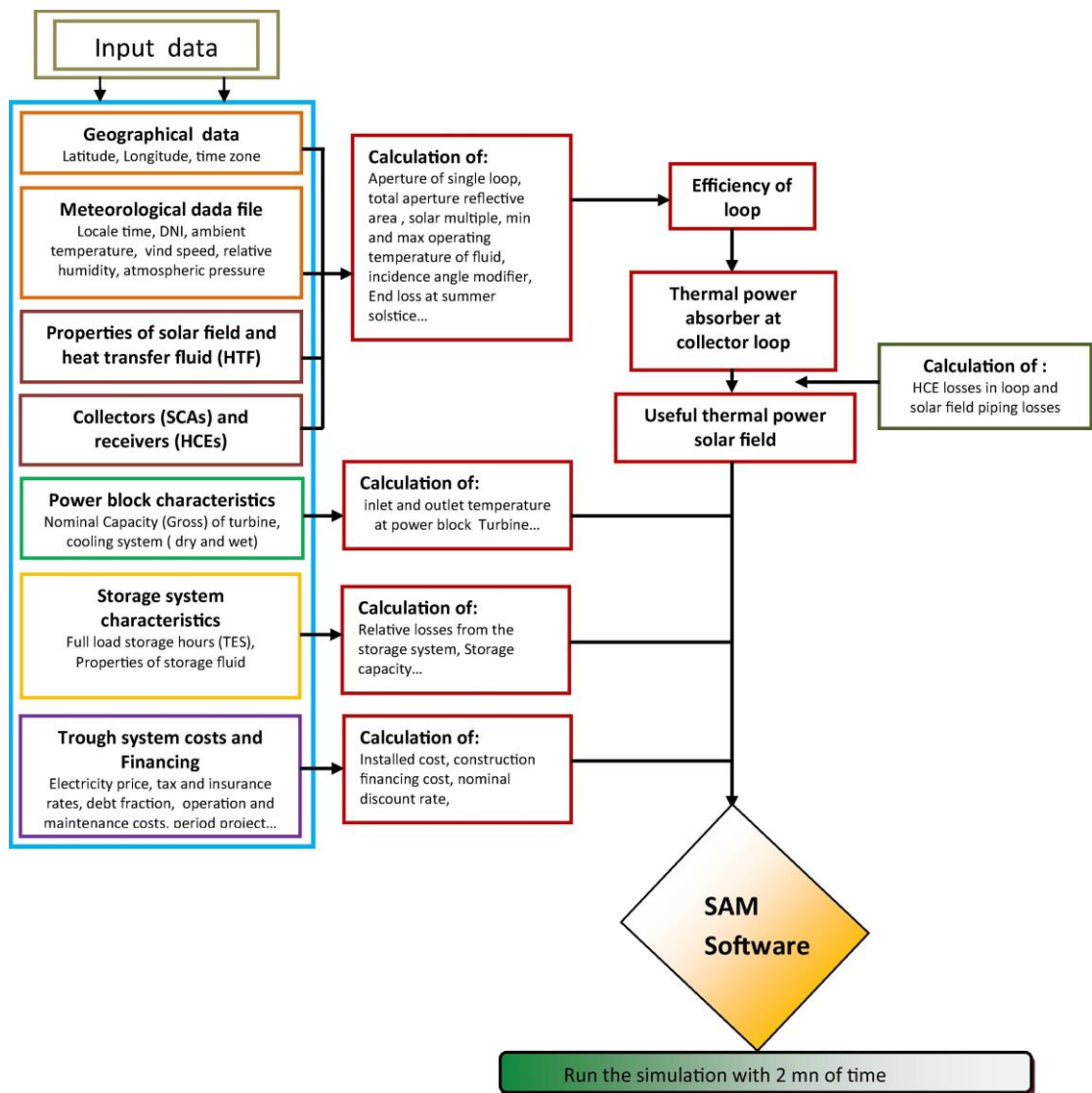


Figure 3. 12 System computational algorithm in SAM [229].

EXCELERGY is an engineering design, performance, and economic model for CSP-PT plants. The model is prepared using Microsoft Excel and Visual Basic programming language. The user can provide inputs based on the desired design, plant operation,

and financial target to determine the impact on plant performance and economics. It should be mentioned that hourly data is used in the performance simulation. In addition, EXCELERGY can run an optimization task to assess the optimal SF system area compared to the TES system volume. Because EXCELERGY is not maintained further, the performance and economic models have been transferred into SAM.

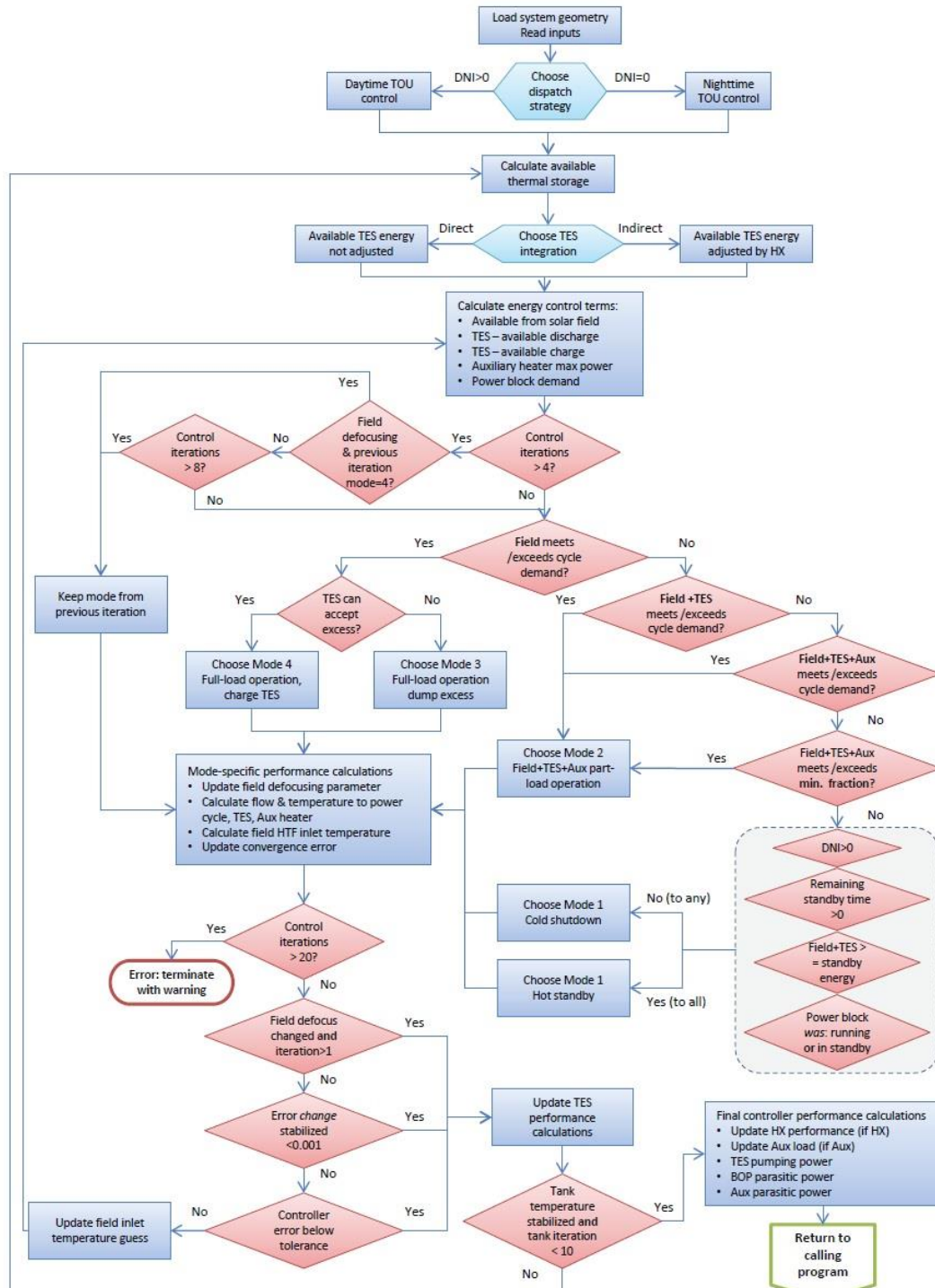


Figure 3. 13 Control flow diagram for the CSP-PT/TES model in SAM [188].

According to a study [230], some efficiency factors are aggregated into single input values in the SF system within SAM. In this work, the input data to the model are provided (see Appendix D). For instance, sources of optical losses are represented by a single optical efficiency number. In addition, a user can enter time-dependent losses to account for soiling and other forms of degradation, such as dust storms. In the PB system, pumping power requirements for the HTF through the PB system are distinguished by a load-based coefficient which is a multiple of the HTF mass flow rate. The user can modify this parameter as needed to match expected parasitic consumption. In SAM, the thermal losses to the ground are negligible as opposed to the losses to the other surroundings. For this reason, it should be recognized that the modeller should increase the thermal loss input to the walls in order to compensate for the losses to the ground. The TES model in SAM uses a single heat loss coefficient for all tank areas; therefore, SAM considers that the temperature along the inner tank surface is constant.

In addition, SAM combines hourly simulation models with performance and economic models to estimate energy output, financial metrics, and cash flows. This is because SAM includes built-in cost and performance models, and it can exchange data with external models developed in Microsoft Excel. Furthermore, SAM can model plant-level simulations since the performance of each of the component models is based on correlations, analytical functions, and factors describing the physical processes. This allows detailed process modelling, including spatial and temporal variability within subcomponents. Also, SAM can handle the detailed optical analysis of the solar collector component. Hence, SAM is selected as one of the analysis tools in this work after surveying numerous software(s).

3.3 Techno-economic competitiveness of concentrating solar power plants with thermal energy storage

In this work, two locations are considered for CSP-PT performance assessment in two different countries (Kuwait and Spain). The meteorological and DNI data used with the reference plant in Spain are provided by NREL. The data for the chosen location in Kuwait is provided by KISR meteorological stations and enhanced with satellite-driven data. Further detailed information about the meteorological data is

provided later (see Section 4.2). In general, these data are used as inputs for performance modelling of the reference 50 MW CSP-PT plant located in Spain using SAM by implementing the following steps:

- i. validation of the CSP-PT/TES model performance against the performance of the reference plant (Andasol-1 in Spain) with 50 MW capacity under the climatic and DNI conditions of Spain in which the reference plant uses a wet-cooled condenser system,
- ii. simulation of the reference plant performance under Spain's climatic and DNI conditions with the dry cooling option instead of the wet cooling option,
- iii. simulation of the reference plant performance under the arid climatic and DNI conditions of the chosen location in Kuwait with the wet and dry cooling options,
- iv. investigation of the influence of the dry-bulb temperature, wet-bulb temperature, and DNI on the plant performance under the conditions of Kuwait and Spain, considering both the wet and dry cooling options,
- v. assessment of the following performance parameters: number of full load hours of steam turbine (operation under the rated design condition), annual net electricity output, overall plant efficiency, solar irradiation on the SF system, thermal power from the SF system, dumped thermal energy from the SF system (due to mirror defocusing), efficiency of the SF system, and total water consumption, and
- vi. evaluation of techno-economic parameters considering several 50 MW CSP-PT design configurations with various TES capacities using the dry cooling option under the arid climatic and DNI conditions of the chosen location in Kuwait, with limited water resources.

Based on an hourly simulation within SAM, the total defocused thermal energy from the SF system (i.e., dumped thermal energy) is tracked throughout, which is the amount of DNI that cannot reach the collector due to mirror defocusing. Moreover, the dumped thermal energy can be calculated from multiple parameters (e.g., the fraction of defocused SCA units and the maximum temperature at which the fluid may exit the collector), as shown later in Chapter 5. It should be noted that the selection of the optimal IAD value, a design point value for a CSP-PT plant, is essential

because it reflects on the amount of auxiliary power needed in the SF system for mirror defocusing and therefore reflects on the total operating cost and LCOE estimations. If the plant's location experiences DNI levels above the design IAD value, the plant operator must perform excessive control by defocusing some mirrors in the SF system. This procedure is necessary to avoid collecting excess thermal energy, which is neither required by the TES system nor the PB system.

3.4. Optimization and performance enhancement of concentrating solar power plants

3.4.1 Parametric analyses

In this work, the optimization and performance enhancement strategies include techno-economic assessment, established by studying the effects of two critical design parameters in a reference CSP-PT plant with a 50 MW rated capacity (Andasol-1 in Spain). The first parameter is the SM, and the second parameter is the number of full load hours of storage (N_h^{TES}). It should be recognized that the SM value is used to determine the SF system area as a multiple of the rated capacity of the PB system (i.e., the design turbine gross output). Table 3.1 shows some design parameters for the reference CSP-PT plant. In the optimization and parametric analyses, thirty-one (31) SM values are considered starting from 1 to 4 with an increment of 0.1. Furthermore, nineteen (19) values of N_h^{TES} are considered starting from 0 to 18 with an increment of 1. Thus, a total of 589 design configurations are evaluated for the CSP-PT model with TES capability. The configuration variations are the product of 31 and 19 (31×19). Later in Chapter 6, performance evaluations of 19 optimal design configurations with optimal SM values based on the lowest LCOE values are evaluated as a function of N_h^{TES} . This means that the performance of the optimal design configuration for each of the 19 categories of N_h^{TES} is evaluated (for $0 \leq N_h^{TES} \leq 18$). It should be noted that each category considers 31 SM values.

The SAM software [187,188,231] is utilized to simulate CSP-PT/TES performance. The model used in this work is validated using actual and simulated published data, provided later in Chapter 5. Moreover, the simulation accuracy and reliability of SAM

are compared with the actual and simulated plant performance data. The results of two simulated cases (Spain and Kuwait) are studied and compared with actual data from the same reference plant (Andasol-1), which became operational in 2009 [8]. Notably, Andasol-1 is the first CSP-PT plant in the world with TES capability.

The TES medium consists of 28,500 t of molten salt, a mixture of 60% sodium nitrate (NaNO_3) and 40% potassium nitrate (KNO_3), which remains in the liquid state throughout the charging and discharging processes of the TES system. The two-tank TES system has a cold tank heater set point of about 292 °C and a hot tank heater set point of about 386 °C. These set points refer to the minimum allowable storage fluid temperature in the storage tanks. If the fluid temperature falls below the set point, the electrical tank heaters deliver energy to the tanks, increasing the temperature to the set point. This energy in the performance model results in the tank freeze protection energy.

It should be recognized that the outcomes from the Kuwait and Spain cases are compared in terms of accuracy and reliability for several CSP-PT plant configurations' technical and financial results, shown later in Chapter 5.

Table 3.1 Design parameters for the reference CSP-PT/TES plant (Andasol-1) used in this work.

Description	Value	Unit
Total land area	477	acres
SF area	329	acres
Number of loops	156	-
Aperture reflective area	510,120	m ²
HTF type	Dowtherm A (see Appendix A)	-
Design loop outlet temperature	393	°C
Design loop inlet temperature	293	°C
Irradiation at Design (IAD)	700	W/m ²
Number of SCA units	624	-
SCA type	EuroTrough ET150 (Skal-ET PT)	-
SCA aperture width	5.77	m
SCA focal length	1.71	m
SCA length	148.5	m
SCA aperture area	817.5	m ²
Absorber tube inner diameter	0.0655	m
Row spacing	17.3	m

Table 3.1 Cont. Design parameters for the reference CSP-PT/TES plant (Andasol-1) used in this work.

Description	Value	Unit
Mirror reflectivity	93.5	%
Absorber absorptivity	96	%
Envelop transmissivity	96.3	%
Total collectors	624	-
Storage medium	Molten salt 60% NaNO ₃ and 40% KNO ₃ 28,500 t (see Table 1. 2 and Appendix B)	-
Number of full load hours of storage (N_h^{TES})	7.5	h
Cold tank heater set point	292	°C
Thermal storage capacity	964	MWh _t
Hot tank heater set point	386	°C
Rated cycle conversion efficiency	38	%
Nominal capacity	50	MW
Total parasitics	5	MW
Turbine inlet conditions: pressure	100	bar
Design back pressure	0.08	bar

In this work, the CSP-PT performance assessment location is within Kuwait's western region, with limited water resources. As mentioned earlier, the meteorological data of the chosen location is provided by meteorological stations and enhanced with satellite-driven data. Additionally, the meteorological data is utilized as inputs for performance modelling using SAM. Furthermore, optimization and performance enhancement of dry-cooled CSP-PT is studied along with the viability of the wind resource for cogeneration by performing the following:

- i. evaluation of the validated CSP-PT model performance with the actual performance of the 50 MW reference plant under the climatic condition of the chosen location in Kuwait,
- ii. assessment of the solar/wind resources and electrical load profiles in Kuwait,
- iii. investigation of the following performance parameters: LCOE, capacity factor, thermal power produced by the SF system, annual energy generation ($E_{ele,a}$), annual overall plant efficiency ($\eta_{overall}$), and cycle electrical power output, and
- iv. assessment of the following performance enhancement strategies:

- a. integration of TES,
- b. integration of wind power,
- c. cogeneration with temperature derating effect,
- d. cogeneration with load consideration,
- e. evaluation of the periods of 24 h continuous generation from CSP-PT/TES without fossil backup, and
- f. comparison of the CSP-PT/TES performance between winter and summer sessions.

3.4.2. Modelling approach

As stated earlier, one of the software(s) used in this work is the SAM software, and it should be recognized that SAM is based on TRNSYS simulation [188]. The selection came after a thorough literature review on various tools for modelling purposes [138,139,148–157,140,158–167,141,168–174,176–178,142,179–187,189,143,190–199,144,200–209,145,210–213,146,147], as shown in Table 2. 8.

SAM allows the user to input design parameters (see Appendix D) for CSP plants to match the desired operation philosophy and design conditions. Furthermore, SAM allows a detailed performance assessment on an hourly basis and provides financial and economic estimations for the project [228,229]. Also, SAM provides dispatch optimization features based on user inputs into the dispatch control algorithms and weekday/weekend schedules. Hence, SAM gives the user options to evaluate the impact of plant performance and economics. Additionally, SAM provides a comprehensive approach for examining the TES energy to electricity conversion [226,232]. In one study, SAM was used to assess water consumption for cooling purposes with an hourly resolution within a year for the Noor 1 power plant [233]. The 160 MW CSP plant (phase I) of the Noor Ouarzazate project has already generated power near the simulation estimates [80].

The primary input data to SAM are as follows: (i) the TES system parameters such as thermal capacity, tank volume, fluid medium properties, heat losses, exergetic efficiency, other parameters including dispatch control, (ii) the PT collector parameters, such as collector geometry, piping distance between assemblies, optical parameters, tracking error, dirt on mirrors, (iii) the HCE parameters, such as

absorber tube inner/outer diameters, glass envelope inner/outer diameter, flow pattern, absorber absorptance/emittance, envelope transmittance, annulus gas type/pressure, shadowing, heat loss at design, (iv) the Typical Meteorological Year (TMY) file (for CSP-PT modelling), (v) the site characteristics, such as elevation, latitude, longitude, (vi) the SF system and HTF characteristics, such as single loop configuration, land area, collector orientation, tilt angle, azimuth, loop optical/conversion efficiencies, (vii) the financial parameters such as analysis periods, interest rate, price escalation, inflation rate, and (viii) the PB system parameters such as gross output, conversion efficiency, net output at design, rated cycle efficiency, ambient temperature at design, condenser pressure ratio.

The detailed meteorological and resource data in the form of a TMY file, which are supplied to SAM, are as follows: (i) day of the year, (ii) time in hourly format, (iii) Global Horizontal Irradiance (GHI), (iv) DNI, (v) diffuse irradiance, (vi) sun azimuth angle, (vii) sun altitude/elevation, (viii) air temperature, (ix) relative humidity, (x) wind speed, (xi) wind direction, (xii) atmospheric pressure, and (xiii) wet-bulb temperature.

3.5. Comparative techno-economic assessment and optimization of wind power plants

3.5.1 Parametric analyses

In this work, the following outcomes are provided using detailed analyses:

- i. daily profiles for wind speed and α at different height levels,
- ii. monthly profiles for wind speed and direction frequencies at the reference 2 MW wind turbine's hub height with normal distributions,
- iii. statistical results of the wind speed in m/s, the wind direction in deg ($^{\circ}$) unit, the ambient temperature in $^{\circ}\text{C}$ unit, and other meteorological data at the reference turbine's hub height, and
- iv. Locally Estimated Scatterplot Smoothing (LOESS) regression analyses for the wind resource.

Additionally, several evaluations are performed by varying the number of rows in the wind power plant (N_r) and the wind power plant layout angle (θ_{plant}), which are the primary investigated design parameters. The impact of varying N_r and θ_{plant} on the annual gross energy, LCOE, performance ratio, capacity factor, and wake losses are evaluated for 2220 configurations, including 60 optimal design configurations. The model simulation is performed for 2220 runs from which 60 optimal configurations are identified corresponding to various row configurations (i.e., 1-row, 2-row, 3-row, ..., 60-row), as will be shown later in Chapter 7. It should be mentioned that the optimization and performance assessment includes a techno-economic evaluation in which it is established by examining the effects of the two primary design parameters as follows:

- i. N_r is varied from 1 to 60 with an increment of 1 row, and
- ii. θ_{plant} is varied from 0 to 360° with an increment of 10°.

The total variations bring the investigated simulation runs to 2220 runs, which are divided into 60 categories as follows:

- i. category 1 of 60:
(1-row x 0°), (1-row x 10°), (1-row x 20°) ..., (1-row x 360°),
- ii. category 2 of 60:
(2-row x 0°), (2-row x 10°), (2-row x 20°) ..., (2-row x 360°),, and
up to,
- iii. category 60 of 60:
(60-row x 0°), (60-row x 10°), (60-row x 20°) ..., 60-row x 360°).

The detailed monthly performance for the following selected 8 of the 60 optimal configurations of wind power plants is further evaluated later in Chapter 7. It should be recognized that the optimal configurations have optimal values of θ_{plant} based on the lowest LCOE values:

- i. category 1 of 60: the optimal 1-row configuration,
- ii. category 2 of 60: the optimal 2-row configuration,
- iii. category 3 of 60: the optimal 3-row configuration,
- iv. category 4 of 60: the optimal 4-row configuration,

- v. category 40 of 60: the optimal 40-row configuration,
- vi. category 46 of 60: the optimal 46-row configuration,
- vii. category 52 of 60: the optimal 52-row configuration, and
- viii. category 58 of 60: the optimal 58-row configuration.

In addition, the frequency profiles for the following 12 assessment parameters are evaluated from January to December:

- i. assessment parameter 1 of 12:
wind speed in m/s unit at the reference turbine's hub height,
- ii. assessment parameter 2 of 12:
wind direction in deg (°) unit at the reference turbine's hub height,
- iii. assessment parameter 3 of 12:
ambient temperature in °C unit at the reference turbine's hub height,
- iv. assessment parameter 4 of 12:
atmospheric pressure in atm unit at the reference turbine's hub height,
- v. assessment parameter 5 of 12 under category 1 of 60:
generation of the optimal 1-row configuration in kW unit,
- vi. assessment parameter 6 of 12 under category 2 of 60:
generation of the optimal 2-row configuration in kW unit,
- vii. assessment parameter 7 of 12 under category 3 of 60:
generation of the optimal 3-row configuration in kW unit,
- viii. assessment parameter 8 of 12 under category 4 of 60:
generation of the optimal 4-row configuration in kW unit,
- ix. assessment parameter 9 of 12 under category 40 of 60:
generation of the optimal 40-row configuration in kW unit,
- x. assessment parameter 10 of 12 under category 46 of 60:
generation of the optimal 46-row configuration in kW unit,
- xi. assessment parameter 11 of 12 under category 52 60:

generation of the optimal 52-row in kW unit, and

- xii. assessment parameter 12 of 12 under category 58 of 60:

generation of the optimal 58-row configuration in kW unit.

Furthermore, the Monthly Frequency Profiles (MFPs) and the Annual Frequency Profiles (AFPs) for the 12 assessment parameters mentioned above are evaluated. Additionally, the Hourly Frequency Profiles (HFPs) for the 12 assessment parameters are evaluated later in Chapter 7.

3.5.2 Modelling approach

In this work, one of the software(s) used in the analysis of wind power performance modelling is the SAM software [187,188]. The flexibility of selecting various design parameters is one of the main reasons for choosing SAM, as it gives the user the capability to set rated design conditions. In addition, SAM allows performing a detailed performance assessment on an hourly basis and provides financial and economic estimations for the project under investigation [228,229]. Furthermore, SAM provides dispatch optimization features based on user inputs (see Appendix D) into the dispatch control algorithm, including weekday and weekend schedules. Hence, it gives the user options to evaluate the impact of wind power plant performance and economics. Finally, the approach used is a comprehensive one in which the plant's energy balance and electricity output are considered [226,232]. Such features strongly support the use of SAM in project assessments for wind power plants to provide feasibility measures before installation and construction stages [80,233].

SAM requires the input of design parameters to run the simulations for wind power modelling. The inputs are as follows: wind turbine design parameters, SRW meteorological file type, location characteristics, and financial input parameters. The input meteorological parameters to the simulation model are as follows: air temperature, relative humidity, wind speed, wind direction, and atmospheric pressure for 8760 hours (i.e., one year). The main risk in modelling a mega-scale system such as a wind power plant consisting of various subsystems is to overcome the computational demand of subsystem models by employing methods to reduce simulation running time. Some techniques that help mitigate intensive computational

time, especially when performing detailed parametric analyses, are the use of software(s) for time-series analyses, which are considered in this work.

3.6. Chapter conclusion

The main findings are summarized as follows:

- i. as part of building the methodology of this work, the system components have been determined for the wind power and CSP-PT model configurations as follows: transmission network for grid connection, wind power-generating units using a reference 2 MW wind turbine, and a reference 50 MW CSP-PT plant (i.e., Andasol-1 in Spain) with energy balance parameters,
- ii. justification has been provided for utilizing the SAM software, based on TRNSYS simulation, to achieve some of the modelling objectives in this work,
- iii. the computational algorithm and control have been explained for a comprehensive performance assessment of the CSP-PT model, along with overall performance metrics such as LCOE and other energy-related parameters with information concerning the performance of subcomponents [228]. The control flow diagram for the model is also provided [188],
- iv. a methodology has been determined for the optimization and parametric analyses in which 31 SM values are considered from 1 to 4 with an increment of 0.1. Furthermore, 19 values of N_h^{TES} are considered from 0 to 18 with an increment of 1. Thus, a total of 589 design configurations are evaluated for the CSP-PT model with TES capability. The configuration variations are the product of 31 and 19 (31×19). The methodology has been determined for the performance evaluations of 19 optimal design configurations for CSP-PT/TES with optimal SM values based on the lowest LCOE values as a function of N_h^{TES} ,
- v. a methodology has been determined to optimise and enhance dry-cooled CSP-PT, considering the viability of wind resources for cogeneration. The methodology includes an evaluation of the validated CSP-PT model

performance with the actual performance of the 50 MW reference plant under the climatic condition of the chosen location in Kuwait, including the assessment of solar/wind resources and the national electrical load profile. Furthermore, the methodology includes an investigation of the following performance parameters:

- a. LCOE,
- b. capacity factor,
- c. thermal power produced by the SF system,
- d. $E_{\text{ele,a}}$,
- e. η_{overall} , and
- f. cycle electrical power output.

Also, the methodology includes an assessment of the following performance enhancement strategies:

- a. integration of TES,
- b. integration of wind power,
- c. cogeneration with temperature derating effect,
- d. cogeneration with load consideration,
- e. evaluation of the periods of 24 h continuous generation from CSP-PT/TES without fossil backup, and
- f. comparison of the CSP-PT/TES performance between winter and summer sessions.

4. NATURAL RESOURCES AND METEOROLOGICAL CHARACTERISTICS

4.1. Chapter journal publications

Some of the work that appears in this chapter is associated with peer-reviewed scientific journal publications. This chapter is associated with publications (1) to (6). The detailed information of these publications is listed in the “Scientific Journal Publications” Section, starting from page (iii) of this thesis.

4.2. Meteorological data

In a few studies [40,234], five locations were evaluated for Kuwait's solar and wind resources. The studies supported the outcome that the chosen location in this work (Shagaya) has high solar and wind resource potentials using data from meteorological stations. In addition, the studies employed ground-measured and satellite-driven data for enhancement purposes. Another study [28] supported the high potential of solar and wind resources in the same location. Furthermore, the wind power density across Kuwait was evaluated by another study [33], which considered the same location attractive for wind power technology implementation.

In this work, a TMY file, which is established on a monthly basis for individual years with long-term monthly characteristics, serves as input to the SAM software. In selecting the most representative month, different weights are considered for the following parameters: DNI, ambient temperature, relative humidity, wind speed, and wind direction. However, these parameters, excluding DNI, have minimal weight in deciding on the choice of the representative month. A higher weight is given to the DNI because it has the highest impact on the annual net electricity output from a CSP-PT plant.

Before the assessment of the techno-economic competitiveness of the CSP-PT technology (using wet and dry-cooled condenser systems), as shown later in Chapter 5, it is required to determine the main design climatic conditions (Table 5.1) for future CSP-PT plants in the chosen location in Kuwait. Therefore, the statistical

results for the DNI and meteorological parameters during a typical year in Kuwait are provided in Table 4. 1.

The primary factor affecting a dry-cooled condenser system is the dry-bulb temperature. Notably, higher dry-bulb temperatures decrease the dry cooling system performance, reducing the Rankine cycle efficiency in a CSP-PT plant. Therefore, the condensing temperature should be close to the dry-bulb temperature in an ideal dry-cooled condenser. It should be recognized that the critical parameter in the dry cooling system is the dry-bulb temperature, which affects the PB system, as shown later in Chapter 6 in Equation 6. 1 and Equation 6. 2. It should be noted that the negative impact of high ambient temperatures on the CSP-PT plant's performance is related to the efficiency of the dry-cooled condenser system.

Furthermore, Kuwait is characteristic of hot summers between May and October and short winters between December and February, as shown in Table 4. 1. In a CSP-PT plant, the better performance is due to the DNI impact, ambient temperature, and wind speed. Table 4. 1 shows the meteorological parameters in Kuwait, the annual mean for the dry-bulb temperature is 25.8 °C, the annual mean for the wet-bulb temperature is 12.1 °C, and the annual mean wind speed is 4 m/s.

It should be recognized that the data (shown in Table 4. 1) is used along with the input data to the model (shown in Table 5. 3). It should be noted that the input data to the model for the condenser system as per design is provided in Table 5. 3. Also, It should be noted that for a wet-cooled condenser system. the condenser is driven by water evaporation (latent heat) to remove heat energy from the PB system; thus, it is dependent on the wet-bulb ambient temperature.

Table 4. 1 Statistical results for the DNI and meteorological parameters during a typical year in Kuwait.

Month	DNI			Dry-bulb temperature			Wet-bulb temperature			Wind speed		
	W/m ²	kW/m ²	W/m ²	°C			°C			m/s		
	Mean	Sum	Maximum	Mean	Maximum	Minimum	Mean	Maximum	Minimum	Mean	Maximum	Minimum
1	186.2	138.5	906	11.3	23.3	0	5.8	14.4	-3.6	3.6	9.6	0.3
2	191.3	128.6	931	15.1	26.2	4.1	7.2	15.2	-0.2	3.6	9.5	0.3
3	220.5	164.1	953	21.1	37.1	6.8	9.4	17.5	0.1	3.4	8.7	0.1
4	188.4	135.7	877	26.9	42.4	12.3	13.3	20.7	3.1	4.3	9.1	0.5
5	207.4	154.3	784	31.9	44.1	17.2	14.5	20.4	6.8	3.8	9.4	0.2
6	251.9	181.4	763	35.4	47.4	22.0	15.4	20.1	9.5	5.2	11.9	0.4
7	257.7	191.7	798	37.1	49.6	24.9	16.5	21.8	11.2	4.5	10.6	0.5
8	245.8	182.9	785	37.6	50.1	26.3	16.8	21.7	11.1	4.2	11.2	0.1
9	246.1	177.2	819	33.7	47.3	20.1	14.9	21.2	7.8	4.1	10.0	0.9
10	210.5	156.6	862	27.2	39.6	14.0	14.5	21.0	7.4	3.8	9.1	0.3
11	171.0	123.1	840	18.8	33.0	6.3	10.0	19.1	0.4	3.6	9.2	0.2
12	165.4	123.1	880.0	13.5	29.4	0.9	6.7	17.6	-3.3	3.5	8.9	0.4
Annual sum	1,857.1											
Annual mean	212.0			25.8			12.1			4.0		

Furthermore, the monthly profiles of hourly DNI are shown in Figure 4. 1. Additionally, Figure 4. 2 shows the monthly profiles of the dry-bulb temperature in Kuwait and Spain. Finally, based on ground measurements from a meteorological station at 10 m, the monthly statistical variations in the ambient temperature and humidity for the chosen location in Kuwait were analyzed, as illustrated in Figure 4. 3.

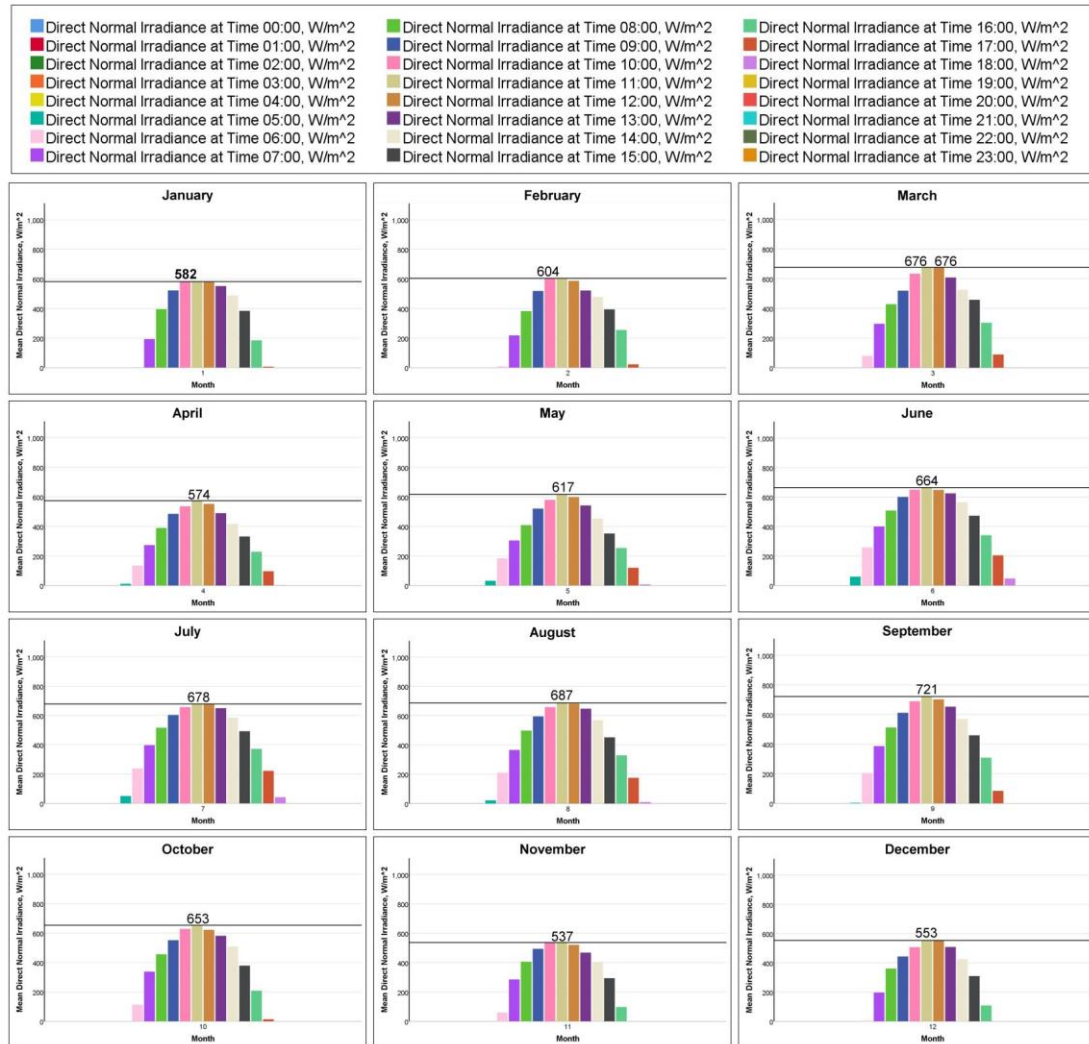


Figure 4. 1 Monthly profiles of the hourly DNI (mean) in Kuwait.

Figure 4. 2 illustrates that the monthly profiles of the dry-bulb temperature in Kuwait are higher than in Spain. Furthermore, the monthly statistical variations in the ambient temperature and humidity for the chosen location in Kuwait, shown in Figure 4. 3, confirm the inverse meteorological relation between ambient temperature and humidity for most monthly representations.

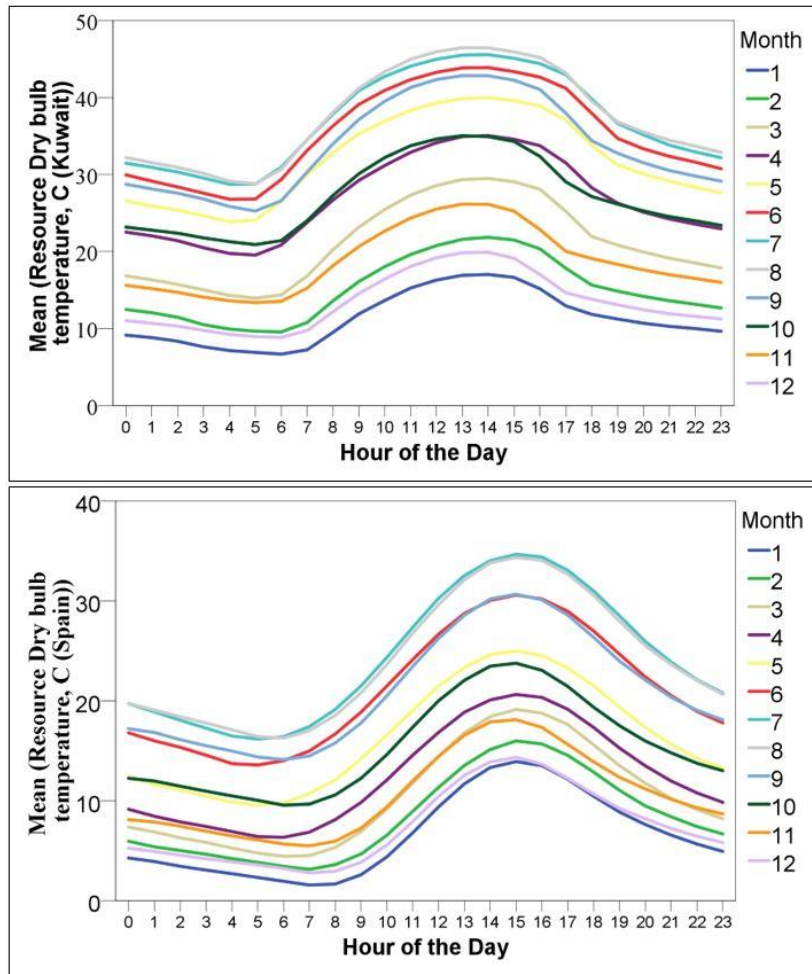


Figure 4. 2 Monthly profiles of the dry-bulb temperature in Kuwait and Spain.

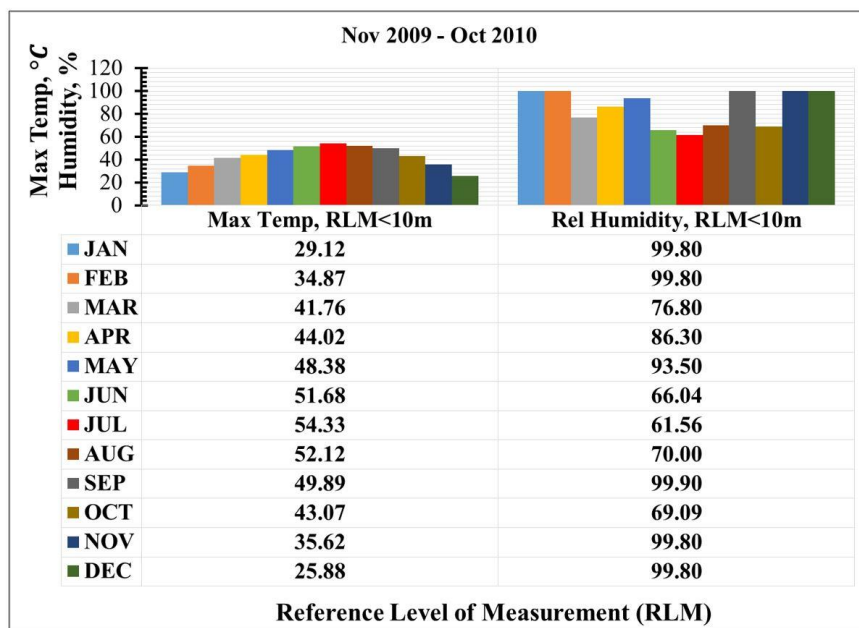


Figure 4. 3 Monthly temperature and humidity profiles based on ground measurements at 10 m in Kuwait.

4.3. Methodology for reliable meteorological data

Within the framework of the KISR renewable energy program and the plan to develop the mentioned above SREP facility, a 12-month wind and solar resource measurement campaign was conducted at five different sites in Kuwait [40]. The selected sites for measuring solar and wind resources were distributed across the centre, north, west, and south regions of Kuwait. Thus, the sites were considered a good representation of the natural resources in the country.

The most important meteorological parameters influencing CSP-PT and wind power technologies are solar irradiance, ambient temperature, relative humidity, wind speed, and wind direction. The solar radiation measurements have been conducted using rotating shadow band pyranometers. The relevant tools used in the ground-measurement campaign are secondary standard pyranometers to measure the GHI/diffuse horizontal irradiance and first-class pyrhemometers to measure the DNI.

This work uses the data from meteorological stations with site adaptation of satellite-based solar resource time series. The long-term estimates are based on the statistical analysis of the SolarGIS [235] multi-year time series of Meteosat satellite-derived solar resource data. The SolarGIS database is operated by GeoModel Solar [236]. The SolarGIS data provided an acceptable estimate of the solar resource for Kuwait. An improved SolarGIS model was mainly applied, and aerosol inputs derived from the MACC atmospheric database were utilized. The improvements in the SolarGIS model and consideration of satellite data with ground-measured solar radiation resulted in an acceptable estimation of the solar resource to be used as input to the CSP-PT performance simulation in this work.

It should be noted that extra-terrestrial radiation depends on the sun's position. The radiation can be calculated from the knowledge of solar geometry and astronomical equations. For simplicity, the extra-terrestrial radiation is considered as a solar constant of about $1,362 \text{ W/m}^2$ [237,238]. The methods for calculating clear-sky irradiance have been the focus of several studies. Some of the best representative models are REST2 [239] and simplified SOLIS [240] (based on radiative transfer equations), in which the SOLIS model is used in SolarGIS [241]. The SolarGIS algorithms' advantage is using multispectral satellite images, precise data correction, gap filling, and applicability for different geographical conditions [239,242]. In some studies, the diffuse models for tilted surfaces were investigated [243,244]. The solar

resource estimation is affected by cloud transmittance, atmospheric status, and terrain [245–247]. The uncertainty in the estimation was also studied [248,249].

The meteorological data are validated using measurements from meteorological stations. The CFSR model [250] and GFS model [251] were considered to validate the meteorological data. Overall, the data indicated that Kuwait has acceptable solar resource potential due to being in a location that rarely experiences cloud covers. In the occasions of clouds, the occurrence is estimated by the cloud index, a parameter within the SolarGIS satellite model.

4.4. Resource and weather characteristics

The chosen location in this work within Kuwait experiences an annual average ambient temperature of about 25 °C and an annual mean wind speed of approximately 4 m/s. The weather condition is affected primarily by a deterministic factor (sun position) and stochastic factors (clouds and aerosols) [237,238]. These factors allow noticeable variations between summer and winter, the dominating seasons. The sun position is the reason behind the lower irradiance values in winter compared to summer. This phenomenon affects solar resource components such as DNI and GHI (see Figure 4. 4, Figure F. 13 to Figure F. 17, and Table 4. 2). Consequently, the DNI is the critical parameter with the most significant impact on CSP-PT performance and energy yield; therefore, establishing high confidence in the DNI values is essential [235,236]. Hence, reducing the uncertainty in the solar resource is of high importance [241,248,249,252–255].

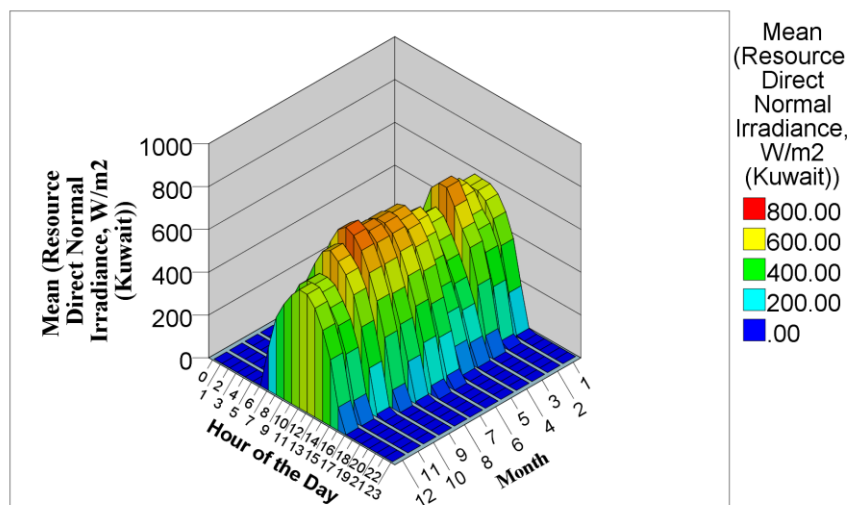


Figure 4. 4 Hourly and monthly DNI levels in Kuwait (W/m^2).

Between November to April, clouds are frequent, with maximum presence in January at the chosen location. Between February to June, aerosols are at their highest levels, reaching a maximum concentration in April/May (i.e., Sarayat). The period of Sarayat is when wind speeds reach up to 17 m/s with low visibility [256,257]. Most areas in Kuwait, including the chosen location, face multi-directional sandstorms, which are analyzed in some studies [258–260] due to their widespread during summer. Therefore, January and February are chosen to represent the winter months in this work. It should be noted that the hot and dry summer months with high aerosol concentration and dust storms pose many challenges for CSP-PT performance in the chosen location due to the soiling effects and harsh operating conditions in such a desert environment [53,258–260].

Figure 4. 5 shows the monthly profiles of temperature and humidity in the chosen location based on different measurement heights, which are defined in this work as the Reference Level of Measurements (RLMs). After a detailed evaluation, July and August are selected to represent the summer months. It should be mentioned that the availability of high DNI levels is a significant factor in making CSP-PT performance exceptionally feasible. In addition, several studies have focused on analyzing solar resources in various locations worldwide and proposing models to study solar resources and forecasting methods.

Having high confidence in the solar resource data is the basis for estimating the performance of various renewable power technologies, not only CSP-PT [239,240,249–251,241–248]. From Table 4. 1, Table 4. 2, Figure 4. 1, Figure 4. 4, and Figure F. 13 to Figure F. 17, the following can be observed concerning the solar resource in the chosen location in this work within Kuwait:

- i. the maximum and mean values for January are 906 and 186.2 W/m², respectively,
- ii. the maximum and mean values for February are 931 and 191.3 W/m², respectively,
- iii. the maximum and mean values for July are 798 and 257.7 W/m², respectively, and
- iv. the maximum and mean values for August are 785 and 245.8 W/m², respectively.

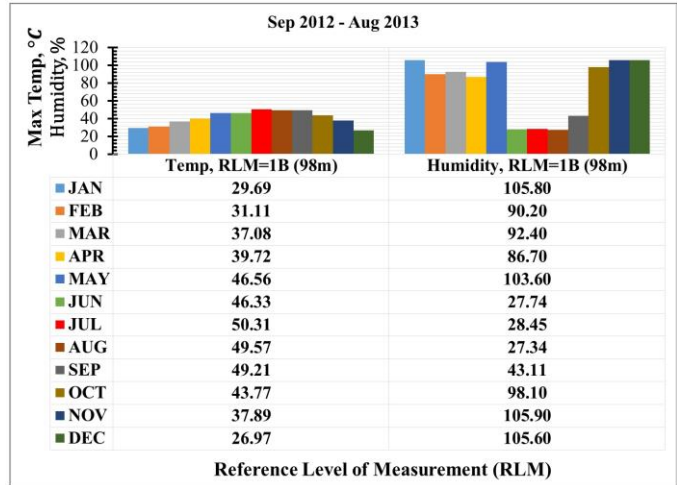
The chosen location has high levels of solar and wind resources [33,40,234]. Both resources are at a peak in this location, which also has the advantage of minimal

concentrations of oil and gas fields [28,29,32–34]. It is concluded that the months with higher wind and solar resources are during the summer. Additionally, the chosen location is a flat desert land with no urban development projects. After assessing a topographical map with elevations for Kuwait [261,262], it is observed that the chosen location has one of the highest elevations, which is the main reason for having a high wind resource potential.

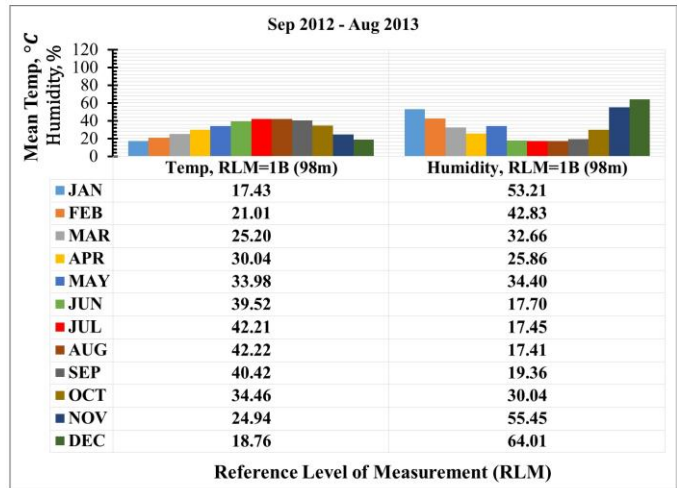
Furthermore, the chosen location's flat desert land and minimal change in topography eliminate the shading effects responsible for optical efficiency degradation of the SF systems inside CSP-PT plants. From Figure 4. 6 to Figure 4. 8, the following can be observed concerning the wind resource: (i) the chosen location has the advantage of high wind resource level, making the construction of wind power plants strongly viable and recommended, (ii) the wind speed at 10 m increases during the afternoon, and (iii) the wind speeds up to 100 m increase during early-day and late-night. Moreover, some studies have reported this effect for other geographical locations [263,264]. It should be recognized that during the nighttime, the atmosphere is relatively stable in the chosen location in this work, which assists in having a pronounced shear of the boundary layer.

Table 4. 2 Statistical comparisons between the DNI and GHI during a typical year in Kuwait.

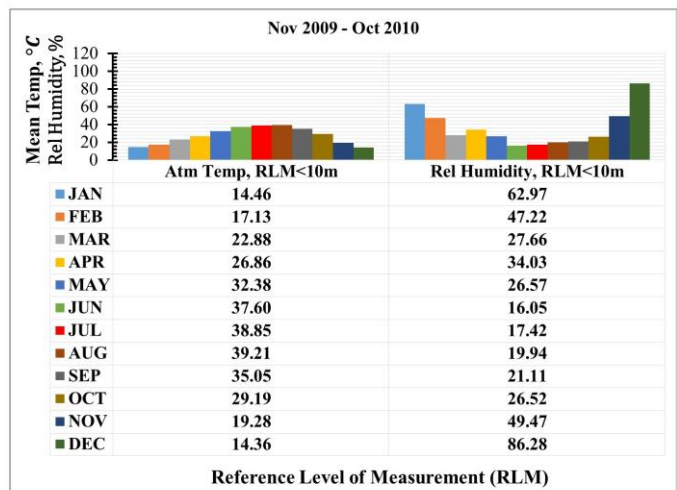
Hour	No. of samples	DNI, W/m ²			GHI, W/m ²		
		Minimum	Maximum	Mean	Minimum	Maximum	Mean
00:00	365	0	0	0	0	0	0
01:00	365	0	0	0	0	0	0
02:00	365	0	0	0	0	0	0
03:00	365	0	0	0	0	0	0
04:00	365	0	1	0	0	1	0
05:00	365	0	131	15	0	70	15
06:00	365	0	394	126	0	260	99
07:00	365	0	680	305	8	472	262
08:00	365	0	814	439	20	675	446
09:00	365	0	889	539	36	848	618
10:00	365	0	932	605	41	977	742
11:00	365	0	953	629	44	1,037	801
12:00	365	0	952	617	44	1,024	786
13:00	365	0	931	571	36	947	702
14:00	365	0	886	499	31	812	564
15:00	365	0	808	398	19	630	392
16:00	365	0	663	249	4	423	210
17:00	365	0	365	87	0	213	69
18:00	365	0	99	9	0	42	7
19:00	365	0	0	0	0	0	0
20:00	365	0	0	0	0	0	0
21:00	365	0	0	0	0	0	0
22:00	365	0	0	0	0	0	0
23:00	365	0	0	0	0	0	0



(i)



(ii)



(iii)

Figure 4. 5 Monthly profiles of the temperature and humidity based on different measurement heights: (i) maximum values at 98 m, (ii) mean values at 98 m, and (iii) mean values at a low height (< 10 m).

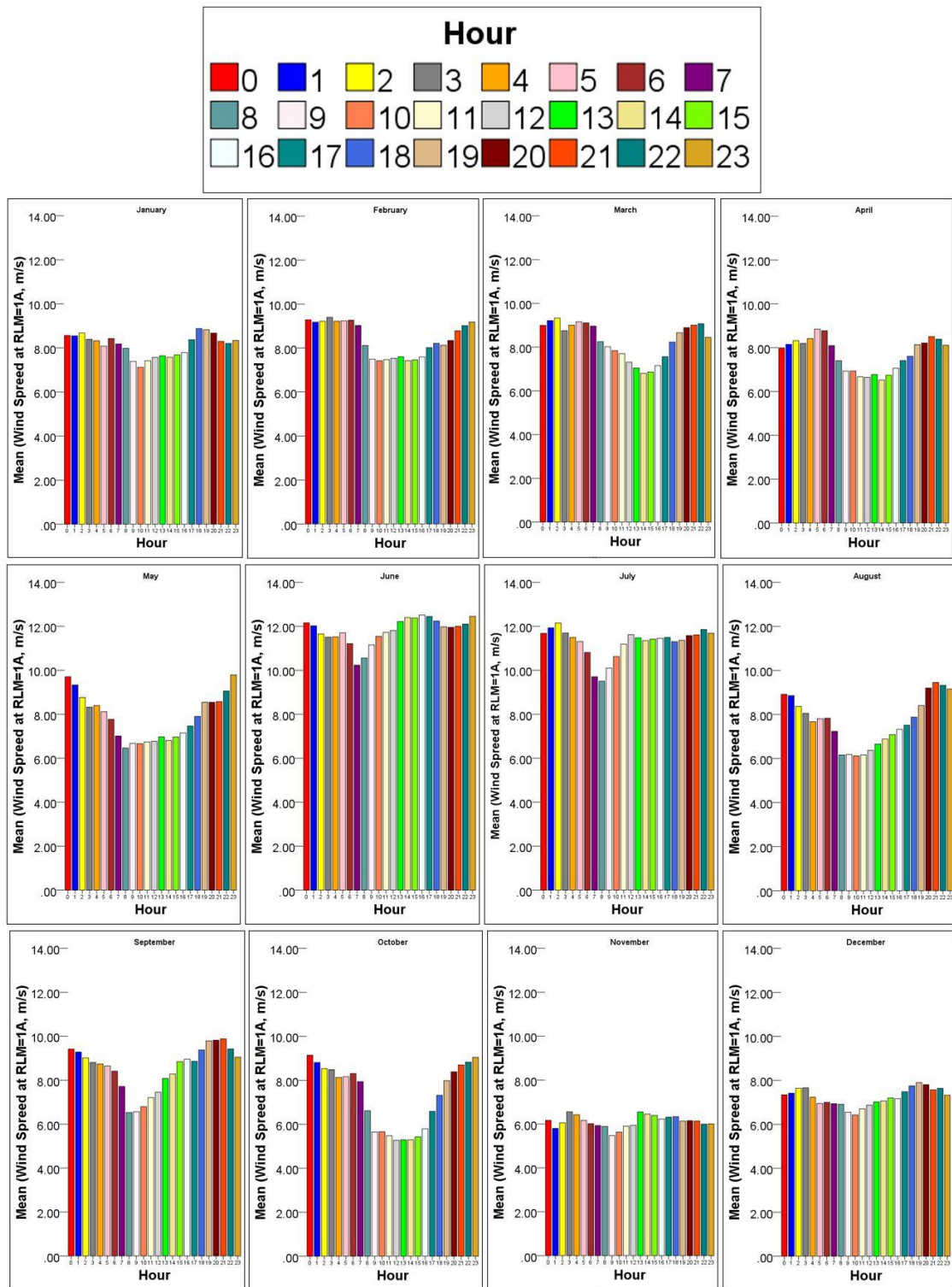
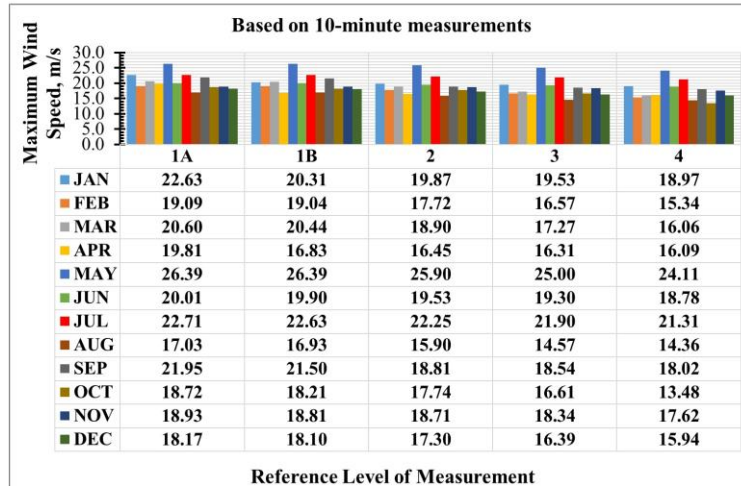
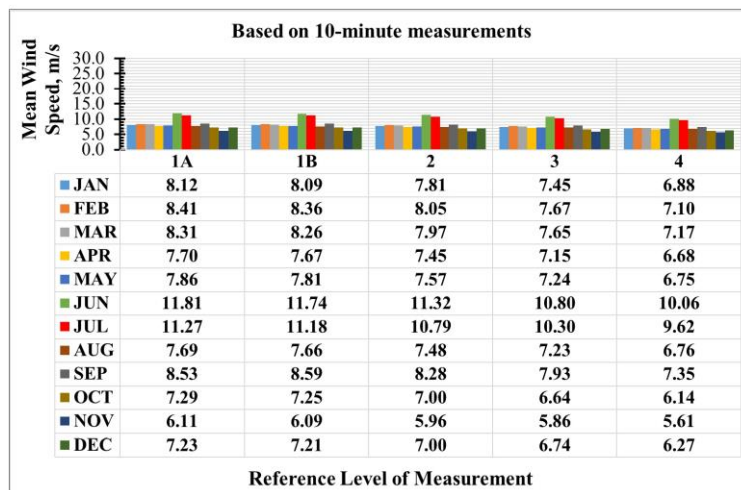


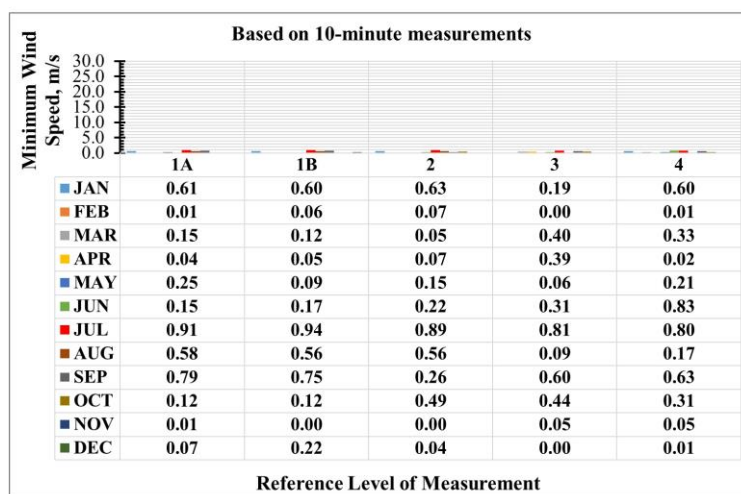
Figure 4. 6 Monthly profiles of the wind speed at 100 m with maximum values occurring during the early day and late night.



(i)



(ii)



(iii)

Figure 4. 7 Monthly statistics of the wind speed at different RLMs: (i) maximum, (ii) mean, and (iii) minimum – (based on a 10-minute analysis).

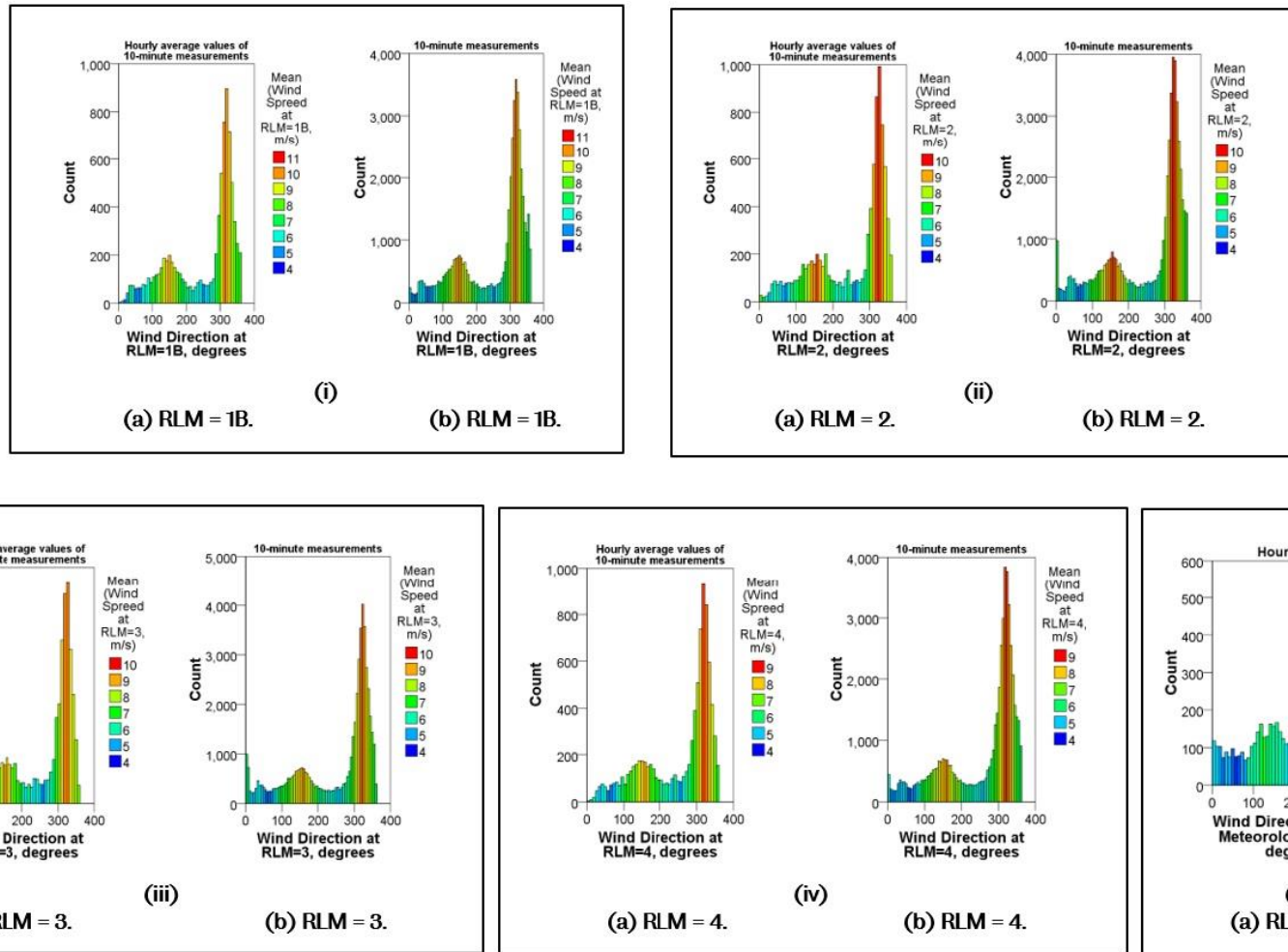


Figure 4. 8 Frequency of the wind direction and wind speed at different RLMs: (i) RLM = 1B (at 97.8 m), (ii) RLM = 2 (at 80 m), (iii) RLM = 3 (at 60 m), (iv) RLM = 4 (at 40 m), and (v) RLM < 10 m – (colours: wind speed ranges, a: hourly analysis, b: 10-minute analysis).

It should be mentioned that the noted cyclic trend of the wind resource can compensate for afternoon peak load shaving/levelling in Kuwait. Hence, this trend can increase wind power generation and Peak Load Shaving Capability (PLSC). In general, The PLSC can be estimated via Equation 4. 1 as follows:

$$PLSC = \sum_{y=1}^k E(N_h^{cr})/N_h^{cr}$$

4.1

where N_h^{cr} is the number of critical hours, $E(N_h^{cr})$ is the amount of electricity produced by a renewable power technology (e.g., wind power, CSP-PT), y is the counting variable for the year, and k is the plant's lifetime. The N_h^{cr} indicates the hours when the load exceeds a certain threshold, typically defined by the plant operator.

The hourly data for the wind speed, direction, and α up to 100 m is evaluated later in Chapters 6 and 7. The outcomes from a detailed analysis of the values for α at high altitudes in the chosen location in this work will aid in confirming the wind behaviour during the day and night times. In addition, an understanding of the solar/wind resources and other meteorological elements is needed to enhance cogeneration from wind/CSP-PT power plants and maximize the capacity factor of future transmission networks, as shown in Figure 3. 1.

4.5. Location characteristics

According to one of the standards of the International Electrotechnical Commission (IEC 61400-1), a wind power plant location is associated with different classes of wind turbines based on the wind resource characteristics, such as the mean wind speed at the turbine's hub height, α average value, turbulence intensity, and gust wind speeds. Wind turbines generally experience static and dynamic load from various sources, including α . The IEC 61400-1 explains the limitation on α and allowed ranges. The design limit is 0.2, indicating that values above 0.2 make the location undesirable for most classes.

After establishing the Reference Level of Calculations (RLCs), the wind speed data from a meteorological mast at the chosen location in Kuwait is assessed, and the α values are calculated. Detailed 10-minute analyses concerning α are performed between two elevations (100 m and 40 m). The mean, maximum, minimum, and

number of values for α were evaluated. The annual mean of α is estimated to be between 0.14-0.18 using Equation 4. 2:

$$\alpha = \frac{\ln(u_2/u_1)}{\ln(z_2/z_1)}$$

4. 2

The calculations of the α values are crucial for estimating the wind energy yield. Therefore, detailed monthly statistical profiles for the wind resource are performed later in Chapter 7.

4.6. Meteorological characteristics

Understanding the wind resource and weather characteristics in the selected sites for wind power projects is vital for estimating the energy yield. In addition, it allows for accurate wind forecasting. From basic principles, the air travels from high to low-pressure regions, thus resulting in the wind flow, a physical measure that allows the mechanical movement of wind turbine blades.

In addition, ambient temperature variations influence air movement, much like the Coriolis effect, which describes the pattern of deflection taken by objects not firmly connected to the ground as they travel long distances around the Earth. Furthermore, other factors influence the wind characteristics, such as northern and southern trades, surface roughness, land topography, and obstacles (e.g., lakes, trees).

The wind speed, wind direction, humidity, and ambient temperature are essential parameters for accurately describing the wind resource since they contribute to the wind's kinetic energy and the potential of mechanical energy creation at the wind turbine's blades (see Appendix E). Thus, the meteorological data used in this work are ground measured, allowing for higher accuracy in estimating the energy yield from the wind.

4.7. Prevailing conditions

The chosen location in this work has one of the highest levels of wind speeds, critical for maximizing the overall efficiency of wind power plants. Kuwait is known for its hot arid weather, long summers, and short winters. During the summer,

temperatures are extremely high, and sandstorms are frequent due to the presence of high winds [53]. The cloudbursts are accompanied by occasional heavy rain with sandstorms lasting for several days. During the “Sarayat” period, wind speeds could reach up to 17 m/s with low visibility due to sandstorms [256]. The average temperature in summer reaches 40 °C, with the maximum temperature reaching up to 54 °C in the shade as of July 2016, reported as the hottest reliably measured air temperature on Earth [15–19].

On 25 March 2011, the recorded visibility was close to zero due to sandstorms, and the wind speed was 13.89 m/s in the capital city [257]. Kuwait experiences frequent sandstorm trajectories [258–260] (see Figure 4. 9 and Figure 4. 10), and extreme temperature and humidity conditions are widespread during summer. Such conditions impose many operational challenges for both wind power and CSP-PT plants.

Figure 4. 9 illustrates a topographical map with elevation for Kuwait, which shows that the western region has the highest elevation. This is the primary reason for the high wind resource and considering the chosen location in this work. From Figure 4. 9, it can be concluded that the chosen location has an elevation of roughly 240 m above sea level.

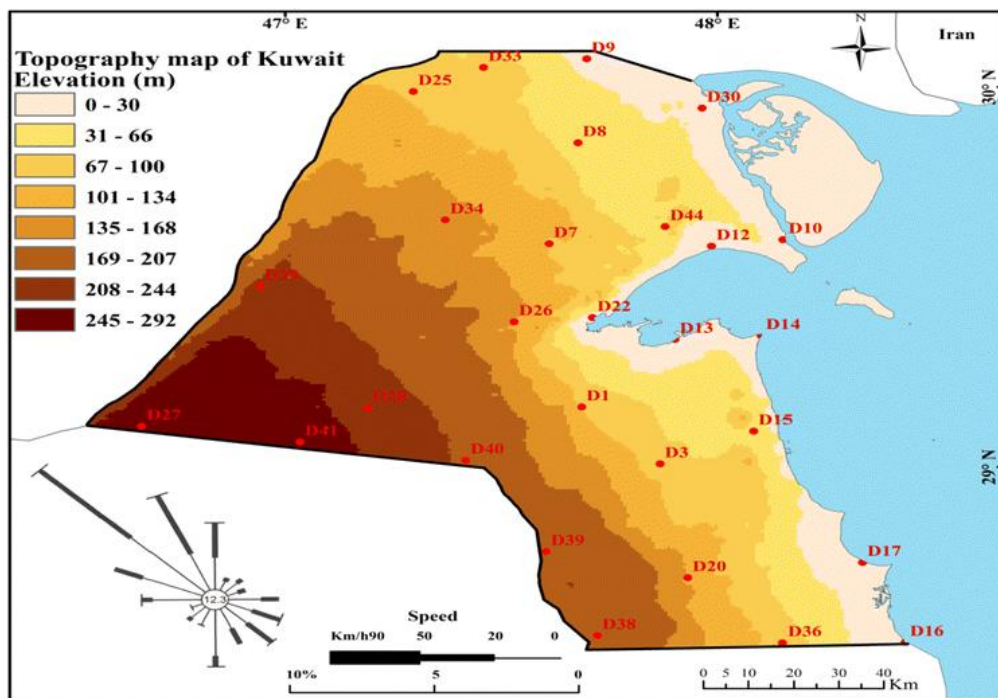
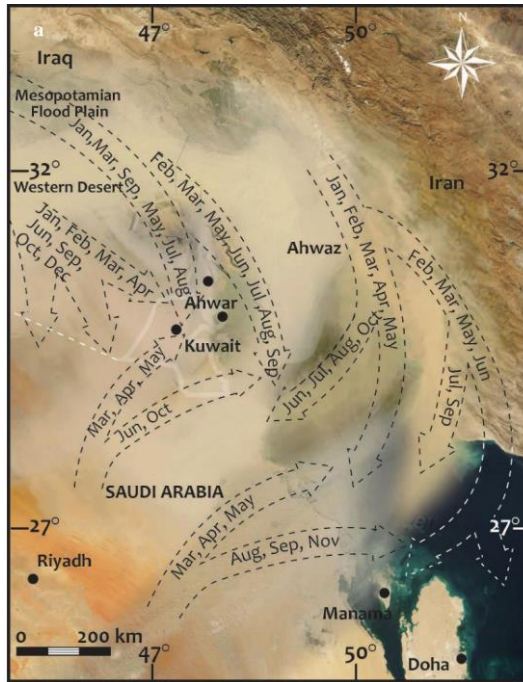


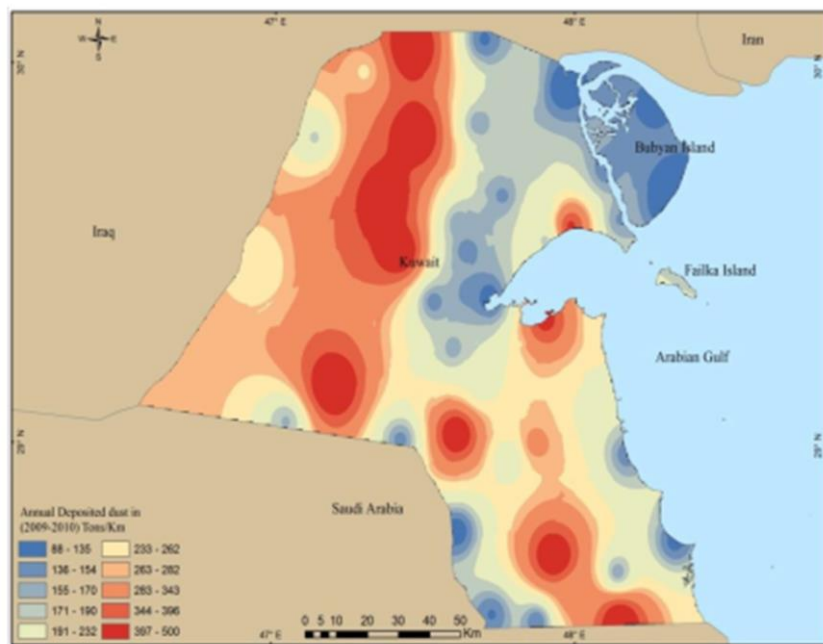
Figure 4. 9 A topographical map with elevation for Kuwait [45].



(i)



(ii)



(iii)

Figure 4. 10 Sandstorm seasons in Kuwait: (i) storm on 25 March 2011 [257], (ii) regional trajectories [258], and (iii) dust deposition rate [259,260].

4.8. Chapter conclusion

The main findings are summarized as follows:

- i. a TMY file, which is established on a monthly basis for individual years with long-term monthly characteristics, serves as input to the SAM software,
- ii. a methodology for reliable meteorological data is provided,
- iii. it was determined that the meteorological parameters relevant to wind power and CSP-PT are ambient temperature, relative humidity, wind speed, and wind direction. Also, the DNI is a critical parameter with the most significant impact on CSP-PT performance, including energy yield.
- iv. It should be recognized that having a high confidence level in the DNI is critical for CSP-PT plant performance assessment [235,236]. Hence, reducing the uncertainty of the solar resource is of high importance [241,248,249,252–255],
- v. it is concluded that the months with high wind and solar resources are during the summer in Kuwait,
- vi. after assessing a topographical map with elevation for Kuwait [261,262], it is observed that the chosen location in this work has one of the highest elevations in the country, which is the primary reason behind having a high wind resource,
- vii. the calculations of α are crucial for estimating the wind energy yield; therefore, detailed monthly statistical profiles for the wind resource are performed,
- viii. the wind speed, direction, humidity, ambient temperature are essential parameters for accurately describing the wind resource since they contribute to the wind's kinetic energy (see Appendix E). Hence, the meteorological data used in this work are ground measured, allowing for higher accuracy in estimating the energy yield from the wind, and
- ix. Kuwait experiences frequent sandstorm trajectories [258–260] and extreme temperature/humidity conditions are widespread during summer. These conditions impose many operational challenges for both wind power and CSP-PT plants.

5. TECHNO-ECONOMIC COMPETITIVENESS OF CONCENTRATING SOLAR POWER PLANTS WITH THERMAL ENERGY STORAGE

5.1. Chapter journal publications

Some of the work that appears in this chapter is associated with peer-reviewed scientific journal publications. This chapter is associated with publications (1) and (4). The detailed information of these publications is listed in the “Scientific Journal Publications” Section, starting from page (iii) of this thesis.

5.2. Climatic conditions

In this work, the chosen location has one of the highest concentrations of DNI, which is critical for maximizing the overall CSP-PT plant efficiency. Generally, Kuwait is known for its hot arid weather, long summer season, and short winter. During summer, temperatures are extremely high, and sandstorms are frequent [53]. During winter, temperatures are warm, and rain is occasional. The weather is the harshest from June to August, with high humidity levels. The months of April and October are more tolerable when temperatures drop to 30 °C. During the spring from March to May, also known as the “Sarayat” period, temperatures fluctuate with strong wind presence. The cloudbursts are accompanied by occasional heavy rain with sandstorms lasting for several days. These conditions jeopardize the visibility significantly and affect CSP-PT performance due to degradation in the optical efficiency of PT collectors. Table 5. 1 lists the main design climatic conditions which should be considered in CSP-PT plants in the chosen location. During the “Sarayat” period, wind speeds can reach up to 17 m/s with low visibility due to sandstorms [256]. The average temperature in summer reaches 40 °C, with a maximum temperature approaching 54 °C in the shade as of July 2016, reported as the hottest reliably measured air temperature on Earth [15–19]. On 25 March 2011, the recorded visibility was close to zero due to sandstorms, and the wind speed was 13.89 m/s in the capital city [257]. Kuwait experiences frequent patterns of sandstorm

trajectories [258–260]. As a result, extreme temperature and humidity conditions are widespread during summer. Such climatic conditions impose many operational challenges for CSP-PT and wind power plants, especially since solar and wind resources peak during summer. Similarly, the electrical load is at a peak during summer due to excessive air conditioning load for comfort cooling in buildings.

From the discussion of the natural resources and meteorological characteristics in Chapter 4, the climatic conditions in Table 5. 1 are assumed for the CSP-PT plant's design in the chosen location in Kuwait. Therefore, it is determined that the CSP-PT plant should provide an acceptable performance (as per the plant's design ratings) at a maximum ambient temperature of 55 °C, a wet-bulb temperature of 45 °C, maximum relative humidity of 95%, and a maximum 3 s wind gust at 1 m height of 17 m/s.

Table 5. 1 Design climatic conditions for CSP-PT plants in the chosen location in this work.

Item	Unit	Value
Annual DNI	kWh/m ² yr	1857.1
Maximum ambient temperature	°C	55
Black-bulb temperature	°C	86
Minimum ambient temperature	°C	-6
Wet-bulb temperature	°C	45
Maximum relative humidity	%	95
Minimum relative humidity	%	5
Maximum ambient air pressure	mbar	1005
Minimum ambient air pressure	mbar	966
Maximum 3 s wind gust at 1 m height	m/s	17
Maximum 3 s wind gust at 10 m height	m/s	49
Average annual rainfall	mm	196
Maximum recorded rainfall in one day	mm	79

5.3. Reference concentrating solar power plant

In a CSP-PT plant, the mirrors concentrate the sunrays by a factor of about 80 onto the HCEs at the focal lines of the SCA units. Figure 5. 1 describes some critical CSP-PT plant components. First, the HTF (Dowtherm A, see Appendix A) circulates in a closed circuit and then heats up to approximately 400 °C in the HCEs. Next, the heated HTF is pumped into the PB system and flows through a heat exchanger. Subsequently, steam is generated to power a steam turbine. It should be recognized that the attractive feature of CSP-PT is the cogeneration of power and heat by employing DNI concentration. Also, Figure 5. 1 shows a description of critical CSP-PT plant components: (i) a PT collector with thermal gradient, (ii) a single unit of SCA,

(iii) a schematic diagram of a typical evacuated receiver, and (iv) HCE manufacturing processes. In addition, the integration of TES allows a CSP-PT plant to function at full capacity on overcast days, dusty climates, and nighttime. Generally, CSP-PT combined with TES provides tremendous benefits considering their dispatch flexibility compared to PV without the battery system [51]. Furthermore, once accompanied by TES, the power delivery flexibility of CSP-PT becomes advantageous, bringing the capability of peak load shaving/levelling and maximization of annual energy yield and capacity factor. These benefits are critical due to the frequent peak load during afternoon periods at both the national level (as previously demonstrated) and the building level, as shown in Figure F. 18 and Figure F. 19 (load data is measured by KISR).

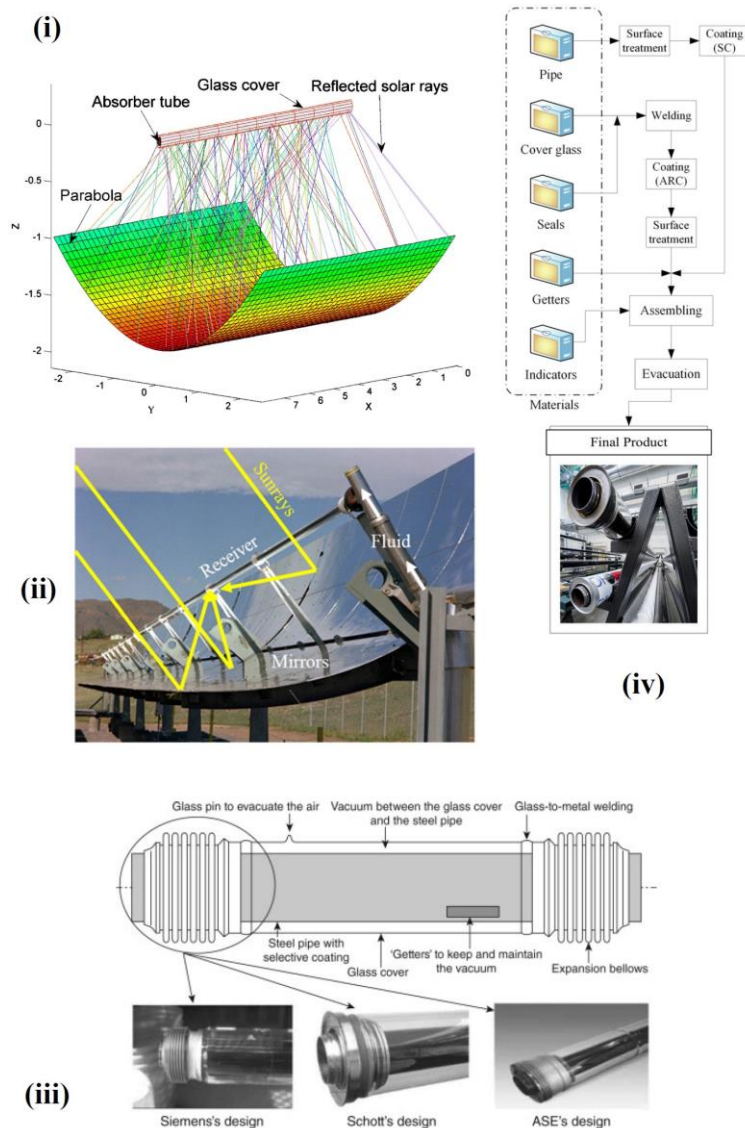


Figure 5.1 Description of critical CSP-PT plant components: (i) a PT collector with thermal gradient [265], (ii) a single unit of SCA [266], (iii) a schematic diagram of a typical evacuated receiver [267], and (iv) HCE manufacturing processes [266].

Although the advantage of combined CSP with TES over the PV technology relies on storing thermal energy for nighttime or 24-hour continuous generation (see Figure 5. 2), the LCOE for PV is still lower [38].

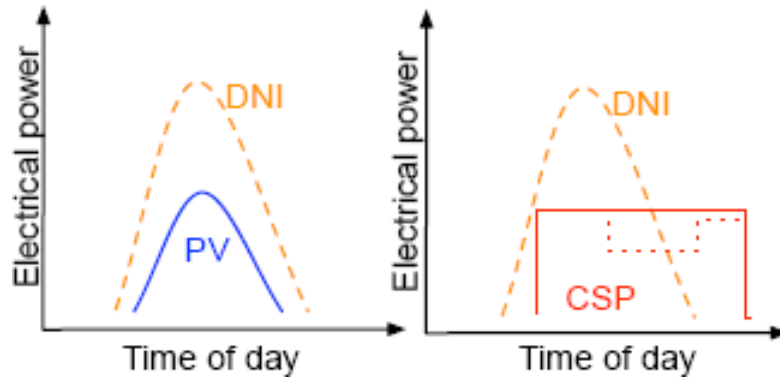


Figure 5. 2 Dispatch flexibility of the CSP and PV technologies under the same solar resource condition [51].

In general, CSP-PT installation costs can be reduced with the drive of technological enhancements in the industry and improving the learning curve by Engineering, Procurement, and Construction (EPC) contractors. In addition, the industry experience can have an influential role in reducing the indirect EPC costs, including the costs of components (see Figure 5. 3 and Figure 5. 4). It should be noted that the reduction in the total installation cost of commercial CSP-PT is estimated to reach 33% by 2025 [268,269]. Several studies have evaluated the CSP-PT technology and its role in dominating the market compared to CSP-Tower, CSP-Fresnel, and CSP-Dish [270,271,280,281,272–279]. In addition, some studies have reviewed CSP plants worldwide [272–276]. At the same time, other studies have evaluated CSP features [272,273,276] and economic benefits, including reliability [274–279].

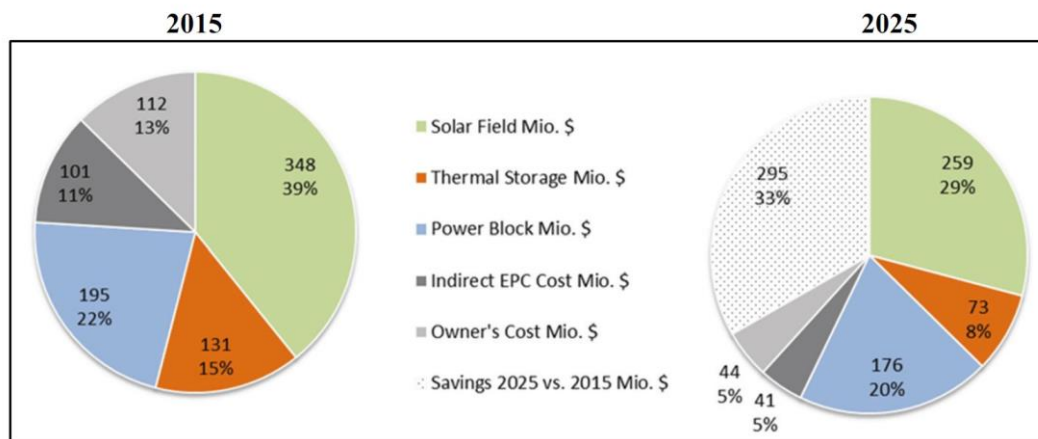


Figure 5. 3 Total installed cost reduction by source for a 160 MW CSP-PT power plant in 2015 and 2025 [269].

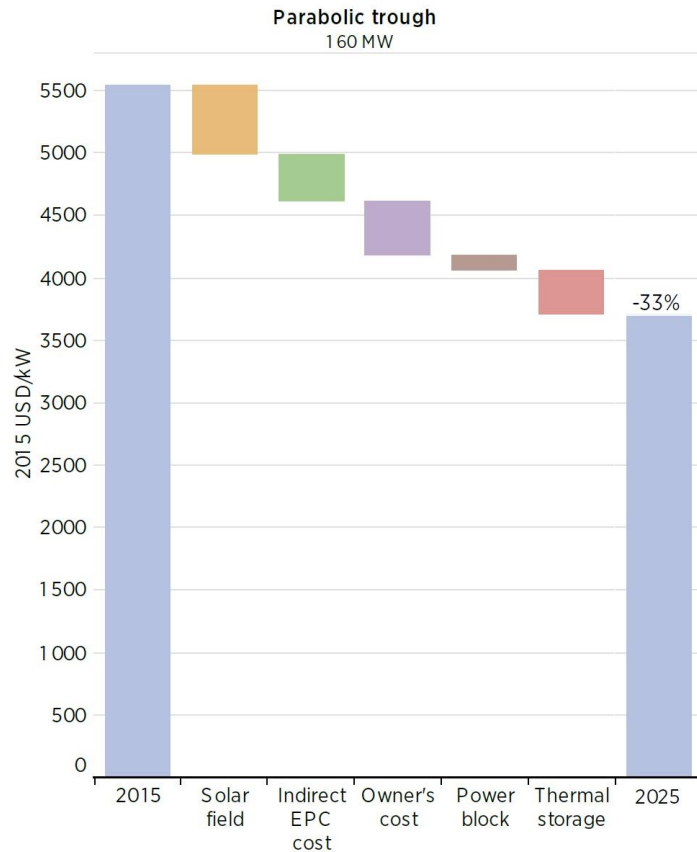


Figure 5. 4 Total installed cost reduction by source for a 160 MW CSP-PT power plant in 2015 and 2025 [268].

It should be recognized that Figure 3. 1, Figure 3. 2, and Appendix C demonstrate the design configuration components for a CSP-PT plant with TES capability. The configuration is concerned with the reference 50 MW CSP-PT plant used in this work, in which the detailed design parameters of the plant are listed in Table 3. 1. It should be noted that the typical estimated costs [282] for the reference 50 MW CSP-PT plant are shown in Table 5. 2. Additionally, a detailed breakdown of the estimated costs for the reference 50 MW CSP-PT plant is provided in this work (see Appendix H).

Table 5. 2 Typical estimated costs for the 50 MW CSP-PT plant [282].

Description	Cost, \$ million	Share, %
Labour cost: Site and solar field	62.4	17.1
Solar field	11.3	3.1
Site preparation and Infrastructure	21.2	5.8
Steel construction	9.1	2.5
Piping	6.4	1.8
Electric installations and others	14.4	4

Table 5. 2. Cont. Typical estimated costs for the 50 MW CSP-PT plant [282].

Description	Cost, \$ million	Share, %
Equipment: Solar field and HTF and system	140.3	38.5
Mirrors	23.1	6.4
Receivers	25.9	7.1
Steel construction	39	10.7
Pylons	3.9	1.1
Foundations	7.8	2.1
Trackers (hydraulics and electrical motors)	1.6	0.4
Swivel joints	2.6	0.7
HTF System (piping, insulation, heat exchangers, pumps)	19.5	5.4
Heat transfer fluid	7.8	2.1
Electronics, controls, electrical and solar equipment	9.1	2.5
Thermal storage system	38.4	10.5
Salt	18.6	5.1
Storage tanks	6.6	1.8
Insulation materials	0.7	0.2
Foundations	2.3	0.6
Heat exchanges	5.1	1.4
Pumps	1.6	0.4
Balance of system	3.5	1
Conventional plant components and plant system	52	14.3
Power block	20.8	5.7
Balance of plant	20.7	5.7
Grid connection	10.5	2.9
Others	71	19.5
Project development	10.5	2.9
Project management (EPC)	28.1	7.7
Financing	21.8	6
Other costs (allowances)	10.5	2.9
Total	364	100

5.4. Cooling options for condenser system

In general, wet cooling for a steam Rankine cycle is preferable to dry cooling because the exit steam from the turbine is cooled down quicker [283], increasing the cycle efficiency. Thus, fossil-based power plants are preferably installed in sites with access to water resources to supply cooling processes within the plants. The chosen location in this work is where future CSP-PT plants should be established to maximize the economic feasibility and capacity factor since this location has high DNI levels. However, the location has limited water resources; hence, it is critical to investigate the competitiveness of employing dry cooling compared to wet cooling for CSP-PT implementation in Kuwait, highlighting the importance of this work.

Some studies have concluded that dry cooling would save more than 90% of water consumption in power plants, but the overall plant performance would decrease. Therefore, an assessment for utilizing dry cooling was studied [283,284]. The results showed that the annual generation decreased by 11% with dry cooling, and the water consumption decreased by 92% compared to wet cooling. Another study [285] concluded that water consumption is crucial in CSP plant construction. Also, the operation of a CSP plant with dry cooling was evaluated [286]. Additionally, a multi-period mixed-integer non-linear mathematical formulation was used to optimize the conditions under different thermal cycles and cooling options.

Further, another study [175] reported the potential of dry cooling, and the study used GATECYCLE, commercial software for heat and mass balance, to evaluate plant performance. The software is used in the modelling of PB systems [173,174]. In addition, it is used in the analysis of a variety of types of plants. It should be mentioned that its library does not include a solar collector. Instead, the software predicts solar power generation [175]. Other studies [229,287–289] investigated the problem of using dry cooling. According to a study [290], dry-cooled plants use 90% less water than wet-cooled ones, thus reducing the LCOE. In addition, dry cooling for CSP-PT has an overall cost penalty, reduced by increasing the size of the dry-cooled condenser [218]. Compared to evaporative cooling, the dry-cooled condenser cost is seven-folds; however, a third of the additional cost is recovered by eliminating the blowdown holding and evaporation ponds [218]. In addition, the SF system is cost-intensive; therefore, it is more economical to invest in an additional condenser space and size than to pay for an extra SF system area for the same energy output from a CSP-PT plant. For example, dry cooling increased the cost of a 110 MW gross turbine to 1140 \$/kW, and when scaled to a dry-cooled 280 MW gross case, the cost fell to 875 \$/kW, according to a study [291].

It should be noted that the schematic diagrams of wet and dry-cooled condensers are shown in Figure 5. 5 and Figure 5. 6 (see Appendix E). It should be recognized that Figure 5. 5 shows schematics of a wet cooling system, and Figure 5. 6 shows schematics of a dry cooling system. It should be noted that the input data to the model for the condenser system as per design is provided in Table 5. 3. In general, the process of modelling the heat and power in a CSP-PT plant depends on the HTF inlet temperature, condenser pressure, and HTF mass flow. The HTF inlet temperature and HTF mass are essential parameters for the SF system and are then inputted into the PB system. In contrast, the condenser pressure is a critical

parameter for the PB system and is dependent on ambient temperature, cooling technology, and cooling load. In this work, attention is given to utilizing wet and dry-cooled condensers, which are needed to perform the process of heat rejection from the PB system under the arid climatic conditions of the chosen location in Kuwait. Furthermore, this location lacks water resources. Such conditions demand the investigation of non-traditional cooling options due to the significant effects on the thermodynamic cycle and water consumption within the CSP-PT plant.

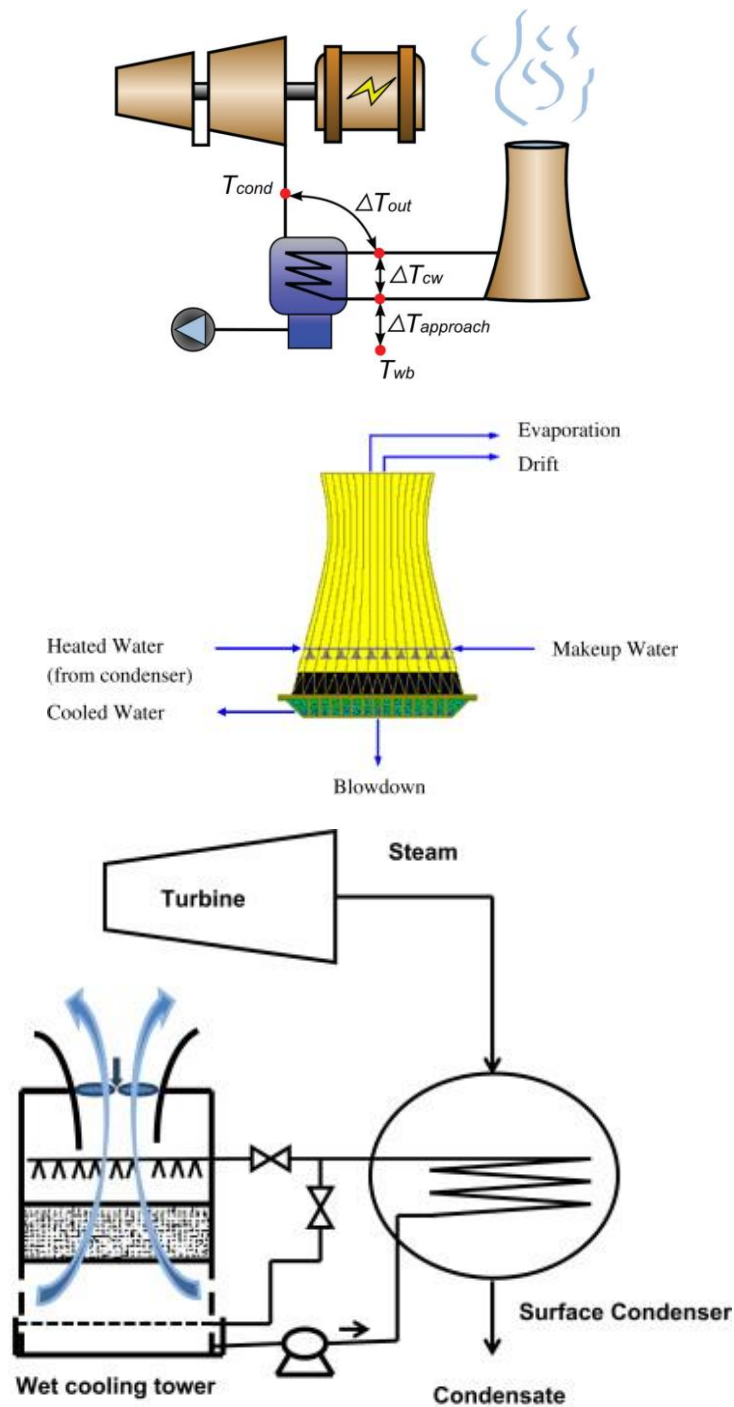


Figure 5. 5 Schematics of a wet cooling system [284,285,290].

Table 5.3 Main input data to the model for the wet and dry-cooled condensers in this work.

	Variable	Description	Value
Wet-cooled condenser system	P_cond_min	Min condenser pressure, inches of mercury	1.25
	dT_cw_ref ($\Delta T_{ce,des}$)	Reference condenser water dT, °C (temperature rise of cooling water across condenser under design conditions)	10
	T_amb_des	Ambient temperature at design	Wet-bulb temperature (see Table 4.1)
	T_approach ($\Delta T_{approach}$)	Cooling water approach temperature, °C (temperature difference between circulating water at condenser inlet and wet bulb ambient temperature)	5
	η_{fan}	Fan mechanical efficiency, %	75
	$\eta_{fan,s}$	Fan isentropic efficiency, %	80
	$\eta_{pump,mechanical}$	Cooling water pump mechanical efficiency, %	75
Dry-cooled condenser system	$\eta_{pump,isentropic}$	Cooling water pump isentropic efficiency, %	80
	P_cond_min	Min condenser pressure, inches of mercury	2
	P_cond_ratio	Condenser pressure ratio	1.0028
	T_amb_des	Ambient temperature at design	Dry-bulb temperature (see Table 4.1)
	T_ITD_des	Initial temperature difference at design (steam to ambient), °C (difference between the temperature of steam at turbine outlet/condenser inlet and ambient dry-bulb temperature)	16
	$\eta_{fan,mechanical}$	Fan mechanical efficiency, %	94
$\eta_{fan,isentropic}$	Fan isentropic efficiency, %	80	

The main difference between the wet and dry cooling options is the heat transfer process between the PB system and the ambient air. In a wet-cooled condenser, the water removes the heat through evaporation. Hence, the cold reservoir temperature is driven by the wet-bulb temperature. On the other hand, in a dry-cooled condenser, the condenser transfer heat directly from the steam working fluid to air (sensible-heat process). Hence, there is a limitation related to the dry-bulb temperature in arid climatic conditions. Thus, it should be recognized that the ambient temperature, condenser pressure, and overall PB system thermodynamic performance are directly affected.

Generally, the dry-bulb temperature refers to the thermodynamic temperature of the air (determined using a thermometer). In comparison, the wet-bulb temperature captures the moisture content of air (i.e., less than the dry-bulb temperature in most cases). It should be realized that wet-cooled condensers use water evaporation to cool the process condensate close to the wet-bulb temperature. In contrast, dry cooled condensers have minimum heat rejection as the dry-bulb temperature. As a result, the dry-cooled condensers are more expensive and less thermodynamically efficient and require more power. However, wet-cooled condensers need more water.

The disadvantage of a wet-cooled condenser is a large amount of water used in the evaporation. The wet-cooled condenser circulates water through a condenser heat exchanger to remove heat from the steam flow. Then, the water passes through a wet cooling tower, where heat is removed by direct evaporation. However, a dry-cooled condenser does not consume water for heat rejection. Both the wet and dry cooled condensers require a condensing heat exchanger to convert high-quality steam from the turbine to feedwater, pumped back through the heat exchanger system. It should be noted that the steam exits the turbine under vacuum conditions and must be piped via ducting to the condenser.

In this work, the wet-cooled condenser model calculates the condenser pressure, parasitic load, and water use for a wet cooled condenser (forced-draft). The model requires several parameters and inputs (see Appendix D) and some property curves to effectively calculate performance. In the dry-cooled condenser model, the cooling airflow generated by the fans is limited to either 100% or 50% flow relative to the design value. The dry-cooled condenser does not consume much water for cooling since a parasitic fan power is required instead.

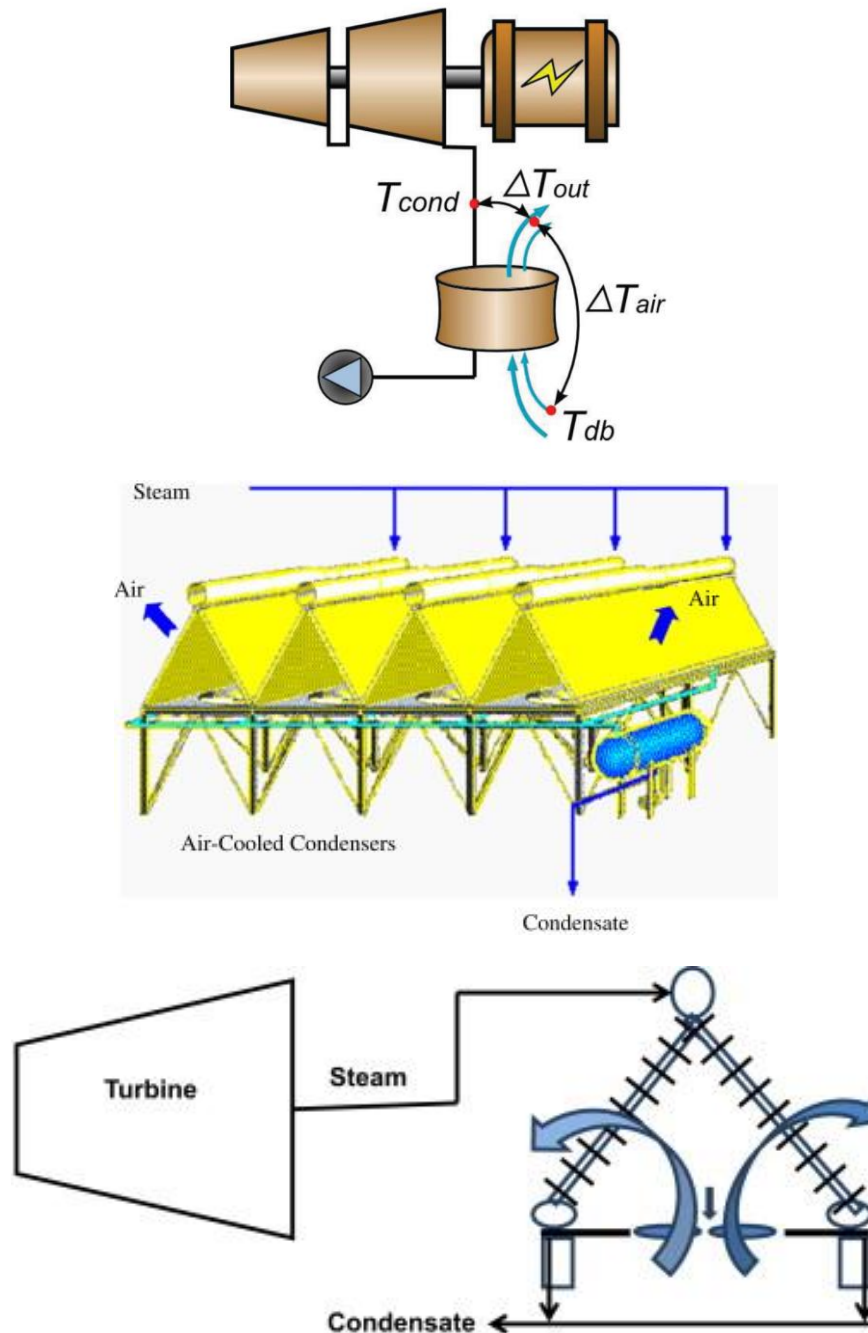


Figure 5. 6 Schematics of a dry cooling system [284,285,290].

It should be noted that a wet-cooled system includes mechanical draft cooling towers, a surface condenser, vacuum pumps, circulating water pumps, underground circulating water pipes, a water treatment system for cooling tower makeup, and an evaporation pond for the cooling tower blowdown. It should be noted that a dry system includes a dry-cooled condenser and vacuum pumps. The different economic parameters of wet and dry cooling systems for the Andasol plant were assessed [292]. The production and cost penalty results are shown in Table 5. 4 and follow those presented by IEA [293–296].

Table 5. 4 Simulation and comparison of Andasol plant for wet and dry cooling systems [285].

General Information		
Number of loops	156	
Effective collector area [m ²]	510,12	
Direct normal irradiance (DNI) [kWh/m ² /yr]	2052	
Comparison element		
	Wet	Dry
Energy field [MWh/yr]	134,715.80	126,184.27
Capacity factor [%]	31.709.968	28.8091941
Thermal output of solar field [MWh/yr]	442,908.30	458,833.01
Economic results		
Internal return rate (IRR) on Equity [%]	9.69	7.28
Net present value (NPV) [€]	109.11	59.32
Payback period [yr]	12.35	13.96
Discounted payback period [yr]	15.88	20.77
Total incremental costs [€]	262,474,023	280,190,787
Min. average debt service coverage ratio	1.01	0.91
Required LCOE tariff [€/kWh]	0.301	0.341
Incremental LCOE [€/kWh]	0.152	0.179
Calculation of LCOE		
Levelized electricity costs (LCOE) [€/kWh]	0.2024	0.2293
Total investment costs (IC) [€]	274,259,498	282,859,352
Annuity of IC	0.0782	0.0782
NPV of operation costs (OC) [€]	74,320,528	75,473,190
Annuity of OC	0.0782	0.0782

According to a study [218], the difference between using dry cooling instead of wet cooling in terms of the used mechanical equipment is the fact that there is the addition of the following equipment: (i) dry-cooled condenser, (ii) condensate tank, (iii) wet surface air cooler, (iv) dry-cooled heat exchanger (fin-fan cooler), (v) wastewater sump blowdown booster, (vi) wet surface air cooler makeup tank, and (vii) wet surface air cooler chemical feed/storage system. On the other hand, the difference between using dry cooling instead of wet cooling in terms of the used mechanical equipment is the fact that there is the deletion of the following

equipment: (i) cooling tower, (ii) steam surface condenser, (iii) closed cooling water heat exchanger, (iv) circulating water pump, (v) auxiliary cooling water (backup/startup), (vi) cooling tower blowdown booster pump, and (vii) cooling tower chemical feed/storage enclosure. A detailed breakdown of the estimated costs for the reference 50 MW CSP-PT plant is provided in this work (see Appendix H).

Table 5. 5 Main characteristics of different cooling systems [285].

Parameter	Cooling systems			
	Dry cooled system			Wet-cooled system
	Indirect natural draft	Indirect mechanical draft	Direct mechanical draft	Circulating evaporative water-cooled system
Investment cost	High	High	High	Low
Power consumption	Low	High	Medium-High	Medium
Energy loss	Medium	High	High	No
Water consumption	Low	Low	Low	High
Noise	No	Medium	Medium	Medium
Wind effect	Medium	Medium	Medium	Medium
Recirculation	No	Low-medium	Medium	Medium
Visible plum	No	No	No	Yes
Polluted water discharge	No	No	No	Yes
Maintenance	Low	Medium	Low-medium	High
Plot area	Medium-High	Medium	Medium	Low
Flexibility in site arrangement	Good	Good	Medium	Good
Lifespan of heat exchanger	High (>30 yrs)	High (>30 yrs)	High (>30 yrs)	Low (10 yrs)

5.5. Description of thermal energy storage system

A portion of the produced heat from the SF system in the reference 50 MW CSP-PT plant in this work (Andasol-1) is not transferred to the PB system. However, it is stored in the TES system, where a mixture of about 28,500 t, a mixture of 60% sodium nitrate (NaNO_3) and 40% potassium nitrate (KNO_3), is heated during the daytime. Generally, the reference plant depends on the TES system to run the steam turbine during nighttime or overcast periods. The TES molten salt mixture has a cold tank heater set point of about 292 °C and a hot tank heater set point of about 386 °C. Moreover, the reference plant has a two-tank TES system, which operates the steam turbine for 7.5 h, allowing for extended operations during the summer. This means that the fully charged TES tanks can hold up the heat, making the steam turbine run at full load for 7.5 h. Therefore, to charge the TES system while operating the steam turbine, the SF system is made larger than that of a CSP-PT plant without a TES system by incorporating more PT collectors. For the most part, the inclusion of TES increases investment costs, but it results in an increased capacity factor [297]. Therefore, reducing the LCOE is expected, highlighting the importance of utilizing a TES system in this work. Figure 5. 7 shows the solar TES system categorizations based on the method of storage and temperature ranges [298,299]. Figure 5. 8 shows the classifications of various materials, latent heat storage, or Phase Change Materials (PCMs) [299], which are commonly used. Figure 5. 9 shows the main TES configurations and mediums for each CSP technology in which molten salt is utilized as a medium in direct and indirect design configurations. For the case of this work, two molten salt tanks are used within the TES system of the reference 50 MW CSP-PT plant.

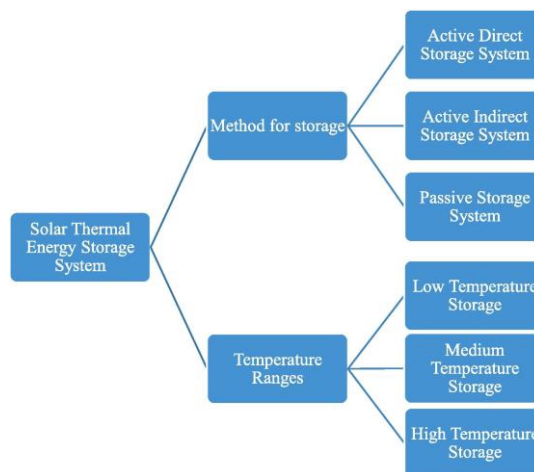


Figure 5. 7 Categorizations of the solar TES system [298,299].

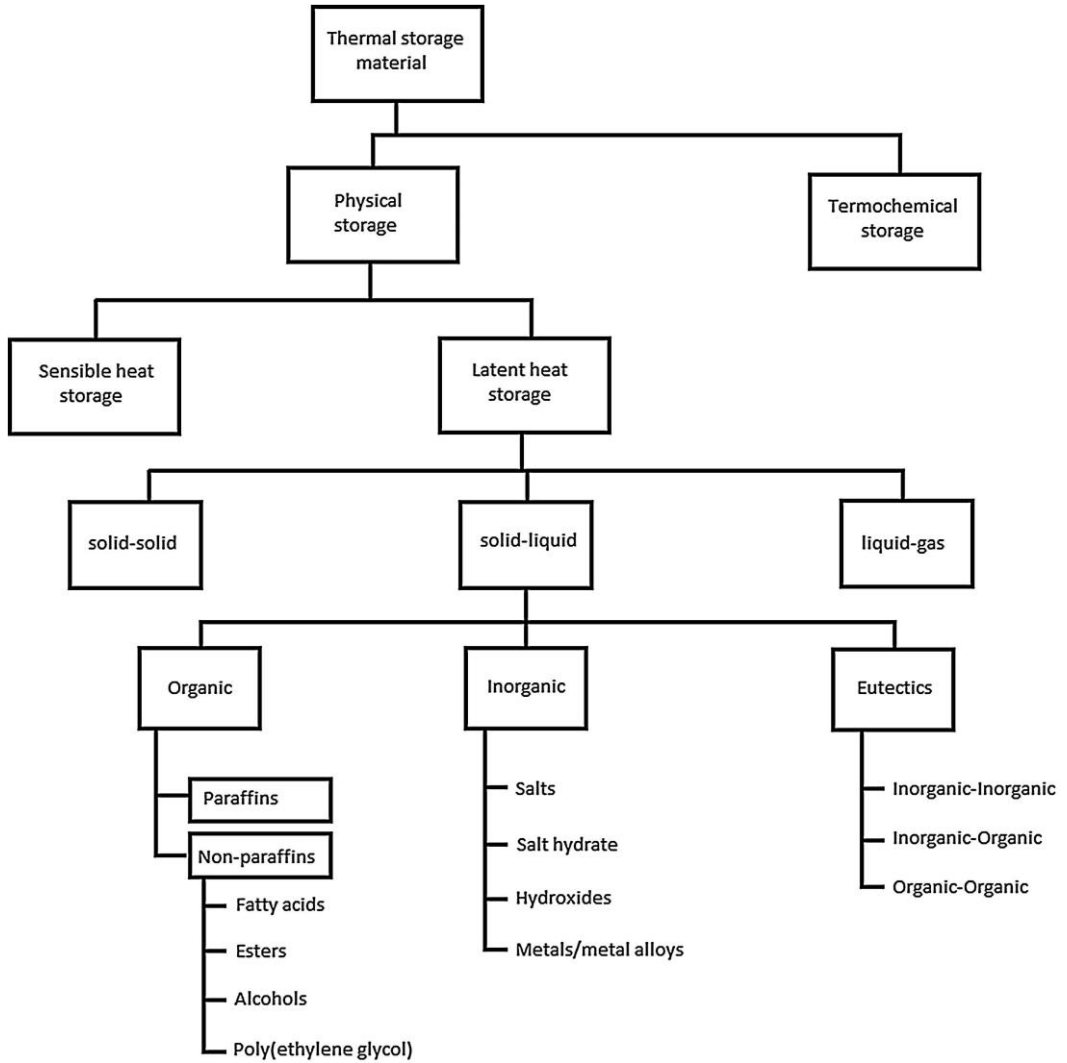


Figure 5. 8 Classifications of various materials, latent heat storage, and PCMs [299].

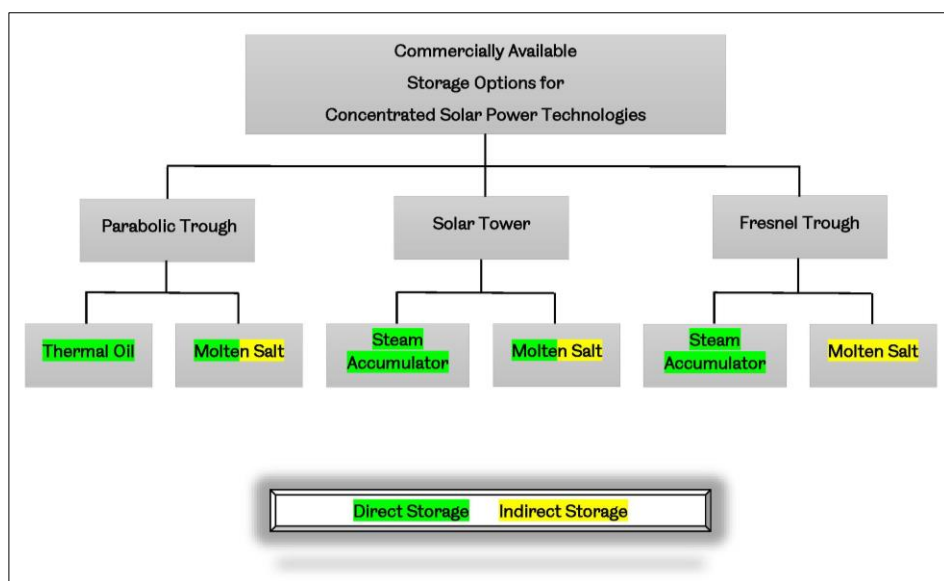


Figure 5. 9 Main TES system configurations for CSP technologies in which molten salt is used as a medium in direct and indirect design configurations.

In short, the TES system stores the heat from the SF system then the heat drives the steam turbine during periods of low or no sunlight. For this reason, TES systems are beneficial in many locations around the world, where peak demand for electricity occurs after sunset. In the direct storage systems, the HTF serves as the TES medium. On the other hand, a separate fluid acts as the TES medium in the indirect storage systems, and heat is transferred from the HTF to the TES medium through heat exchangers. Thus, a two-tank TES system consists of a hot tank to store heat from the SF system and a cold tank for the cooled TES medium.

5.6. Mathematical description

In this work, the design configuration, shown in Figure 3. 1, Figure 3. 2, and Appendix C, is investigated for CSP-PT plant operations from the total system-level simulation viewpoint (see Figure 3. 11 and Figure 3. 12). The solar radiation is recognized as it becomes incident on the total aperture area of the SF system (A_{ap}). Figure 5. 10 shows a schematic for the processing of solar heat between the CSP-PT plant systems.

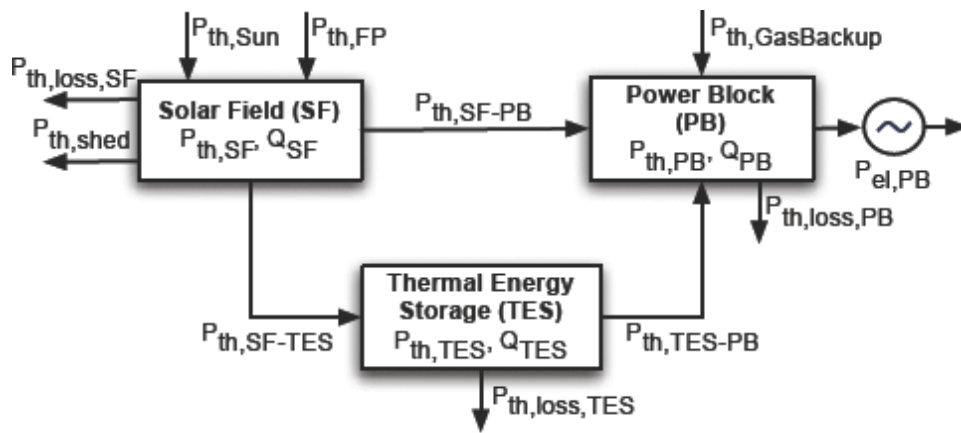


Figure 5. 10 Schematic of the processing of solar heat between CSP-PT plant systems [51].

It should be noted that the detailed mathematical derivations are provided by some studies [300,301], which define the radiative solar power incident on the net aperture area of the mirrors (E_{sun}) as:

$$E_{sun} = \sum_{i=1}^{365} \sum_{j=0}^{23} DNI_{ij} A_{ap}$$

5. 1

where the total aperture area of the SF system, A_{ap} , is given by:

$$A_{ap} = W_{ap} L M N = \sum_{i=1}^{N_{SCA}} A_{collector,i}$$

5. 2

where W_{ap} is the collector aperture width, L is the collector length, M is the number of rows of the collectors in series, N is the number of parallel lines, and N_{SCA} is the total number of collectors. Furthermore, other studies [289,302–307] have estimated five efficiencies of critical components in the CSP-PT plant to evaluate the impact on $\eta_{overall}$, which is defined along with the five efficiencies as follows:

$$\begin{aligned} \eta_{optical} &= \frac{E_{receiver}}{E_{sun}} = \eta_{optical,peak} \eta_{shadow} F_{fou,mirror} F_{fou,glass} F_{track} \\ &= \rho_{clean} \gamma \tau_{glass} \alpha K(\theta) \eta_{shadow} F_{fou,mirror} F_{fou,glass} F_{track} \end{aligned}$$

5. 3

$$\eta_{thermal} = \frac{E_{HTF}}{E_{receiver}} = 1 - \frac{E_{th,loss}}{E_{sun} \eta_{optical}}$$

5. 4

$$\eta_{piping} = \frac{E_{HTF} - E_{loss,piping}}{E_{HTF}} = \frac{E_{boiler}}{E_{HTF}}$$

5. 5

$$\eta_{net,PB} = \frac{E_{ele,turb} - E_{ele,pump} - E_{aux,cond}}{E_{boiler}} = \frac{E_{ele,net,PB}}{E_{boiler}}$$

5. 6

$$\eta_{aux,SF} = \frac{E_{ele,net,PB} - E_{ele,aux,SF}}{E_{ele,net,PB}}$$

5. 7

$$\eta_{overall} = \eta_{optical} \eta_{thermal} \eta_{piping} \eta_{net,PB} \eta_{aux,SF} = \frac{E_{ele,a}}{E_{sun}}$$

5. 8

where $E_{ele,a}$ is the annual net electricity output, and the above listed five efficiencies represent the following: (i) optical efficiency ($\eta_{optical}$), which compares the radiation on the receiver to the incident radiation on the mirror from the sun, (ii) thermal efficiency ($\eta_{thermal}$), which takes into account the collector thermal energy losses, (iii) piping efficiency (η_{piping}), which evaluates the impact of piping thermal losses, including nighttime losses on the HTF transferred thermal power, (iv) net PB

efficiency ($\eta_{\text{net,PB}}$), which expresses the conversion efficiency of the thermal input into the electricity output and considers the heat exchanger thermal losses, and (v) efficiency of the SF auxiliary ($\eta_{\text{aux,SF}}$), which expresses the impact of the SF system circulating pumps and tracking consumptions on the net PB system output.

It should be recognized that Equation 5. 9 to Equation 5. 18 are assigned from some studies [229,283,300], which define the collector thermal performance as follows:

$$F'U_L = \begin{cases} F_R U_L & \text{if } \frac{F_R U_L}{g_{\text{test}} C_{p\text{fluid}} \text{ConcRat}} \geq 1 \\ g_{\text{test}} C_{p\text{fluid}} \left(1 - e^{-\left(\frac{F_R U_L}{g_{\text{test}} C_{p\text{fluid}} \text{ConcRat}}\right)} \right) & \text{if } \frac{F_R U_L}{g_{\text{test}} C_{p\text{fluid}} \text{ConcRat}} < 1 \end{cases}$$

5. 9

where

F_R : collector heat removal factor (–)

F' : collector efficiency factor (–)

U_L : loss coefficient ($\text{W}/\text{m}^2 \text{ } ^\circ\text{C}$)

$F'U_L$: modified loss coefficient based on $F_R U_L$ ($\text{W}/\text{m}^2 \text{ } ^\circ\text{C}$)

$F_R U_L$: collector loss coefficient ($\text{W}/\text{m}^2 \text{ } ^\circ\text{C}$)

ConcRat: Concentration Ratio

and

$$\text{ConcRat} = \frac{A_{\text{ap}}}{A_{\text{receiver}}}$$

5. 10

The thermal power output from the collector (Q_u) is given by:

$$Q_u = A_{\text{collector}} [F_R (\tau\alpha)_n I_t - F_R U_L \Delta T]$$

5. 11

where the term $F_R (\tau\alpha)_n$ represents the efficiency when the solar radiation is absorbed by the plate and removed by the fluid flowing through the collector, I_t is the amount of solar radiation incident on the plane of the surface, and ΔT is the temperature difference representing either the collector inlet temperature minus the ambient temperature or the mean collector fluid temperature minus the ambient temperature. For PT collectors, two constant modifiers (R_1 and R_2) are

applied to Equation 5. 11 to account for flow rates/collectors in series and can be expressed as shown below in which R_1 includes a term defined as R_{test} :

$$R_{\text{test}} = g_{\text{test}} C_{p\text{fluid}} \left(1 - e^{(-F' U_L / (g_{\text{test}} C_{p\text{fluid}}))} \right) \quad 5.12$$

$$R_1 = \frac{N_{\text{series}} \dot{m} C_{p\text{fluid}}}{A_{\text{ap}}} \left(\frac{1 - e^{((-F' U_L A_{\text{ap}}) / (N_{\text{series}} \dot{m} C_{p\text{fluid}}))}}{R_{\text{test}}} \right) \quad 5.13$$

$$R_2 = \frac{1 - \left(1 - \left((R_1 A_{\text{ap}} F_R U_L) / (\dot{m} C_{p\text{fluid}} N_{\text{series}} \text{ConcRat}) \right) \right)^{N_{\text{series}}}}{N_{\text{series}} \left((R_1 A_{\text{ap}} F_R U_L) / (\dot{m} C_{p\text{fluid}} N_{\text{series}} \text{ConcRat}) \right)} \quad 5.14$$

where \dot{m} is the mass flow rate of the fluid, and N_{series} is the number of collectors in series. After considering the above definitions of R_1 and R_2 , then Equation 5. 11 is reformulated as follows:

$$Q_u = R_1 R_2 A_{\text{ap}} N_{\text{parallel}} \left[F_R (\tau\alpha)_n \text{IAM} I_{\text{beam}} - \frac{F_R U_L}{\text{ConcRat}} (T_{\text{in}} - T_{\text{amb}}) \right] \quad 5.15$$

where N_{parallel} is the number of series collector strings in parallel, IAM is the Incidence Angle Modifier, I_{beam} is the amount of the beam solar radiation incident on the collector surface, T_{in} is the temperature of the fluid entering the collector array, and T_{amb} is the ambient temperature. Besides, the temperature of the fluid at the collector outlet (T_{out}) is given by:

$$T_{\text{out}} = \begin{cases} T_{\text{in}} + \frac{Q_u}{\dot{m} C_{p\text{fluid}}} & \text{if } \dot{m} > 0 \\ T_{\text{amb}} + F_R (\tau\alpha)_n \text{IAM} I_{\text{beam}} \frac{\text{ConcRat}}{F_R U_L} & \text{if } \dot{m} = 0 \end{cases} \quad 5.16$$

The mean annual collector efficiency at the design condition ($\eta_{\text{collector}}$) is given by:

$$\eta_{\text{collector}} = \frac{Q_u}{\text{DNI} A_{\text{ap}}} \quad 5.17$$

Based on an hourly simulation, the total defocused thermal energy from the SF system (i.e., dumped energy) is tracked throughout, which is the amount of DNI that

cannot reach the collector due to mirror defocusing. Moreover, the dumped energy (Q_{dump}) is given as:

$$Q_{\text{dump}} = A_{\text{ap}} \text{DNI} \eta_{\text{optical}} \eta_{\text{def}} = \dot{m} C_{p,\text{fluid}} (T_{\text{out}} - T_{\text{max}}) \quad 5.18$$

where η_{def} is the fraction of defocused SCA units, and T_{max} is the maximum temperature at which the fluid may exit the collector.

In most cases, the critical parameter for consideration in the TES sizing stage is the maximum storage capacity ($Q_{\text{m}}^{\text{TES}}$) [188], which is given as follows:

$$Q_{\text{m}}^{\text{TES}} = N_{\text{h}}^{\text{TES}} Q_{\text{in,th}}^{\text{PB}} \quad 5.19$$

where $Q_{\text{in,th}}^{\text{PB}}$ is the design turbine thermal input (i.e., the design-point PB thermal requirement). In general, $Q_{\text{m}}^{\text{TES}}$ is expressed by the number of hours that the thermal energy is delivered at the PB design thermal-input level, which is the thermal input requirement of the PB system to operate at the design point condition. Apart from this, the thermodynamic PB system efficiency (η_{PB}) is determined by dividing the work output by the required heat input, as shown in Equation 5. 20. With this in mind, Equation 5. 19 is reformulated, as shown in Equation 5. 21.

$$\eta_{\text{PB}} = \frac{\dot{W}}{Q_{\text{in,th}}^{\text{PB}}} \quad 5.20$$

$$Q_{\text{m}}^{\text{TES}} = N_{\text{h}}^{\text{TES}} \frac{\dot{W}}{\eta_{\text{PB}}} \quad 5.21$$

Apart from this, $Q_{\text{m}}^{\text{TES}}$ is used to calculate the following dispatch parameters: the PB input limits, the PB load requirement, and the start-up requirement. On the whole, the maximum power to the TES system is expressed as $Q_{\text{m}}^{\text{to TES}}$ which is the maximum TES charge rate used in the dispatch calculation whenever energy from the SF system exceeds the PB load requirement. If the fluid type in the TES system is different from that of the SF system, the TES will consist of a heat exchanger system. Thus, a heat exchanger duty (D_{hex}), which is an adjustment factor greater than one, is defined as:

$$Q_m^{\text{to TES}} = D_{\text{hex}} Q_{\text{in,th}}^{\text{PB}}$$

5. 22

Alternatively, the maximum power from the TES system ($Q_m^{\text{frm TES}}$), which is the maximum TES discharge rate used in the dispatch calculation whenever the energy from the SF system is less than or equal to the PB load requirement. As a rule, $Q_m^{\text{frm TES}}$ is calculated as follows:

$$Q_m^{\text{frm TES}} = \frac{Q_m^{\text{to TES}} F_{\text{gross}}^{\text{TES}}}{F_{\eta}^{\text{TES}}}$$

5. 23

where $F_{\text{gross}}^{\text{TES}}$ and F_{η}^{TES} are adjustment factors: the turbine-storage adjustment gross output factor and the turbine-storage adjustment efficiency factor, respectively. In a CSP-PT plant, the TES dispatch control is critical since it determines the TES system operation. The dispatch control will evaluate the backup function if the power plant is equipped with fossil backup. Above all, there are two main fractions for consideration in TES dispatch control. Firstly, the storage dispatch fraction with solar ($F_{\text{WS}}^{\text{TES}}$), which is the fraction of energy required for the TES system to start when the SF thermal energy is greater than zero [308]. This means that $F_{\text{WS}}^{\text{TES}}$ is only applied when the TES system did not operate in the previous hour. Therefore, $F_{\text{WS}}^{\text{TES}}$ is the fraction of the TES maximum storage capacity indicating the minimum level of charge that the TES can discharge while the SF system produces power during the daytime. A value of zero should dispatch the TES system at any hour assigned to the given dispatch period, whereas a value of one will never dispatch the TES. Secondly, the storage dispatch fraction without solar ($F_{\text{WOS}}^{\text{TES}}$), which is the fraction of energy in the TES system required for the TES to start whenever the SF thermal energy equals zero. This means that $F_{\text{WOS}}^{\text{TES}}$ is only applied when the TES system did not operate in the previous hour. Thus, $F_{\text{WOS}}^{\text{TES}}$ is the fraction of the TES maximum storage capacity indicating the minimum level of charge that the TES can discharge while no solar resource is available during the nighttime.

Undoubtedly, the TES system helps overcome short periods of passing clouds, which backup burners can overcome, if applicable. Likewise, the TES system allows shifting and extending the power production into the nighttime. However, up to a specific point determined during the plant design stage, the heat produced by the SF system is separated into a heat flow feeding the steam turbine for a full load operation, and

the remaining heat flow is used for loading the TES system. Therefore, the distribution will not always resemble an equal-division percentage between the heat flow feeding the steam turbine and the TES system throughout the daytime. Significantly, priority should always mandate securing the steam turbine operation at the nominal load, highlighting the importance of this work (see Section 5.7). As a rule of thumb, the surplus energy is stored in the TES system to perform the following accordingly:

- i. allowing constant full load operation of the steam turbine,
- ii. reducing the number of daily operations of the power plant, and
- iii. maintaining continuous operation of the steam turbine at rated capacity.

Consequently, the power export to the grid remains at optimal design conditions as a result. In general, the economic feasibility of a CSP-PT plant can be evaluated by different methods. Still, the LCOE method is the most common because it considers project installation costs, electricity generation, operations, and maintenance costs. In this respect, the LCOE calculation is performed as follows [309]:

$$\text{LCOE} = \frac{\sum_{y=1}^k S_y + M_y + F_y}{\sum_{y=1}^k E_y / (1 + r)^y}$$

5. 24

where

S_y : investment expenditures in the year y .

M_y : operation and maintenance expenditures in the year y .

F_y : fuel expenditures in the year y .

E_y : electricity generation in the year y .

r : discount rate.

k : lifetime of the plant.

5.7. Results and discussions

5.7.1. Validation

The simulation results obtained in this work for the reference 50 MW CSP-PT plant (Andasol-1) are compared and validated with actual and simulated data published by Herrmann et al. [8], Liqreina et al. [283], Trabelsi et al. [229], and Bataineh et al. [310]. Table 5. 6 compares the results obtained with other published literature findings, which suggest acceptable variations.

Furthermore, Table 5. 7 shows the percentage difference values between the actual and simulated results for the reference plant performance under the climatic conditions of Spain, which is the actual location of the reference plant. The values, shown in Table 5. 7, indicate that the results obtained from the SAM software are more conservative than the actual data reported for the reference plant in the literature. Hence, the results confirm that SAM is reliable; thus, it is used to yield realistic findings in further analyses later within this Chapter by undergoing simulations with two cooling options using wet and dry-cooled condensers. Moreover, the outcome from this work compared to the published data by Herrmann et al. [8], which is the actual published data for the reference plant, suggests higher accuracy for the following parameters:

- i. 14.6% for the annual overall plant efficiency (η_{overall}), which leads to a difference of -0.63%,
- ii. 479,609.8 MWh/yr for the thermal power from the SF system, which leads to a difference of -6.34%, and
- iii. 46.2% for the annual efficiency of the SF system, which leads to a difference of 0.27%.

Table 5. 6 Actual and simulated results for the performance of the reference 50 MW CSP-PT plant (Andasol-1) used in this work under the climatic conditions of Spain.

Description	Unit	Actual	Simulated	Simulated	Simulated	Simulated
		published data, Herrmann et al. [8]	published data, Liqreina et al. [283]	published data, Trabelsi et al. [229]	published data, Bataineh et al. [310]	published data from this work
Annual DNI	kWh/m ² yr	2,202	2,052	2,052	2,052	2,033.3
Number of full load hours of steam turbine	h	3,144	3,089	3,089	3,098	3,003
Annual net electricity output ($E_{ele,a}$)	MWh _e /yr	157,206	141,110.1	142,381	153,560	151,569.8
Annual overall plant efficiency ($\eta_{overall}$)	%	14.7	13.5	13.6	13.1	14.6
Solar irradiation on the SF system	MWh/yr	1,105,430	1,046,919.3	1,046,919.3	-	1,037,586.6
Thermal power from the SF system	MWh/yr	510,030	439,782	438,180	-	479,609.8
Annual efficiency of the SF system	%	46.1	42	41.8	44.2	46.2
Total water consumption	m ³ /yr	612,000	540,520.1	587,100	-	508,949

Table 5. 7 Percentage difference values with actual and simulated results for the performance of the reference 50 MW CSP-PT plant (Andasol-1) used in this work under the climatic conditions of Spain.

Description	Percentage difference values, ± %									
	Liqreina et al. compared to	Trabelsi et al. compared to		Bataineh et al. compared to			Simulated data from this work compared to			
	Herrmann et al.	Herrmann et al.	Liqreina et al.	Herrmann et al.	Liqreina et al.	Trabelsi et al.	Herrmann et al.	Liqreina et al.	Trabelsi et al.	Bataineh et al.
Annual DNI	-7.31	-7.31	0	-7.31	0	0	-8.30	-0.92	-0.92	-0.92
Number of full load hours of steam turbine	-1.78	-1.78	0	-1.48	0.29	0.29	-4.70	-2.86	-2.86	-3.16
Annual net electricity output ($E_{ele,a}$)	-11.41	-10.41	0.89	-2.37	8.11	7.28	-3.72	6.90	6.06	-1.31
Annual overall plant efficiency ($\eta_{overall}$)	-8.89	-8.09	0.74	-12.30	-3.13	-3.90	-0.63	7.58	6.90	10.39
Solar irradiation on the SF system	-5.59	-5.59	0	-	-	-	-6.54	-0.90	-0.90	-
Thermal power from the SF system	-15.97	-16.40	-0.37	-	-	-	-6.34	8.30	8.64	-
Annual efficiency of the SF system	-9.76	-10.29	-0.48	-4.28	5.00	5.45	0.27	9.14	9.57	4.36
Total water consumption	-13.22	-4.24	7.93	-	-	-	-20.25	-6.20	-15.36	-

5.7.2. Effects of temperature and solar irradiance

Unlike a conventional power plant, the control strategy from a CSP-PT plant operator's viewpoint depends on the DNI level. Therefore, DNI forecasting can be critical for this particular renewable technology in arid environments with frequent sandstorms. Several studies [241,248,249,252–255] proposed different methods for characterizing and estimating the DNI to provide confidence in the solar resource and hence the energy generation output obtained from plant simulations. Essentially, such methods minimize the uncertainty in the DNI to increase the accuracy of the energy yield predictions. To illustrate the importance of DNI, Figure 5. 11 shows that the increase in the net electricity output ($E_{ele,a}$) is proportional to DNI. Concerning the two cases of Spain and Kuwait with both wet and dry cooling options, the net electricity output difference increases in the summer when experiencing high DNI levels as the ambient temperature increases.

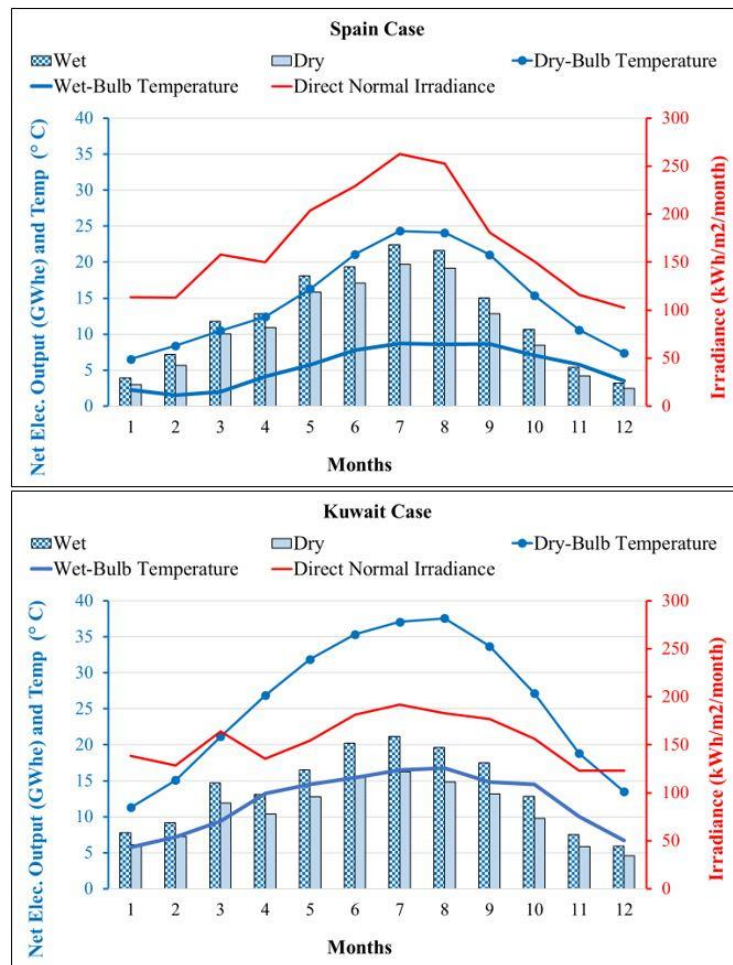


Figure 5. 11 Monthly profiles of the net electricity output using wet/dry cooling options, the DNI level ($\text{kWh}/\text{m}^2/\text{month}$), and the wet/dry bulb temperatures for the Spain and Kuwait cases.

Additionally, it can also be concluded from Figure 5. 11 that during the spring in Kuwait, also known as the “Sarayat” period, the month of April records lower DNI values than March due to sandstorms while the ambient temperature is superior. This is because the chosen location is influenced by the presence of sandstorms during the Sarayat period. This variation decreases mainly the amount of electricity generation by the air-cooled condenser system within the CSP-PT plant. With this scenario, the condensation temperature increases, which increases the pressure of the dry-cooled condenser while reducing the PB efficiency (see Figure 5. 17).

Figure 5. 12 shows the effect of the ambient temperature on the overall plant efficiency, which is noticeable in the Kuwait case for the range of average monthly temperatures close to 40 °C during the summer. The difference in the overall plant efficiency between the dry and wet cooling options increases during the summer. In contrast, the dry cooling option performs more competitively in the winter due to the lower ambient temperature.

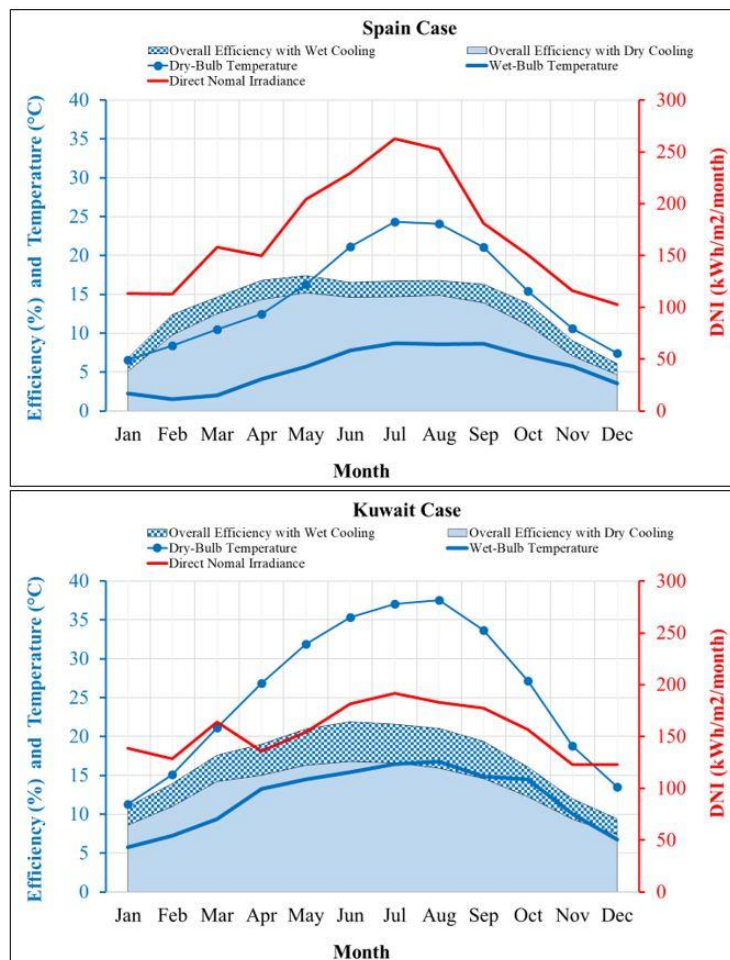


Figure 5. 12 Monthly profiles of the overall plant efficiency using wet/dry cooling, the DNI level ($\text{kWh/m}^2/\text{month}$), and the wet/dry bulb temperatures for the Spain and Kuwait cases.

Before the stage of CSP-PT plant design, a critical consideration is the number of full load hours at which the steam turbine in the PB system produces electricity under the rated design condition. Figure 5. 13 shows that selecting an IAD value of 700 W/m^2 (illustrated by the dark blue area), provides the maximum number of hours during the summer in the Kuwait case for the DNI level in the range of $600\text{-}700 \text{ W/m}^2$. With this specific IAD value, the steam turbine produces electricity at full load hours during the summer more often in the Kuwait case compared to the Spain case. This is critical since the summer months are when the maximum DNI and peak electrical load occur for the chosen location in this work within Kuwait. For the same IAD value of 700 W/m^2 , the number of full load hours of steam turbine in the Spain case is 3003 h, and in the Kuwait case is 3306 h, as shown in Table 5. 8. Hence, the IAD value of 700 W/m^2 is selected as a design value for the reference 50 MW CSP-PT plant and thus used as an input parameter to SAM (see Appendix D).

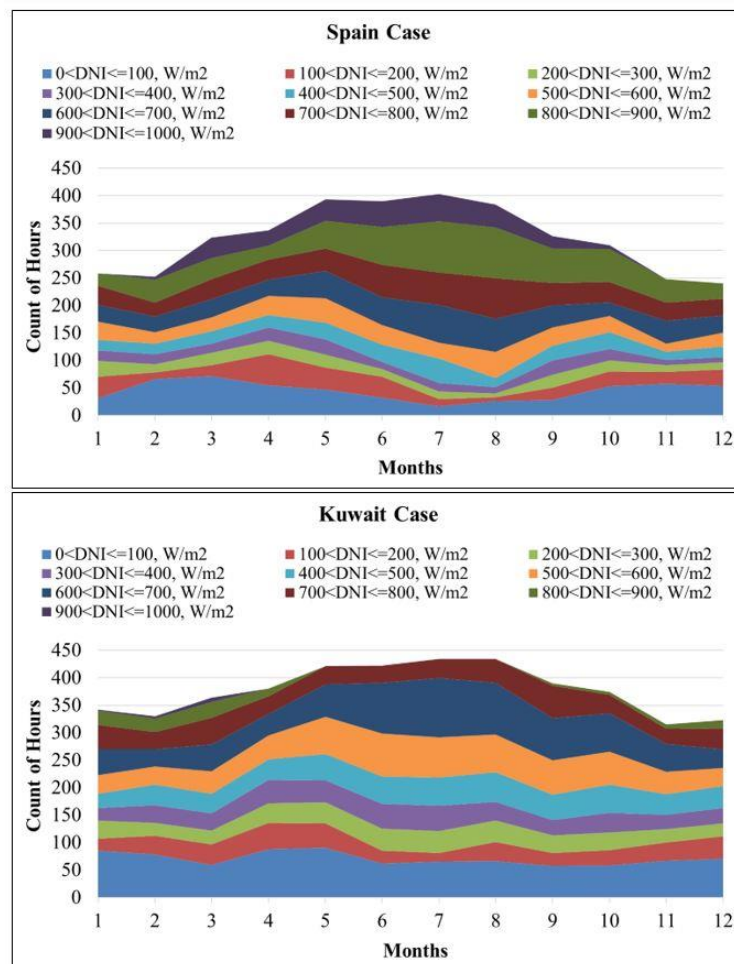


Figure 5. 13 Comparison of the number of hours for different ranges of DNI (W/m^2) during each month for the Spain and Kuwait cases.

After comparing the performance results of the reference 50 MW CSP-PT plant under the climatic and DNI conditions of Spain and Kuwait, one can conclude that the IAD value of 700 W/m^2 is very suitable for Kuwait. The selection of an IAD value of 700 W/m^2 is one of the contributing factors towards the higher annual and monthly overall plant efficiency values for the Kuwait case compared to that of Spain under both the wet and dry cooling options. Due to the importance of IAD, a parametric analysis is performed (in Section 5.7.4) on various IAD values. The parametric analysis focuses on further understanding the impacts on $E_{\text{ele,a}}$ and Q_{dump} especially since the annual/monthly profiles and frequency of high DNI values in Kuwait are usually lower compared to Spain, as shown in Table 5. 8, Figure 5. 11, and Figure 5. 14.

Table 5. 8 Performance results for the reference 50 MW CSP-PT plant (Andasol-1) under the wet/dry cooling options for the Kuwait and Spain cases.

Description	Unit	Simulated data from this work for the Spain case		Simulated data from this work for the Kuwait case	
		Wet	Dry	Wet	Dry
Annual DNI	$\text{kWh/m}^2 \text{ yr}$	2033.3	2033.3	1857.1	1857.1
Number of full load hours of steam turbine	h	3003	2709	3306	2792
Annual net electricity output ($E_{\text{ele,a}}$)	MWh_e/yr	151,569.8	129,345.1	166,104.0	128,595.3
Annual overall plant efficiency (η_{overall})	%	14.6	12.5	17.5	13.6
Solar irradiation on the SF system	MWh/yr	1,037,586.6	1,037,586.6	947,718.8	947,718.8
Thermal power from the SF system	MWh/yr	479,609.8	494,715.0	477,073.1	480,063.7
Annual dumped thermal energy from the SF system (Q_{dump})	MWh/yr	37,513.0	21,132.2	4362.5	857.0
Annual efficiency of the SF system	%	46.2	47.7	50.3	50.7
Annual capacity factor	%	38	33	42	33
Total water consumption	m^3/yr	508,949	38,984	592,799	39,299

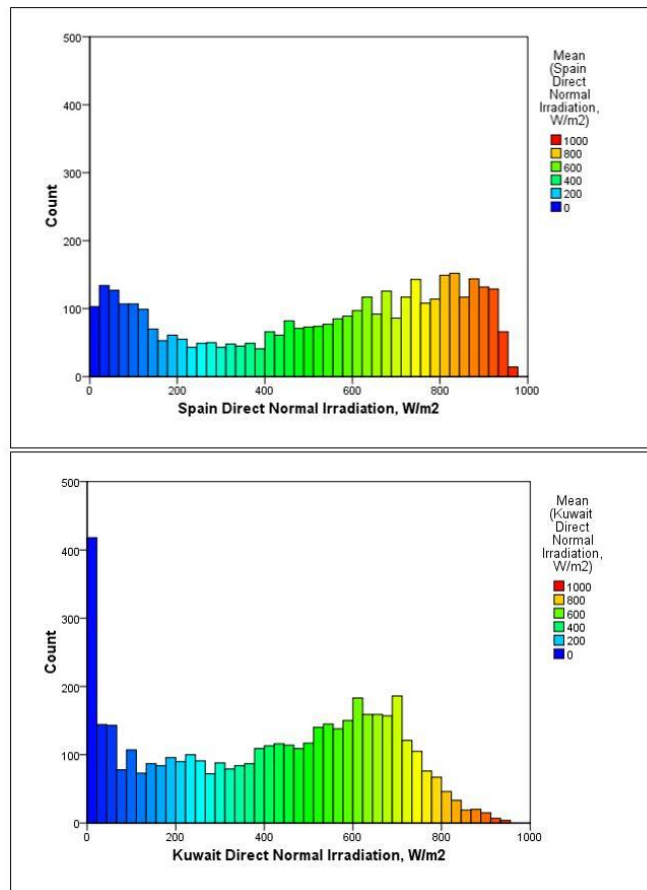


Figure 5. 14 Frequency of DNI (W/m^2) during a typical year in Spain and Kuwait.

The selection of the optimal IAD value, a design point value for a CSP-PT plant, is essential because it reflects on the amount of auxiliary power needed in the SF system for mirror defocusing and therefore reflects on the total operating cost and LCOE estimations. If the plant's location experiences DNI levels above the design IAD value, the plant operator must perform excessive control by defocusing some mirrors in the SF system. This procedure is necessary to avoid collecting excess thermal energy, which is neither required by the TES system nor the PB system. Figure 5. 15 shows that the values of Q_{dump} in the Spain case are higher compared to that of Kuwait. This means that the IAD value of $700 W/m^2$ for the reference 50 MW CSP-PT plant in this work is more suitable for the DNI conditions of Kuwait than that of Spain. This is because the number of hours when the DNI reaches values above the IAD of $700 W/m^2$ (i.e., the selected design value) is more significant in the Spain case compared to the Kuwait case, as shown in Figure 5. 13 and Figure 5. 14. Thus, the level of DNI in relation to the IAD value is the primary factor in estimating Q_{dump} . In addition, Q_{dump} is proportional to the seasonal variations of DNI in both the wet and dry cooling options for the Spain and Kuwait cases (see Figure 5. 15).

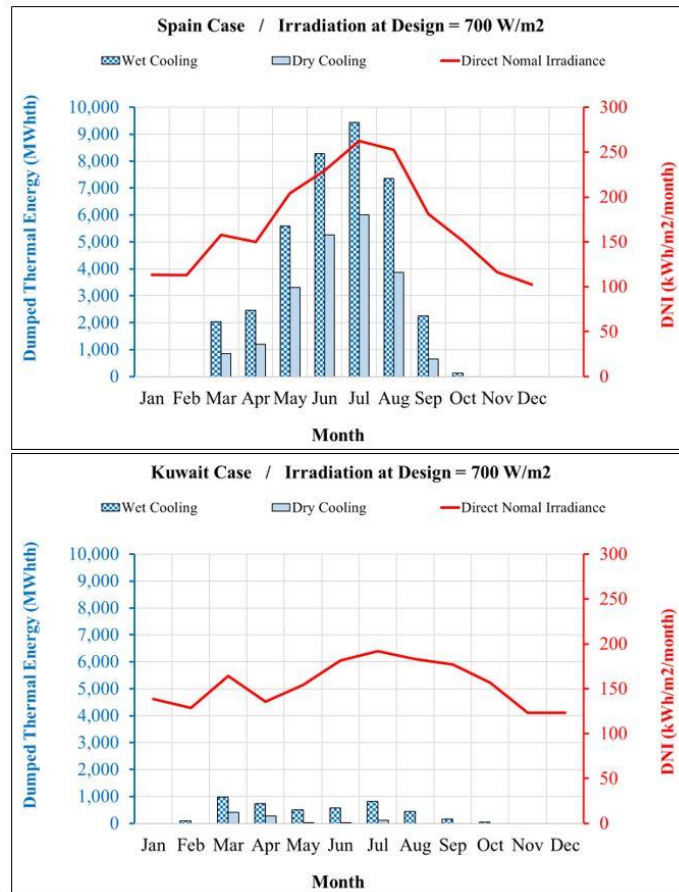


Figure 5. 15 Monthly profiles of the dumped energy with the wet/dry cooling options and the DNI level ($\text{kWh/m}^2/\text{month}$) for the Spain and Kuwait cases ($y\text{-axis} \leq 10,000 \text{ MWh}_t$).

The reason for the lower Q_{dump} values with dry cooling compared to wet cooling in the Spain and Kuwait cases is that with evaporative cooling (wet-cooled condenser), heat is rejected at a higher rate than with air fans (dry-cooled condenser). The effect of the number of hours when the DNI reaches values above the IAD of 700 W/m^2 is observed during March when the highest amount of Q_{dump} is recorded in the Kuwait case. Although the monthly DNI of July for the Kuwait case is higher than that of March, the value of Q_{dump} (in March) is higher due to experiencing a more significant number of hours when the DNI reaches values above IAD of 700 W/m^2 (see Figure 5. 13). Besides, the Q_{dump} values with the dry cooling option are less than that of the wet cooling option (see Figure 5. 15) because the dry cooling option uses the excess DNI to compensate for the lower overall plant efficiency. This is especially true since evaporative cooling in a wet-cooled condenser system rejects heat at a higher/faster rate than with air fans in a dry-cooled condenser system.

It is observed from Figure 5. 16 that the DNI variations between the summer (April to September) and winter (January to March and October to December) are

noticeable in the Spain case compared to the Kuwait case because the location of Kuwait is characterized as being a desert land, influenced by sandstorms. Such characteristics of meteorological variation decrease mainly the PB system efficiency for the dry-cooling option, as illustrated in Figure 5. 17 (i.e., orange-coloured curve), which shows lower performance during the summer for the Kuwait case compared to the Spain case. It should be noted that under the arid climatic conditions of summer in Kuwait, the condensation temperature is usually higher, increasing the pressure of the dry-cooled condenser and reducing the PB efficiency as a result (see Figure 5. 17).

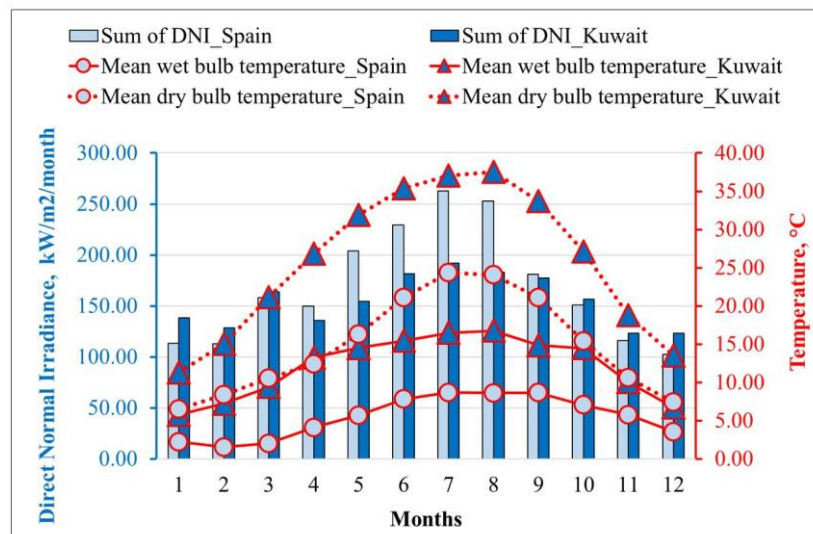


Figure 5. 16 Comparison of the monthly DNI level (kWh/m²/month) and the wet/dry bulb temperatures in Spain and Kuwait.

Figure 5. 18 shows the cycle cooling water mass flow rate (makeup) for the Spain and Kuwait cases. The flow rate is higher in the Kuwait case due to the higher ambient temperatures resulting in increased water consumption, as shown in Table 5. 8. It should be recognized that water consumption is not related to evaporative cooling since air fans are utilized with the dry-cooling option. This means that water consumption is mainly for mirror cleaning and plant auxiliaries. Although, Table 5. 8 shows that the annual sum of DNI in Kuwait is less than that in Spain by a difference of only 176.2 kWh/m² yr, the simulation results show that the reference plant performance under Kuwait's meteorological and DNI conditions has a higher annual SF efficiency and overall plant efficiency (for both cooling options) than the performance under Spain's conditions. This is because the steam turbine operates under the rated design condition for more hours in the Kuwait case. The difference is 303 full load hours with the wet cooling option and 83 hours with the dry cooling

option, favouring the Kuwait case. As shown in Table 5. 8, the calculated capacity factor for the simulated Spain case (38%) matches well with the published data for the reference plant (Andasol-1) [311]. Also, the simulation results in this work for the total water consumption match well with the published estimates for water consumption in CSP-PT plants, according to some studies [312–314], which is 3.0 m³/MWh using the wet cooling option and 0.3 m³/MWh using the dry cooling option.

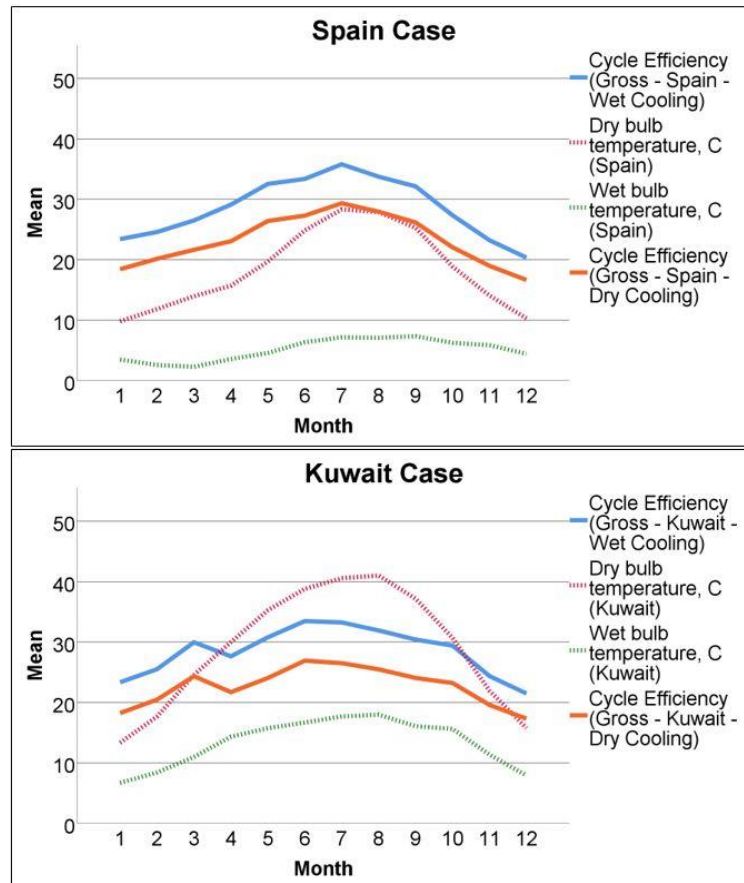


Figure 5.17 The effects of the wet/dry bulb temperatures and DNI levels on the PB cycle efficiency with the wet/dry cooling options for the Spain and Kuwait cases.

Table 5. 9 compares the cycle cooling water mass flow rate (makeup) for the reference 50 MW CSP-PT plant (Andasol-1) under the wet/dry cooling options for the Kuwait and Spain cases. It is concluded that the percentage reduction in water consumption is 96.61% (Spain case) and 97.05% (Kuwait case) due to replacing a wet-cooled condenser with a dry-cooled one. It should be recognized that a small amount of makeup water is necessary to support a wet-surface air cooler to provide low-temperature cooling water for the PB system.

Furthermore, Table 5. 10 shows the energy balance results of the reference 50 MW CSP-PT plant (Andasol-1) under the wet/dry cooling options for the Spain and

Kuwait cases. It should be recognized that a small amount of makeup water is necessary to support a wet-surface air cooler to provide low-temperature cooling water for the PB system.

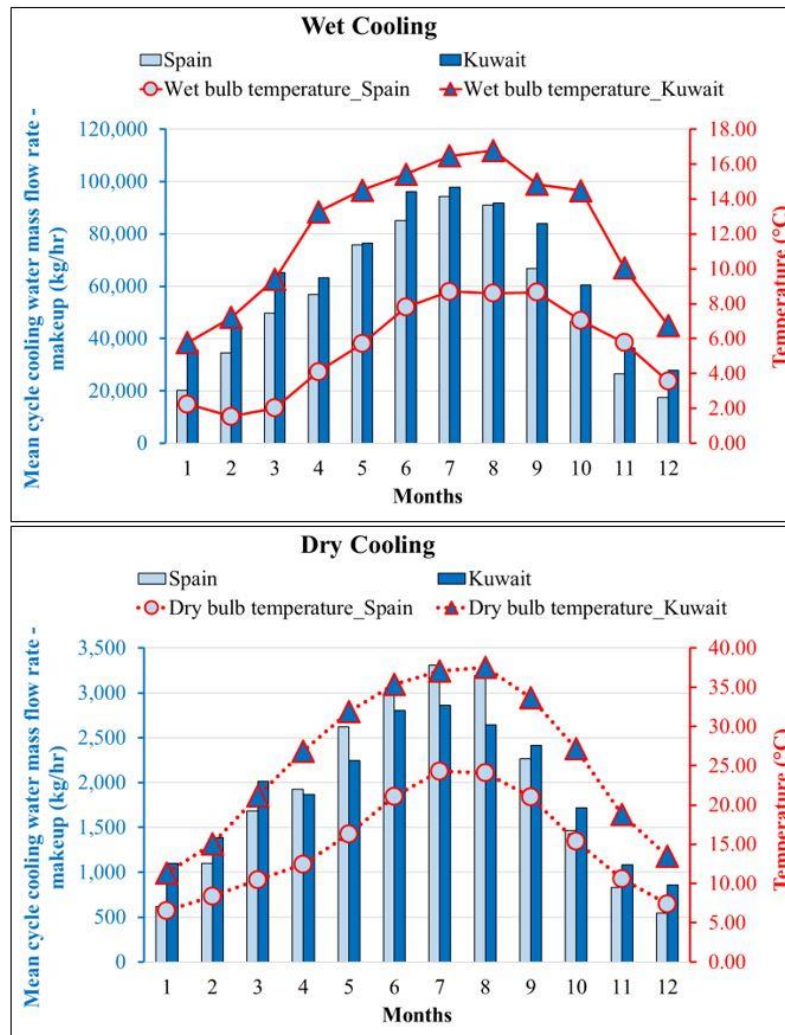


Figure 5. 18 Cycle cooling water mass flow rate (makeup) with the wet/dry cooling options for the Spain and Kuwait cases.

Table 5. 9 Cycle cooling water mass flow rate (makeup) for the reference 50 MW CSP-PT plant (Andasol-1) under the wet/dry cooling options for the Kuwait and Spain cases.

		Cycle cooling water mass flow rate - makeup,			Percentage reduction in water
		Sum	Mean	Maximum	
Spain	Wet	486,452,569	55,531	155,532	96.61
	Dry	16,487,985	1,882	5,127	
Kuwait	Wet	570,302,807	65,103	156,756	97.05
	Dry	16,802,957	1,918	5,130	

Table 5. 10 Energy balance results of the reference 50 MW CSP-PT plant (Andasol-1) under the wet/dry cooling options for the Spain and Kuwait cases.

	Spain		Kuwait	
	Wet-cooled condenser	Dry-cooled condenser	Wet-cooled condenser	Dry-cooled condenser
	Sum	Sum	Sum	Sum
PB Cycle electrical power output (gross), MW _e	168,830.58	150,592.50	183,454.57	149,682.32
PB Cycle electrical power output (net), MW _e	157,885.24	134,734.50	173,024.99	133,953.47
PB Cycle thermal power input, MWh _t	441,621.52	475,099.88	480,070.90	484,466.62
SF HTF energy inertial (consumed), MWh _t	55,476.33	55,805.94	56,051.44	56,272.72
SF collector DNI-cosine product, W/m ²	1,780,409.21	1,780,409.21	1,662,779.59	1,662,779.59
SF thermal power absorbed, MWh _t	505,392.18	520,682.34	503,258.95	506,394.00
SF thermal power avg. receiver loss, W/m	861,117.17	864,354.95	876,314.37	879,422.23
SF thermal power dumped, MWh _t	37,513.04	21,132.17	4,362.51	856.95
SF thermal power header pipe losses, MWh _t	4,273.44	4,282.12	4,175.53	4,184.85
SF thermal power incident, MWh _t	1,037,586.59	1,037,586.59	947,718.78	947,718.78
SF thermal power incident after cosine, MWh _t	908,222.33	908,222.33	848,217.11	848,217.11
SF thermal power produced, MWh _t	479,609.77	494,714.97	477,073.06	480,063.65
SF thermal power receiver loss, MWh _t	80,171.21	80,472.16	81,514.51	81,803.29
Parasitic power TES and cycle HTF pump, MW _e	1,970.84	2,078.88	2,102.25	1,910.69
Parasitic power condenser operation, MW _e	1,400.50	5,715.52	2,737.04	7,980.27
Parasitic power field collector drives, MW _e	314.04	318.21	327.64	328.68
Parasitic power fixed load, MW _e	2,409.00	2,409.00	2,409.00	2,409.00
Parasitic power solar field HTF pump, MW _e	2,117.78	2,406.69	1,617.03	1,675.33
Parasitic thermal TES freeze protection, MWh _t	1,772.53	2,052.58	909.66	1,095.83
Parasitic thermal field freeze protection, MWh _t	924.62	835.40	308.46	306.85
Direct Normal Irradiance (DNI), W/m ²	2,033,305.00	2,033,305.00	1,857,135.00	1,857,135.00

5.7.3. Evaluation of thermal energy storage

For the Kuwait case, the impact of sandstorms on CSP-PT plant performance can be minimized by occasionally operating the TES system instead of the SF system to supply heat to the PB system. Therefore, integrating TES systems in future CSP-PT plants in Kuwait should be inevitable.

In this work, the simulation results show a high level of accuracy in assessing CSP-PT performance, which is directly and primarily affected by the DNI level. Furthermore, the control algorithm in the simulation is verified after tracing the charged and discharged TES energy. For example, the DNI level of Spain extends further to two hours compared to the DNI of Kuwait (see Figure 5. 19). Figure 5. 20 shows the comparison results between the charged/discharged TES energy for the Spain and Kuwait cases using the wet/dry cooling options for an entire typical year. As a result, the TES operation extends further to two hours for the discharged TES energy in the Spain case (see Figure 5. 21 and Figure 5. 22).

Additionally, Table 5. 11 shows a comparison between the DNI statistical results in Spain and Kuwait, which can also be checked in conjunction with Figure 5. 20 by tracing the TES energy. Moreover, Figure 5. 20 shows an accurate estimation of the number of cycles for the charged and discharged TES energy concerning the wet and dry cooling options in Kuwait and Spain.

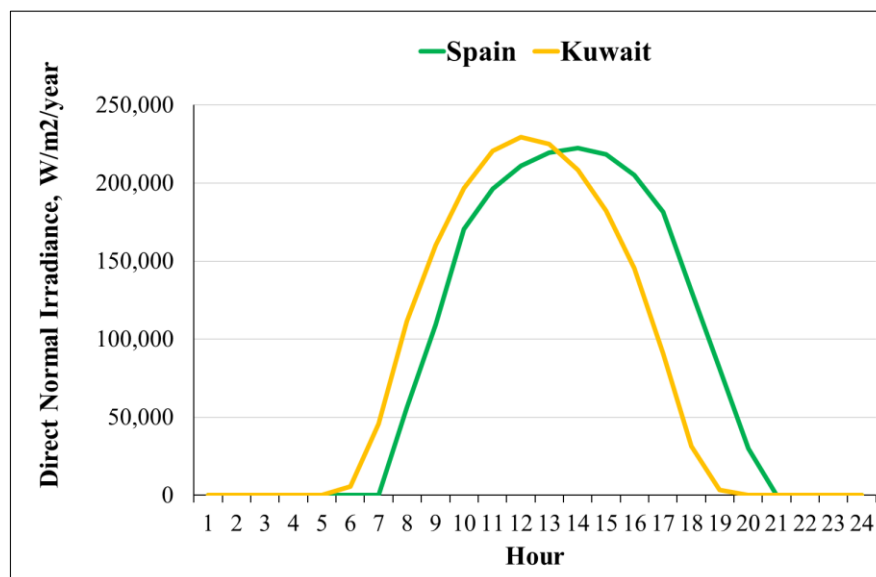


Figure 5. 19 Annual profiles (sum) of the DNI in Spain and Kuwait.

Table 5. 11 Comparison of the statistical results for the DNI levels during a typical year in Spain and Kuwait.

Hour	Spain DNI level, W/m ²			Kuwait DNI level, W/m ²		
	Mean	Sum	Maximum	Mean	Sum	Maximum
0	0	0	0	0	0	0
1	0	0	0	0	0	0
2	0	0	0	0	0	0
3	0	0	0	0	0	0
4	0	0	0	0	2	1
5	0	0	0	15	5,535	131
6	0	0	0	126	45,845	394
7	154	56,058	611	305	111,332	680
8	300	109,411	722	439	160,204	814
9	468	170,661	810	539	196,674	889
10	538	196,468	914	605	220,799	932
11	579	211,154	936	629	229,511	953
12	602	219,571	968	617	225,150	952
13	610	222,621	974	571	208,434	931
14	598	218,280	952	499	182,305	886
15	562	205,145	902	398	145,392	808
16	497	181,508	835	249	90,945	663
17	359	131,147	772	87	31,638	365
18	222	81,207	687	9	3,369	99
19	82	30,074	539	0	0	0
20	0	0	0	0	0	0
21	0	0	0	0	0	0
22	0	0	0	0	0	0
23	0	0	0	0	0	0

Hour	Discharged TES Thermal Energy, MWh				Charged TES Thermal Energy, MWh			
	Spain Case -	Kuwait Case -	Spain Case -	Kuwait Case -	Spain Case -	Kuwait Case -	Spain Case -	Kuwait Case -
	Wet Cooling	Wet Cooling	Dry Cooling	Dry Cooling	Wet Cooling	Wet Cooling	Dry Cooling	Dry Cooling
0	-15,503.52	-25.76	-15,459.00					
1	-8,614.01		-8,788.12					
2								
3								
4								
5								
6								
7		-129.55		-294.09		779.91		534.50
8	-1.34	-240.48	-35.57	-370.45	6,698.87	9,861.19	5,314.21	6,454.18
9	-88.90	-94.44	-180.87	-228.38	18,939.35	19,666.09	15,991.65	14,377.97
10	-124.06	-437.32	-269.32	-336.55	25,287.07	24,227.89	21,611.31	18,810.45
11	-564.59	-387.72	-683.23	-312.45	25,785.58	25,387.85	22,136.59	19,926.19
12	-886.79	-612.46	-921.74	-687.80	21,916.77	23,801.46	22,073.09	19,024.08
13	-495.64	-900.52	-615.18	-603.11	13,418.71	20,053.82	18,755.10	16,624.58
14	-855.39	-1,228.19	-957.60	-1,209.78	8,497.97	13,350.59	12,091.45	11,700.51
15	-913.14	-2,441.35	-1,058.46	-3,009.09	6,995.67	5,354.52	9,899.72	5,034.04
16	-1,487.45	-10,765.92	-1,641.03	-11,638.11	5,855.06	279.94	6,932.80	392.41
17	-5,120.49	-22,017.70	-4,187.79	-21,178.20	1,584.68	17.43	2,328.64	36.14
18	-9,263.70	-25,619.88	-8,952.90	-23,356.44	141.31		227.66	
19	-18,206.68	-22,555.54	-18,940.98	-18,376.77	53.93		138.84	
20	-20,126.23	-19,008.60	-20,975.58	-13,275.13				
21	-18,847.08	-15,424.06	-18,779.43	-9,197.42				
22	-17,581.83	-11,476.92	-18,275.33	-4,761.62				
23	-16,494.79	-7,203.27	-17,157.75	-1,886.30				
Total	-135,175.61	-140,569.69	-137,879.90	-110,721.70	135,174.97	142,780.70	137,501.06	112,915.05
No. cycles	-140.22	-145.82	-143.03	-114.86	140.22	148.11	142.63	117.13

Figure 5. 20 Comparison between the charged and discharged TES energy levels for the Spain and Kuwait cases using both the wet/dry cooling options.

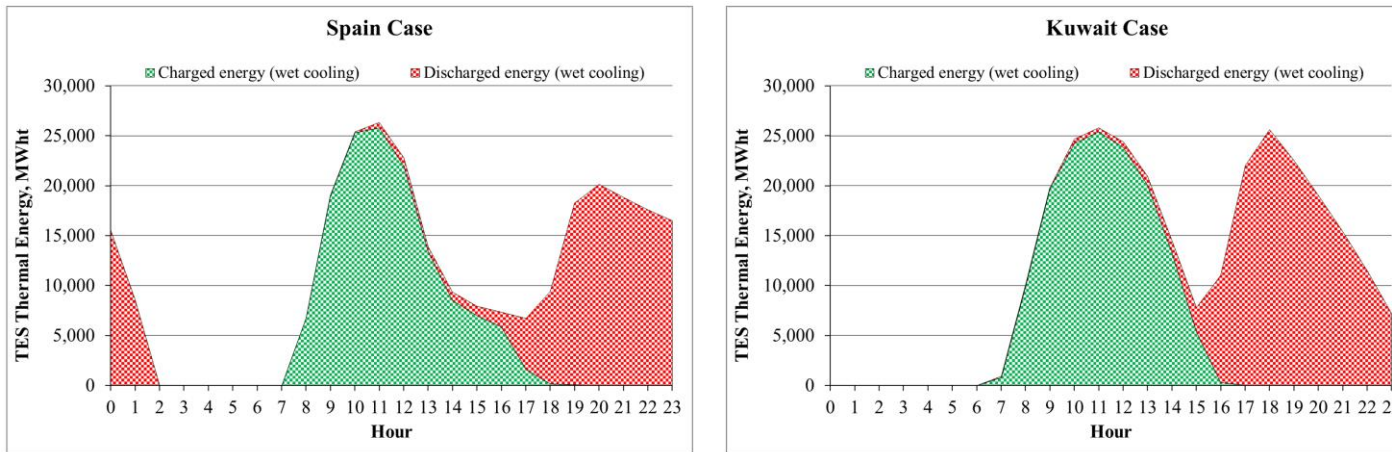


Figure 5.21 Total charged and discharged TES energy using the wet cooling option for the Spain and Kuwait cases.

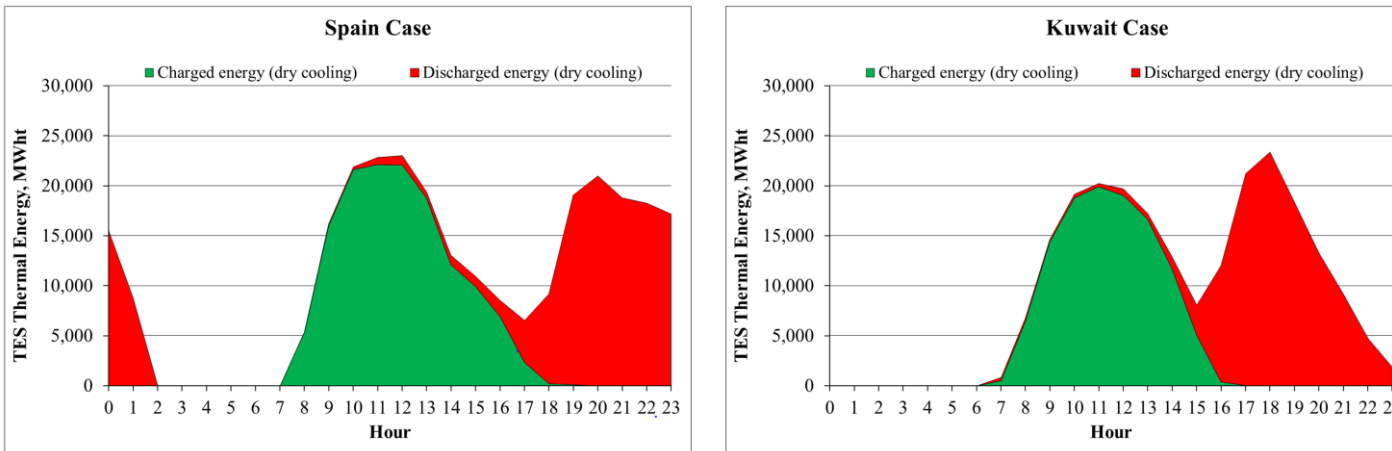


Figure 5.22 Total charged and discharged TES energy using the dry cooling option for the Spain and Kuwait cases.

5.7.4. Parametric analysis

5.7.4.1. Electricity output

It should be noted that the complete range of IAD values considered in the simulation runs is as follows: 300, 400, 500, 600, 700, 800, 900, and 1000 W/m², respectively. With the wet cooling option, the parametric analysis shows that the annual net electricity output ($E_{ele,a}$) for the Kuwait case is higher compared to the Spain case with the following differences: 21150, 18724, 16777, 15543, 14534, 14009, 13675, and 13025 MWh_e, respectively. This is because the number of full load hours at which the steam turbine produces electricity under the rated design condition is always higher for the Kuwait case compared to the Spain case with the following differences: 419, 361, 359, 319, 303, 311, 314, and 301 full load hours, respectively as shown in Figure 5. 23. With the dry cooling option, the parametric analysis shows that the value of $E_{ele,a}$ for the Kuwait case is higher compared to the Spain case for the IAD values of 300, 400, 500, and 600 W/m², with the following differences: 6655, 3977, 1867, and 364 MWh_e, respectively. However, the value of $E_{ele,a}$ for the Kuwait case is lower compared to the Spain case for the IAD values of 700, 800, 900, and 1000 W/m² with the following differences: 750, 1546, 1414, and 1931 MWh_e respectively. It is concluded that the number of full load hours at which the steam turbine produces electricity under the rated design condition is always higher for the Kuwait case compared to the Spain case with the following differences: 179, 148, 117, 89, 83, 61, 69, and 56 full load hours, respectively as shown in Figure 5. 23.

The different performance behaviours between the wet and dry cooling options are because, under the arid climatic conditions of summer in Kuwait, the condensation temperature becomes higher, which increases the pressure of the dry-cooled condenser system. As a result, this leads to a reduction in PB system efficiency (see Figure 5. 17). Thus, a relatively lower difference in the value of $E_{ele,a}$ is observed for the Kuwait case. However, the steam turbine operates with a higher number of full load hours for the complete range of the IAD values (i.e., 300 to 1000 W/m²), as shown in Figure 5. 23.

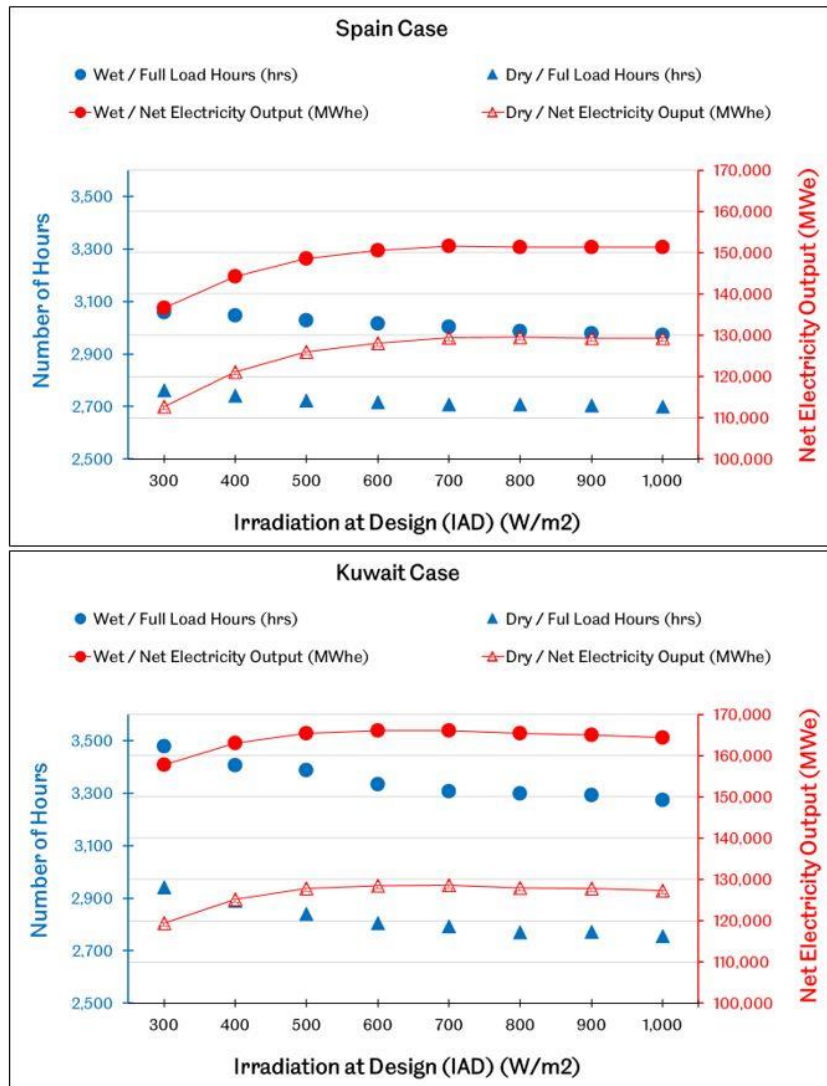


Figure 5. 23 The annual net electricity output and the number of full load hours when the PB system operates at the rated design condition using the wet/dry cooling options for the Spain and Kuwait cases.

5.7.4.2. Dumped thermal energy

With the wet cooling option, Figure 5. 24 shows that the value of Q_{dump} due to mirror defocusing in the SF system for the Kuwait case is 86-89% less than the Spain case for the full range of the IAD values mentioned above. With the dry cooling option, Figure 5. 25 shows that Q_{dump} for the Kuwait case is 95-96% less than the Spain case for the full range of the IAD values. Therefore, it is established that Q_{dump} has a decreasing trend for the majority of the IAD values. The parametric analysis revealed that when selecting values of IAD between 300 and 1000 (W/m^2), with an increment of 100, then the values of Q_{dump} in the SF system varied as follows:

- i. 35,814.4 – 37,801.7 MWh_t (Spain, wet cooling),

- ii. 3718.75 – 4968.76 MWh_t (Kuwait, wet cooling),
- iii. 20,047.90 – 22,140.30 MWh_t (Spain, dry cooling), and
- iv. 739.55 – 919.04 MWh_t (Kuwait, dry cooling).

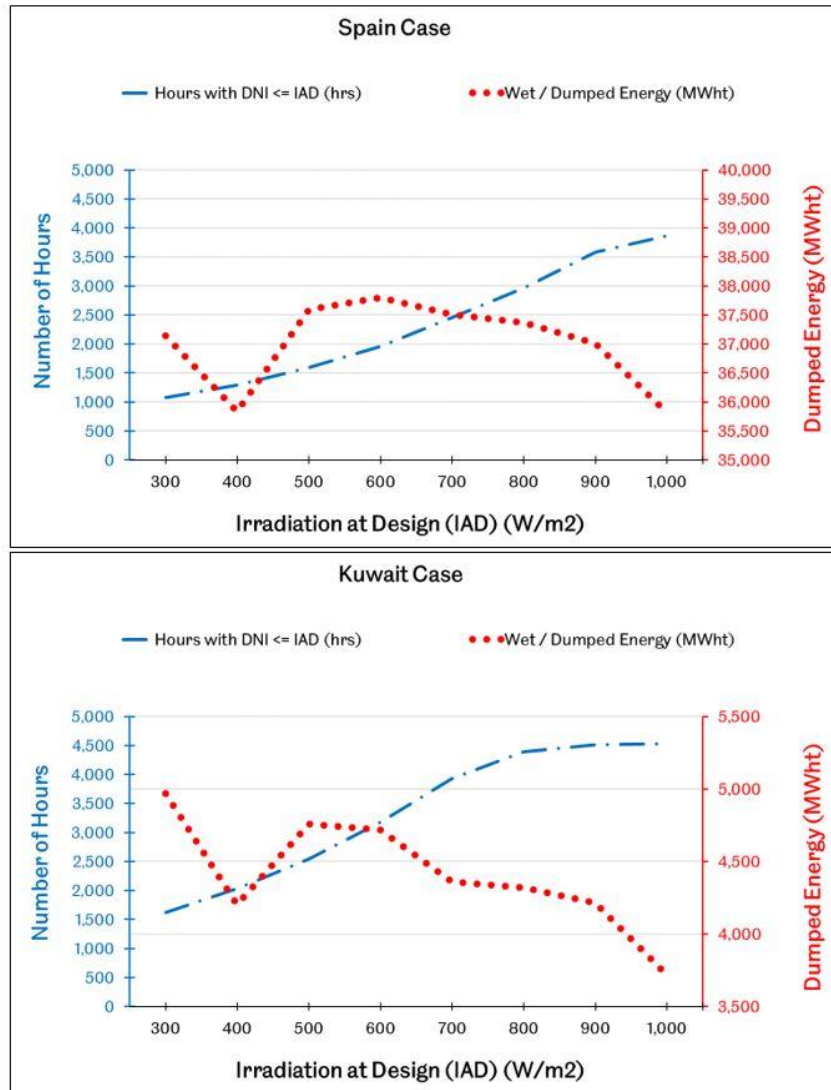


Figure 5. 24 The dumped energy and the number of hours when the DNI value is less than or equal to a particular IAD value using the wet cooling option for the Spain and Kuwait cases.

After considering the decreasing trend of Q_{dump} and the increasing trend of the number of hours when the DNI reaches a particular IAD value (see Figure 5. 24 and Figure 5. 25), it is revealed that this inverse relationship highlights the importance of DNI assessment before the stage of CSP-PT plant design. This is critical so that an optimal IAD value is selected. In addition, the parametric analysis suggested that the IAD value for the CSP-PT plant design must differ from one geographical location to another depending on the DNI profile and meteorological characteristics. Moreover, it was observed that the number of hours when the DNI reaches a particular IAD

value has an increasing trend for the wet and dry cooling options. It should be recalled from Figure 5. 23 that the number of full load hours at which the steam turbine in the PB system produces electricity under the rated design condition slightly decreases as the IAD value increases. Thus, one can conclude that the values of Q_{dump} slightly decrease at the expense of the slight reduction in the number of full load hours of steam turbine.

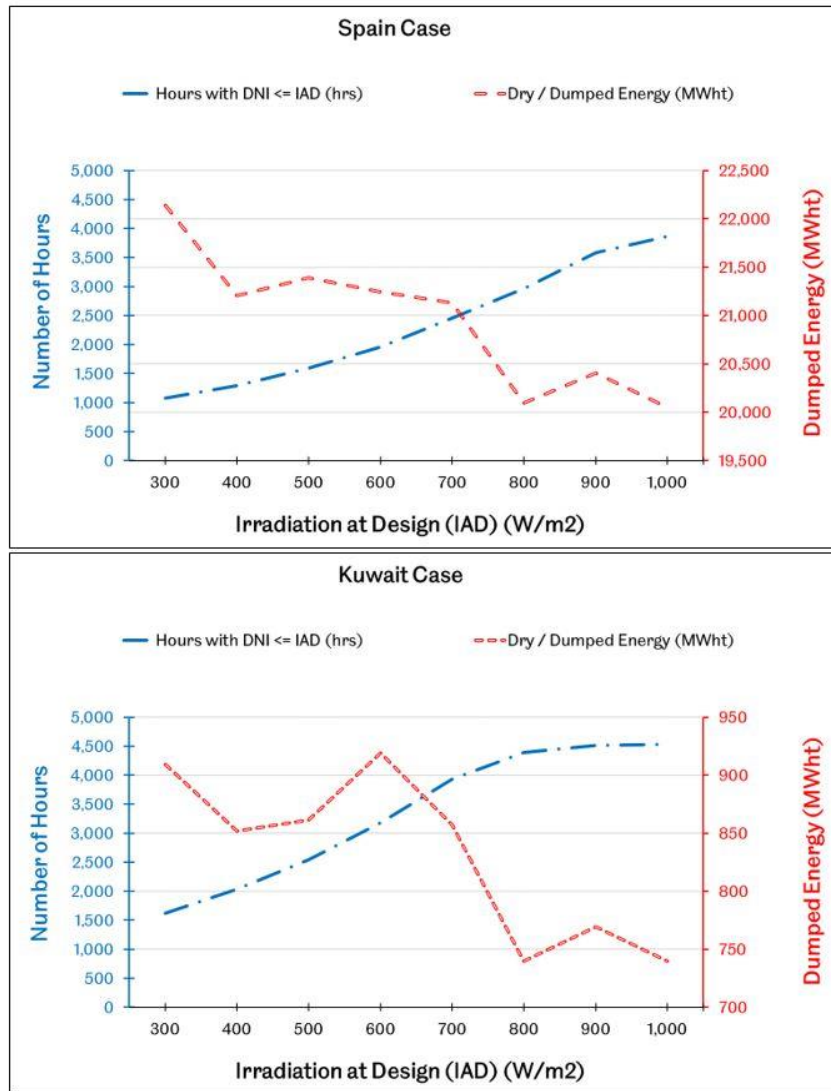


Figure 5. 25 The dumped energy and the number of hours when the DNI value is less than or equal to a particular IAD value using the dry cooling option for the Spain and Kuwait cases.

5.7.4.3. Techno-economic analysis

In this section, the effects of the SM and N_h^{TES} are considered in determining the LCOE values for different design configurations utilizing the dry cooling option in Kuwait. In this evaluation, the dry cooling option is selected for the techno-economic

assessment due to limited water resources in the chosen location with one of Kuwait's highest DNI levels. The values of SM and N_h^{TES} are varied to identify the optimal configurations that provide the lowest LCOE for the validated CSP-PT model of the reference plant with 50 MW capacity. Figure 5. 26 shows LCOE values for 589 (31x19) different design configurations, based on the previously validated model from this work, with the consideration of SM values between 1 and 4 with an increment of 0.1 (31 values), and N_h^{TES} values between 0 and 18 h with an increment of 1 h (19 values).

Table 5. 12 shows the results of the optimal SM values for the different design configurations, which provide the lowest LCOE values (i.e., the lowest point at each of the 19 curves shown in Figure 5. 26). Furthermore, Table 5. 12 indicates that the lowest LCOE when N_h^{TES} equals 0 h (without TES) is at SM of 1.4 and the lowest LCOE when N_h^{TES} equals 18 h is at SM of 3.5. The parametric analysis revealed that the optimal SM value is at 3.3, corresponding to the lowest LCOE of 15.0663 ¢/kWh for N_h^{TES} of 16 h. Moreover, Table 5. 12 shows the technical benefits of TES for the various 50 MW design configurations, such as increasing the annual net electricity output ($E_{ele,a}$) from 90,511.5 to 249,227 MWh and increasing the capacity factor from 22% to 63.2%. From Table 5. 12, it is observed that the $\eta_{overall}$ values for these configurations with optimal SM and lowest LCOE varied between 11.7% and 13.2%. Furthermore, Table 5. 12 shows that the thermal energy into TES, which represents an annual sum, has negative values for N_h^{TES} of 0, 1, and 2. It should be noted that these particular design configurations do not depend highly on the TES operation. This means that as the N_h^{TES} value increases, the thermal energy into the TES increases. Also, Table 5. 12 shows that the total water consumption increases as the SM value increases, which is expected because the water consumption with the dry cooling option is not related to evaporative cooling due to the use of air fans (dry-cooled condenser system). In contrast, the water consumption is mainly for mirror cleaning and plant auxiliaries (i.e., higher SM values correspond to a higher number of PT collectors).

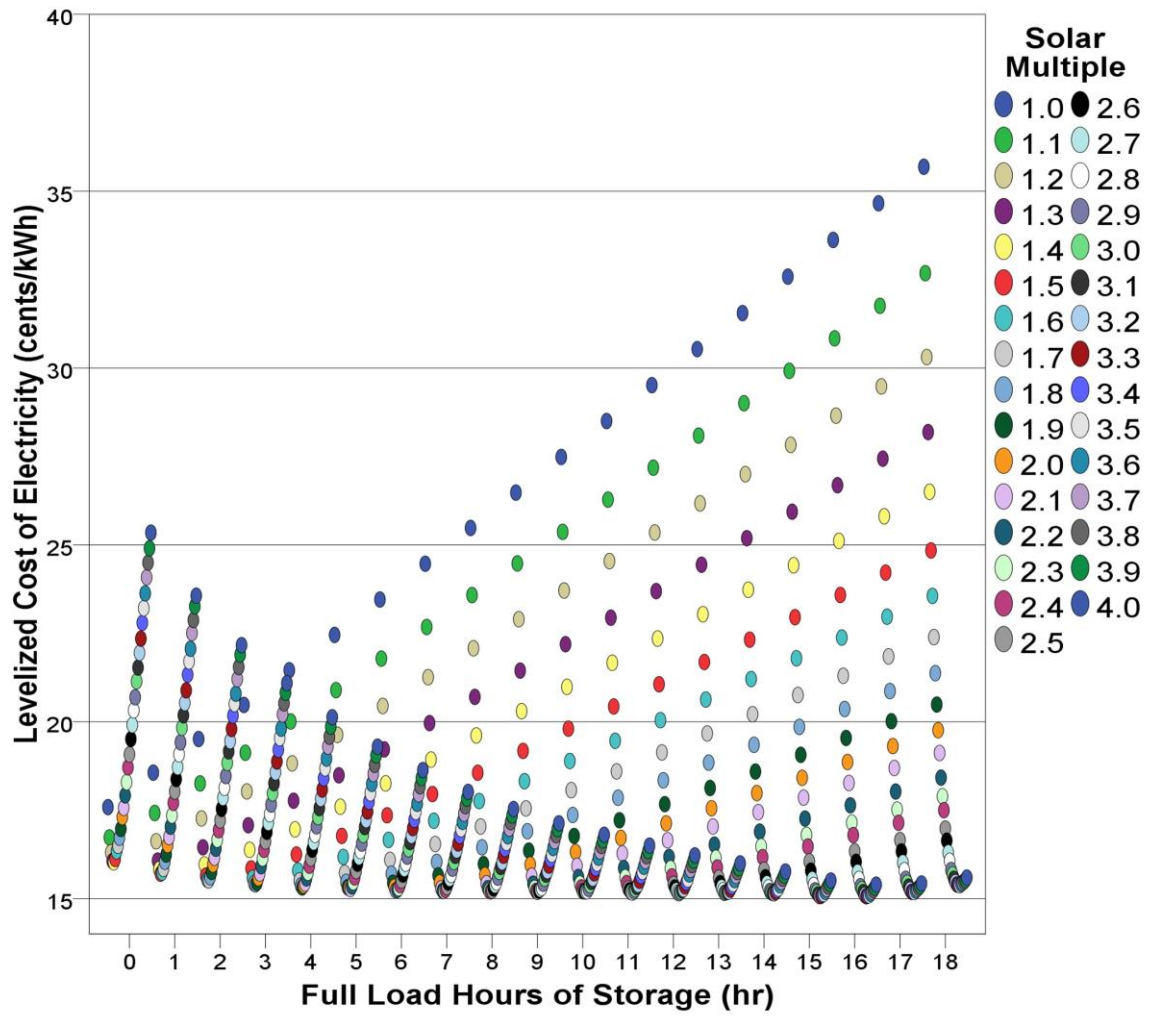


Figure 5. 26 The LCOE values of 589 different design configurations for 50 MW CSP-PT power plants.

Table 5. 12 Comparison between the optimal design configurations and their performance measures using the validated CSP-PT model for the reference plant (50 MW capacity) with optimal SM values based on the lowest LCOE.

N_h^{TES} (h)	LCOE (¢/kWh)	Optimal SM (-)	Gross to net conversion factor (%)	Capacity factor (%)	Q_{dump} (MWh _t)	Thermal power from the SF system (MWh _t)	Total absorbed energy (MWh _t)	Total power incident on the SF (MWh _t)	Thermal energy to the PB system (MWh _t)	Thermal energy into the TES (MWh _t)	Total water consumption (m ³ /yr)	$E_{ele,a}$ (MWh)	$\eta_{overall}$ (%)
0	16.0244	1.4	89.6	23.0	16,526.2	378,117	398,797	771,540	344,662	0	30,290.8	90,511.5	11.7
1	15.7029	1.5	88.7	25.4	14,277.2	407,244	429,561	826,216	387,122	-2,567.3	33,056.5	100,256	12.1
2	15.5148	1.7	89.6	28.7	19,891.1	455,794	482,057	935,569	428,523	-230.6	37,078.1	112,941	12.1
3	15.4020	1.8	89.7	30.9	19,249.9	483,567	511,355	990,245	460,118	296.9	39,468.1	121,791	12.3
4	15.3152	1.9	89.8	33.1	18,765.6	511,238	540,642	1,044,920	490,787	929.2	41,824.2	130,547	12.5
5	15.2719	2.1	89.9	36.2	24,755.5	558,207	591,926	1,154,270	532,408	1,486.4	45,860.0	142,550	12.3
6	15.2287	2.1	89.9	37.4	17,537.6	565,038	598,749	1,154,270	549,985	1,946.6	46,467.9	147,495	12.8
7	15.2170	2.2	89.9	39.5	18,105.0	591,555	626,858	1,208,950	579,090	2,420.2	48,772.6	155,713	12.9
8	15.2048	2.4	90.0	42.5	23,603.5	638,741	679,716	1,318,300	619,860	3,523.1	52,780.3	167,518	12.7
9	15.1930	2.5	90.0	44.6	24,685.7	665,102	706,940	1,372,980	648,680	3,824.9	55,075.2	175,765	12.8
10	15.2038	2.7	90.1	47.5	31,448.7	709,894	755,517	1,482,330	688,062	4,650.2	59,030.5	187,314	12.6
11	15.1695	2.8	90.1	49.7	30,113.1	738,521	787,862	1,537,010	718,379	5,220.3	61,380.4	195,876	12.7
12	15.1544	2.9	90.1	51.8	31,356.1	764,410	814,616	1,591,680	747,710	5,332.6	63,693.9	204,211	12.8
13	15.1643	2.9	90.0	52.9	24,875.2	770,594	820,814	1,591,680	763,028	5,776.6	64,224.5	208,624	13.1
14	15.1518	3.2	90.1	56.8	37,405.8	836,854	895,968	1,755,710	816,379	6,618.0	69,965.1	224,101	12.8
15	15.0713	3.2	90.1	58.3	30,200.3	843,245	902,886	1,755,710	832,673	7,046.3	70,532.4	229,909	13.1
16	15.0663	3.3	90.1	60.4	32,455.0	867,855	928,074	1,810,390	858,231	7,535.6	72,716.7	238,172	13.2
17	15.1844	3.5	90.3	62.9	41,892.9	907,532	972,464	1,919,740	887,534	8,293.6	76,321.3	247,962	12.9
18	15.3789	3.5	90.3	63.2	39,996.7	909,234	974,238	1,919,740	891,348	8,688.4	76,453.9	249,227	13.0

5.8. Chapter conclusion

5.8.1. Concluding remarks

This work emphasizes the sustainable realization of the CSP-PT technology for electricity generation under arid climatic conditions with limited water resources, such as in the case of the chosen location in the western region of Kuwait. Due to the high impact of DNI on CSP-PT plant performance, two locations are selected to demonstrate techno-economic competitiveness. One location is in Kuwait (a MENA/GCC member), reported as having the hottest reliably measured air temperature on Earth [15–19]. Another location is in Spain, which has the world's largest installed share of CSP. In addition, this work supports using CSP-PT with a significant share in the 2030 renewable power technology mix for Kuwait by demonstrating its competitiveness. The techno-economic assessment is performed using two design options (wet and dry cooling) under the climatic conditions of Kuwait and Spain. Although the annual DNI for the Kuwait case ($1857.1 \text{ kW/m}^2 \text{ yr}$) is lower than that of Spain ($2033.3 \text{ kW/m}^2 \text{ yr}$), the justification for the overall exceeding performance of the Kuwait case is as follows:

- i. the steam turbine in the PB system produces electricity at full load hours for the Kuwait case more often than that of Spain. This means that the number of full load hours of steam turbine for the Spain case (3,003 h) is less than that of Kuwait (3,306 h) under the same IAD of 700 W/m^2 (i.e., design point value),
- ii. the results for the number of full load hours of steam turbine are as follows: 3003 h (wet cooling, Spain), 2709 h (dry cooling, Spain), 3306 h (wet cooling, Kuwait), and 2792 h (dry cooling, Kuwait),
- iii. the annual mean ambient temperature in Kuwait ($25.8 \text{ }^\circ\text{C}$) is higher than that of Spain ($14.9 \text{ }^\circ\text{C}$),
- iv. the annual mean wind speed in Kuwait (4 m/s) is lower than that of Spain (6.7 m/s),
- v. the differences in the meteorological conditions from (ii) and (iii) have led to a decrease in the annual heat loss from the SF system in the Kuwait case compared to that of Spain, and

- vi. the dumped energy, Q_{dump} , due to mirror defocusing from the SF system in the Spain case is greater than that of Kuwait at both the annual and monthly levels.

The techno-economic assessment considered several design configurations utilizing the dry cooling option in Kuwait due to limited water resources in the chosen location, which has one of the highest DNI levels. The values of SM and N_h^{TES} are varied to identify the optimal configurations that provide the lowest LCOE for the validated CSP-PT model for the reference 50 MW plant, using 589 (31x19) different design configurations. The parametric analysis revealed that the optimal SM value is at 3.3, corresponding to the lowest LCOE of 15.0663 ¢/kWh for N_h^{TES} of 16 h.

In this work, it was also demonstrated that there are many benefits to utilizing a TES system, such as increasing the annual net electricity output ($E_{\text{ele,a}}$) from 90,511.5 to 249,227 MWh and increasing the capacity factor from 22% to 63.2%. For the most part, the η_{overall} values for design configurations with optimal SM and lowest LCOE varied between 11.7% and 13.2%.

5.8.2. Recommendations

Generally, Kuwait experiences relatively low wind speeds at low altitudes, high ambient temperatures, and suitable DNI levels. These conditions significantly impact CSP-PT plant performance. For example, lower wind speeds minimize the heat loss from the SF system and increase efficiency compared to other geographical locations with higher wind speeds. Furthermore, the DNI has the most substantial impact on the overall plant efficiency. It should be noted that relatively high ambient temperatures contribute to maintaining the HTF at the design reference point with minimal auxiliary power consumption for various functions, such as HTF freeze protection (advantage). However, high ambient temperatures affect the plant's heat rejection process, leading to excess water consumption with a wet-cooled condenser system (disadvantage).

Additionally, the simulation results show that the DNI level in the chosen location provides an optimal condition for making dry-cooled CSP-PT plants technically competitive in the arid desert environment where water is limited. Hence, it is recommended that the outcomes from this work be considered in the planning stage for future mega-scale projects in line with the strategic target for achieving

15% of electricity demand from renewable technologies by 2030 in Kuwait. One way to accomplish this is by increasing the CSP-PT technology share in the mix of other renewable technologies, especially since such a mix is still not finalized. In addition, it is recommended to perform research on different technologies, such as wind power technology (i.e., provided later in Chapter 7), to assess the potential of cogeneration under arid climatic conditions of the chosen location in this work. The combined analysis approach between wind power and CSP-PT should increase the capacity factor of future transmission networks.

Consequently, attention should be given to studying the wind speed profiles at different heights, which initiate sandstorms and contribute to the degradation of CSP-PT performance (i.e., provided later in Chapters 6 and 7). Another critical area of concern is the effect of sandstorms on the erosion of the reflectors/collectors. Hence, it is recommended that CSP-PT plant operators consider the following instructions for optimal plant performance in climatic conditions similar to that of Kuwait and the MENA/GCC region. Following these instructions will lead to trouble-free operation by maintaining the rated design conditions and reducing the effects of dust and suspended particle contents in the air:

- i. the power equipment should be protected against corrosion since the climate is mostly dry and hot with minimal rainfall during the winter months,
- ii. the main risk in a CSP-PT plant is the loss of DNI due to unscattered solar radiation passing through the atmosphere between March and September for the Kuwait case when sandstorms leave suspended particles in the air; therefore, barriers are considered necessary to hold sand movements outside of the plant's borders. Furthermore, scheduled cleaning of sand buildup outside of the barriers would be needed, and
- iii. the turbidity due to sand and dust storms poses the most significant real risk to CSP-PT plants, where losses in DNI would lead to reductions in the energy yield and the capacity factor values. Thus, cleaning the reflecting mirrors in the SF system should be a routine process.

6. OPTIMIZATION AND PERFORMANCE

ENHANCEMENT OF CONCENTRATING SOLAR

POWER PLANTS

6.1. Chapter journal publications

Some of the work that appears in this chapter is associated with peer-reviewed scientific journal publications. This chapter is associated with publications (2) and (5). The detailed information of these publications is listed in the “Scientific Journal Publications” Section, starting from page (iii) of this thesis.

6.2. Design parameters

As previously mentioned, the reference 50 MW CSP-PT plant used in this work (Andasol-1) is located in Spain. Table 3. 1 shows a list of design parameters for this plant. The plant selection came after conducting a thorough survey considering various technical specifications for different plants worldwide [112,113,122–131,114,132–137,115–121]. The total land area of the plant is 477 acres, of which 329 acres are allocated for the SF system. The PT collectors are aligned in a north-south direction in the SF system, consisting of 156 loops (see Figure 1. 1) on an area of 510,120 m². The thermal HTF oil (Dowtherm A, see Appendix A) flows with a temperature of 293 °C at the inlet and 393 °C at the outlet. The SF system size is selected such that under normal conditions, the rated power is produced while the TES system is fully charged. The TES medium consist of molten salt, a mixture of 60% sodium nitrate (NaNO₃) and 40% potassium nitrate (KNO₃), inside two tanks (hot and cold). It should be recognized that the N_h^{TES} value is chosen initially as 7.5 h.

6.3. Dry-cooled condenser

To a certain extent, a relatively high ambient temperature contributes to maintaining the HTF condition at the design reference point with low auxiliary power consumption for freeze protection purposes. However, this high temperature also

affects the PB heat rejection process, leading to additional water consumption when a wet-cooled condenser is utilized. Therefore, a dry-cooled condenser system is an effective alternative for the chosen location in this work within Kuwait. The use of a dry-cooled condenser instead of a wet-cooled one is recommended due to the positive effects on the technical performance, economic feasibility, and reasons related to limited water resources. The primary factor affecting dry-cooled condensers is the dry-bulb temperature. Notably, higher dry-bulb temperatures decrease the dry cooling system performance, reducing the Rankine cycle efficiency in a CSP-PT plant. Therefore, the condensing temperature should be close to the dry-bulb temperature in an ideal dry-cooled condenser. It should be recognized that the critical parameter in the dry cooling system is the dry-bulb temperature, which affects the PB system, as shown in Equation 6. 1 and Equation 6. 2. The relation between the efficiency of the Rankine cycle and the ambient temperature is defined as follows [175]:

$$\eta_{d,c} = -0.1468 T_d + 22.526 \tag{6.1}$$

$$\eta_{d,i} = -0.1324 T_d + 30.503 \tag{6.2}$$

where $\eta_{d,c}$ is the cycle efficiency of the power plant with the conventional dry cooling system, $\eta_{d,i}$ is the cycle efficiency of the plant with the ideal dry cooling system, and T_d is the dry-bulb temperature. In fact, several studies have investigated the advantages and disadvantages of using dry-cooled condenser systems in typical thermodynamic cycles [175,218,291,229,283–289]. Due to the crucial influence of the meteorological conditions on the overall CSP-PT performance and PB system efficiency, the chosen location’s monthly temperature and humidity profiles (based on ground measurements) are shown in Figure 4. 3 and Figure 4. 5.

6.4. Performance enhancement using thermal energy storage

The advantage of a TES system is that it allows electricity generation during periods of insufficient solar radiation and offers dispatchability on demand, especially at nighttime [77,315]. Furthermore, it is possible to reduce the cost of electricity

generation from the CSP-PT technology once combined with a TES system by means of the following: (i) optimizing TES dispatch control, (ii) making the CSP-PT technology more efficient for nighttime operations [79], (iii) increasing the capacity factor of CSP-PT plants, and (iv) providing ancillary grid services and shifting generation [297]. In this work, the TES system primarily consists of two tanks (hot and cold). The TES medium is a mixture of molten salt. The value of the maximum TES capacity (Q_m^{TES}), which is a critical parameter for TES sizing, is selected as 964 MWh_t. Additionally, the cold tank heater set point is 292 °C, and the hot tank heater set point is 386 °C. The TES system design for the reference plant provides a rated power output of 7.5 hours. Also, the TES system has a cold tank temperature of 292 °C and a hot tank temperature of 386 °C. It should be noted that the CSP-PT technology is expected to lead the way among other solar thermal technologies as the installation cost continues to decrease [268,269]. Compared to other CSP technologies, it has more potential to dominate the global markets [270,271,280,281,272–279]. Several studies have been conducted to assess and evaluate the roles of CSP technologies [272–276]. The dispatchability of CSP-PT with TES makes the technology more attractive to investors [272,273,276]. Moreover, CSP-PT is reliable with economic benefits that compete with fossil-based power [274–279].

6.5. Performance enhancement using wind power

Theoretically, various factors directly affect the performance of wind power-generating units [316]. The first and most critical factor in estimating a unit's energy output is the wind speed, as shown in Equation 6. 3. The importance of wind speed comes from the fact that the unit's blades will spin faster at a higher wind speed. This means that the energy yield will increase compared to the case of lower wind speeds. The output of the wind power-generating unit (P_w) is calculated from Equation 6. 3, which is referred to as Betz's law, which is derived from the principles of the conservation of mass and momentum. The theory of Betz's law is concerned with the maximum possible energy produced from the wind, which is independent of any wind turbine design. It was developed in 1919 by the German physicist Albert Betz who determined that no turbine can capture more than (59.3%) of the potential energy in the wind at any location. Hence, the factor 16/27 (0.593) is known as the Betz's coefficient (see Appendix E).

$$P_w = (1/2) C_p \rho A_b u_h^3$$

6.3

where C_p is the wind turbine power coefficient or performance coefficient (i.e., an indicator of turbine efficiency), ρ is the air density, A_b is the blade's swept area of the turbine, and u_h is the wind speed at the turbine's hub height. The second factor is the value of α , which is investigated later in Chapters 6 and 7. It should be noted that the α value relates the wind speed and installation height level. The optimal hub height at which the unit is installed depends on the α value. If the value of α is substantial, then the wind load on the blade's swept area will be imbalanced. This negatively impacts the blades and nacelle's performance, leading to a shorter life span with operational problems. The third most important factor is the ambient temperature. An apparent influence is detected on the energy output when the ambient temperature is beyond the unit's normal operating range; hence, this is the reason for investigating the ambient temperature in Chapters 6 and 7 for the case of the chosen location in Kuwait. Due to the high ambient temperature, the air density value and the energy output decrease accordingly, as shown in Equation 6.3. Generally, the blades can freeze when the ambient temperature is too low, leading to a necessary unit shutdown. The fourth factor is the tower height on which the wind power-generating unit is mounted. The unit's energy output increases as the tower height increases, resulting from increasing the wind speed with height above ground. The fifth factor in estimating the energy output from the unit is the air density, as shown in Equation 6.3. When the air density is low, the wind becomes weaker. This means that the unit's rated wind speed and cut-in speed will increase accordingly, reducing the energy output. The sixth factor, which will affect the annual energy output, is the unit's rated capacity. The lower is the rated capacity (i.e., the rated power or maximum power that the unit's generator can produce); the lesser is the annual energy output. Finally, the seventh factor is the yearly valid operating period. The shorter is the active working period, the smaller is the annual energy output. It should be noted that zero production periods are counted against the capacity factor calculations. Therefore, estimating the unit's availability in a mega-scale power plant is crucial since it directly affects the economic feasibility.

6.6. Mathematical formulation

In this work, the design configuration, shown in Figure 3. 1, Figure 3. 2 and Appendix C, is analyzed using a comprehensive system-level approach. The solar radiation is taken into consideration while it is incident on the total aperture area of the SF system (A_{ap}). It should be mentioned that some mathematical derivations are summarized from a few studies [300,301]. The radiative solar power incident on the net aperture area of the mirrors (E_{sun}) is calculated from Equation 5. 1. Additionally, A_{ap} is estimated by Equation 5. 2. Other studies [289,302–307] have defined five efficiencies of critical systems in a CSP-PT plant to evaluate $\eta_{overall}$ as observed from Equation 5. 3 to Equation 5. 8. The collector thermal performance is derived from the literature [229,283,300], as observed in Equation 5. 9.

For a reliable economic assessment of a CSP-PT plant, the LCOE criterion is the most popular because it considers the project construction costs, electricity production, operations, and maintenance costs. Specifically, the LCOE criterion is the most frequently used economic indicator in the literature for comparing electricity generation technologies [38,192,194,309]. The LCOE is the net present value of the unit cost of electricity over the thermal power generating unit's lifetime. Thus, the LCOE resembles the price that the technology must receive to break even over the plant's lifetime. Consequently, Equation 5. 24 is used in estimating the LCOE values in this work [309]. In addition, a detailed breakdown of the estimated costs for the reference 50 MW CSP-PT plant is provided in this work (see Appendix H).

6.7. Results and discussions

6.7.1. Levelized cost of electricity

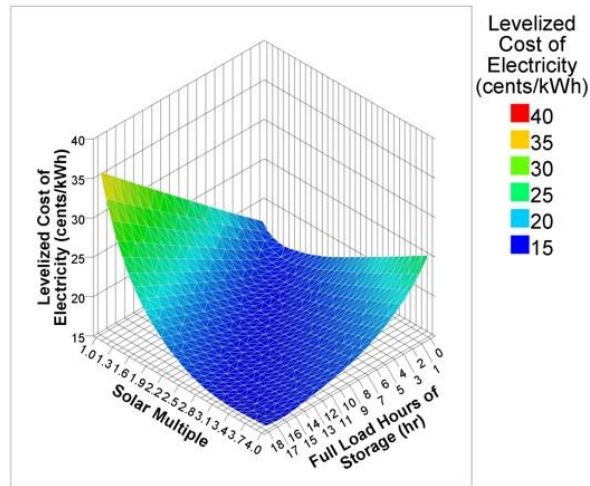
From Figure 5. 26, critical results for the previously-mentioned 589 CSP-PT design configurations are considered. These results include, most specifically, 19 design configurations that have optimal SM values based on the lowest LCOE (the lowest points at each of the 19 curves shown in Figure 5. 26). The 19 design configurations relate to this work's validated 50 MW CSP-PT model for the reference plant (see Table 5. 6 and Table 5. 7). The 19 configurations are selected based on the LCOE-minimization criterion. It should be recognized that the results concerning the

589 configurations are used in demonstrating the LCOE variations for the selected range of values for SM and N_h^{TES} .

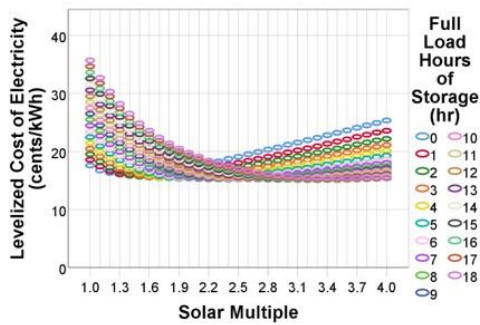
The results, including the profiles of LCOE for all configurations, are shown in Figure 6. 1. It should be noted that Figure 6. 1(i) shows the three-dimensional (3-D) variation in LCOE using a dry-cooled condenser. Figure 6. 1(ii) shows that selecting a design configuration with a higher N_h^{TES} value leads to achieving the lowest LCOE at higher SM values. This means that the TES capacity demands the use of a larger SF system area (higher SM value) to justify the economic feasibility of the plant. Furthermore, the common theoretical assumption that increasing the TES capacity decreases the LCOE does not stand, as shown in Figure 6. 1(iii). It is realized that the LCOE may increase beyond the optimal value for plants with larger TES capacities. Therefore, the following findings should be noted against this assumption:

- i. the optimal LCOE value for a plant with N_h^{TES} of 9 h is less than the optimal LCOE values for a plant with N_h^{TES} of 10 h,
- ii. the optimal LCOE value for a plant with N_h^{TES} of 12 h is less than the optimal LCOE values for a plant with N_h^{TES} of 13 h,
- iii. the optimal LCOE value for a plant with N_h^{TES} of 16 h is less than the optimal LCOE values for a plant with N_h^{TES} of 17 h, and
- iv. the optimal LCOE value for a plant with N_h^{TES} of 17 h is less than the optimal LCOE values for a plant with N_h^{TES} of 18 h.

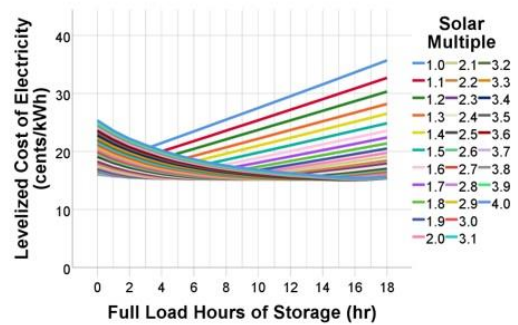
In addition, the optimal configuration for the N_h^{TES} value of zero (0 h) is at the SM value of 1.4, and the optimal configuration for the N_h^{TES} value of 18 h is at the SM value of 3.5. Thus, the optimal SM value for the optimal configuration increases with increasing N_h^{TES} values.



(i)



(ii)



(iii)

Figure 6.1 Profiles of LCOE using a dry-cooled condenser: (i) 3-D variation of LCOE, (ii) LCOE as a function of SM, and (iii) LCOE as a function of N_h^{TES} .

6.7.2. Capacity factor

Figure 6. 2(i) shows the 3-D variation in the capacity factor using a dry-cooled condenser. Figure 6. 2(ii) shows the capacity factor values for the 589 design configurations in a two-dimensional (2-D) illustration. Figure 6. 2(iii) shows that when increasing the SM beyond the value of 1.3, the capacity factor rises rapidly. This rapid increase continues to grow at a faster rate, with an increase in N_h^{TES} . Up to a specific point, the capacity factor growth rate stabilizes, in which increasing the SF system area becomes less significant from an economic perspective. On the other hand, analyzing the capacity factor as a function of N_h^{TES} brings a crucial finding. One should note that excessively increasing the SM value has minimal effect on the capacity factor for any TES capacity, as shown in Figure 6. 2(iv). Moreover, the closeness of the coloured data points at larger values of SM for the entire range of N_h^{TES} confirms this finding, as shown in Figure 6. 2(ii).

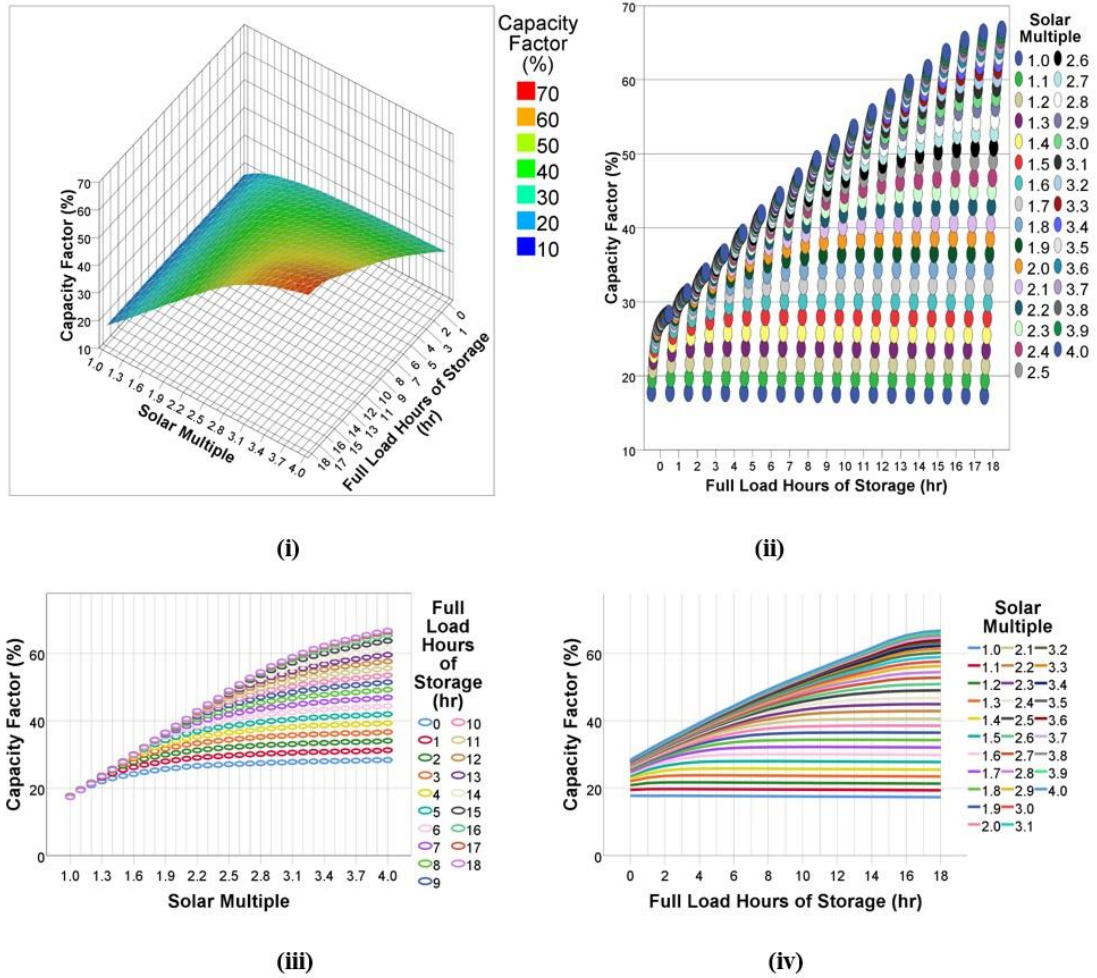


Figure 6. 2 Profiles of capacity factor using a dry-cooled condenser: (i) 3-D variation of capacity factor, (ii) capacity factor for 589 design configurations, (iii) capacity factor as a function of SM, and (iv) capacity factor as a function of N_h^{TES} .

6.7.3. Thermal power produced by the solar field

Figure 6. 3(i) shows the 3-D variation in the thermal power produced by the SF system using a dry-cooled condenser. Figure 6. 3(ii) shows the thermal power for the 589 design configurations in a 2-D illustration. From initial observation, a linear trend appears concerning the impact of SM and N_h^{TES} on the thermal power for the selected range ($1 \leq SM \leq 1.3$). Furthermore, Figure 6. 3(iii) shows the SF thermal power as a function of SM. It is observed that for $1 \leq SM \leq 1.3$, the variation in the thermal power remains almost constant as the N_h^{TES} value increases. For SM values larger than 1.3, the variation starts to become more noticeable as the value of N_h^{TES} increases. Moreover, Figure 6. 3(iv) shows the thermal power as a function of N_h^{TES} .

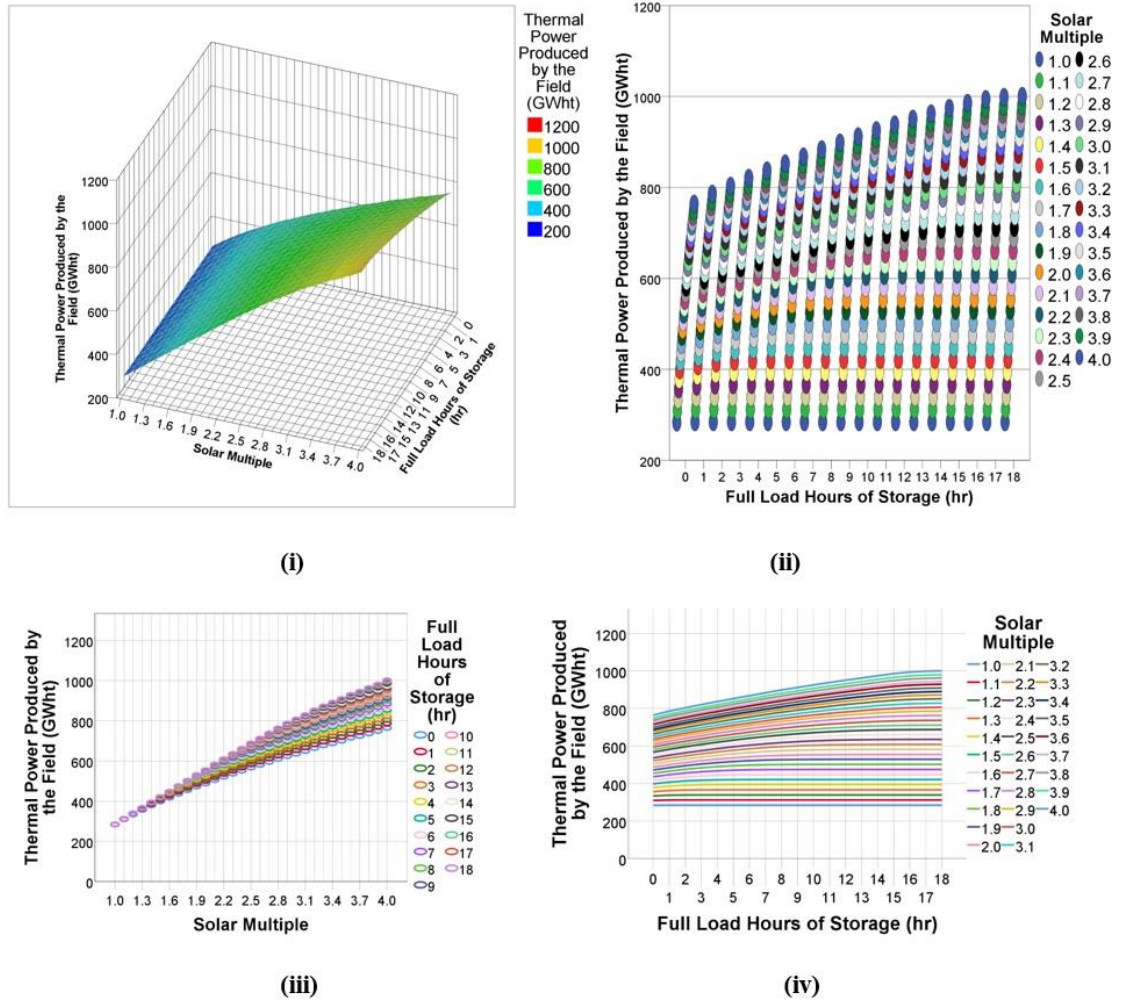


Figure 6.3 Profiles of thermal power produced by the SF system using a dry-cooled condenser: (i) 3-D variation of power, (ii) power for 589 design configurations, (iii) power as a function of SM, and (iv) power as a function of N_h^{TES} .

Considering the above finding is essential for maximizing CSP-PT plant performance and application beyond electricity generation (heat utilization). For this case, the levelized cost of heat value should be investigated along with LCOE. It is observed that, at higher SM values, the benefit of increasing N_h^{TES} becomes evident since the SF system produces more thermal power leading to higher SF efficiency. For $1 \leq SM \leq 1.3$, the thermal power remains almost constant even with the increase in the N_h^{TES} . This suggests that investing in a larger TES capacity should always accompany a larger SF area (above SM of 1.3), as shown in Figure 6.3(ii) and Figure 6.3(iv).

6.7.4. Annual energy generation

Figure 6. 4(i) shows the 3-D variation of $E_{ele,a}$ using a dry-cooled condenser. Figure 6. 4(ii) shows the $E_{ele,a}$ values for the 589 design configurations in a 2-D illustration. Figure 6. 4(iii) shows that when increasing the SM beyond the value of 1.3, then $E_{ele,a}$ starts to increase rapidly. This rapid increase continues to grow at a faster rate, with an increase in the value of N_h^{TES} . In a similar behaviour to the capacity factor, the growth rates of $E_{ele,a}$ stabilize, which indicates that increasing the SF system area becomes unjustified from an economic viewpoint for $1 \leq SM \leq 1.3$.

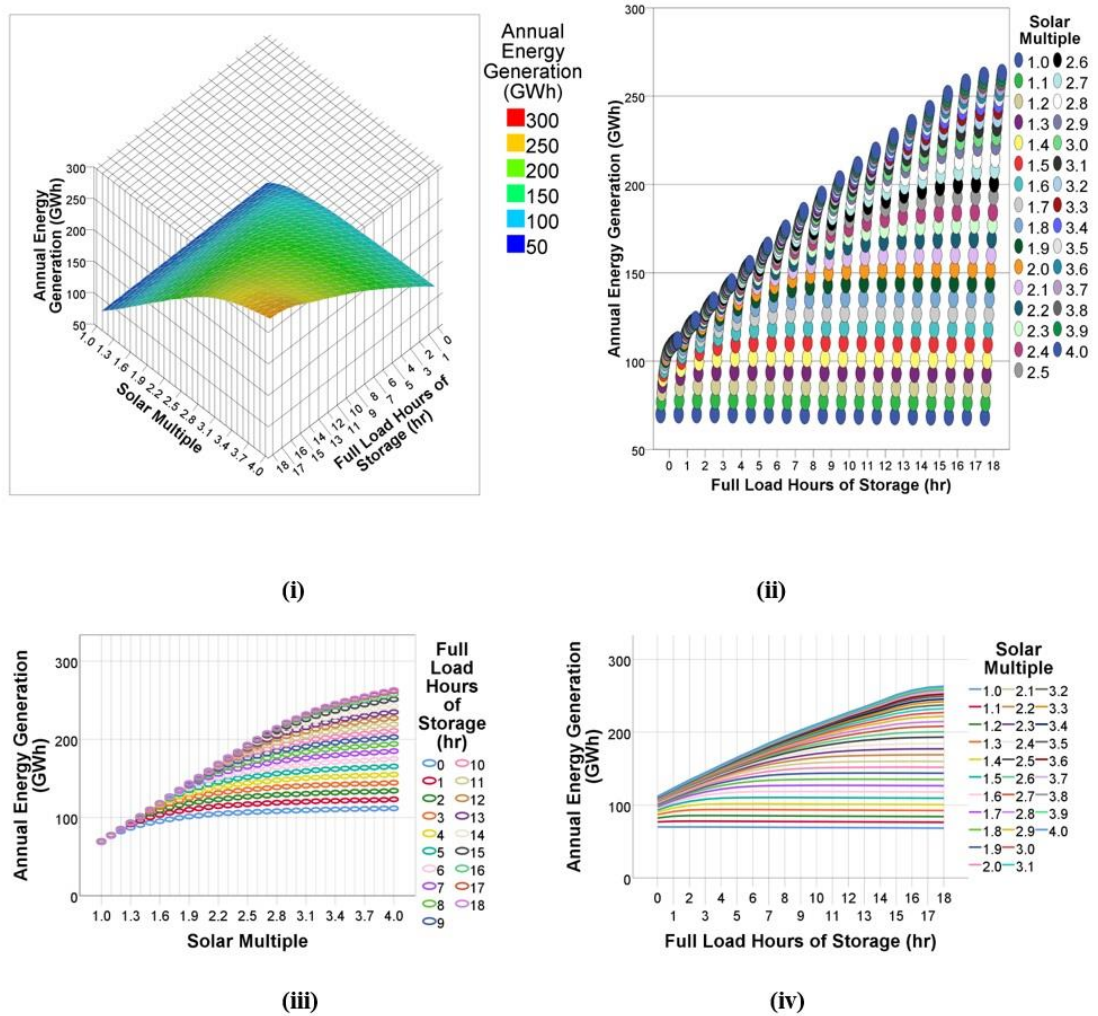


Figure 6. 4 Profiles of $E_{ele,a}$ using a dry-cooled condenser: (i) 3-D variation of $E_{ele,a}$, (ii) $E_{ele,a}$ for 589 design configurations, (iii) $E_{ele,a}$ as a function of SM, and (iv) $E_{ele,a}$ as a function of N_h^{TES} .

Thus, increasing the TES capacity has minimal effect on $E_{ele,a}$ for $1 \leq SM \leq 1.3$. This is because the SF aperture area cannot produce enough thermal energy to the PB system to generate power at the rated conditions of the CSP-PT plant. Hence, the

TES system does not receive adequate thermal energy to charge during the daytime and discharge at nighttime. As a result, a linear trend is observed for $1 \leq SM \leq 1.3$, as shown in Figure 6. 4(iii). Additionally, analyzing the $E_{ele,a}$ as a function of N_h^{TES} brings about another finding. Significantly, increasing the SM values has minimal effect on $E_{ele,a}$ under all TES capacities for $1 \leq SM \leq 1.3$, as shown in Figure 6. 4(ii) and Figure 6. 4(iv). Further confirmation is obtained from noticing the closeness of the coloured data points at higher values of SM for all categories of N_h^{TES} , as shown in Figure 6. 4(ii).

6.7.5. Annual overall plant efficiency

The value of $\eta_{overall}$ is calculated from the ratio of $E_{ele,a}$ to the total power incident on the SF system. Consequently, $\eta_{overall}$ can be calculated from Equation 5. 8. In addition, Figure 6. 5(i) shows the 3-D variation in $\eta_{overall}$ using a dry-cooled condenser. Figure 6. 5(ii) shows the $\eta_{overall}$ values for the 589 design configurations in a 2-D illustration. Figure 6. 5(iii) shows that $\eta_{overall}$ increases with increasing values of SM up to the maximum point of each of the illustrated curves. After that, the trend of $\eta_{overall}$ tends to decrease at higher SM values. In particular, Figure 6. 4(iii) shows that the slope of the $E_{ele,a}$ curves changes at different points depending on the value of N_h^{TES} . Because $\eta_{overall}$ is dependent on $E_{ele,a}$, the maximum values of the $\eta_{overall}$ curves, which are also the turning points, represent the points when the $E_{ele,a}$ changes slope. It is observed that to maximize $\eta_{overall}$, the SM value should not exceed 2.6 since below this value, the maximum $\eta_{overall}$ values occur for the investigated range of N_h^{TES} . Moreover, the impact of N_h^{TES} on $\eta_{overall}$ is insignificant. As proof, one should note that $\eta_{overall}$ equals 11.7% for one optimal configuration ($N_h^{TES} = 0$ h) when the optimal SM value equals 1.4 for the lowest LCOE of 16.0244 ¢/kWh. Whereas, $\eta_{overall}$ equals 13% for another optimal configuration ($N_h^{TES} = 18$ h) when the optimal SM value equals 3.5 for the lowest LCOE of 15.3789 ¢/kWh. Hence, N_h^{TES} has a minimal impact on $\eta_{overall}$. Another finding is that the value of $\eta_{overall}$ never exceeds 14.3%, even at higher SM and N_h^{TES} values as shown in Figure 6. 5(ii) and Figure 6. 5(iv). For example, this can be confirmed by observing the trend of the black-coloured data points at higher SM values.

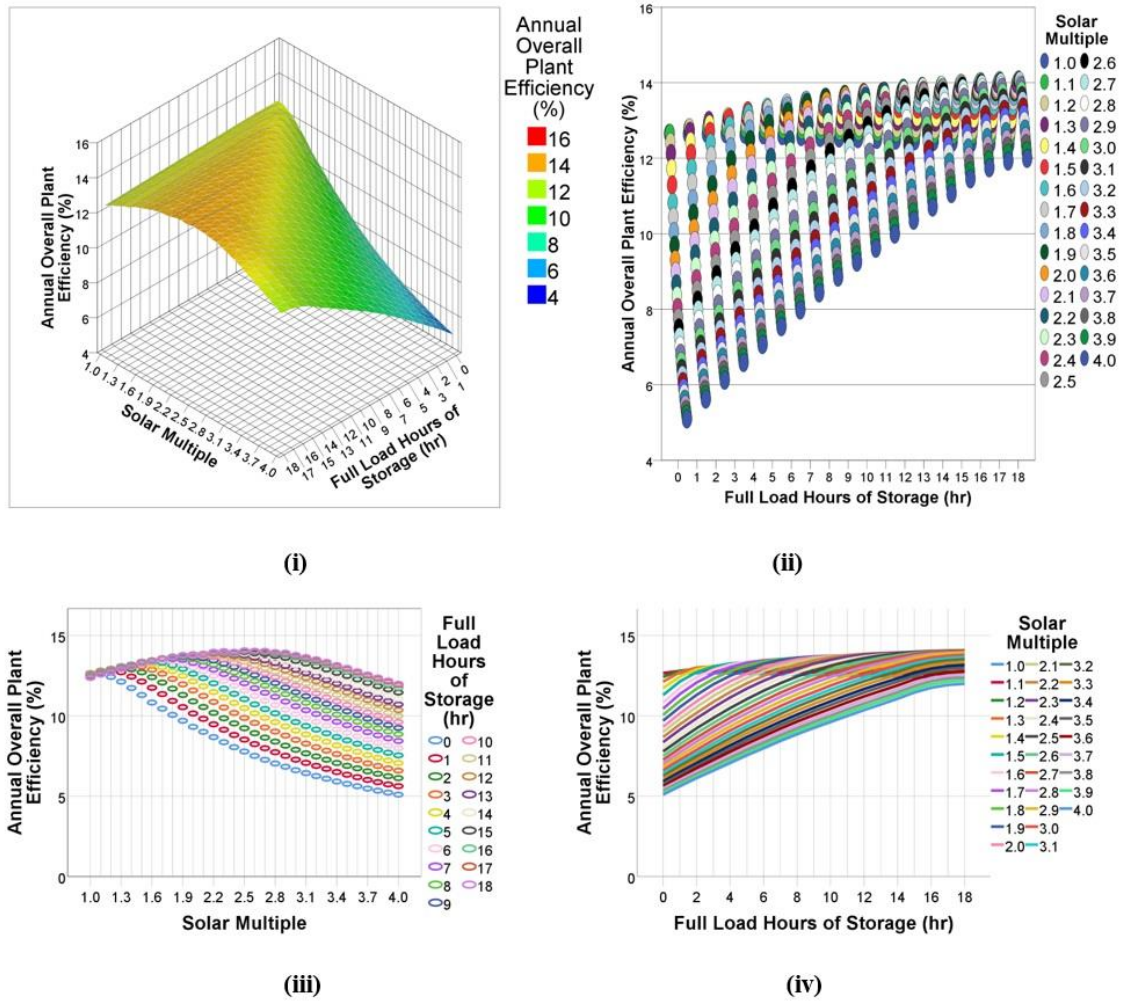


Figure 6. 5 Profiles of η_{overall} using dry-cooled condenser: (i) 3-D variation of η_{overall} , (ii) η_{overall} for 589 design configurations, (iii) η_{overall} as a function of SM, and (iv) η_{overall} as a function of N_h^{TES} .

6.7.6. Cycle electrical power output

After carefully evaluating the solar resource from Table 4. 1, Table 4. 2, Figure 4. 1, Figure 4. 4, Figure F. 13 to Figure F. 17, Figure 5. 14, and Figure 5. 16, it is determined that January and February provide the best representation for the winter season in the chosen location in Kuwait. Furthermore, it was determined that July and August provide the best representation of the summer season. Therefore, detailed illustrations for the profiles of January, February, July, and August are shown in Figure 6. 6 to Figure 6. 9, respectively. These illustrations are concerned with a critical performance measuring parameter, i.e., the cycle electrical power output.

The primary purpose is to present the cycle electrical power output of the previously-mentioned 19 optimal configurations with optimal SM values based on the lowest LCOE for $0 \leq N_h^{\text{TES}} \leq 18$. These illustrations show the performance of the

reference 50 MW CSP-PT plant. It should be recognized that the main benefit of selecting a CSP-PT plant configuration with higher SM and N_h^{TES} values is to extend the electricity generation into the night. Another critical benefit is that the PB steam turbine becomes capable of smooth operations at rated capacity for a maximal number of hours, increasing the PB system efficiency.

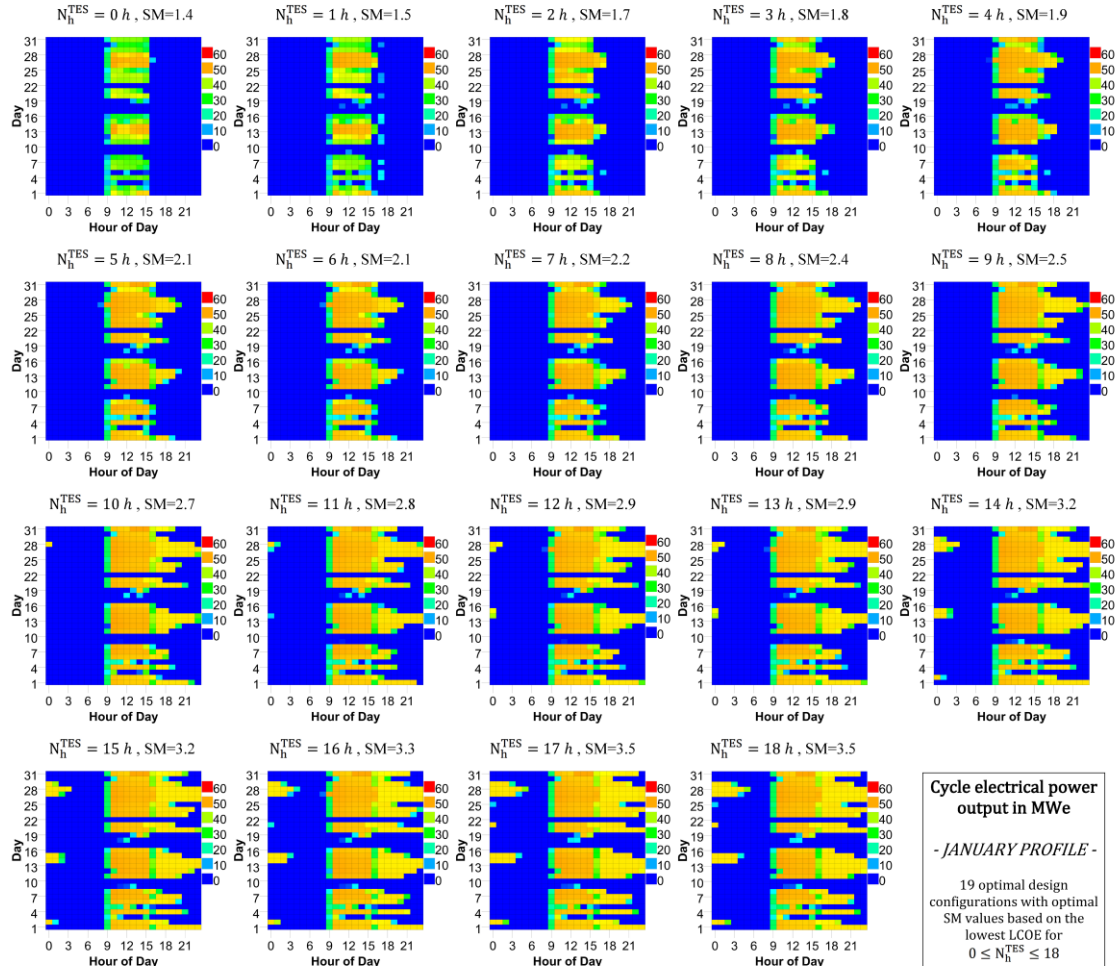


Figure 6. 6 Cycle electrical power output of a sample winter month (January profile) showing the 19 optimal design configurations with optimal SM values based on the lowest LCOE for $0 \leq N_h^{TES} \leq 18$.

During the winter season, 24 h continuous generations without fossil backup in February occur more often than in January due to the high cloud presence during the latter month. Therefore, it is concluded that 24 h continuous generations without fossil backup in January are unlikely to occur, as shown in Figure 6. 6. Additionally, 24 h continuous generations without fossil backup in February occur for the following configurations:

- i. SM value of 3.5 and N_h^{TES} value of 17 h, and

ii. SM value of 3.5 and N_h^{TES} value of 18 h, as shown in Figure 6. 7.

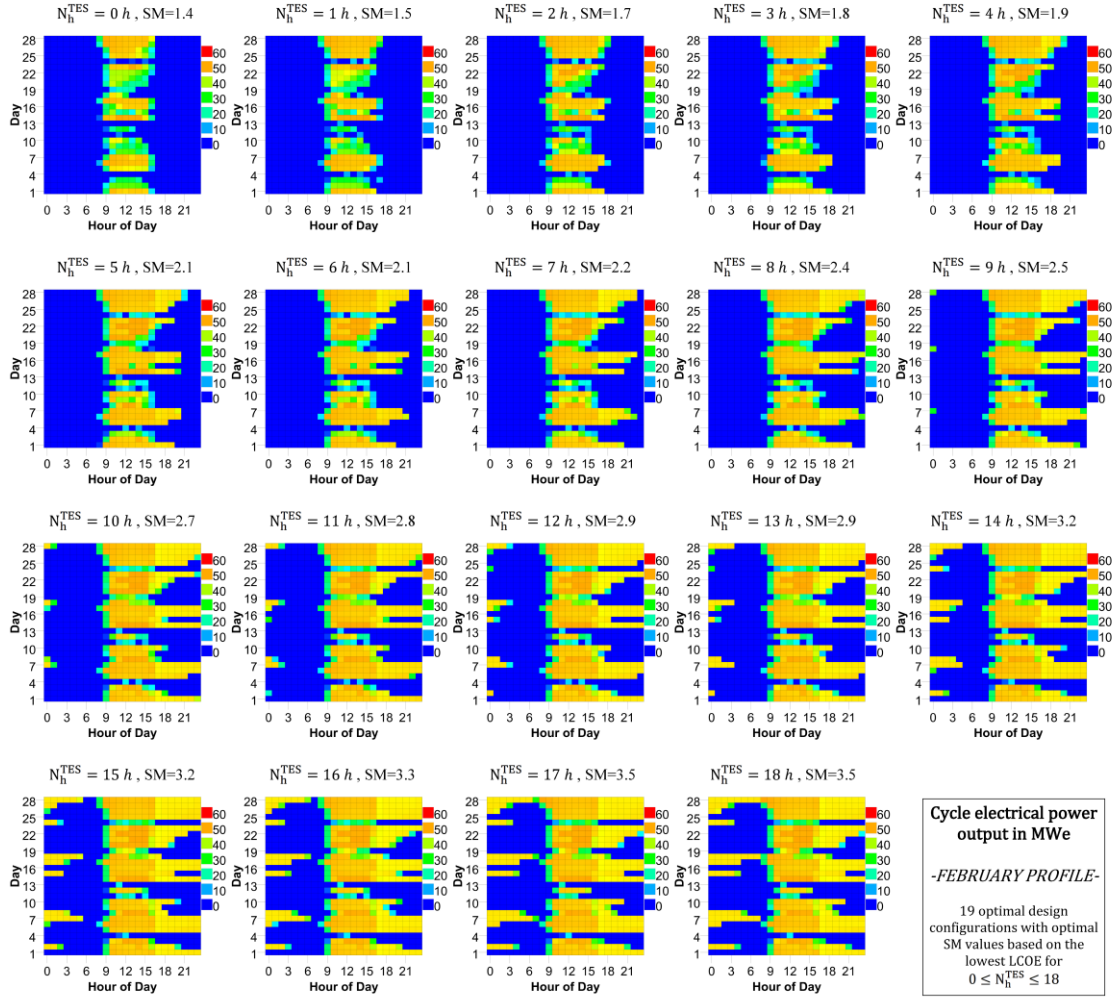


Figure 6. 7 Cycle electrical power output of a sample winter month (February profile) showing the 19 optimal design configurations with optimal SM values based on the lowest LCOE for $0 \leq N_h^{\text{TES}} \leq 18$.

During the summer season, 24 h continuous generations without fossil backup in July occur more often than in August. As shown in Figure 6. 8, it is concluded that the 24 h continuous generations without fossil backup in July occur for the following configurations:

- i. SM value of 3.2 and N_h^{TES} value of 15 h,
- ii. SM value of 3.3 and N_h^{TES} value of 16 h,
- iii. SM value of 3.5 and N_h^{TES} value of 17 h, and
- iv. SM value of 3.5 and N_h^{TES} value of 18 h.

Additionally, as shown in Figure 6. 9, the 24 h continuous generations without fossil backup in August occur for the following configurations:

- i. SM value of 3.2 and N_h^{TES} value of 15 h,
- ii. SM value of 3.3 and N_h^{TES} value of 16 h,
- iii. SM value of 3.5 and N_h^{TES} value of 17 h, and
- iv. SM value of 3.5 and N_h^{TES} value of 18 h.

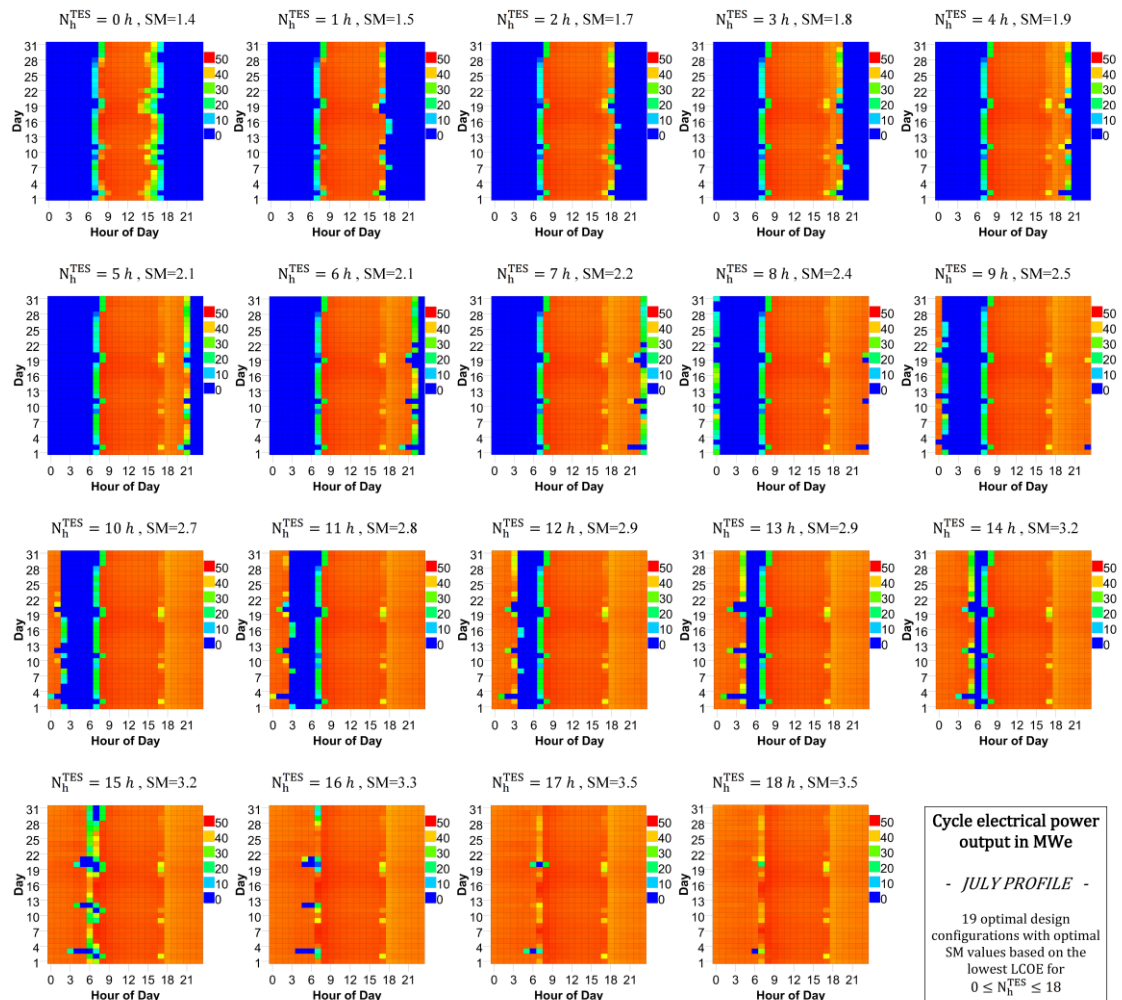


Figure 6. 8 Cycle electrical power output of a sample summer month (July profile) showing the 19 optimal design configurations with optimal SM values based on the lowest LCOE for $0 \leq N_h^{TES} \leq 18$.

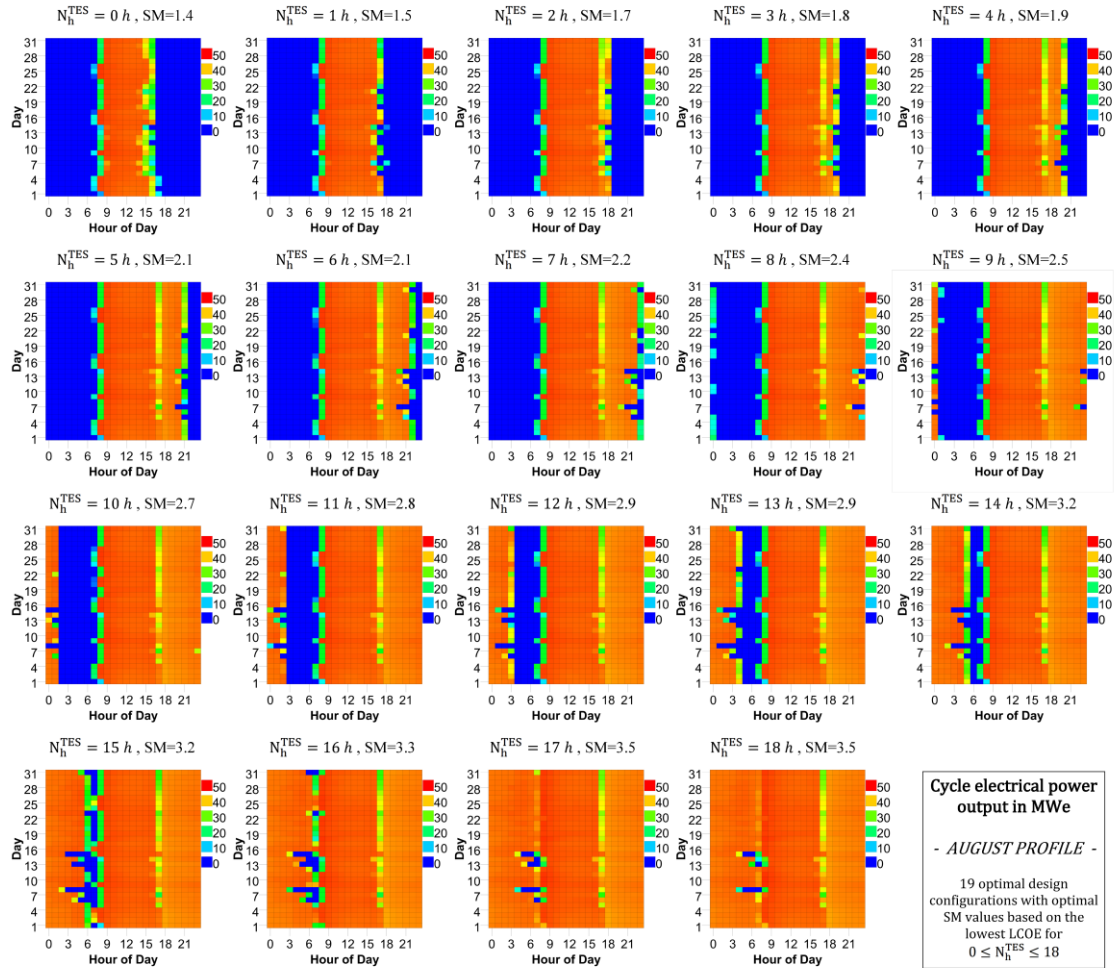


Figure 6.9 Cycle electrical power output of a sample summer month (August profile) showing the 19 optimal design configurations with optimal SM values based on the lowest LCOE for $0 \leq N_h^{TES} \leq 18$.

6.7.7. Performance enhancement strategies

6.7.7.1. Dispatch control of thermal energy storage

The CSP-PT technology can reduce peak load during daytime and address nighttime peak once integrated with a capable TES system [99]. This approach requires evaluating optimal CSP-PT/TES deployment schedules, enhancement strategies, and detailed solar resource assessments for the location and climatic conditions under consideration. Understanding optimal deployment schedules are vital for knowing the periods with cogeneration possibilities from renewable power technologies; thus, the analysis results in Figure 6.6 to Figure 6.9 are provided.

Moreover, Figure 6. 10 illustrates the effect of the previously explained TES dispatch control fractions (F_{WOS}^{TES} and F_{WS}^{TES}) on $E_{ele,a}$ to assist in understanding the performance of the reference 50 MW CSP-PT power plant under the climatic and DNI conditions of the chosen location in Kuwait. It should be noted that the range, $0 \leq F_{WOS}^{TES} \leq 1$, is investigated through the following variations:

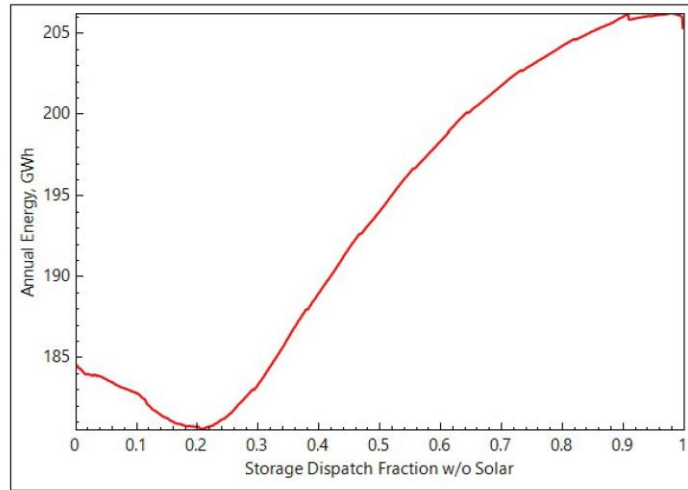
- i. $F_{WS}^{TES} = 0$,
- ii. $F_{WS}^{TES} = 0.5$, and
- iii. $F_{WS}^{TES} = 1$.

It is observed that the role of the TES dispatch control fractions in maximizing $E_{ele,a}$ is significant from approximately 124 GWh to 206 GWh, which is an increase of 66.1%. This means that the effect of the TES dispatch control strategies using F_{WOS}^{TES} and F_{WS}^{TES} can also affect the LCOE estimations. Furthermore, the capacity factor of the CSP-PT plant is directly influenced.

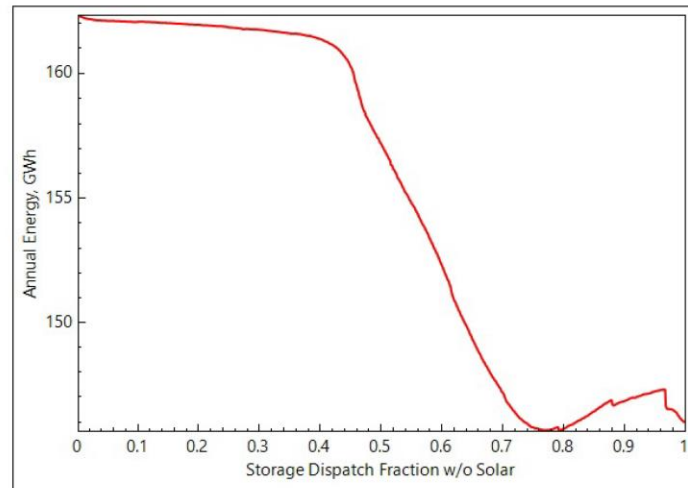
Figure 6. 11 illustrates the performance of the reference 50 MW CSP-PT plant under the conditions of the chosen location for one typical day. It is observed that the nighttime generation is possible by means of optimal TES integration. It should be mentioned that Figure 6. 11 demonstrates the performance assessment of the reference plant with a focus on the following critical parameters:

- i. DNI level,
- ii. SF system thermal output,
- iii. thermal energy to thermal storage (i.e., TES).
- iv. dumped thermal energy, and
- v. net electric power output.

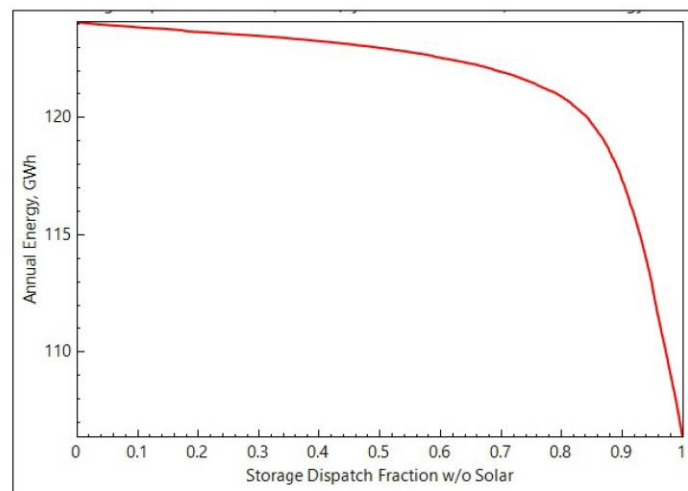
It should be mentioned that the thermal energy to thermal storage, representing the TES performance (blue curve), directly affects the smoothness of the net electric power output (dark-red curve at the 50 MW rated capacity), as shown in Figure 6. 11. This means that the TES performance effect is extended to the number of full load hours of steam turbine and eventually the PB system efficiency, highlighting the importance of this analysis approach.



(i)



(ii)



(iii)

Figure 6. 10 Role of TES dispatch control fractions in maximizing $E_{ele,a}$ in the reference 50 MW CSP-PT plant for $0 \leq F_{WoS}^{TES} \leq 1$ with the following variations: (i) $F_{WoS}^{TES} = 0$, (ii) $F_{WoS}^{TES} = 0.5$, and (iii) $F_{WoS}^{TES} = 1$.

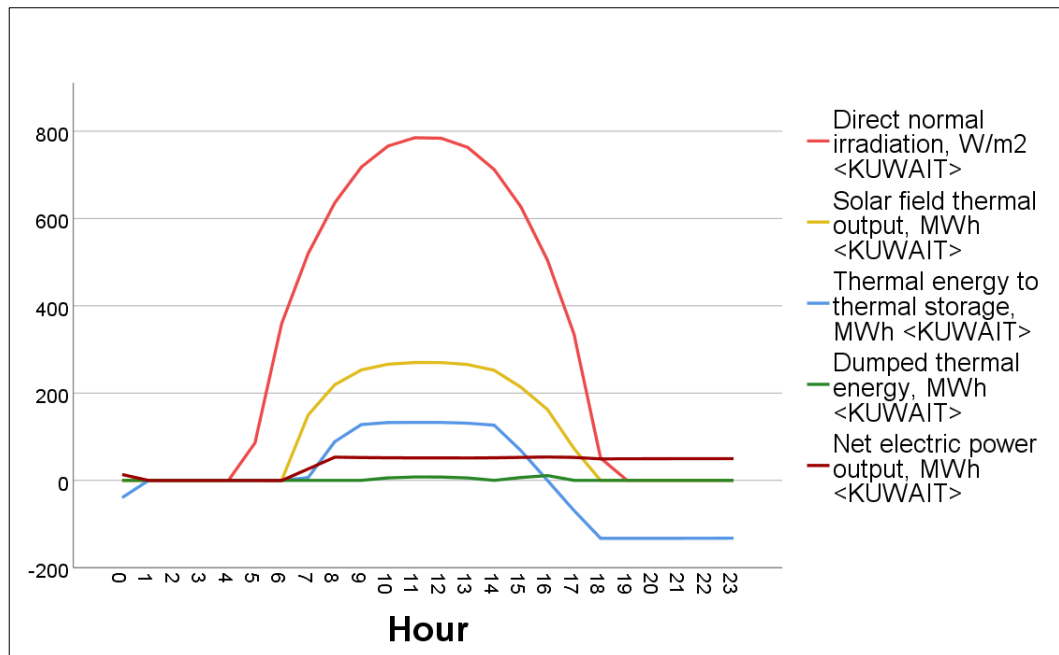


Figure 6. 11 Simulation results for the reference 50 MW CSP-PT plant performance during a typical day in the chosen location in Kuwait.

After evaluating the performance of various daily profiles under different seasons, it is concluded that peak generation from CSP-PT occurs in the late morning and the afternoon due to the DNI and climatic conditions of the chosen location in Kuwait whenever the TES system is not discharged. Therefore, CSP-PT generation can coincide with the peak load from fossil-based power plants (see Table G. 1). Hence, CSP-PT can replace peaking power units (gas turbines) in fossil-based power plants in Kuwait. Figure F. 20 shows the conventional power capacities and future projections in Kuwait. Additionally, implementing the CSP-PT technology at a mega-scale can reduce fossil fuel consumption (see Figure F. 21 and Figure F. 22).

It should be mentioned that combining CSP-PT with an optimal TES system offers dispatchability and tremendous economic benefits, as shown in Figure 5. 26 and Figure 6. 1. These benefits can extend to peak load shaving and levelling and savings in fuel consumption. Figure 6. 12 and Figure 6. 13 show the simulated results of the reference 50 MW CSP-PT plant under the DNI and climatic conditions of the chosen location during a sample winter month (January), which is a month with a high cloud presence. Hence, it is revealed that the TES system role is maximized by increasing the F_{WOS}^{TES} values (0, 0.3, 0.6, and 0.9, respectively). Further, the maximization of the TES system role leads to an increase in the cycle electrical power output, as shown in Figure 6. 12 and Figure 6. 13, for both the low values and high values of F_{WOS}^{TES} (respectively).

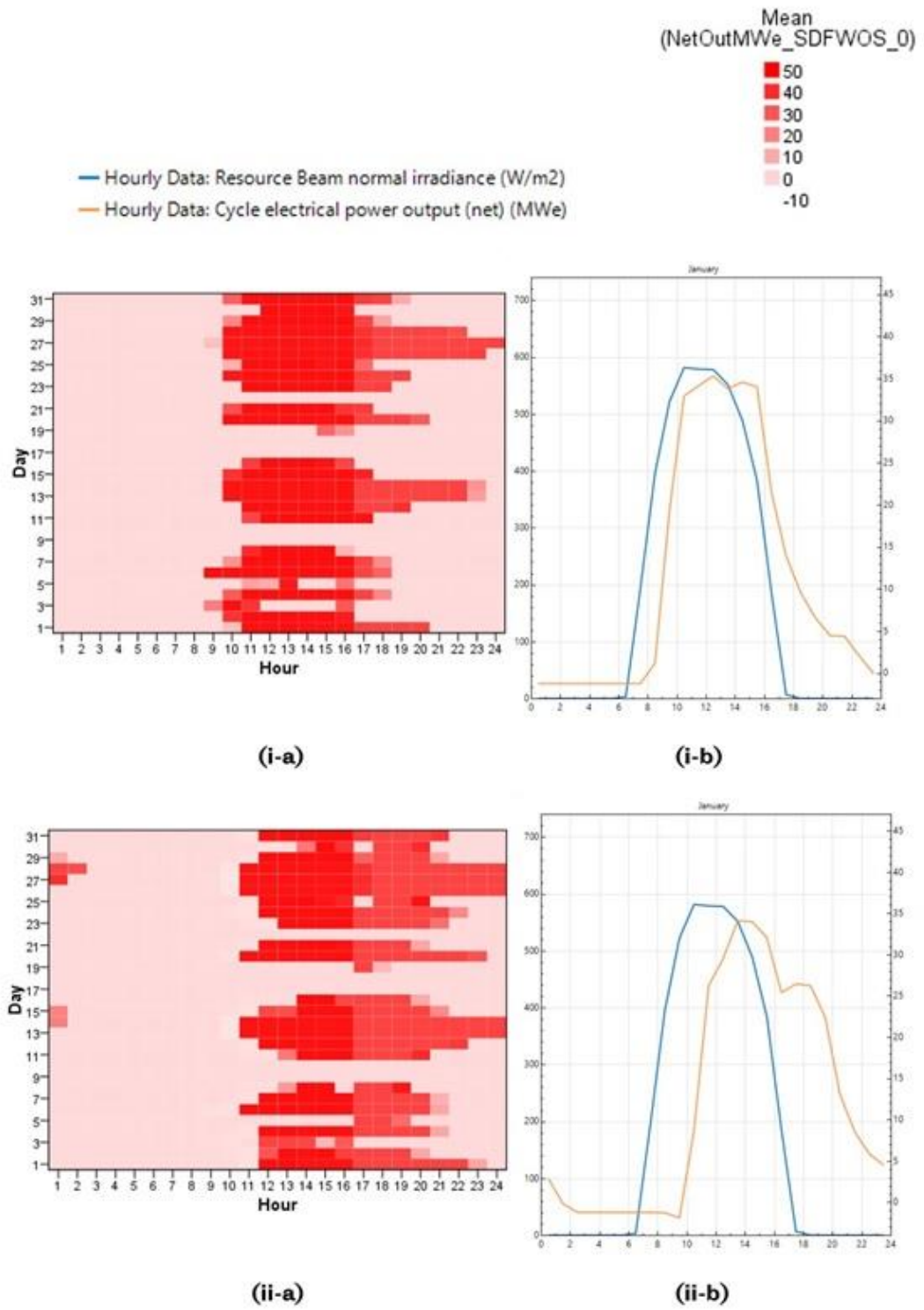


Figure 6. 12 Cycle electrical power output and direct/beam normal irradiance (i.e., DNI) during a sample winter month with high cloud presence (January profile) with maximization of TES role by increasing the value of F_{WOS}^{TES} as follows: (i) 0 and (ii) 0.3 – (low values of F_{WOS}^{TES}).

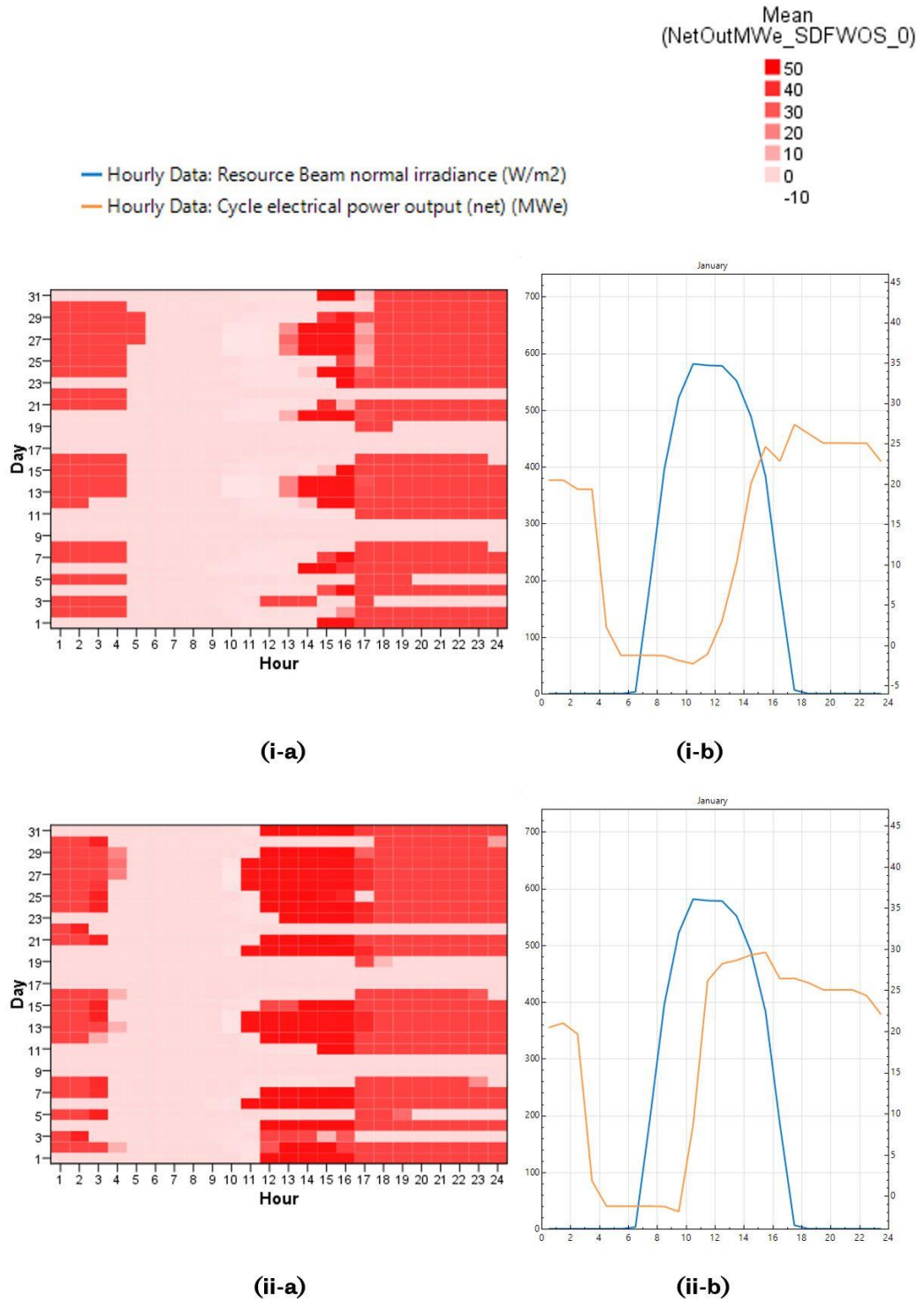


Figure 6. 13 Cycle electrical power output and direct/beam normal irradiance (i.e., DNI) during a sample winter month with high cloud presence (January profile) with maximization of TES role by increasing the value of F_{WOS}^{TES} as follows: (i) 0.6 and (ii) 0.9 – (high values of F_{WOS}^{TES}).

6.7.7.2. Integration of wind power

Figure 6. 14 shows the locations of two Meteorological Masts (MM) in Kuwait at 100 m (MM-1) and 10 m (MM-2). As shown in Figure 6. 14, both masts are at approximately 240 m elevation above sea level and 10 km apart in the chosen location in this work [261,262]. The elevation above sea level makes this location an excellent candidate for wind power generation. Besides, the location has high solar resource potential, making CSP-PT technically and economically viable, as previously demonstrated. It should be mentioned that the RLMs are established for some meteorological elements at different height levels of the MM-1 mast, as shown in Table 6. 1. Also, it should be recognized that various meteorological elements are measured at different height levels, enabling a detailed analysis of the vertical wind speed, wind direction, and α for this location.

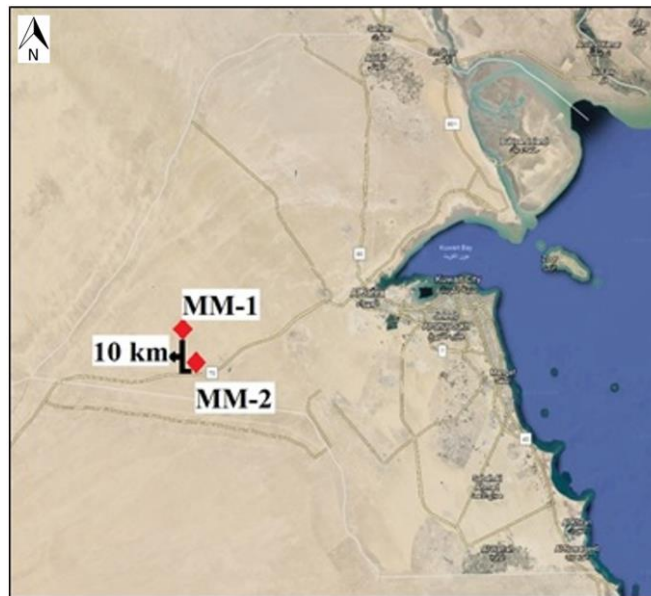


Figure 6. 14 A map of Kuwait showing the locations of two meteorological masts (about 10 km apart) in the chosen location: MM-1 at 100 m and MM-2 at 10 m.

Figure 4. 7 illustrates statistical results concerning the monthly maximum, mean, and minimum wind speed values based on a 10-minute analysis approach. It is observed that the wind resource in the chosen location reaches maximum levels during the summer, which is also the period of peak load from fossil-based power plants in Kuwait. Hence, there is a significant advantage to utilizing wind power during peak load periods, leading to increasing the economic feasibility of wind power plants. Moreover, the cogeneration using wind power and CSP-PT/TES is considered an optimal performance enhancement strategy since the solar resource is at maximum levels during the summer, as previously explained.

Table 6. 1 Established RLMs for some measured meteorological elements from the MM-1 mast at 100 m.

RLMs	Temperature measurement height, m	Humidity measurement height, m	Pressure measurement height, m	Wind speed measurement height, m	Wind direction measurement height, m
1A	-	-	-	100	-
	-	-	-	-	-
1B	98	98	-	-	-
	-	-	-	97.8	-
	-	-	-	-	97.5
	-	-	96	-	-
2	-	-	-	80	-
	-	-	-	-	79.3
3	-	-	-	60	-
	-	-	-	-	59.3
4	-	-	-	40	-
	-	-	-	-	39.3

Figure 4. 8 shows the frequency of wind speed and direction (based on hourly and 10-minute analyses) for ground measurements from different RLMs using the MM-1 and MM-2 masts. After a detailed evaluation of the measured data, it is observed that the dominant wind direction is at approximately 318° (northwesterly direction). Also, it is observed that the wind speed and direction profiles from various measurement heights (i.e., RLMs) follow similar trends during the same periods. Thus, this observation provides confidence that the used wind resource data broadly represents the wind behaviour in the chosen location.

Notably, the measured data, shown in Figure 4. 8(v) from the MM-2 mast, is used to confirm the wind direction dominance. It should be recalled that the MM-2 mast is about 10 km away from the MM-1 mast, as shown in Figure 6. 14. Thus, it is confirmed that the northwesterly wind direction is dominant. After establishing the RLCs, the wind speed data from MM-1 is further analyzed by calculating the α values. Detailed 10-minute calculations of α are performed between RLM-1A (100 m) and RLM-4 (40 m), in which the mean, maximum, minimum, and number of α values are determined. The annual mean of α is calculated to be between 0.14-0.18, as illustrated in Table 6. 2 using Equation 4. 2, showing cyclic behaviour. The calculations of α are critical for the accurate estimation of wind energy yield. The statistical profiles for the analysis of α are shown in Figure 6. 15 and Table 6. 2.

A detailed analysis is performed to understand the wind speed behaviour at high and low altitudes during the daytime and nighttime. This analysis is recommended to size and enhance a CSP-PT/TES plant performance by integrating wind power-

generating units, as shown in Figure 3. 1. The detailed wind speed analysis results are shown in Figure 4. 6 to Figure 4. 8. After evaluating the ground-measured wind data, it is concluded that the wind speed profile reaches maximum values at high altitudes during early-day and late-night periods. Whereas during the afternoon, the wind speed reaches maximum values at low altitudes (< 10 m). Hence, these findings are critical for future wind turbine sizing using centralized and decentralized power generation for mega/small-scale applications in Kuwait.

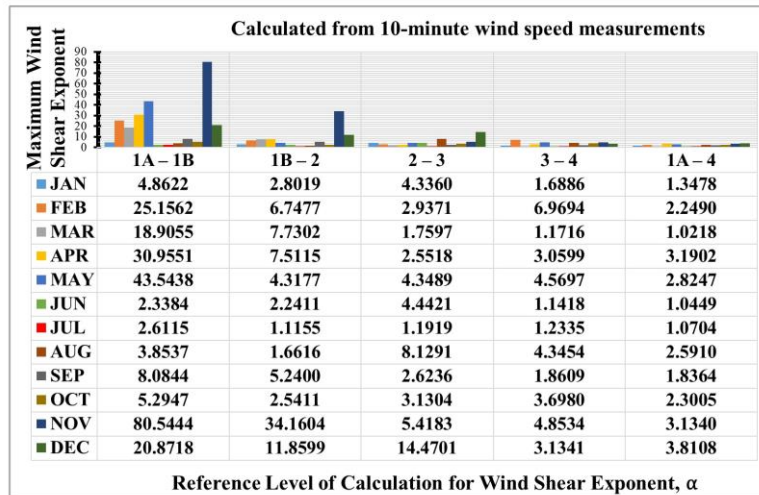
Table 6. 2 Statistics of calculated α values based on a 10-minute analysis during a typical year.

α	Mean	Maximum	Minimum	No. of values
Complete values	0.14186	3.81084	-3.70584	52442
excluding values < 0	0.18759	3.81084	0	45921
excluding values < 0 and values ≥ 1	0.18378	0.99885	0	45769
excluding values < 0 and values ≥ 0.5	0.16352	0.49999	0	43752

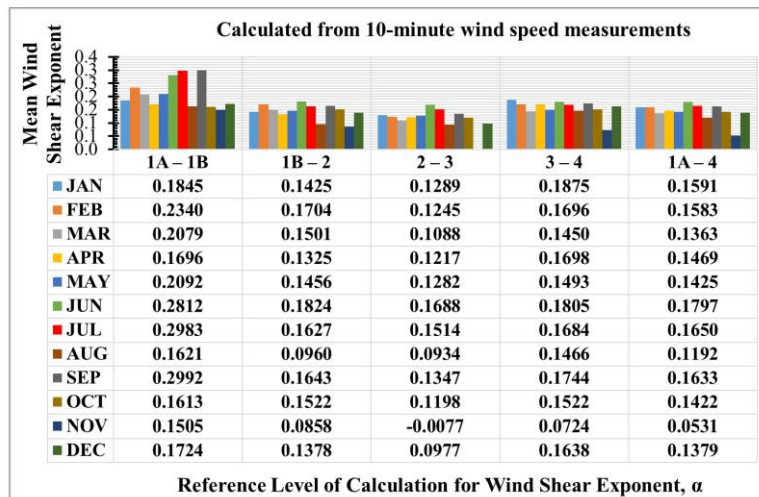
6.7.7.3. Cogeneration with temperature derating effect

The ambient temperature derating effect negatively impacts both CSP-PT and wind power technologies. This is especially true because high ambient temperatures negatively affect the dry-cooled condenser performance and Rankine cycle efficiency in dry-cooled CSP-PT plants, as shown in Equation 6. 1 and Equation 6. 2. One of the reasons for the performance assessment of wind power-generating units is to quantify the losses in power output. For the chosen location in this work in Kuwait, the power and heat losses are expected to result from the constraints imposed by the arid climatic conditions, such as high ambient temperatures between 40-53 °C and high humidity levels during the summer season.

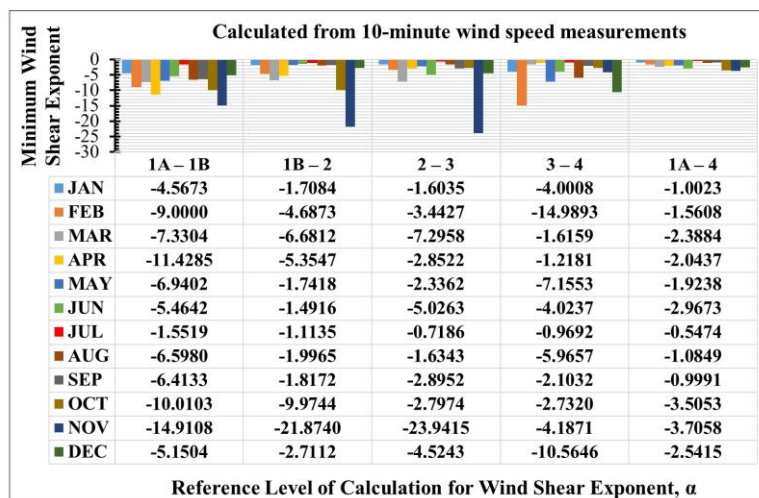
Figure 6. 16(i) illustrates the frequency of the ambient temperature exceeding a specific value in the chosen location during a typical year. In addition, the temperature corrected gross annual generation from the reference 2 MW wind turbine used in this work is estimated, as shown in Figure 6. 16(iii). Consequently, it is recommended that the effects on the wind turbine unit performance should be further evaluated in the future due to the following factors: (i) turbine's blade soiling due to dust and sand storms, (ii) high ambient temperature shutdown of the turbine, and (iii) high ambient temperature derating effect of the turbine power curve, as shown in Figure 6. 16(iii).



(i)



(ii)



(iii)

Figure 6. 15 Monthly statistics for α based on 10-minute calculations at different RLCs: (i) maximum, (ii) mean, and (iii) minimum.

6.7.7.4. Cogeneration with load consideration

Cogeneration from CSP-PT/TES and wind power can have numerous benefits, such as peak load shaving and levelling. It should be noted that TES systems are usually used for various purposes, including demand time shifting, power quality improvement, and spinning reserve to maximize renewable power integration into the grid [317–323]. Hence, an evaluation is performed to utilize a TES system in a CSP-PT plant under the wind and solar resource conditions of the chosen location in this work. The assessment considers combining the solar resource, wind speed, and electrical load profiles to determine whether an optimal scheduling strategy is possible. Figure 6. 17 shows a potential TES utilization technique (from non-renewable power) for peak load shaving and levelling application with national load consideration, which is demonstrated to serve as the base scenario (i.e., zero renewable penetration). The orange-shaded area is when energy can be produced and stored between 04:00 and 07:00 from non-renewable power. The peak load is at 14:00 (13,340 MW), and the possible period of TES discharging is shown in the green-shaded area. Once an optimal TES dispatch scenario is selected, the peak demand can decrease to above 12,930 MW. The minimum load equals 10,480 MW in this scenario instead of 10,020 MW. It should be noted that this scenario resembles zero renewable power penetration instead of the ideal scenario of achieving 15% penetration from renewable power by 2030, as previously explained. Figure 6. 18 shows the coordination between the wind/solar resources and load for the day of maximum peak load in 2016 (August 15th) with zero renewable penetration.

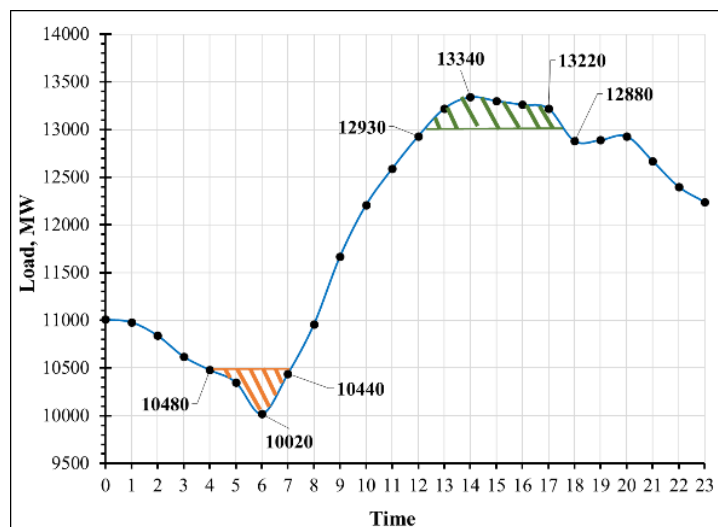


Figure 6. 17 Potential periods for TES charging (orange-shaded) and discharging (green-shaded) for the day of maximum peak load during 2016 (August 15th) in Kuwait under the zero renewable penetration scenario – (i.e., combined load from all fossil-based power plants).

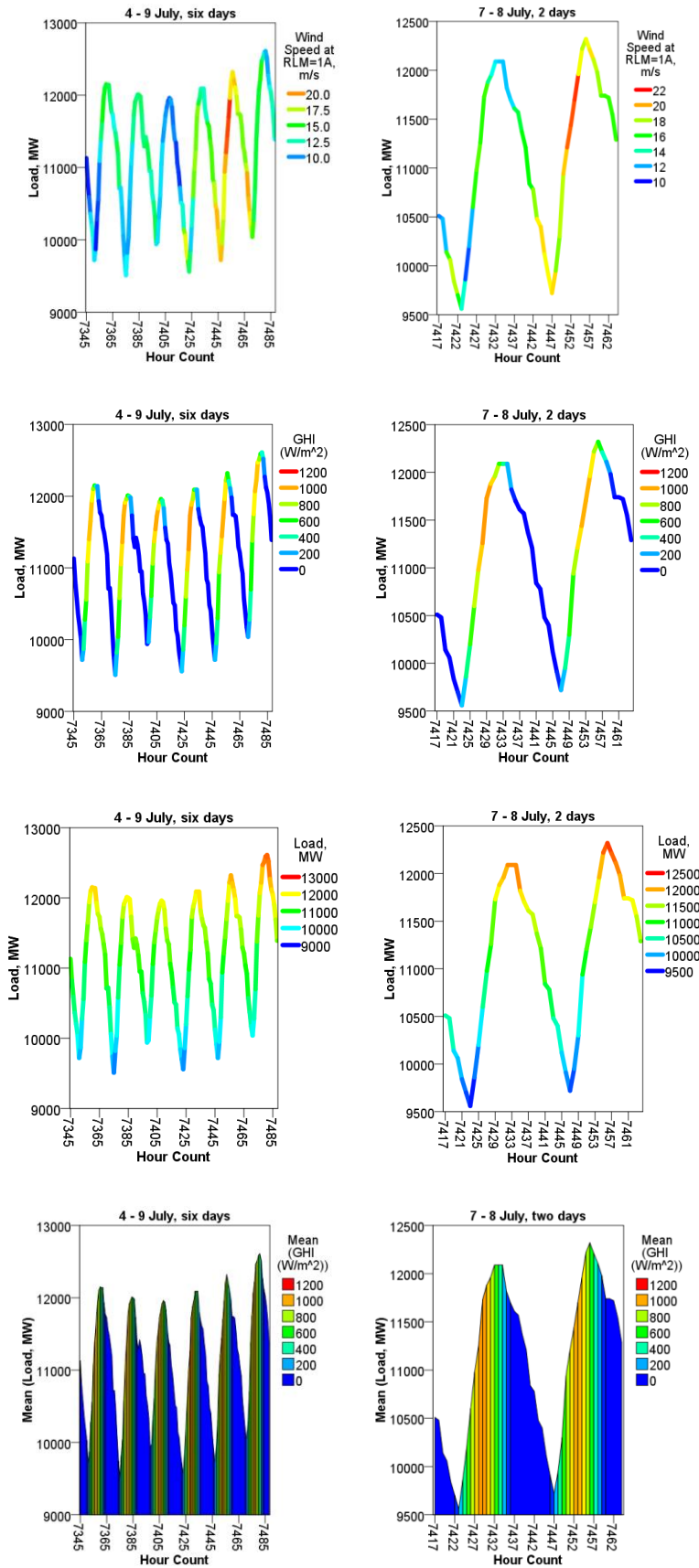


Figure 6. 18 Coordination between the wind resource from the MM-1 mast at 100 m, solar resource, and electrical load in Kuwait.

After evaluation, it is confirmed that the peak load in Kuwait is during the summer and afternoon due to the excess air conditioning load for comfort cooling in buildings (see Figure F. 1, Figure 2. 13 to Figure 2. 17, Figure 2. 19, Figure F. 18, and Figure F. 19). Besides, the summertime is when the peaks occur for both the wind and solar resources. Therefore, the coinciding peak trends of electrical load and solar/wind resources should be analyzed (as previously demonstrated in Chapter 2) along with the techno-economic assessment and renewable share allocation optimisation. The focus should be on estimating the feasibility of wind and solar power. This is critical since a scheduled power shutdown was implemented in Kuwait because conventional electricity generation did not meet local demand when the peak load as a percentage of installed capacity was 87% (13% reserve) [107], as shown in Figure 2. 18. The detailed evaluation of the wind resource, solar resource, and electrical load has revealed the periods of optimal coordination, as shown in Figure 6. 18. As peak generation from CSP-PT occurs during the afternoon; therefore,

CSP-PT generation can be dispatched to coincide with the peak load from the fossil-based power plants. For this reason, the CSP-PT technology can replace electricity generation from peaking power units (gas turbines), reducing the consumption of conventional fuels, such as heavy fuel, crude oil, NG, and gas oil [108].

The generation from CSP-PT with an optimal TES system can offer tremendous economic benefits, exceeding peak load shaving and levelling due to the additional fuel savings. A TES system in a CSP-PT plant is essential to serve the peak load in the afternoon and achieve high annual energy yields. Also, maximum TES utilization (i.e., higher N_h^{TES} values) promote achieving 24 h continuous generation with a higher capacity factor for the reference 50 MW CSP-PT plant used in this work, as shown in Figure 6. 6 to Figure 6. 9. It should be noted that the capacity factor measures how efficiently a plant's nominal capacity is utilized, directly linked to the plant's economic figures. Consequently, the primary contributor to capacity factor increase is using an optimal TES system in a CSP-PT plant. The electrical load profile in Kuwait suggests that the peak load occurs in the afternoon most of the year when ambient temperatures are at high levels, and the air conditioning load is at maximum levels. Therefore, wind power and CSP-PT with TES can effectively reduce the afternoon peak load and replace fossil-based generation.

6.8. Chapter conclusion

In this work, the simulation results based on a CSP-PT/TES model are examined for the Kuwait case. Several analyses are performed as follows: model validation, assessment of the temperature effects on performance, evaluation of an optimal dry cooling option for CSP-PT, optimization of the SF system, optimization of the PB system, and optimization of the TES system. Furthermore, the performance assessment of CSP-PT/TES under the climatic conditions of the chosen location in Kuwait is performed from technical and economic viewpoints. The main findings are: (i) the implementation of dry-cooled CSP-PT plants in this location has been justified because of the limited water resources and high potential of solar/wind resources, (ii) the summertime and afternoon are when the peak electrical load occurs at the consumer level, similar to the national load, which also peaks during the same periods, (iii) the coinciding peaks of load and solar/wind resources promote cogeneration from CSP-PT/TES and wind power, (iv) the wind speed is maximum at high altitudes in early daytime and late nighttime. Whereas during the afternoon, it reaches maximum values at low altitudes (< 10 m), (v) the annual mean of α is calculated between 0.14-0.18 and shows cyclic behaviour in the wind resource, promoting wind power generation and compensating for afternoon peak load shaving/levelling, (vi) the optimal SM for CSP-PT plants with different values of N_h^{TES} has been determined using the LCOE-minimization criterion. It was concluded that the optimal SM value for optimal plant configurations increases with increasing N_h^{TES} values, (vii) the value of N_h^{TES} value has significant effects on $E_{ele,a}$, capacity factor, and LCOE. However, the impact of N_h^{TES} on $\eta_{overall}$ is insignificant, (viii) the optimal SM value is at 3.3, corresponding to the lowest LCOE of approximately 15 ϕ /kWh for 16 h of TES. It is observed that the range of lowest LCOE is between 15-16 ϕ /kWh for the optimal configurations out of the total 589 configurations, (ix) the selection of a CSP-PT plant configuration with higher SM and N_h^{TES} values provide benefits, such as inclusion of electricity generation into nighttime and maximization of steam turbine/cycle efficiency by increasing the rated capacity operation periods, (x) 24 h continuous electricity generation without fossil backup is possible during February for the optimal CSP-PT plant configurations with SM value of 3.5 and N_h^{TES} values of 17 h and 18 h, and (xi) During winter, continuous generation from CSP-PT/TES without fossil backup occurs in February but not in January due to the high cloud presence. During summer, generation occurs in July more often than in August.

7. COMPARATIVE TECHNO-ECONOMIC ASSESSMENT AND OPTIMIZATION OF WIND POWER PLANTS

7.1. Chapter journal publications

Some of the work that appears in this chapter is associated with peer-reviewed scientific journal publications (under revising process). This chapter is associated with publications (3) and (6). The detailed information of these publications is listed in the “Scientific Journal Publications” Section, starting from page (iii) of this thesis.

7.2. Technology description

This work presents a comparative techno-economic assessment and minimization of the LCOE for increasing capacity wind power plants by row and angle layout optimization. In particular, each wind turbine within the defined rows in the wind power plants has a rated capacity of 2 MW (i.e., the reference wind turbine as explained earlier). Furthermore, the reference 2 MW wind turbine has a cut-in wind speed of 3 m/s, rated wind speed of 11 m/s, and cut-out wind speed of 25 m/s. Figure 7.1 shows a simplified illustration for a single row configuration to be used as the base for analyzing 2220 design configurations in total. These configurations have increasing power capacities and are connected to the following components:

- i. electrical grid,
- ii. substations (step-up/down),
- iii. overhead lines, and
- iv. residential units.

Figure 7.2 shows the reference 2 MW wind turbine’s power curve used in the simulation. It should be recognized that the design characteristics for the wind turbine type used in this work are shown in Table 7.1.

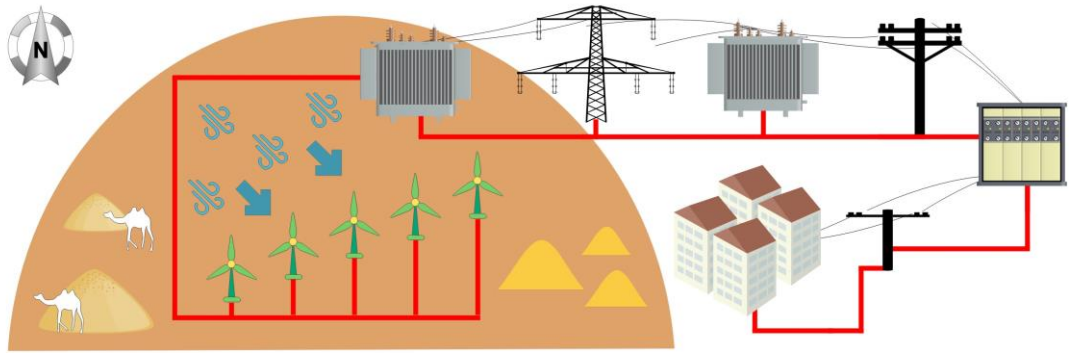


Figure 7. 1 A simplified illustration of a single row configuration with grid connection, substations, overhead lines, and residential units.

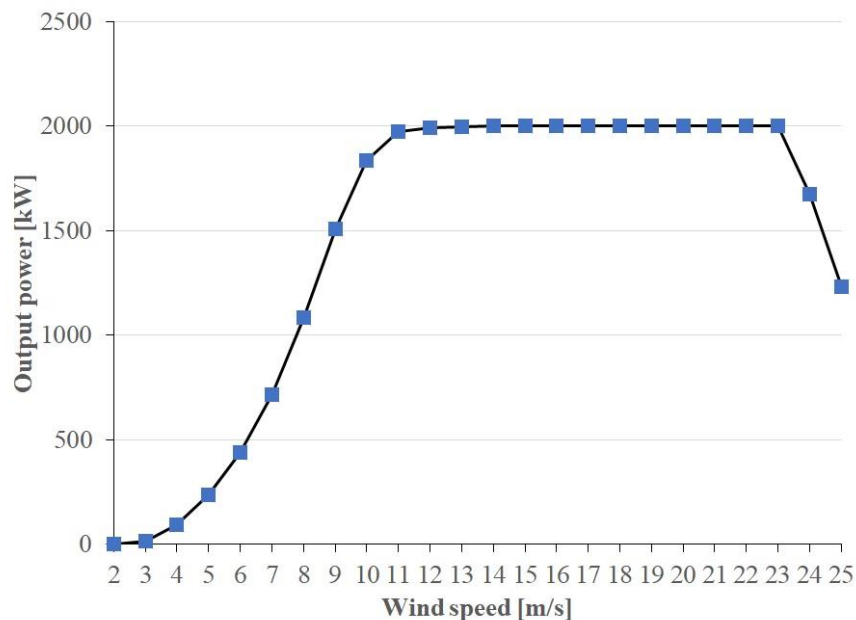


Figure 7. 2 Power curve for the reference 2 MW wind turbine used in this work.

Like most mega-scale wind turbines, this work's reference 2 MW wind turbine has technical specifications and service requirements. According to the turbine's mechanical design, the turbine platform considers improved mechanical capacity in the turbine components (e.g., yaw system, framework, central axis, blade bearings). These improvements increase the reliability of the turbine's components and make it possible to use larger rotors to harness the wind kinetic energy and maximize the power generated in different wind strengths.

Furthermore, as per the turbine's drive train, the main axis is supported by two spherical bearings, providing additional benefits when the surrounding loads are transmitted to the framework through a rack. As a result, this prevents the gearbox

from the extra loads, leading to reduced breakdown and providing a longer lifetime for the turbine.

Table 7.1 Design characteristics for the reference wind turbine used in this work.

Description	Value	Unit
Make and model	Siemens-Gamesa G97	-
Power capacity	2000	kW
Number of blades	3	-
Cut-in wind speed	3	m/s.
Rated wind speed	11	m/s.
Cut-out wind speed	25	m/s.
Rotor diameter	97	m
Swept area	7390	m ²
Rotational speed	9.6 - 17.8	rpm
Blade material	pre-impregnated epoxy glass fiber + carbon fiber	-
Blade length	47.5	m
Blade cord, maximum	3,41	m
Blade cord, minimum	0,057	m
Blade torsion	8,5	m
Turbine cover dimensions	10.583 x 3,505 x 4,487	m
Turbine cover material	reinforced matrix composite	-
Turbine hub material	Nodular cast iron	-
Main shaft type	Cast shaft	-

In addition, a lightning protection system, which is designed according to the IEC 62305 standard, is impeded as per the turbine's design. The lightning protection conducts the lightning from the sides of the blade's tip to the root, then through the nacelle, tower structure, leading to the foundation (ground). Such protection maintains the blades and protects the bearings and main axis from possible lightning travelling through them. In addition, this protection saves the electrical and electronic equipment from burnout situations.

Furthermore, the turbine has a controlled braking system, represented by the aerodynamic brakes and mechanical emergency brakes at the output of the high-speed axis of the gearbox. Also, a hydraulic control system provides braking when experiencing excessive transmission load.

Table 7.1 Cont. Design characteristics for the reference wind turbine used in this work.

Description	Value	Unit
Main shaft support	Nodular cast iron	-
Front frame material	Nodular cast iron	-
Yaw system type	Yaw ring with friction bearing	-
Tower type	Tubular truncated	-
Tower material	Structural carbon steel	-
Tower surface treatment	Painted	-
Gearbox type	1 planetary stage, 2 parallel stages	-
Gearbox ratio	1:106.8 (50 Hz) 1:127.1 (60 Hz)	-
Main shaft coupling	Cone collar	-
High-speed shaft coupling	Flexible coupling	-
Generator type	Doubly-fed machine	-
Generator nominal power	2,070	kW
Generator voltage	690	Vac
Generator frequency	50 / 60	Hz
Mechanical brake type	Disc	-
Hydraulic unit operating pressure	220	bar
Control unit voltage	24	Vdc
Transformer type	Three-phase, dry-type encapsulated	-
Nacelle weight	72	t
Rotor weight	47	t
Tower weight	165	t

7.3. Mathematical description

In this work, the LCOE is calculated as follows [324]:

$$LCOE = \frac{FCR \times ICC + FOC}{AEP} + VOC$$

7.1

where

FCR: Fixed Charge Rate (-).

ICC: Installed Capital Cost (\$).

FOC: Fixed Operating Cost, or operations and maintenance costs (\$).

VOC: Variable Operating Cost, or operations and maintenance costs per unit of annual electricity production (\$/kWh).

AEP: Annual Electricity Production (kWh).

Additionally, the output of a single wind power-generating unit (P_w) is calculated from Equation 6. 3. Furthermore, the wind power density (P_d) in the unit of W/m^2 is calculated as follows (see Appendix E):

$$P_d = (1/2) \rho u_h^3$$

7. 2

7.4. Results and discussions

7.4.1 Locally estimated scatterplot smoothing regression analyses

Figure 7. 3 shows the hourly wind speed and α profiles for one day in the chosen location in Kuwait at different height levels. The comparison between daytime and nighttime reveals that the difference in the vertical α is noticeable. The wind speeds are distributed equally and vertically during the day with lower α values (on average, $\alpha = 0.15$). In comparison, the wind speeds increase for higher elevations above the ground at night, thus increasing the α values ($\alpha > 0.29$).

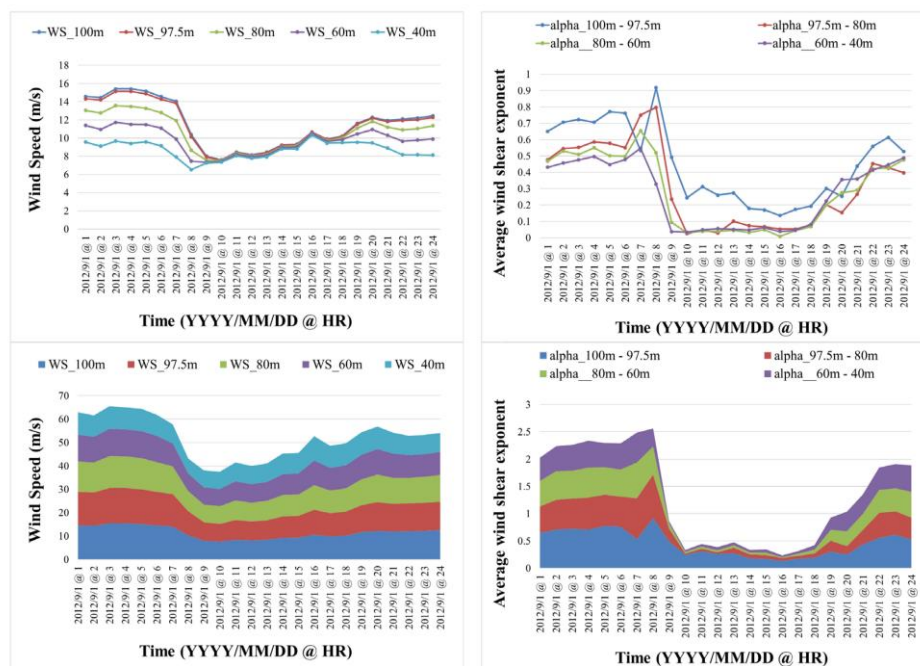


Figure 7. 3 Profiles for the wind speed and α at different height levels during one day.

It should be noted that understanding the wind behaviour and class is crucial for assessing the chosen location's suitability for mega-scale wind power installations since mega-scale wind turbines are designed to withstand certain design conditions. Considering a mean air density of 1.12 kg/m^3 , a rotor swept area of 7390 m^2 for the reference wind turbine with a rated capacity of 2 MW, a rotor diameter of 97 m, and a mean wind speed of 8.02 m/s (as shown in Table 7. 1); therefore, the P_d value is calculated to be 289 W/m^2 using Equation 7. 2 (see Appendix E).

Generally, an annual frequency evaluation of wind speed and direction is insufficient for wind power assessment. Therefore, the corresponding monthly profiles have been investigated in this work. A detailed resource assessment focusing on wind speed and direction has also been performed for the chosen location in Kuwait. The evaluation resulted in identifying wind dominance in the northwest direction. It can be concluded that the months of June and July have maximum wind speed profiles and dominant wind direction with consistent two levels compared to other months, showing relative dominance in the same wind direction.

In particular, the wind resource assessment incorporated several regression analyses of LOESS. This work utilizes the LOESS regression method to find the best fit for the wind data points. It should be recognized that the LOESS analysis is an investigation in which least squares regression is performed in localized subsets, such as in the case of hourly wind speed and wind direction data. The complete LOESS analyses concluded that the wind direction and distribution ranges showed consistent and robust northwest components. In addition, the seasonal wind direction distribution is evaluated, and it is observed that the dominant wind direction is maintained without significant variations throughout the year (see Figure 7. 4 and Figure 7. 5). Essentially, Figure 7. 4 shows various plots corresponding to separate monthly LOESS analyses. It should be noted that the horizontal axes indicate the wind direction in the deg ($^\circ$) unit, whereas the vertical axes indicate the wind speed in the m/s unit. The boxplots, shown on the right and top sides of the plots, provide helpful information concerning the range, average, maximal, and minimal values.

In statistical modelling, a regression analysis is defined as a set of statistical processes for the estimation of the relationship between a dependent variable and other independent variables (one or more). The LOESS regression analyses reveal that the correlations between wind speed and direction provide essential

information for identifying the months with the highest contribution toward wind power generation. Hence, such findings can be used in wind power scheduling to increase the energy yield of future mega-scale installations of wind power plants (i.e., high power capacities) in the chosen location within Kuwait.

As illustrated in Figure 7. 4, the large markers represent the hour count in which the early hours of the day are represented with smaller markers compared to later hours. Furthermore, the wind speed and direction correlations show that the months of June, July, August, and September have consistent trends. Thus, it is revealed that a high concentration exists at a specific wind direction, i.e., approximately 318° . Additionally, it is concluded that the highest concentrations occur during the months of June and July, with a mean wind speed of 11.27 m/s and 10.74 m/s, respectively. Additionally, as shown in Figure 7. 4, the red curves indicate sharp spikes at approximately 318° , confirming the previous finding

Table 7. 2 shows statistical results (annual) for the primary meteorological data at the reference wind turbine's hub height. It is crucial to understand the wind resource if dispatching wind power is accompanied by other renewable energy technologies, such as CSP-PT. Additionally, CSP-PT with TES capability is considered a dispatchable power source and can provide additional economic benefits once combined with wind power, an intermittent source.

For the chosen location in Kuwait, it is essential to realize that the wind resource is at maximal levels during the nighttime when CSP-PT can be dispatched using a TES system. Such dispatch operation will increase the economic feasibility and reduce the curtailment of renewable power cogeneration. It should be recognized that the wind resource assessment and the LOESS regression analyses have provided an acceptable correlation between the wind speed and direction, resulting in the nighttime showing maximal values. Therefore, CSP-PT and wind power complement each other for the case of the chosen location in this work within Kuwait.

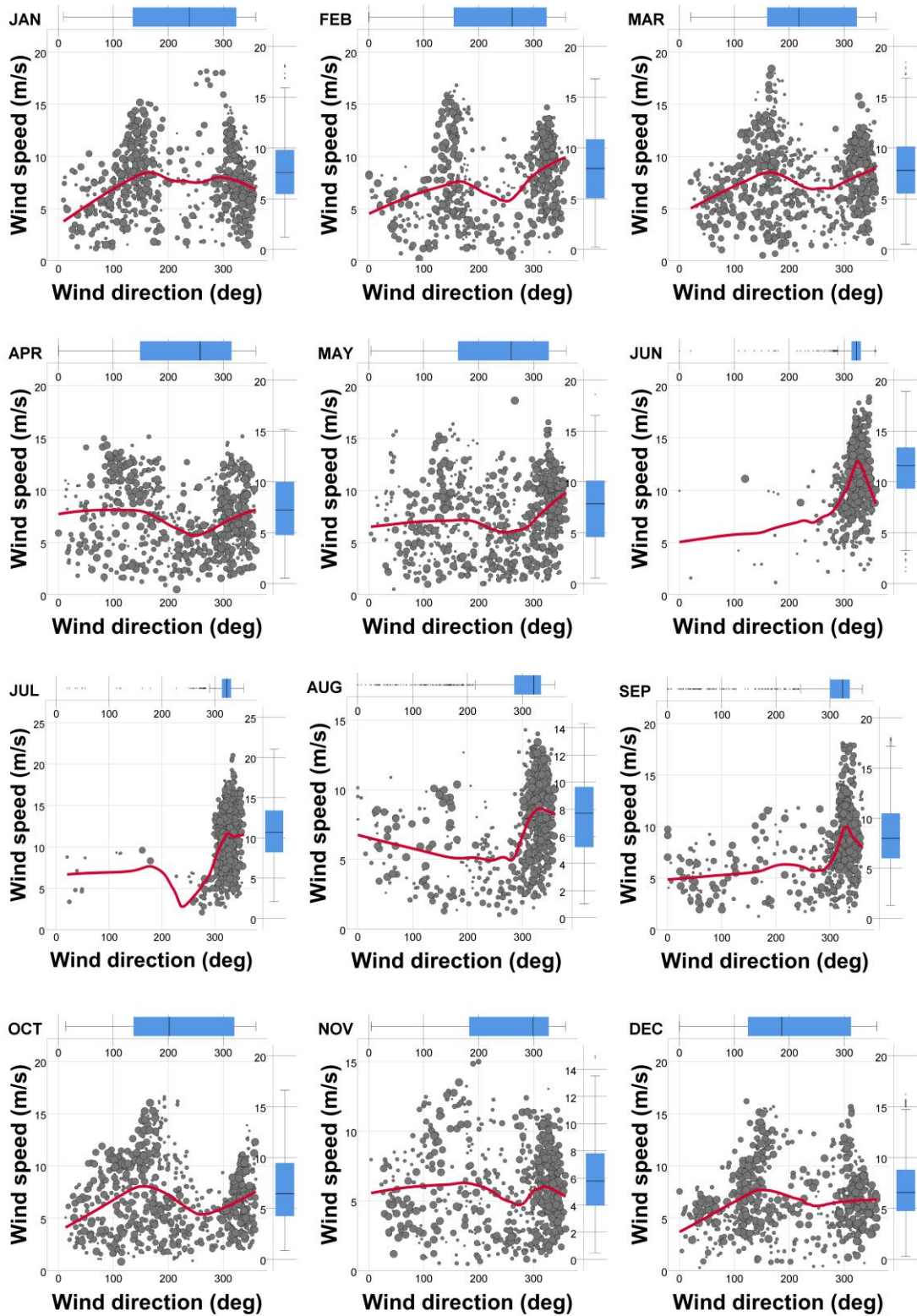


Figure 7. 4 Results of the LOESS regression analyses (monthly) for the wind resource during hours 0 to 23 for a typical year in the chosen location in this work.

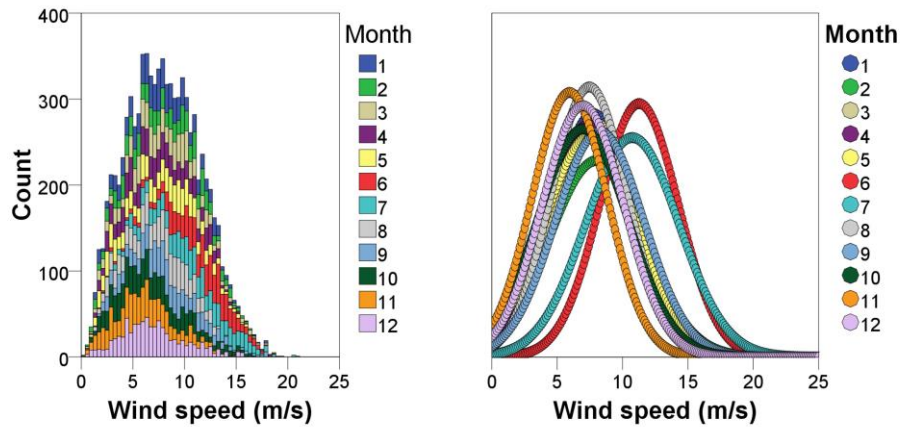


Figure 7. 5 Monthly profiles for the wind speed frequency (left) at the reference wind turbine's hub height with normal distributions (right).

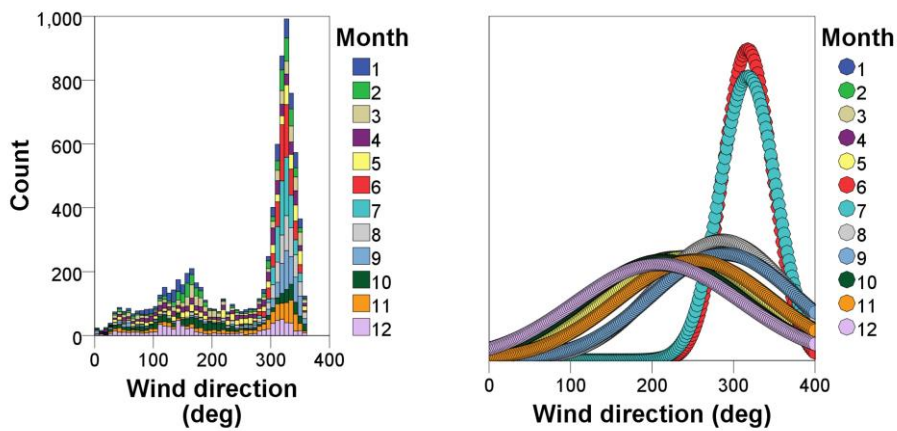


Figure 7. 6 Monthly profiles for the wind direction frequency (left) at the reference wind turbine's hub height with normal distributions (right).

Table 7. 2 Statistical results (annual) for primary meteorological data at the reference wind turbine's hub height during a typical year.

Description	Wind speed, (m/s)	Wind direction, (°)	Atmospheric pressure, (atm)	Ambient temperature, (°C)
Mean	8.02	253.30	0.9646	30.89
Median	7.85	306.11	0.9654	31.98
Maximum	21.05	359.91	0.9832	50.20
Minimum	0.22	0.24	0.9493	7.88
Range	20.83	359.67	0.0339	42.32
Standard Deviation	3.59	95.73	0.0067	9.78

7.4.2 Optimization analyses

As mentioned earlier in Section 3.5, the model simulation is performed for a total of 2220 design configurations, from which 60 optimal configurations are identified corresponding to different row configurations. The optimization is accompanied by techno-economic evaluation, which is established through studying the effects of varying two primary parameters (N_r and θ_{plant}) for several wind power plants using the reference 2 MW wind turbine. The variations bring the total investigated simulations to 2220 runs, divided into 60 categories. While interpreting the following sections, it should be noted that the results of the 2220 configurations are shown in 3-D illustrations, i.e., Figure 7. 7(a,b), Figure 7. 8(a,b), Figure 7. 9(a,b), and Figure 7. 10(a,b). Whereas the 60 optimal configurations (one for each of the 60 categories as mentioned earlier) are shown in 2-D illustrations, i.e., Figure 7. 7(c), Figure 7. 8(c), Figure 7. 9(c), and Figure 7. 10(c).

7.4.2.1. Impact on levelized cost of electricity

This section examines the impact of varying N_r and θ_{plant} on the LCOE and annual gross energy. Figure 7. 7(a) shows the results of a parametric analysis, which reveals that the change in the LCOE occurs as the N_r and θ_{plant} values differ. As the N_r value increases, an increase in the LCOE occurs for the following ranges of θ_{plant} : 110-140° and 280-320° (red areas). Whereas at small values of N_r , a decrease in the LCOE occurs for the following ranges of θ_{plant} : 0-75°, 160-260°, and 340-360° (dark-blue areas). Figure 7. 7(b) shows a linear increase in annual gross energy as the N_r value increases for almost all ranges of θ_{plant} . Figure 7. 7(c) shows the LCOE, N_r , and θ_{plant} for each of the 60 optimal configurations based on the LCOE-minimization criterion.

7.4.2.2. Impact on wake losses

This section examines the impact of varying N_r and θ_{plant} on the wake losses and annual gross energy. Figure 7. 8(a) shows the results of a parametric analysis, which reveals that the change in the wake losses occurs as the N_r and θ_{plant} values differ. As the N_r value increases, an increase in the wake losses occurs for the following ranges of θ_{plant} : 110-140° and 280-320° (red areas). Whereas at small values of N_r , a decrease in the wake losses occurs for the following ranges of θ_{plant} : 0-75°, 160-260°,

and 340-360° (dark-blue areas). Figure 7. 8(b) shows a linear increase in annual gross energy as the N_r value increases for almost all ranges of θ_{plant} . Also, Figure 7. 8(c) shows the wake losses, N_r , and θ_{plant} for each of the 60 optimal configurations based on the LCOE-minimization criterion.

7.4.2.3. Impact on performance ratio

This section examines the impact of varying N_r and θ_{plant} on the performance ratio and annual gross energy. Figure 7. 9(a) shows the results of a parametric analysis, which reveals that the change in the performance ratio occurs as the N_r and θ_{plant} values differ. As the N_r value increases, a decrease in the performance ratio occurs for the following ranges of θ_{plant} : 110-140° and 280-320° (dark-blue areas). Whereas at small values of N_r , an increase in the performance ratio occurs for the following ranges of θ_{plant} : 0-75°, 160-260°, and 340-360° (red areas). Figure 7. 9(b) shows a linear increase in annual gross energy as the N_r value increases for almost all ranges of θ_{plant} . Also, Figure 7. 9(c) shows the performance ratio, N_r , and θ_{plant} for each of the 60 optimal configurations based on the LCOE-minimization criterion.

7.4.2.4. Impact on capacity factor

This section examines the impact of varying N_r and θ_{plant} on the capacity factor and annual gross energy. Figure 7. 10(a) shows the results of a parametric analysis, which reveals that the change in the capacity factor occurs as the N_r and θ_{plant} values differ. As the N_r value increases, a decrease in the capacity factor occurs for the following ranges of θ_{plant} : 110-140° and 280-320° (dark-blue areas). Whereas at small values of N_r , an increase in the capacity factor occurs for the following ranges of θ_{plant} : 0-75°, 160-260°, and 340-360° (red areas). Figure 7. 10(b) shows a linear increase in annual gross energy as the N_r value increases for almost all ranges of θ_{plant} . Also, Figure 7. 10(c) shows the capacity factor, N_r , and θ_{plant} for each of the 60 optimal configurations based on the LCOE-minimization criterion.

7.4.2.5. Impact of wind resource

Firstly, Figure 7. 5 to Figure 7. 7 reveal that the frequency of the wind resource has a clear impact on the LCOE and annual gross energy once linked with the variation of

N_r and θ_{plant} . Because there are more wind turbines for higher N_r values, the turbines create more turbulence at high wind speeds, leading to increased wake losses. As a result, the generation decreases, and the LCOE rises accordingly. This explanation justifies the continuous increase in the LCOE shown in Figure 7. 7(a) for θ_{plant} : 110-140° and 280-320° (red areas). Furthermore, this explanation justifies the initial slight increase and continuous decrease in the LCOE for θ_{plant} : 0-75°, 160-260°, and 340-360° (dark-blue areas).

Secondly, Figure 7. 5 to Figure 7. 7 and Figure 7. 8 reveal that the frequency of the wind resource has a clear impact on the wake losses and annual gross energy once linked with the variation of N_r and θ_{plant} . Because there are more wind turbines at higher N_r values, the turbines create more turbulence at high wind speeds, leading to increased wake losses. As a result, the generation decreases, and the wake losses increase accordingly. This explanation justifies the continuous increase in the wake losses shown in Figure 7. 8(a) for θ_{plant} : 110-140° and 280-320° (red areas). Furthermore, this explanation justifies the initial slight increase and continuous decrease in the wake losses for θ_{plant} : 0-75°, 160-260°, and 340-360° (dark-blue areas).

Thirdly, Figure 7. 5 to Figure 7. 7 and Figure 7. 9 reveal that the frequency of the wind resource has a clear impact on the performance ratio and annual gross energy once linked with the variation of N_r and θ_{plant} . Because there are more wind turbines for higher N_r values, the turbines create more turbulence at high wind speeds, leading to increased wake losses. As a result, the generation decreases, and the performance ratio drops accordingly.

Lastly, Figure 7. 5 to Figure 7. 7 and Figure 7. 10 reveal that the frequency of the wind resource has a clear impact on the capacity factor and annual gross energy once linked with the variation of N_r and θ_{plant} . Because there are more wind turbines for higher N_r values, the turbines create more turbulence at high wind speeds, leading to increased wake losses. As a result, the generation decreases, and the capacity factor decreases accordingly.

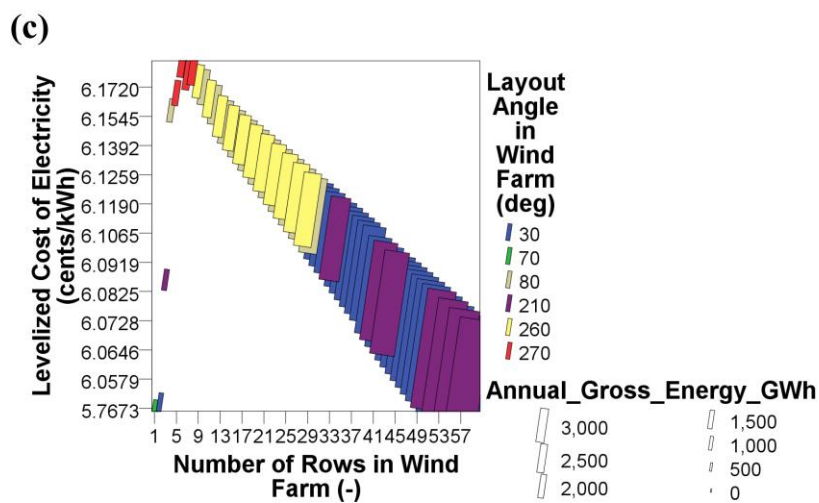
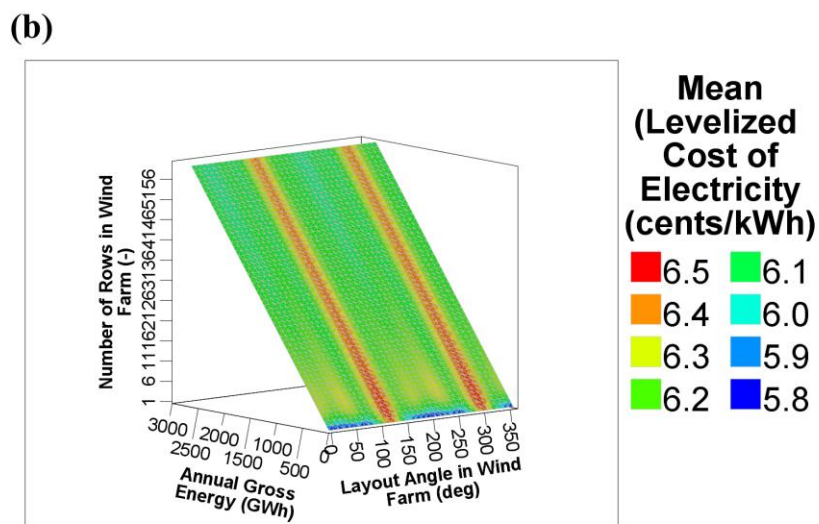
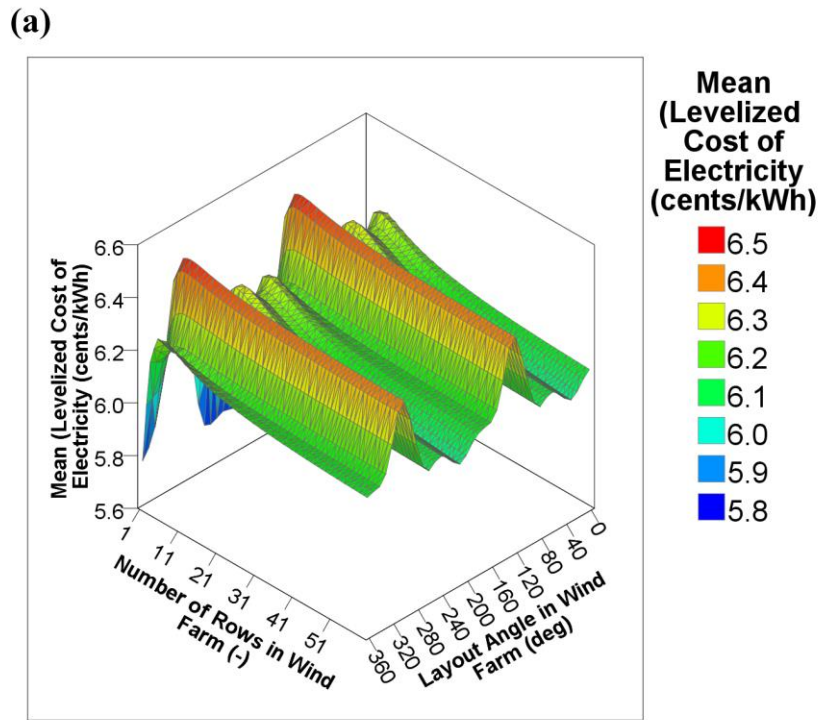


Figure 7. 7 Impact of varying N_r and θ_{plant} on the LCOE and annual gross energy: (a) for 2220 configurations, (b) for 2220 configurations, and (c) for 60 optimal configurations.

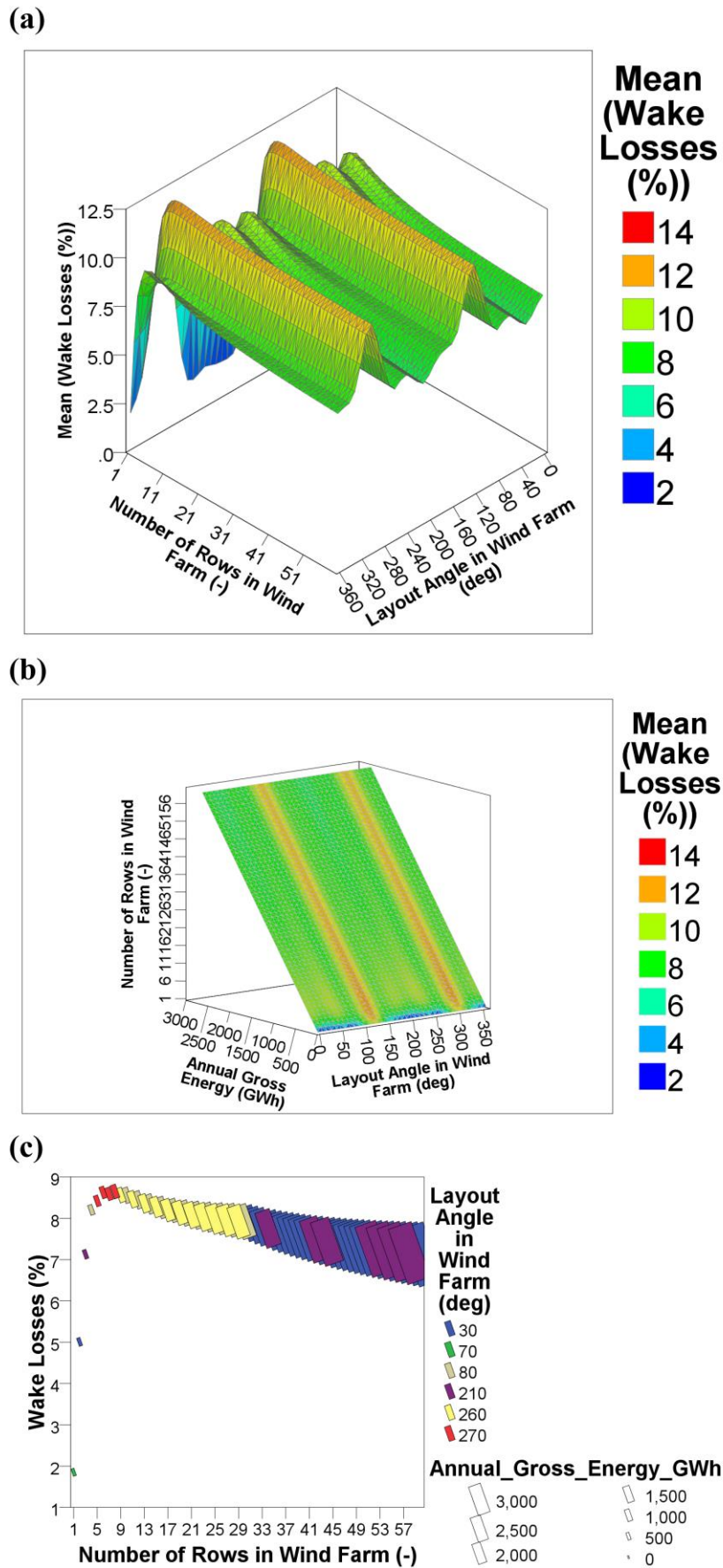


Figure 7. 8 Impact of varying N_r and θ_{plant} on the wake losses and annual gross energy: (a) for 2220 configurations, (b) for 2220 configurations, and (c) for 60 optimal configurations.

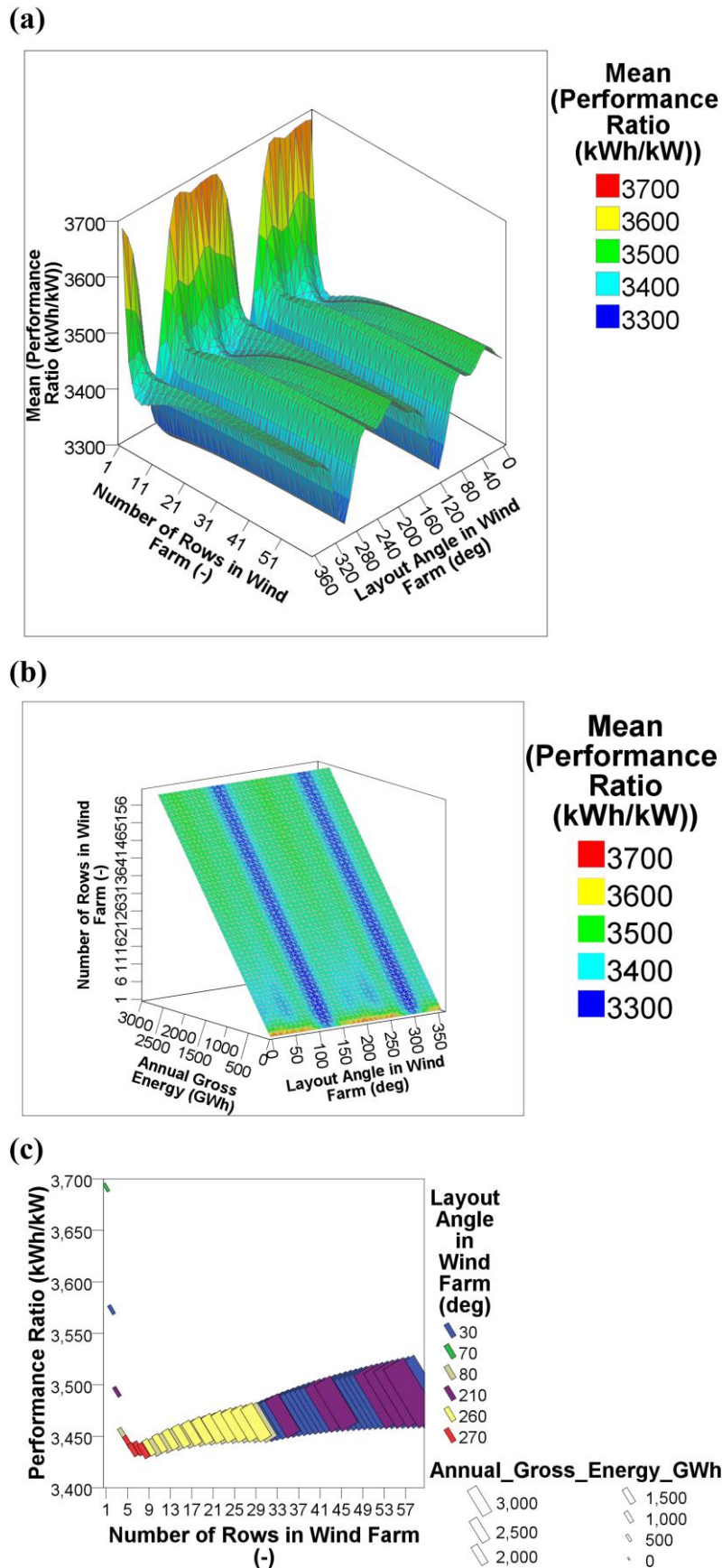


Figure 7. 9 Impact of varying N_r and θ_{plant} on the performance ratio and annual gross energy: (a) for 2220 configurations, (b) for 2220 configurations, and (c) for 60 optimal configurations.

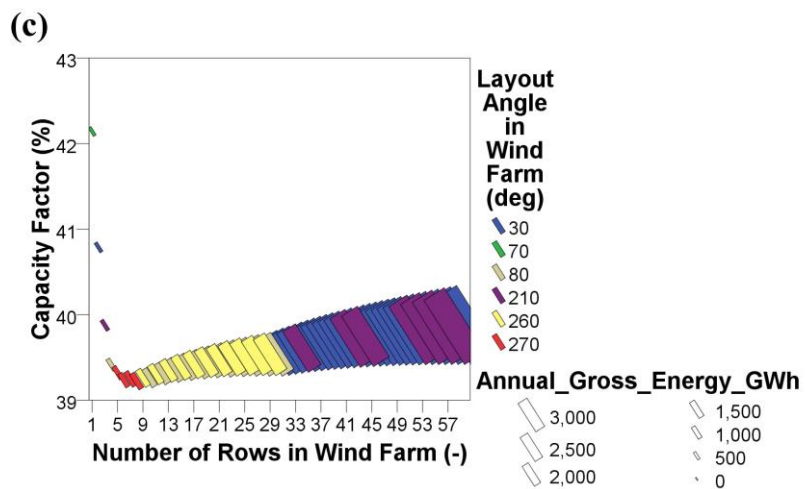
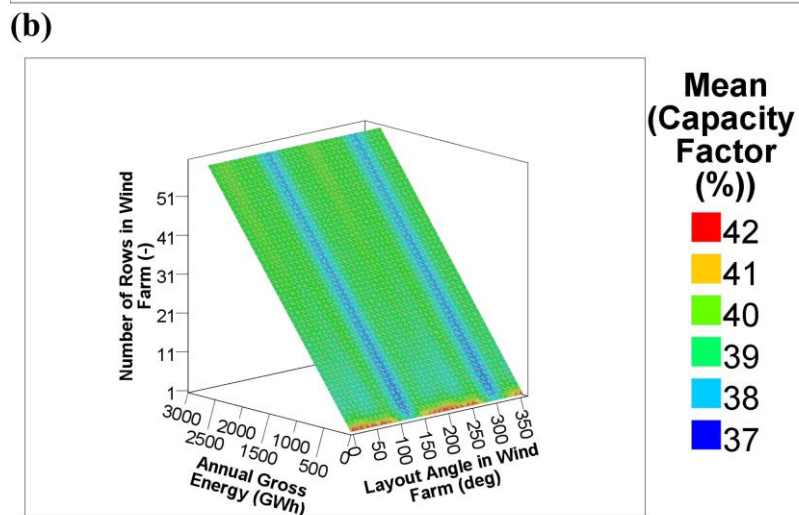
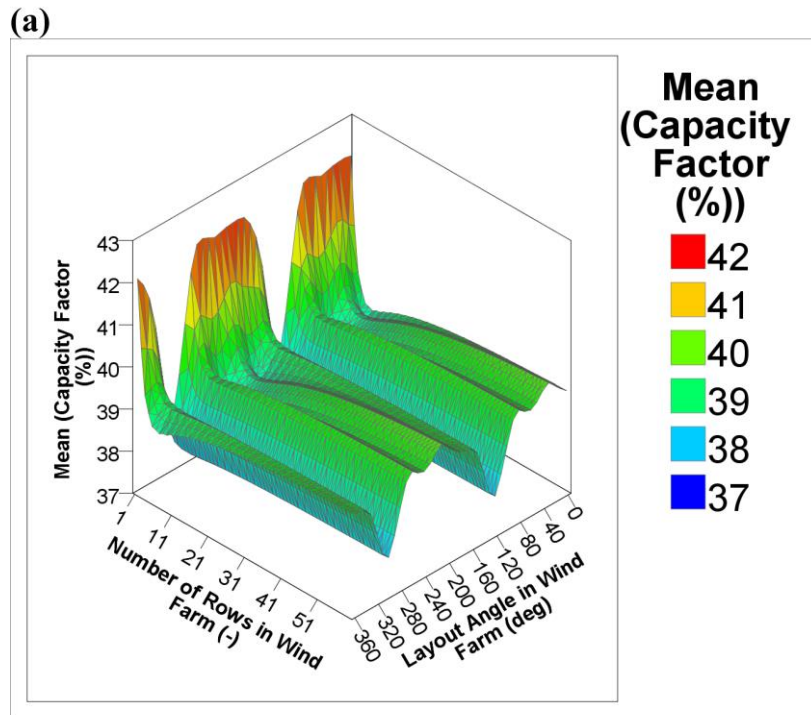


Figure 7. 10 Impact of varying N_r and θ_{plant} on the capacity factor and annual gross energy: (a) for 2220 configurations, (b) for 2220 configurations, and (c) for 60 optimal configurations.

7.4.3. Monthly performance assessment

This section evaluates the Monthly Frequency Profiles (MFPs) of the selected 8 of the 60 optimal configurations (i.e., for categories 1, 2, 3, 4, 40, 46, 52, and 58 of 60) in relation to the Annual Frequency Profiles (AFPs). The optimal selection is based on the LCOE-minimization criterion, and the selected eight optimal configurations are as follows:

- i. the optimal 1-row configuration at 70° ($N_r = 1$ and $\theta_{\text{plant}} = 70^\circ$),
- ii. the optimal 2-row configuration at 30° ($N_r = 2$ and $\theta_{\text{plant}} = 30^\circ$),
- iii. the optimal 3-row configuration at 210° ($N_r = 3$ and $\theta_{\text{plant}} = 210^\circ$),
- iv. the optimal 4-row configuration at 80° ($N_r = 4$ and $\theta_{\text{plant}} = 80^\circ$),
- v. the optimal 40-row configuration at 30° ($N_r = 40$ and $\theta_{\text{plant}} = 30^\circ$),
- vi. the optimal 46-row configuration at 30° ($N_r = 46$ and $\theta_{\text{plant}} = 30^\circ$),
- vii. the optimal 52-row configuration at 210° ($N_r = 52$ and $\theta_{\text{plant}} = 210^\circ$), and
- viii. the optimal 58-row configuration at 210° ($N_r = 58$ and $\theta_{\text{plant}} = 210^\circ$).

It should be recognized that the MFPs of the 12 assessment parameters are shown in Figure 7. 11 to Figure 7. 14 for the January to December months. Additionally, the 12 assessment parameters are listed in the following order from left to right in Figure 7. 11 to Figure 7. 14:

- i. wind speed,
- ii. wind direction,
- iii. ambient temperature,
- iv. atmospheric pressure,
- v. generation of run 421 of 2220: “the optimal 1-row configuration”,
- vi. generation of run 182 of 2220: “the optimal 2-row configuration”,
- vii. generation of run 1263 of 2220: “the optimal 3-row configuration”,
- viii. generation of run 484 of 2220: “the optimal 4-row configuration”,
- ix. generation of run 220 of 2220: “the optimal 40-row configuration”,
- x. generation of run 226 of 2220: “the optimal 46-row configuration”,

- xi. generation of run 1312 of 2220: “the optimal 52-row configuration”, and
- xii. generation of run 1318 of 2220: “the optimal 58-row configuration”.

For each of the 12 assessment parameters, the following applies concerning Figure 7. 11 to Figure 7. 14:

- i. the white areas represent the MFPs,
- ii. the dark-blue areas represent the AFPs, and
- iii. the light-blue areas represent the intersection areas.

Firstly, to understand the MFPs illustrations for the 12 assessment parameters, the ambient temperature parameter (assessment parameter 3 of 12) is chosen. It should be noted that since the summer months have higher temperatures than the winter months, the white areas travel from left to right, then from right to left, starting from January and ending in December. This visual understanding should aid in interpreting the data of the MFPs for the 12 assessment parameters, which are shown in Figure 7. 11 to Figure 7. 14.

Secondly, the following can be observed from Figure 7. 11 to Figure 7. 14 concerning the wind speed (assessment parameter 1 of 12) profiles:

- i. June and July have a wide range of high wind speeds,
- ii. October, November, and December have a narrow range of low wind speeds, and
- iii. the remaining months have mid-range wind speeds close to the annual average.

Thirdly, after considering the results of the LOESS regression analyses for the wind resource (see Figure 7. 4) along with the MFPs (see Figure 7. 11 to Figure 7. 14), the following can be observed concerning the wind direction (assessment parameter 2 of 12) profiles:

- i. June, July, August, and September have concentrated range wind direction close to 318° with high wind speeds, and
- ii. the remaining months have scattered range wind direction at low and high wind speeds.

Fourthly, the following can be observed from Figure 7. 11 to Figure 7. 14 concerning the atmospheric pressure (assessment parameter 4 of 12) profiles, the frequency pattern of the atmospheric pressure is opposite to the ambient temperature (assessment parameter 3 of 12).

Finally, the following can be observed from Figure 7. 11 to Figure 7. 14 concerning assessment parameters 5, 6, 7, 8, 9, 10, 11, and 12 of 12 (generation of the optimal 1, 2, 3, 4, 40, 46, 52, and 58-row configuration, respectively):

- i. for January and March:
the MFPs slightly match the AFPs at the lowest and highest (full load) generation ranges. Also, the MFPs exceed the AFPs in the majority of the moderate generation ranges,
- ii. for February:
the MFPs exceed the AFPs at the highest generation (full load) range,
- iii. for April to May:
the MFPs slightly match the AFPs at the highest (full load) generation range and the majority of the moderate generation ranges. Additionally, the MFPs exceed the AFPs at the lowest generation range,
- iv. for June to July:
the MFPs exceed the AFPs at the highest (full load) generation range and upper-moderate generation ranges,
- v. for August:
the MFPs exceed the AFPs in the majority of the moderate generation ranges. Moreover, the MFPs perfectly match the AFPs at the lowest generation range,
- vi. for September:
the MFPs perfectly match the AFPs at the highest (full load) generation range. Additionally, the MFPs exceed the AFPs in the majority of the moderate generation ranges. Also, the MFPs slightly match the AFPs at the lowest generation range,
- vii. for October to December:
the MFPs exceed the AFPs at the lowest generation range,

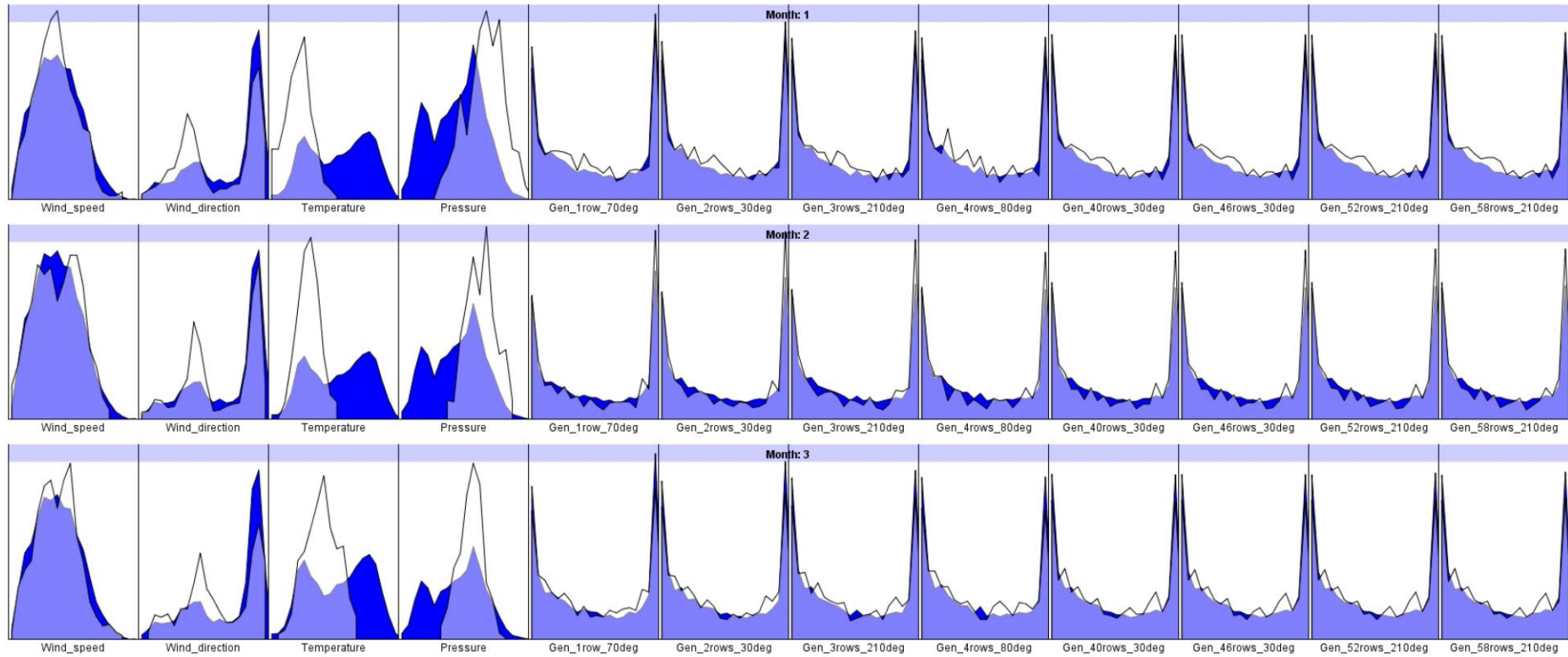


Figure 7. 11 MFPs and AFPs with their intersection areas (January to March months) for assessment parameters 1 to 12, namely from left to right, wind speed, wind direction, ambient temperature, atmospheric pressure, and generation of the selected 8 of the 60 optimal configurations (the optimal 1, 2, 3, 4, 40, 46, 52, and 58-row configurations): (i) MFPs (white areas), (ii) AFPs (dark-blue areas), and (iii) intersection areas (light-blue areas).

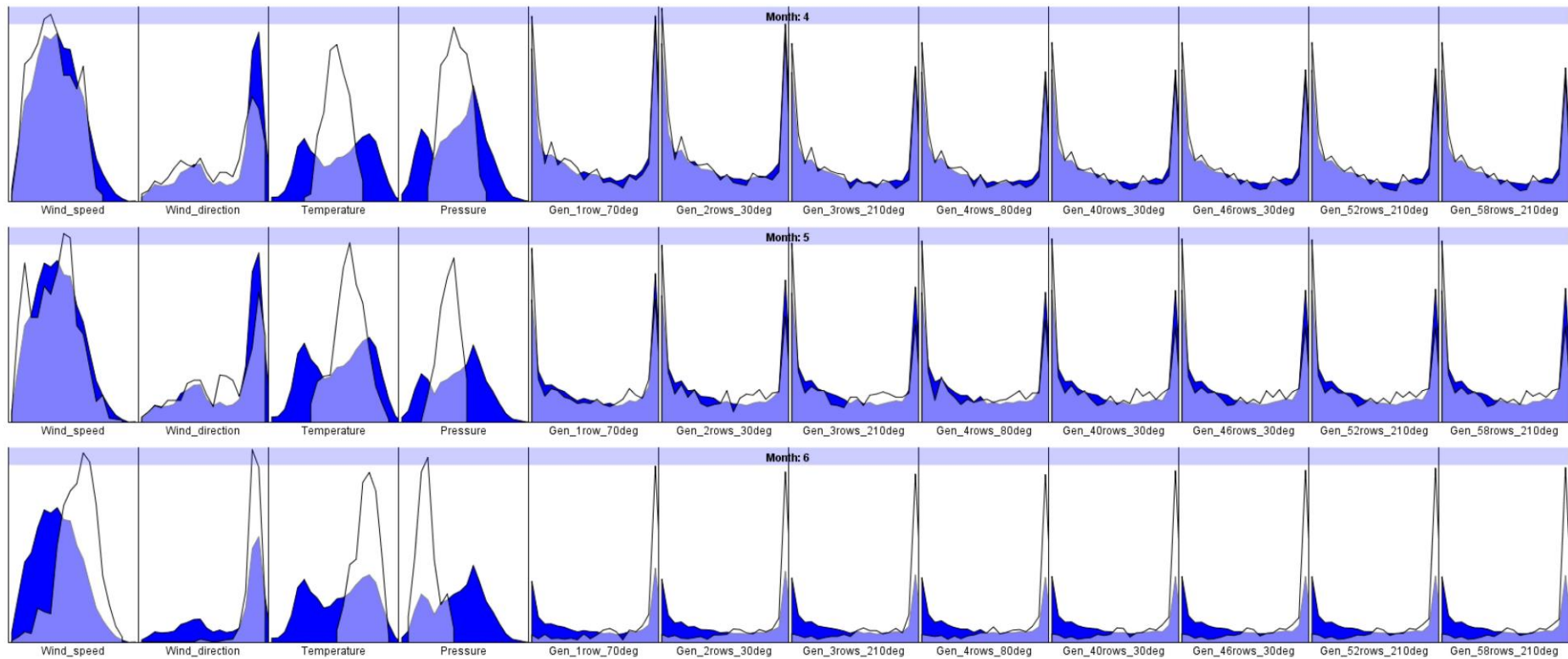


Figure 7. 12 MFPs and AFPs with their intersection areas (April to June months) for assessment parameters 1 to 12, namely from left to right, wind speed, wind direction, ambient temperature, atmospheric pressure, and generation of the selected 8 of the 60 optimal configurations (the optimal 1, 2, 3, 4, 40, 46, 52, and 58-row configurations): (i) MFPs (white areas), (ii) AFPs (dark-blue areas), and (iii) intersection areas (light-blue areas).

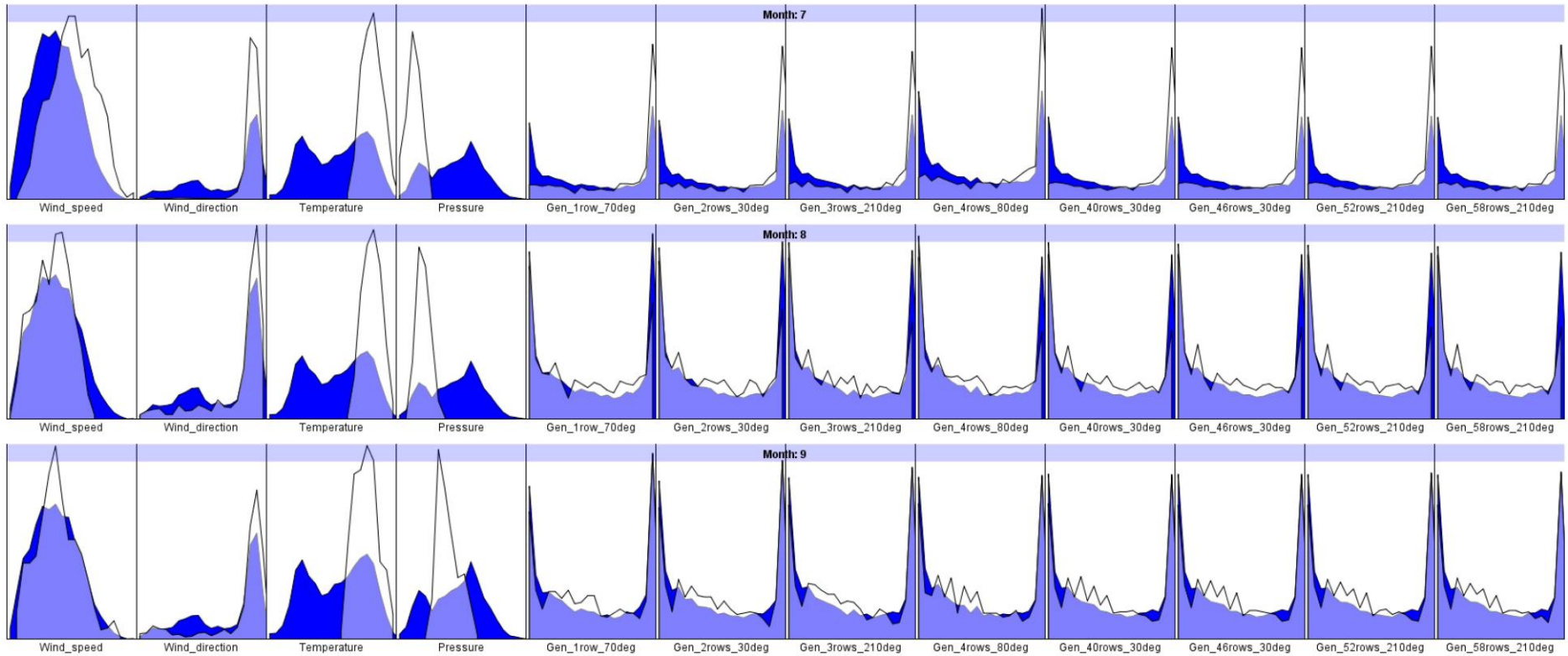


Figure 7. 13 MFPs and AFPs with their intersection areas (July to September months) for assessment parameters 1 to 12, namely from left to right, wind speed, wind direction, ambient temperature, atmospheric pressure, and generation of the selected 8 of the 60 optimal configurations (the optimal 1, 2, 3, 4, 40, 46, 52, and 58-row configurations): (i) MFPs (white areas), (ii) AFPs (dark-blue areas), and (iii) intersection areas (light-blue areas).

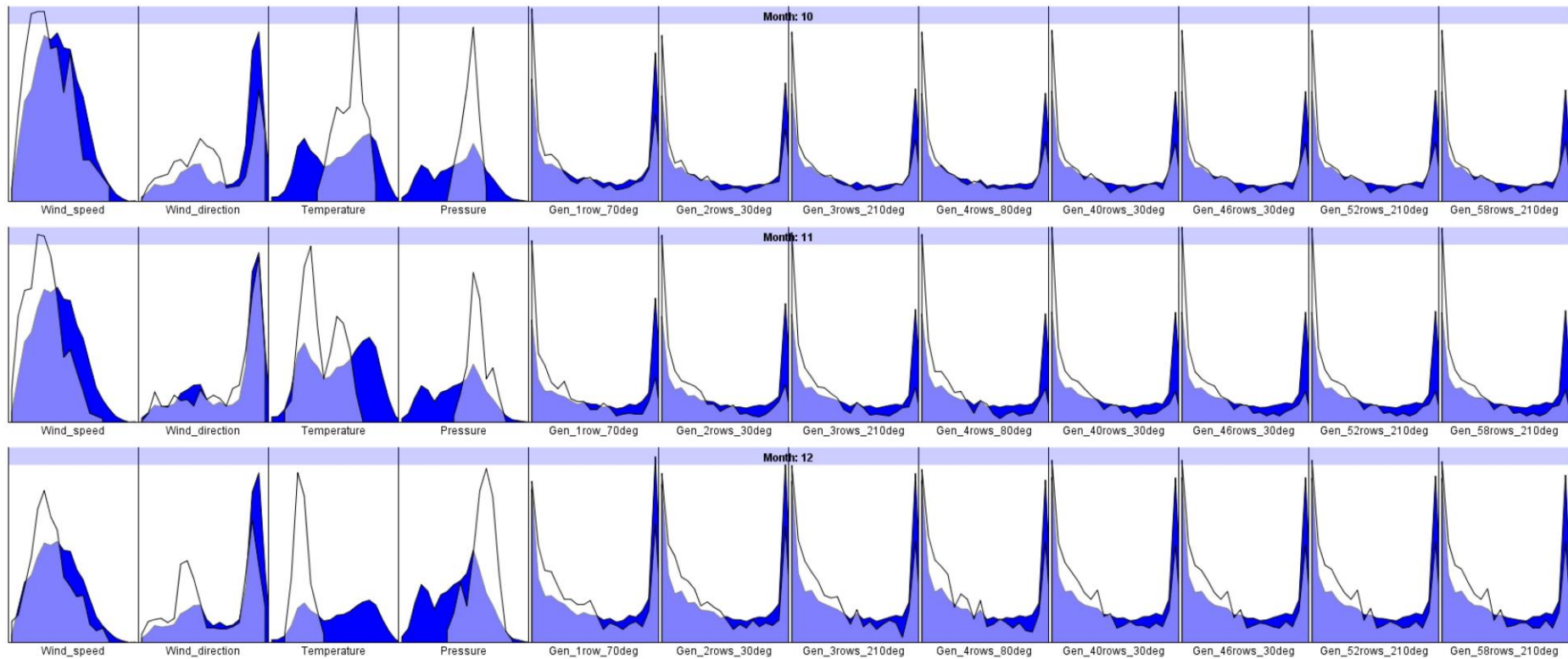


Figure 7. 14 MFPs and AFPs with their intersection areas (October to December months) for assessment parameters 1 to 12, namely from left to right, wind speed, wind direction, ambient temperature, atmospheric pressure, and generation of the selected 8 of the 60 optimal configurations (the optimal 1, 2, 3, 4, 40, 46, 52, and 58-row configurations): (i) MFPs (white areas), (ii) AFPs (dark-blue areas), and (iii) intersection areas (light-blue areas).

7.4.4. Hourly performance assessment

This section evaluates the Hourly Frequency Profiles (HFPs) of the selected 8 of the 60 optimal configurations (i.e., for categories 1, 2, 3, 4, 40, 46, 52, and 58 of 60) in relation to the Annual Frequency Profiles (AFPs). The optimal selection is based on the LCOE-minimization criterion, and the selected eight optimal configurations are previously explained in Section 7.4.3. It should be recognized that the HFPs of the 12 assessment parameters are shown in Figure 7. 15 to Figure 7. 22 for the 00:00 to 23:00 hours in the same order explained in Section 7.4.3. For each of the 12 assessment parameters, the following applies concerning Figure 7. 15 to Figure 7. 22:

- i. the white areas represent the HFPs,
- ii. the dark-red areas represent the AFPs, and
- iii. the light-red areas represent the intersection areas.

Firstly, to understand the HFPs illustrations for the 12 assessment parameters in Figure 7. 15 to Figure 7. 22, the ambient temperature parameter (assessment parameter 3 of 12) is chosen. It should be recognized that since most day hours have higher temperatures than night hours, the white area travels from left to right, then from right to left, starting from the daytime and ending with the nighttime. This visual understanding should aid in interpreting the data of the HFPs for the 12 assessment parameters, which are shown in Figure 7. 15 to Figure 7. 22.

Secondly, the following can be observed from Figure 7. 15 to Figure 7. 22 concerning the wind speed (assessment parameter 1 of 12) profiles:

- i. the HFPs of the hours from 00:00 to 05:00 and 18:00 to 23:00 reach upper-high wind speed ranges, and
- ii. the HFPs of the hours from 06:00 to 17:00 stay within moderate wind speed ranges.

Thirdly, after considering the results of the LOESS regression analyses for the wind resource (see Figure 7. 4) along with the HFPs (see Figure 7. 15 to Figure 7. 22), the following can be observed concerning the wind direction (assessment parameter 2 of 12) profiles:

- i. the HFPs of hours from 00:00 to 23:00 have a high concentrated range wind direction close to 318° with high wind speeds, and

- ii. the HFPs of hours from 00:00 to 23:00 have a low concentrated range wind direction close to 150° with high wind speeds.

Fourthly, the following can be clearly observed from Figure 7. 15 to Figure 7. 22 concerning the atmospheric pressure (assessment parameter 4 of 12) profiles, the frequency pattern of the atmospheric pressure is opposite to the ambient temperature (assessment parameter 3 of 12).

Finally, the following can be observed from Figure 7. 15 to Figure 7. 22 concerning assessment parameters 5, 6, 7, 8, 9, 10, 11, and 12 of 12 (generation of the optimal 1, 2, 3, 4, 40, 46, 52, and 58-row configuration, respectively):

- i. for the 00:00 to 01:00 (early-day) hours:
the HFPs exceed the AFPs at the highest (full load) generation range and the majority of the moderate generation ranges,
- ii. for the 03:00 to 06:00 (early-day) hours:
the HFPs match the AFPs at the highest (full load) generation range and upper-moderate generation ranges, and
- iii. for the 18:00 to 23:00 (late-night) hours:
the HFPs exceed the AFPs at the highest (full load) generation range and upper-moderate generation ranges.

7.4.5. Full load generation at rated wind speed

This section evaluates the full load generation at the rated wind speed according to the wind turbine specifications (see Figure 7. 2) for the selected 8 of the 60 optimal configurations (i.e., for categories 1, 2, 3, 4, 40, 46, 52, and 58 of 60). Figure 7. 23 and Figure 7. 24 show that the optimal 1-row configuration (category 1 of 60) has the highest full load generation at the rated wind speed due to having the slightest wind disturbance and wake losses as it corresponds to a 1-row configuration (single row). It can be observed that the full load generation at the rated wind speed decreases as the N_r value increases. Furthermore, it can be observed that the full load generation at the rated wind speed is independent of θ_{plant} . It is concluded that the order from highest to lowest full load generation at the rated wind speed is as follows: the optimal 1, 2, 3, 4, 40, 46, 52, and 58-row configuration, respectively.

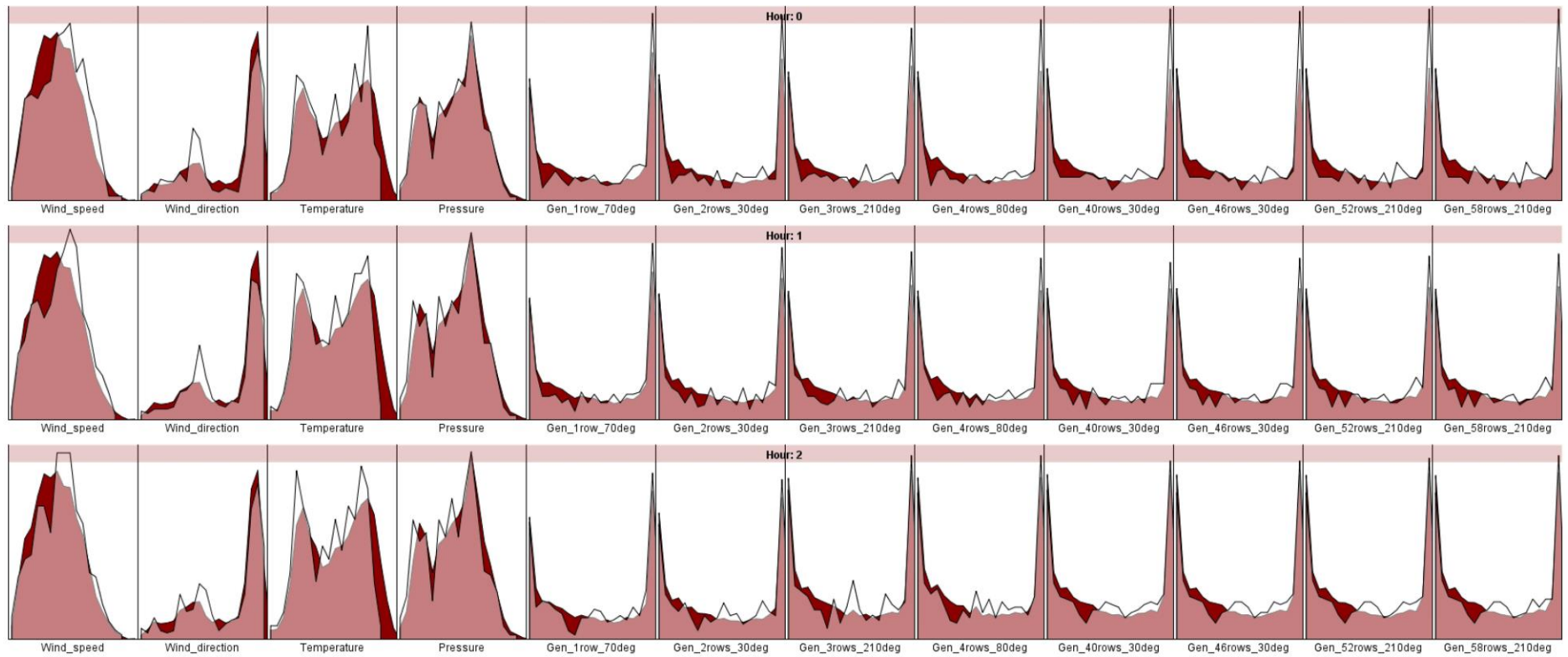


Figure 7. 15 HFPs and AFPs with their intersection areas (00:00 to 02:00 hours) for assessment parameters 1 to 12, namely from left to right, wind speed, wind direction, ambient temperature, atmospheric pressure, and generation of the selected 8 of the 60 optimal configurations (the optimal 1, 2, 3, 4, 40, 46, 52, and 58-row configurations): (i) HFPs (white areas), (ii) AFPs (dark-red areas), and (iii) intersection areas (light-red areas).

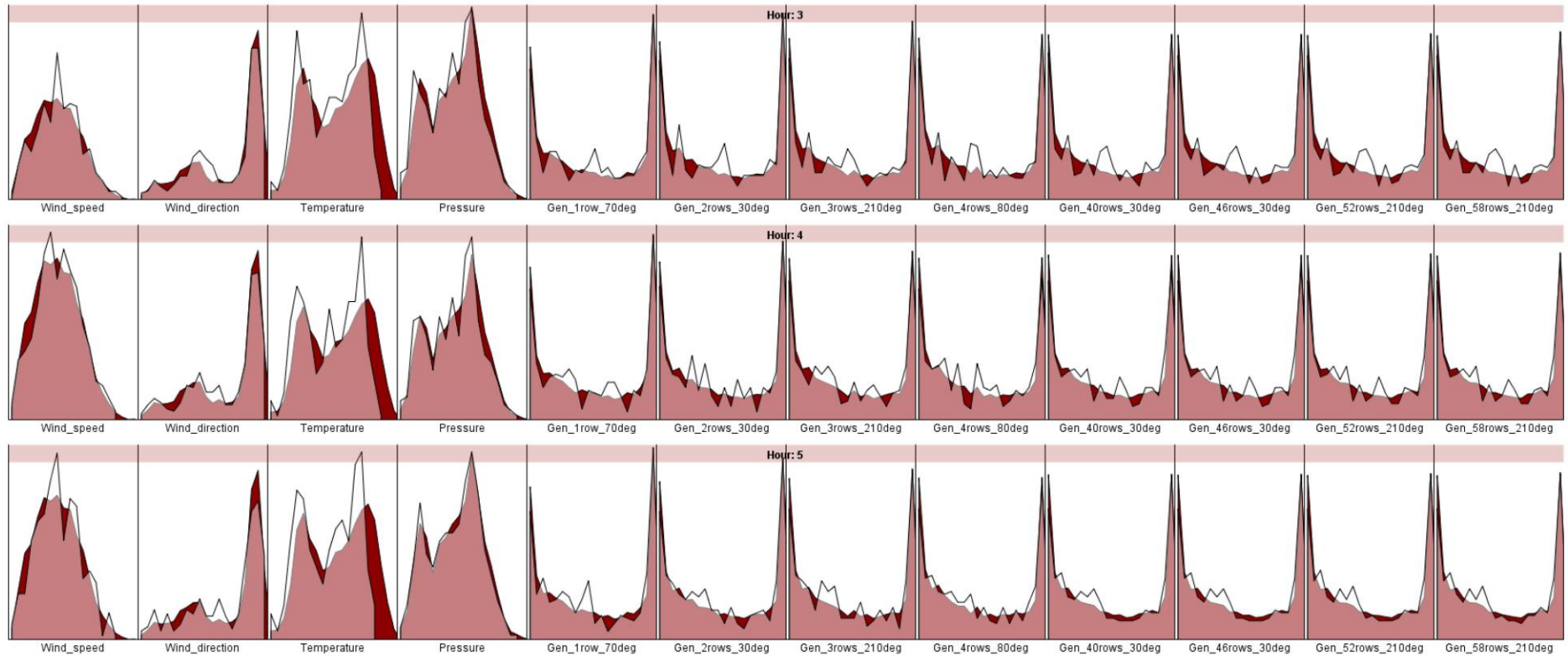


Figure 7. 16 HFPs and AFPs with their intersection areas (03:00 to 05:00 hours) for assessment parameters 1 to 12, namely from left to right, wind speed, wind direction, ambient temperature, atmospheric pressure, and generation of the selected 8 of the 60 optimal configurations (the optimal 1, 2, 3, 4, 40, 46, 52, and 58-row configurations): (i) HFPs (white areas), (ii) AFPs (dark-red areas), and (iii) intersection areas (light-red areas).

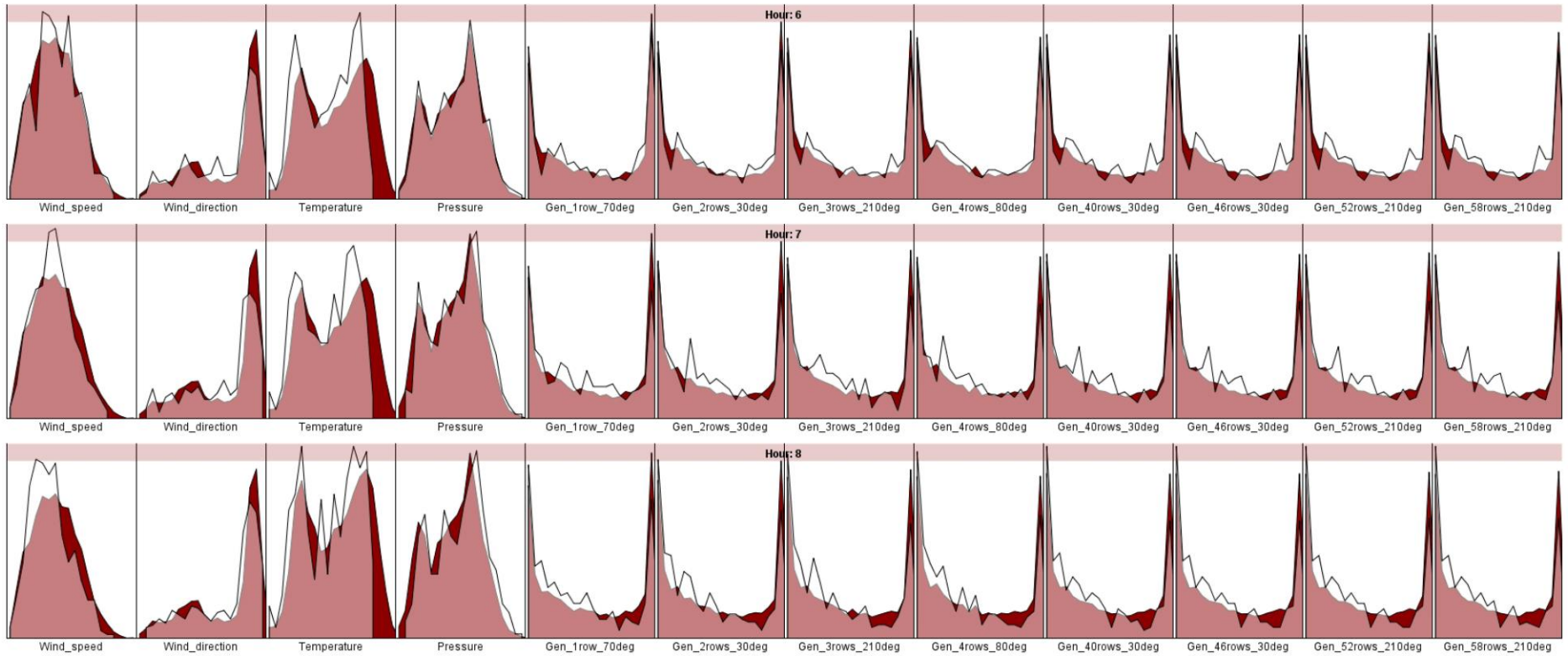


Figure 7. 17 HFPs and AFPs with their intersection areas (06:00 to 08:00 hours) for assessment parameters 1 to 12, namely from left to right, wind speed, wind direction, ambient temperature, atmospheric pressure, and generation of the selected 8 of the 60 optimal configurations (the optimal 1, 2, 3, 4, 40, 46, 52, and 58-row configurations): (i) HFPs (white areas), (ii) AFPs (dark-red areas), and (iii) intersection areas (light-red areas).

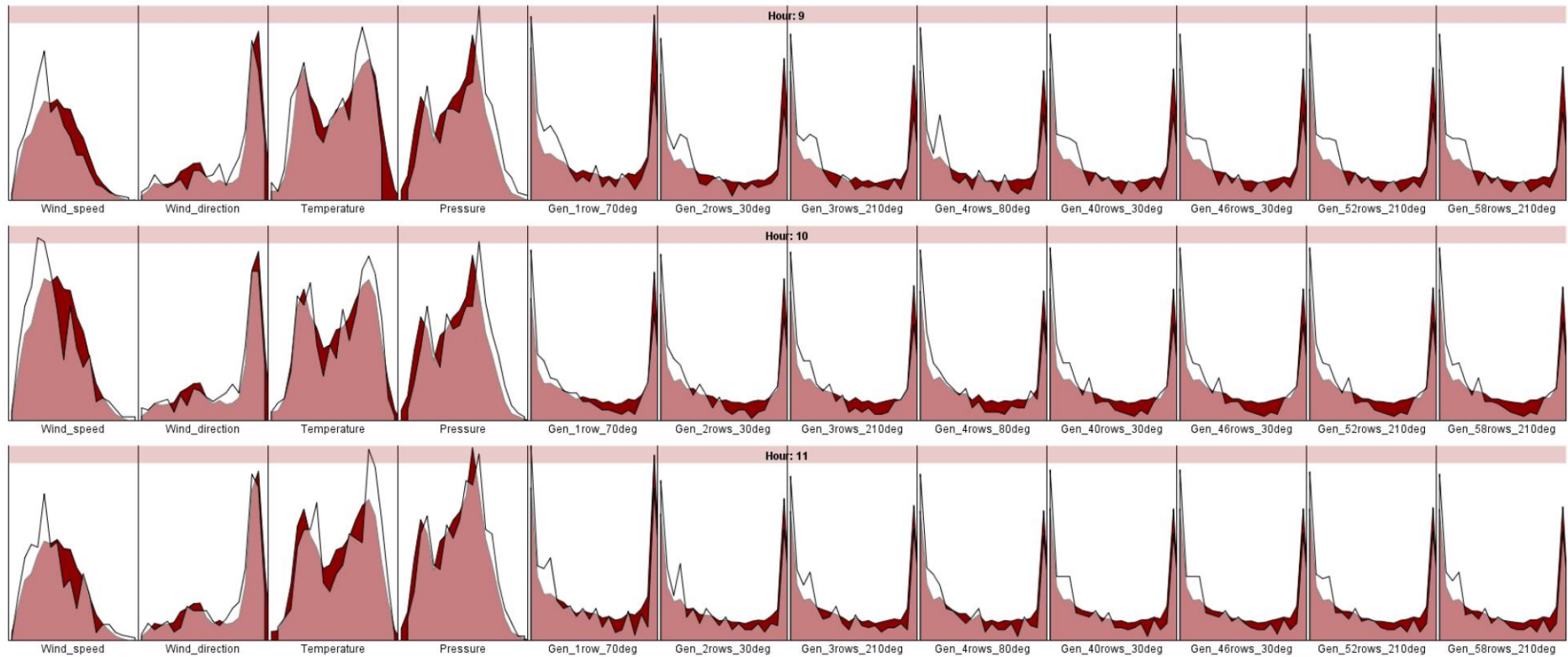


Figure 7.18 HFPs and AFPs with their intersection areas (09:00 to 11:00 hours) for assessment parameters 1 to 12, namely from left to right, wind speed, wind direction, ambient temperature, atmospheric pressure, and generation of the selected 8 of the 60 optimal configurations (the optimal 1, 2, 3, 4, 40, 46, 52, and 58-row configurations): (i) HFPs (white areas), (ii) AFPs (dark-red areas), and (iii) intersection areas (light-red areas).

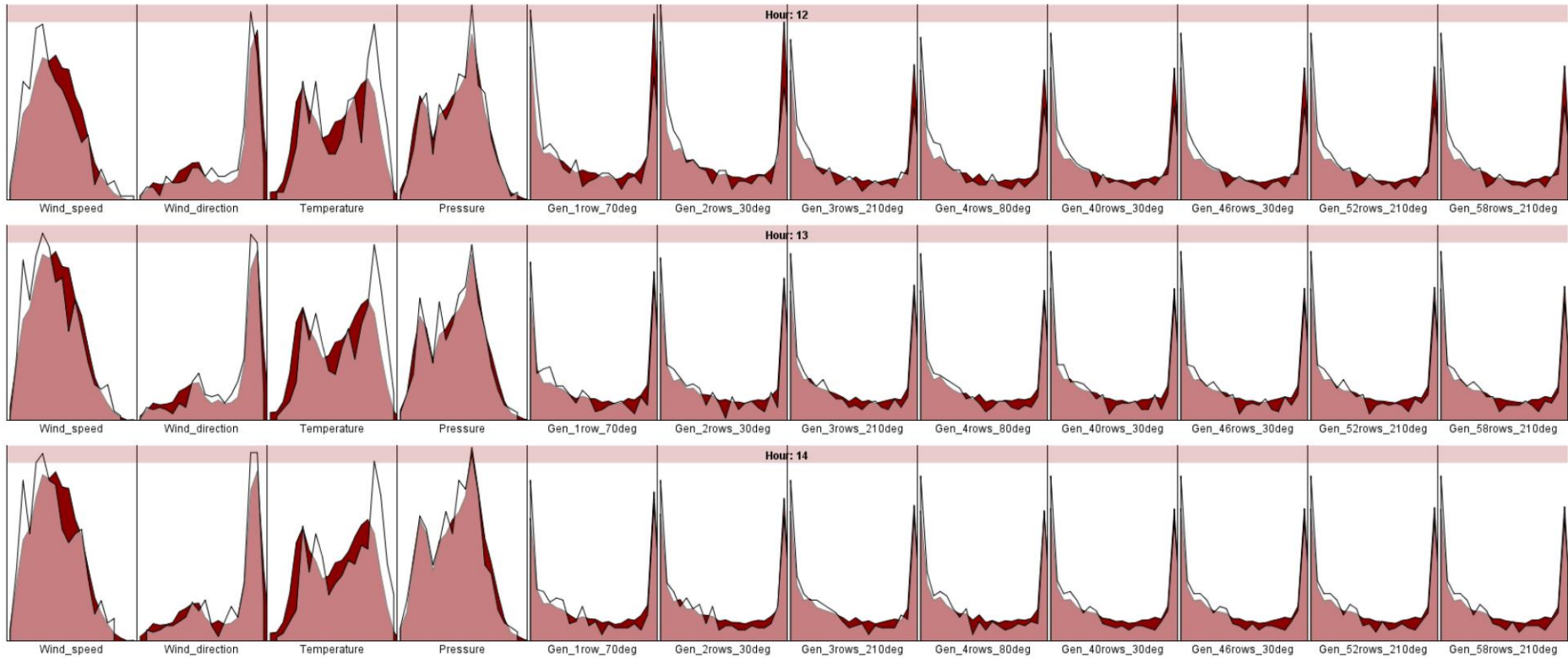


Figure 7.19 HFPs and AFPs with their intersection areas (12:00 to 14:00 hours) for assessment parameters 1 to 12, namely from left to right, wind speed, wind direction, ambient temperature, atmospheric pressure, and generation of the selected 8 of the 60 optimal configurations (the optimal 1, 2, 3, 4, 40, 46, 52, and 58-row configurations): (i) HFPs (white areas), (ii) AFPs (dark-red areas), and (iii) intersection areas (light-red areas).

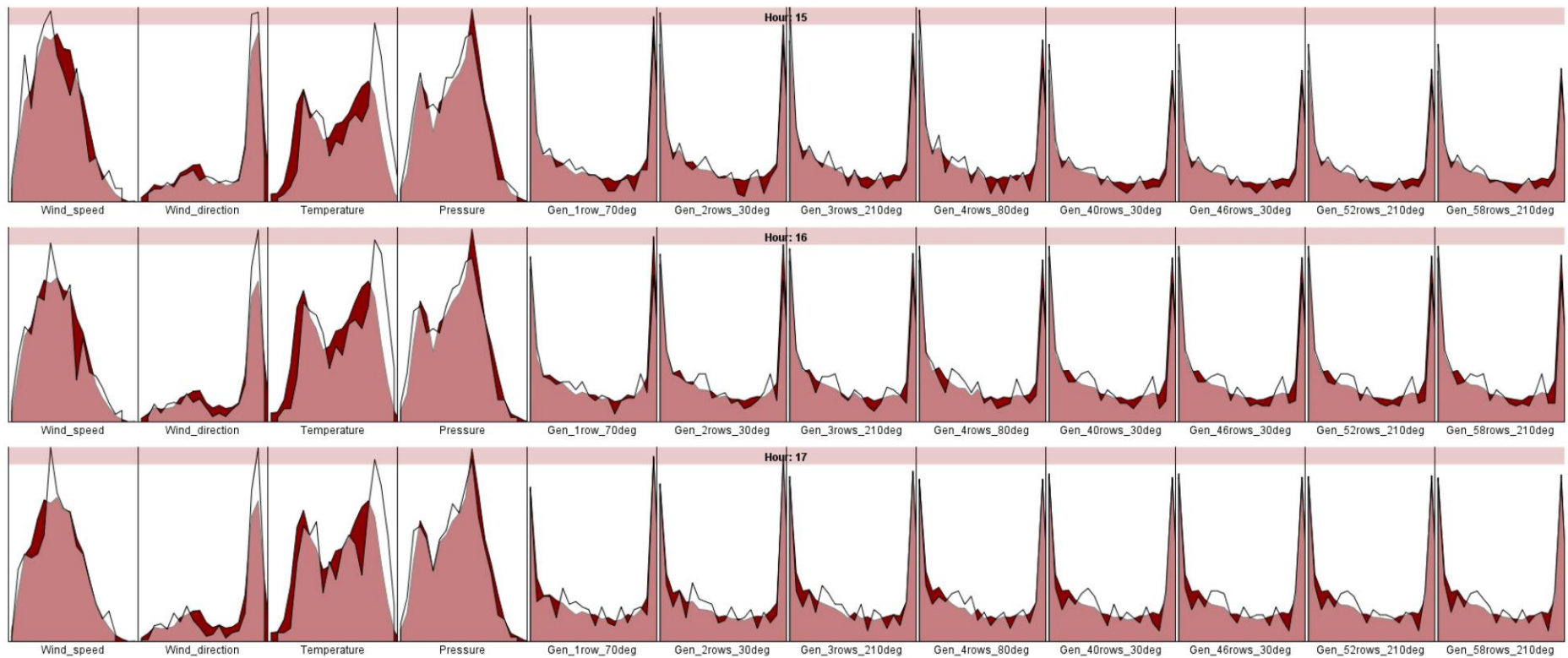


Figure 7. 20 HFPs and AFPs with their intersection areas (15:00 to 17:00 hours) for assessment parameters 1 to 12, namely from left to right, wind speed, wind direction, ambient temperature, atmospheric pressure, and generation of the selected 8 of the 60 optimal configurations (the optimal 1, 2, 3, 4, 40, 46, 52, and 58-row configurations): (i) HFPs (white areas), (ii) AFPs (dark-red areas), and (iii) intersection areas (light-red areas).

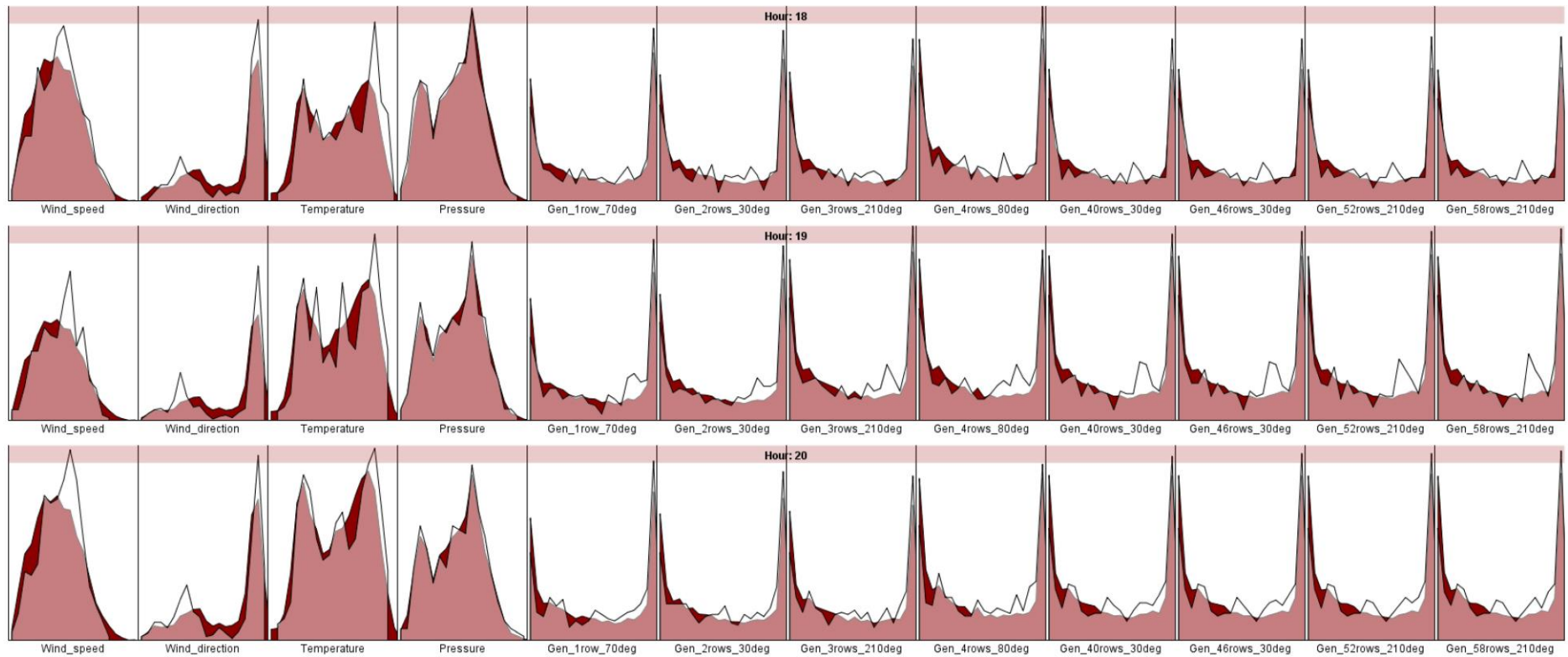


Figure 7. 21 HFPs and AFPs with their intersection areas (18:00 to 20:00 hours) for assessment parameters 1 to 12, namely from left to right, wind speed, wind direction, ambient temperature, atmospheric pressure, and generation of the selected 8 of the 60 optimal configurations (the optimal 1, 2, 3, 4, 40, 46, 52, and 58-row configurations): (i) HFPs (white areas), (ii) AFPs (dark-red areas), and (iii) intersection areas (light-red areas).

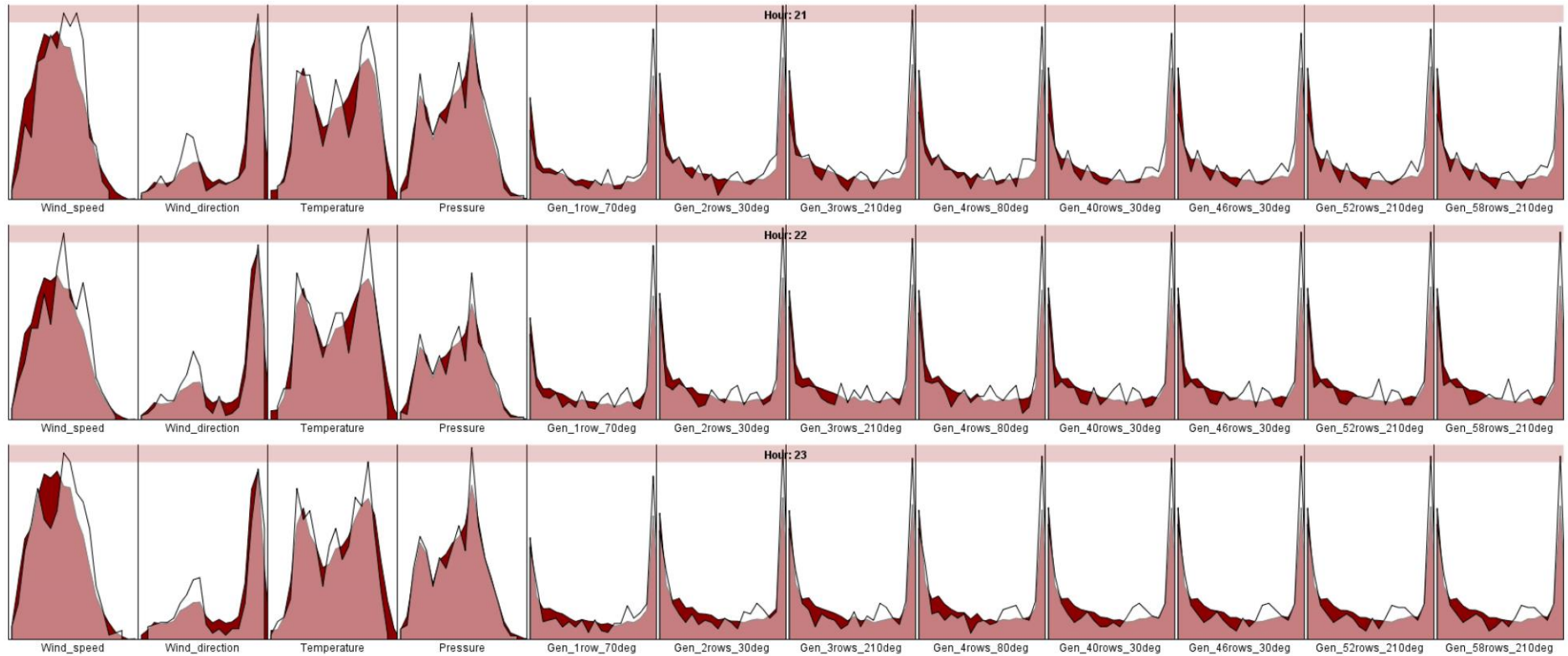
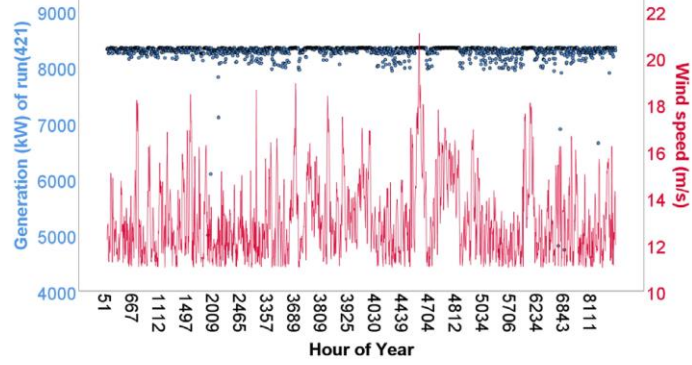
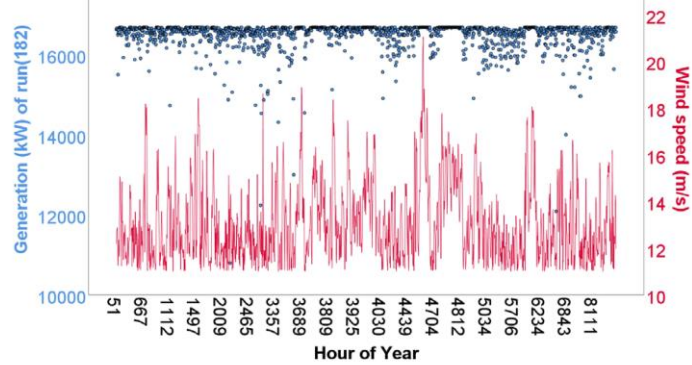


Figure 7. 22 HFPs and AFPs with their intersection areas (21:00 to 23:00 hours) for assessment parameters 1 to 12, namely from left to right, wind speed, wind direction, ambient temperature, atmospheric pressure, and generation of the selected 8 of the 60 optimal configurations (the optimal 1, 2, 3, 4, 40, 46, 52, and 58-row configurations): (i) HFPs (white areas), (ii) AFPs (dark-red areas), and (iii) intersection areas (light-red areas).

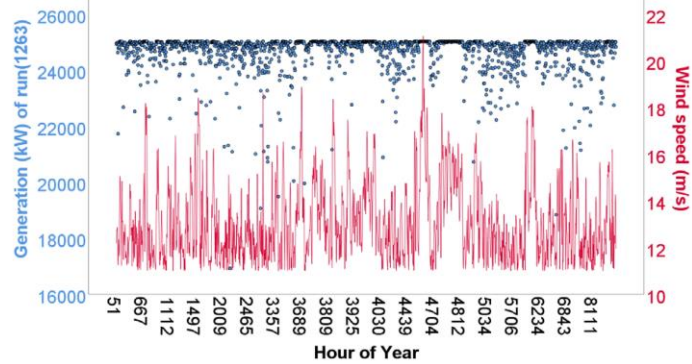
The optimal 1-row configuration (i.e., at 70-degree layout)



The optimal 2-row configuration (i.e., at 30-degree layout)



The optimal 3-row configuration (i.e., at 210-degree layout)



The optimal 4-row configuration (i.e., at 80-degree layout)

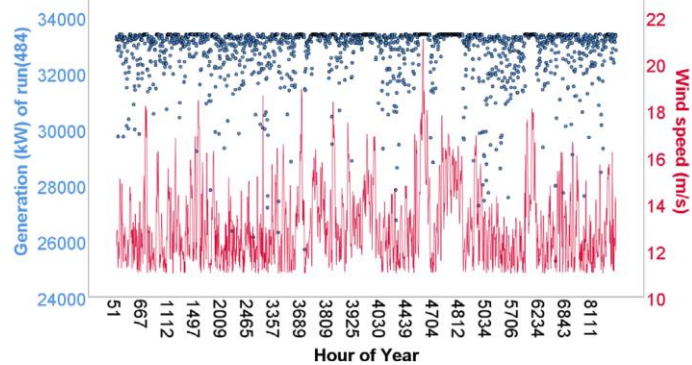
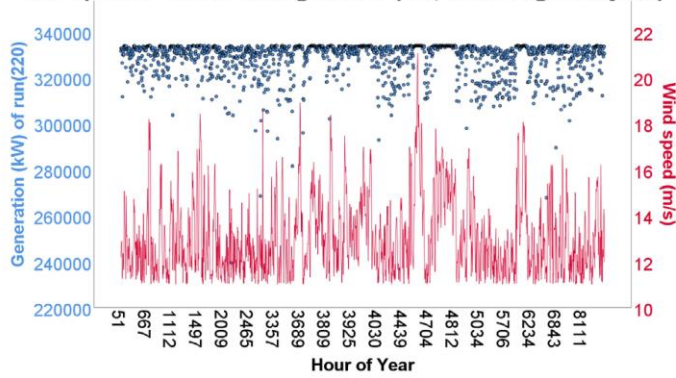
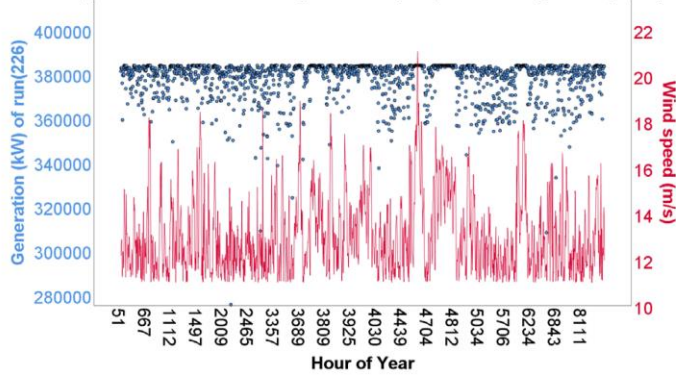


Figure 7. 23 Full load generation at the rated wind speed for selected 4 of the 60 optimal configurations (the optimal 1, 2, 3, and 4-row configurations) – (optimal low row-count configurations).

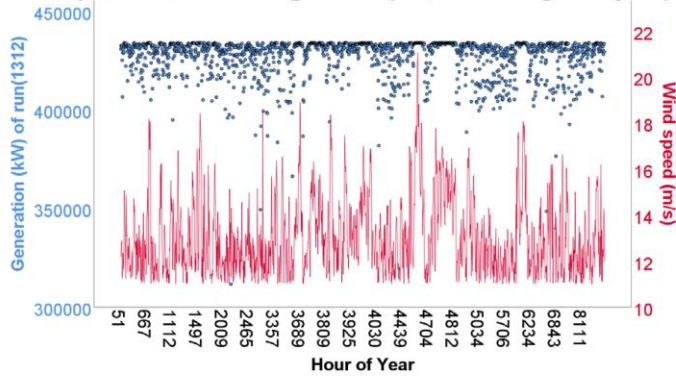
The optimal 40-row configuration (i.e., at 30-degree layout)



The optimal 46-row configuration (i.e., at 30-degree layout)



The optimal 52-row configuration (i.e., at 210-degree layout)



The optimal 58-row configuration (i.e., at 210-degree layout)

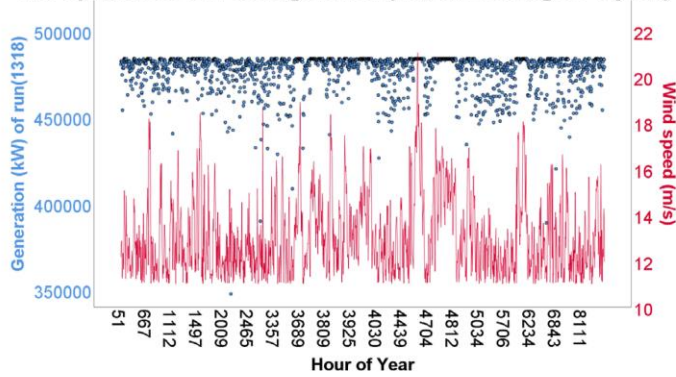


Figure 7. 24 Full load generation at the rated wind speed for selected 4 of the 60 optimal configurations (the optimal 40, 46, 52, and 58-row configurations) – (optimal high row-count configurations).

7.4.6. Economic analysis

This section performs an economic assessment for the 60 optimal configurations of the wind power plants based on the LCOE-minimization criterion. The impact of varying N_r and θ_{plant} on the financial indicators for these configurations is assessed. The following indicators are evaluated for the selected 8 of the 60 optimal configurations (i.e., several designs of mega-scale wind power plants): (i) the installed cost per watt, (ii) the present value of annual energy, (iii) the net present value (annual costs) with relation to annual energy and annual gross energy, (iv) the internal rate of return at the end of the analysis period, (v) the project return (after-tax project maximum internal rate of return), (vi) the required Power Purchase Agreement (PPA) price, (vii) the flip actual percentage, (viii) the flip target percentage, (ix) the flip target year, and (x) the cash flow over the project lifetime.

Figure 7. 25 shows the installed cost per watt as a function of N_r for the 60 optimal configurations. For the selected 8 of the 60 optimal configurations, the corresponding installed costs are as follows: 2.0616, 2.0386, 2.0312, 2.0275, 2.0166, 2.0165, 2.0163, 2.0162 \$/W, which correspond to the LCOE values of 5.76734, 5.94352, 6.0849, 6.15907, 6.08697, 6.0745, 6.06462, 6.05662 ¢/kWh, respectively. From the analysis results, it can be concluded that there exists an exponential relation between the installed cost per watt and N_r .

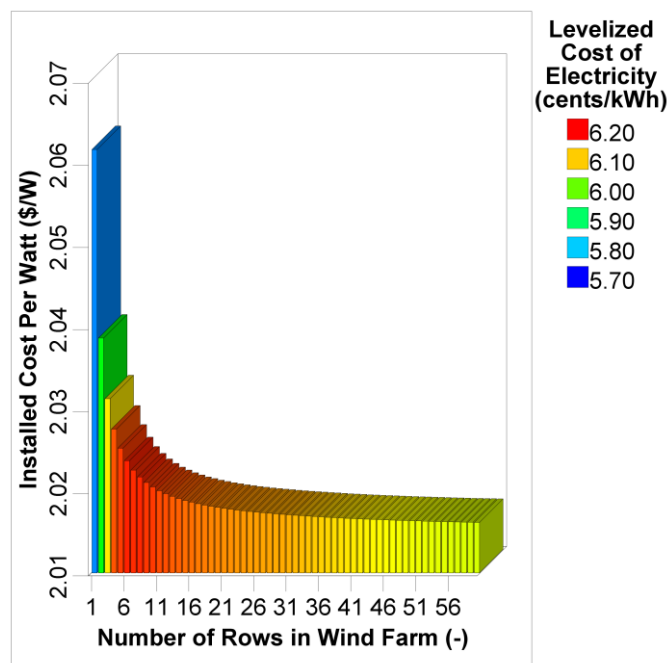


Figure 7. 25 The installed cost per watt as a function of N_r for the 60 optimal configurations of wind power plants (the optimal 1-row to 60-row configurations from left to right).

Figure 7. 26 shows the present value of annual energy, the net present value (annual costs), the annual energy, and the annual gross energy as a function of N_r for the 60 optimal configurations. It is clear that these have increasing linear trends as N_r increases. Thus, there exist linear relations between these and N_r . Figure 7. 27 shows the internal rate of return at the end of the analysis period (25 years), the project return (i.e., after-tax project maximum internal rate of return), and the required PPA price. Figure 7. 28 shows multiple profiles for the 60 optimal design configurations of the wind power plants: the flip actual percentage, the flip target percentage, and the flip target year. Figure 7. 29 to Figure 7. 31 show the cash flow over the project lifetime (25 years) for the selected 8 of the 60 optimal configurations (i.e., for categories 1, 2, 3, 4, 40, 46, 52, and 58 of 60). The optimal configurations demonstrated the profitability during the lifetime of these projects except for the initial year due to the capital expenses. It is revealed that the optimal configurations require a PPA price of at least 7.03 ¢/kWh to make a positive return on investment.

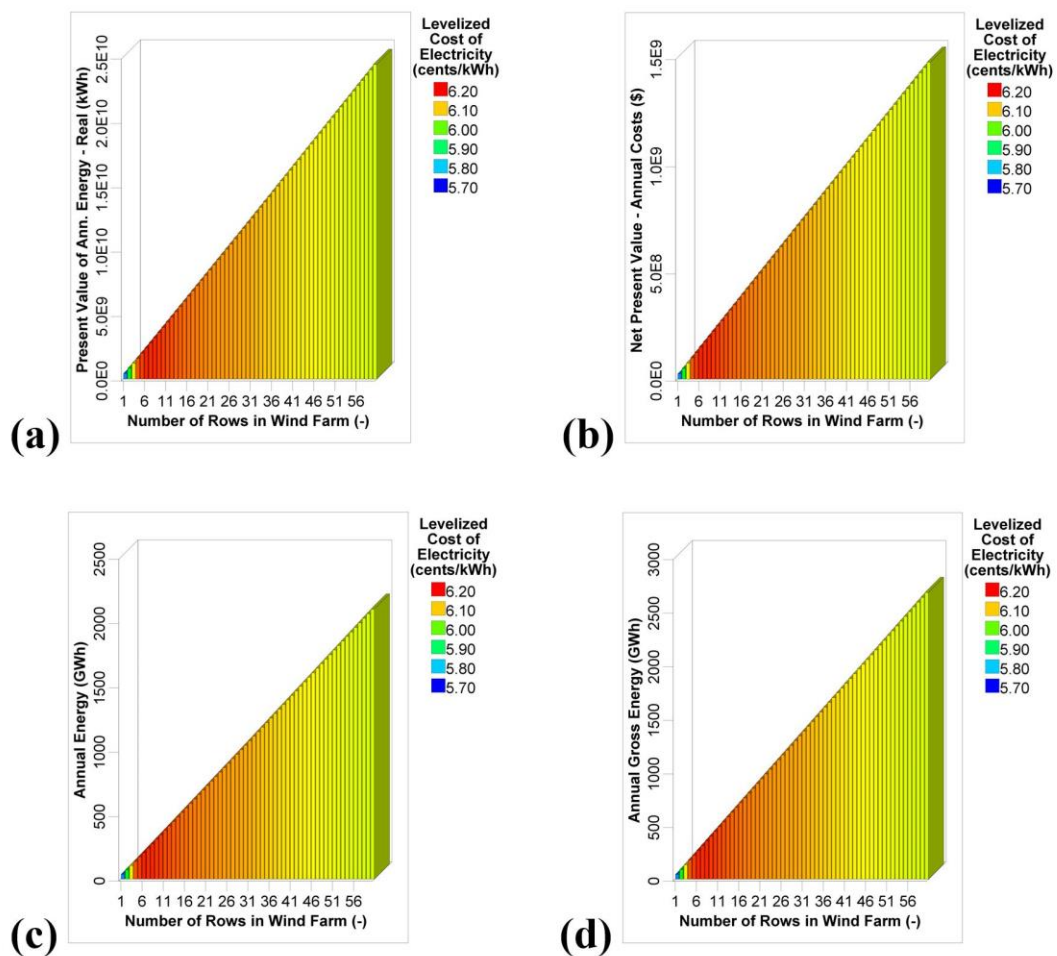


Figure 7. 26 Multiple profiles for the 60 optimal configurations (the optimal 1-row to 60-row configurations from left to right): (a) the present value of annual energy, (b) the net present value (annual costs), (c) the annual energy, and (d) the annual gross energy.

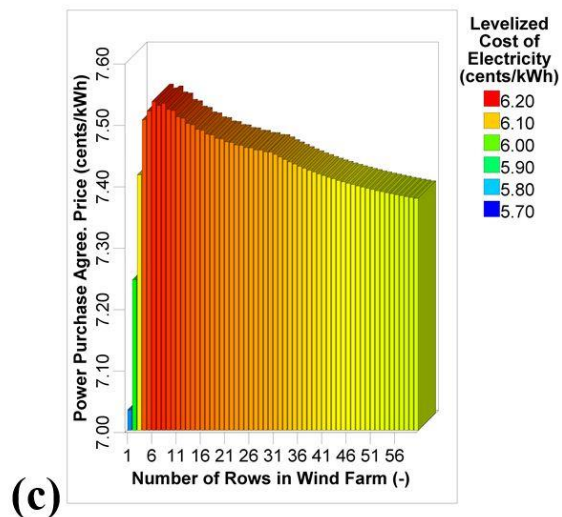
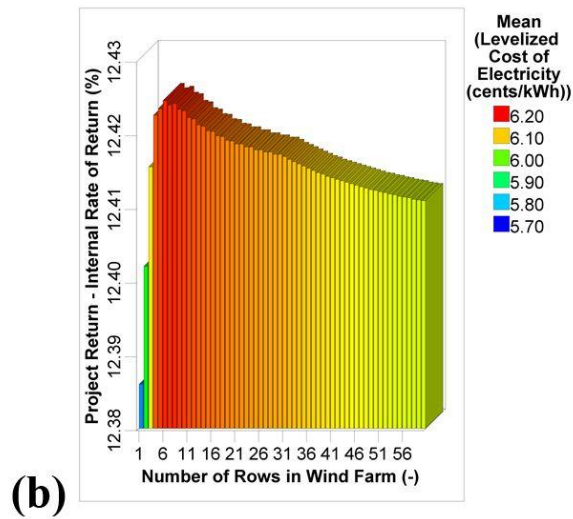
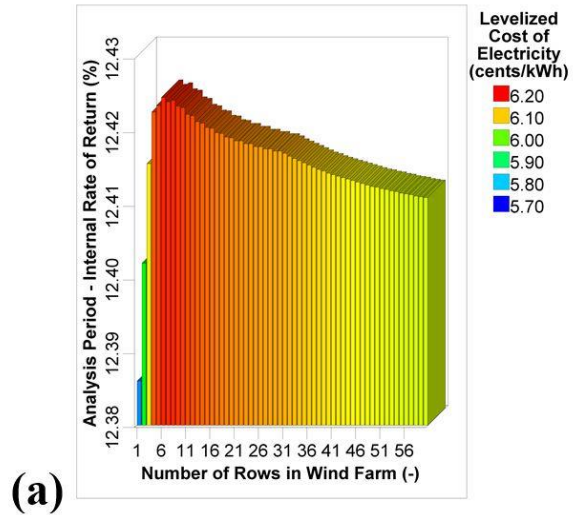


Figure 7. 27 Multiple profiles for the 60 optimal design configurations of (the optimal 1-row to 60-row configurations from left to right): (a) the internal rate of return at the end of the analysis period (i.e., 25 years), (b) the project return (i.e., after-tax project maximum internal rate of return), and (c) the required PPA price.

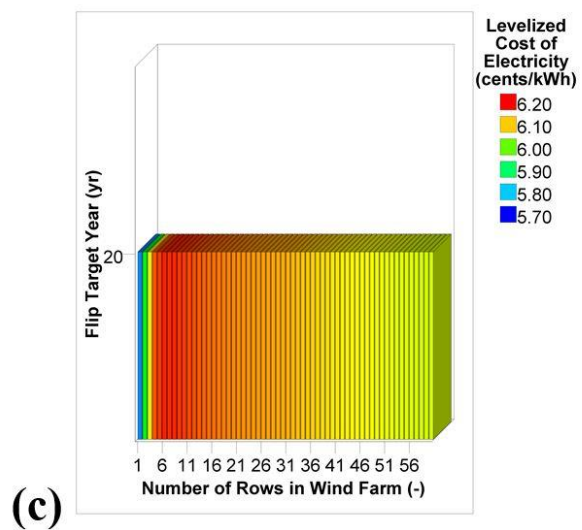
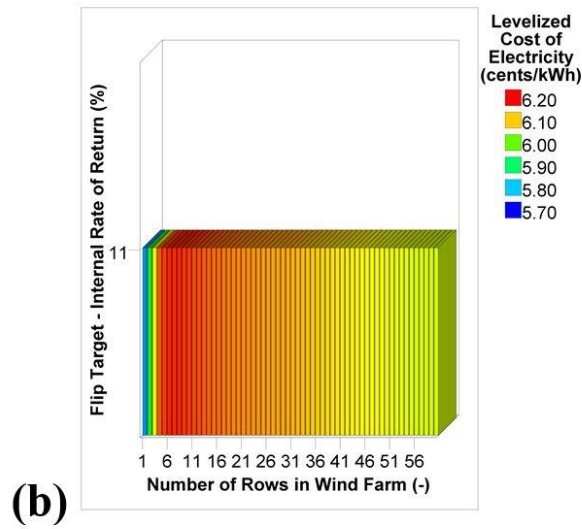
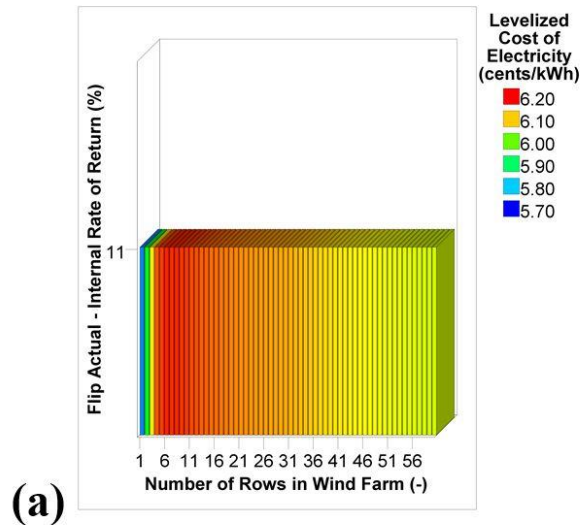


Figure 7. 28 Multiple profiles for the 60 optimal design configurations (the optimal 1-row to 60-row configurations from left to right): (a) the flip actual percentage, (b) the flip target percentage, and (c) the flip target year.

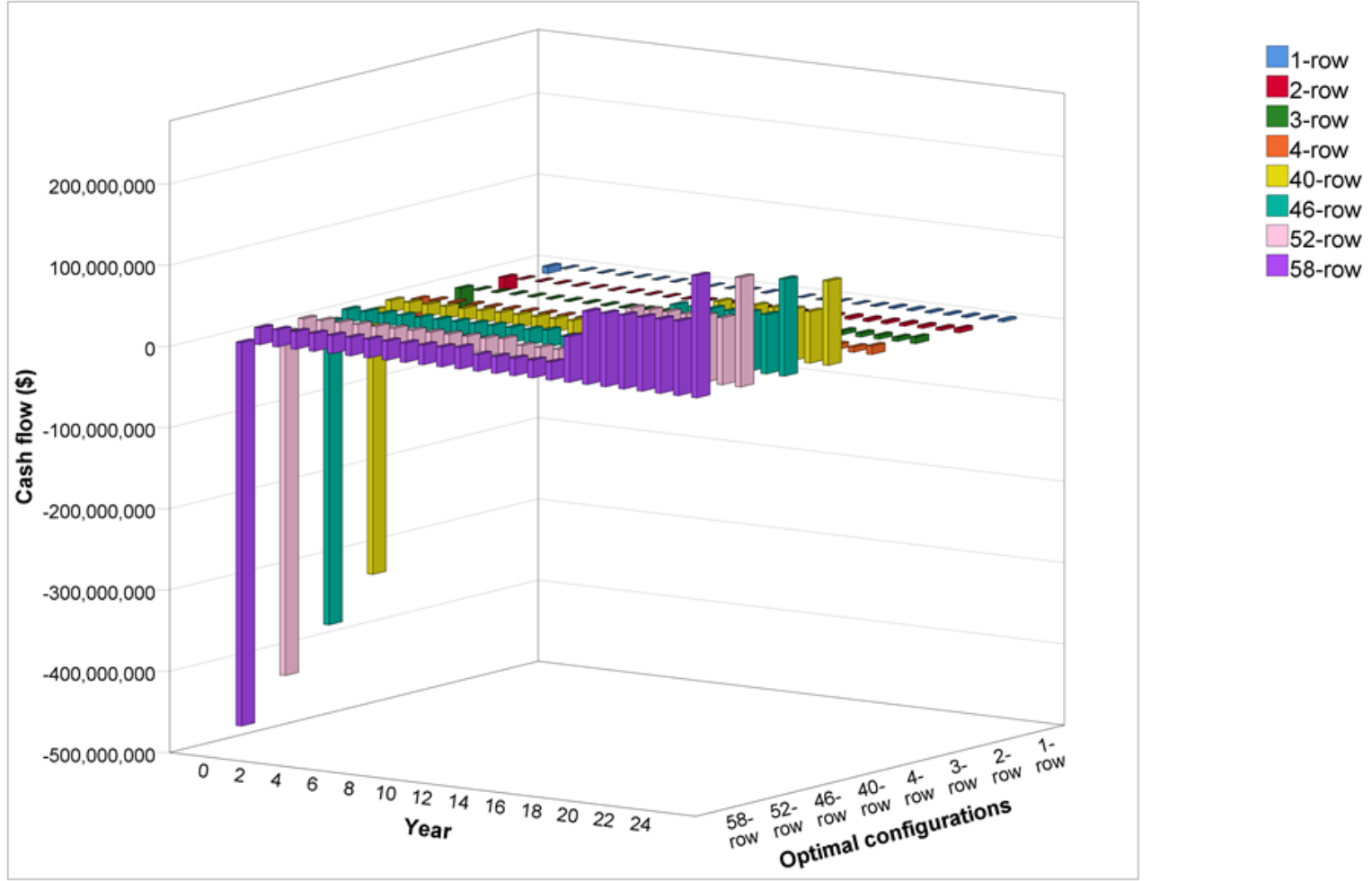


Figure 7. 29 Illustration (3D) of the cash flow over the project lifetime (25 years) for the selected 8 of the 60 optimal configurations (the optimal 1, 2, 3, 4, 40, 46, 52, and 58-row configurations).

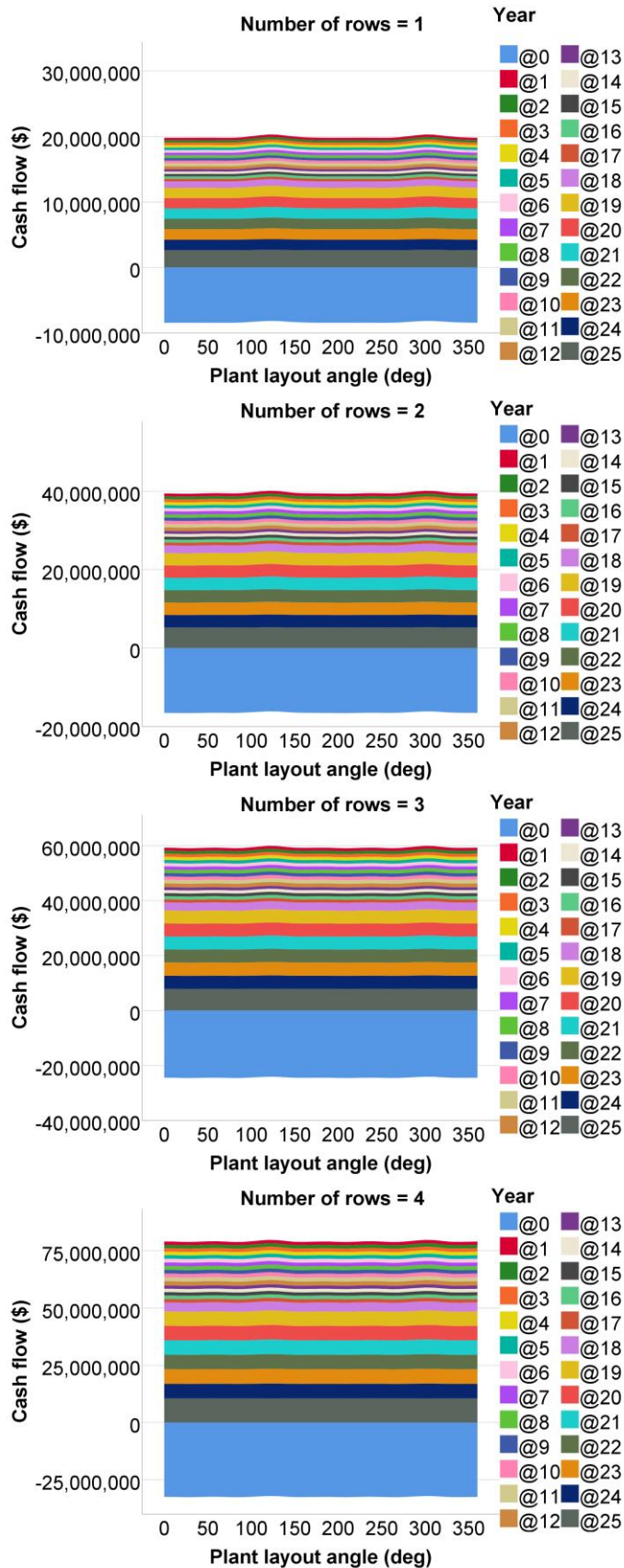


Figure 7. 30 Illustration (2-D) of the cash flow over the project lifetime (25 years) for selected 4 of the 60 optimal configurations (the optimal 1, 2, 3, and 4-row configurations) – (optimal low row-count configurations).

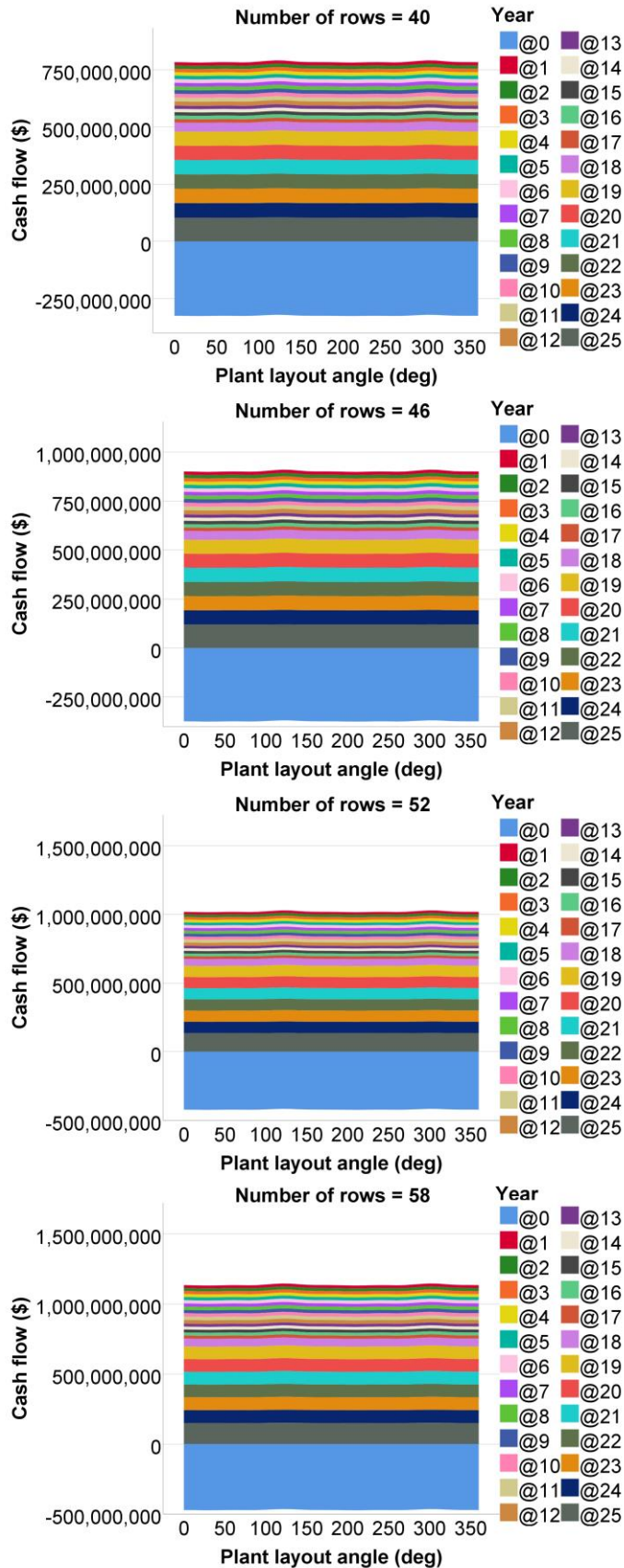


Figure 7. 31 Illustration (2D) of the cash flow over the project lifetime (25 years) for selected 4 of the 60 optimal configurations (the optimal 40, 46, 52, and 58-row configurations) – (optimal high row-count configurations).

7.5. Chapter conclusion

In this work, the critical findings are summarized as follows:

- i. the α value is calculated to be 0.15 and larger than 0.29 for the daytime and nighttime, respectively, The P_d value is calculated to be 289 W/m^2 (see Appendix E),
- ii. the months of June and July have high levels of generation, wind speed, temperature, and humidity. Also, the wind speed is at maximal levels during the nighttime, leading to an increase in economic feasibility and reduction of curtailment from renewable power cogeneration if wind power is accompanied by CSP/TES,
- iii. the LOESS regression analyses confirmed that the wind direction and distribution ranges have consistent and robust northwest components throughout the year,
- iv. 60 design configurations with optimal θ_{plant} values based on the LCOE-minimization criterion are identified. A linear increase in annual gross energy occurs as the N_r value increases for almost all ranges of θ_{plant} ,
- v. as the N_r value increases, an increase in the LCOE occurs for the following ranges of θ_{plant} : $110\text{-}140^\circ$ and $280\text{-}320^\circ$ (red areas). At small values of N_r , a decrease in the LCOE occurs for the following ranges of θ_{plant} : $0\text{-}75^\circ$, $160\text{-}260^\circ$, and $340\text{-}360^\circ$ (dark-blue areas),
- vi. as the N_r value increases, an increase in the wake losses occur for the following ranges of θ_{plant} : $110\text{-}140^\circ$ and $280\text{-}320^\circ$ (red areas). At small values of N_r , a decrease in the wake losses occurs for the following ranges of θ_{plant} : $0\text{-}75^\circ$, $160\text{-}260^\circ$, and $340\text{-}360^\circ$ (dark-blue areas),
- vii. as the N_r value increases, a decrease in the performance ratio occurs for the following ranges of θ_{plant} : $110\text{-}140^\circ$ and $280\text{-}320^\circ$ (dark-blue areas). At small values of N_r , an increase in the performance ratio occurs for the following ranges of θ_{plant} : $0\text{-}75^\circ$, $160\text{-}260^\circ$, and $340\text{-}360^\circ$ (red areas),
- viii. as the N_r value increases, a decrease in the capacity factor occurs for the following ranges of θ_{plant} : $110\text{-}140^\circ$ and $280\text{-}320^\circ$ (dark-blue areas). At

small values of N_r , an increase in the capacity factor occurs for the following ranges of θ_{plant} : 0-75°, 160-260°, and 340-360° (red areas),

- ix. the wind speed and direction frequencies have various impacts on the LCOE, wake losses, performance ratio, capacity factor, and annual gross energy once linked with the variation of N_r and θ_{plant} . Since there are more wind turbines for higher N_r values, the turbines create more turbulence at high wind speeds, leading to increased wake losses. As a result, the LCOE increases while the performance ratio, capacity factor, and generation decrease accordingly,
- x. the monthly and hourly performance have been evaluated for the selected 8 of the 60 optimal configurations (i.e., for categories 1, 2, 3, 4, 40, 46, 52, and 58 of 60). It should be recognized that the optimal selection is based on the LCOE-minimization criterion, and the evaluations are performed considering the frequency profiles of 12 assessment parameters.
- xi. It can be observed that the full load generation at the rated wind speed decreases as the N_r value increases. Furthermore, it can be observed that the full load generation at the rated wind speed is independent of θ_{plant} . Thus, the order from highest to lowest full load generation at the rated wind speed is as follows: the optimal 1, 2, 3, 4, 40, 46, 52, and 58-row configuration, respectively,
- xii. For the selected 8 of the 60 optimal configurations (i.e., for categories 1, 2, 3, 4, 40, 46, 52, and 58 of 60), the corresponding installed costs are as follows: 2.0616, 2.0386, 2.0312, 2.0275, 2.0166, 2.0165, 2.0163, 2.0162 \$/W, which correspond to the LCOE values of 5.76734, 5.94352, 6.0849, 6.15907, 6.08697, 6.0745, 6.06462, 6.05662 ¢/kWh, respectively. Thus, it can be concluded that there exists an exponential relation between the installed cost per watt and N_r .
- xiii. the present value of annual energy, net present value (annual costs), annual energy, and annual gross energy have increasing linear trends as N_r increases. Thus, there exist linear relations between these and N_r , and
- xiv. It is revealed that the optimal configurations require a PPA price of at least 7.03 ¢/kWh to make a positive return on investment.

8. CONCLUSION AND FUTURE WORK

8.1. Chapter journal publications

Some of the work that appears in this chapter is associated with peer-reviewed scientific journal publications. This chapter is associated with publications (1), (2), and (3). The detailed information of these publications is listed in the “Scientific Journal Publications” Section, starting from page (iii) of this thesis.

8.2. Benefits and applications

From a mega-scale viewpoint, the assessment of wind power and CSP-PT/TES technologies to achieve the 15% strategic target of electricity demand from renewables by the year 2030 has never been investigated prior to this work under the arid desert climate of Kuwait (i.e., dust storms, high humidity, extreme temperatures). Several technical/operational guidelines and economic yield figures have been provided for potential developers and investors to promote renewable installations through multiple wind power and CSP-PT/TES performance evaluations. Furthermore, recommendations have been addressed on the validation, optimal design configurations, and operating conditions for future possibilities of wind power and CSP-PT/TES plants. Many objectives are achieved by performance assessment, integrating optimal design parameters/operating conditions, and utilizing ground measured meteorological data. Also, guidelines have been provided for optimal performance and performance degradation evaluation.

This work has identified areas of concern for efficiency, design, and operational improvements for the CSP-PT/TES technology. It was established that an essential step towards increasing η_{overall} is maximizing the work potential of the heat collected from solar radiation. Therefore, the heat collection process has been analyzed. One of the objectives was to perform a performance assessment of the 50 MW reference plant (Andasol-1 in Spain) and compare the performance under the climatic conditions of the chosen location in Kuwait. It should be recognized that many scenarios exist for utilizing the validated CSP-PT model, which can be used in thermal performance comparisons between field-tested PT collectors and newly

manufactured ones. It should be recalled that MEW is the exclusive provider of electricity and water in Kuwait. The benefits from this work extend to the power sector, which can retrofit renewable technologies, such as wind power and CSP-PT/TES, rather than burning oil and gas for electricity generation. Moreover, the oil and gas sector can also benefit from renewable technology implementations. This work has also provided solutions to optimization and operational problems concerning wind power technology.

8.3. Novelty

Novelty is driven by the desire to offer beneficial solutions to specified problems and challenges. This work has provided various optimal configurations of CSP-PT/TES with performance assessment measures. Furthermore, techno-economic assessment and optimization of mega-scale wind power plant configurations have been performed for the Kuwait case, which has never been investigated prior to this work. In addition, a validated model has been provided to assist in improving thermal efficiency for future CSP-PT plant installations. One of the motivations was to identify performance degradation factors along with location, cause, and magnitude of heat loss. In addition, one source of innovation came from using the model to maximize thermal efficiency and economic feasibility. This work has applicable significance because of the need to maintain optimal performance in wind power and CSP-PT/TES plants. Also, recommendations have been addressed concerning the validation, optimal design configurations, and operating conditions for future possibilities of CSP-PT/TES and wind power plant installations. The outcomes can be used in identifying operational challenges and innovative solutions specific to the arid climate of Kuwait.

Currently, the energy demand of Kuwait is fulfilled by burning oil and gas. While 10% of production was consumed locally in 1980, this percentage increased to 20% in 2005 and was expected to reach 40% in 2015 [325]. Thus, the most effective solution for economic savings and generating additional revenues is utilizing renewable energy technologies such as wind power and CSP-PT/TES to meet local energy demand. It should be noted that providing guidelines for cost reduction and optimal configuration with the lowest LCOE, as presented in this work, is crucial for mega-scale renewable technology implementation for a major oil-producing country, such as Kuwait. Furthermore, techno-economic findings are essential since economic

savings directly result from improving the efficiency of renewable power plants, which has been investigated in this work.

8.4. Challenges and solutions

One of the main challenges facing wind power and CSP-PT/TES technologies is lower economic feasibility than fossil-based technologies. The advancements in the design of system components and configurations of renewable power plants are ongoing. Still, the problems of variability, uncertainty, and intermittency in the wind and solar resources have different solutions due to the high dependency on geographical location. Also, these problems affect the outcome of other optimization tasks. This work has focused on answering important questions related to the day-to-day operations of renewable power plants. The case of Kuwait was chosen since such problems highlight essential research and knowledge gaps in the literature. Hence, the optimization of various CSP-PT and wind power plants was investigated. The electrical load under consideration was the national electrical load of Kuwait, a country with one of the highest per capita electricity consumption. In addition, Kuwait experiences an arid desert climate and environmental conditions, such as dust, sand storms, and high ambient temperature/humidity. Therefore, one of the objectives was to identify the technical limitations and economic feasibility under harsh and extreme climatic conditions.

The importance of this work comes from the fact that wind power and CSP-PT should contribute toward the strategic target of achieving 15% of electricity demand from renewables in Kuwait by 2030. Thus, optimization and scenario-based investigation of these technologies are critical since Kuwait is a country that needs regulated incentives for renewable energy implementation to promote future installations. Some of these incentives are feed-in tariffs, cash grants, soft government loans, public auctions for specified capacities of renewable energy technologies, and regulations. As of the time of this writing, financial metrics, such as LCOE, net present value, and payback period, are not widely available based on techno-economic justification for centralized generation of wind power and CSP-PT technologies under the arid desert climate of Kuwait. However, these metrics are essential for potential developers and investors. Therefore, the objectives of this work are imperative to promote the commercialization of mega-scale wind power and CSP-PT installations and offer economic benefits to Kuwait's power sector and

economy, which are currently reliant on fossil fuels and oil export revenues, respectively.

8.5. Study justification

This section provides an overview of some key findings from Chapter 1. The CSP-PT technology is the most popular and represents 76.6-82% of the global installed CSP capacity share. Therefore, the CSP-PT technology is investigated in this work. The Andasol-1 power plant in Spain is a milestone for the CSP-PT technology because it is the first CSP-PT plant with TES capability. Approximately 45.9% of the global CSP-PT installations have 50 MW capacity ratings [5,6]. Therefore, a CSP-PT plant with a 50 MW capacity (Andasol-1) is selected for performance assessment and optimization of the CSP-PT/TES technology. Kuwait experiences extreme climatic conditions; for example, the maximum temperature reached 54 °C in July 2016 in the shade, reported as the hottest reliably measured air temperature on Earth [15–19].

Kuwait has a strategic target for achieving 15% of the electricity demand from renewable technologies by 2030, and the technology mix shares have not, as yet, been finalized. Kuwait is a MENA/GCC member [11] and has one of the heavily subsidized prices of electricity in the world, with 0.66 ¢/kWh from fossil-based power plants [20–22]. Dispatchable renewable power, such as combined CSP-PT with TES, should be considered an attractive solution for electricity generation in Kuwait. Such design configuration provides electricity on demand, similar to fossil-based power technologies (e.g., gas turbines). Also, dispatchable CSP-PT with TES accompanied by wind power can minimize the intermittences in the solar and wind resources.

It should be recognized that the detailed coordination of wind power and CSP-PT/TES has never been investigated for the Kuwait case prior to this work. The Kuwait case represents a challenging one for evaluating the techno-economic competitiveness of renewable technologies due to various economic, environmental, and political constraints, including the national target for achieving a 15% penetration in electricity demand from solar and wind power technologies by the year 2030.

8.6. Selection criteria

This section provides an overview of some key findings from Chapter 2. It should be mentioned that renewable energy had a 26.5% electricity production share, and the global capacity of CSP reached 4.9 GW [57]. Also, Spain has the largest installed share of CSP globally. Notably, wind power has the maximum share (5.6%) of the total renewable energy electricity production share (26.5%), and the non-renewable electricity share accounts for 73.5%. Thus, an existing CSP-PT plant in Spain is selected as the reference plant in this work for performance assessment and optimization of the CSP-PT/TES technology. For the per capita electricity consumption, Kuwait is at the top rank [73,74] in the range of 16,000-17,000 kWh per capita from 2003 to 2011 [68]. According to a study [82], the most advanced technology for solar thermal power is CSP. The MENA desert has the advantage of high solar resources, which contribute to the popularity of CSP [83,84]. Therefore, the initiative to utilize such desert to construct power plants and export electricity to Europe is the most encouraging near-term prospect for CSP [85,86].

The DLR has promoted renewable energy in the MENA region. There exists a network of meteorological stations under the cooperation between the DLR, international research institutes, and industry partners [87]. The aim is to provide reliable meteorological data of MENA, critical for CSP performance predictions. This network of meteorological stations is established as part of the enerMENA initiative to shut down nuclear plants in Germany by 2022. The existing and planned grid interconnection between countries in the GCC, MENA, and Europe has encouraged Germany to support this initiative, which also motivated the creation of the Europe-MENA partnerships with Morocco [88]. Kuwait is part of the grid interconnection in the Middle East [88]; therefore, the Kuwait case was investigated in this work along with the Spain case for performance assessment and optimization of CSP-PT/TES.

Kuwait has one of the heavily subsidized prices of electricity worldwide, with 0.66 ¢/kWh [20–22]. As of 2014, Kuwait's total installed renewable energy capacity was 0.2 MW [20]. The chosen location in Kuwait has no future development plans, which makes it ideal for development projects toward the 15% target to fulfil local electricity demand from renewable energy by 2030. Besides, this location has minimal oil and gas field concentrations [52]. Furthermore, this location has a peak in both solar and wind resources. Hence, investigating the different optimal design configurations of dispatchable CSP-PT with TES accompanied by wind power can

minimize the intermittences in the solar and wind resources. As a result, the chosen location is used for the performance assessment and optimization of wind power and CSP-PT/TES plants for the Kuwait case.

Kuwait's oil/gas sector accounts for about 40% of the gross domestic product and about 92% of the export revenues [106]. As of 2018, Kuwait's oil production reached 2.7 Mbbl/d, and the marketed production of NG reached 17.1 Bm³ [106]. It can be estimated that approximately 342,842 bbl were used for electricity generation in 2016 [107]. This estimation corresponds to 12.7% of domestic oil production. Kuwait's domestically consumed fossil fuels are gas oil, crude oil, heavy oil, and NG [108]. Domestic oil consumption for electricity generation is estimated to reach 1 Mbbl/d by 2030 [109,110]. Such consumption equals approximately 37% of the 2017 oil production, leaving Kuwait with 63% for oil exports if the 2030 oil production remains as that of 2017. MEW has estimated that the peak load would reach 33,000 MW in 2030, rising from 13,390 MW in 2016 [107]. Kuwait's total installed power assets are about 18,850.4 MW [107] (i.e., 47.6% steam turbines, 12.2% combined cycle gas turbines, and 40.2% open cycle gas turbines). Most of these assets are categorized under thermal generation units with a high potential for CSP-PT retrofit applications by integrating solar heat augmentation processes within the conventional power plants (i.e., supplying steam side-to-side to boilers). The third quarter (summer) is when peak generation occurs due to the excess air conditioning load (comfort cooling in buildings). In Kuwait, the peak load is during the summer. The fuel consumption for electricity and water production accounted for 55% in Kuwait. According to a study and official announcements, the cost of electricity production from fossil-based power plants is averaged at approximately 14 ¢/kWh in Kuwait [35–37]. However, most residential consumers pay as low as 6% of this average actual cost.

This work has provided detailed review material on various software(s) and tools. The SAM software has been selected for performance assessment and optimization of wind power and CSP-PT/TES; in addition, other time-series analysis software(s) have been used. The result of a detailed review on the specifications of selected CSP plants worldwide is provided [112,113,122–131,114,132–137,115–121]. It should be noted that the Andasol-1 plant with TES capability is located in Spain and has a 50 MW capacity rating [5,6]; therefore, it is used as the reference CSP-PT plant for performance assessment and optimization purposes.

8.7. Optimization and assessment approach

This section provides an overview of some key findings from Chapter 3. As part of building the methodology of this work, the system components have been determined for the wind power and CSP-PT model configurations (i.e., transmission network, reference 2 MW wind turbine, and reference 50 MW CSP-PT plant). In several analyses, justification has been provided for utilizing the SAM software based on TRNSYS simulation. The computational algorithm and control have been explained for a comprehensive performance assessment of the CSP/TES technology, among other performance metrics such as LCOE and energy-related parameters concerning the performance of plant subcomponents [228]. In addition, a methodology has been determined for the optimization and parametric analyses in which 31 SM values are considered from 1 to 4 with an increment of 0.1. Furthermore, 19 values of N_h^{TES} are considered from 0 to 18 with an increment of 1. Thus, a total of 589 design configurations are evaluated for the CSP-PT model with TES capability. The configuration variations are the product of 31 and 19 (31×19). Additionally, the methodology has included performance evaluations of 19 optimal design configurations for CSP-PT/TES with optimal SM values based on the lowest LCOE as a function of N_h^{TES} .

Moreover, a methodology has been determined to optimise and enhance dry-cooled CSP-PT, considering the viability of wind resources for cogeneration. The methodology has been selected to evaluate the validated CSP-PT model performance with the actual performance for the 50 MW reference plant under the climatic condition of the chosen location in Kuwait, including the assessment of solar/wind resources and the national electrical load. Furthermore, the methodology has investigated the following performance parameters: LCOE, capacity factor, thermal power produced by the SF system, $E_{\text{ele,a}}$, η_{overall} , and cycle electrical power output.

Additionally, the methodology has included an assessment of the following performance enhancement strategies: integration of TES, integration of wind power, cogeneration with temperature derating effect, cogeneration with load consideration, evaluation of the periods of 24 h continuous generation from CSP-PT/TES without fossil backup, and comparison of the CSP-PT/TES performance between winter and summer sessions.

8.8. Natural resources and meteorological characteristics

This section provides an overview of some key findings from Chapter 4. In this work, a TMY file, which is established on a monthly basis for individual years with long-term monthly characteristics, serves as input to the SAM software. In addition, the methodology for reliable meteorological data is provided. The meteorological parameters relevant to wind power and CSP-PT are the ambient temperature, relative humidity, wind speed, and wind direction. Consequently, the DNI is the critical parameter with the most significant impact on the CSP-PT performance, including energy yield. High confidence in the DNI values is necessary [235,236] for performance assessment; therefore, reducing the uncertainty of the solar resource is of high importance [241,248,249,252–255]. It is concluded that the months with high potential wind and solar resources are during the summer. After evaluating a topographical map with elevations for Kuwait [261,262], it is observed that the chosen location has one of the highest elevations in the country, which is the primary reason behind having a high wind resource potential. The calculations of α are crucial for estimating the wind energy yield. Therefore, detailed monthly statistical profiles for the wind resource are performed. The wind speed, direction, humidity, and ambient temperature are essential parameters for accurately describing the wind resource. This is because they all contribute to the wind's kinetic energy and the potential of mechanical energy creation at the wind turbine's blades (see Appendix E). Thus, the meteorological data used in this work are ground measured, allowing for higher accuracy in estimating wind energy yield. It should be recognized that Kuwait experiences frequent sandstorm trajectories [258–260], and extreme temperature/humidity conditions are widespread during summer. These conditions impose many operational challenges for wind power and CSP-PT plants.

8.9. Techno-economic competitiveness of concentrating solar power plants with thermal energy storage

This section provides an overview of some key findings from Chapter 5. One of the objectives is to evaluate the CSP-PT technology for electricity generation under arid

climatic conditions. The assessment is performed on an existing plant in Spain, and the model is validated using published data. The DNI of Spain exceeds that of Kuwait by a difference of 176.2 kWh/m² yr, but the overall performance of the Kuwait case exceeds that of Spain. With a wet-cooled condenser system, the Kuwait case performance exceeds that of Spain for η_{overall} by 2.9% and the annual efficiency of the SF system by 4.1%. Additionally, the annual net electricity output of the Kuwait case exceeds that of Spain by 14,534 MWh_e. With a dry-cooled condenser system, the Kuwait case performance exceeds that of Spain for η_{overall} by 1.1% and the annual efficiency of the SF system by 3.0%. However, the annual net electricity output of the Spain case exceeds that of Kuwait by only 749.8 MWh_e. The better performance of the Kuwait case is due to the DNI impact on the number of full load hours of steam turbine, ambient temperature, wind speed, and SF heat loss/dumped energy. The techno-economic assessment considered numerous design configurations utilizing dry cooling in Kuwait due to limited water resources. The SM and N_h^{TES} values are varied to identify optimal configurations. It is concluded that the optimal SM is at 3.3, corresponding to the lowest LCOE of 15.0663 ¢/kWh for 16 h of storage.

Thus, the following are concluded: (i) the design climatic conditions for CSP-PT plants in Kuwait are determined, (ii) the effects of dry and wet cooling options on CSP-PT plant performance are investigated, (iii) the number of full load hours of steam turbine and electricity output is evaluated, (iv) the water consumption, plant efficiency, and SF performance measures are estimated, and (v) the techno-economic parameters for 50 MW CSP-PT plants are calculated and compared.

8.10. Optimization and performance enhancement of concentrating solar power plants

This section provides an overview of some key findings from Chapter 6. It should be recognized that the CSP-PT technology with a dry-cooled condenser system is an alternative option for arid climate locations, such as Kuwait. This work evaluates the performance of various CSP-PT design configurations, including 19 configurations reported as optimal. These have optimal SM values based on the lowest LCOE. Furthermore, CSP-PT with TES, including wind power potential, is evaluated. It is revealed that coinciding peaks of electrical load, solar, and wind resources promote

cogeneration from CSP-PT/TES and wind power with significant benefits. Also, the wind speed is found to be at maximum levels at high altitudes in the early daytime and late nighttime. Whereas in the afternoon, it reaches maximum values at low altitudes. The calculated α is between 0.14-0.18 and shows a cyclic behaviour. Such findings promote mega-scale wind power generation. From the techno-economic assessment, it is concluded that the SM value for optimal CSP-PT/TES configurations increases with increasing N_h^{TES} . In addition, the N_h^{TES} value has significant effects on $E_{ele,a}$, capacity factor, and LCOE. However, the impact of N_h^{TES} on $\eta_{overall}$ is insignificant. Furthermore, the optimal SM and lowest LCOE values are determined. Also, the periods of 24 h continuous electricity generation from CSP-PT/TES without fossil backup have been identified.

Thus, the following are concluded: (i) the coinciding peaks of electrical load, solar, and wind resources promote cogeneration, (ii) the wind increases in early-day/late-night at high altitudes and in the afternoon at low altitudes, (iii) the α value is calculated to be 0.14-0.18 and shows cyclic behaviour in the wind resource, (iv) the N_h^{TES} value has maximal effects on $E_{ele,a}$, capacity factor, and LCOE but minimal effect on $\eta_{overall}$, and (v) the periods of 24 h generation from CSP-PT/TES without fossil backup are identified.

8.11. Comparative techno-economic assessment and optimization of wind power plants

This section provides an overview of some key findings from Chapter 7. It should be recognized that optimal scheduling of wind power can be achieved once an accurate prediction of the wind resource is performed. In general, feasible power generation is reached after wind resource assessment for different locations since surface roughness changes based on the type and elevation of land and topography, directly affecting wind speeds. One of the most promising technologies, which has a high potential for implementation in Kuwait, is wind power. Therefore, wind power performance assessment and optimization are performed as an alternative solution to electricity generation from fossil fuels.

In this work, one of the objectives is to assess the performance of multi-row design configurations for wind power plants. The configurations have optimal values of θ_{plant} based on the lowest LCOE. The optimal selection comes after evaluating

2220 configurations. The optimal configurations are determined for various N_r values. The wind power potential is assessed technically and economically. It is concluded that N_r and θ_{plant} values impact the LCOE, wake losses, performance ratio, capacity factor, and annual gross energy. Additionally, 60 optimal design configurations with θ_{plant} based on the LCOE-minimization criterion are identified. The LOESS regression analyses confirm that wind speed, direction, and distribution ranges have consistent and robust northwest components. Hence, the following are concluded: (i) the N_r and θ_{plant} values impact the LCOE, wake losses, performance ratio, and capacity factor, (ii) the 60 configurations with optimal θ_{plant} values based on the LCOE-minimization criterion are identified, (iii) the α and P_d values are determined, (iv) the months of June and July have high levels of generation, wind speed, temperature, and humidity, and (v) the LOESS analyses confirm prevailing wind with a consistent northwest component.

Moreover, the monthly and hourly performance have been evaluated for the selected 8 of the 60 optimal configurations (i.e., for categories 1, 2, 3, 4, 40, 46, 52, and 58 of 60). It should be recognized that the evaluations are performed considering the frequency profiles of the 12 assessment parameters. It is concluded that the full load generation at the rated wind speed decreases as the N_r value increases. Furthermore, it is observed that the full load generation at the rated wind speed is independent of θ_{plant} . It is concluded that the order from highest to lowest full load generation at the rated wind speed is as follows: the optimal 1, 2, 3, 4, 40, 46, 52, and 58-row configuration, respectively. For the selected 8 of the 60 optimal configurations, the corresponding installed costs are as follows: 2.0616, 2.0386, 2.0312, 2.0275, 2.0166, 2.0165, 2.0163, 2.0162 \$/W, which correspond to the LCOE values of 5.76734, 5.94352, 6.0849, 6.15907, 6.08697, 6.0745, 6.06462, 6.05662 ¢/kWh, respectively.

Thus, it can be concluded that there exists an exponential relation between the installed cost per watt and N_r . Additionally, the present value of annual energy, the net present value (annual costs), the annual energy, and the annual gross energy have increasing linear trends as N_r increases. Therefore, there exist linear relations between these and N_r . It is revealed that the optimal configurations require a PPA price of at least 7.03 ¢/kWh to make a positive return on investment.

8.12. Future work and recommendations

The results obtained from this work constitute an attempt to provide recommendations for optimal operating conditions of future possibilities of CSP-PT/TES and wind power plant installations under arid climatic conditions. This work has investigated these technologies by analyzing various performance parameters. In addition, many modelling skills and expertise in performance assessment and optimization have been demonstrated.

It is recommended that the environmental effects on wind power plant performance should be further evaluated in the future for the following reasons: (i) wind turbine's blade soiling due to dust and sandstorms, (ii) high ambient temperature shutdown of the wind turbine, and (iii) high ambient temperature derating effect of the turbine power curve. In addition, one area of concern is the effect of sandstorms on the erosion of the reflectors/collectors in CSP-PT plants. Thus, the following instructions for optimal CSP-PT plant performance will lead to trouble-free operation: (i) the power equipment should be protected against corrosion, (ii) barriers are considered necessary to hold sand movements outside the CSP-PT plant's borders; hence, scheduled cleaning of sand buildup outside of the barriers would be needed, and (iii) cleaning the reflecting mirrors in the SF system should be a routine process.

Moreover, this work is best to be followed by developing a testing facility to validate and assess the performance of different brands of HCEs for the CSP-PT technology (i.e., experimental testing). Establishing a testing facility is beneficial for future CSP-PT installations in Kuwait and the MENA/GCC regions. In this aspect, the testing facility's role can be to certify after performing quality control and testing on collectors to determine if they suit the operation under arid climatic conditions. Also, photogrammetric testing can be performed to evaluate the optical efficiency of the collectors. This approach can guarantee the technical performance of various collector brands and their efficiency profiles. Especially since the typical lifetime of a CSP-PT plant is about 25 years, and performance degradation throughout the plant lifetime is widespread in various plant subsystems. Therefore, a testing facility can generate thermal efficiency profiles to guarantee the overall collector performance for specified periods. Additionally, the CSP-PT/TES technology is relatively new to Kuwait; therefore, establishing a training facility for skill and expertise development in photogrammetry is necessary.

References

- [1] Sultan AJ, Hughes KJ, Ingham DB, Ma L, Pourkashanian M. Techno-economic competitiveness of 50 MW concentrating solar power plants for electricity generation under Kuwait climatic conditions. *Renew Sustain Energy Rev* 2020;134:110342. <https://doi.org/10.1016/j.rser.2020.110342>.
- [2] Sultan AJ, Ingham DB, Hughes KJ, Ma L, Pourkashanian M. Optimization and performance enhancement of concentrating solar power in a hot and arid desert environment. *Renew Sustain Energy Rev* 2021;149:111411. <https://doi.org/10.1016/J.RSER.2021.111411>.
- [3] Sultan AJ, Hughes KJ, Ingham DB, Ma L, Pourkashanian M. Supplementary material for research article 110342 “Techno-economic competitiveness of 50 MW concentrating solar power plants for electricity generation under Kuwait climatic conditions”. *Renew Sustain Energy Rev* 2020;134:110342. <https://doi.org/10.1016/j.rser.2020.110342> (download from “Appendix A. Supplementary data” in DOI).
- [4] Sultan AJ, Ingham DB, Hughes KJ, Ma L, Pourkashanian M. Supplementary material for research article 111411 “Optimization and performance enhancement of concentrating solar power in a hot and arid desert environment”. *Renew Sustain Energy Rev* 2021;149:111411. <https://doi.org/10.1016/j.rser.2021.111411> (download from “Appendix A. Supplementary data” in DOI).
- [5] Balghouthi M, Trabelsi SE, Amara M Ben, Ali ABH, Guizani A. Potential of concentrating solar power (CSP) technology in Tunisia and the possibility of interconnection with Europe. *Renew Sustain Energy Rev* 2016;56:1227–48. <https://doi.org/10.1016/j.rser.2015.12.052>.
- [6] Xu X, Vignarooban K, Xu B, Hsu K, Kannan AM. Prospects and problems of concentrating solar power technologies for power generation in the desert regions. *Renew Sustain Energy Rev* 2016. <https://doi.org/10.1016/j.rser.2015.09.015>.
- [7] Price H, Lüpfer E, Kearney D, Zarza E, Cohen G, Gee R, et al. Advances in parabolic trough solar power technology. *J Sol Energy Eng Trans ASME*

2002;124:109–25. <https://doi.org/10.1115/1.1467922>.

- [8] Herrmann U, Geyer M, Kistner R. The AndaSol Project. Workshop on Thermal Storage for Trough Power Systems. 2002. <https://p2infohouse.org/ref/46/45523.pdf>.
- [9] Dunn R. A Global Review of Concentrated Solar Power Storage. 2010.
- [10] Energy Storage Technology for Concentrating Solar Power n.d.
- [11] Al-Matrouk A, Alqallaf M, AlShemmeri A, BoJbarah H. Identification of synthetic cannabinoids that were seized, consumed, or associated with deaths in Kuwait in 2018 using GC–MS and LC–MS-MS analysis. *Forensic Sci Int* 2019;303. <https://doi.org/10.1016/j.forsciint.2019.109960>.
- [12] Millennium S. The parabolic trough power plants Andasol 1 to 3 The largest solar power plants in the world-Technology premiere in Europe. 2008.
- [13] Ahmad Khaled. TECHNICAL AND ECONOMIC PERFORMANCE OF PARABOLIC TROUGH IN JORDAN n.d. [http://edge.rit.edu/content/P15484/public/Detailed Design Documents/Solar Trough Preliminary analysis references/Technical and economic performance of parabolic trough in Jordan.pdf](http://edge.rit.edu/content/P15484/public/Detailed%20Design%20Documents/Solar%20Trough%20Preliminary%20analysis%20references/Technical%20and%20economic%20performance%20of%20parabolic%20trough%20in%20Jordan.pdf) (accessed November 25, 2021).
- [14] 1 John O'Donnell Solar Thermal Power. - ppt download n.d. <https://slideplayer.com/slide/5276365/> (accessed April 2, 2022).
- [15] Fletcher S. “The world’s hottest day EVER is recorded in Kuwait as temperature soars to 54C” [Online]. Daily Mail, Mail Online, News. Published by Associated Newspapers Ltd, Part of the Daily Mail, The Mail on Sunday & Metro Media Group 2016. <https://www.dailymail.co.uk/news/article-3704601/The-hottest-day-recorded-Kuwait-temperature-soars-54C.html>.
- [16] Burt CC. “CHRIS BURT: Hottest Reliably Measured Air Temperatures on Earth” [Online]. 2016. <http://www.markvoganweather.com/2016/07/29/chris-burt-hottest-reliably-measured-air-temperatures-on-earth/> (accessed December 12, 2019).
- [17] Burt CC. “Hottest Reliably Measured Air Temperatures on Earth” [Online]. 2016. <https://www.wunderground.com/blog/weatherhistorian/hottest-reliably-measured-air-temperatures-on-earth.html> (accessed December 12,

2019).

- [18] Livingston I. "Scorching temperatures in Kuwait and Pakistan among hottest measured" [Online]. 2019. <https://www.smh.com.au/environment/climate-change/scorching-temperatures-in-kuwait-and-pakistan-among-hottest-measured-20190619-p51z4k> (accessed December 12, 2019).
- [19] WMO. "WMO verifies 3rd and 4th hottest temperature recorded on Earth" [Online]. An article by the World Meteorological Organization. 2019. <https://public.wmo.int/en/media/press-release/wmo-verifies-3rd-and-4th-hottest-temperature-recorded-earth> (accessed December 12, 2019).
- [20] IRENA. Renewable Energy Market Analysis: The GCC Region. A Report by the International Renewable Energy Agency. 2016. <https://doi.org/10.1017/S1740355311000283>.
- [21] IRENA. Renewables Readiness Assessment: Sultanate of Oman. A Report by the International Renewable Energy Agency. 2014.
- [22] Hertog S. The private sector and reform in the Gulf Cooperation Council Countries. 2013. Kuwait Programme on Development; Governance and Globalisation in the Gulf States. No. 30. London School of Economics and Political Science. 2013.
- [23] Atalla TN, Hunt LC. Modelling residential electricity demand in the GCC countries. *Energy Econ* 2016;59:149–58. <https://doi.org/10.1016/j.eneco.2016.07.027>.
- [24] World Development Indicators (2019). GDP per capita, The World Bank. [Online]. Available: <https://data.worldbank.org/indicator/NY.GDP.PCAP.CD> 2019.
- [25] H. Ritchie and M. Roser, "CO₂ and Greenhouse Gas Emissions" Our World in Data, 2017. [Online]. Available: <https://ourworldindata.org/co2-and-other-greenhouse-gas-emissions>. 2017.
- [26] H. Ritchie and M. Roser, "Energy," Our World in Data, 2014. [Online]. Available: <https://ourworldindata.org/energy>. 2014.
- [27] Khatti SS, Woodruff GW. TECHNO-ECONOMIC OPTIMIZATION AND MARKET POTENTIAL STUDY OF SMALL-SCALE PARTICLE HEATING RECEIVER BASED

CENTRAL RECEIVER POWER TOWER PLANTS IN MENA REGION A Dissertation
Presented to The Academic Faculty. Georgia Institute of Technology; 2021.

- [28] Alhajraf S, Heil O. Feasibility study of renewable energy technologies in the State of Kuwait. Project No. EU060C. Report No. KISR 10673. Kuwait Institute for Scientific Research (KISR). Final Report. 2011.
- [29] Shams HM, Bradley DA, Regan PH. Determination of levels of naturally occurring radioactive materials in lagoon samples containing produced water from the Minagish oil field in the state of Kuwait. *Radiat Phys Chem* 2017;137:193–7. <https://doi.org/10.1016/j.radphyschem.2016.03.006>.
- [30] GENI. National Energy Grid Kuwait. Global Energy Network Institute. 4420 Rainier Avenue, Suite 308, San Diego, California 92120 USA. 2017. http://www.geni.org/globalenergy/library/national_energy_grid/kuwait/kuwaitnationalelectricitygrid.shtml (accessed September 16, 2019).
- [31] ISES. Concentrating Solar Thermal Power with Built in Storage. A Webinar by the International Solar Energy Society (ISES). Jan 2018. 2018. <https://www.youtube.com/watch?v=9oxR7BNx8nU>.
- [32] Mirza A. “Kuwait looks at crude oil expansion as neutral zone row drags” [Online]. 2018. <https://www.platts.ru/news-feature/2018/oil/2018-oil-natgas-outlook/2018-kuwait-crude-expansion> (accessed August 8, 2018).
- [33] Alnassar W, Alhajraf S, Alenizi A AL. Potential wind power generation in the State of Kuwait. *Renewable Energy*, Volume 30, Issue 14, November 2005, Pages 2149-2161. <https://doi.org/10.1016/j.renene.2005.01.002>. 2005. <https://www.sciencedirect.com/science/article/pii/S0960148105000145#fig5>.
- [34] SolarGIS. Solar resource maps of Kuwait. 2019. <https://solargis.com/maps-and-gis-data/download/kuwait>.
- [35] Ali H, Alsabbagh M. Residential Electricity Consumption in the State of Kuwait. *Environ Pollut Clim Chang* 2018;02. <https://doi.org/10.4172/2573-458x.1000153>.
- [36] Ansari M. Kuwait Utilities Sector. Industry Research. 2013:1–15. [http://www.infomercatiesteri.it/public/images/paes1/107/files/Kuwait Utilities Sector Report_pdf 6_13.pdf](http://www.infomercatiesteri.it/public/images/paes1/107/files/Kuwait%20Utilities%20Sector%20Report_pdf%206_13.pdf).
- [37] Alrai. “Newspaper article in Arabic” [online]. Alrai Media Group (Newspaper).

Published: 29 September 2015. 2015.

<http://www.alraimedia.com/Home/Details?id=53ab9db2-2245-4fd7-8d91-c5caf47a1d57>.

- [38] IRENA. Renewable Power Generation Costs in 2017, A Report by the International Renewable Energy Agency, Abu Dhabi, UAE. 2018. 2018. https://doi.org/10.1007/SpringerReference_7300.
- [39] Alhajraf S, Alabdullah Y, Sultan AJ, Alnahedh S, Alnassar W, Alsenafy M, et al. Performance assessment of renewable energy applications in the State of Kuwait. Final Report. EU057C. Kuwait Institute for Scientific Research (KISR). 2011.
- [40] Al-Rasheedi M, Gueymard C, Al-Hajraf S, Ismail A. Solar Resource Assessment over Kuwait: Validation of Satellite-derived Data and Reanalysis Modeling. EuroSun 2014, Aix-les-Bains (France), 16 – 19 Sept. 2014, 2015, p. 1–10. <https://doi.org/10.18086/eurosun.2014.08.01>.
- [41] Sultan AJ, Alotaibi A. Feasibility of implementing photovoltaic systems at Kuwait National Petroleum Company premises. EA005S. KISR 13336. Kuwait Institute for Scientific Research (KISR). 2016.
- [42] Sultan AJ. An exergy-based approach for performance assessment of a solar thermal energy collecting converting system. Final report. EA048G. Kuwait Institute for Scientific Research (KISR). 2017.
- [43] Sebzali M, Sultan AJ, Altabtabaei M. Design of self-reliant, sustainable protected environment food protection system. Int. report. EA070K. Kuwait Institute for Scientific Research (KISR). 2016.
- [44] Alrashidi MS, Alsudairawi M, Ramadan A, Aldabbous AN, Sultan AJ. Air Quality Assessment in the Ali Sabah Alsaleem Urban Community, Phase II. KISR 10656. Kuwait Institute for Scientific Research (KISR). 2011.
- [45] Al-Dousari AM, Ibrahim MI, Al-Dousari N, Ahmed M, Al-Awadhi S. Pollen in aeolian dust with relation to allergy and asthma in Kuwait. *Aerobiologia* (Bologna) 2018;34:325–36. <https://doi.org/10.1007/s10453-018-9516-8>.
- [46] RCREEE. Provision of technical support/services for an economical, technological and environmental impact assessment of national regulations and incentives for renewable energy and energy efficiency : country report

Morocco (draft), Cairo. 2010.

- [47] Chen HM. IEA, CO2 emissions from fuel combustion Highlights 2017, A Report by the International Energy Agency, 2017. *Libr Technol Rep* 2017;53:28. <http://www.indiaenvironmentportal.org.in/files/file/CO2EmissionsfromFuelCombustionHighlights2017.pdf>.
- [48] World Bank. CO2 emissions (metric tons per capita). 2019. <https://data.worldbank.org/indicator/EN.ATM.CO2E.PC>.
- [49] BP. BP statistical review of world energy. A Report by British Petroleum. 2018.
- [50] K-EPA. Kuwait's Initial National Communications under the United Nations Framework Convention on Climate Change. Kuwait Environment Public Authority, November 2012. 2012. <https://unfccc.int/resource/docs/natc/kwtnc1.pdf>.
- [51] Dallmer-Zerbe K, Bucher MA, Ulbig A, Andersson G. Assessment of capacity factor and dispatch flexibility of concentrated solar power units. 16-20 June 2013. 2013 IEEE Grenoble Conf. PowerTech, POWERTECH 2013, 2013, p. 1–6. <https://doi.org/10.1109/PTC.2013.6652252>.
- [52] MOO. Kuwait Oil Field Map. Kuwait Ministry of Oil. 2016. <http://www.moo.gov.kw/About-Us/Programs/Technical-Affairs/Kuwait-Oil-Field-Map.aspx>.
- [53] Al-Dousari A, Al-Nassar W, Al-Hemoud A, Alsaleh A, Ramadan A, Al-Dousari N, et al. Solar and wind energy: Challenges and solutions in desert regions. *Energy* 2019;176:184–94. <https://doi.org/10.1016/j.energy.2019.03.180>.
- [54] Al-Dousari A, Al-Nassar W, Ahmed M. Photovoltaic and wind energy: Challenges and solutions in desert regions. *E3S Web Conf.*, vol. 166, EDP Sciences; 2020. <https://doi.org/10.1051/e3sconf/202016604003>.
- [55] Al-Nassar WK, Neelamani S, Al-Salem KA, Al-Dashti HA. Feasibility of offshore wind energy as an alternative source for the state of Kuwait. *Energy* 2019;169:783–96. <https://doi.org/10.1016/j.energy.2018.11.140>.
- [56] Al-Salem K, Al-Nassar W. Assessment of wind energy potential at Kuwaiti Islands by statistical analysis of wind speed data. *E3S Web Conf.*, vol. 51, EDP Sciences; 2018. <https://doi.org/10.1051/e3sconf/20185101001>.

- [57] REN21. Renewables 2018 Global Status Report. A Report by the Renewable Energy Policy Network for the 21st Century. 2018.
- [58] IEA. Key world energy statistics 2018. A Report by the International Energy Agency. 2018.
- [59] Hessari FA. Sectoral energy consumption in Iran. *Renew Sustain Energy Rev* 2005;9:203–14. <https://doi.org/10.1016/j.rser.2004.03.002>.
- [60] Nejat P, Morsoni AK, Jomehzadeh F, Behzad H, Saeed Vesali M, Majid MZA. Iran's achievements in renewable energy during fourth development program in comparison with global trend. *Renew Sustain Energy Rev* 2013;22:561–70. <https://doi.org/10.1016/j.rser.2013.01.042>.
- [61] Hrayshat ES. Analysis of renewable energy situation in Jordan. *Energy Sources, Part B Econ Plan Policy* 2008;3:89–102. <https://doi.org/10.1080/15567240600815000>.
- [62] Ramanathan R. An analysis of energy consumption and carbon dioxide emissions in countries of the Middle East and North Africa. *Energy* 2005;30:2831–42. <https://doi.org/10.1016/j.energy.2005.01.010>.
- [63] M. KA. Assessments of primary energy consumption and its environmental consequences in the United Arab Emirates. *Renew Sustain Energy Rev* 2007;11:426–46.
- [64] Alnaser WE. Fuel consumption by vehicles in the state of Bahrain. *Appl Energy* 1995;50:31–40. [https://doi.org/10.1016/0306-2619\(95\)90762-6](https://doi.org/10.1016/0306-2619(95)90762-6).
- [65] Darwish MA, Al-Awadhi FM, Darwish AM. Energy and water in Kuwait Part I. A sustainability view point. *Desalination* 2008;225:341–55. <https://doi.org/10.1016/j.desal.2007.06.018>.
- [66] Al-Ismaily HA, Probert SD. Energy overview for the Sultanate of Oman. *Appl Energy* 1997;57:287–325. [https://doi.org/10.1016/s0306-2619\(97\)00029-9](https://doi.org/10.1016/s0306-2619(97)00029-9).
- [67] Almasri R, Muneer T, Cullinane K. The effect of transport on air quality in urban areas of Syria. *Energy Policy* 2011;39:3605–11. <https://doi.org/10.1016/j.enpol.2011.03.062>.
- [68] Nematollahi O, Hoghooghi H, Rasti M, Sedaghat A. Energy demands and renewable energy resources in the Middle East. *Renew Sustain Energy Rev*

2016;54:1172–81. <https://doi.org/10.1016/j.rser.2015.10.058>.

- [69] Rahman SM, Khondaker AN. Mitigation measures to reduce greenhouse gas emissions and enhance carbon capture and storage in Saudi Arabia. *Renew Sustain Energy Rev* 2012;16:2446–60. <https://doi.org/10.1016/j.rser.2011.12.003>.
- [70] Fath HES, Hashem HH. Energy use and efficiencies in the Arab countries. *Energy* 1988;13:861–70. [https://doi.org/10.1016/0360-5442\(88\)90051-5](https://doi.org/10.1016/0360-5442(88)90051-5).
- [71] Ibrahim SMA. Estimates of oil and natural gas (NG) reserves in Egypt. *Energy* 1998;23:997–1005. [https://doi.org/10.1016/S0360-5442\(98\)00047-4](https://doi.org/10.1016/S0360-5442(98)00047-4).
- [72] Marktanner M, Salman L. Economic and geopolitical dimensions of renewable vs. nuclear energy in North Africa. *Energy Policy* 2011;39:4479–89. <https://doi.org/10.1016/j.enpol.2010.12.047>.
- [73] IEA. Key World Energy Statistics 2017. A Report by the International Energy Agency. 2017.
- [74] World-Bank. Electric power consumption (kWh per capita). 2014. <https://data.worldbank.org/indicator/EG.USE.ELEC.KH.PC> (accessed November 3, 2019).
- [75] IEA. World Energy Balances 2018; Report by the International Energy Agency. 2018. <https://doi.org/10.1787/3a876031-en>.
- [76] IEA. Statistics: Electricity Information 2018; Report by the International Energy Agency. 2018.
- [77] Kousksou T, Allouhi A, Belattar M, Jamil A, El Rhafiki T, Arid A, et al. Renewable energy potential and national policy directions for sustainable development in Morocco. *Renew Sustain Energy Rev* 2015;47:46–57. <https://doi.org/10.1016/j.rser.2015.02.056>.
- [78] MEMEE. Ministère de l’Energie; des Mines; de l’Eau et de l’Environnement (MEMEE); Les Energies Renouvelables au Maroc: Stratégie et plan d’action; Casablanca; November; 2012. 2012.
- [79] Vidican G, Böhning M, Burger G, Regueira E de S, Müller S. Achieving inclusive competitiveness in the emerging solar energy sector in Morocco; Report by the German Development Institute. vol. 79. 2013.

- [80] Ashurst. Renewables in Morocco [Online]. Africa energy forum. 2016.
<https://www.ashurst.com/en/news-and-insights/legal-updates/renewables-in-morocco---june-2016/> (accessed November 3, 2019).
- [81] Promotion of renewable energy and energy efficiency – the “PEREN” project (2012b): 2012. <http://www.giz.de/Themen/de/dokumente/giz2012-renewableenergy-peren-en.pdf>.
- [82] Bouhal T, Agrouaz Y, Kousksou T, Allouhi A, El Rhafiki T, Jamil A, et al. Technical feasibility of a sustainable Concentrated Solar Power in Morocco through an energy analysis. *Renew Sustain Energy Rev* 2018;81:1087–95.
<https://doi.org/10.1016/j.rser.2017.08.056>.
- [83] Mahia R, De Arce R, Medina E. Assessing the future of a CSP industry in Morocco. *Energy Policy* 2014;69:586–97.
<https://doi.org/10.1016/j.enpol.2014.02.024>.
- [84] Brand B, Boudghene Stambouli A, Zejli D. The value of dispatchability of CSP plants in the electricity systems of Morocco and Algeria. *Energy Policy* 2012;47:321–31. <https://doi.org/10.1016/j.enpol.2012.04.073>.
- [85] ESTELA. Solar power from Europe’s sun belt – a European solar thermo-electric industry initiative contributing to the European Commission Strategic Energy Technology Plan. Brussels: European Solar Thermal Electricity Association. 2009.
- [86] Komendantova N, Patt A. Employment under vertical and horizontal transfer of concentrated solar power technology to North African countries. *Renew Sustain Energy Rev* 2014;40:1192–201.
<https://doi.org/10.1016/j.rser.2014.07.072>.
- [87] DLR (Deutsches Zentrum für Luft- und Raumfahrt) (2013), “A Solar Research and Test Centre for Morocco”, 23 May. 2013.
www.dlr.de/dlr/en/desktopdefault.aspx/tabid-10081/151_read-7107/year-all/#gallery/10409 (accessed September 15, 2013).
- [88] Zhang XP, Ou M, Song Y, Li X. Review of Middle East energy interconnection development. *J Mod Power Syst Clean Energy* 2017;5:917–35.
<https://doi.org/10.1007/s40565-017-0335-7>.
- [89] DLR. Trans-Mediterranean Interconnection for Concentrating Solar Power. A

report by German Aerospace Center (DLR). 2006.

https://www.dlr.de/tt/Portaldata/41/Resources/dokumente/institut/system/projects/TRANS-CSP_Full_Report_Final.pdf.

- [90] Petrollese M, Cocco D, Cau G, Cogliani E. Comparison of three different approaches for the optimization of the CSP plant scheduling. *Sol Energy* 2017;150:463–76. <https://doi.org/10.1016/j.solener.2017.04.060>.
- [91] Madaeni SH, Sioshansi R, Denholm P. Estimating the capacity value of concentrating solar power plants with thermal energy storage: A case study of the southwestern united states. *IEEE Trans Power Syst* 2013;28:1205–15. <https://doi.org/10.1109/TPWRS.2012.2207410>.
- [92] Stekli J; Irwin L; Pitchumani R. Technical Challenges and Opportunities for Concentrating Solar Power With Thermal Energy Storage. *Journal of Thermal Science and Engineering Applications*. June 2013; Vol. 5 / 021011-1. DOI: 10.1115/1.4024143. 2019.
- [93] Ebrahimi M, Cheshme Ghasabani N. Forecasting OPEC crude oil production using a variant Multicyclic Hubbert Model. *J Pet Sci Eng* 2015;133:818–23. <https://doi.org/10.1016/j.petrol.2015.04.010>.
- [94] OPEC. UAE facts and figures. Statistics by the Organization of Petroleum Exporting Countries. 2019. https://www.opec.org/opec_web/en/about_us/170.htm (accessed December 3, 2019).
- [95] IEA. World Energy Statistics and Balances. International Energy Agency; p. 1–1. (19-Apr-2015). 2014.
- [96] Sgouridis S, Abdullah A, Griffiths S, Saygin D, Wagner N, Gielen D, et al. RE-mapping the UAE's energy transition: An economy-wide assessment of renewable energy options and their policy implications. *Renew Sustain Energy Rev* 2016;55:1166–80. <https://doi.org/10.1016/j.rser.2015.05.039>.
- [97] Krarti M, Dubey K. Review analysis of economic and environmental benefits of improving energy efficiency for UAE building stock. *Renewable and Sustainable Energy Reviews* 82 (2018) 14–24. 2018. <https://www.sciencedirect.com/science/article/pii/S1364032117312455?via%3Dihub>.

- [98] UAE-Government. Energy: The energy sector. 2019.
<https://government.ae/en/information-and-services/environment-and-energy/water-and-energy/energy-> (accessed December 3, 2018).
- [99] Said Z, Alshehhi AA, Mehmood A. Predictions of UAE's renewable energy mix in 2030. *Renew Energy* 2018;118:779–89.
<https://doi.org/10.1016/j.renene.2017.11.075>.
- [100] Sgouridis S, Griffiths S, Kennedy S, Khalid A, Zurita N. A sustainable energy transition strategy for the United Arab Emirates: Evaluation of options using an Integrated Energy Model. *Energy Strateg Rev* 2013;2:8–18.
<https://doi.org/10.1016/j.esr.2013.03.002>.
- [101] Arab-Weekly. "Kuwait launches ambitious development plan" [Online]. The Arab Weekly Newspaper, Al Arab Publishing House Quadrant Building 177-179 Hammersmith Road London W6 8BS. Issue date: February 5, 2017, Page No. 20. 2017. <https://thearabweekly.com/sites/default/files/pdf/2017/02/05-02/p1000.pdf#page=20> (accessed October 13, 2019).
- [102] Gulf Consult, "Physical Development Plan of the Northern Sub-Regional Area, Full Master Planning Services including Town Planning, Architectural and Engineering" [Online]. 2012. http://gckuwait.com/portfolio_page/physical-development-plan-of-the-northern-sub-regional-area/.
- [103] Kuwait Municipality. "Third Kuwait Master Plan Review" [Online]. 2009. <http://ud.baladia.gov.kw/main-web/masterplan/masterplan05.htm> (accessed November 7, 2018).
- [104] GSSCPD. "Kuwait National Development Plan" [Online]. General Secretariat of the Supreme Council for Planning and Development, Kuwait. 2016.
https://s3.amazonaws.com/assets.newkuwait.gov.kw/wp-content/uploads/2016/09/KNDP_Inforgraphics_ProjectOverview_ENG.pdf.
- [105] US-EIA. Kuwait is one of the world's top producers and net exporters of oil. Report by the US Energy Information Administration. 2013.
- [106] OPEC. UAE facts and figures. Statistics by the Organization of Petroleum Exporting Countries. 2019.
https://www.opec.org/opec_web/en/about_us/170.htm (accessed December 3, 2018).

- [107] MEW. Statistical yearbook for 2016. A Report by the Ministry of Electricity and Water. Kuwait. 2017. 2017.
- [108] Aljandal S; Alsayegh O; Clean Energy Policy Options: Modeling Possible Deployment Scenarios. EcoMod 2015 Conference; 14-17 July 2015; Boston College; MA. 2015. [https://ecomod.net/system/files/Al_Jandal.Clean energy policy options - Modeling deployment scenarios Final.docx](https://ecomod.net/system/files/Al_Jandal.Clean%20energy%20policy%20options%20-%20Modeling%20deployment%20scenarios%20Final.docx).
- [109] Binamer AO. Al-Abdaliya integrated solar combined cycle power plant: Case study of Kuwait, part I. *Renew Energy* 2019;131:923–37. <https://doi.org/10.1016/j.renene.2018.07.076>.
- [110] Alrai. “Newspaper Article in Arabic” [Online]. Alrai Media Group. Kuwait. Published: 2 Aug 2017. 2017. <http://www.alraimedia.com/Home/Details?Id=3bc2f51e-b8f6-4dc2-8441-484b589d6e21>.
- [111] Alshahed. “Arabic Newspaper Article” [Online]. An article published by Alshahed Newspaper, Kuwait. Published: 21-Jul-2017. 2017. http://www.alshahedkw.com/index.php?option=com_content&view=article&id=172282:2017-07-20-18-10-44&catid=31:03&Itemid=419.
- [112] Kuravi S, Trahan J, Goswami DY, Rahman MM, Stefanakos EK. Thermal energy storage technologies and systems for concentrating solar power plants. *Prog Energy Combust Sci* 2013;39:285–319. <https://doi.org/10.1016/j.pecs.2013.02.001>.
- [113] PSA. Annual technical report 1996. Plataforma Solar de Almeria. 1997. 2004. <https://www.psa.es/es/techrep/1996/report96.pdf>.
- [114] Plaza DM. Plataforma Solar de Almería: The European Solar Thermal Test Centre. 2006.
- [115] Pacheco J, Gilbert R. “Overview of Recent Results of the Solar Two Test and Evaluations Program, Renewable and Advanced Energy Systems for the 21st Century,” *Proceedings of 1999 ASME Int. Solar Energy Conf., Maui, HI. 1999.*
- [116] Dinter F, Geyer M, Tamm R. *Thermal Energy Storage for Commercial Applications*, Springer-Verlag, New York. 1990. 1991. <https://www.springer.com/gp/book/9783540530541>.

- [117] NREL. Concentrating solar power projects. National Renewable Energy Laboratory. 2019. http://www.nrel.gov/csp/solarpaces/by_technology.cfm; 2011 (accessed December 11, 2019).
- [118] Richter C, Blanco J, Heller P, Mehos M, Meier A, Meyer R. Solar Power and Chemical Energy Systems. SolarPACES Annual Report 2006. Int Energy Agency 2009. <http://www.solarpaces.org/wp-content/uploads/ATR2006.pdf>.
- [119] NREL. "Aalborg CSP-Brønderslev CSP with ORC project" [Online]. National Renewable Energy Laboratory. 2017. <https://solarpaces.nrel.gov/aalborg-csp-bronderslev-csp-orc-project> (accessed February 1, 2019).
- [120] CSP Today. Weekly Intelligence Brief: September 13 - September 20. CSP Today. 2010. <https://newenergyupdate.com/csp-today/weekly-intelligence-brief-september-13-september-20>.
- [121] Dreigacker V, Müller-Steinhagen H, Zunft S. Thermo-mechanical analysis of packed beds for large-scale storage of high temperature heat. *Heat Mass Transf Und Stoffuebertragung* 2010;46:1199–207. <https://doi.org/10.1007/s00231-010-0684-5>.
- [122] NREL. "Arcosol 50" [Online]. National Renewable Energy Laboratory. 2017. <https://solarpaces.nrel.gov/arcosol-50> (accessed February 1, 2019).
- [123] Tamme R. Development of storage systems for SP plants. Brussels. 2006.
- [124] Solucar. 10 MW Solar Thermal Power Plant for Southern Spain. Final Tech Prog Rep 2006:1–10. http://ec.europa.eu/energy/res/sectors/doc/csp/ps10_final_report.pdf.
- [125] NREL. "ASE Demo" [Online]. National Renewable Energy Laboratory. 2015. <https://solarpaces.nrel.gov/ase-demo-plant> (accessed February 1, 2019).
- [126] NREL. "Diwakar" [Online]. National Renewable Energy Laboratory. 2013. <https://solarpaces.nrel.gov/diwakar> (accessed February 1, 2019).
- [127] Dunn RI, Hearps PJ, Wright MN. Molten-salt power towers: newly commercial concentrating solar storage. *Proceedings of the IEEE* 2012;100(2):504e15. DOI: 10.1109/JPROC.2011.2163739. 2012. <https://ieeexplore.ieee.org/stamp/stamp.jsp?tp=&arnumber=6035949&tag=1>.
- [128] NREL. "Gujarat Solar One" [Online]. National Renewable Energy Laboratory.

2014. <https://solarpaces.nrel.gov/gujarat-solar-one>.
- [129] Sener. Andasol 1 & 2: 50 MW, 7 h molten salt heat storage. National Renewable Energy Laboratory, NREL trough technology workshop. 2018. http://www.nrel.gov/csp/troughnet/pdfs/2007/martin_andasol_pictures_storage.pdf.
- [130] NREL. “Gulang 100MW Thermal Oil Parabolic Trough project” [Online]. National Renewable Energy Laboratory. 2016. <https://solarpaces.nrel.gov/gulang-100mw-thermal-oil-parabolic-trough-project> (accessed February 1, 2019).
- [131] NREL. “Ilanga I” [Online]. National Renewable Energy Laboratory. 2018. <https://solarpaces.nrel.gov/ilanga-i> (accessed February 1, 2019).
- [132] NREL. “Extresol-1” [Online]. National Renewable Energy Laboratory. 2017. <https://solarpaces.nrel.gov/extresol-1> (accessed February 1, 2019).
- [133] NREL. “Kathu Solar Park” [Online]. National Renewable Energy Laboratory. 2019. <https://solarpaces.nrel.gov/kathu-solar-park> (accessed February 1, 2019).
- [134] NREL. “KaXu Solar One” [Online]. National Renewable Energy Laboratory. 2015. <https://solarpaces.nrel.gov/kaxu-solar-one> (accessed February 1, 2019).
- [135] NREL. “KVK Energy Solar Project” [Online]. National Renewable Energy Laboratory. 2013. <https://solarpaces.nrel.gov/kvk-energy-solar-project> (accessed February 1, 2019).
- [136] Xu E, Yu Q, Wang Z, Yang C. Modeling and simulation of 1 MW DAHAN solar thermal power tower plant. *Renew Energy* 2011;36:848–57. <https://doi.org/10.1016/j.renene.2010.08.010>.
- [137] ADB - Technical Assistance Consultant’s Report Project. People’s Republic of China : Concentrating Solar Thermal Power Development 2012. <https://www.solarthermalworld.org/sites/default/files/China CSP development.pdf>.
- [138] Scott P, Alonso ADLC, Hinkley JT, Pye J. SolarTherm: A flexible Modelica-based simulator for CSP systems. *AIP Conf. Proc.*, vol. 1850, 2017. <https://doi.org/10.1063/1.4984560>.

- [139] Hogan RE. AEETES—A solar reflux receiver thermal performance numerical model. *Sol Energy* 1994;52:167–78. [https://doi.org/10.1016/0038-092X\(94\)90066-3](https://doi.org/10.1016/0038-092X(94)90066-3).
- [140] Hogan R. AEETES a solar reflux receiver thermal performance numerical model. In: *Proceedings of the 1992 ASME international solar energy conference, Maui, HI; 1992*. 1992.
- [141] Hogan R. Heat transfer analysis of radiant heating panels-Hot water pipes in concrete slab floor, M.S. thesis, Louisiana Tech University (1979). 1979.
- [142] Schneider G, Zedan M. Control volume based finite element formulation of the heat conduction equation, AIAA-82-0909, AIAA/ASME Proceedings of the 3rd Joint Thermophysics, Fluids, Plasma and Heat Transfer Conference, St. Louis, MO, June 7-11 (1982). 1982.
- [143] Sandia. “Solar Glare and Flux Analysis Tools”. Sandia National Laboratories, National Technology and Engineering Solutions of Sandia, LLC., Honeywell International, Inc., U.S. Department of Energy’s National Nuclear Security Administration. 2013. <https://share-ng.sandia.gov/glare-tools/>.
- [144] Goswami D. *Principles of Solar Engineering*. Third Edition. CRC Press; Taylor and Francis Group. 2015. https://books.google.co.uk/books?id=v4GbbgAAQBAJ&source=gbs_navlinks_s (accessed December 10, 2018).
- [145] Breault. *The ASAP Primer: A basic course of study of ASAP software, the most powerful set of tools for optical analysis*. A report by Breault Research Organization. 2012. http://www.breault.com/sites/default/files/knowledge_base/broman0955_primer.pdf.
- [146] Breault Research Organization. *Introduction to Wave Optics Analysis in ASAP*. 2019. <http://www.breault.com/software/asap-applications>.
- [147] Ho C, Sims C. *Tower Illuminance Model*. U.S. Department of Energy Office of Scientific and Technical Information. 2017. <https://www.osti.gov/biblio/1399217-tower-illuminance-model>.
- [148] Christian JM, Ho CK. CFD simulation and heat loss analysis of the solar two power tower receiver. *ASME 2012 6th Int. Conf. Energy Sustain. ES 2012*,

Collocated with ASME 2012 10th Int. Conf. Fuel Cell Sci. Eng. Technol., 2012, p. 227–35. <https://doi.org/10.1115/ES2012-91030>.

- [149] Moghimi MA, Craig KJ, Meyer JP. A novel computational approach to combine the optical and thermal modelling of Linear Fresnel Collectors using the finite volume method. *Sol Energy* 2015;116:407–27. <https://doi.org/10.1016/j.solener.2015.04.014>.
- [150] Bofill M, Palah M. SIMPLY : a Compiler from a CSP Modeling Language to the SMT-LIB Format. Eighth Int. Work. Constraint Model. Reformul., 2009.
- [151] Ratzel A, Boughton B. CIRCE.001: a computer code for analysis of point focus concentrators with flat targets. Albuquerque: Sandia National Laboratories; 1987. SAND86-1866. 1987. <https://prod.sandia.gov/techlib-noauth/access-control.cgi/1986/861866.pdf>.
- [152] Romero VJ. CIRCE2/DEKGEN2: a software package for facilitated optical analysis of 3-D distributed solar energy concentrators - Theory and user manual. Albuquerque; NM: Sandia National Laboratories; 1994. SAND91-2238. 1992.
- [153] El Hefni B. Dynamic modeling of concentrated solar power plants with the ThermoSysPro library (Parabolic Trough collectors, Fresnel reflector and Solar-Hybrid). *Energy Procedia* 2013;49:1127–37. <https://doi.org/10.1016/j.egypro.2014.03.122>.
- [154] Kistler BL. A User's Manual for DELSOL3: A Computer Code for Calculating the Optical Performance and Optimal System Design for Solar Thermal Central Receiver Plants. Sandia National Laboratories; Albuquerque; SAND86-8018. 1986. <https://doi.org/SAND86-8018>.
- [155] Weinrebe G, Von Reeken F, Wöhrbach M, Plaz T, Göcke V, Balz M. Towards holistic power tower system optimization. *Energy Procedia* 2014;49:1573–81. <https://doi.org/10.1016/j.egypro.2014.03.166>.
- [156] Dellin T, Fish M, Yang C. A User's Manual For DELSOLP: A Computer Code For Calculating the Optical Performance and Optimal System Design For Solar-Thermal Central-Receiver Plant. Sandia National Laboratories. 1981. Available: <https://www.osti.gov/servlets> 1981.
- [157] Falcone P. A handbook for solar central receiver design. SAND86-8009. Sandia

- National Laboratories; 1986. C-9. 1986. <https://prod-ng.sandia.gov/techlib-noauth/access-control.cgi/1986/868009.pdf>.
- [158] Qi F, Wen F, Liu X A-SM. A Residential Energy Hub Model with a Concentrating Solar Power Plant and Electric Vehicles. *Energies* 2017, 10, 1159; doi:10.3390/en10081159. 2017. <https://www.mdpi.com/1996-1073/10/8/1159>.
- [159] Igo J, Andraka CE. Solar dish field system model for spacing optimization. *Proc. Energy Sustain. Conf.* 2007, 2007, p. 981–8. <https://doi.org/10.1115/ES2007-36154>.
- [160] Blair N, Mehos M, Short W, Heimiller D. Concentrating Solar Deployment System (CSDS) - A new model for estimating U.S. concentrating solar power (CSP) market potential. vol. 2. 2006.
- [161] Winters W. DRAC: A User-Friendly Computer Code for Modeling Transient -1 - Thermohydraulic Phenomena in Solar-Receiver Tubing. Sandia National Laboratories, Livermore, US. 1983.
- [162] W. W. TOPAZ-A Computer Code for Modeling Heat Transfer and Fluid Flow in Arbitrary Networks of Pipes, Flow Branches, and Vessels. Sandia National Laboratories for the US Department of Energy. 1984.
- [163] Winters WS. TOPAZ e the transient one-dimensional pipe flow analyzer: an update on code improvements and increased capabilities. Livermore, CA: Sandia National Laboratories; 1987. SAND87-8225. 1985.
- [164] Häggståhl D, Dahlquist E. Evaluation of Prosim and IPSEpro, Two Heat and Mass Balance Simulation Softwares; *Proc. of SIMS 2003 - 44th Conference on Simulation and Modeling*, Västerås, Sweden., 2003, p. 6.
- [165] Solid Works. Introducing COSMOSWorks. Solid Work Co. 2003. <https://www.clear.rice.edu/mech403/HelpFiles/IntroducingCW.pdf> (accessed December 10, 2018).
- [166] Kohnke P. ANSYS. Theory reference. Knowl Creat Diffus Util 2009;3304:724–46. <http://research.me.udel.edu/~lwang/teaching/MEx81/ansys56manual.pdf>.
- [167] Introducing solidworks (manual book). 1995-2015, Dassault Systemes SolidWorks Corporation, a Dassault Systèmes SE company, 175 Wyman Street, Waltham, Mass. 02451 USA. 2015.

https://my.solidworks.com/solidworks/guide/SOLIDWORKS_Introduction_EN.pdf.

- [168] Schmitz M, Schwarzbözl P, Buck R, Pitz-Paal R. Assessment of the potential improvement due to multiple apertures in central receiver systems with secondary concentrators. *Sol Energy* 2006;80:111–20.
<https://doi.org/10.1016/j.solener.2005.02.012>.
- [169] Rheinländer J, Perz EW, Goebel O. Performance simulation of integrated water and power systems - Software tools IPSEpro and RESYSpro for technical, economic and ecological analysis. *Desalination* 2003;157:57–64.
[https://doi.org/10.1016/S0011-9164\(03\)00383-7](https://doi.org/10.1016/S0011-9164(03)00383-7).
- [170] ANSYS Fluent. Fluid dynamics solutions. 2019.
<https://www.ansys.com/products/fluids/ansys-fluent>.
- [171] Christian JM, Ortega JD, Ho CK. Novel tubular receiver panel configurations for increased efficiency of high-temperature solar receivers. *ASME 2015 9th Int. Conf. Energy Sustain. ES 2015, collocated with ASME 2015 Power Conf. ASME 2015 13th Int. Conf. Fuel Cell Sci. Eng. Technol. ASME 2015 Nucl. Forum, vol. 1, 2015*. <https://doi.org/10.1115/ES2015-49431>.
- [172] Mills B, Ho CK. Annualized thermal performance of intermediate-scale falling particle receivers. *AIP Conference Proceedings* 2033, 040026 (2018);
<https://doi.org/10.1063/1.5067062>. *AIP Conf. Proc.*, vol. 2033, 2018.
<https://doi.org/10.1063/1.5067062>.
- [173] Cau G, Cocco D, Tola V. Performance and cost assessment of integrated solar combined cycle systems (ISCCS) using CO₂ as heat transfer fluid. *30th ISES Bienn Sol World Congr 2011, SWC 2011* 2011;5:4000–11.
<https://doi.org/10.18086/swc.2011.25.07>.
- [174] GE Energy. Fact sheet/GateCycle-Heat Balance Software for Power Plant Simulation. 2005. http://www.epcmart.co.kr/data/Gate_Cycle_FactSheet.pdf.
- [175] Deng H, Boehm RF. An estimation of the performance limits and improvement of dry cooling on trough solar thermal plants. *Appl Energy* 2011;88:216–23.
<https://doi.org/10.1016/j.apenergy.2010.05.027>.
- [176] INSEL. Getting started with INSEL 8. Stuttgart:INSEL 2014.
https://www.insel.eu/files/public/gettingStarted_en.pdf.

- [177] Biggs F VC. The Helios Model for the Optical Behavior of Reflecting Solar Concentrators. A report by the Sandia National Laboratories, US. 1979. <https://prod.sandia.gov/techlib-noauth/access-control.cgi/1976/760347.pdf>.
- [178] Vittitoe C, Biggs F. User's guide to HELIOS: part 1, introduction and code input. A computer program for modeling the optical behavior of reflecting concentrators. Albuquerque, NM: Sandia National Laboratories; 1981.SAND81-1180. 1981.
- [179] de Lucena AFP, Schaeffer R, Szklo AS. Least-cost adaptation options for global climate change impacts on the Brazilian electric power system. *Glob Environ Chang* 2010;20:342–50. <https://doi.org/10.1016/j.gloenvcha.2010.01.004>.
- [180] Garcia P, Ferriere A, Bezia JJ. Codes for solar flux calculation dedicated to central receiver system applications: A comparative review. *Sol Energy* 2008;82:189–97. <https://doi.org/10.1016/j.solener.2007.08.004>.
- [181] Leary P, Hankins J. User's guide for MIRVAL e a computer code for modeling the optical behavior of reflecting solar concentrators. Livermore, CA: Sandia National Laboratories; 1979. SAND77-8280. 1979. <https://www.osti.gov/servlets/purl/6371450>.
- [182] Fichter T, Trieb F, Moser M, Kern J. Optimized integration of renewable energies into existing power plant portfolios. *Energy Procedia* 2014;49:1858–68. <https://doi.org/10.1016/j.egypro.2014.03.197>.
- [183] Abrams M. RADSOLVER - A Computer Program for Calculating Spectrally Dependent Radiative Heat Transfer in Solar Cavity Receivers, SAND81-8248, Sandia National Laboratories, September 1981. 1981. <https://www.osti.gov/servlets/purl/6254943>.
- [184] Hess D. The empirical probability of integrating CSP and its cost optimal configuration in a low carbon energy system of EUMENA. *Sol Energy* 2018;166:267–307. <https://doi.org/10.1016/j.solener.2018.03.034>.
- [185] Blair N, Dobos A, Freeman J, Neises T, Wagner M, Ferguson T, Gilman P, Janzou S. System Advisor Model, SAM 2014.1.14: General Description. NREL/TP-6A20-61019. National Renewable Energy Laboratory. Golden, CO. 2014:13. <https://www.nrel.gov/docs/fy14osti/61019.pdf> (accessed December 10, 2018).
- [186] Gilman P, Blair N, Mehos M, Christensen C, Janzou S. Solar Advisor Model user

guide for version 2.0. NREL/TP-670-43704 2008. 2008.

- [187] System Advisor Model (SAM). National Renewable Energy Laboratory. 2019. <https://sam.nrel.gov/download.html>.
- [188] Wagner M, Gilman P. Technical Manual for the SAM Physical Trough Model. A Report by NREL. 2011. <https://www.nrel.gov/docs/fy11osti/51825.pdf>.
- [189] Guzman L, Henao A, Vasquez R. Simulation and optimization of a parabolic trough solar power plant in the city of Barranquilla by using system advisor model (SAM). *Energy Procedia* 2014;57:497–506. <https://doi.org/10.1016/j.egypro.2014.10.203>.
- [190] Llorente García I, Álvarez JL, Blanco D. Performance model for parabolic trough solar thermal power plants with thermal storage: Comparison to operating plant data. *Sol Energy* 2011;85:2443–60. <https://doi.org/10.1016/j.solener.2011.07.002>.
- [191] Blair N, Mehos M, Christensen C. Sensitivity of concentrating solar power trough performance, cost, and financing with the solar advisor model. 2008 14th Biennial CSP SolarPACES (Solar Power and Chemical Energy Systems) Symposium, 4-7 March 2008, Las Vega 2008. <https://www.nrel.gov/docs/fy08osti/42852.pdf>.
- [192] Branker K, Pathak MJM, Pearce JM. A review of solar photovoltaic levelized cost of electricity. *Renew Sustain Energy Rev* 2011;15:4470–82. <https://doi.org/10.1016/j.rser.2011.07.104>.
- [193] Santos JJCS, Palacio JCE, Reyes AMM, Carvalho M, Freire AJR, Barone MA. Concentrating Solar Power. vol. 1. 2018. <https://doi.org/10.1016/B978-0-12-812959-3.00012-5>.
- [194] Hoffmann W. PV solar electricity in EUMENA: headway in the world. Mediterranean solar plan-introduction. European Photovoltaic Industry Association (EPIA); Valencia; May 11th 2010. 2010.
- [195] Gils HC, Simon S. Carbon neutral archipelago – 100% renewable energy supply for the Canary Islands. *Appl Energy* 2017;188:342–55. <https://doi.org/10.1016/j.apenergy.2016.12.023>.
- [196] Stoddard MC, Faas SE, Chiang CJ, Dirks J a. SOLERGY - A Computer Code for

- Calculating the Annual Energy from Central Receiver Power Plants 1987:153.
<https://prod.sandia.gov/techlib-noauth/access-control.cgi/1986/868060.pdf>.
- [197] Müller-Steinhagen H. Concentrating solar thermal power. *Phil Trans R Soc A* 371: 20110433. <http://dx.doi.org/10.1098/rsta.2011.0433> 2013:655–763.
<https://royalsocietypublishing.org/doi/10.1098/rsta.2011.0433>.
- [198] Eck M, Steinmann WD. Modelling and design of direct solar steam generating collector fields. *J Sol Energy Eng Trans ASME* 2005;127:371–80.
<https://doi.org/10.1115/1.1849225>.
- [199] Wendelin T, Dobos A, Lewandowski A. SolTrace: A Ray-Tracing Code for Complex Solar Optical Systems. A Report by the National Renewable Energy Laboratory, Golden, Colorado. 2013;303:275–3000.
<https://www.nrel.gov/docs/fy14osti/59163.pdf>.
- [200] NREL. SolTrace description. National Renewable Energy Laboratory. 2018.
<https://www.nrel.gov/csp/soltrace.html>.
- [201] Aung KT. Simulation Tools for Renewable Energy Projects. 2011 ASEE Annual Conference & Exposition, Vancouver, BC 2011.
<https://peer.asee.org/simulation-tools-for-renewable-energy-projects>.
- [202] THERMOFLOW. Program Overview – Program: STEAM PRO & STEAM MASTER. A Report by THERMOFLOW Inc., US. 2015.
https://www.thermoflow.com/Images/PROGRAM_BROCHURE_2015.pdf.
- [203] Thermoflow Inc. STEAM PRO: Conventional steam power plant creation. 2018.
https://www.thermoflow.com/products_conventionalsteam.html.
- [204] Pacheco J. Final Test and Evaluation Results from the Solar Two Project. National Renewable Energy Laboratory. 2002. <https://prod-ng.sandia.gov/techlib-noauth/access-control.cgi/2002/020120.pdf>.
- [205] Study E, View SP. Matlab Simulation of 10 MW Molten Salt Solar Power Tower Plant in Aswan Matlab Simulation of 10 MW Molten Salt Solar Power Tower Plant in Aswan 2017;1:34–43.
- [206] Kolb G, Diver R. Conceptual design of an advanced trough utilizing a molten salt working fluid. *SolarPACES Symp Las Vegas* 2008:1–8.
<http://energy.sandia.gov/wp/wp->

content/gallery/uploads/SolarPACES_2X_Trough.pdf.

- [207] The Center for Solar Energy and Hydrogen Research (ZSW, Stuttgart, Germany) upgraded Sandia's HELIOS software in the mid 1990's to model trough mirrors. Available from Greg J. Kolb, Sandia National Laboratories MS 1127 Albuquerque, NM, 87185-5800. 1999.
- [208] Denholm P, Wan YH, Hummon M, Mehos M. The value of CSP with thermal energy storage in the western United States. *Energy Procedia* 2014;49:1622–31. <https://doi.org/10.1016/j.egypro.2014.03.171>.
- [209] Dobos A, Neises T, Wagner M. Advances in CSP simulation technology in the System Advisor Model. *Energy Procedia* 2014;49:2482–9. <https://doi.org/10.1016/j.egypro.2014.03.263>.
- [210] TRNSYS. A transient systems simulation program. Thermal Energy System Specialists, LLC. 2019. <http://www.trnsys.com/demo/index.html>.
- [211] Mondejar ME, Thern M. A new IPSEpro library for the simulation of binary mixtures of real fluids in power cycle analysis. *Journal of Postdoctoral Research. J Postdr Res* 2014;2. <https://doi.org/10.14304/surya.jpr.v2n3.1>.
- [212] SimTech. What is IPSEpro? [Online]. SimTech Simulation Technology. SimTech GmbH - Riesstr. 120, 8010 Graz, Austria. 2019. <http://simtechnology.com/CMS/index.php/ipsepro>.
- [213] Mondejar ME, Thern M. A new IPSEpro® library for the simulation of binary mixtures of real fluids in power cycle analysis. *Postdoc J* 2014;2. <https://doi.org/10.14304/surya.jpr.v2n3.1>.
- [214] Casablanca | Concentrating Solar Power Projects | NREL n.d. <https://solarpaces.nrel.gov/project/casablanca> (accessed April 4, 2022).
- [215] CGN Delingha - 50MW Trough | Concentrating Solar Power Projects | NREL n.d. <https://solarpaces.nrel.gov/project/cgn-delingha-50mw-trough> (accessed April 4, 2022).
- [216] SZWGroup | CSP Focus China 2016 n.d. http://www.szwgroup.com/csp-focus-china-2016/news_detail.aspx?pid=86 (accessed April 4, 2022).
- [217] World Bank. Project Information Document, Appraisal Stage. Report No.: 55106, 2010. 2010.

- [218] Turchi C. Parabolic Trough Reference Plant for Cost Modeling with the Solar Advisor Model (SAM). Technical Report. National Renewable Energy Laboratory. NREL/TP-550-47605. 2010.
- [219] Burkholder F, Kutscher C. Heat Loss Testing of Schott's 2008 PTR70 Parabolic Trough Receiver. 2008.
- [220] Wang Y, Zhu Y, Chen H, Yang L, Yang M. Thermal Performance of a Single-Pass All-Glass Parabolic Trough Receiver 2016.
[https://doi.org/10.1061/\(ASCE\)EY.1943-7897.0000381](https://doi.org/10.1061/(ASCE)EY.1943-7897.0000381).
- [221] Morales A, San Vicente G. A new generation of absorber tubes for concentrating solar thermal (CST) systems. *Adv Conc Sol Therm Res Technol* 2017:59–73. <https://doi.org/10.1016/B978-0-08-100516-3.00004-6>.
- [222] Giostri A, Binotti M, Astolfi M, Silva P, Macchi E, Manzolini G. Comparison of different solar plants based on parabolic trough technology 2012.
<https://doi.org/10.1016/j.solener.2012.01.014>.
- [223] Transient effects in linear concentrating solar thermal power plant 2014.
https://www.researchgate.net/publication/272163920_Transient_effects_in_linear_concentrating_solar_thermal_power_plant?channel=doi&linkId=54dca39b0cf282895a3acec1&showFulltext=true (accessed August 12, 2021).
- [224] Realising the Potential of Concentrating Solar Power in Australia. 2012.
- [225] Experiments: Planning, Analysis, and Optimization, 2nd Edition | Wiley n.d.
<https://www.wiley.com/en-gb/Experiments:+Planning,+Analysis,+and+Optimization,+2nd+Edition-p-9780471699460> (accessed April 3, 2022).
- [226] Wagner M. Simulation and predictive performance modeling of utility-scale central receiver system power plants. 2008.
- [227] Methodology for Constructing Reduced-Order Power Block Performance Models for CSP Applications: Preprint - UNT Digital Library n.d.
<https://digital.library.unt.edu/ark:/67531/metadc1013788/> (accessed April 3, 2022).
- [228] Ho CK. SANDIA. Software and Codes for Analysis of Concentrating Solar Power Technologies. Sandia National Laboratories. 2008. Available:

<https://www.osti.gov/biblio/946571>. 2008.

- [229] Trabelsi SE, Chargui R, Qoaidar L, Liqreina A, Guizani AA. Techno-economic performance of concentrating solar power plants under the climatic conditions of the southern region of Tunisia. *Energy Convers Manag* 2016;119:203–14. <https://doi.org/10.1016/j.enconman.2016.04.033>.
- [230] Kesseli D, Wagner M, Guédez R, Turchi CS. KTH Royal Institute of Technology Presented at the SolarPACES Conference 2018 Casablanca n.d.
- [231] National Renewable Energy Laboratory (NREL) 2021. <https://www.nrel.gov/> (accessed September 25, 2020).
- [232] Hamilton WT, Newman AM, Wagner MJ, Braun RJ. Off-design performance of molten salt-driven Rankine cycles and its impact on the optimal dispatch of concentrating solar power systems. *Energy Convers Manag* 2020;220. <https://doi.org/10.1016/j.enconman.2020.113025>.
- [233] Fares MS Ben, Abderafi S. Water consumption analysis of Moroccan concentrating solar power station. *Sol Energy* 2018;172:146–51. <https://doi.org/10.1016/j.solener.2018.06.003>.
- [234] Al-Rasheedi M, Gueymard CA, Ismail A, Hussain T. Comparison of two sensor technologies for solar irradiance measurement in a desert environment. *Sol Energy* 2018;161:194–206. <https://doi.org/10.1016/j.solener.2017.12.058>.
- [235] SolarGIS. Solargis s.r.o. Mýtna 48, 811 07 Bratislava, Slovakia. 2019. www.solargis.com.
- [236] GeoModel Solar. “GeoModel Solar Launches New Generation Online Tools for Solar Site Prospecting and Bankable Photovoltaic Yield Assessment/About GeoModel Solar” [Online]. 2012. https://solargis.info/doc/_docs/pr/GeoModelSolar_PressRelease_New-Generation-Online-Tools-for-Solar-Site-Prospecting-and-Bankable-Photovoltaic-Yield-Assessment_20120117.pdf.
- [237] Gueymard CA. Solar Radiation, Introduction. In: Meyers R.A. (eds) *Encyclopedia of Sustainability Science and Technology*. Springer, New York, NY 2012. https://link.springer.com/referenceworkentry/10.1007%2F978-1-4419-0851-3_929.

- [238] Gueymard CA. Solar resource assessment for CSP and CPV. Leonardo Energy webinar. 2010. <https://www.slideshare.net/sustenergy/csp-training-series-solar-resource-assessment-12>.
- [239] Gueymard CA. REST2: High-performance solar radiation model for cloudless-sky irradiance, illuminance, and photosynthetically active radiation - Validation with a benchmark dataset. *Sol Energy* 2008;82:272–85. <https://doi.org/10.1016/j.solener.2007.04.008>.
- [240] Ineichen P. A broadband simplified version of the Solis clear sky model. *Sol Energy* 2008;82:758–62. <https://doi.org/10.1016/j.solener.2008.02.009>.
- [241] Cebecauer T, Perez R, Suri M. Comparing performance of solargis and suny satellite models using monthly and daily aerosol data. 30th ISES Bienn Sol World Congr 2011, SWC 2011 2011;5:3564–71. <https://doi.org/10.18086/swc.2011.24.05>.
- [242] Younes S, Claywell R, Muneer T. Quality control of solar radiation data: Present status and proposed new approaches. *Energy* 2005;30:1533–49. <https://doi.org/10.1016/j.energy.2004.04.031>.
- [243] Perez R, Seals R, Ineichen P, Stewart R, Menicucci D. A new simplified version of the perez diffuse irradiance model for tilted surfaces. *Sol Energy* 1987;39:221–31. [https://doi.org/10.1016/S0038-092X\(87\)80031-2](https://doi.org/10.1016/S0038-092X(87)80031-2).
- [244] Gueymard CA. An anisotropic solar irradiance model for tilted surfaces and its comparison with selected engineering algorithms. *Sol Energy* 1987;38:367–86. [https://doi.org/10.1016/0038-092X\(87\)90009-0](https://doi.org/10.1016/0038-092X(87)90009-0).
- [245] Perez R., Cebecauer T. SM. Semi-Empirical Satellite Models. In Kleissl J. (ed.) *Solar Energy Forecasting and Resource Assessment*. Academic press. 2013. <https://www.sciencedirect.com/science/article/pii/B9780123971777000024>.
- [246] Cebecauer T, Šúri M, Perez R. High performance msg satellite model for operational solar energy applications. 39th ASES Natl Sol Conf 2010, *Sol* 2010 2010;1:1–22.
- [247] Cebecauer T, Šúri M. Correction of Satellite-Derived DNI Time Series Using Locally-Resolved Aerosol Data. *Proceedings of the SolarPACES Conference, Marrakech, Morocco, September 2012*. 2012.

- [248] Šúri M, Cebecauer T, Perez R. Quality procedures of SolarGIS for provision site-specific solar resource information. Conf SolarPACES 2010:1–5.
- [249] Cebecauer T, Marcel Š, Gueymard CA. Uncertainty Sources in Satellite-Derived Direct Normal Irradiance: How Can Prediction Accuracy Be Improved Globally? Proc. SolarPACES Conf., 2011, p. 20–3.
- [250] NCAR/UCAR. “Climate Forecast System Reanalysis (CFSR)” [Online]. National Center for Atmospheric Research/University Corporation for Atmospheric Research. 2019. <https://climatedataguide.ucar.edu/climate-data/climate-forecast-system-reanalysis-cfsr>.
- [251] NOAA. “NCEP Products Inventory- GFS model” [Online]. NOAA/National Weather Service National Centers for Environmental Prediction. 2019. <http://www.nco.ncep.noaa.gov/pmb/products/gfs/>.
- [252] Cebecauer T, Šúri M, Perez R. High performance MSG satellite model for operational solar energy applications. 39th ASES Natl. Sol. Conf. 2010, Sol. 2010, vol. 1, 2010, p. 1–22.
- [253] Cebecauer T, Suri M. Accuracy improvements of satellite-derived solar resource based on GEMS re-analysis aerosols. Conf. SolarPACES 2010, vol. 2009, 2010, p. 1–4.
- [254] Perez RR, Ineichen P, Maxwell EL, Seals RD, Zelenka A. Dynamic global-to-direct irradiance conversion models. ASHRAE Transactions-Research Series. ASHRAE Trans 1992;98:354–69.
- [255] Ineichen P. Five satellite products deriving beam and global irradiance validation on data from 23 ground stations. A Report by the University of Geneva/IEA SHC Task 36. Univ Geneva 2011. http://www.task24.iea-shc.org/data/sites/1/publications/Five_Satellite_Products_Deriving_Beam_and_Global_Irradiance_Validation_on_Data_from_23_Ground_Stations.pdf.
- [256] Gulf-Insider. “Sarayat season in Kuwait brings unstable weather” [Online]. 2017. <https://www.gulf-insider.com/sarayat-season-kuwait-brings-unstable-weather/>.
- [257] Al-Hemoud A, Al-Sudairawi M, Neelamanai S, Naseeb A, Behbehani W. Socioeconomic effect of dust storms in Kuwait. Arab J Geosci 2017;10. <https://doi.org/10.1007/s12517-016-2816-9>.

- [258] Al-Dousari A, Doronzo D, Ahmed M. Types, indications and impact evaluation of sand and dust storms trajectories in the Arabian Gulf. *Sustain* 2017;9. <https://doi.org/10.3390/su9091526>.
- [259] Steensma G, Román R, Marshall C, Bermejo J, Iyer K, Al-Hajraf S, et al. Shagaya renewable energy park project. *AIP Conf Proc* 2019;2126. <https://doi.org/10.1063/1.5117583>.
- [260] Aldousari AM, Aldousari N, Ramadhan A, Ahmed M AA "A. Assessments of dust fallout within Kuwait. *ProScience 1* (2014) 149-155. Conference: International Conference on Atmospheric Dust, At Italy, 2014.
- [261] KISR. GIS. Map of Kuwait with meteorological masts. Kuwait Institute for Scientific Research, Kuwait. 2015.
- [262] KISR. GIS. Map of Kuwait with elevations. Kuwait Institute for Scientific Research, Kuwait. 2015.
- [263] The Diurnal Wind Variation in the Lowest 1500 ft in Central Oklahoma. June 1966–May 1967 in: *Journal of Applied Meteorology and Climatology* Volume 12 Issue 1 (1973) 1973. https://journals.ametsoc.org/view/journals/apme/12/1/1520-0450_1973_012_0127_tdwwit_2_0_co_2.xml?tab_body=fulltext-display (accessed December 5, 2020).
- [264] Mahrt L. The early evening boundary layer transition. *Q J R Meteorol Soc* 2007;107:329–43. <https://doi.org/10.1002/qj.49710745205>.
- [265] Agagna B, Smaili A, Behar O. An improved model for predicting the performance of parabolic trough solar collectors. *Int J Energy Res* 2018;42:4512–21. <https://doi.org/10.1002/ER.4165>.
- [266] Tagle-Salazar PD, Nigam KDP, Rivera-Solorio CI. Parabolic trough solar collectors: A general overview of technology, industrial applications, energy market, modeling, and standards. *Green Process Synth* 2020;9:595–649. <https://doi.org/10.1515/GPS-2020-0059>.
- [267] Moya EZ. Parabolic-trough concentrating solar power (CSP) systems. *Conc Sol Power Technol* 2012:197–239. <https://doi.org/10.1533/9780857096173.2.197>.

- [268] IRENA. The Power to Change: Solar and Wind Cost Reduction Potential to 2025. International Renewable Energy Agency 2016:112.
https://www.irena.org/documentdownloads/publications/irena_power_to_change_2016.pdf.
- [269] Pitz-Paal R. Concentrating Solar Power Systems. DLR Institute of Solar Research - Linder Höhe, 51147 Cologne, Germany. EPJ Web of Conferences 148, 00008 (2017) LNES 2016. DOI: 10.1051/epjconf/201714800008. 2017.
https://www.epj-conferences.org/articles/epjconf/pdf/2017/17/epjconf_eps-sif2017_00008.pdf.
- [270] Ummadisingu A, Soni MS. Concentrating solar power - Technology, potential and policy in India. *Renew Sustain Energy Rev* 2011;15:5169–75.
<https://doi.org/10.1016/j.rser.2011.07.040>.
- [271] Py X, Azoumah Y, Olives R. Concentrated solar power: Current technologies, major innovative issues and applicability to West African countries. *Renew Sustain Energy Rev* 2013;18:306–15. <https://doi.org/10.1016/j.rser.2012.10.030>.
- [272] Pavlović TM, Radonjić IS, Milosavljević DD, Pantić LS. A review of concentrating solar power plants in the world and their potential use in Serbia. *Renew Sustain Energy Rev* 2012;16:3891–902.
<https://doi.org/10.1016/j.rser.2012.03.042>.
- [273] Mendelsohn M; Lowder T; Canavan B. Utility-Scale Concentrating Solar Power and Photovoltaics Projects: A Technology and Market Overview. A Report by the National Renewable Energy Laboratory; United States. April 2012 . 2012.
<https://www.nrel.gov/docs/fy12osti/51137.pdf>.
- [274] CSPA. The economic and reliability benefits of CSP with thermal energy storage: literature review and research needs. A Report by the Concentrating Solar Power Alliance. 2014.
- [275] Jorgenson J, Denholm P, Mehos M, Turchi C. Estimating the Performance and Economic Value of Multiple Concentrating Solar Power Technologies in a Production Cost Model. A Report by the National Renewable Energy Laboratory, United States. 2013.
- [276] IRENA. Concentrating Solar Power: Technology Brief. A Report by the International Renewable Energy Agencies. 2006.

[https://doi.org/10.1061/40802\(189\)109](https://doi.org/10.1061/40802(189)109).

- [277] Chu Y. Review and Comparison of Different Solar Energy Technologies, Global Energy Network Institute (GENI). 2011. <https://doi.org/10.1002/ejoc.201200111>.
- [278] Morin G, Dersch J, Platzer W, Eck M, Häberle A. Comparison of Linear Fresnel and Parabolic Trough Collector power plants. *Sol Energy* 2012;86:1–12. <https://doi.org/10.1016/j.solener.2011.06.020>.
- [279] Suresh NS, Thirumalai NC, Rao BS, Ramaswamy MA. Methodology for sizing the solar field for parabolic trough technology with thermal storage and hybridization. *Sol Energy* 2014;110:247–59. <https://doi.org/10.1016/j.solener.2014.09.020>.
- [280] Yilmaz IH, Söylemez MS. Thermo-mathematical modeling of parabolic trough collector. *Energy Convers Manag* 2014;88:768–84. <https://doi.org/10.1016/j.enconman.2014.09.031>.
- [281] Ouagued M, Khellaf A, Loukarfi L. Estimation of the temperature, heat gain and heat loss by solar parabolic trough collector under Algerian climate using different thermal oils. *Energy Convers Manag* 2013;75:191–201. <https://doi.org/10.1016/j.enconman.2013.06.011>.
- [282] Renewable Energy Agency I. RENEWABLE ENERGY TECHNOLOGIES: COST ANALYSIS SERIES Concentrating Solar Power Volume 1: Power Sector Issue 2/5 Acknowledgement 2012.
- [283] Liqreina A, Qoaidar L. Dry cooling of concentrating solar power (CSP) plants, an economic competitive option for the desert regions of the MENA region. *Sol Energy* 2014;103:417–24. <https://doi.org/10.1016/j.solener.2014.02.039>.
- [284] Zhai H, Rubin ES. Performance and cost of wet and dry cooling systems for pulverized coal power plants with and without carbon capture and storage. *Energy Policy* 2010;38:5653–60. <https://doi.org/10.1016/j.enpol.2010.05.013>.
- [285] Colmenar-Santos A, Borge-Diez D, Molina CP, Castro-Gil M. Water consumption in solar parabolic trough plants: Review and analysis of the southern Spain case. *Renew Sustain Energy Rev* 2014;34:565–77. <https://doi.org/10.1016/j.rser.2014.03.042>.
- [286] Martín M. Optimal annual operation of the dry cooling system of a

- concentrated solar energy plant in the south of Spain. *Energy* 2015;84:774–82.
<https://doi.org/10.1016/j.energy.2015.03.041>.
- [287] Poullikkas A, Hadjipaschalis I, Kourtis G. A comparative overview of wet and dry cooling systems for Rankine cycle based CSP plants, *Trends in Heat & Mass Transfer*, Vol. 13, 2013, pp.27-50. 2013.
- [288] Qoaider L, Liqreina A. Optimization of dry cooled parabolic trough (CSP) plants for the desert regions of the Middle East and North Africa (MENA). *Sol Energy* 2015;122:976–85. <https://doi.org/10.1016/j.solener.2015.10.021>.
- [289] Trabelsi SE, Qoaider L, Guizani A. Investigation of using molten salt as heat transfer fluid for dry cooled solar parabolic trough power plants under desert conditions. *Energy Convers Manag* 2018;156:253–63.
<https://doi.org/10.1016/j.enconman.2017.10.101>.
- [290] DOE. Concentrating Solar Power Commercial Application Study: Reducing Water Consumption of Concentrating Solar Power Electricity Generation. U.S. Department of Energy, US. 2011:175–205.
https://www1.eere.energy.gov/solar/pdfs/csp_water_study.pdf.
- [291] Turchi C, Mehos M, Ho CK, Kolb GJ. Current and Future Costs for Parabolic Trough and Power Tower Systems in the US Market. National Renewable Energy/Laboratory Sandia National Laboratories. 2010:11.
<http://www.nrel.gov/docs/fy11osti/49303.pdf>.
- [292] Abdel A., Liqreina LM. Evaluation of dry cooling option for parabolic trough (CSP) plants including related technical and economic assessment: Case study CSP Plant in Ma'an/Jordan. German Aerospace Center-DLR, 2012. n.d.
- [293] Behar O, Khellaf A, Mohammedi K. A review of studies on central receiver solar thermal power plants. *Renew Sustain Energy Rev* 2013;23:12–39.
<https://doi.org/10.1016/J.RSER.2013.02.017>.
- [294] International Energy Agency. Technology Roadmap - concentrating solar power. OECD international energy agency. Publications Service; 2010. n.d.
- [295] International Energy Agency. Technology roadmap solar photovoltaic energy, OECD/IEA; 2010. n.d.
- [296] International Energy Agency. Experience curves for energy technology policy,

OECD/IEA; 2000. n.d.

- [297] IRENA - International Renewable Energy Agency. Renewable Power Generation Costs full report on 2014 2012:12. [http://www.homepages.ed.ac.uk/shs/Tidal Stream/IRENA_RE_Power_Costs_2014_report.pdf](http://www.homepages.ed.ac.uk/shs/TidalStream/IRENA_RE_Power_Costs_2014_report.pdf).
- [298] Kumar L, Hasanuzzaman M, Rahim NA. Global advancement of solar thermal energy technologies for industrial process heat and its future prospects: A review. *Energy Convers Manag* 2019;195:885–908. <https://doi.org/10.1016/J.ENCONMAN.2019.05.081>.
- [299] Crespo A, Barreneche C, Ibarra M, Platzer W. Latent thermal energy storage for solar process heat applications at medium-high temperatures – A review. *Sol Energy* 2019;192:3–34. <https://doi.org/10.1016/J.SOLENER.2018.06.101>.
- [300] Duffie JA, Beckman WA. *Solar Engineering of Thermal Processes*, Fourth Edition. John Wiley & Sons, Inc. 2013. [https://www.sku.ac.ir/Datafiles/BookLibrary/45/John A. Duffie, William A. Beckman\(auth.\)-Solar Engineering of Thermal Processes, Fourth Edition \(2013\).pdf](https://www.sku.ac.ir/Datafiles/BookLibrary/45/John%20A.%20Duffie,%20William%20A.%20Beckman(auth.)-Solar%20Engineering%20of%20Thermal%20Processes,%20Fourth%20Edition%20(2013).pdf).
- [301] Elmohlawy AE, Kazanjian BI, Ochkov VF. Modeling and performance prediction of solar parabolic trough collector for hybrid thermal power generation plant under different weather conditions. *AIP Conf. Proc.*, vol. 2047, 2018. <https://doi.org/10.1063/1.5081635>.
- [302] Giostri A, Binotti M, Astolfi M, Silva P, Macchi E, Manzolini G. Comparison of different solar plants based on parabolic trough technology. *Sol Energy* 2012;86:1208–21. <https://doi.org/10.1016/j.solener.2012.01.014>.
- [303] Manzolini G, Giostri A, Saccilotto C, Silva P, Macchi E. Development of an innovative code for the design of thermodynamic solar power plants part B: Performance assessment of commercial and innovative technologies. *Renew Energy* 2011;36:2465–73. <https://doi.org/10.1016/j.renene.2011.02.003>.
- [304] Mittelman G, Epstein M. A novel power block for CSP systems. *Sol Energy* 2010;84:1761–71. <https://doi.org/10.1016/j.solener.2010.06.004>.
- [305] Praveen RP, Baseer MA, Awan AB, Zubair M. Performance analysis and optimization of a parabolic trough solar power plant in the middle east region. *Energies* 2018;11. <https://doi.org/10.3390/en11040741>.

- [306] Desideri U, Campana PE. Analysis and comparison between a concentrating solar and a photovoltaic power plant. *Appl Energy* 2014;113:422–33. <https://doi.org/10.1016/j.apenergy.2013.07.046>.
- [307] Manzolini G, Giostri A, Saccilotto C, Silva P, MacChi E. A numerical model for off-design performance prediction of parabolic trough based solar power plants. *J Sol Energy Eng Trans ASME* 2012;134. <https://doi.org/10.1115/1.4005105>.
- [308] System Advisor Model (SAM). SAM's Help system (full version). 2020.
- [309] Renewable Energy Agency I. RENEWABLE ENERGY TECHNOLOGIES: COST ANALYSIS SERIES Concentrating Solar Power Volume 1: Power Sector Issue 2/5 Acknowledgement. 2012.
- [310] Bataineh KM, Gharaibeh A. Optimization analyses of parabolic trough (CSP) plants for the desert regions of the middle east and North Africa (MENA). *Jordan J Mech Ind Eng* 2018;12:33–43.
- [311] Wikipedia, The Free Encyclopedia . Andasol Solar Power Station. 2019. https://en.wikipedia.org/wiki/Andasol_Solar_Power_Station (accessed September 19, 2019).
- [312] Belgasim B, Aldali Y, Abdunnabi MJR, Hashem G, Hossin K. The potential of concentrating solar power (CSP) for electricity generation in Libya. *Renew Sustain Energy Rev* 2018;90:1–15. <https://doi.org/10.1016/j.rser.2018.03.045>.
- [313] Ziuku S, Seyitini L, Mapurisa B, Chikodzi D, van Kuijk K. Potential of Concentrated Solar Power (CSP) in Zimbabwe. *Energy Sustain Dev* 2014;23:220–7. <https://doi.org/10.1016/j.esd.2014.07.006>.
- [314] Purohit I, Purohit P. Technical and economic potential of concentrating solar thermal power generation in India. *Renew Sustain Energy Rev* 2017;78:648–67. <https://doi.org/10.1016/j.rser.2017.04.059>.
- [315] Ban M, Krajačić G, Grozdek M, Čurko T, Duić N. The role of cool thermal energy storage (CTES) in the integration of renewable energy sources (RES) and peak load reduction. *Energy* 2012;48:108–17. <https://doi.org/10.1016/j.energy.2012.06.070>.
- [316] Aeolos. “Which factors will affect the annual energy output of the wind

turbine? ". Hieff Wind Energy, Ltd (Europe & America) [available online] 2020.
<https://www.windturbinestar.com/wind-turbine-annual-output.html>
(accessed December 22, 2020).

- [317] Dolan MJ, Gill S, Ault GW, Barnacle M, Foote C, Bell G. C I R E D 22nd International Conference on Electricity Distribution MODELLING AND DELIVERY OF AN ACTIVE NETWORK MANAGEMENT SCHEME FOR THE NORTHERN ISLES NEW ENERGY SOLUTIONS PROJECT. 2013.
- [318] Gill S, Ault GW, Kockar I. Using dynamic optimal power flow to inform the design and operation of active network management schemes. IET Conf. Publ., vol. 2013, 2013. <https://doi.org/10.1049/cp.2013.1185>.
- [319] Tan CW, Green TC, Hernandez-Aramburo CA. A stochastic method for battery sizing with uninterruptible-power and demand shift capabilities in PV (photovoltaic) systems. *Energy* 2010;35:5082–92.
<https://doi.org/10.1016/j.energy.2010.08.007>.
- [320] Purvins A, Papaioannou IT, Debarberis L. Application of battery-based storage systems in household-demand smoothening in electricity-distribution grids. *Energy Convers Manag* 2013;65:272–84.
<https://doi.org/10.1016/j.enconman.2012.07.018>.
- [321] Papič I. Simulation model for discharging a lead-acid battery energy storage system for load leveling. *IEEE Trans Energy Convers* 2006;21:608–15.
<https://doi.org/10.1109/TEC.2005.853746>.
- [322] International Electrotechnical Commission (IEC). *Electrical Energy Storage: White Paper*. Geneva, Switzerland : IEC; 2011.
- [323] Agamah SU, Ekonomou L. Peak demand shaving and load-levelling using a combination of bin packing and subset sum algorithms for electrical energy storage system scheduling. 2016. <https://doi.org/10.1049/iet-smt.2015.0218>.
- [324] Short W, Packey DJ, Holt T. *A Manual for the Economic Evaluation of Energy Efficiency and Renewable Energy Technologies* 1995.
- [325] Sorour A. Energy Consumption in Kuwait: Prospects and Future Approaches. *Energy Policy*. 39 (2011) 637–643. 2011.
- [326] Dow Inc. DOWTHERM™ A Heat Transfer Fluid. A Tech Data Sheet Synth Org

- Heat Transf Fluid – Liq Vap Phase Data 2022:4. <https://www.dow.com/en-us/pdp.dowtherm-a-heat-transfer-fluid.238000z.html> (accessed March 27, 2022).
- [327] German] KWE einer A zur M der W von S [dissertation] A (Germany): R-A 1985 [in. No Title. n.d.
- [328] Kato Y, Furukawa K, Araki N, Kobayasi K. Thermal diffusivity measurement of molten salts by use of a simple ceramic cell. *High Temp - High Press* 1983;15:191–8.
- [329] Ohta H, Ogura G, Waseda Y, Suzuki M. Thermal diffusivity measurements of molten salts using a three-layered cell by the laser flash method. *Rev Sci Instrum* 1990;61:2645–9. <https://doi.org/10.1063/1.1141853>.
- [330] Sci. AT-AJA, 1961 undefined. The thermal conductivity of molten salts. II. Theory and results for pure salts. OstiGov n.d.
- [331] Kitade S, Kobayashi Y, Nagasaka Y, Nagashima A. Measurement of the thermal conductivity of molten KNO₃ and NaNO₃ by the transient hot-wire method with ceramic-coated probes. *High Temp - High Press* 1989;21:219–24.
- [332] Santini R, Tadriss L, Pantaloni J, Cerisier P. Measurement of thermal conductivity of molten salts in the range 100–500°C. *Int J Heat Mass Transf* 1984;27:623–6. [https://doi.org/10.1016/0017-9310\(84\)90034-6](https://doi.org/10.1016/0017-9310(84)90034-6).
- [333] White LR, Davis HT. Thermal Conductivity of Molten Alkali Nitrates. *J Chem Phys* 2004;47:5433. <https://doi.org/10.1063/1.1701811>.
- [334] Tufeu R, Petitet JP, Denielou L, Le Neindre B. Experimental determination of the thermal conductivity of molten pure salts and salt mixtures. *Int J Thermophys* 1985;6:315–30. <https://doi.org/10.1007/BF00500266>.
- [335] Omotani T, Nagasaka Y, Nagashima A. Measurement of the thermal conductivity of KNO₃-NaNO₃ mixtures using a transient hot-wire method with a liquid metal in a capillary probe. *Int J Thermophys* 1982;3:17–26. <https://doi.org/10.1007/BF00503955>.
- [336] Foosnaes: Thermal conductivity of nitrate mixtures - Google Scholar n.d. [https://scholar.google.com/scholar_lookup?title=Thermal conductivity of nitrate mixtures&author=T. Foosnæs&publication_year=1982](https://scholar.google.com/scholar_lookup?title=Thermal+conductivity+of+nitrate+mixtures&author=T.+Foosnæs&publication_year=1982) (accessed April

6, 2022).

- [337] McDonald J, Davis HT. Thermal conductivity of binary mixtures of alkali nitrates. *J Phys Chem* 2002;74:725–30. <https://doi.org/10.1021/J100699A007>.
- [338] Tricklebank SB. Molten Salt Mixtures. IX. The Thermal Conductivities of Molten Nitrate Systems. *Aust J Chem* 1965;18:1171–6. <https://doi.org/10.1071/CH9651171>.
- [339] Jriri T, Rogez J, Bergman C, Mathieu JC. Thermodynamic study of the condensed phases of NaNO₃, KNO₃ and CsNO₃ and their transitions. *Thermochim Acta* 1995;266:147–61. [https://doi.org/10.1016/0040-6031\(95\)02337-2](https://doi.org/10.1016/0040-6031(95)02337-2).
- [340] Gustafsson SE, Halling NO, Kjellander RAE. Optical Determination of Thermal Conductivity with a Plane Source Technique: I. Molten Sodium Nitrate and Potassium Nitrate. *Zeitschrift Fur Naturforsch - Sect A J Phys Sci* 1968;23:44–7. <https://doi.org/10.1515/ZNA-1968-0106/MACHINEREADABLECITATION/RIS>.
- [341] Carling RW. Heat capacities of NaNO₃ and KNO₃ from 350 to 800 K. *Thermochim Acta* 1983;60:265–75. [https://doi.org/10.1016/0040-6031\(83\)80248-2](https://doi.org/10.1016/0040-6031(83)80248-2).
- [342] Takahashi Y, Sakamoto R, Kamimoto M. Heat capacities and latent heats of LiNO₃, NaNO₃, and KNO₃. *Int J Thermophys* 1988;9:1081–90. <https://doi.org/10.1007/BF01133275>.
- [343] Rogers DJ, Janz GJ. Melting-crystallization and premelting properties of sodium nitrate-potassium nitrate. Enthalpies and heat capacities. *J Chem Eng Data* 2002;27:424–8. <https://doi.org/10.1021/JE00030A017>.
- [344] Ichikawa K, Matsumoto T. The Heat Capacities of Lithium, Sodium, Potassium, Rubidium, and Caesium Nitrates in the Solid and Liquid States. <Http://DxDoiOrg/101246/Bcsj562093> 2006;56:2093–100. <https://doi.org/10.1246/BCSJ.56.2093>.
- [345] Zavoico A. Solar power tower design basis document, revision 0; Topical 2001.
- [346] Pacheco J, Ralph M, Chavez J, Dunkin S. Results of molten salt panel and component experiments for solar central receivers: cold fill, freeze/thaw, thermal cycling and shock, and instrumentation tests 1995.

- [347] Scopus - Document details - Specific weight of alloys from nitrate and nitrite systems of potassium and sodium | Signed in n.d.
https://www.scopus.com/record/display.uri?eid=2-s2.0-84883050790&origin=inward&featureToggles=FEATURE_NEW_DOC_DETAIL_S_EXPORT:1 (accessed April 6, 2022).
- [348] Murgulescu IG, Zuca S. Viscosity of binary mixtures of molten nitrates as a function of ionic radius—II. *Electrochim Acta* 1969;14:519–26.
[https://doi.org/10.1016/0013-4686\(69\)87037-4](https://doi.org/10.1016/0013-4686(69)87037-4).
- [349] Murgulescu: Die elektrische Leitfähigkeit binärer... - Google Scholar n.d.
[https://scholar.google.com/scholar_lookup?title=Die elektrische Leitfähigkeit binärer Salzgemische im geschmolzenem Zustand – die Systeme%3AKNO3%2BNaNO3%3Ba\(NO3\)2%2BKNO3%3BMnCl2%2BKCl&author=I.G. Murgulescu&publication_year=1959&pages=227-241](https://scholar.google.com/scholar_lookup?title=Die+elektrische+Leitf%C3%A4higkeit+bin%C3%A4rer+Salzgemische+im+geschmolzenem+Zustand+%20%E2%80%93+die+Systeme%3AKNO3%2BNaNO3%3Ba(NO3)2%2BKNO3%3BMnCl2%2BKCl&author=I.G.+Murgulescu&publication_year=1959&pages=227-241) (accessed April 6, 2022).
- [350] Janz GJ, Krebs U, Siegenthaler HF, Tomkins RPT. Molten Salts: Volume 3 Nitrates, Nitrites, and Mixtures: Electrical Conductance, Density, Viscosity, and Surface Tension Data. *J Phys Chem Ref Data* 2009;1:581.
<https://doi.org/10.1063/1.3253103>.
- [351] Bradshaw RW. Effect of composition on the density of multi-component molten nitrate salts. 2009. <https://doi.org/10.2172/983681>.
- [352] Bauer T, Pflieger N, Breidenbach N, Eck M, Laing D, Kaesche S. Material aspects of Solar Salt for sensible heat storage. *Appl Energy* 2013;111:1114–9.
<https://doi.org/10.1016/J.APENERGY.2013.04.072>.
- [353] Burton T, Sharpe D, Jenkins N, Bossanyi E. WIND ENERGY HANDBOOK. JOHN WILEY & SONS, LTD; 2001.
- [354] Boukelia TE, Bouraoui A, Laouafi A, Djimli S, Kabar Y. 3E (Energy-Exergy-Economic) comparative study of integrating wet and dry cooling systems in solar tower power plants. *Energy* 2020;200:117567.
<https://doi.org/10.1016/J.ENERGY.2020.117567>.

Appendices

Appendix A. Thermophysical properties of the Heat Transfer Fluid (HTF)

This appendix contains the technical data sheet for the HTF (Dowtherm A) used in the reference CSP-PT plant in this work.



Technical Data Sheet

DOWTHERM™ A

Product Type Synthetic organic heat transfer fluid – Liquid and Vapor Phase Data

Applications

- Indirect heat transfer

Recommended Use Temperature Range Liquid phase: 15°C (60°F) to 400°C (750°F)
Vapor phase: 257°C (495°F) to 400°C (750°F)

Description DOWTHERM™ A heat transfer fluid is a eutectic mixture of two very stable compounds, biphenyl (C₁₂H₁₀) and (C₁₂H₁₀O). These compounds have practically the same vapor pressures, so the mixture can be handled as if it were a single compound. DOWTHERM A fluid may be used in systems employing either liquid phase or vapor phase heating.

Typical Properties†

Composition		
Diphenyl Oxide/Biphenyl Blend		
Property	SI Units	English Units
Color	Clear to light yellow	
Freeze Point	12.0°C	53.6°F
Atmospheric Boiling Point	257.1°C	494.8°F
Flash Point ¹	113°C	236°F
Fire Point ²	118°C	245°F
Autoignition Temperature ³	599°C	1110°F
Density at 25°C (75°F)	1056 kg/m ³	66.0 lb./ft. ³
Surface Tension in Air at:		
20°C (68°F)	40.1 Dynes/cm	40.1 Dynes/cm
40°C (104°F)	37.6 Dynes/cm	37.6 Dynes/cm
60°C (140°F)	35.7 Dynes/cm	35.7 Dynes/cm
Estimated Critical Temperature	497°C	927°F
Estimated Critical Pressure	31.34 bar	30.93 atm
Estimated Critical Volume	3.17 l/kg	0.0508 ft. ³ /lb.
Average Molecular Weight	166.0	
Heat of Combustion	36,053 kJ/kg	15,500 Btu/lb.

†Not to be construed as specifications.

¹SETA

²C.O.C.

³ASTM E659-78

Figure A. 1 The technical data sheet for the HTF used in this work (Dowtherm A) [326].

Saturated Liquid Properties of DOWTHERM™ A Fluid (English Units)

Temperature °F	Specific Heat Btu/lb. °F	Density lb./ft. ³	Thermal Conductivity Btu/hr. ft. ² (°F/ft.)	Viscosity (cP)	Vapor Pressure (psia)
60	0.373	66.37	0.0805	4.91	0.000
120	0.396	64.72	0.0775	2.12	0.003
180	0.418	63.03	0.0744	1.22	0.028
240	0.441	61.30	0.0713	0.81	0.16
300	0.463	59.51	0.0682	0.59	0.64
360	0.485	57.65	0.0651	0.45	2.03
420	0.507	55.72	0.0620	0.35	5.38
480	0.529	53.70	0.0590	0.28	12.25
540	0.552	51.57	0.0559	0.23	24.72
600	0.575	49.29	0.0528	0.19	45.31
660	0.599	46.82	0.0497	0.16	76.89
720	0.627	44.08	0.0466	0.14	122.7
780	0.665	40.93	0.0436	0.12	186.4

Saturated Liquid Properties of DOWTHERM™ A Fluid (SI Units)

Temperature °C	Specific Heat kJ/kg K	Density kg/m ³	Thermal Conductivity W/mK	Viscosity mPa sec	Vapor Pressure (bar)
15	1.558	1063.5	0.1395	5.00	0.00
65	1.701	1023.7	0.1315	1.58	0.00
105	1.814	990.7	0.1251	0.91	0.01
155	1.954	947.8	0.1171	0.56	0.06
205	2.093	902.5	0.1091	0.38	0.28
255	2.231	854.0	0.1011	0.27	0.97
305	2.373	801.3	0.0931	0.20	2.60
355	2.527	742.3	0.0851	0.16	5.80
405	2.725	672.5	0.0771	0.12	11.32

Saturated Vapor Properties of DOWTHERM™ A Fluid (English Units)

Temperature °F	Vapor Pressure (psia)	Liquid Enthalpy Btu/lb.	Latent Heat Btu/lb.	Vapor Enthalpy Btu/lb.	Vapor Density lb./ft. ³	Vapor Viscosity cP	Vapor Thermal Cond. Btu/hr. ft. ² (°F/ft.)	Z _{vapor}	Specific Heat (c _p) Btu/lb. °F	Ratio of Specific Heats c _p /c _v
60	0.000	2.5	175.1	177.6		0.0054	0.0044	1.000	0.250	1.050
120	0.003	26.2	167.3	193.5		0.0060	0.0055	1.000	0.279	1.045
300	0.64	103.0	148.0	251.1	0.0130	0.0079	0.0092	0.996	0.361	1.035
360	2.03	131.1	142.0	273.1	0.0388	0.0086	0.0106	0.989	0.385	1.034
420	5.38	160.6	135.8	296.3	0.0967	0.0092	0.0120	0.977	0.409	1.034
480	12.25	191.4	129.2	320.5	0.2100	0.0098	0.0135	0.959	0.433	1.035
540	24.72	223.5	122.1	345.5	0.4102	0.0105	0.0150	0.932	0.456	1.039
600	45.31	256.9	114.2	371.1	0.7389	0.0166	0.0166	0.895	0.480	1.045
660	76.89	291.7	105.3	397.0	1.254	0.0183	0.0183	0.848	0.505	1.055
720	122.7	327.9	95.0	422.9	2.045	0.0200	0.0200	0.789	0.534	1.073
780	186.4	365.9	82.5	448.4	3.270	0.0219	0.0219	0.714	0.571	1.108

®™ Trademark of The Dow Chemical Company ("Dow") or an affiliated company of Dow

Form 176-01472-0417

Figure A. 1 Cont. The technical data sheet for the HTF used in this work (Dowtherm A) [326].

Saturated Vapor Properties of DOWTHERM™ A Fluid (SI Units)

Temperature °F	Vapor Pressure (bar)	Liquid Enthalpy kJ/kg	Latent Heat kJ/kg	Vapor Enthalpy kJ/kg	Vapor Density Kg/m ³	Vapor Viscosity mPa·s	Vapor Thermal Cond. W/mK	Z _{vapor}	Specific Heat (c _p) kJ/kg K	Ratio of Specific Heats c _p /c _v
15	0.00	4.9	407.2	412.1		0.0054	0.0075	1.000	1.044	1.050
65	0.00	88.1	380.9	469.4	0.0040	0.0063	0.0104	1.000	1.227	1.043
105	0.01	158.1	362.7	520.9	0.0341	0.0071	0.0129	0.999	1.366	1.038
155	0.06	251.2	341.5	592.7	0.2583	0.0080	0.0163	0.995	1.528	1.035
205	0.28	351.2	320.2	671.5	1.179	0.0090	0.0200	0.982	1.681	1.034
255	0.97	458.2	297.4	755.6	3.831	0.0100	0.0238	0.954	1.829	1.036
305	2.60	572.2	271.5	843.6	9.896	0.0110	0.0279	0.908	1.976	1.042
355	5.80	693.1	240.6	933.8	22.03	0.0122	0.0322	0.838	2.133	1.057
405	11.32	822.0	201.7	1023.7	45.17	0.0138	0.0368	0.740	2.333	1.094

Product Stewardship

The Dow Chemical Company and its subsidiaries ("Dow") has a fundamental concern for all who make, distribute, and use its products, and for the environment in which we live. This concern is the basis for our Product Stewardship philosophy by which we assess the safety, health, and environmental information on our products and then take appropriate steps to protect employee and public health and our environment. The success of our Product Stewardship program rests with each and every individual involved with Dow products—from the initial concept and research, to manufacture, use, sale, disposal, and recycle of each product.

Safety Considerations

Material Safety Data (MSD) sheets are available from The Dow Chemical Company. MSD sheets are provided to help customers satisfy their own handling, safety and disposal needs and those that may be required by locally applicable health and safety regulations. MSD sheets are updated regularly, therefore, please request and review the most current MSD sheet before handling or using any product. These are available from the nearest Dow sales office.

Customer Notice

Dow encourages its customers to review their application of Dow products from the standpoint of human health and environmental quality. To help ensure that Dow products are not used in ways for which they were not intended or tested, Dow personnel will assist customers in dealing with ecological and products safety. Your Dow sales representative can arrange the proper contacts.

Contact information:
For more information about this product please call The Dow Chemical Company.

North America: +1 (800) 447-4369
Latin America: +55 (115) 184-6722
Europe: +31 (11) 567-2626
Asia/Pacific: +6 (037) 965-5392
<http://www.dowtherm.com>

NOTICE: No freedom from infringement of any patent owned by Dow or others is to be inferred. Because use conditions and applicable laws may differ from one location to another and may change with time, Customer is responsible for determining whether products and the information in this document are appropriate for Customer's use and for ensuring that Customer's workplace and disposal practices are in compliance with applicable laws and other government enactments. The product shown in this literature may not be available for sale and/or available in all geographies where Dow is represented. The claims made may not have been approved for use in all countries. Dow assumes no obligation or liability for the information in this document. References to "Dow" or the "Company" mean the Dow legal entity selling the products to Customer unless otherwise expressly noted. NO WARRANTIES ARE GIVEN; ALL IMPLIED WARRANTIES OF MERCHANTABILITY OR FITNESS FOR A PARTICULAR PURPOSE ARE EXPRESSLY EXCLUDED.

®™ Trademark of The Dow Chemical Company ("Dow") or an affiliated company of Dow

Form 176-01472-0417

Figure A. 1 Cont. The technical data sheet for the HTF used in this work (Dowtherm A) [326].

Appendix B. Thermophysical properties of the Thermal Energy Storage (TES) medium

This appendix contains the properties of the molten salt (TES medium) used in the reference CSP-PT plant in this work.

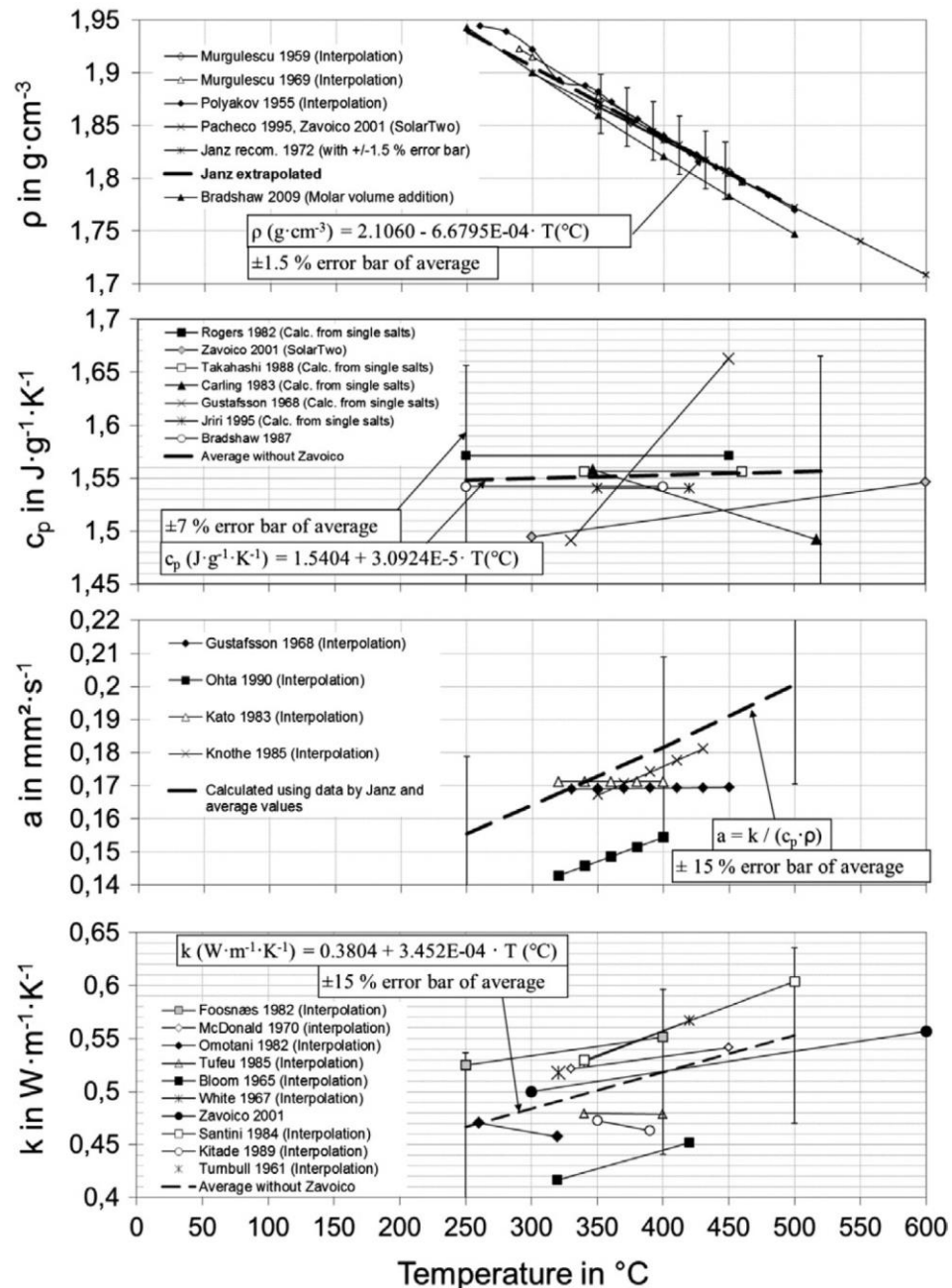


Figure B. 1 Thermophysical properties (density, heat capacity, thermal diffusivity and thermal conductivity - top to bottom) of a commonly used storage medium, a mixture of 60% sodium nitrate (NaNO_3) and 40% potassium nitrate (KNO_3) [327,328,335–344,329,345–352,330,331,331,331–334].

Appendix C. Process flow diagrams for the reference 50 MW CSP-PT plant (wet/dry)

This appendix contains the process flow diagrams for the wet and dry cooling options, as shown in Figure C. 1 to Figure C. 3, for the reference 50 MW CSP-PT plant used in this work. It should be noted that the plant's components were determined after assessment of the used model in Ref. [218]. In addition, a detailed breakdown of the estimated costs for the plant is provided in this work (see Appendix H).

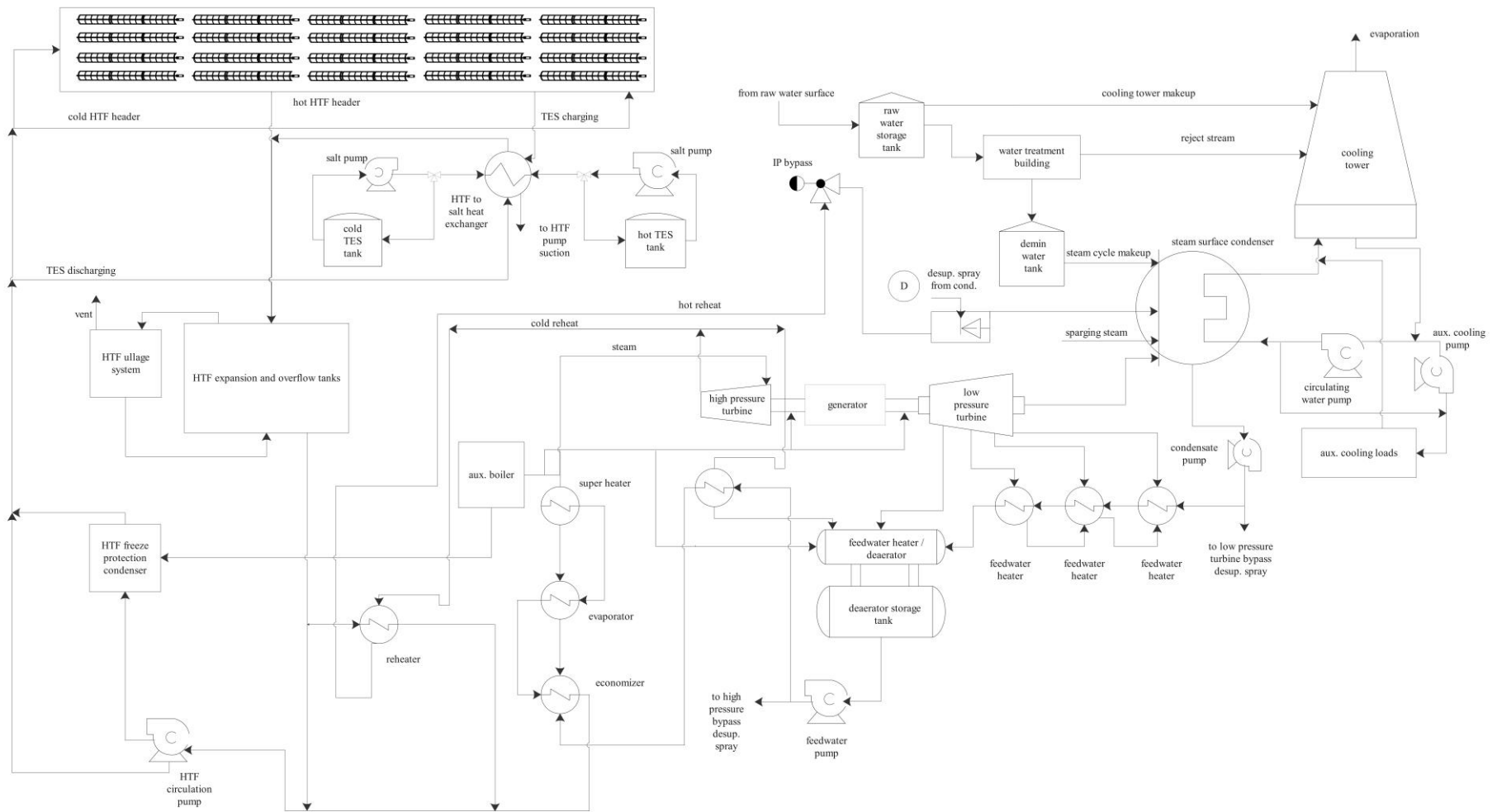


Figure C. 2 Process flow diagram for the reference 50 MW CSP-PT plant with the wet cooling option.

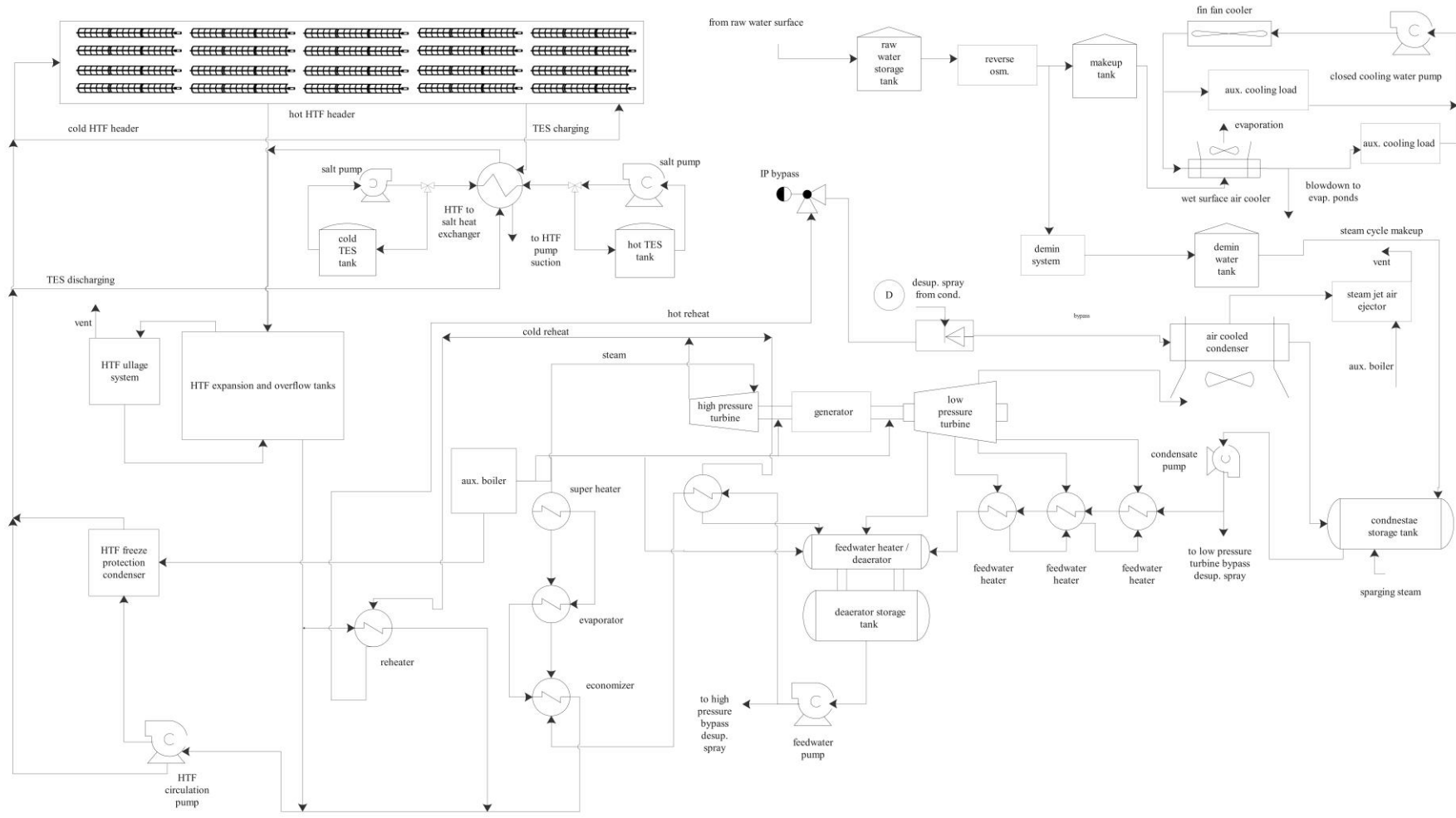


Figure C. 3 Process flow diagram for the reference 50 MW CSP-PT plant with the dry cooling option.

Appendix D. Input data to the model

This appendix contains the following: (i) input data to the CSP-PT/TES model for the reference CSP-PT plant used in this work, and (ii) input data to the wind power model for the reference 2 MW wind turbine used in this work.

D.1. Input data to the CSP-PT/TES model

Table D. 1 Input data to the CSP-PT/TES model used in this work.

Variable	Description	Value
DP_SGS	Pressure drop within the steam generator	0
HDR_rough	Header pipe roughness	4.57E-05
IAMs_1	Incidence angle modifier coefficients	1;0.0506;-0.1763;0;
IAMs_2	Incidence angle modifier coefficients	1;0.0506;-0.1763;0;
IAMs_3	Incidence angle modifier coefficients	1;0.0506;-0.1763;0;
IAMs_4	Incidence angle modifier coefficients	1;0.0506;-0.1763;0;
I_bn_des	Irradiation at design	700
L_rnr_pb	Length of runner pipe in pb	25
L_rnr_per_xpan	Threshold length of straight runner pipe without an expansion loop	70
L_xpan_hdr	Combined perpendicular lengths of each header expansion loop	20
L_xpan_rnr	Combined perpendicular lengths of each runner expansion loop	20
Min_rnr_xpans	Minimum number of expansion loops per single-diameter runner section	1
N_hdr_per_xpan	Number of collector loops per expansion loop	2
N_max_hdr_diams	Max header diameters	10
P_ref	Design gross output	50
Pipe_hl_coef	Piping thermal loss coefficient	0.45
SCA_drives_elec	Tracking power	125
T_approach	Approach temperature	5
T_fp	Freeze protection temp	150
T_loop_in_des	Design loop inlet temp	293
T_loop_out	Design loop outlet temp	393
T_startup	Minimum required startup temp	300
T_tank_cold_ini	Initial TES fluid temp	300
T_tank_hot_inlet_min	Minimum hot tank htf inlet temperature	400
V_hdr_cold_max	Header design max flow velocity	3
V_hdr_cold_min	Header design min flow velocity	2
V_hdr_hot_max		3
V_hdr_hot_min		2
V_tes_des	Design-point velocity to size the TES pipe diameters	1.85
analysis_period	Analysis period	25

azimuth	Collector azimuth	0
calc_design_pipe_vals	Calculate temps and pressures at design conditions for runners and headers	1
cold_tank_Thtr	Cold tank heater set point	292
collector_library	Collector library	EuroTrough ET150
combo_FieldConfig	Number of field subsections	2
combo_feather	Defocusing strategy	Simultaneous
combo_htf_type	Field HTF fluid	User-defined...
csp.dtr.cost.contingency_percent	Contingency	7
csp.dtr.cost.epc.cost_per_watt		0
csp.dtr.cost.epc.percent	EPC Costs % direct	11
csp.dtr.cost.site_improvements.cost_per_m2	Site Improvement Cost per m2	28
csp.dtr.par.aux_c0	Aux heater parasitic coeff 0	0.483
csp.dtr.par.aux_c1	Aux heater parasitic coeff 1	0.517
csp.dtr.par.aux_c2	Aux heater parasitic coeff 2	0
csp.dtr.par.aux_pf	Aux heater parasitic factor	1
csp.dtr.par.aux_val	Aux heater parasitic value	0.02273
csp.dtr.par.bop_c0	BOP parasitic coeff 0	0.483
csp.dtr.par.bop_c1	BOP parasitic coeff 1	0.517
csp.dtr.par.bop_c2	BOP parasitic coeff 2	0
csp.dtr.par.bop_pf	BOP parasitic factor	1
csp.dtr.par.bop_val	BOP parasitic value	0
csp.dtr.pwr.b.gross_net_conversion_factor	Estimated gross to net conversion factor	0.9
csp_dtr_hce_absorber_material_1	Absorber material type	304L
csp_dtr_hce_absorber_material_2	Absorber material type	304L
csp_dtr_hce_absorber_material_3	Absorber material type	304L
csp_dtr_hce_absorber_material_4	Absorber material type	304L
csp_dtr_hce_diam_absorber_inner_1	Absorber tube inner diameter	0.066
csp_dtr_hce_diam_absorber_inner_2	Absorber tube inner diameter	0.066
csp_dtr_hce_diam_absorber_inner_3	Absorber tube inner diameter	0.066
csp_dtr_hce_diam_absorber_inner_4	Absorber tube inner diameter	0.066
csp_dtr_hce_diam_absorber_outer_1	Absorber tube outer diameter	0.07
csp_dtr_hce_diam_absorber_outer_2	Absorber tube outer diameter	0.07
csp_dtr_hce_diam_absorber_outer_3	Absorber tube outer diameter	0.07
csp_dtr_hce_diam_absorber_outer_4	Absorber tube outer diameter	0.07
csp_dtr_hce_diam_envelope_inner_1	Glass envelope inner diameter	0.115
csp_dtr_hce_diam_envelope_inner_2	Glass envelope inner diameter	0.115

csp_dtr_hce_diam_envelope_inner_3	Glass envelope inner diameter	0.115
csp_dtr_hce_diam_envelope_inner_4	Glass envelope inner diameter	0.115
csp_dtr_hce_diam_envelope_outer_1	Glass envelope outer diameter	0.12
csp_dtr_hce_diam_envelope_outer_2	Glass envelope outer diameter	0.121
csp_dtr_hce_diam_envelope_outer_3	Glass envelope outer diameter	0.12
csp_dtr_hce_diam_envelope_outer_4	Glass envelope outer diameter	0.12
csp_dtr_hce_flow_type_1	Absorber flow pattern	Tube flow
csp_dtr_hce_flow_type_2	Absorber flow pattern	Tube flow
csp_dtr_hce_flow_type_3	Absorber flow pattern	Annular flow
csp_dtr_hce_flow_type_4	Absorber flow pattern	Tube flow
csp_dtr_hce_inner_roughness_1	Internal surface roughness	4.50E-05
csp_dtr_hce_inner_roughness_2	Internal surface roughness	4.50E-05
csp_dtr_hce_inner_roughness_3	Internal surface roughness	4.50E-05
csp_dtr_hce_inner_roughness_4	Internal surface roughness	4.50E-05
csp_dtr_hce_notify_text_1	Receiver name from library	Schott PTR70 2008
csp_dtr_hce_var1_abs_abs_1	Variation 1 Absorber Absorptance	0.96
csp_dtr_hce_var1_abs_abs_2	Variation 1 Absorber Absorptance	0.96
csp_dtr_hce_var1_abs_abs_3	Variation 1 Absorber Absorptance	0.96
csp_dtr_hce_var1_abs_abs_4	Variation 1 Absorber Absorptance	0.96
csp_dtr_hce_var1_annulus_pressure_1	Variation 1 Annulus Pressure	0.0001
csp_dtr_hce_var1_annulus_pressure_2	Variation 1 Annulus Pressure	0.0001
csp_dtr_hce_var1_annulus_pressure_3	Variation 1 Annulus Pressure	0.0001
csp_dtr_hce_var1_annulus_pressure_4	Variation 1 Annulus Pressure	0.0001
csp_dtr_hce_var1_bellows_shadowing_1	Variation 1 Bellows Shadowing	0.96
csp_dtr_hce_var1_bellows_shadowing_2	Variation 1 Bellows Shadowing	0.971
csp_dtr_hce_var1_bellows_shadowing_3	Variation 1 Bellows Shadowing	0.96
csp_dtr_hce_var1_bellows_shadowing_4	Variation 1 Bellows Shadowing	0.96
csp_dtr_hce_var1_broken_glass_1	Variation 1 Broken Glass	0
csp_dtr_hce_var1_broken_glass_2	Variation 1 Broken Glass	0
csp_dtr_hce_var1_broken_glass_3	Variation 1 Broken Glass	0
csp_dtr_hce_var1_broken_glass_4	Variation 1 Broken Glass	0
csp_dtr_hce_var1_env_abs_1	Variation 1 Envelope Absorptance	0.02
csp_dtr_hce_var1_env_abs_2	Variation 1 Envelope Absorptance	0.02
csp_dtr_hce_var1_env_abs_3	Variation 1 Envelope Absorptance	0.02
csp_dtr_hce_var1_env_abs_4	Variation 1 Envelope Absorptance	0.02

csp_dtr_hce_var1_env_emis_1	Variation 1 Envelope Emittance	0.86
csp_dtr_hce_var1_env_emis_2	Variation 1 Envelope Emittance	0.86
csp_dtr_hce_var1_env_emis_3	Variation 1 Envelope Emittance	0.86
csp_dtr_hce_var1_env_emis_4	Variation 1 Envelope Emittance	0.86
csp_dtr_hce_var1_env_trans_1	Variation 1 Envelope Transmittance	0.963
csp_dtr_hce_var1_env_trans_2	Variation 1 Envelope Transmittance	0.96
csp_dtr_hce_var1_env_trans_3	Variation 1 Envelope Transmittance	0.963
csp_dtr_hce_var1_env_trans_4	Variation 1 Envelope Transmittance	0.963
csp_dtr_hce_var1_field_fraction_1	Variation 1 Field Fraction	0.985
csp_dtr_hce_var1_field_fraction_2	Variation 1 Field Fraction	1
csp_dtr_hce_var1_field_fraction_3	Variation 1 Field Fraction	1
csp_dtr_hce_var1_field_fraction_4	Variation 1 Field Fraction	1
csp_dtr_hce_var1_gas_type_1	Variation 1 Gas Type	Hydrogen
csp_dtr_hce_var1_gas_type_2	Variation 1 Gas Type	Hydrogen
csp_dtr_hce_var1_gas_type_3	Variation 1 Gas Type	Hydrogen
csp_dtr_hce_var1_gas_type_4	Variation 1 Gas Type	Hydrogen
csp_dtr_hce_var1_hce_dirt_1	Variation 1 Dirt on receiver	0.98
csp_dtr_hce_var1_hce_dirt_2	Variation 1 Dirt on receiver	0.98
csp_dtr_hce_var1_hce_dirt_3	Variation 1 Dirt on receiver	0.98
csp_dtr_hce_var1_hce_dirt_4	Variation 1 Dirt on receiver	0.98
csp_dtr_hce_var1 Rated Heat Loss_1	Variation 1 Rated Heat Loss	150
csp_dtr_hce_var1 Rated Heat Loss_2	Variation 1 Rated Heat Loss	175
csp_dtr_hce_var1 Rated Heat Loss_3	Variation 1 Rated Heat Loss	150
csp_dtr_hce_var1 Rated Heat Loss_4	Variation 1 Rated Heat Loss	150
csp_dtr_hce_var2_abs_abs_1	Variation 2 Absorber Absorptance	0.96
csp_dtr_hce_var2_abs_abs_2	Variation 2 Absorber Absorptance	0.96
csp_dtr_hce_var2_abs_abs_3	Variation 2 Absorber Absorptance	0.96
csp_dtr_hce_var2_abs_abs_4	Variation 2 Absorber Absorptance	0.96
csp_dtr_hce_var2_annulus_pressure_1	Variation 2 Annulus Pressure	750
csp_dtr_hce_var2_annulus_pressure_2	Variation 2 Annulus Pressure	750
csp_dtr_hce_var2_annulus_pressure_3	Variation 2 Annulus Pressure	750
csp_dtr_hce_var2_annulus_pressure_4	Variation 2 Annulus Pressure	750
csp_dtr_hce_var2_bellows_shadowing_1	Variation 2 Bellows Shadowing	0.96

csp_dtr_hce_var2_bellows_shadowing_2	Variation 2 Bellows Shadowing	0.971
csp_dtr_hce_var2_bellows_shadowing_3	Variation 2 Bellows Shadowing	0.96
csp_dtr_hce_var2_bellows_shadowing_4	Variation 2 Bellows Shadowing	0.96
csp_dtr_hce_var2_broken_glass_1	Variation 2 Broken Glass	0
csp_dtr_hce_var2_broken_glass_2	Variation 2 Broken Glass	0
csp_dtr_hce_var2_broken_glass_3	Variation 2 Broken Glass	0
csp_dtr_hce_var2_broken_glass_4	Variation 2 Broken Glass	0
csp_dtr_hce_var2_env_abs_1	Variation 2 Envelope Absorptance	0.02
csp_dtr_hce_var2_env_abs_2	Variation 2 Envelope Absorptance	0.02
csp_dtr_hce_var2_env_abs_3	Variation 2 Envelope Absorptance	0.02
csp_dtr_hce_var2_env_abs_4	Variation 2 Envelope Absorptance	0.02
csp_dtr_hce_var2_env_emis_1	Variation 2 Envelope Emittance	0.86
csp_dtr_hce_var2_env_emis_2	Variation 2 Envelope Emittance	0.86
csp_dtr_hce_var2_env_emis_3	Variation 2 Envelope Emittance	0.86
csp_dtr_hce_var2_env_emis_4	Variation 2 Envelope Emittance	0.86
csp_dtr_hce_var2_env_trans_1	Variation 2 Envelope Transmittance	0.963
csp_dtr_hce_var2_env_trans_2	Variation 2 Envelope Transmittance	0.96
csp_dtr_hce_var2_env_trans_3	Variation 2 Envelope Transmittance	0.963
csp_dtr_hce_var2_env_trans_4	Variation 2 Envelope Transmittance	0.963
csp_dtr_hce_var2_field_fraction_1	Variation 2 Field Fraction	0.01
csp_dtr_hce_var2_field_fraction_2	Variation 2 Field Fraction	0
csp_dtr_hce_var2_field_fraction_3	Variation 2 Field Fraction	0
csp_dtr_hce_var2_field_fraction_4	Variation 2 Field Fraction	0
csp_dtr_hce_var2_gas_type_1	Variation 2 Gas Type	Air
csp_dtr_hce_var2_gas_type_2	Variation 2 Gas Type	Air
csp_dtr_hce_var2_gas_type_3	Variation 2 Gas Type	Air
csp_dtr_hce_var2_gas_type_4	Variation 2 Gas Type	Air
csp_dtr_hce_var2_hce_dirt_1	Variation 2 Dirt on receiver	0.98
csp_dtr_hce_var2_hce_dirt_2	Variation 2 Dirt on receiver	0.98
csp_dtr_hce_var2_hce_dirt_3	Variation 2 Dirt on receiver	0.98
csp_dtr_hce_var2_hce_dirt_4	Variation 2 Dirt on receiver	0.98

csp_dtr_hce_var2 Rated Heat Loss 1	Variation 2 Rated Heat Loss	1100
csp_dtr_hce_var2 Rated Heat Loss 2	Variation 2 Rated Heat Loss	1100
csp_dtr_hce_var2 Rated Heat Loss 3	Variation 2 Rated Heat Loss	1100
csp_dtr_hce_var2 Rated Heat Loss 4	Variation 2 Rated Heat Loss	1100
csp_dtr_hce_var3 Absorber Absorption 1	Variation 3 Absorber Absorption	0.8
csp_dtr_hce_var3 Absorber Absorption 2	Variation 3 Absorber Absorption	0.9
csp_dtr_hce_var3 Absorber Absorption 3	Variation 3 Absorber Absorption	0.8
csp_dtr_hce_var3 Absorber Absorption 4	Variation 3 Absorber Absorption	0.8
csp_dtr_hce_var3 Annulus Pressure 1	Variation 3 Annulus Pressure	750
csp_dtr_hce_var3 Annulus Pressure 2	Variation 3 Annulus Pressure	750
csp_dtr_hce_var3 Annulus Pressure 3	Variation 3 Annulus Pressure	750
csp_dtr_hce_var3 Annulus Pressure 4	Variation 3 Annulus Pressure	750
csp_dtr_hce_var3 Bellows Shadowing 1	Variation 3 Bellows Shadowing	0.96
csp_dtr_hce_var3 Bellows Shadowing 2	Variation 3 Bellows Shadowing	0.971
csp_dtr_hce_var3 Bellows Shadowing 3	Variation 3 Bellows Shadowing	0.96
csp_dtr_hce_var3 Bellows Shadowing 4	Variation 3 Bellows Shadowing	0.96
csp_dtr_hce_var3 Broken Glass 1	Variation 3 Broken Glass	1
csp_dtr_hce_var3 Broken Glass 2	Variation 3 Broken Glass	1
csp_dtr_hce_var3 Broken Glass 3	Variation 3 Broken Glass	1
csp_dtr_hce_var3 Broken Glass 4	Variation 3 Broken Glass	1
csp_dtr_hce_var3 Envelope Absorptance 1	Variation 3 Envelope Absorptance	0
csp_dtr_hce_var3 Envelope Absorptance 2	Variation 3 Envelope Absorptance	0
csp_dtr_hce_var3 Envelope Absorptance 3	Variation 3 Envelope Absorptance	0
csp_dtr_hce_var3 Envelope Absorptance 4	Variation 3 Envelope Absorptance	0
csp_dtr_hce_var3 Envelope Emittance 1	Variation 3 Envelope Emittance	1
csp_dtr_hce_var3 Envelope Emittance 2	Variation 3 Envelope Emittance	1
csp_dtr_hce_var3 Envelope Emittance 3	Variation 3 Envelope Emittance	1
csp_dtr_hce_var3 Envelope Emittance 4	Variation 3 Envelope Emittance	1
csp_dtr_hce_var3 Envelope Transmittance 1	Variation 3 Envelope Transmittance	1
csp_dtr_hce_var3 Envelope Transmittance 2	Variation 3 Envelope Transmittance	1
csp_dtr_hce_var3 Envelope Transmittance 3	Variation 3 Envelope Transmittance	1
csp_dtr_hce_var3 Envelope Transmittance 4	Variation 3 Envelope Transmittance	1
csp_dtr_hce_var3 Field Fraction	Variation 3 Field Fraction	0.005

ion_1		
csp_dtr_hce_var3_field_fraction_2	Variation 3 Field Fraction	0
csp_dtr_hce_var3_field_fraction_3	Variation 3 Field Fraction	0
csp_dtr_hce_var3_field_fraction_4	Variation 3 Field Fraction	0
csp_dtr_hce_var3_gas_type_1	Variation 3 Gas Type	Air
csp_dtr_hce_var3_gas_type_2	Variation 3 Gas Type	Air
csp_dtr_hce_var3_gas_type_3	Variation 3 Gas Type	Air
csp_dtr_hce_var3_gas_type_4	Variation 3 Gas Type	Air
csp_dtr_hce_var3_hce_dirt_1	Variation 3 Dirt on receiver	1
csp_dtr_hce_var3_hce_dirt_2	Variation 3 Dirt on receiver	1
csp_dtr_hce_var3_hce_dirt_3	Variation 3 Dirt on receiver	1
csp_dtr_hce_var3_hce_dirt_4	Variation 3 Dirt on receiver	1
csp_dtr_hce_var3_rated_heat_loss_1	Variation 3 Rated Heat Loss	1500
csp_dtr_hce_var3_rated_heat_loss_2	Variation 3 Rated Heat Loss	1500
csp_dtr_hce_var3_rated_heat_loss_3	Variation 3 Rated Heat Loss	1500
csp_dtr_hce_var3_rated_heat_loss_4	Variation 3 Rated Heat Loss	1500
csp_dtr_hce_var4_abs_abs_1	Variation 4 Absorber Absorptance	0
csp_dtr_hce_var4_abs_abs_2	Variation 4 Absorber Absorptance	0
csp_dtr_hce_var4_abs_abs_3	Variation 4 Absorber Absorptance	0
csp_dtr_hce_var4_abs_abs_4	Variation 4 Absorber Absorptance	0
csp_dtr_hce_var4_annulus_pressure_1	Variation 4 Annulus Pressure	0
csp_dtr_hce_var4_annulus_pressure_2	Variation 4 Annulus Pressure	0
csp_dtr_hce_var4_annulus_pressure_3	Variation 4 Annulus Pressure	0
csp_dtr_hce_var4_annulus_pressure_4	Variation 4 Annulus Pressure	0
csp_dtr_hce_var4_bellows_shadowing_1	Variation 4 Bellows Shadowing	0.963
csp_dtr_hce_var4_bellows_shadowing_2	Variation 4 Bellows Shadowing	0.963
csp_dtr_hce_var4_bellows_shadowing_3	Variation 4 Bellows Shadowing	0.963
csp_dtr_hce_var4_bellows_shadowing_4	Variation 4 Bellows Shadowing	0.963
csp_dtr_hce_var4_broken_glass_1	Variation 4 Broken Glass	0
csp_dtr_hce_var4_broken_glass_2	Variation 4 Broken Glass	0
csp_dtr_hce_var4_broken_glass_3	Variation 4 Broken Glass	0
csp_dtr_hce_var4_broken_glass_4	Variation 4 Broken Glass	0

ass_4		
csp_dtr_hce_var4_env_abs_1	Variation 4 Envelope Absorptance	0
csp_dtr_hce_var4_env_abs_2	Variation 4 Envelope Absorptance	0
csp_dtr_hce_var4_env_abs_3	Variation 4 Envelope Absorptance	0
csp_dtr_hce_var4_env_abs_4	Variation 4 Envelope Absorptance	0
csp_dtr_hce_var4_env_emis_1	Variation 4 Envelope Emittance	0
csp_dtr_hce_var4_env_emis_2	Variation 4 Envelope Emittance	0
csp_dtr_hce_var4_env_emis_3	Variation 4 Envelope Emittance	0
csp_dtr_hce_var4_env_emis_4	Variation 4 Envelope Emittance	0
csp_dtr_hce_var4_env_trans_1	Variation 4 Envelope Transmittance	0
csp_dtr_hce_var4_env_trans_2	Variation 4 Envelope Transmittance	0
csp_dtr_hce_var4_env_trans_3	Variation 4 Envelope Transmittance	0
csp_dtr_hce_var4_env_trans_4	Variation 4 Envelope Transmittance	0
csp_dtr_hce_var4_field_fraction_1	Variation 4 Field Fraction	0
csp_dtr_hce_var4_field_fraction_2	Variation 4 Field Fraction	0
csp_dtr_hce_var4_field_fraction_3	Variation 4 Field Fraction	0
csp_dtr_hce_var4_field_fraction_4	Variation 4 Field Fraction	0
csp_dtr_hce_var4_gas_type_1	Variation 4 Gas Type	Hydrogen
csp_dtr_hce_var4_gas_type_2	Variation 4 Gas Type	Hydrogen
csp_dtr_hce_var4_gas_type_3	Variation 4 Gas Type	Hydrogen
csp_dtr_hce_var4_gas_type_4	Variation 4 Gas Type	Hydrogen
csp_dtr_hce_var4_hce_dirt_1	Variation 4 Dirt on receiver	0.98
csp_dtr_hce_var4_hce_dirt_2	Variation 4 Dirt on receiver	0.98
csp_dtr_hce_var4_hce_dirt_3	Variation 4 Dirt on receiver	0.98
csp_dtr_hce_var4_hce_dirt_4	Variation 4 Dirt on receiver	0.98
csp_dtr_hce_var4RatedHeatLoss_1	Variation 4 Rated Heat Loss	0
csp_dtr_hce_var4RatedHeatLoss_2	Variation 4 Rated Heat Loss	0
csp_dtr_hce_var4RatedHeatLoss_3	Variation 4 Rated Heat Loss	0
csp_dtr_hce_var4RatedHeatLoss_4	Variation 4 Rated Heat Loss	0
csp_dtr_sca_aperture_1	Reflective aperture area	817.5
csp_dtr_sca_aperture_2	Reflective aperture area	817.5
csp_dtr_sca_aperture_3	Reflective aperture area	817.5
csp_dtr_sca_aperture_4	Reflective aperture area	817.5
csp_dtr_sca_ave_focal_len_1	Average surface-to-focus path length	2.11

csp_dtr_sca_ave_focal_len_2	Average surface-to-focus path length	2.11
csp_dtr_sca_ave_focal_len_3	Average surface-to-focus path length	2.11
csp_dtr_sca_ave_focal_len_4	Average surface-to-focus path length	2.11
csp_dtr_sca_clean_reflectivity_1	Mirror reflectance	0.935
csp_dtr_sca_clean_reflectivity_2	Mirror reflectance	0.935
csp_dtr_sca_clean_reflectivity_3	Mirror reflectance	0.935
csp_dtr_sca_clean_reflectivity_4	Mirror reflectance	0.935
csp_dtr_sca_general_error_1	General optical error	0.99
csp_dtr_sca_general_error_2	General optical error	0.99
csp_dtr_sca_general_error_3	General optical error	0.99
csp_dtr_sca_general_error_4	General optical error	0.99
csp_dtr_sca_geometry_effects_1	Geometry effects	0.98
csp_dtr_sca_geometry_effects_2	Geometry effects	0.98
csp_dtr_sca_geometry_effects_3	Geometry effects	0.98
csp_dtr_sca_geometry_effects_4	Geometry effects	0.98
csp_dtr_sca_length_1	Length of collector assembly	148.5
csp_dtr_sca_length_2	Length of collector assembly	148.5
csp_dtr_sca_length_3	Length of collector assembly	148.5
csp_dtr_sca_length_4	Length of collector assembly	148.5
csp_dtr_sca_mirror_dirt_1	Dirt on mirror	0.95
csp_dtr_sca_mirror_dirt_2	Dirt on mirror	0.95
csp_dtr_sca_mirror_dirt_3	Dirt on mirror	0.95
csp_dtr_sca_mirror_dirt_4	Dirt on mirror	0.95
csp_dtr_sca_ncol_per_sca_1	Number of modules per assembly	12
csp_dtr_sca_ncol_per_sca_2	Number of modules per assembly	12
csp_dtr_sca_ncol_per_sca_3	Number of modules per assembly	12
csp_dtr_sca_ncol_per_sca_4	Number of modules per assembly	12
csp_dtr_sca_notify_text_1	Collector name from library	EuroTrough ET150
csp_dtr_sca_notify_text_2	Collector name from library	EuroTrough ET150
csp_dtr_sca_notify_text_3	Collector name from library	EuroTrough ET150
csp_dtr_sca_notify_text_4	Collector name from library	EuroTrough ET150
csp_dtr_sca_piping_dist_1	Piping distance between assemblies	1
csp_dtr_sca_piping_dist_2	Piping distance between assemblies	1
csp_dtr_sca_piping_dist_3	Piping distance between assemblies	1
csp_dtr_sca_piping_dist_4	Piping distance between assemblies	1
csp_dtr_sca_tracking_error_1	Tracking error	0.99
csp_dtr_sca_tracking_error_2	Tracking error	0.99
csp_dtr_sca_tracking_error_3	Tracking error	0.99
csp_dtr_sca_tracking_error_4	Tracking error	0.99
csp_dtr_sca_w_profile_1	Aperture width total structure	5.77
csp_dtr_sca_w_profile_2	Aperture width total structure	5.77
csp_dtr_sca_w_profile_3	Aperture width total structure	5.77
csp_dtr_sca_w_profile_4	Aperture width total structure	5.77

custom_sf_pipe_sizes	Use custom solar field pipe diameter, wall thickness, and length	0
custom_sgs_pipe_sizes	Use custom SGS pipe diameter, wall thickness, and length	0
custom_tes_p_loss	TES pipe losses are based on custom lengths and coeffs	0
cycle_cutoff_frac	Min turbine operation	0.25
cycle_max_frac	Max turbine over design operation	1.05
dT_cw_ref	Reference condenser water dT	10
debt_option	Debt mode (0=debt percent input1=DSCR input)	1
debt_percent	Debt percent	50
depr_alloc_macrs_15_percent	15-yr MACRS depreciation allocation	1.5
depr_alloc_macrs_5_percent	5-yr MACRS depreciation allocation	90
depr_alloc_sl_15_percent	15-yr Straight Line depreciation allocation	2.5
depr_alloc_sl_20_percent	20-yr Straight Line depreciation allocation	3
depr_alloc_sl_39_percent	39-yr Straight Linedepreciation allocation	0
depr_alloc_sl_5_percent	5-yr Straight Line depreciation allocation	0
dscr_reserve_months	Debt service reserve account	6
dt_hot	Hot side HX approach temp	5
equip1_reserve_cost	Replacement reserve 1 cost	0
equip1_reserve_freq	Replacement reserve 1 frequency	12
equip2_reserve_cost	Replacement reserve 2 cost	0
equip2_reserve_freq	Replacement reserve 2 frequency	15
equip3_reserve_cost	Replacement reserve 3 cost	0
equip3_reserve_freq	Replacement reserve 3 frequency	3
equip_reserve_depr_fed	Replacement reserves federal depreciation method	5-yr MACRS
equip_reserve_depr_sta	Replacement reserves state depreciation method	5-yr MACRS
eta_lhv	Fossil backup boiler LHV efficiency	0.9
eta_pump	HTF pump efficiency	0.85
eta_ref	Rated cycle conversion efficiency	0.389
eta_tes_htr	Tank heater efficiency	0.98
federal_tax_rate	Federal income tax rate	30;
flip_target_percent	IRR target	12
flip_target_year	IRR target year	20
fthrok	Allow partial defocusing	1
h_tank	Tank height	14
h_tank_min	Tank fluid min height	1
has_hot_tank_bypass	Bypass valve connects field outlet to cold tank	0
hce_2_is_shown	Current selection for Receiver Type 2	1
hce_3_is_shown	Current selection for Receiver Type 3	1
hce_4_is_shown	Current selection for Receiver Type 4	1
hot_tank_Thtr	Hot tank heater set point	386
in_nsrdb_options	NSRDB Options	
in_time_step	Time Step Option (0=60 min1=30 min)	0
inflation_rate	Inflation rate	2.5

roe_input	Return on equity	0;
sca_2_is_shown	Current selection for Collector Type 2	1
sca_3_is_shown	Current selection for Collector Type 3	1
sca_4_is_shown	Current selection for Collector Type 4	1
sf_hdr_diams	Custom header diameters	-1;
sf_hdr_lengths	Custom header lengths	-1;
sf_hdr_wallthickness	Custom header wall thicknesses	-1;
sf_rnr_diams	Custom runner diameters	-1;
sf_rnr_lengths	Custom runner lengths	-1;
sf_rnr_wallthickness	Custom runner wall thicknesses	-1;
sgs_diams	Custom SGS diameters	-1;
sgs_lengths	Custom SGS lengths	0;90;100;120;0;0;0;0;80;120;80;
sgs_wallthickness	Custom SGS wall thicknesses	-1;
specified_total_aperture	Field aperture	510120
startup_frac	Fraction of thermal power needed for startup	0.2
startup_time	Power block startup time	0.5
store_fl_props	User-defined HTF fluid	[1]
t_standby_reset	Low resource standby period	2
tank_max_heat	Tank heater capacity	25
tank_pairs	Parallel tank pairs	1
tanks_in_parallel	Tanks are in parallel not in series with solar field	1
term_int_rate	Annual interest rate	7
tes_pump_coef	Required pumping power for HTF through storage	0.15
theta_dep	Deploy angle	10
theta_stow	Stow angle	170
tilt	Collector tilt	0
tod_library	TOD factors and schedule library	Generic Summer Peak
tshours	Full load hours of TES	7.5
u_tank	Tank loss coeff	0.4
ud_T_amb_des	Ambient temperature	43
ud_T_amb_high	High ambient temperature	55
ud_T_amb_ind_od	Off-design parametric on ambient temperature	[0]
ud_T_amb_levels	Number of levels	20
ud_T_amb_low	Low ambient temperature	0
ud_T_htf_high	High HTF temperature	410
ud_T_htf_ind_od	Off-design parametric on htf temperature	[0]
ud_T_htf_levels	Number of levels	20
ud_T_htf_low	Low HTF temperature	300
ud_f_W_dot_cool_des	Gross power consumed by cooling system	0
ud_m_dot_htf_high	High normalized HTF \dot{m}	1.2
ud_m_dot_htf_ind_od	Off-design parametric on HTF mass flow rate	[0]
ud_m_dot_htf_levels	Number of levels	20
ud_m_dot_htf_low	Low normalized HTF \dot{m}	0.3

ud_m_dot_water_cool_des	Cooling system water usage	0
ui_disp_1_nosolar	Dispatch Fraction Without Solar Period 1	0
ui_disp_1_solar	Dispatch Fraction With Solar Period 1	0
ui_disp_1_turbout	Turbine Output Fraction Period 1	1
ui_disp_2_nosolar	Dispatch Fraction Without Solar Period 2	0
ui_disp_2_solar	Dispatch Fraction With Solar Period 2	0
ui_disp_2_turbout	Turbine Output Fraction Period 2	1
ui_disp_3_fossil	Fossil Fill Fraction Period 3	0
ui_disp_3_nosolar	Dispatch Fraction Without Solar Period 3	0
ui_disp_3_solar	Dispatch Fraction With Solar Period 3	0
ui_disp_3_turbout	Turbine Output Fraction Period 3	1
ui_disp_4_fossil	Fossil Fill Fraction Period 4	0
ui_disp_4_nosolar	Dispatch Fraction Without Solar Period 4	0
ui_disp_4_solar	Dispatch Fraction With Solar Period 4	0
ui_disp_4_turbout	Turbine Output Fraction Period 4	1
ui_disp_5_fossil	Fossil Fill Fraction Period 5	0
ui_disp_5_nosolar	Dispatch Fraction Without Solar Period 5	0
ui_disp_5_solar	Dispatch Fraction With Solar Period 5	0
ui_disp_5_turbout	Turbine Output Fraction Period 5	1
ui_disp_6_fossil	Fossil Fill Fraction Period 6	0
ui_disp_6_nosolar	Dispatch Fraction Without Solar Period 6	0
ui_disp_6_solar	Dispatch Fraction With Solar Period 6	0
ui_disp_6_turbout	Turbine Output Fraction Period 6	1
ui_disp_7_fossil	Fossil Fill Fraction Period 7	0
ui_disp_7_nosolar	Dispatch Fraction Without Solar Period 7	0
ui_disp_7_solar	Dispatch Fraction With Solar Period 7	0
ui_disp_7_turbout	Turbine Output Fraction Period 7	1
ui_disp_8_fossil	Fossil Fill Fraction Period 8	0
ui_disp_8_nosolar	Dispatch Fraction Without Solar Period 8	0
ui_disp_8_solar	Dispatch Fraction With Solar Period 8	0
ui_disp_8_turbout	Turbine Output Fraction Period 8	1
ui_disp_9_fossil	Fossil Fill Fraction Period 9	0
ui_disp_9_nosolar	Dispatch Fraction Without Solar Period 9	0
ui_disp_9_solar	Dispatch Fraction With Solar Period 9	0
ui_disp_9_turbout	Turbine Output Fraction Period 9	1
washing_frequency	Washes per year	63
water_usage_per_wash	Water usage per wash	0.7

D.2. Input data to the wind power model

Table D. 2 Input data to the wind power model used in this work.

Variable	Description	Value
analysis_period	Analysis period	25
anchor	Anchor type	0
avail_bop_loss	Balance of plant	0.5
avail_bop_uncert	Balance of plant	0.3
avail_grid_loss	Grid	1.5
avail_grid_uncert	Grid	0.94
avail_turb_loss	Turbine	3.58
avail_turb_uncert	Turbine	2.3
bos_cost_fixed	BOS fixed costs	0
bos_cost_per_kw	BOS cost per kW	0
bos_cost_per_turbine	BOS cost per turbine	0
buryDepth	Electrical cable burial depth	2
cableOptimizer	Electrical cable cost optimizer	0
depr_alloc_macrs_15_percent	15-yr MACRS depreciation allocation	1.5
depr_alloc_macrs_5_percent	5-yr MACRS depreciation allocation	90
depr_alloc_sl_15_percent	15-yr Straight Line depreciation allocation	2.5
depr_alloc_sl_20_percent	20-yr Straight Line depreciation allocation	3
depr_alloc_sl_39_percent	39-yr Straight Linedepreciation allocation	0
depr_alloc_sl_5_percent	5-yr Straight Line depreciation allocation	0
depr_bonus_fed	Federal bonus depreciation percentage	0
depth	Turbine foundation depth	1
desired_farm_size	Desired farm size	50000
dispatch_data_filename	TOD factor inputs file	
dispatch_factor1	TOD factor 1	1
dispatch_factor2	TOD factor 2	1
dispatch_factor3	TOD factor 3	1
dispatch_factor4	TOD factor 4	1
dispatch_factor5	TOD factor 5	1
dispatch_factor6	TOD factor 6	1
dispatch_factor7	TOD factor 7	1
dispatch_factor8	TOD factor 8	1
dispatch_factor9	TOD factor 9	1
distAtoS	Distance from inshore assembly area to site	90
distInterCon	Distance over land to grid interconnect	3
distPort	Distance from installation port to site	90
distPtoA	Distance from installation port to	90

	inshore assembly area	
distShore	Distance to landfall	90
distance_to_interconnect_mi	Distance to interconnect	0
dscr	DSCR	1.3
dscr_reserve_months	Debt service reserve account	6
elecCont	Electrical install weather contingency	30
elec_eff_loss	Efficiency	1.91
elec_eff_uncert	Electrical efficiency	1
elec_parasitic_loss	Parasitic consumption	0.1
elec_parasitic_uncert	Facility parasitic consumption	0.05
en_landbosse	Enable LandBOSSE model	0
enable_interconnection_limit	Enable interconnection limit	0
env_degrad_loss	Degradation	1.8
env_degrad_uncert	Degradation	2.2
env_env_loss	Environmental	0.4
env_env_uncert	Environmental	1
env_exp_uncert	Exposure changes	0
env_exposure_loss	Exposure changes	0
env_icing_loss	Icing	0.21
env_icing_uncert	Icing	3.8
equip1_reserve_cost	Replacement reserve 1 cost	0.25
equip1_reserve_freq	Replacement reserve 1 frequency	12
equip2_reserve_cost	Replacement reserve 2 cost	0
equip2_reserve_freq	Replacement reserve 2 frequency	15
equip3_reserve_cost	Replacement reserve 3 cost	0
equip3_reserve_freq	Replacement reserve 3 frequency	3
est_bos_cost		0
est_turbine_cost		0
eval_climate_10yr_uncert	10 year	1.3
eval_climate_20yr_uncert	20 year	1.3
eval_climate_uncert	Climate change Year 1	1.3
eval_perf_10yr_uncert	10 year	1
eval_perf_20yr_uncert	20 year	1
eval_perf_uncert	Plant performance Year 1	1
eval_period_10yr_uncert	10 year	1.5
eval_period_20yr_uncert	20 year	1.5
eval_period_uncert	Modelled period Year 1	1.5
grid_curtailment_price	Curtailed energy compensation rate	0
grid_curtailment_price_esc	Curtailed compensation escalation	0
grid_interconnection_limit_kwac	Grid interconnection limit	100000
hextrap_inputs_uncert	Model inputs	1.7
hextrap_sens_uncert	Model sensitivity and stress	1.3
inflation_rate	Inflation rate	2.5
installStrategy	Installation vessel strategy	0
install_type	Land based or offshore installation	0

interConVolt	Grid interconnect voltage	345
interconnect_voltage_kv	Interconnect voltage	137
labor_cost_multiplier	Labor cost multiplier	0
lib_dispatch_factor1	TOD factor 1 from TOD library	1
lib_dispatch_factor2	TOD factor 2 from TOD library	1
lib_dispatch_factor3	TOD factor 3 from TOD library	1
lib_dispatch_factor4	TOD factor 4 from TOD library	1
lib_dispatch_factor5	TOD factor 5 from TOD library	1
lib_dispatch_factor6	TOD factor 6 from TOD library	1
lib_dispatch_factor7	TOD factor 7 from TOD library	1
lib_dispatch_factor8	TOD factor 8 from TOD library	1
lib_dispatch_factor9	TOD factor 9 from TOD library	1
meas_atm_uncert	Other atmospheric parameters	0.3
meas_data_uncert	Data integrity and documentation	0.3
meas_dir_uncert	Wind direction measurement and rose	0
meas_speed_uncert	Wind speed measurement	2
mera_name1	Replacement reserve 1 name	Replacement Reserve 1
mera_name2	Replacement reserve 2 name	Replacement Reserve 2
mera_name3	Replacement reserve 3 name	Replacement Reserve 3
months_receivables_reserve	Receivables reserve	0
months_working_reserve	Working capital reserve	6
moorLines	Number of mooring lines	3
number_install_seasons	Number of installation seasons	1
om_capacity_escal	Fixed cost per capacity escalation	0
om_fixed	Fixed annual cost	0
om_fixed_escal	Fixed annual cost escalation	0
om_fuel_cost	Fossil fuel cost	0
om_fuel_cost_escal	Fossil fuel cost escalation	0
om_production	Variable cost by generation	0
om_production_escal	Variable cost by generation escalation	0
om_replacement_cost1	Battery replacement cost	0
om_replacement_cost_escal	Escalation cost for battery replacements	0
ops_env_loss	Environmental and permit curtailment	1
ops_env_uncert	Environmental and permit curtailment	1.8
ops_strategies_loss	Operational strategies	0
ops_strategies_uncert	Operational strategies	0
payment_option	Debt payment mode (0=Equal payments1=Fixed principal declining interest)	0
pbi_fed_amount	Federal PBI amount	0
ppa_escalation	PPA price escalation	1
ppa_multiplier_model	TOD factor mode	0

rated_thrust_N	Turbine rated thrust	0
real_discount_rate	Real discount rate	7
reserves_interest	Interest on reserves	1.75
resource_adj_uncert	Long-term adjustment (MCP)	1
resource_datasync_uncert	On-site data synthesis (gap filling)	0
resource_definition_type		0
resource_dist_uncert	Speed distribution uncertainty	2
resource_period_uncert	Long-term period (IAV)	2
resource_refdata_uncert	Reference data	0
revenue_TOD_is_shown	Current selection for Time of Delivery	0
revenue_capacity_payments_is_shown	Current selection for Capacity Payments	0
revenue_curtailment_is_shown	Current selection for Curtailment Payments	0
roe_input	Return on equity	0
sensitivity_uncert	Sensitivity (% Δ Energy/% Δ Wind Speed)	1.8
substructCont	Substructure install weather contingency	30
substructure	Substructure type	0
system_use_lifetime_output		0
term_int_rate	Annual interest rate	7
tod_library	TOD factors and schedule library	Uniform Dispatch
turbCont	Turbine install weather contingency	30
turbInstallMethod	Turbine installation method	0
turb_generic_loss	Generic power curve adjustment	1.7
turb_generic_uncert	Generic power curve adjustment	3.72
turb_hysteresis_loss	High wind hysteresis	0.4
turb_hysteresis_uncert	High wind hysteresis	1
turb_perf_loss	Sub-optimal performance	1.1
turb_specific_loss	Site-specific power curve adjustment	0.81
turb_specific_uncert	Site-specific power curve adjustment	1.2
turb_subopt_uncert	Sub-optimal performance	2
turbine_cost_fixed	Turbine fixed costs	0
turbine_cost_per_turbine	Turbine cost per turbine	0
user_specified_wf_wind	Wind resource user-specified file	
vextrap_comp_uncert	Model components	0
vextrap_inputs_uncert	Model inputs	1.5
vextrap_stress_uncert	Model stressor	0.8
wake_ext_loss	External wake	1.1
wake_ext_uncert	External wake	1.1
wake_future_loss	Future wake	0
wake_future_uncert	Future wake	0
wake_int_uncert	Internal wake	2.8
wake_loss	Constant loss	11.02
waterD	Maximum water depth	30

weibull_reference_height	Reference height for wind speed	50
weibull_wind_speed	Average annual wind speed	7.25
wind.turbine.blade_design	Blade design	Advanced Design
wind.turbine.drive_train	Drive train design	3 Stage Planetary
wind.turbine.elevation	Turbine elevation (above sea level)	0
wind.turbine.max_tip_speed	Maximum tip speed	80
wind.turbine.max_tspeed_ratio	Maximum tip-speed ratio	8
wind.turbine.radio_list_or_design		0
wind.turbine.region2nhalf_slope		5
wind.turbine.tower_design	Tower design	Advanced Design
wind_bos_shown	Current selection for Land-Based Balance of System Cost Model (v2.3.0.3)	0
wind_climate.msg		
wind_climate.msg_is_error		0
wind_farm_sizing_mode		2
wind_obos_shown	Current selection for Offshore Balance of System Cost Model	0
wind_resource.lat_requested		0
wind_resource.lon_requested	Longitude	0
wind_resource_distribution		[0;0;1]
wind_resource_model_choice	Current selection for Wind Resource	0
wind_resource_shear	Shear coefficient	0.14
wind_resource_turbulence_coeff	Turbulence coefficient	0.1
wind_turbine_cut_out	Cut-out wind speed	25
wind_turbine_kw_rating_input	User-defined rated output	1500
windfarm.farm.layout_angle	Row orientation	70
windfarm.farm.layout_slider		0
windfarm.farm.number_of_rows	Number of rows	1
windfarm.farm.offset	Offset for rows	1.7
windfarm.farm.offset_type	Offset type	Every Other Row
windfarm.farm.shape	Shape	
windfarm.farm.turbines_per_row	Turbines per row	5
windfarm.layout.file_or_controls		1
wspd_uncert	Total wind speed-based uncertainty	9.10558

Appendix E. Mathematical modelling

E.1. Wind power density

The kinetic energy (E_k) of an object with total mass (m) and velocity (U) is expressed as follows:

$$E_k = \frac{1}{2} m U^2$$

It should be noted that the above can represent E_k of moving wind blow (an imaginary volume of air) with a geometry of a collection of air molecules, passing through a plane, of a wind turbine's blades in which the blade sweeps out a cross-sectional area (A) with a thickness (δ) over a given time (t). Here, the volume (φ) of this imaginary volume of air is determined by the area multiplied by its thickness:

$$\varphi = A \delta$$

ρ is the density of the air in this imaginary volume of air and is calculated as follows:

$$\rho = m/\varphi \quad (\text{or}) \quad m = \rho \varphi$$

If t is the required time for the imaginary volume of air to move through the plane of the blades, then the imaginary volume of air's velocity, U , is expressed as follows:

$$U = \delta / t \quad (\text{or}) \quad \delta = U t$$

Thus, E_k can be expressed as follows:

$$E_k = \frac{1}{2} m U^2$$

$$E_k = \frac{1}{2} (\rho \varphi) U^2$$

$$E_k = \frac{1}{2} (\rho A \delta) U^2$$

$$E_k = \frac{1}{2} (\rho A U t) U^2$$

$$E_k = \frac{1}{2} \rho U^3 A t$$

After changing the above expression of E_k using the power (P), the outcome becomes as follows:

$$P = E_k / t = (\frac{1}{2} \rho U^3 A t) / t = \frac{1}{2} \rho U^3 A$$

$$P/A = \frac{1}{2} \rho U^3$$

It can be concluded that P/A only depends on ρ and U ; hence, there is no dependency on size, efficiency or other characteristics of wind turbines when determining P/A . It should be recognized that the term P/A is the "wind power density (P_d)" and has units of W/m^2 , which is calculated as follows:

$$P_d = P/A = \frac{1}{2} \rho U^3 = \frac{1}{2} * 1.12 \text{ kg/m}^3 * (8.02 \text{ m/s})^3 = 289 \text{ W/m}^2$$

E.2. Betz's coefficient

It should be noted that understanding the aerodynamics of any type of wind turbine comes initially from analyzing the process of energy extraction. Figure E. 1 shows an energy extracting actuator disc and stream tube.

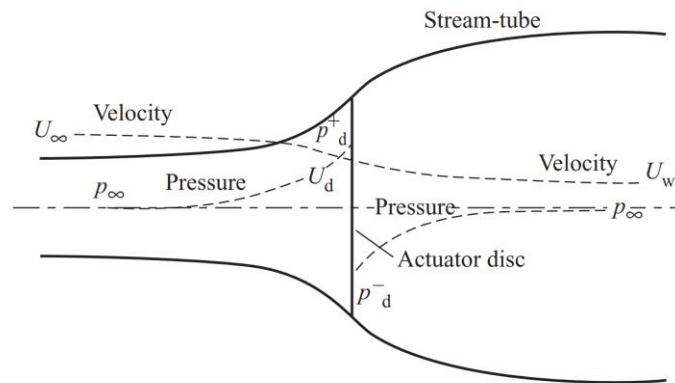


Figure E. 1 A stream tube and actuator disc [353].

At the location far upstream of the disc, it should be noted that the stream tube has an area which is smaller than that of the actuator disc and larger than the disc downstream. Thus, the expansion of the stream tube is because the mass flow rate must be the same everywhere.

The air mass flow rate through a cross-section of the stream tube in a unit length of time is $\rho \cdot \sigma \cdot U^3$, where U is the flow velocity. According to the conservation of mass law, the mass flow rate must be the same everywhere along the stream tube; therefore, the following relation is valid:

$$\rho U_\infty A_\infty = \rho U_d A_d = \rho U_w A_w$$

where ∞ refers to the conditions at the location far upstream, d refers to the conditions at the disc, and w refers to the conditions in the far wake. As the actuator disc induces a velocity, therefore, the effective component of flow is - a U_∞ and the net stream velocity is calculated follows [353]:

$$U_d = U_\infty (1 - a)$$

where a is the inflow factor. The rate of change of momentum (R) is calculated as follows:

$$R = \rho U_d A_d (U_\infty - U_w)$$

After applying Bernoulli's equation under steady conditions while considering the total energy in the flow, kinetic energy, static pressure and gravitational energy for a unit volume of air, then the following relations hold [353]:

$$\frac{1}{2} \rho U^2 + p + \rho g h = \text{constant}$$

The force causing R to be effective is as follows:

$$A_d (p_d^+ - p_d^-) = \rho U_\infty A_d (U_\infty - U_w) (1 - a)$$

where $(p_d^+ - p_d^-)$ is the pressure difference across the actuator disc. The force (F) on the air becomes as follows:

$$F = A_d (p_d^+ - p_d^-) = 2 \rho U_\infty^2 A_d a (1 - a)$$

Thus, the power extraction (P_{ex}) from the air is calculated as follows:

$$P_{ex} = F U_d = 2 \rho U_\infty^3 A_d a (1 - a)^2$$

Then, the power coefficient (C_p) is defined as follows:

$$\begin{aligned} C_p &= \frac{\text{power extraction from air}}{\text{power in the air in the absence of an actuator disc}} \\ &= \frac{P_{ex}}{\frac{1}{2} \rho U_\infty^3 A_d} \\ &= \frac{2 \rho U_\infty^3 A_d a (1 - a)^2}{\frac{1}{2} \rho U_\infty^3 A_d} \\ &= 4 a (1 - a)^2 \end{aligned}$$

E.3. Betz's limit

As shown earlier, the power coefficient (C_p) is defined as follows:

$$\begin{aligned} C_p &= \frac{\text{power extraction from air}}{\text{power in the air in the absence of an actuator disc}} \\ &= \frac{P_{ex}}{\frac{1}{2} \rho U_\infty^3 A_d} \end{aligned}$$

$$\begin{aligned}
&= \frac{2 \rho U_{\infty}^3 A_d a (1 - a)^2}{\frac{1}{2} \rho U_{\infty}^3 A_d} \\
&= 4 a (1 - a)^2
\end{aligned}$$

The maximum value of C_p occurs when the following relation holds:

$$\frac{dC_p}{da} = 4 (1 - 3a)(1 - a) = 0$$

Solving the above gives a value of 0.33 for a ; thus, the maximum value that C_p can theoretically have (Betz's limit) is as follows:

$$C_p = \frac{16}{27} = 0.593$$

E.4. Condenser systems (wet and dry)

In this section, the cooling performances with the mathematical derivations and calculations used in the simulations are summarized as follows [188,354]. Here, attention is given to utilizing cooling condensers (see Figure E. 2), which are needed to perform the process of heat rejection from the PB system due to the significant effects on the thermodynamic cycle and water consumption within the CSP-PT plant. For the cycle heat rejection, which is essential for the estimation of the system cooling as per the plant's design, it can be calculated as follows:

$$\dot{Q}_{rej} = (1 - \eta_{PB,des}) \dot{Q}_{in,PB} = \left(\frac{1}{\eta_{PB,des}} - 1 \right) \dot{W}_{des}$$

In both the wet and dry-cooled condenser systems, the mass flow rate of the circulating fluid, which are either water or air respectively, can be expressed as a function of the cooling fluid temperature rise through the condenser and the heat rejection load as follows:

$$\dot{m}_{cw} = \frac{\dot{Q}_{rej}}{C_{p,cw} \Delta T_{cw,des}}$$

$$\dot{m}_{ca} = \frac{\dot{Q}_{rej}}{C_{p,ca} \Delta T_{ca,des}}$$

The power consumed by the pump in order to circulate the water through the condenser system can be determined as follows:

$$\dot{W}_{cw,pump} = \frac{(h_{cw,pump\ out} - h_{cw,pump\ in}) \dot{m}_{cw}}{\eta_{pump,isentropic} \eta_{pump,mechanical}}$$

The power consumed by the fan in order to drive the cooling air inside the cooling tower can be determined by the same equation as the pump:

$$\dot{W}_{fan} = \frac{(h_{fan\ out} - h_{fan\ in}) \dot{m}_{air}}{\eta_{fan,isentropic} \eta_{fan,mechanical}}$$

It should be noted that the air and water enthalpies in the previous two equations are illustrated based on empirical models presented in the study [188]. Thus, the cooling tower water consumption for the wet-cooled condenser system is determined as the sum of water for evaporative loss (in which the evaporative segment of the equation is determined based on latent heat:), cooling tower blowdown, and drift loss as follows:

$$\begin{aligned} \dot{m}_{water,cooling} &= \dot{m}_{water} + \dot{m}_{drift} + \dot{m}_{blowdown} \\ &= \frac{\dot{Q}_{rej}}{\Delta h_{evaporation}} + f_{drift} \dot{m}_{cw} + f_{blowdown} \dot{m}_{cw} \end{aligned}$$

It should be recognized that the complete mathematical model of the condenser system, including operating pressure, parasitic load energy, and water consumption, can be found in Ref. [188]. Also, the input data to the model for the condenser system as per design is provided in Table 5. 3.

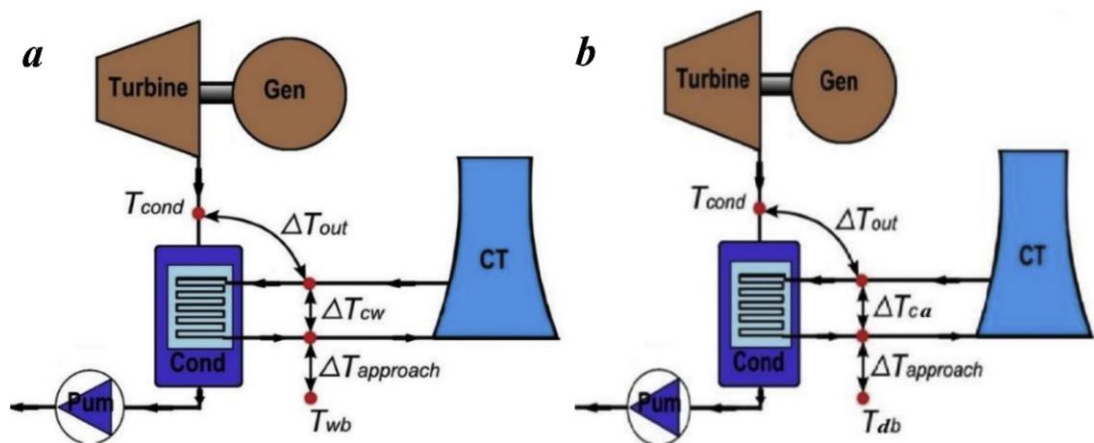


Figure E. 2 Schematics of cooling options alongside various temperature evaluations: (a) wet-cooled condenser system, and (b) dry-cooled condenser system [188,354].

Appendix F. Supplementary figures

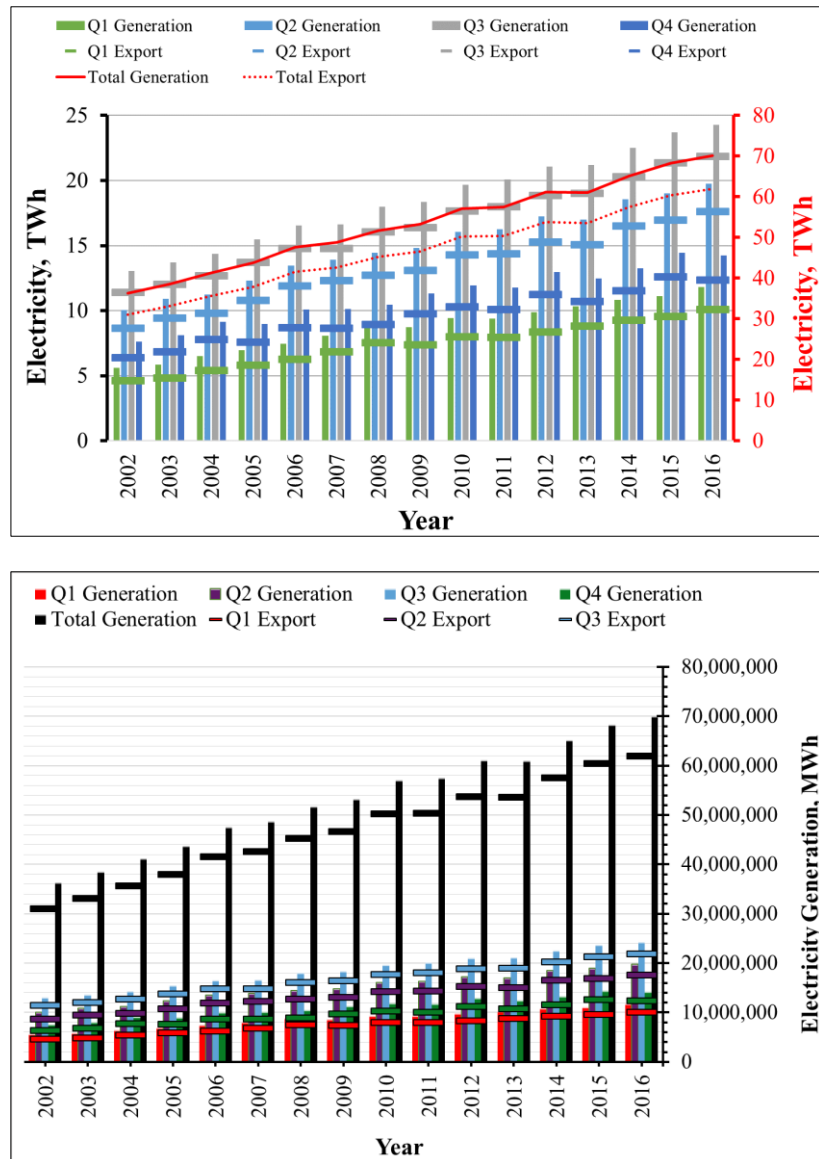


Figure F. 1 Electricity generation and export from 2002 to 2016 with the summertime represented by the third quarter (Q3) showing peak levels across the years in Kuwait.

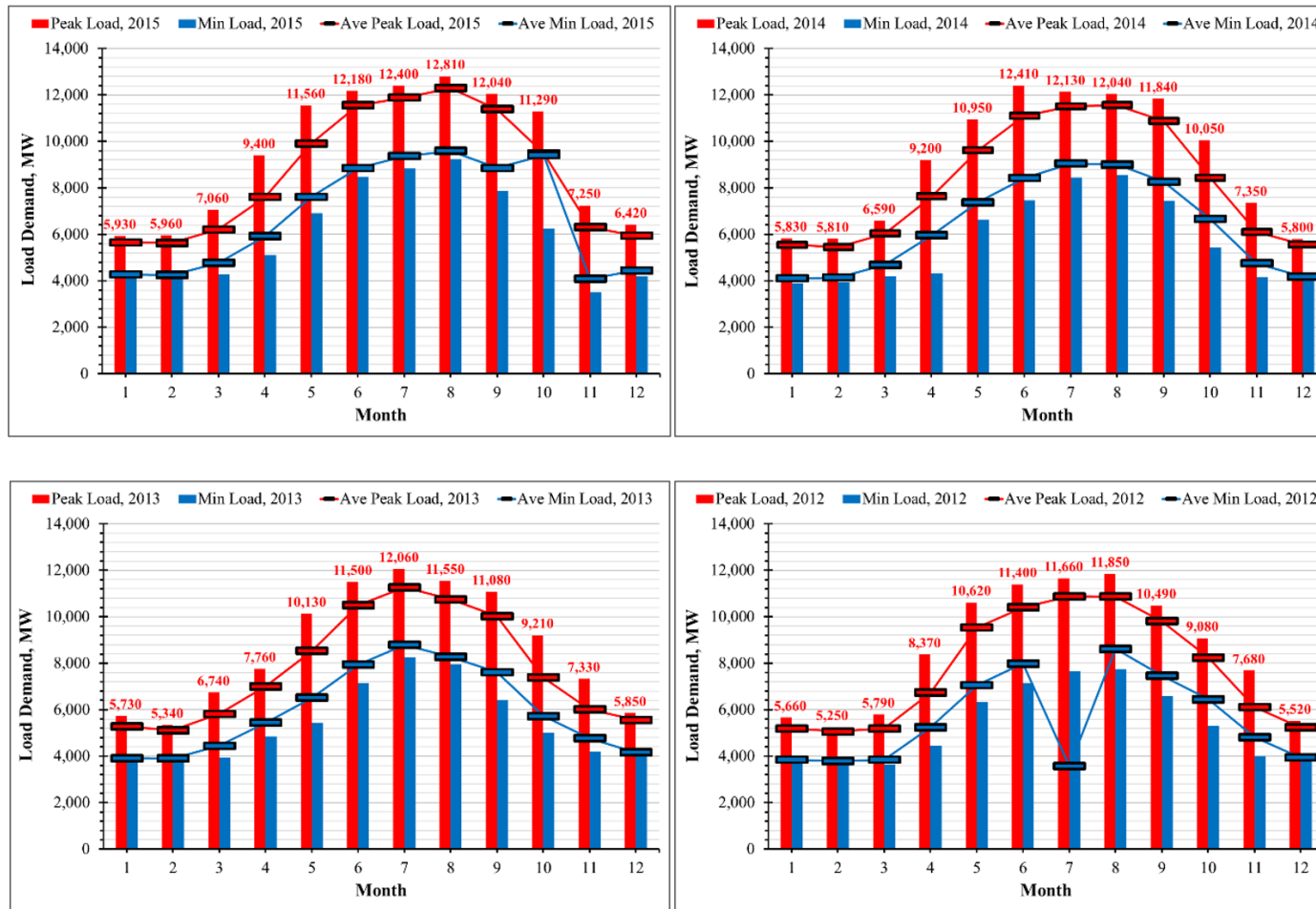


Figure F. 2 Monthly peak load, average peak load, minimum load, and average minimum load for 2015, 2014, 2013, and 2012 in Kuwait.

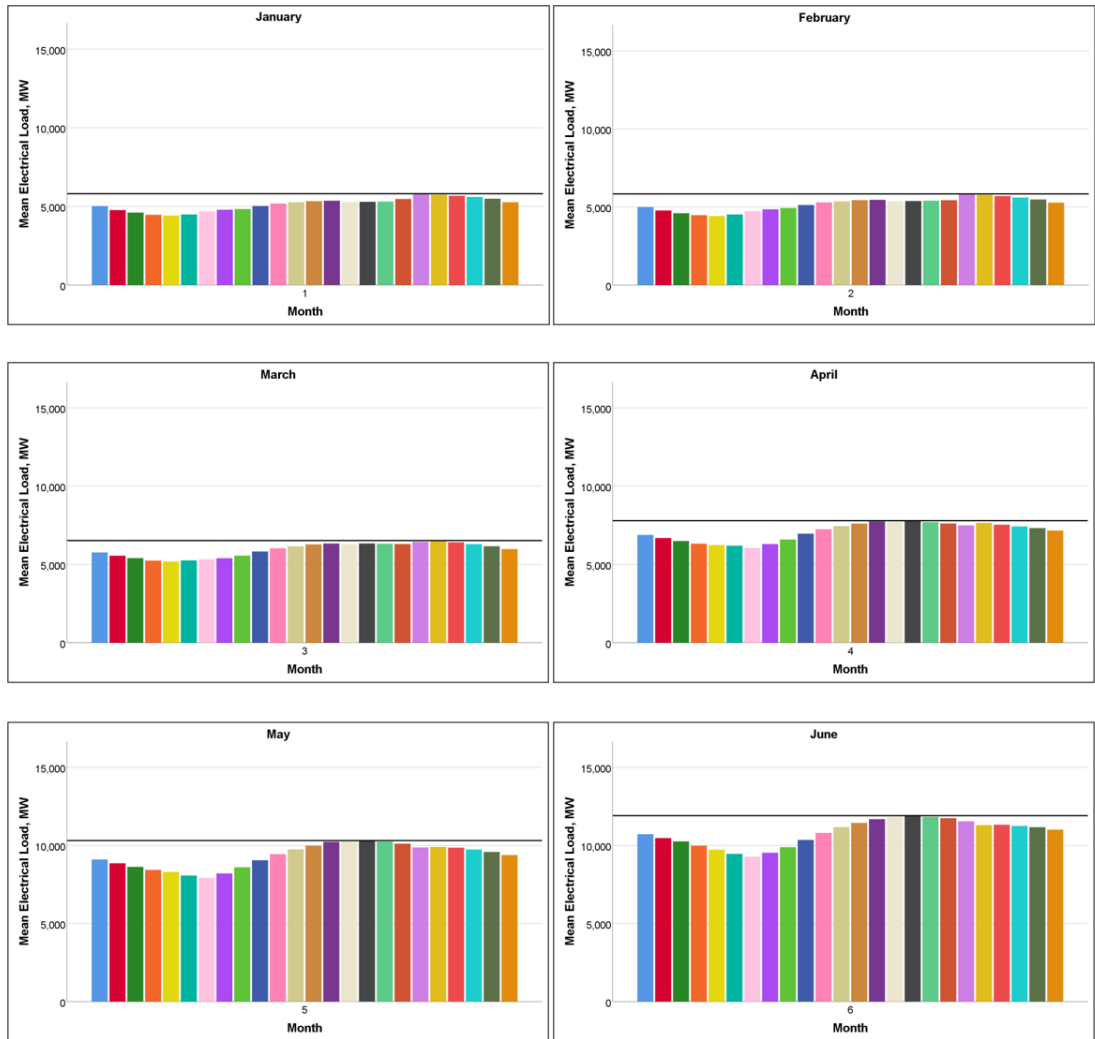
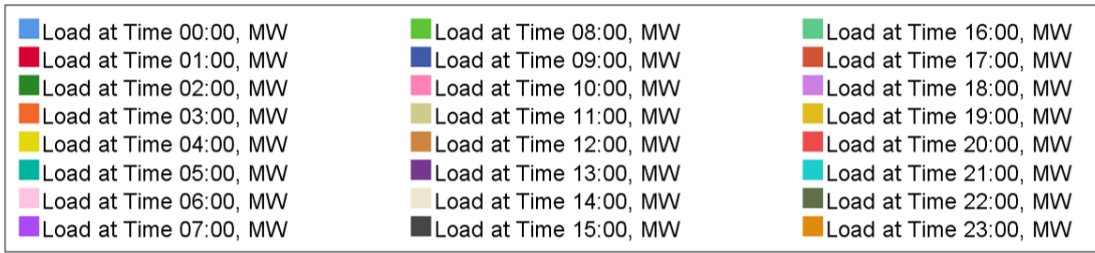


Figure F. 3 Monthly electrical load profiles (January to June) for 2016 in Kuwait (y-axis: 0-15,000 MW).

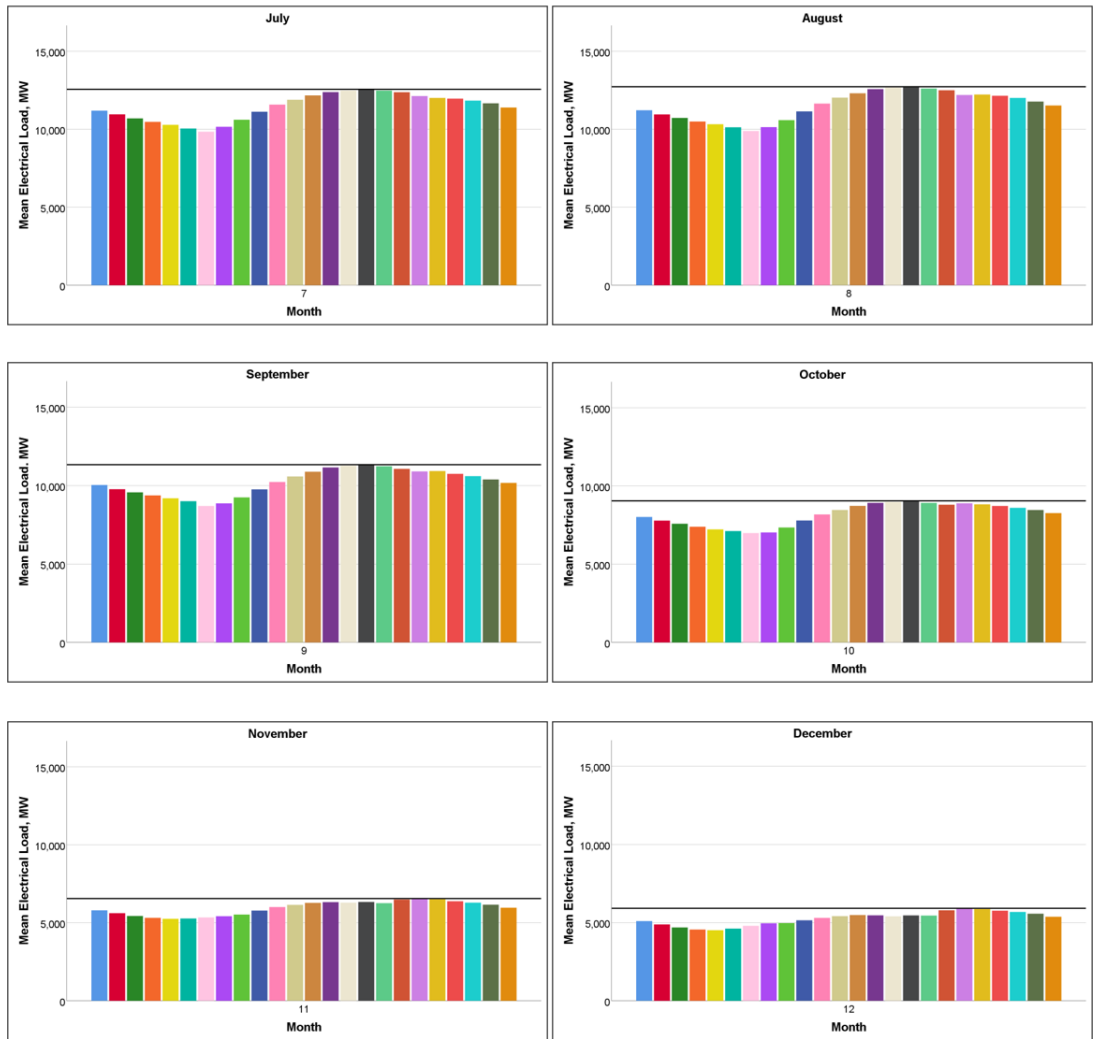
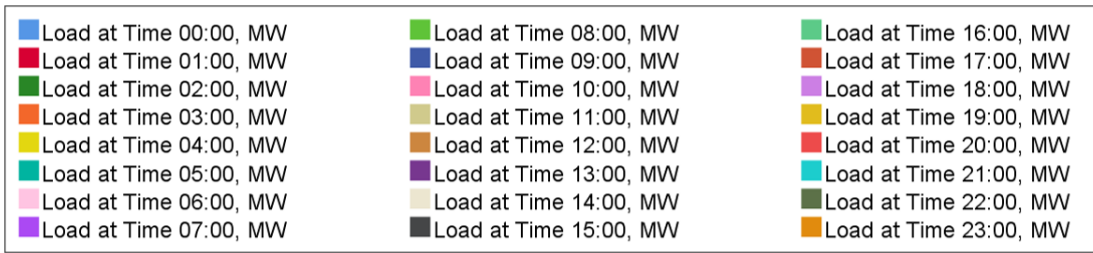


Figure F. 4 Monthly electrical load profiles (July to December) for 2016 in Kuwait (y-axis: 0-15,000 MW).

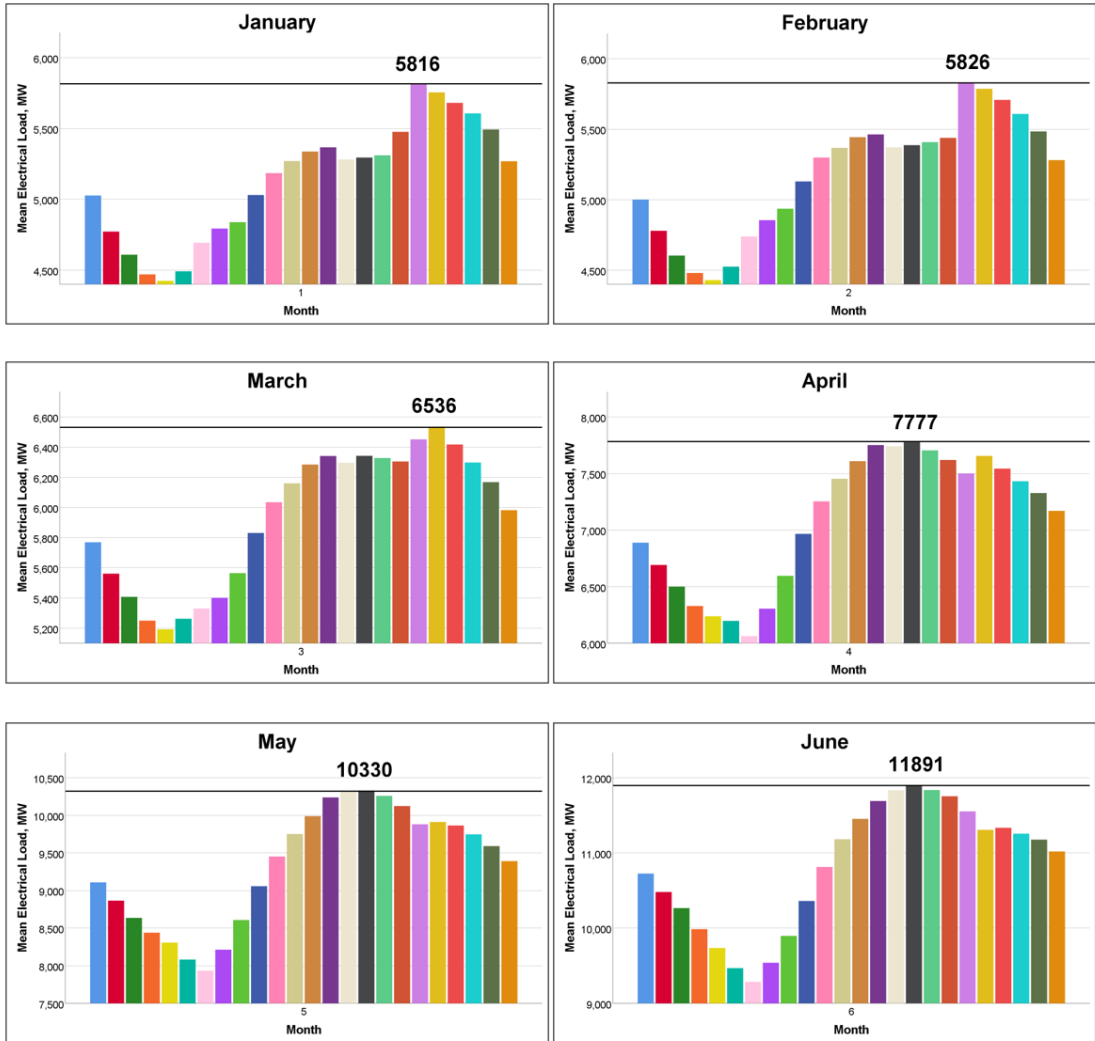
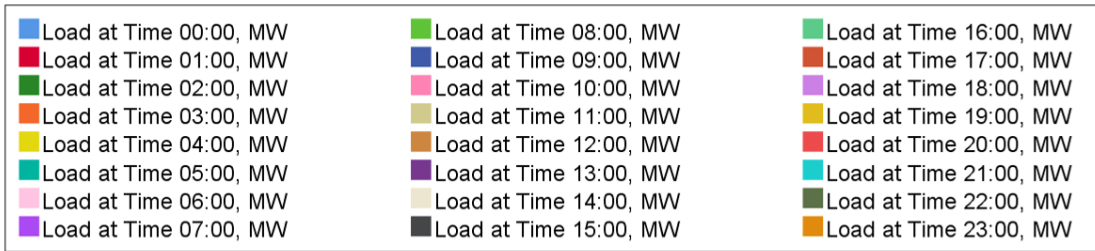


Figure F. 5 Monthly electrical load profiles (January to June) for 2016 in Kuwait (variable scale y-axis).

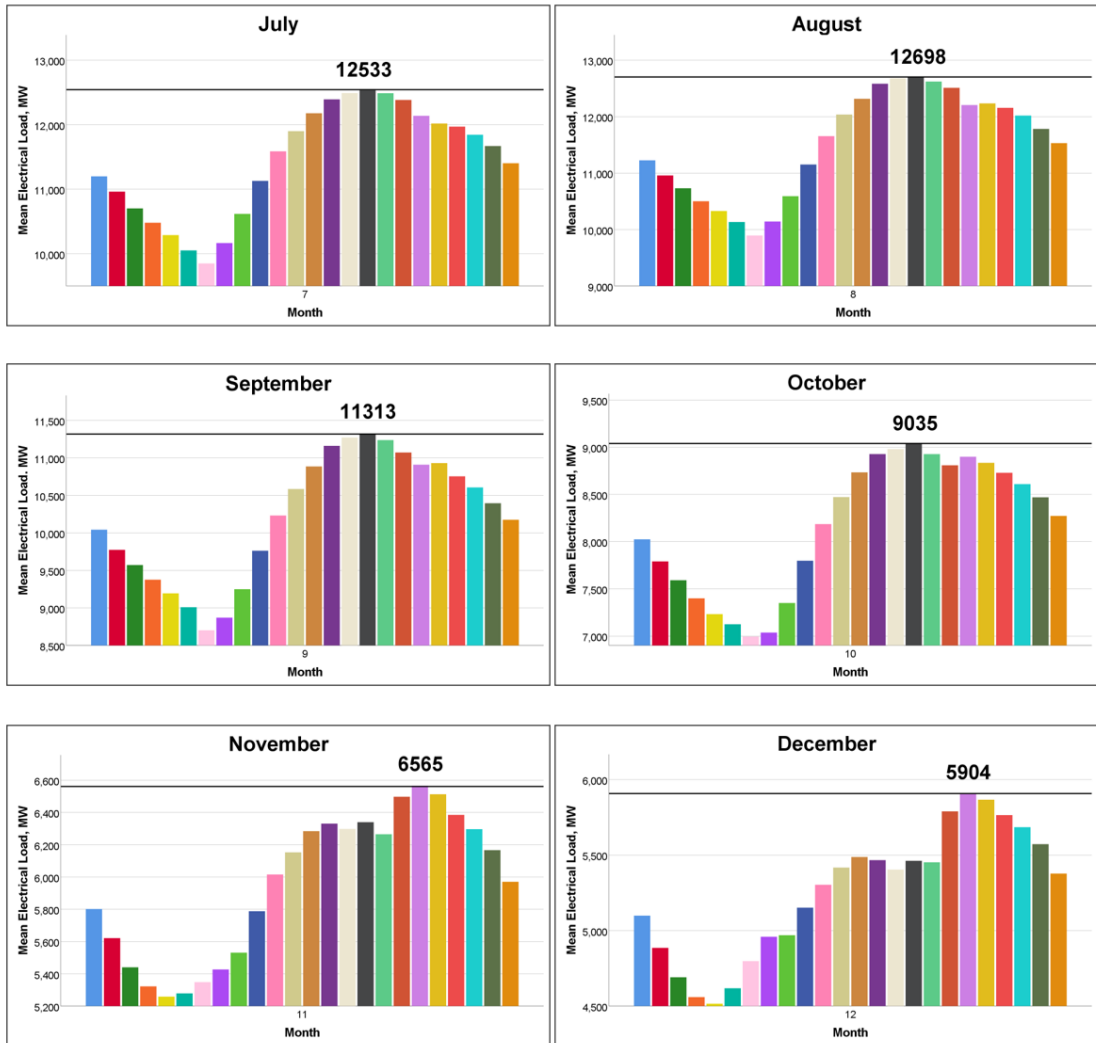
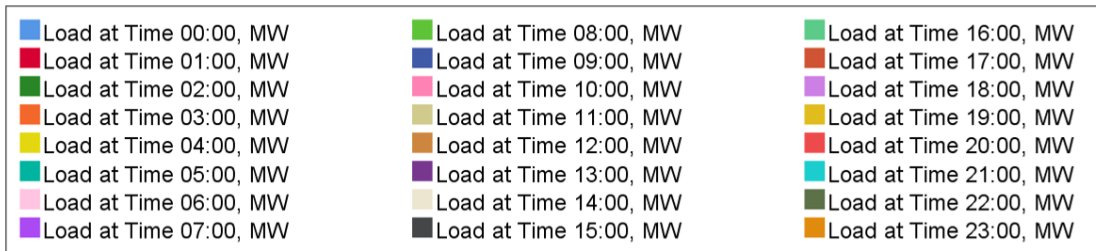


Figure F. 6 Monthly electrical load profiles (July to December) from the fossil-based power plants for 2016 in Kuwait (variable scale y-axis).

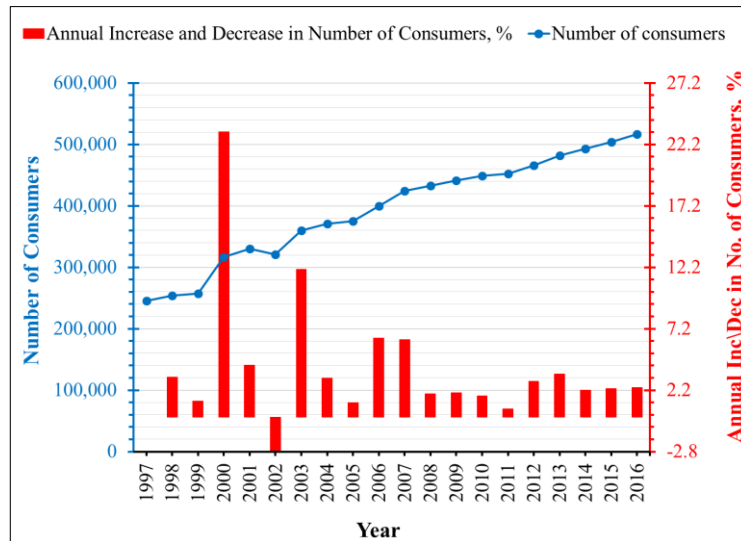
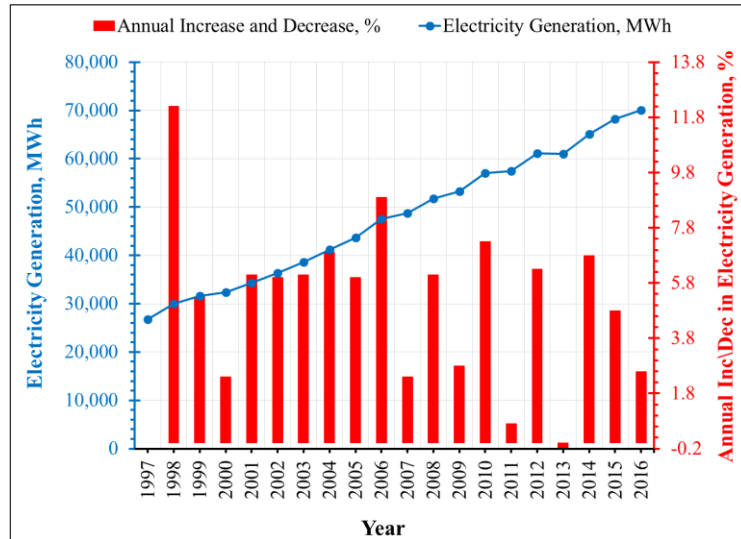


Figure F. 7 Annual profiles of the electricity generation and the number of consumers in Kuwait from 1997 to 2016.

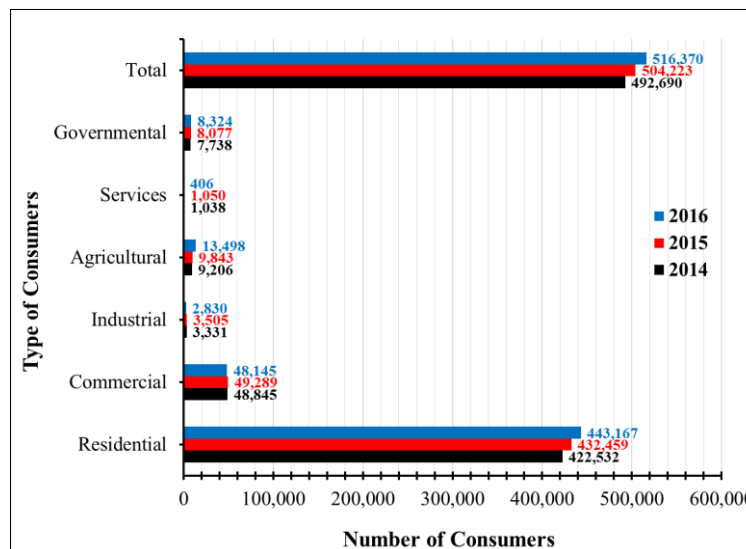


Figure F. 8 Type of electricity consumers from 2014 to 2016 in Kuwait.

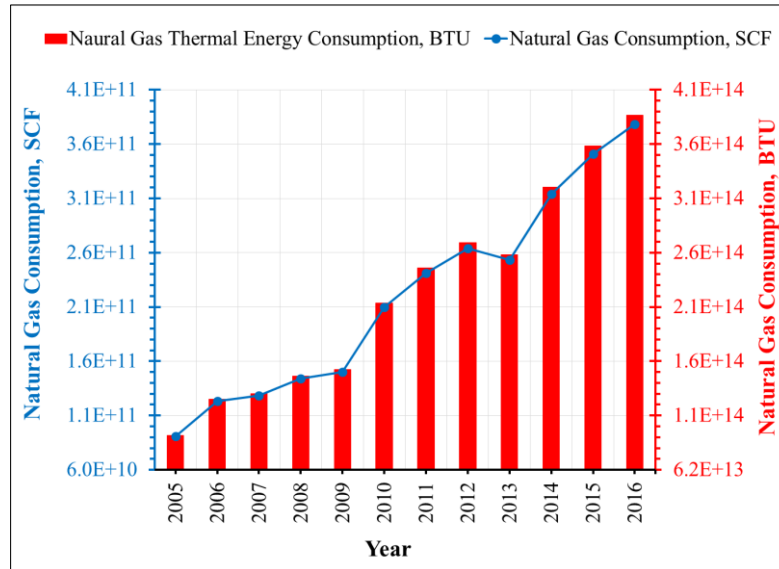
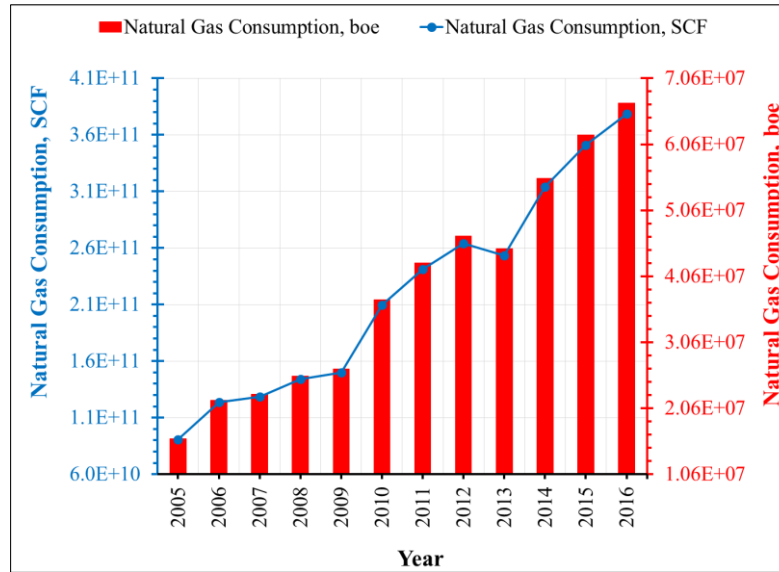


Figure F. 9 Consumption of NG in SCF/boe and thermal energy in SCF/BTU in Kuwait.

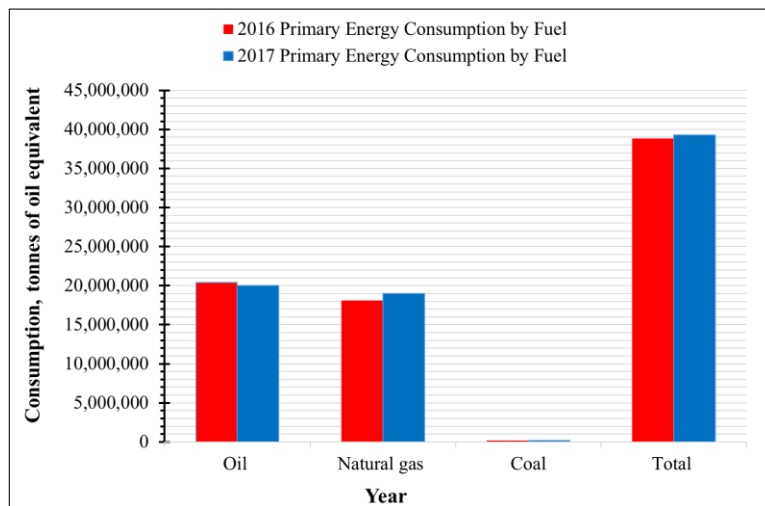
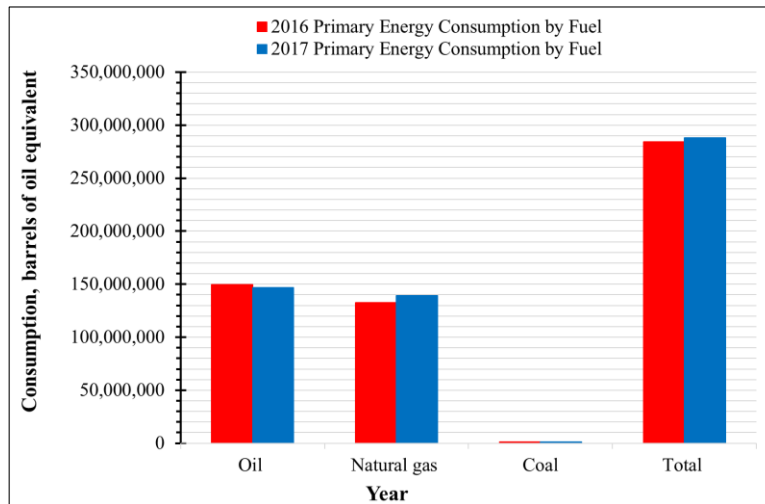
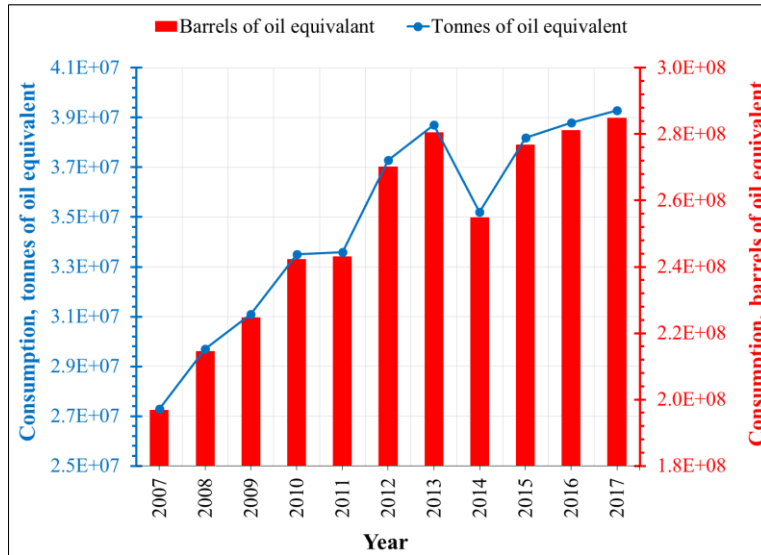


Figure F. 10 Primary energy consumption from 2007 to 2017 and fuel type from 2016 to 2017 in boe and toe units in Kuwait.

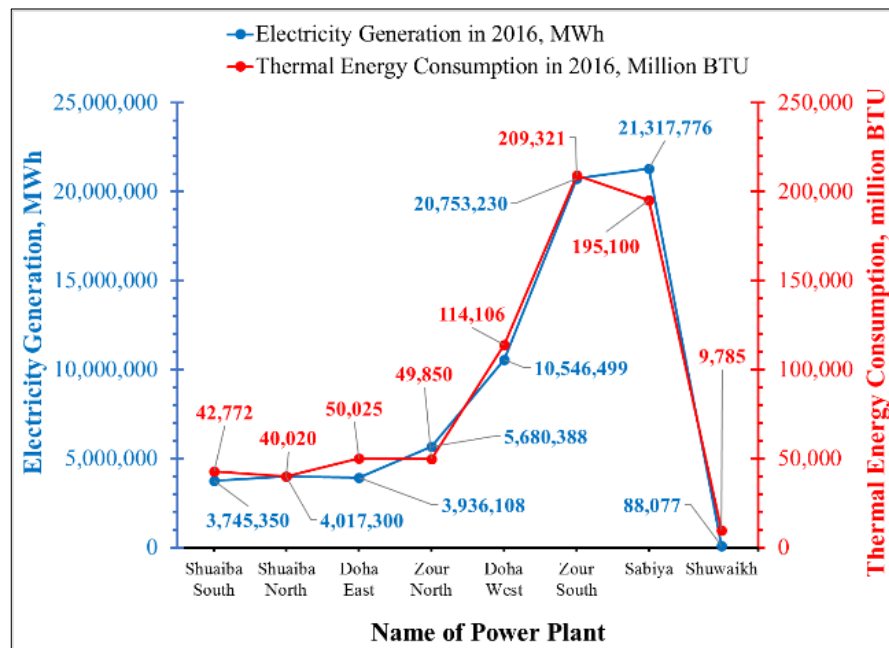
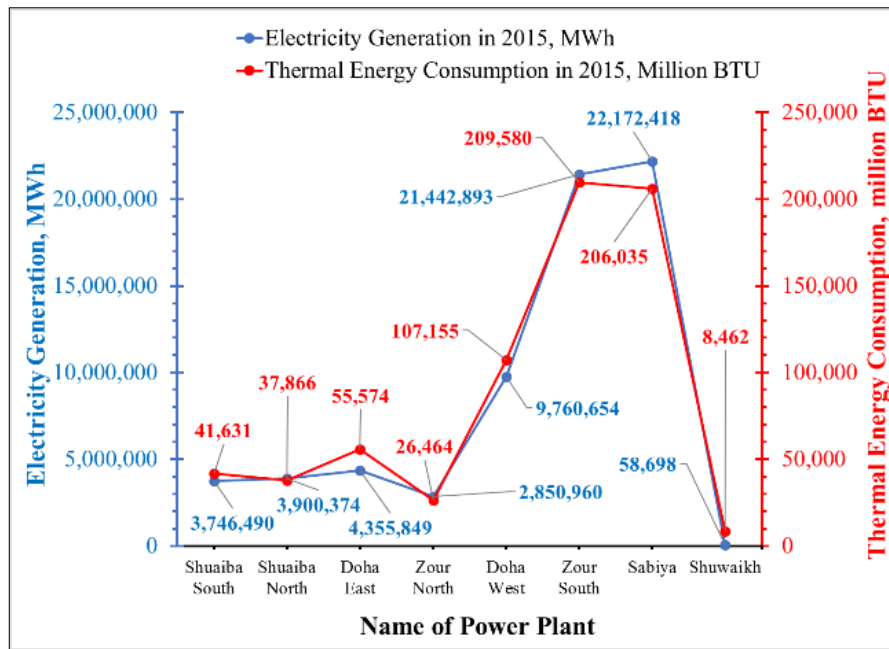


Figure F. 11 Calculated thermal energy consumption and electricity generation at Kuwait's fossil-based power plants from 2015 to 2016.

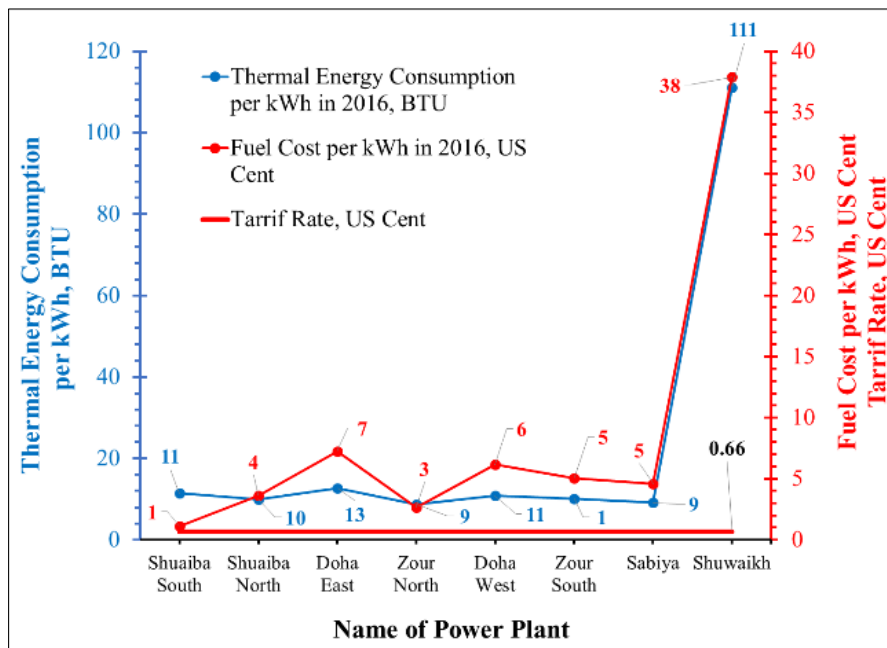
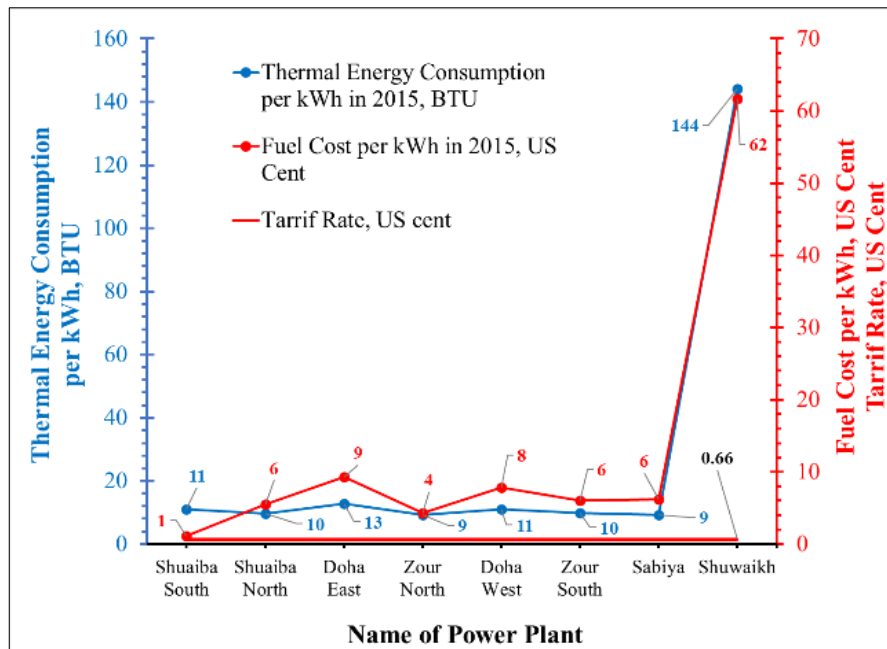


Figure F. 12 Calculated thermal energy consumption and related fossil fuel costs at Kuwait's fossil-based power plants from 2015 to 2016.

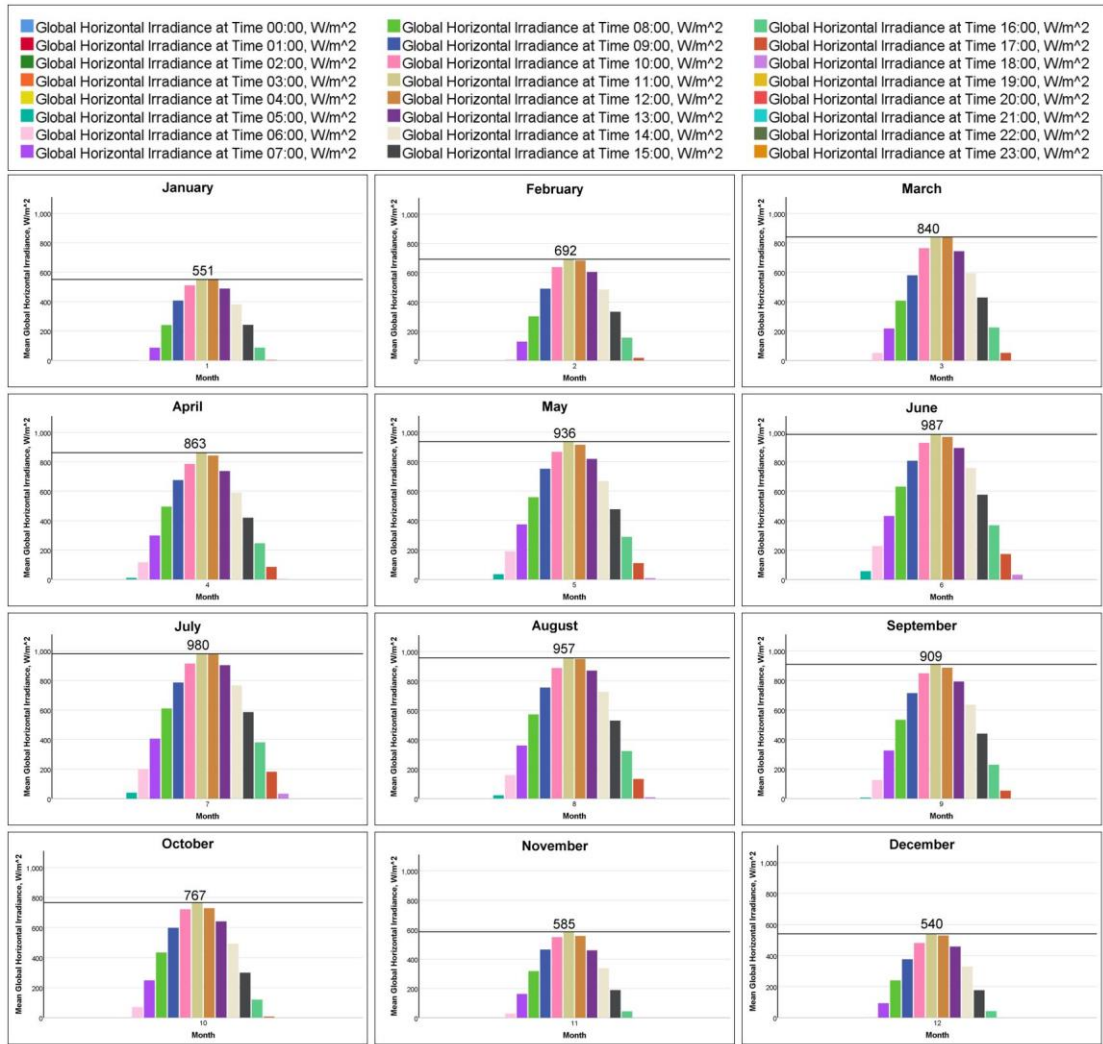


Figure F. 13 Monthly profiles of the GHI for a typical year in Kuwait.

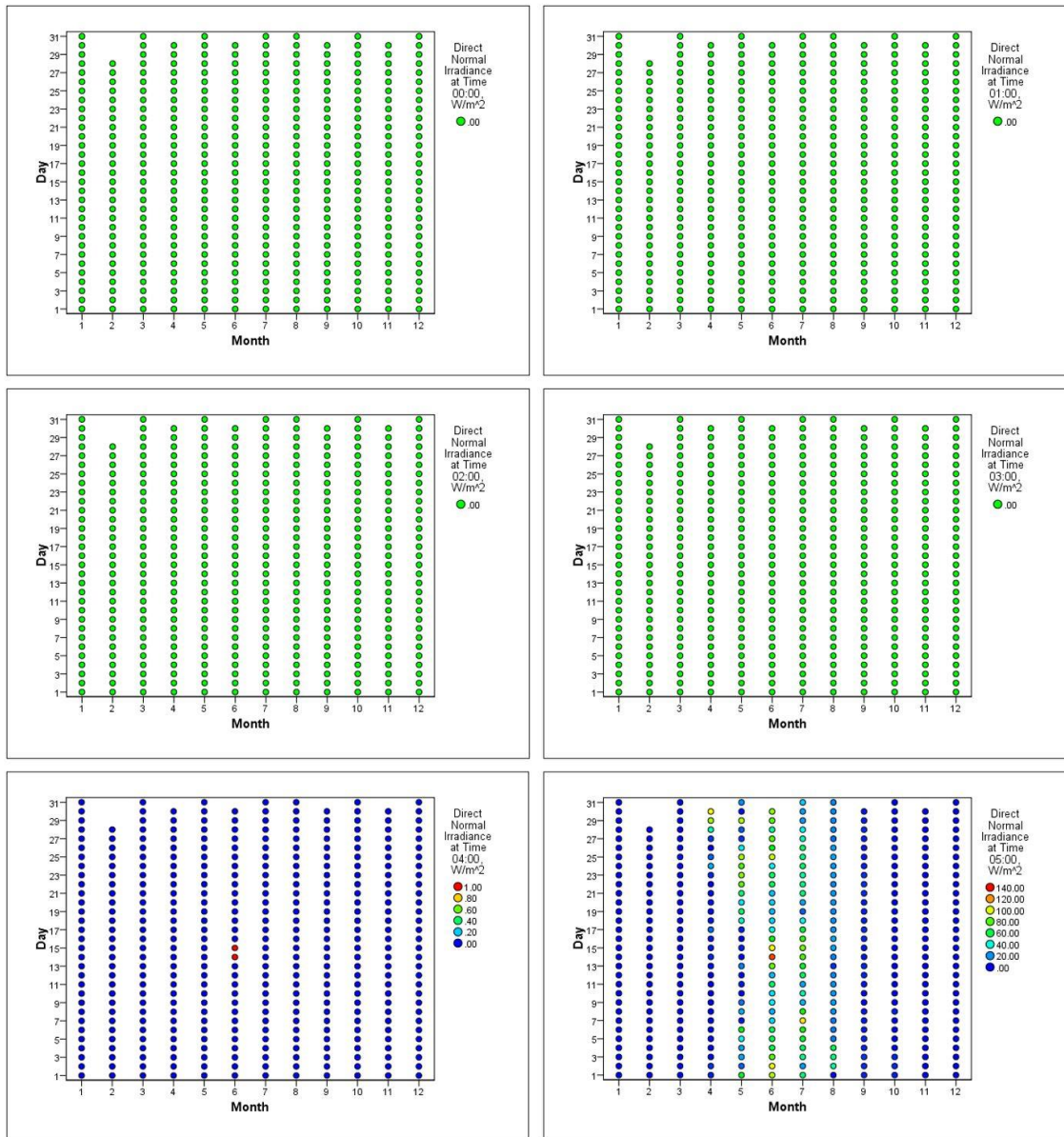


Figure F. 14 Hourly profiles of the DNI for 00:00 to 05:00 in Kuwait (x-axis: month of the year, y-axis: day of the month).

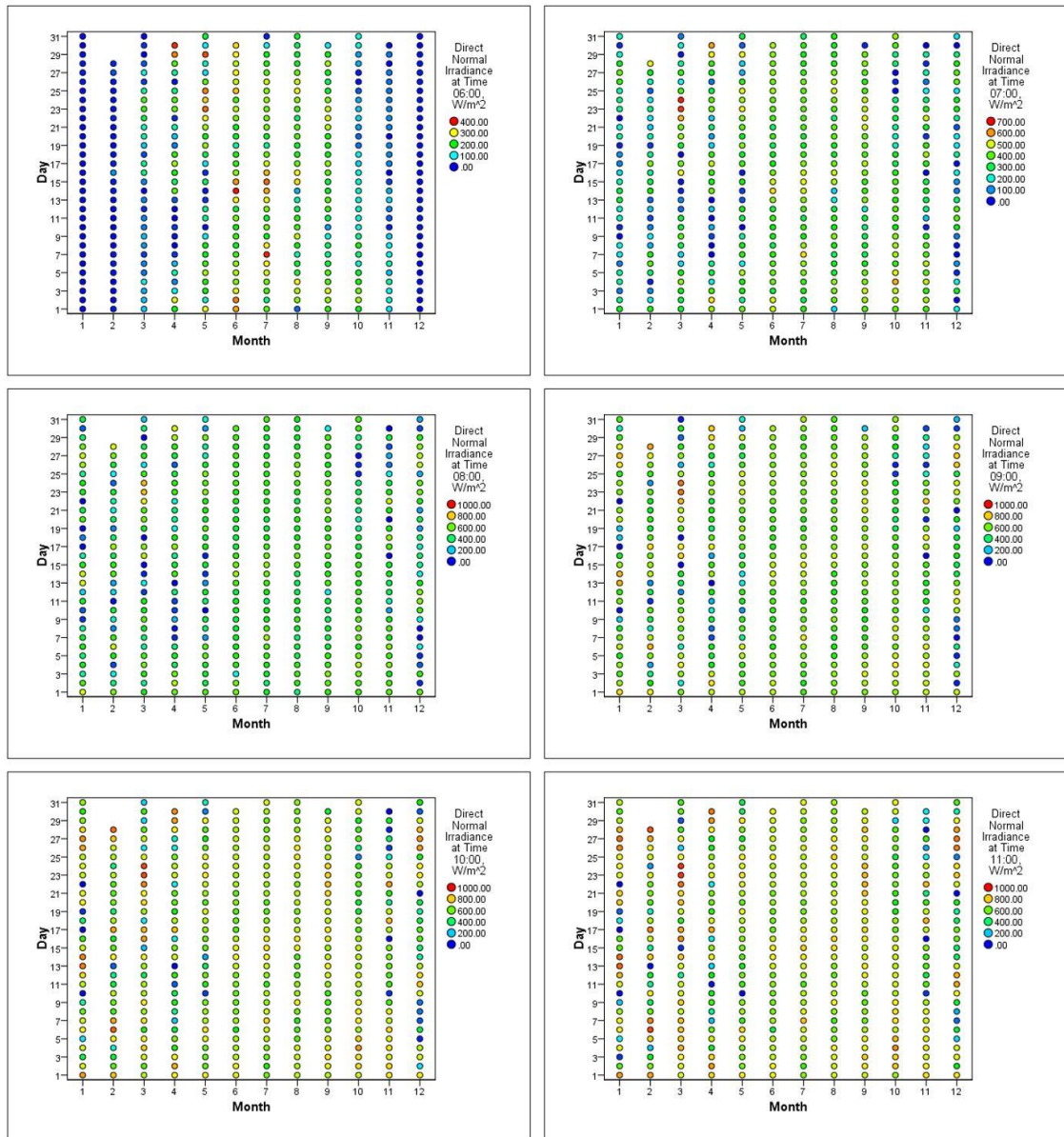


Figure F. 15 Hourly profiles of the DNI for 06:00 to 11:00 in Kuwait (x-axis: month of the year, y-axis: day of the month).

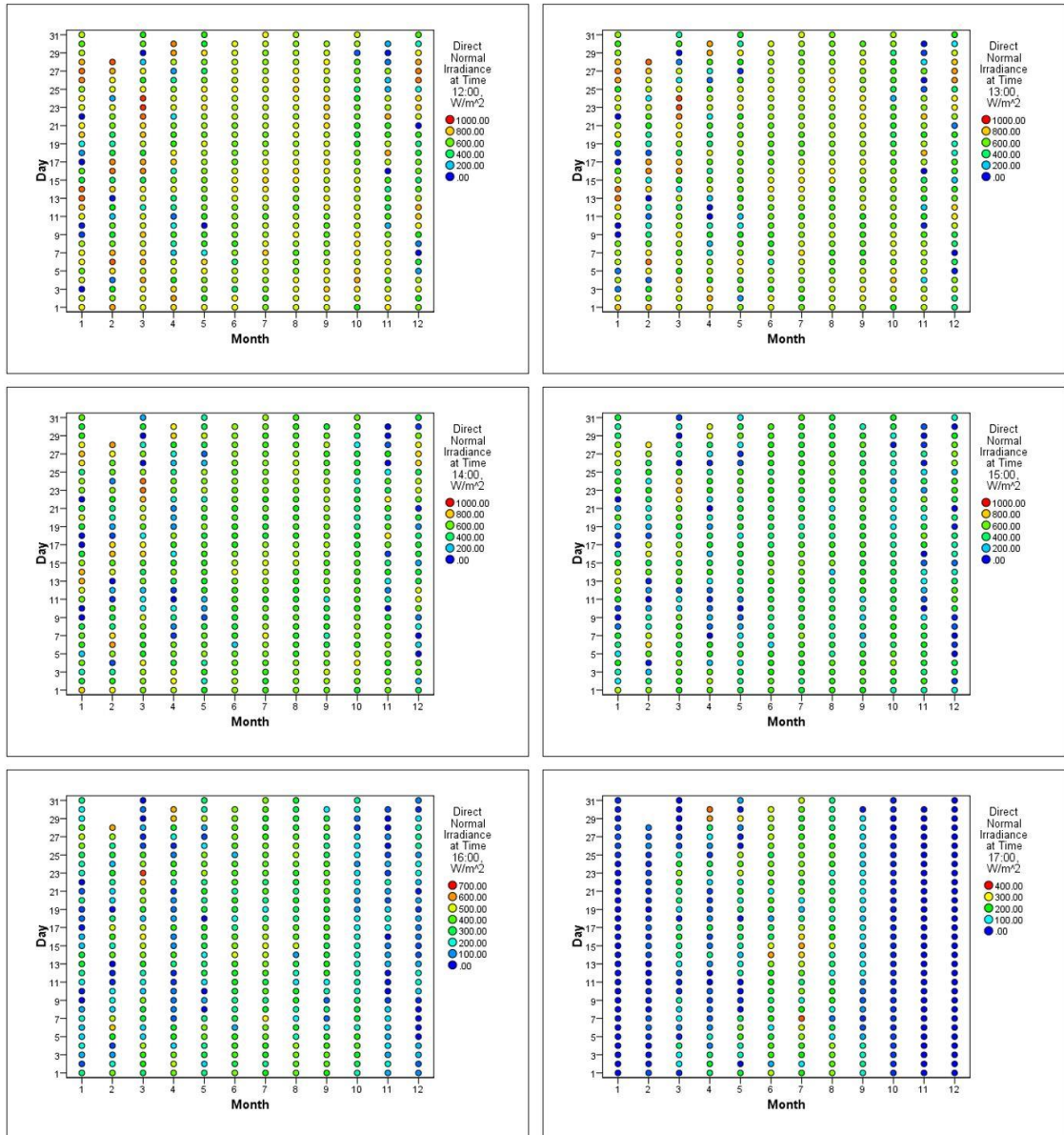


Figure F. 16 Hourly profiles of the DNI for 12:00 to 17:00 in Kuwait (x-axis: month of the year, y-axis: day of the month).

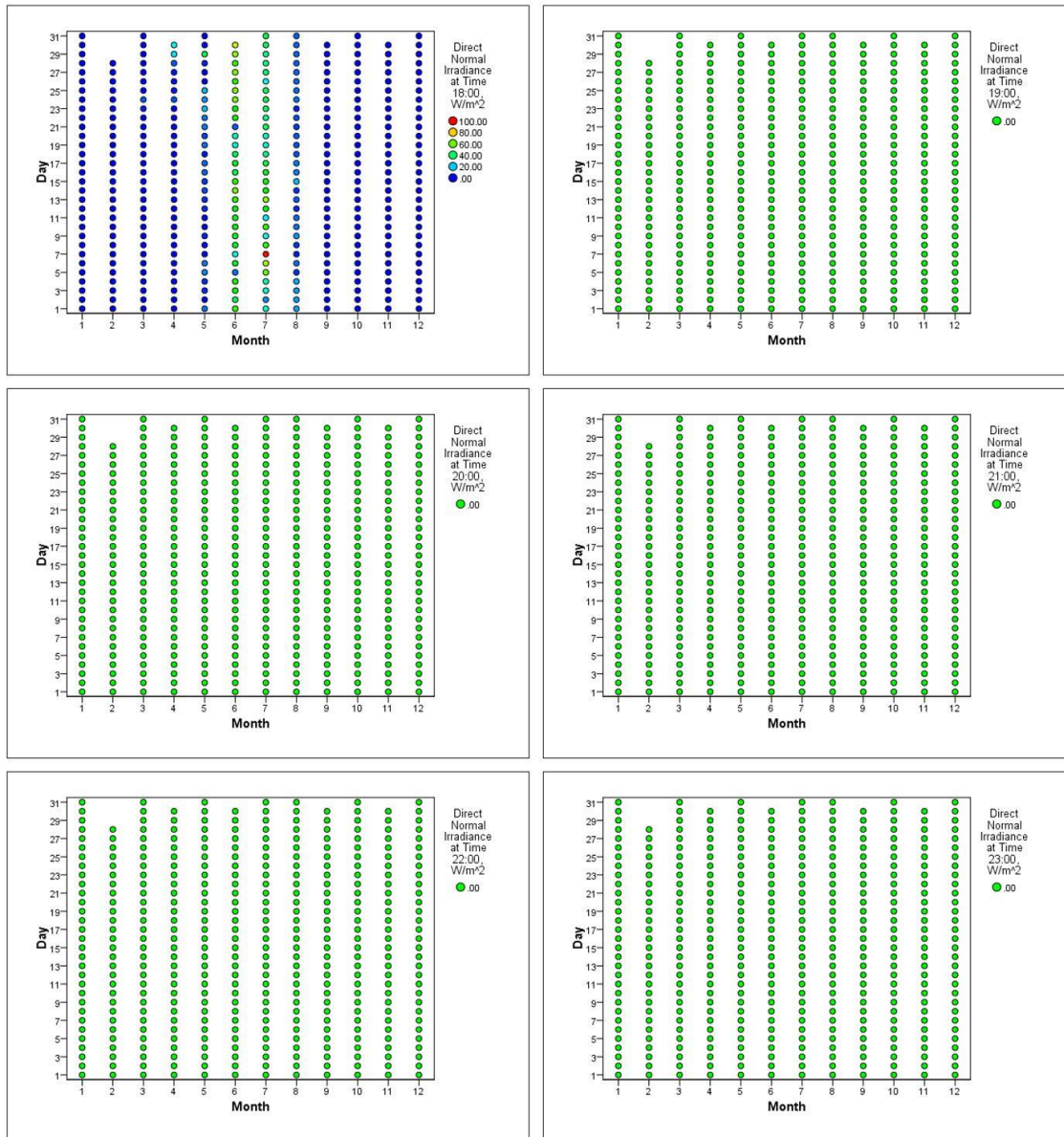


Figure F. 17 Hourly profiles of the DNI for 18:00 to 23:00 in Kuwait (x-axis: month of the year, y-axis: day of the month).

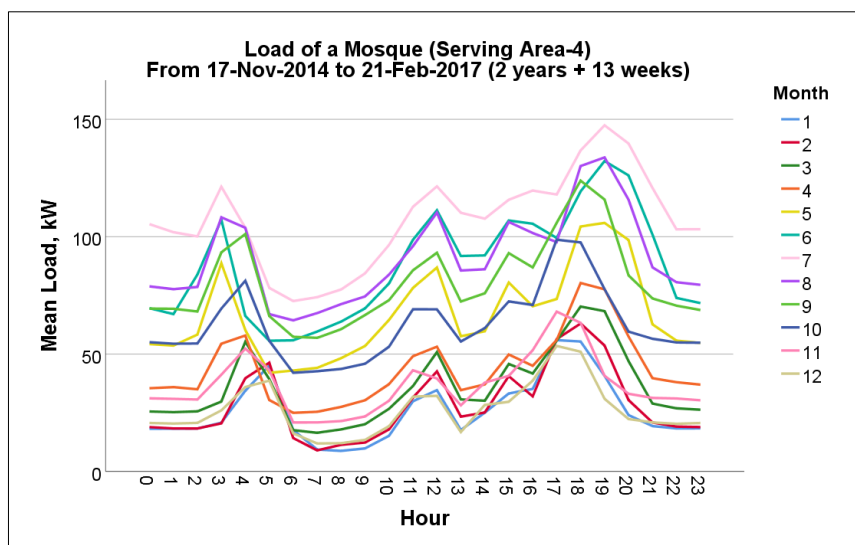
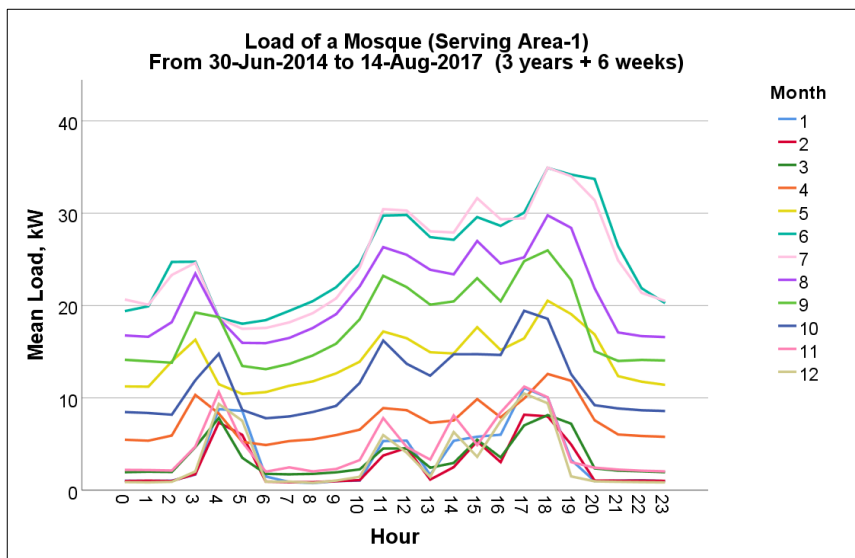
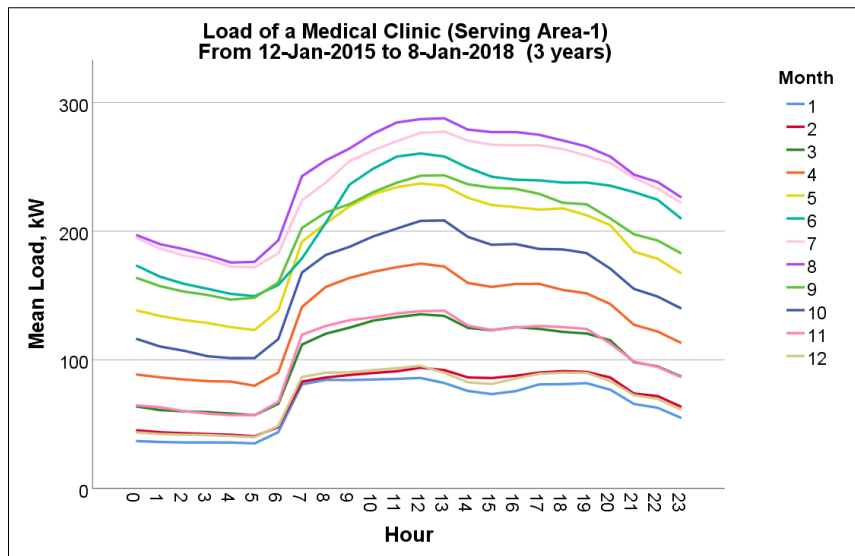


Figure F. 18 Monthly load profiles for different building types (a medical clinic and mosques) in Kuwait.

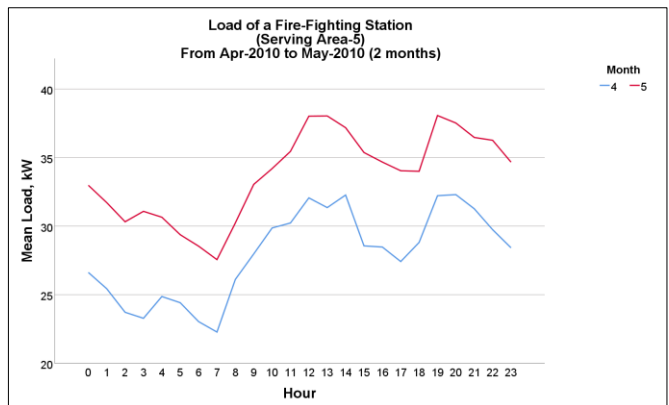
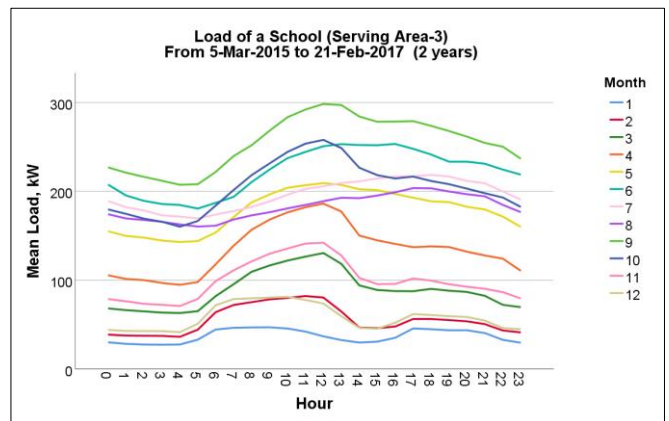
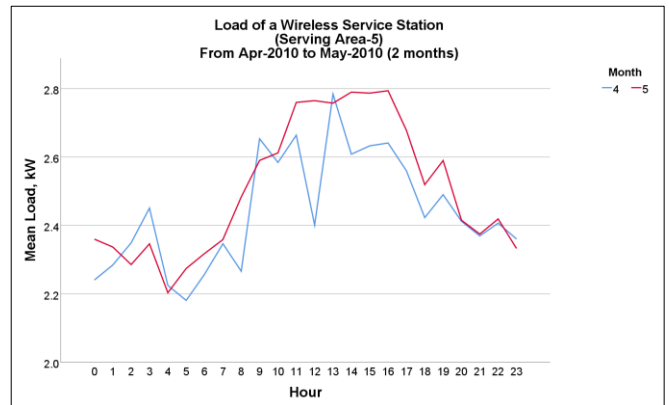
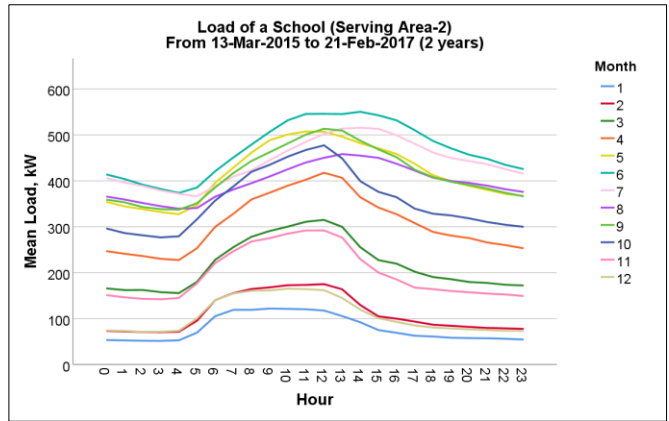


Figure F. 19 Monthly load profiles for different building types (schools, a wireless service station, and a fire-fighting station) in Kuwait.

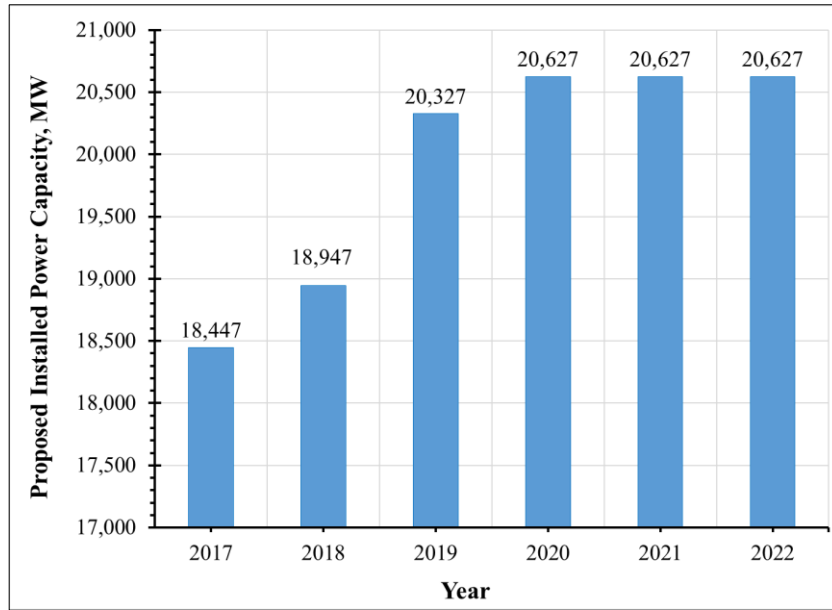


Figure F. 20 Fossil-based power capacities and future projections in Kuwait.

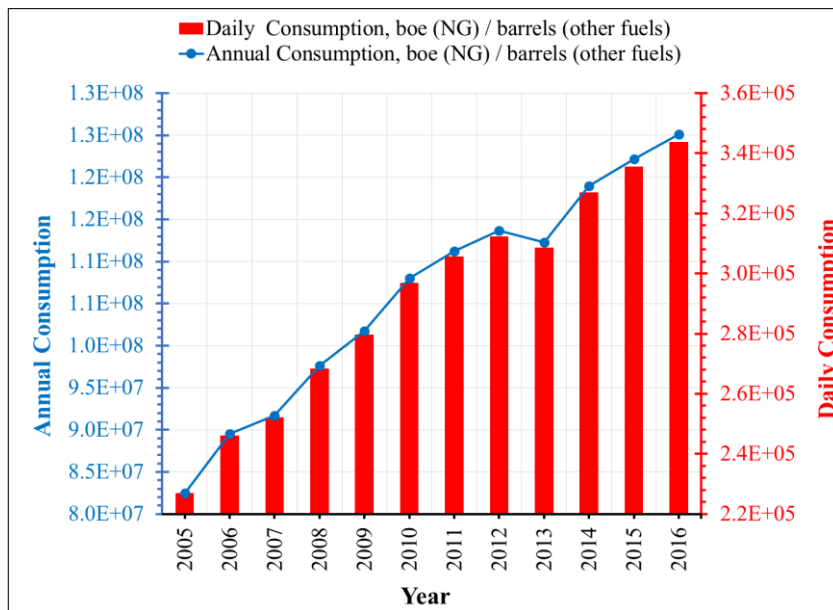


Figure F. 21 Consumption of fuels (gas, crude, heavy) and NG for 2005-2016 in Kuwait.

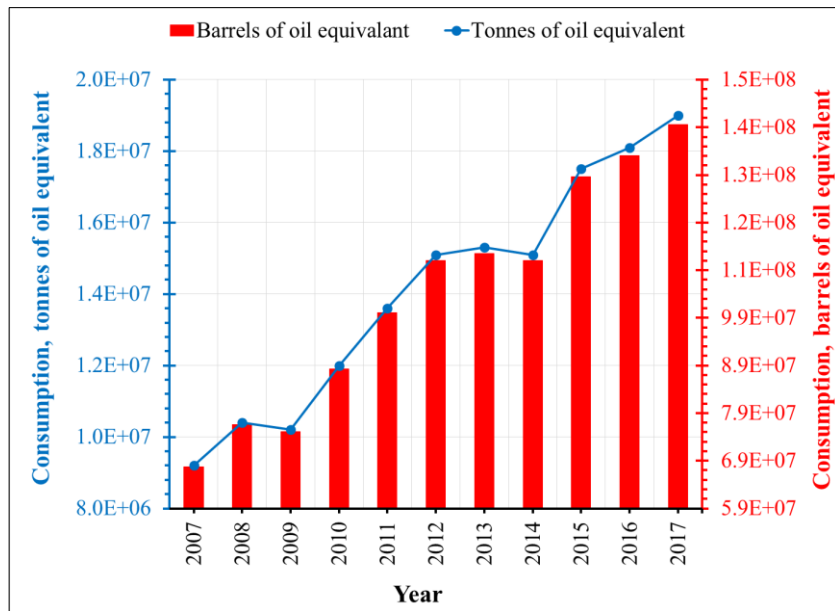
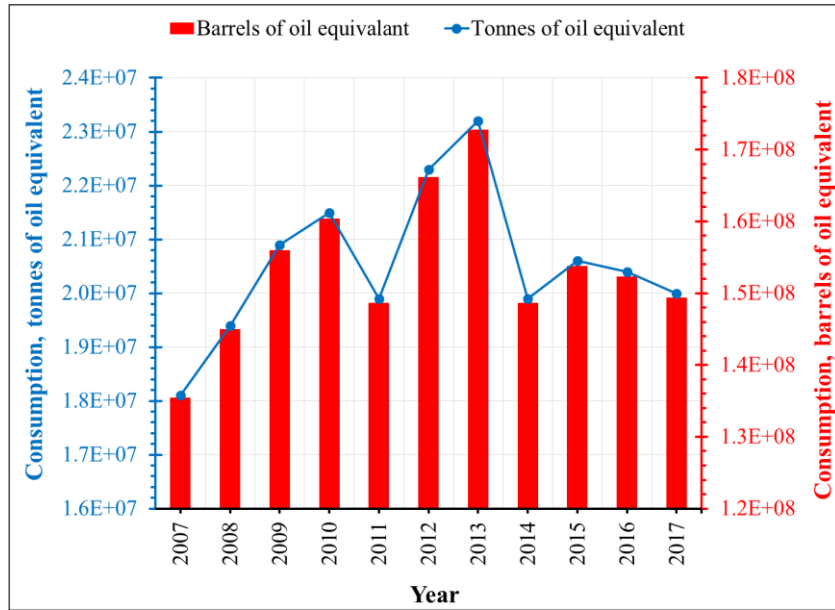


Figure F. 22 Consumption of fuels (oil and NG) for 2007-2017 in Kuwait in boe and toe units.

Appendix G. Supplementary tables

Table G. 1 Statistics of the 2016 electrical load from all fossil-based power plants in Kuwait.

Hour	Minimum load, MW	Maximum load, MW	Mean load, MW	Hour	Minimum load, MW	Maximum load, MW	Mean load, MW
00:00	4,760	12,320	7,836	12:00	5,050	13,130	8,511
01:00	4,540	12,100	7,605	13:00	5,080	13,260	8,655
02:00	4,330	11,800	7,406	14:00	4,960	13,340	8,677
03:00	4,270	11,600	7,226	15:00	4,980	13,350	8,712
04:00	4,230	11,240	7,105	16:00	4,880	13,300	8,665
05:00	4,330	10,900	7,029	17:00	5,010	13,270	8,660
06:00	4,430	10,580	6,978	18:00	5,290	12,880	8,648
07:00	4,360	11,150	7,151	19:00	5,340	12,890	8,623
08:00	4,450	11,530	7,405	20:00	5,290	12,930	8,537
09:00	4,720	12,000	7,773	21:00	5,250	12,680	8,428
10:00	4,860	12,570	8,095	22:00	5,110	12,530	8,285
11:00	5,050	12,840	8,324	23:00	4,970	12,400	8,080

Appendix H. Estimated costs

This appendix contains a detailed breakdown of the estimated costs for the reference 50 MW CSP-PT plant, including the condenser system, as follows:

Table H.1 A breakdown of the estimated costs for the reference 50 MW CSP-PT plant.

Description	Cost, (10K*\$)	Percentage share, %
Studies:		
Resource, Environmental, and Testing	55.37	0.16
Sub Total	55.37	0.16
Preparation Work: Site Monitoring	1,117.71	3.17
Sub Total	1,117.71	3.17
Civil Work		
Infrastructure works	205.19	0.58
Road preparation including lighting installation	263.11	0.75
Security border and outdoor barrier	286.58	0.81
Gate building	8.06	0.02
Other structures	22.04	0.06
Administration, control, and electrical	100.48	0.29
Staff housing	606.33	1.72
Amenities	52.84	0.15
Workshops	103.04	0.29
Solar field system	1,754.58	4.98
Heat transfer fluid	150.21	0.43
Thermal energy storage	393.60	1.12
Power block	388.74	1.10
Water plants	19.28	0.05
Sewage and waste	48.98	0.14
Fuel oil	6.12	0.02
Electrical, instrumentation and control	50.01	0.14
Sub Total	4,459.19	12.66
Mechanical Work of Solar Field		
Solar collector assemblies:		
Mirrors	1,743.27	4.95
Receivers	2,336.66	6.64
Steel Structure	5,818.26	16.52
Foundation	230.01	0.65
Tracking	335.72	0.95
Others (joints)	116.69	0.33
Heat transfer fluid:		
Storage Tanks	4.45	0.01
Overflow tank	189.07	0.54
Nitrogen equipment	4.60	0.01
Pumps and valves	1,107.83	3.15
Piping	791.84	2.25
Others (tanks)	154.22	0.44
Thermal energy storage:		
tanks	674.70	1.92
heat exchanger	600.33	1.70
pumps and valves	608.91	1.73
piping	124.97	0.35
Others (structural steel)	78.66	0.22
Sub Total	14,920.19	42.37

Table H.1 Cont. A breakdown of the estimated costs for the reference 50 MW CSP-PT plant.

Description	Cost, (10K*\$)	Percentage share, %
Mechanical Work of Power Block		
Solar steam generator system:		
Solar steam generator	511.13	1.45
Steam turbine generator system		
Steam turbine	1,431.43	4.06
Condenser system		
Air cooled condenser	588.05	1.67
Structure	65.34	0.19
Fuel Oil Fired Heaters		
Heat transfer fluid heater	100.91	0.29
Burner	15.33	0.04
Steam, feedwater and condensate	635.51	1.80
Water treatment	115.27	0.33
Waste water treatment	94.31	0.27
Fuel oil	37.40	0.11
Compressed air	30.67	0.09
Fire fighting and alarm	122.67	0.35
air conditioning	383.35	1.09
Miscellaneous	562.72	1.60
Initial inventory	404.94	1.15
Others (structural Steel and balance of plant)	243.86	0.69
Sub Total	5,342.90	15.17
Electrical Work		
Interconnection from generators to substation	108.87	0.31
Plant auxiliaries supply	1,620.84	4.60
Sub Total	1,729.71	4.91
Instrumentation, Control, and Communication		
Sub Total	374.74	1.06
Other Works		
Piping and valves	448.68	1.27
control room	14.69	0.04
Software	91.88	0.26
Signal line and connection	28.16	0.08
Heat transfer fluid	1,265.55	3.59
Molten salt	3,085.00	8.76
Fuel oil	338.85	0.96
Others	178.91	0.51
Transportation costs	419.48	1.19
Project expenses	267.79	0.76
cars	64.30	0.18
Insurance policies	210.74	0.60
technical costs	801.40	2.28
Sub Total	7,215.45	20.49
TOTAL	35,215.26	100.00